Universiteit Leiden
The Netherlands

# Accurate modeling of the dynamics of dissociative chemisorption on metal surfaces

Gerrits, N.

**Citation**

Gerrits, N. (2021, September 23). *Accurate modeling of the dynamics of dissociative chemisorption on metal surfaces*. Retrieved from https://hdl.handle.net/1887/3213516

| | |
|---|---|
| Version: | Publisher's Version |
| License: | Licence agreement concerning inclusion of doctoral thesis in the Institutional Repository of the University of Leiden |
| Downloaded from: | https://hdl.handle.net/1887/3213516 |

**Note:** To cite this publication please use the final published version (if applicable).

# Accurate Modeling of the Dynamics of Dissociative Chemisorption on Metal Surfaces

Proefschrift

ter verkrijging van
de graad van doctor aan de Universiteit Leiden,
op gezag van rector magnificus prof. dr. ir. H. Bijl,
volgens besluit van het college voor promoties
te verdedigen op donderdag 23 september 2021
klokke 13:45 uur

door

Nick Gerrits
geboren te Dordrecht, Nederland, 1992

## Promotiecommissie

| | |
|---|---|
| Promoter: | Prof. dr. G.J. Kroes |
| Copromoter: | Dr. Jörg Meyer |
| Overige leden: | Prof. dr. H.S. Overkleeft (voorzitter)<br>Prof. dr. M.T.M. Koper (secretaris)<br>Prof. dr. B. Jackson (University of Massachusetts Amherst)<br>Prof. dr. P. Saalfrank (Universität Potsdam)<br>Dr. L.B.F. Juurlink<br>Dr. C. Díaz (Universidad Autónoma de Madrid) |

ISBN: 978-94-6421-474-1

The research reported in this thesis has been performed in the Theoretical Chemistry group at the Leiden Institute of Chemistry (Einsteinweg 55, 2333 CC, Leiden, the Netherlands). This work has been made possible by financial support by the Nederlandse Organisatie voor Wetenschappelijk Onderzoek (NWO) through an NWO/CW TOP Grant (No. 715.017.001), and with computer time granted by NWO Exacte Wetenschappen, EW (NWO Physical Sciences Division).

*"En 's avond?" werd gevraagd, na een nieuwe stilte.*
*"'s Avonds is het donker", zei ik.*

- Willem Elsschot

*Ik weet niet of er een speciaal talent bestaat voor humor, maar zeker is dat humor en intelligentie bij elkaar horen.*

- Vic van de Reijt

# Contents

**1 General Introduction** **1**
1.1 Heterogeneous Catalysis . . . . . 1
1.2 Molecule-Metal Surface Reactions . . . . . 2
1.3 Aims of This Thesis . . . . . 5
1.4 Main Results . . . . . 7
1.5 Outlook . . . . . 11

**2 Methods and Theory** **23**
2.1 Density Functional Theory . . . . . 23
2.1.1 Exchange-Correlation Functionals . . . . . 24
Local Density Approximation . . . . . 25
Generalized Gradient Approximation . . . . . 25
Meta-Generalized Gradient Approximation . . . . . 26
Non-local Exchange . . . . . 28
Non-local Correlation . . . . . 29
Specific Reaction Parameter Approach . . . . . 30
2.1.2 Plane Wave DFT . . . . . 30
2.2 Dynamics Methods . . . . . 31
2.2.1 Integration Algorithm . . . . . 31
Velocity Verlet . . . . . 32
Leapfrog . . . . . 32
Bulirsch-Stoer . . . . . 32
2.2.2 (Quasi-)Classical and Quantum Dynamics . . . . . 33
2.3 Fitting Potential Energy Surfaces . . . . . 33
2.3.1 Corrugation Reducing Procedure (CRP) . . . . . 34
2.3.2 Behler-Parrinello Approach to High-Dimensional Neural Network Potentials (HD-NNPs) . . . . . 35
2.4 Initial Condition Sampling . . . . . 36
2.4.1 Metal Surface . . . . . 36
2.4.2 Molecular Beam . . . . . 37
2.5 Calculation of Observables . . . . . 40

**3 Closing the Gap Between Experiment and Theory: Reactive Scattering of HCl from Au(111 51**
3.1 Introduction . . . . . 52
3.2 Method . . . . . 54
3.2.1 Theory . . . . . 54
3.2.2 Experiment . . . . . 58
3.3 Results . . . . . 59
3.3.1 Experimental Sticking Probabilities . . . . . 59
3.3.2 Potential Energy Surface . . . . . 61
3.3.3 Sticking Probabilities Computed by Theory . . . . . 68
3.3.4 Dynamics During the Reaction Obtained with Theory . 71
Vibrational Excitation . . . . . 71
Energy Transfer . . . . . 74
Site Specific Reaction . . . . . 78
3.4 Additional Discussion . . . . . 85
3.5 Conclusions . . . . . 87
3.A Convergence . . . . . 89
3.B Symmetry Functions . . . . . 92
3.C Vibrational Excitation Probabilities . . . . . 92
3.D Elbow Plots of the Potential Energy Surface . . . . . 94

**4 Large Effect of Rotational Pre-excitation of HCl on its Reaction on Au(111): A Rotational Phase Lock-in Effect 109**
4.1 Introduction . . . . . 110
4.2 Results . . . . . 112
4.2.1 Rotational and Vibrational Efficacies . . . . . 112
4.2.2 Reaction Mechanism . . . . . 117
4.2.3 Sticking Probabilities . . . . . 119
4.3 Conclusion . . . . . 122
4.A Definition of the Sticking Probability . . . . . 123
4.B Determination of Effective Barrier Heights and Concomitant Vibrational Efficacy . . . . . 124
4.C Experimental State-Specific Sticking Probabilities . . . . . 126
4.D The Two Experimental Data Sets and the Origin of Their Differences . . . . . 127
4.E The Mechanism Underlying the High Rotational Efficacy . . . 131
4.F Synergistic Effect of Rotational and Vibrational Pre-excitation 139

**5 When Does GGA-DFT Get Molecule-Metal Surface Reaction Barriers Right, and What to Do if it Doesn't 147**
5.1 Introduction . . . . . 148
5.2 Analysis of Previous Results . . . . . 151
5.3 Method . . . . . 154
5.4 Results . . . . . 156
5.4.1 Potential Energy Surface . . . . . 156
5.4.2 Sticking Probability . . . . . 158
5.4.3 Functional-Driven Error . . . . . 161
5.5 Conclusion . . . . . 163
5.A Method . . . . . 165
5.A.1 Density Functionals Used in This Chapter . . . . . 165
5.A.2 Work Function and Electron Affinity Values . . . . . 166
5.B Results . . . . . 167
5.B.1 Self-Consistent DFT Results for $O_2$ + Al(111) . . . . . 167
5.B.2 Non-Self-Consistent DFT Results for $O_2$ + Al(111), HCl + Au(111), and $NH_3$ + Ru(0001) . . . . . 171
5.B.3 Correlation Between $(W - E_{ea})$ and Charge Transfer at the TS . . . . . 172
5.B.4 Dynamics: Dependence of $S_0$ on Molecular Beam Conditions . . . . . 172
5.B.5 Dynamics: Dependence of $S_0$ on the Alignment of $O_2$ . 175
5.B.6 Dynamics: Dependence of $S_0$ on Incidence Angle . . . 176
5.C Discussion . . . . . 176
5.C.1 $O_2$ + Metal Systems That Are Useful Benchmark Systems for Dissociative Chemisorption . . . . . 176
5.C.2 Towards an SRP Density Functional for $O_2$ + Al(111) . 178

**6 The Curious Reaction Mechanism of Ammonia on Ru(0001) 197**
6.1 Introduction . . . . . 198
6.2 Method . . . . . 201
6.3 Results . . . . . 206
6.3.1 Activation Barriers and Adsorption Energies . . . . . 206
6.3.2 Sticking Probability . . . . . 209
6.3.3 Dynamics During the Reaction . . . . . 213
6.4 Discussion of the Comparison of Experiment and Theory . . . 220
6.5 Conclusions . . . . . 220
6.A Convergence . . . . . 223
6.B Trapping . . . . . 226

**7 $CHD_3$ + Cu(111), Cu(211), and Single-Atom Cu(111) Alloys 235**
7.1 Introduction . . . . . 236
7.2 Method . . . . . 237
7.3 Results . . . . . 242
7.3.1 Activation Barriers and Adsorption Energies . . . . . 242
7.3.2 Minimum Energy Path . . . . . 245
7.3.3 Sticking Probability . . . . . 249
7.3.4 Reaction Site . . . . . 252
7.4 Conclusions . . . . . 254
7.A Electronic Structure Calculations . . . . . 257
7.B Minimum Energy Paths . . . . . 259
7.C Energy Transfer . . . . . 260
7.D Surface Atom Displacement . . . . . 264

**8 A High-Dimensional Neural Network Potential for the dissociative chemisorption of $CHD_3$ + Cu(111) 273**
8.1 Introduction . . . . . 274
8.2 Method . . . . . 275
8.2.1 Neural Network . . . . . 275
8.2.2 Molecular Initial Conditions . . . . . 276
8.3 Results . . . . . 278
8.4 Conclusions . . . . . 285
8.A Symmetry Functions . . . . . 287
8.B Elbow Plots . . . . . 287
8.C Statistical Analysis . . . . . 287

**9 Dissociative Chemisorption of $CHD_3$ on Pd(111) 301**
9.1 Introduction . . . . . 302
9.2 Method . . . . . 304
9.3 Results . . . . . 305
9.3.1 Activation Barriers . . . . . 305
9.3.2 Sticking Probability . . . . . 309
9.3.3 Dynamics of the Reaction . . . . . 311
9.3.4 Discussion of Reactivity of Pd(111) vs Ni(111) and Pt(111); Comparison with Experiment . . . . . 319
9.4 Conclusions . . . . . 323
9.A Convergence . . . . . 325
9.B Site-Specific Reaction Probability . . . . . 325

**10 Dissociative Chemisorption of Methanol on Cu(111) with Implications for Formaldehyde Formation** **339**
10.1 Introduction . . . . . 340
10.2 Method . . . . . 341
10.3 Results . . . . . 346
10.3.1 Barriers . . . . . 346
10.3.2 Minimum Energy Path . . . . . 347
10.3.3 Sticking Probability . . . . . 348
10.3.4 Reaction Site . . . . . 349
10.3.5 Energy Transfer to the Surface . . . . . 351
10.3.6 Angular Distributions . . . . . 351
10.3.7 Formation of Formaldehyde . . . . . 353
10.4 Conclusions . . . . . 355
10.A Electronic Structure Calculations . . . . . 357
10.B Impact Site . . . . . 360

**Samenvatting** **367**

**Curriculum Vitae** **377**

**List of Publications** **379**

**Afterword** **381**

# Chapter 1

# General Introduction

## 1.1 Heterogeneous Catalysis

Catalysis plays an extremely important role in chemistry: Catalysts alter reaction pathways by, e.g., stabilizing reaction intermediates and changing barrier heights. This way, different (milder) reaction conditions and a considerable selectivity towards the desired products can be achieved. Thus, many chemicals can be produced efficiently, which would have been impossible without catalysis. For example, the Haber-Bosch process has been instrumental in feeding a large part of the world population and is responsible for the population explosion[1]. In order to improve sustainability, better catalysts are needed, for which fundamental understanding of the working of catalysts is instrumental.

An important subclass of catalysis is heterogeneous catalysis. Here, two different phases can be distinguished for the catalyst and reactants. Typically, a solid catalyst interacts with reactants in the gas or liquid phase. Such a catalyst is not only able to lower barrier heights for bond-breaking, but also involves kinetic effects such as diffusion of reaction intermediates[2], making heterogeneously catalyzed processes complex multi-step processes with multiple possible reaction outcomes. Fortunately, such processes are often rate-controlled by only one or a few states[3–5], which ensures that fundamental research only has to focus on a few reaction steps. However, at the industrial level, heterogeneous catalysts are also structurally complex due to varying sizes and shapes of the catalytic nanoparticles involved. As a result, many different facets are available, which exhibit different elementary reaction rates. Similar to a rate-controlling state, often only a single or a few facets, or edges, dominate the reaction[6]. Therefore, research is often limited to the reaction of molecules on surfaces with specific Miller indices, although this does exclude diffusion effects between different facets. Another aspect to industrial heterogeneous catalysis is the high pressure involved. The high surface density

of molecules that may results complicates the extrapolation of experiments and is at present extremely hard, if not intractable, to model at an atomistic level. Thus, fundamental research tends to be performed for reactions in an ultra-high vacuum (i.e., a low pressure), which allows for a relatively straightforward investigation of elementary reaction steps[7]. These aforementioned complexities and their pragmatic solutions also outline the type of research (i.e., surface science) presented in this thesis: Simulations are performed for single molecules reacting on or scattering from well-defined metal surfaces in order to understand reaction mechanisms relevant for heterogeneous catalysis.

## 1.2 Molecule-Metal Surface Reactions

Although reactive scattering of molecules from well-defined metal surfaces in UHV is considerably less complex than reactions of molecules on nanoparticles under heterogeneous catalytic conditions, the former topic still presents major challenges, both from a theoretical and an experimental point of view. In experiments, typically a well-defined molecular beam (MB), of which the velocity and the rovibrational state distribution are characterized, is directed toward a metal crystal. Thermal rate experiments are possible as well, but are less well-defined than MB studies[8] and are therefore not the focus in this thesis. The characteristics of the MB can be altered via the nozzle temperature and the seeding gas mixture. The nozzle, through which the MB is produced, and its temperature have an effect on the translational, vibrational, and rotational temperatures. Control over only the translational energy can also be achieved by altering the seeding gas mixture. If a heavy molecule is mixed with a light, often inert gas, a considerably higher translational energy can be achieved than by increasing the nozzle temperature, while the rovibrational temperatures are (by approximation) unaffected. Obviously, with a heavy seeding gas the opposite effect for the translational energy is achieved.

The incidence angle of the MB with respect to the surface normal can also be used to control the incidence energy normal to the surface. This is especially useful if normal energy scaling (NES)[9] holds, i.e., if the reaction probability only depends on the molecule's translational energy normal to the surface. Moreover, the rovibrational state population in an MB can be altered not only via the nozzle temperature, but also via state-selective excitation with laser pumping. Also, the alignment of many molecules relative to the surface can be controlled by employing a magnetic field[10] or polarized laser light[11, 12].

So far, only ways of controlling the molecular conditions have been discussed, but the metal surface also plays an important role. As discussed in Section 1.1, different surface facets display different reaction rates, and as such the choice of the surface facet in the experiment is important as well since typically only a single facet is investigated at a time. On the other hand, with a curved crystal, both flat and stepped (or kinked) surfaces can be investigated simultaneously with varying step density[13–15]. Furthermore, the surface temperature controls whether (unwanted) reaction products desorb or not, and may influence the barrier height through surface atom motion, where the latter increases with the surface temperature[16, 17]. Additionally, the surface can be pre-covered with adsorbates[18]. This way, the surface can be (partially) passivated or a specific reaction involving multiple reactants can be investigated. In short, a large degree of control over both the molecule and the metal surface in experiments can be achieved.

From the reactive scattering of molecules from surfaces many different aspects of the mechanisms involved can be gleaned. The so-called sticking probability (i.e., the fraction of the molecules sticking to instead of scattering from the surface) is often easy to measure using the King and Wells method[19]. In the King and Wells method, the initial pressure drop in the UHV chamber when the MB first hits the surface and the initial pressure rise when the MB enters the UHV chamber without hitting the surface can be used to determine the initial sticking probability ($S_0$). The advantage of this method is that it is internally calibrated, and as such does not require additional calibration of the data. Other approaches to measure the sticking or reaction probability exist as well (note that sticking and reaction are not necessarily the same due to the possibility of adsorption and subsequent desorption of molecularly adsorbed molecules in the case of sticking), e.g., measuring the desorption of products during the reaction or performing temperature-programmed desorption after the reaction. However, these approaches are indirect, and require calibration of the data and assumptions about the overall reaction. Not only reacting, but also scattering molecules are often the focus of the study. For instance, the scattering angle, translational energy change, and rovibrational state-to-state scattering can be investigated to learn about the interaction between the molecule and the metal surface[9, 20–37].

However, in experiments, reaction mechanisms are mostly studied indirectly. Fortunately, theoretical studies can investigate these reaction mechanisms directly. Static calculations can investigate the potential energy surface (PES) the molecule experiences in the vicinity of the surface. Especially transition states (TSs) are of interest since they tend to be a good indicator of the reactivity. Still, instead of a single TS, molecule-metal surface reactions deal

with a collection of TSs, where reaction does not necessarily occur over the TS with the lowest barrier height. Furthermore, dynamical effects arising from traveling over the PES are difficult to study with static calculations. Therefore, dynamical studies that simulate a MB hitting a surface are used to investigate both the reactivity and reaction mechanism. In such a dynamical study, many trajectory calculations are performed, with each trajectory simulating the reactive scattering for only a single initial condition. The generation of the initial conditions of the trajectories requires special care in order to mimic the experimental conditions. The benefit is that dynamical effects are included and that all relevant TSs are probed. Moreover, most, if not all, of the aforementioned experimentally obtained results can be obtained in theoretical dynamical studies as well, making comparison between experiment and theory relatively easy. Unfortunately, dynamical studies are computationally more demanding than static studies. Thus, the latter are more often performed than the former.

At present, the biggest challenge of theoretical studies is to improve their accuracy. Most theoretical studies rely on density functional theory (DFT), which requires an exchange-correlation density functional (XC-DF). In principle, an exact XC-DF exists, but its form is unknown and therefore many different approximate XC-DFs exist. Much of the ongoing research is involved with the improvement of existing XC-DFs. For example, semi-empirical DFs are developed by fitting experimental or theoretical (obtained at a higher level of theory) databases, e.g., the Minnesota DFs developed by Truhlar and coworkers[38]. In contrast, so-called non-empirical DFs are developed by ensuring that the DF fulfills several known exact limits, with the PBE DF[39] perhaps being the most famous example. In the specific reaction parameter (SRP) approach to molecule-metal surface reactions can be considered as an extreme example of a semi-empirical method: Two first-principles DFs are mixed with an empirically determined mixing parameter, yielding a chemically accurate SRP-DF for a specific molecule-metal surface reaction. Interestingly, in some cases, SRP-DFs have been found to be transferable to chemically related systems[40–42]. In this thesis, both non-empirical and SRP-DFs are employed.

Many other challenges for theoretical studies remain. The computational cost of calculations increases rapidly with the number of atoms and degrees of freedom (DOFs). Direct, or *ab initio*, molecular dynamics methods can deal with a large number of DOFs, but at a large computational cost, strongly limiting the tractability of studies employing ab initio molecular dynamics. Especially surface atom motion causes the number of DOFs to increase rapidly. Precomputed PESs can lower the computational cost considerably, but tend to struggle with a large number of DOFs, thus often neglecting surface atom motion. Fortunately, recent advances, such as the application of atomistic

neural network potentials[43] and reactive force fields[44], allow for computationally relatively cheap studies with many DOFs. Furthermore, most theoretical studies neglect quantum effects in the propagation of the atoms since the cost of quantum dynamics calculations scales unfavorably with the number of DOFs. However, this neglect can be a too severe approximation, especially when light atoms such as hydrogen are involved. Another important approximation in theoretical studies is the Born-Oppenheimer approximation (BOA)[45], which separates the motion of nuclei and electrons, greatly simplifying calculations. Unfortunately, for many molecule-metal surface systems a non-negligible interaction exists between the motion of the molecule and electronic excitations in the metal surface[24, 30, 46–54], i.e., the BOA can break down due to electron-hole pair (ehp) excitation (a non-adiabatic effect). Non-adiabatic effects in molecular simulations can be treated with, for instance, mean-field (e.g., Ehrenfest dynamics[55]) or surface hopping[56] approaches. Unfortunately, those methods rely on both the ground state and the excited state(s) PESs, but the continuum of the metal surface's electrons makes the excited state PESs of molecule-metal surface systems ill-defined, limiting use of the aforementioned methods for molecule-metal surface reactions. In addition to the independent electron surface hopping model[57], which might be more accurate for molecule-metal surface systems than other surface hopping models if electron transfer to the molecule occurs or if excited electronic states of the molecule also play a role, friction models have been developed to model the dissipative effect of ehp excitation, e.g., the local density friction approximation[47] and the orbital dependent friction[49] model.

## 1.3 Aims of This Thesis

Many molecule-metal surface reaction mechanisms remain unclear due to their complexity. To fully understand a reaction mechanism, theoretical studies have to move beyond a static point of view (e.g., transition state theory). Therefore, in this thesis, several molecule-metal surface reaction mechanisms are studied in detail and clarified by use of molecular dynamics (MD). However, MD studies are expensive and are still limited to only a handful of molecule-metal surface reactions. To increase the range of tractable molecule-metal surface systems, not only relatively expensive *ab initio* MD studies are performed, but also the corrugation reducing procedure and the Behler-Parrinello approach to neural network potentials are employed to obtain pre-computed potential energy surfaces with which to perform MD calculations. Furthermore, at present the predictive power of theoretical studies

towards experiments still wildly varies, where sometimes even the SRP approach is not sufficient in yielding a quantitative, or in some cases even a qualitatively correct, prediction. For a large part, this discrepancy between experiment and theory can be attributed to the DFT calculations, where often the DF is the culprit. Thus, the XC-DF will be given additional consideration for a few reactions in this thesis. In short, MB simulations of molecules reacting on well-defined metal surfaces are performed, with special consideration for the XC-DF and dynamical effects. The chapters in this thesis address the aforementioned aims as follows:

**Chapter 2** discusses the techniques employed throughout this thesis. A brief summary of DFT is provided, with special attention to the many different available approximations to the XC-DF. We also discuss methods for pre-computing PESs with a view to enabling accurate dynamics calculations of small reaction probabilities. Furthermore, some approaches in performing MD are discussed. Finally, the calculation of the observables obtained from MD calculations is described.

**Chapter 3** focuses on improving the description of the HCl + Au(111) interaction through employing a state-of-the-art XC-DF and a neural network PES. The XC-DF is tested with a thorough comparison between computed and (re-analyzed) experimental results. Moreover, this chapter tries to identify the shortcomings of the XC-DF to provide guidance in future development of an accurate XC-DF for the HCl + Au(111) system.

**Chapter 4** tries to elucidate the reaction mechanism behind the large effect of rotational pre-excitation of HCl on its reaction on Au(111). The state-of-the-art PES developed in Chapter 3 is employed. Especially the dynamic reorientation of the polar angle of HCl during the dissociation is investigated closely.

In **Chapter 5**, a criterium is sought that can predict when DFT at the generalized gradient approximation (GGA) level will fail at accurately describing molecule-metal surface reaction barriers. The reason for the potential failure of GGA-DFT and a potential solution to address this problem are investigated as well. Here, the focus is on the infamous $O_2$ + Al(111) benchmark system.

**Chapter 6** tries to improve the theoretical description of the $NH_3$ + Ru(0001) system by including surface atom motion and Van der Waals correlation in the simulations. In some of the simulations, surface atom motion is excluded to gauge its effect on the reactivity. For the most part, the reaction mechanism is investigated since it is unexpectedly peculiar.

**Chapter 7** provides predictions for the dissociation of $CHD_3$ on the flat surface Cu(111), the stepped surface Cu(211), and the flat single-atom alloy surfaces Pt-Cu(111) and Pd-Cu(111). The chemically accurate SRP-DF for

$CHD_3$ + Ni(111), Pt(111), and Pt(211) is employed in the hope to test the SRP-DF's transferability to $CHD_3$ + Cu surfaces with future experiments. Several dynamical effects are investigated to explain the trends observed in the reactivity of the methane-Cu surface systems.

**Chapter 8** investigates the applicability of the Behler-Parrinello approach[43] to neural network potentials for reactive scattering of polyatomic molecules from mobile metal surfaces. The $CHD_3$ + Cu(111) system is taken as a benchmark since the associated reaction probability is too low to obtain statistically relevant data with Born-Oppenheimer MD (BOMD) for a comparison with an experimental study. Furthermore, the cause of the unusually large effect of vibrational pre-excitation of $CHD_3$ on the sticking probability is investigated.

**Chapter 9** searches for trends in the reaction dynamics of methane on group 10 metal (111) surfaces, where BOMD is performed for the first time for $CHD_3$ + Pd(111). Also, the aforementioned SRP-DF for $CHD_3$ + Ni(111) and Pt(111) is employed. This should enable tests of the transferability of the SRP32-vdW-DF1 DF among the systems in which methane interacts with all group 10 metal (111) surfaces by experiments on $CHD_3$ + Pd(111) in the future.

Finally, **Chapter 10** tries to elucidate the potential reaction pathways for the dissociation of methanol and subsequent formation of formaldehyde. Moreover, the role of dynamical effects in the branching ratio of initial CH or OH dissociation is considered. The subsequent reaction step after the initial dissociation of a CH or OH bond, i.e., the formation of formaldehyde, is analyzed as well.

## 1.4 Main Results

Several systems have been the object of study in this thesis. Chapters 3 and 4 describe the reaction of HCl on Au(111) with a high-dimensional neural network potential (HD-NNP). This reaction is of fundamental interest since a large discrepancy between theoretical[58] and experimental[59] $S_0$ existed at the onset of this thesis work, despite a large effort from both a theoretical and an experimental point of view[25, 31, 58–62]. Chapter 3 shows that improvements in the DF combined with an improved analysis of experimental sticking probabilities[63] manage to largely close the gap between experiment and theory, without including non-adiatic effects. Furthermore, dynamical effects play an important role in the overall reactivity, leading to a dependence of the reactivity on impact sites that cannot be explained on the basis of site-specific barrier heights and geometries only. Interestingly, surface atom motion only

has a minor influence on the sticking probability. Moreover, Chapter 4 shows that the orientation and angular momentum of HCl have a huge effect on the sticking probability on Au(111). This effect cannot be ascribed to rotational steering, but to a lock-in effect, where specific combinations of initial angular momentum and orientation allow the reaction to occur. When rotational excitation is combined with vibrational excitation an even larger effect is observed due to a mutually enforcing effect: Vibrational excitation causes the bottleneck to the dissociation to occur later along the reaction path whereas rotational excitation causes a larger distribution in the orientation to be accessible for dissociation. A very large rotational efficacy is observed, i.e., pre-exiting the molecule rotationally is much more effective at promoting reaction than increasing the collision energy or pre-exiting the molecule vibrationally.

In Chapter 5, the difference between the work function of a metal surface and the electron affinity of a molecule ($W - E_{\mathrm{ea}}$) is found to be related to a GGA DF's ability to correctly describe a molecule-metal surface reaction. If this difference is smaller, the functional also has to be made more "repulsive" in order to obtain an SRP DF. Furthermore, if $(W - E_{\mathrm{ea}}) < 7\,\mathrm{eV}$, even one of the most repulsive GGA DFs (i.e., RPBE[64]) underestimates barrier heights due to an increase in electron transfer and concomitant increase of the delocalization error fundamental to DFT[65]. Fortunately, DFs that include some (approximate) way of correcting for the so-called self-interaction error (SIE) are expected to be less susceptible to the delocalization error at the transition state, and thus potentially do not underestimate barrier heights when $(W - E_{\mathrm{ea}})$ is small. This is indeed shown to be true for the benchmark $O_2$ + Al(111) system. Here, the results obtained with the MS-RPBEl DF[66] suggest that meta-GGA DFs of the "made simple" (MS) kind[67] can slightly remedy the SIE problem, but not sufficiently for this system. Screened hybrid GGA DFs like HSE03-1/3X[68–70] offer an even further improved description of $O_2$ + Al(111) in that they yield sticking probabilities in semi-quantitative agreement with experiment[71, 72], thus offering more promise.

Dissociative chemisorption of polyatomic molecules on metal surfaces usually proceeds through either a rotationally adiabatic or a rotational sudden mechanism. The reaction is usually either direct, or proceeds through a trapped molecular physisorped state. However, Chapter 6 shows with BOMD that the reaction mechanism of $NH_3$ + Ru(0001) is neither rotationally adiabatic nor rotational sudden, with clearly distinct and non-statistical initial and time-of-reaction orientation distributions. Under the conditions investigated the reaction of $NH_3$ on Ru(0001) is not described by a simple direct, or by an indirect trapping-mediated reaction mechanism, but rather by a direct reaction mechanism in which $NH_3$ goes through a very short-lived

molecularly chemisorbed state. Also, the lack of surface temperature dependence at high incidence energy observed by experiment[73] is confirmed with BOMD, although the modeling of surface motion is still required to accurately describe the sticking probability. Not only is surface atom motion included for this reaction for the first time, a DF incorporating attractive Van der Waals correlation[74] (RPBE-vdW-DF1) is employed as well. With respect to earlier work[75] employing the PBE DF[39] and modeling the Ru(0001) surface as static the computed sticking probability is found to be in improved agreement with experiment[73], showing reasonably good agreement between experiment and theory. This improvement is attributed to both modeling the Ru(0001) as a mobile surface and using the RPBE-vdW-DF1 DF instead of the PBE DF.

In Chapter 7, predictions are made made for the reaction of $CHD_3$ on Cu(111), Cu(211), and the single-atom alloys (SAAs) Pt-Cu(111) and Pd-Cu(111). The results have been obtained using static DFT and BOMD calculations with the SRP32-vdW-DF1 DF originally developed for $CHD_3$ + Ni(111)[76], which was later found to be chemically accurate for $CHD_3$ + Pt(111) and Pt(211) as well[41]. The results predict a much lower reactivity for Cu(111) than for Ni(111) and Pt(111) due to the higher and later barrier found on Cu(111), requiring higher kinetic and/or vibrational energies in order to observe reaction. Furthermore, rather surprisingly, $CHD_3$ has the same reaction probability on Cu(211) as on Cu(111), but with the reaction occurring only at the steps, which can be understood from the lower barriers at the step and higher barriers at the terrace relative to Cu(111). For the SAAs, the reactivity is only increased for Pt–Cu(111). In this system, reaction occurs primarily near the alloyed atom, which is not only caused by the reduction of the barrier height but also by changes in the dynamical pathway and reduction of energy transfer from methane to the surface atoms.

BOMD studies are limited to reaction probabilities larger than 1% and smaller than 99% due to the computational cost associated with the statistical accuracy requirements of reaction probabilities that fall outside of the aforementioned range. Therefore, in Chapter 8 the Behler-Parrinello approach[43] is used to develop an HD-NNP that describes a polyatomic molecule reacting on a mobile metal surface, i.e., $CHD_3$ + Cu(111). Here, it is shown that it is possible to use an HD-NNP for a polyatomic molecule-metal surface reaction that yields results at the accuracy level of BOMD, but with considerably reduced computational effort. While including surface atom motion explicitly, reaction probabilities as low as $5 \times 10^{-5}$ have been obtained, which is intractable with BOMD at present. It is observed that the reaction probability is influenced considerably by dynamical effects such as the bobsled effect[77, 78] and sur-

face recoil[79, 80]. A special observation for $CHD_3$ + Cu(111) is that a higher vibrational efficacy is obtained for two quanta in the CH stretch mode than for a single quantum, and this can be explained on the basis of the bobsled effect.

Although the SRP32-vdW-DF1 SRP-DF has been shown to be chemically accurate for $CHD_3$ + Ni(111) and Pt(111)[41, 76] (both group 10 metals), its transferability to Pd(111) (also a group 10 metal surface) remains unclear. Therefore, in Chapter 9, predictions have been made for the reaction of $CHD_3$ on Pd(111) using BOMD, while also performing a rough comparison with experimental data for $CH_4$ + Pd(111) obtained for lower incidence energies[81]. The reactivity of $CHD_3$ on Pd(111) is found to be intermediate between and similar to either Pt(111) or Ni(111), with the degree of similarity depending on the incidence energy and the initial vibrational state distribution. This is surprising because the barrier height and experiments[81] performed at lower incidence energies than investigated here suggest that the reactivity of Pd(111) should be similar to that of Pt(111) only. The relative decrease in the reactivity of Pd(111) at high incidence energies is attributed to the site specificity of the reaction and to dynamical effects such as the bobsled effect[77, 78] and energy transfer from methane to the surface atoms. In general, at the lowest incidence energy and laser-off conditions when these dynamical effects are smaller, the reaction probability on Pd(111) is comparable to that on Pt(111), which is also observed by experiment[81]. However, at higher incidence energies, these dynamical effects play a larger role and the computed reaction probability is more similar to that on Ni(111). Furthermore, under laser-on conditions ($\nu_1 = 1$) all three systems investigated show similar reaction probabilities, which is related to the aforementioned dynamical effects. The low reactivity of Pd(111) compared to that of Pt(111) is consistent with the low reactivity of Pd-Cu(111) relative to that of Pt-Cu(111) (Chapter 7), with the difference being greater than expected from the difference in barrier heights only.

An important industrial process is methanol steam reforming, which is typically used in conjunction with copper catalysts. However, little agreement exists on the reaction mechanisms involved on a copper catalyst[82]. Therefore, in Chapter 10 BOMD calculations have been performed yielding additional insight into the reaction mechanism for the dissociative chemisorption of methanol on Cu(111). Static DFT calculations on the molecule-metal surface interaction have also been performed. Here, it is shown that Cu(111) is a highly selective catalyst in that it primarily breaks the OH bond due to the difference in barrier heights and in other features of the MEPs for OH and CH cleavage. Furthermore, after the initial dissociation, formaldehyde is observed to form through three different mechanisms: Two mechanisms involve a hot hydrogen atom that either abstracts another hydrogen atom forming

molecular hydrogen or knocks off another hydrogen atom resulting in two hydrogen atoms (i.e., atomically adsorbed hydrogen is formed) at the surface. In the third mechanism, the OH and CH bonds are broken simultaneously or subsequently without the influence of a hot hydrogen atom. Additionally, it is observed that at high energy, CH cleavage is the dominant pathway instead of the formerly presumed OH cleavage pathway. Finally, in order to describe the interaction of methanol with the metal surface, the SRP32-vdW-DF1 DF is used, in the hope that future experiments can validate the transferability of this SRP-DF from $CH_4$ + Ni(111), Pt(111), and Pt(211) to chemically related molecule-metal surface systems, like the $CHD_3$ + Cu(111) and Pd(111) systems investigated here.

## 1.5 Outlook

Here, several open questions and possible future research directions are discussed. First, the results of HCl + Au(111) (Chapters 3 and 4), $O_2$ + Al(111) (Chapter 5), and to a lesser extent $NH_3$ + Ru(0001) (Chapter 6) suggest that the XC-DF still poses a large challenge for chemically accurate predictions from DFT. Especially the delocalization error and SIE seem to play a large role in the failure of DFT to reproduce quantatively, or even qualitatively, several experiments on systems where $(W - E_{\mathrm{ea}}) > 7\,\mathrm{eV}$. Fortunately, MGGA and hybrid DFs seem to be both a pragmatic and fundamental step forward towards a correct description of such molecule-metal surface reactions. Future research could further investigate such DFs in an effort to (semi-)quantitatively reproduce experiments where charge transfer plays an important role, e.g., the aforementioned systems and systems in which $O_2$ interacts Cu surfaces. Additionally, non-local correlation should be included as well since it can play an important role. At present, MGGA and hybrid DFs have not yet been paired with non-local correlation in calculations on barriers for molecule-metal surface reactions. Also, the exploratory calculations in Chapter 5 suggest that non-self-consistent calculations using screened hybrid DFs might yield accurate results, but additional testing is required to validate this approach. Furthermore, it might be possible to use an HD-NNP to upscale a PES obtained at a lower level of theory (e.g., with a GGA DF) to a higher level of theory (e.g., with a hybrid DF)[83]. This way, accurate PESs can be developed while lowering the computational cost associated with accurate calculations using a high level of theory.

HCl + Au(111) remains an enigmatic system, both for theory and experiment. In order to further improve and test theory, experimental sticking prob-

abilities with a lower error margin than presented in Chapter 3 are required. Moreover, experiments probing the rovibrational efficacies are required to validate the theoretical predictions in Chapter 4 of a huge rotational effect, in addition to a mutually enforcing effect of rotational and vibrational excitation.

A systematic experimental comparison of methane reacting on several transition metals is still lacking. For example, a large body of experimental work on methane + Ni(111) and Pt(111) exists, but a systematic comparison is difficult since the experimental conditions vary wildly. Moreover, the theoretical predictions for methane + Cu(111) and Pd(111) (Chapters 7 and 9) have yielded interesting comparisons with Ni(111) and Pt(111). However, for the Cu(111) and Pd(111) surfaces, the employed SRP32-vdW-DF1 DF is still untested against experiments using $CHD_3$, and therefore additional experiments are required in order to validate the SRP-DF. Likewise, the reactivity of Cu(211) and the Pt-Cu(111) and Pd-Cu(111) SAAs towards the dissociative chemisorption of methane also warrants experiments. Furthermore, although HD-NNPs allow the computation of sticking probabilities lower than 1% for methane, it is still to be seen whether the quasi-classical approach is sufficient, or whether quantum effects also need to be included for methane-metal surface systems at low incidence energies. Ring polymer MD simulations[84–86] might include quantum effects in both an efficient and an accurate manner, but requires additional testing[86].

The predictions for $NH_3$ + Ru(0001) in Chapter 6 warrant additional theoretical and experimental research. The accuracy of the employed XC-DF (RPBE-vdW-DF1) is questionable, in view of both the comparison to experiment and $(W - E_{\mathrm{ea}})$ being lower than 7 eV, and questions about the quality of the experimental sticking probabilities also remain. Therefore, an experiment is required to validate the previously published sticking results. Additionally, measured sticking probabilities of vibrationally pre-excited ammonia (or, preferably, $NHD_2$) would be a great benchmark for theory. Furthermore, an experiment where ammonia is orientationally aligned prior to hitting the metal surface, potentially using several different isotopologues of ammonia, would be able to test our prediction that the reaction is neither rotationally adiabatic nor rotational sudden, with clearly distinct and non-statistical initial and time-of-reaction orientation distributions.

The theoretical predictions for methanol + Cu(111) in Chapter 10 present several interesting conclusions, but at present no experiments are available to directly compare against. Such experiments would not only help with testing XC-DFs, but also with testing predictions of the reaction pathways, in particular concerning the formation of formaldehyde.

# References


(1) Smil, V. Detonator of the Population Explosion. *Nature* **1999**, *400*, 415–415, DOI: 10.1038/22672.

(2) Zhdanov, V. P. Impact of Surface Science on the Understanding of Kinetics of Heterogeneous Catalytic Reactions. *Surf. Sci.* **2002**, *500*, 966–985, DOI: 10.1016/S0039-6028(01)01626-0.

(3) Ertl, G. Elementary Steps in Heterogeneous Catalysis. *Angew. Chem. Int. Ed.* **1990**, *29*, 1219–1227, DOI: 10.1002/anie.199012191.

(4) Sabbe, M. K.; Reyniers, M.-F.; Reuter, K. First-Principles Kinetic Modeling in Heterogeneous Catalysis: An Industrial Perspective on Best-Practice, Gaps and Needs. *Catal. Sci. Technol.* **2012**, *2*, 2010–2024, DOI: 10.1039/C2CY20261A.

(5) Wolcott, C. A.; Medford, A. J.; Studt, F.; Campbell, C. T. Degree of Rate Control Approach to Computational Catalyst Screening. *J. Catal.* **2015**, *330*, 197–207, DOI: 10.1016/j.jcat.2015.07.015.

(6) Somorjai, G. A.; York, R. L.; Butcher, D.; Park, J. Y. The Evolution of Model Catalytic Systems; Studies of Structure, Bonding and Dynamics from Single Crystal Metal Surfaces to Nanoparticles , and from Low Pressure ($<10^{-3}$ Torr) to High Pressure ($>10^{-3}$ Torr) to Liquid Interfaces. *Phys. Chem. Chem. Phys.* **2007**, *9*, 3500–3513, DOI: 10.1039/B618805B.

(7) Imbihl, R.; Behm, R.; Schlögl, R. Bridging the Pressure and Material Gap in Heterogeneous Catalysis. *Phys. Chem. Chem. Phys.* **2007**, *9*, 3459, DOI: 10.1039/b706675a.

(8) Kroes, G.-J. Toward a Database of Chemically Accurate Barrier Heights for Reactions of Molecules with Metal Surfaces. *J. Phys. Chem. Lett.* **2015**, *6*, 4106–4114, DOI: 10.1021/acs.jpclett.5b01344.

(9) Balooch, M.; Cardillo, M. J.; Miller, D. R.; Stickney, R. E. Molecular Beam Study of the Apparent Activation Barrier Associated with Adsorption and Desorption of Hydrogen on Copper. *Surf. Sci.* **1974**, *46*, 358–392, DOI: 10.1016/0039-6028(74)90315-X.

(10) Kurahashi, M.; Yamauchi, Y. Production of a Single Spin-Rotational State [(J,M)=(2,2)] Selected Molecular Oxygen ($^3\Sigma_g^-$) Beam by a Hexapole Magnet. *Rev. Sci. Instrum.* **2009**, *80*, 083103, DOI: 10.1063/1.3206299.

(11) Yoder, B. L.; Bisson, R.; Beck, R. D. Steric Effects in the Chemisorption of Vibrationally Excited Methane on Ni(100). *Science* **2010**, *329*, 553–556, DOI: 10.1126/science.1191751.

(12) Vattuone, L.; Savio, L.; Pirani, F.; Cappelletti, D.; Okada, M.; Rocca, M. Interaction of Rotationally Aligned and of Oriented Molecules in Gas Phase and at Surfaces. *Prog. Surf. Sci.* **2010**, *85*, 92–160, DOI: 10.1016/j.progsurf.2009.12.001.

(13) Van Lent, R.; Auras, S. V.; Cao, K.; Walsh, A. J.; Gleeson, M. A.; Juurlink, L. B. F. Site-Specific Reactivity of Molecules with Surface Defects—the Case of $H_2$ Dissociation on Pt. *Science* **2019**, *363*, 155–157, DOI: 10.1126/science.aau6716.

(14) Roorda, T.; Auras, S. V.; Juurlink, L. B. F. Chiral Surface Characterisation and Reactivity Toward H–D Exchange of a Curved Platinum Crystal. *Top. Catal.* **2020**, *63*, 1558–1568, DOI: 10.1007/s11244-020-01371-3.

(15) Auras, S. V.; van Lent, R.; Bashlakov, D.; Bastidas, J. M. P.; Roorda, T.; Spierenburg, R.; Juurlink, L. B. F. Scaling Platinum-Catalyzed Hydrogen Dissociation on Corrugated Surfaces. *Angew. Chem. Int. Ed.* **2020**, *59*, 20973–20979, DOI: 10.1002/anie.202005616.

(16) Tiwari, A. K.; Nave, S.; Jackson, B. Methane Dissociation on Ni(111): A New Understanding of the Lattice Effect. *Phys. Rev. Lett.* **2009**, *103*, 253201, DOI: 10.1103/PhysRevLett.103.253201.

(17) Tiwari, A. K.; Nave, S.; Jackson, B. The Temperature Dependence of Methane Dissociation on Ni(111) and Pt(111): Mixed Quantum-Classical Studies of the Lattice Response. *J. Chem. Phys.* **2010**, *132*, 134702, DOI: 10.1063/1.3357415.

(18) Kroes, G.-J.; Díaz, C. Quantum and Classical Dynamics of Reactive Scattering of $H_2$ from Metal Surfaces. *Chem. Soc. Rev.* **2016**, *45*, 3658–3700, DOI: 10.1039/C5CS00336A.

(19) King, D. A.; Wells, M. G. Reaction Mechanism in Chemisorption Kinetics: Nitrogen on the {100} Plane of Tungsten. *Proc. R. Soc. Lond. A* **1974**, *339*, 245–269, DOI: 10.1098/rspa.1974.0120.

(20) Kay, B. D.; Raymond, T. D.; Coltrin, M. E. Observation of a Dynamical Propensity Rule in Rotationally Inelastic Gas-Surface Scattering: $NH_3$ on Au(111). *Phys. Rev. B* **1987**, *36*, 6695–6697, DOI: 10.1103/PhysRevB.36.6695.

(21) Tenner, M. G.; Geuzebroek, F. H.; Kuipers, E. W.; Wiskerke, A. E.; Kleyn, A. W.; Stolte, S.; Namiki, A. Orientation Dependence of Rotational Excitation in NO Scattering from Ag(111). *Chem. Phys. Lett.* **1990**, *168*, 45–50, DOI: 10.1016/0009-2614(90)85100-Q.

(22) LaVilla, M. E.; Ionov, S. I. Molecular Self-Diffraction on a Surface: Inversion Symmetry Changes in Scattering of State-Selected $ND_3$ on Graphite (0001). *Phys. Rev. Lett.* **1992**, *68*, 129–132, DOI: 10.1103/PhysRevLett.68.129.

(23) Hou, H.; Rettner, C. T.; Auerbach, D. J.; Huang, Y.; Gulding, S. J.; Wodtke, A. M. The Interaction of Highly Vibrationally Excited Molecules with Surfaces: Vibrational Relaxation and Reaction of NO($v$) at Cu(111) and O/Cu(111). *Faraday Discuss.* **1999**, *113*, 181–199, DOI: 10.1039/A902660F.

(24) White, J. D.; Chen, J.; Matsiev, D.; Auerbach, D. J.; Wodtke, A. M. Vibrationally Promoted Electron Emission from Low Work-Function Metal Surfaces. *J. Chem. Phys.* **2006**, *124*, 064702, DOI: 10.1063/1.2166360.

(25) Rahinov, I.; Cooper, R.; Yuan, C.; Yang, X.; Auerbach, D. J.; Wodtke, A. M. Efficient Vibrational and Translational Excitations of a Solid Metal Surface: State-to-State Time-of-Flight Measurements of HCl($v$=2,J=1) Scattering from Au(111). *J. Chem. Phys.* **2008**, *129*, 214708, DOI: 10.1063/1.3028542.

(26) Nahler, N. H.; White, J. D.; LaRue, J.; Auerbach, D. J.; Wodtke, A. M. Inverse Velocity Dependence of Vibrationally Promoted Electron Emission from a Metal Surface. *Science* **2008**, *321*, 1191–1194, DOI: 10.1126/science.1160040.

(27) Cooper, R.; Rahinov, I.; Yuan, C.; Yang, X.; Auerbach, D. J.; Wodtke, A. M. Efficient Translational Excitation of a Solid Metal Surface: State-to-State Translational Energy Distributions of Vibrational Ground State HCl Scattering from Au(111). *J. Vac. Sci. Technol. A* **2009**, *27*, 907–912, DOI: 10.1116/1.3071971.

(28) Nieto, P.; Farías, D.; Miranda, R.; Luppi, M.; J. Baerends, E.; F. Somers, M.; van der Niet, M. J. T. C.; A. Olsen, R.; J. Kroes, G. Diffractive and Reactive Scattering of $H_2$ from Ru(0001): Experimental and Theoretical Study. *Phys. Chem. Chem. Phys.* **2011**, *13*, 8583–8597, DOI: 10.1039/C0CP02425B.

(29) Cooper, R.; Bartels, C.; Kandratsenka, A.; Rahinov, I.; Shenvi, N.; Golibrzuch, K.; Li, Z.; Auerbach, D. J.; Tully, J. C.; Wodtke, A. M. Multiquantum Vibrational Excitation of NO Scattered from Au(111): Quantitative Comparison of Benchmark Data to Ab Initio Theories of Nonadiabatic Molecule–Surface Interactions. *Angew. Chem. Int. Ed.* **2012**, *51*, 4954–4958, DOI: 10.1002/anie.201201168.

(30) Bünermann, O.; Jiang, H.; Dorenkamp, Y.; Kandratsenka, A.; Janke, S.; Auerbach, D. J.; Wodtke, A. M. Electron-Hole Pair Excitation Determines the Mechanism of Hydrogen Atom Adsorption. *Science* **2015**, *350*, 1346–1349, DOI: 10.1126/science.aad4972.

(31) Geweke, J.; Shirhatti, P. R.; Rahinov, I.; Bartels, C.; Wodtke, A. M. Vibrational Energy Transfer near a Dissociative Adsorption Transition State: State-to-State Study of HCl Collisions at Au(111). *J. Chem. Phys.* **2016**, *145*, 054709, DOI: 10.1063/1.4959968.

(32) Krüger, B. C.; Barratt Park, G.; Meyer, S.; V. Wagner, R. J.; M. Wodtke, A.; Schäfer, T. Trapping-Desorption and Direct-Scattering of Formaldehyde at Au(111). *Phys. Chem. Chem. Phys.* **2017**, *19*, 19896–19903, DOI: 10.1039/C7CP03907G.

(33) Al Taleb, A.; Anemone, G.; Zhou, L.; Guo, H.; Farias, D. Diffraction of $CH_4$ from a Metal Surface. *J. Phys. Chem. Lett.* **2019**, *10*, 1574–1580, DOI: 10.1021/acs.jpclett.9b00158.

(34) Geweke, J.; Wodtke, A. M. Vibrationally Inelastic Scattering of HCl from Ag(111). *J. Chem. Phys.* **2020**, *153*, 164703, DOI: 10.1063/5.0026228.

(35) Alkoby, Y.; Chadwick, H.; Godsi, O.; Labiad, H.; Bergin, M.; Cantin, J. T.; Litvin, I.; Maniv, T.; Alexandrowicz, G. Setting Benchmarks for Modelling Gas–Surface Interactions Using Coherent Control of Rotational Orientation States. *Nat. Commun.* **2020**, *11*, 3110, DOI: 10.1038/s41467-020-16930-1.

(36) Borodin, D.; Rahinov, I.; Shirhatti, P. R.; Huang, M.; Kandratsenka, A.; Auerbach, D. J.; Zhong, T.; Guo, H.; Schwarzer, D.; Kitsopoulos, T. N.; Wodtke, A. M. Following the Microscopic Pathway to Adsorption through Chemisorption and Physisorption Wells. *Science* **2020**, *369*, 1461–1465, DOI: 10.1126/science.abc9581.

(37) Werdecker, J.; Chen, B.-J.; Van Reijzen, M. E.; Farjamnia, A.; Jackson, B.; Beck, R. D. State-to-State Methane-Surface Scattering as a Probe of Catalytic Activity. *Phys. Rev. Research* **2020**, *2*, 043251, DOI: 10.1103/PhysRevResearch.2.043251.

(38) Mardirossian, N.; Head-Gordon, M. How Accurate Are the Minnesota Density Functionals for Noncovalent Interactions, Isomerization Energies, Thermochemistry, and Barrier Heights Involving Molecules Composed of Main-Group Elements? *J. Chem. Theory Comput.* **2016**, *12*, 4303–4325, DOI: 10.1021/acs.jctc.6b00637.

(39) Perdew, J. P.; Burke, K.; Ernzerhof, M. Generalized Gradient Approximation Made Simple. *Phys. Rev. Lett.* **1996**, *77*, 3865–3868, DOI: 10.1103/PhysRevLett.77.3865.

(40) Sementa, L.; Wijzenbroek, M.; van Kolck, B. J.; Somers, M. F.; Al-Halabi, A.; Busnengo, H. F.; Olsen, R. A.; Kroes, G. J.; Rutkowski, M.; Thewes, C.; Kleimeier, N. F.; Zacharias, H. Reactive Scattering of $H_2$ from Cu(100): Comparison of Dynamics Calculations Based on the Specific Reaction Parameter Approach to Density Functional Theory with Experiment. *J. Chem. Phys.* **2013**, *138*, 044708, DOI: 10.1063/1.4776224.

(41) Migliorini, D.; Chadwick, H.; Nattino, F.; Gutiérrez-González, A.; Dombrowski, E.; High, E. A.; Guo, H.; Utz, A. L.; Jackson, B.; Beck, R. D.; Kroes, G.-J. Surface Reaction Barriometry: Methane Dissociation on Flat and Stepped Transition-Metal Surfaces. *J. Phys. Chem. Lett.* **2017**, *8*, 4177–4182, DOI: 10.1021/acs.jpclett.7b01905.

(42) Smeets, E. W. F.; Kroes, G.-J. Designing New SRP Density Functionals Including Non-Local vdW-DF2 Correlation for $H_2$ + Cu(111) and Their Transferability to $H_2$ + Ag(111), Au(111) and Pt(111). *Phys. Chem. Chem. Phys.* **2021**, *23*, 7875–7901, DOI: 10.1039/D0CP05173J.

(43) Behler, J.; Parrinello, M. Generalized Neural-Network Representation of High-Dimensional Potential-Energy Surfaces. *Phys. Rev. Lett.* **2007**, *98*, 146401, DOI: 10.1103/PhysRevLett.98.146401.

(44) Senftle, T. P.; Hong, S.; Islam, M. M.; Kylasa, S. B.; Zheng, Y.; Shin, Y. K.; Junkermeier, C.; Engel-Herbert, R.; Janik, M. J.; Aktulga, H. M.; Verstraelen, T.; Grama, A.; van Duin, A. C. T. The ReaxFF Reactive Force-Field: Development, Applications and Future Directions. *NPJ Comput. Mater.* **2016**, *2*, 1–14, DOI: 10.1038/npjcompumats.2015.11.

(45) Born, M.; Oppenheimer, R. Zur Quantentheorie Der Molekeln. *Ann. Phys.* **1927**, *389*, 457–484, DOI: 10.1002/andp.19273892002.

(46) White, J. D.; Chen, J.; Matsiev, D.; Auerbach, D. J.; Wodtke, A. M. Conversion of Large-Amplitude Vibration to Electron Excitation at a Metal Surface. *Nature* **2005**, *433*, 503–505, DOI: 10.1038/nature03213.

(47) Juaristi, J. I.; Alducin, M.; Muiño, R. D.; Busnengo, H. F.; Salin, A. Role of Electron-Hole Pair Excitations in the Dissociative Adsorption of Diatomic Molecules on Metal Surfaces. *Phys. Rev. Lett.* **2008**, *100*, 116102, DOI: 10.1103/PhysRevLett.100.116102.

(48) Novko, D.; Blanco-Rey, M.; Alducin, M.; Juaristi, J. I. Surface Electron Density Models for Accurate Ab Initio Molecular Dynamics with Electronic Friction. *Phys. Rev. B* **2016**, *93*, 245435, DOI: 10.1103/PhysRevB.93.245435.

(49) Askerka, M.; Maurer, R. J.; Batista, V. S.; Tully, J. C. Role of Tensorial Electronic Friction in Energy Transfer at Metal Surfaces. *Phys. Rev. Lett.* **2016**, *116*, 217601, DOI: 10.1103/PhysRevLett.116.217601.

(50) Maurer, R. J.; Askerka, M.; Batista, V. S.; Tully, J. C. Ab Initio Tensorial Electronic Friction for Molecules on Metal Surfaces: Nonadiabatic Vibrational Relaxation. *Phys. Rev. B* **2016**, *94*, 115432, DOI: 10.1103/PhysRevB.94.115432.

(51) Maurer, R. J.; Jiang, B.; Guo, H.; Tully, J. C. Mode Specific Electronic Friction in Dissociative Chemisorption on Metal Surfaces: $H_2$ on Ag(111). *Phys. Rev. Lett.* **2017**, *118*, 256001, DOI: 10.1103/PhysRevLett.118.256001.

(52) Spiering, P.; Meyer, J. Testing Electronic Friction Models: Vibrational De-Excitation in Scattering of $H_2$ and $D_2$ from Cu(111). *J. Phys. Chem. Lett.* **2018**, *9*, 1803–1808, DOI: 10.1021/acs.jpclett.7b03182.

(53) Spiering, P.; Shakouri, K.; Behler, J.; Kroes, G.-J.; Meyer, J. Orbital-Dependent Electronic Friction Significantly Affects the Description of Reactive Scattering of $N_2$ from Ru(0001). *J. Phys. Chem. Lett.* **2019**, *10*, 2957–2962, DOI: 10.1021/acs.jpclett.9b00523.

(54) Box, C. L.; Zhang, Y.; Yin, R.; Jiang, B.; Maurer, R. J. Determining the Effect of Hot Electron Dissipation on Molecular Scattering Experiments at Metal Surfaces. *JACS Au* **2020**, DOI: 10.1021/jacsau.0c00066.

(55) Li, X.; Tully, J. C.; Schlegel, H. B.; Frisch, M. J. Ab Initio Ehrenfest Dynamics. *J. Chem. Phys.* **2005**, *123*, 084106, DOI: 10.1063/1.2008258.

(56) Wang, L.; Akimov, A.; Prezhdo, O. V. Recent Progress in Surface Hopping: 2011–2015. *J. Phys. Chem. Lett.* **2016**, *7*, 2100–2112, DOI: 10.1021/acs.jpclett.6b00710.

(57) Shenvi, N.; Roy, S.; Tully, J. C. Nonadiabatic Dynamics at Metal Surfaces: Independent-Electron Surface Hopping. *J. Chem. Phys.* **2009**, *130*, 174107, DOI: 10.1063/1.3125436.

(58) Füchsel, G.; del Cueto, M.; Díaz, C.; Kroes, G.-J. Enigmatic HCl + Au(111) Reaction: A Puzzle for Theory and Experiment. *J. Phys. Chem. C* **2016**, *120*, 25760–25779, DOI: 10.1021/acs.jpcc.6b07453.

(59) Shirhatti, P. R.; Geweke, J.; Steinsiek, C.; Bartels, C.; Rahinov, I.; Auerbach, D. J.; Wodtke, A. M. Activated Dissociation of HCl on Au(111). *J. Phys. Chem. Lett.* **2016**, *7*, 1346–1350, DOI: 10.1021/acs.jpclett.6b00289.

(60) Liu, T.; Fu, B.; Zhang, D. H. Six-Dimensional Quantum Dynamics Study for the Dissociative Adsorption of HCl on Au(111) Surface. *J. Chem. Phys.* **2013**, *139*, 184705, DOI: 10.1063/1.4829508.

(61) Liu, Q.; Zhou, X.; Zhou, L.; Zhang, Y.; Luo, X.; Guo, H.; Jiang, B. Constructing High-Dimensional Neural Network Potential Energy Surfaces for Gas–Surface Scattering and Reactions. *J. Phys. Chem. C* **2018**, *122*, 1761–1769, DOI: 10.1021/acs.jpcc.7b12064.

(62) Füchsel, G.; Zhou, X.; Jiang, B.; Juaristi, J. I.; Alducin, M.; Guo, H.; Kroes, G.-J. Reactive and Nonreactive Scattering of HCl from Au(111): An Ab Initio Molecular Dynamics Study. *J. Phys. Chem. C* **2019**, *123*, 2287–2299, DOI: 10.1021/acs.jpcc.8b10686.

(63) Geweke, J. D. Scattering HCl Molecules from Au(111) and Ag(111) Surfaces, Lausanne: EPFL, 2019, DOI: 10.5075/epfl-thesis-9742.

(64) Hammer, B.; Hansen, L. B.; Nørskov, J. K. Improved Adsorption Energetics within Density-Functional Theory Using Revised Perdew-Burke-Ernzerhof Functionals. *Phys. Rev. B* **1999**, *59*, 7413–7421, DOI: 10.1103/PhysRevB.59.7413.

(65) Perdew, J. P.; Ruzsinszky, A.; Constantin, L. A.; Sun, J.; Csonka, G. I. Some Fundamental Issues in Ground-State Density Functional Theory: A Guide for the Perplexed. *J. Chem. Theory Comput.* **2009**, *5*, 902–908, DOI: 10.1021/ct800531s.

(66) Smeets, E. W.; Voss, J.; Kroes, G.-J. Specific Reaction Parameter Density Functional Based on the Meta-Generalized Gradient Approximation: Application to $H_2$ + Cu(111) and $H_2$ + Ag(111). *J. Phys. Chem. A* **2019**, *123*, 5395–5406, DOI: 10.1021/acs.jpca.9b02914.

(67) Sun, J.; Xiao, B.; Fang, Y.; Haunschild, R.; Hao, P.; Ruzsinszky, A.; Csonka, G. I.; Scuseria, G. E.; Perdew, J. P. Density Functionals That Recognize Covalent, Metallic, and Weak Bonds. *Phys. Rev. Lett.* **2013**, *111*, 106401, DOI: 10.1103/PhysRevLett.111.106401.

(68) Heyd, J.; Scuseria, G. E.; Ernzerhof, M. Hybrid Functionals Based on a Screened Coulomb Potential. *J. Chem. Phys.* **2003**, *118*, 8207–8215, DOI: 10.1063/1.1564060.

(69) Heyd, J.; Scuseria, G. E.; Ernzerhof, M. Erratum: "Hybrid Functionals Based on a Screened Coulomb Potential" [J. Chem. Phys. 118, 8207 (2003)]. *J. Chem. Phys.* **2006**, *124*, 219906, DOI: 10.1063/1.2204597.

(70) Guido, C. A.; Brémond, E.; Adamo, C.; Cortona, P. Communication: One Third: A New Recipe for the PBE0 Paradigm. *J. Chem. Phys.* **2013**, *138*, 021104, DOI: 10.1063/1.4775591.

(71) Österlund, L.; Zorić, I.; Kasemo, B. Dissociative Sticking of $O_2$ on Al(111). *Phys. Rev. B* **1997**, *55*, 15452–15455, DOI: 10.1103/PhysRevB.55.15452.

(72) Kurahashi, M.; Yamauchi, Y. Steric Effect in $O_2$ Sticking on Al(111): Preference for Parallel Geometry. *Phys. Rev. Lett.* **2013**, *110*, 246102, DOI: 10.1103/PhysRevLett.110.246102.

(73) Mortensen, H.; Diekhöner, L.; Baurichter, A.; Jensen, E.; Luntz, A. C. Dynamics of Ammonia Decomposition on Ru(0001). *J. Chem. Phys.* **2000**, *113*, 6882–6887, DOI: 10.1063/1.1310662.

(74) Dion, M.; Rydberg, H.; Schröder, E.; Langreth, D. C.; Lundqvist, B. I. Van Der Waals Density Functional for General Geometries. *Phys. Rev. Lett.* **2004**, *92*, 246401, DOI: 10.1103/PhysRevLett.92.246401.

(75) Hu, X.; Yang, M.; Xie, D.; Guo, H. Vibrational Enhancement in the Dynamics of Ammonia Dissociative Chemisorption on Ru(0001). *J. Chem. Phys.* **2018**, *149*, 044703, DOI: 10.1063/1.5043517.

(76) Nattino, F.; Migliorini, D.; Kroes, G.-J.; Dombrowski, E.; High, E. A.; Killelea, D. R.; Utz, A. L. Chemically Accurate Simulation of a Polyatomic Molecule-Metal Surface Reaction. *J. Phys. Chem. Lett.* **2016**, *7*, 2402–2406, DOI: 10.1021/acs.jpclett.6b01022.

(77) Marcus, R. A. On the Analytical Mechanics of Chemical Reactions. Quantum Mechanics of Linear Collisions. *J. Chem. Phys.* **1966**, *45*, 4493–4499, DOI: 10.1063/1.1727528.

(78) McCullough, E. A.; Wyatt, R. E. Quantum Dynamics of the Collinear (H, $H_2$) Reaction. *J. Chem. Phys.* **1969**, *51*, 1253–1254, DOI: 10.1063/1.1672133.

(79) Jackson, B.; Nattino, F.; Kroes, G.-J. Dissociative Chemisorption of Methane on Metal Surfaces: Tests of Dynamical Assumptions Using Quantum Models and Ab Initio Molecular Dynamics. *J. Chem. Phys.* **2014**, *141*, 054102, DOI: 10.1063/1.4891327.

(80) Guo, H.; Farjamnia, A.; Jackson, B. Effects of Lattice Motion on Dissociative Chemisorption: Toward a Rigorous Comparison of Theory with Molecular Beam Experiments. *J. Phys. Chem. Lett.* **2016**, *7*, 4576–4584, DOI: 10.1021/acs.jpclett.6b01948.

(81) Tait, S. L.; Dohnálek, Z.; Campbell, C. T.; Kay, B. D. Methane Adsorption and Dissociation and Oxygen Adsorption and Reaction with CO on Pd Nanoparticles on MgO(100) and on Pd(111). *Surf. Sci.* **2005**, *591*, 90–107, DOI: 10.1016/j.susc.2005.06.024.

(82) Sá, S.; Silva, H.; Brandão, L.; Sousa, J. M.; Mendes, A. Catalysts for Methanol Steam Reforming—A Review. *Appl. Catal. B* **2010**, *99*, 43–57, DOI: 10.1016/j.apcatb.2010.06.015.

(83) Nandi, A.; Qu, C.; Houston, P. L.; Conte, R.; Bowman, J. M. Δ-Machine Learning for Potential Energy Surfaces: A PIP Approach to Bring a DFT-Based PES to CCSD(T) Level of Theory. *J. Chem. Phys.* **2021**, *154*, 051102, DOI: 10.1063/5.0038301.

(84) Craig, I. R.; Manolopoulos, D. E. Quantum Statistics and Classical Mechanics: Real Time Correlation Functions from Ring Polymer Molecular Dynamics. *J. Chem. Phys.* **2004**, *121*, 3368–3373, DOI: 10.1063/1.1777575.

(85) Habershon, S.; Manolopoulos, D. E.; Markland, T. E.; Miller, T. F. Ring-Polymer Molecular Dynamics: Quantum Effects in Chemical Dynamics from Classical Trajectories in an Extended Phase Space. *Annu. Rev. Phys. Chem.* **2013**, *64*, 387–413, DOI: 10.1146/annurev-physchem-040412-110122.

(86) Liu, Q.; Zhang, L.; Li, Y.; Jiang, B. Ring Polymer Molecular Dynamics in Gas–Surface Reactions: Inclusion of Quantum Effects Made Simple. *J. Phys. Chem. Lett.* **2019**, *10*, 7475–7481, DOI: 10.1021/acs.jpclett.9b02570.

# Chapter 2

# Methods and Theory

In this chapter, the theoretical framework for the electronic structure calculations and molecular dynamics (MD) for molecule-metal surface reactions is introduced. Section 2.1 concerns the electronic structure calculations, for which density functional theory (DFT) is employed. Section 2.2 discusses how the MD is performed. In Section 2.3 two different methods for fitting potential energy surfaces (PESs) are briefly discussed. Finally, Section 2.4 explains how the initial conditions for MD simulations are generated and Section 2.5 shows how observables can be computed from the MD simulations.

## 2.1 Density Functional Theory

In theoretical chemistry, typically the Born-Oppenheimer approximation (BOA) is used, which separates the motion of nuclei and electrons[1]. From the BOA follows that the most important and difficult property to be addressed by MD simulations is the electronic structure. The most popular method in calculating the electronic structure is DFT. Its success lies in its relatively low computational cost and favorable scaling with system size, combined with its accuracy. The basis of DFT relies on the fact that the ground state wave function is uniquely defined by the electron density, which has been proposed by Hohenberg and Kohn[2]. Hereafter, Kohn and Sham proposed a strategy in actually obtaining the ground state electronic density and concomitant wave function[3]. Their strategy involved introducing a fictitious system of non-interacting electrons and solving the one-electron Kohn-Sham (KS) equations:

$$\left[-\frac{1}{2}\nabla^2 + V_\mathrm{s}(\mathbf{r})\right]\psi_i(\mathbf{r}) = \epsilon_i\psi_i(\mathbf{r}), \tag{2.1}$$

where the first term is the kinetic energy operator, $V_\mathrm{s}$ is the effective potential, $\psi_i(\mathbf{r})$ is the KS wave function at $\mathbf{r} = (x, y, z)$, and $\epsilon_i$ is the KS orbital energy.

Note that all equations in this section are given in Hartree atomic units, i.e., $\hbar = e = m_e = 1$. From the KS orbitals the electron density $\rho$ can be constructed:

$$\rho(\mathbf{r}) = \sum_i |\psi_i(\mathbf{r})|^2. \tag{2.2}$$

Furthermore, the effective potential is defined as

$$V_\mathrm{s}(\mathbf{r}) = \int \frac{\rho(\mathbf{r}')}{|\mathbf{r} - \mathbf{r}'|}\,\mathrm{d}\mathbf{r}' - \sum_N \frac{Z_N}{|\mathbf{r} - \mathbf{R}_N|} + V_\mathrm{XC}(\mathbf{r}), \tag{2.3}$$

where $Z_N$ and $\mathbf{R}_N$ are the charges and positions of the nuclei, respectively. The first term is the electron-electron repulsion, the second term is the electron-nuclei attraction, and the final term is the exchange-correlation (XC) potential, which contains all non-classical interaction energy terms and is the derivative of the XC-energy with respect to the electron density as follows:

$$V_\mathrm{XC}(\mathbf{r}) = \frac{\delta E_\mathrm{XC}(\mathbf{r})}{\delta \rho(\mathbf{r})}. \tag{2.4}$$

Although DFT is in principle exact, the exact functional form of the exchange-correlation potential is unknown and is at present still improved upon in order to increase the accuracy of DFT. Different functional forms and approximations will be discussed in the next Section.

### 2.1.1 Exchange-Correlation Functionals

Unfortunately, the exact expression for the exchange-correlation (XC) density functional (DF) is unknown, requiring approximations to the exact XC-DF. It is tempting to refer to the so-called Jacob's ladder[4] when discussing the many available approximations to the exact XC-DF. This ladder attempts to systematically rank the approximations and their "ingredients" in terms of accuracy (and coincidentally of computational cost). For instance, the first rung only relies on the local electron density, whereas the second and third rungs add the first and second derivatives of the electron density, respectively. Regrettably, Jacob's ladder contains several inconsistencies. For example, Perdew and Schmidt stated that in the design of Jacob's ladder ingredients of lower rungs cannot be removed when climbing the ladder[4]. However, the fourth rung includes, among others, the hybrid generalized gradient approximation (GGA), which does not make use of the Laplacian employed in the meta-GGA (MGGA) belonging to the third rung. Furthermore, neither the dispersion corrected nor the vdW non-local correlation DFs currently

have a place on the ladder, and it is unclear where they should be positioned since they also do not belong to the fifth rung of the non-local exact partial correlation methods. Some attempts have been made to improve Jacob's ladder (e.g., by introducing rungs between the existing rungs), but it remains rather inconsistent. Therefore, in the discussion of several approximations to the XC-DF, here, I will refrain from employing a "ranking" such as Jacob's ladder and merely try to categorize the approximations.

### Local Density Approximation

The most simple approximation is the local density approximation (LDA), where the electrons are assumed to behave as a homogeneous electron gas (or jellium). The XC energy $E_{\mathrm{XC}}^{\mathrm{LDA}}$ only depends on the local electron density $\rho(\mathbf{r})$ and can be written as

$$E_{\mathrm{XC}}^{\mathrm{LDA}}(\rho(\mathbf{r})) = \int \rho(\mathbf{r}) \left[\epsilon_{\mathrm{X}}(\rho(\mathbf{r})) + \epsilon_{\mathrm{C}}(\rho(\mathbf{r}))\right] \mathrm{d}\mathbf{r}, \tag{2.5}$$

where $\epsilon_{\mathrm{X}}$ and $\epsilon_{\mathrm{C}}$ are the exchange and correlation energies per electron, respectively. The exchange energy in a jellium can be analytically computed as[5]

$$\epsilon_{\mathrm{X}}(\rho(\mathbf{r})) = -\frac{3}{4}\left(\frac{3}{\pi}\rho(\mathbf{r})\right)^{\frac{1}{3}}. \tag{2.6}$$

However, for the correlation energy in a jellium, exact analytical expressions only exist for the low- and high-density limits. Therefore, analytical correlation DFs are either fitted to accurate quantum Monte Carlo results for a jellium[6–9] or derived from physical constraints[10].

### Generalized Gradient Approximation

The LDA can be extended by including the gradient of the local electron density as well, being the so-called GGA:

$$E_{\mathrm{XC}}^{\mathrm{GGA}}\left(\rho(\mathbf{r}), \nabla\rho(\mathbf{r})\right) = \int f\left[\rho(\mathbf{r}), \nabla\rho(\mathbf{r})\right] \mathrm{d}\mathbf{r}, \tag{2.7}$$

which subsequently can be separated into a separate exchange ($E_{\mathrm{X}}^{\mathrm{GGA}}$) and correlation ($E_{\mathrm{C}}^{\mathrm{GGA}}$) energy (as is done for the LDA). Note that a non-separable gradient approximation also exists, which is similar to the GGA but where the exchange and correlation are non-separable[11, 12]. The exchange part is

defined as

$$E_{\mathrm{X}}^{\mathrm{GGA}}\left(\rho(\mathbf{r}), \nabla\rho(\mathbf{r})\right) = \int \rho(\mathbf{r})\epsilon_{\mathrm{X}}(\rho(\mathbf{r}))F(s)\,\mathrm{d}\mathbf{r}, \tag{2.8}$$

where $F(s)$ is the enhancement factor and $s$ is the dimensionless reduced density gradient:

$$s = \frac{|\nabla\rho|}{2(3\pi^2)^{1/3}\rho(\mathbf{r})^{4/3}}. \tag{2.9}$$

In the Perdew, Burke and Ernzerhof (PBE) GGA DF[13] the enhancement factor is defined as

$$F^{\mathrm{PBE}}(s) = 1 + \kappa\left(1 - \frac{1}{1 + \mu s^2/\kappa}\right), \tag{2.10}$$

where $\kappa = 0.804$ and $\mu = \beta(\pi^2/3) \simeq 0.21951$, which are constants derived from physical constraints[13]. Furthermore, for the revised PBE (RPBE) DF[14] the enhancement factor is defined in a slightly different manner than for the PBE DF, while keeping the $\kappa$ and $\mu$ constants from the PBE DF, in an effort to improve chemisorption energies without violating the Lieb-Oxford bound[15–17]:

$$F^{\mathrm{RPBE}}(s) = 1 + \kappa\left(1 - e^{-\mu s^2/\kappa}\right). \tag{2.11}$$

This change in the functional form of the enhancement factor is also the reason why the PBE DF is more attractive, i.e., yields lower molecule-metal surface interaction energies, than the RPBE DF as both DFs use the same correlation DF[14]. The GGA correlation DF is typically expressed as

$$E_{\mathrm{C}}^{\mathrm{GGA}}\left(\rho(\mathbf{r}), \nabla\rho(\mathbf{r})\right) = \int \rho(\mathbf{r})\left[\epsilon_{\mathrm{C}}(\rho(\mathbf{r})) + H\left(\rho(\mathbf{r}), \nabla\rho(\mathbf{r})\right)\right]\,\mathrm{d}\mathbf{r}, \tag{2.12}$$

where $H$ is the gradient contribution, which is specific to the DF used.

### Meta-Generalized Gradient Approximation

The next obvious extension to make to the approximation of the exact XC-DF is to include the second derivative of the electron density (i.e., the Laplacian), resulting in the MGGA DFs. The inclusion of the Laplacian solves the issue of GGA DFs not being able to satisfy all the theoretical constraints on the exact functional, which is also the reason why GGA DFs tend to be good for either molecules or solids, but never for both[12, 18]. However, for numerical reasons, typically the kinetic energy density $\tau(\mathbf{r})$ for the occupied KS orbitals (i.e., the Laplacian of the KS orbitals) is used instead of the Laplacian of

the electron density[12, 19]. Nevertheless, the two are related since the KS orbitals are non-local functionals of the electron density and can therefore be interchanged in the design of an MGGA DF[20]. Similar to the LDA and GGA XC energy, the MGGA XC energy is expressed as

$$E_{\mathrm{XC}}^{\mathrm{MGGA}}\left(\rho(\mathbf{r}), \nabla\rho(\mathbf{r}), \tau(\mathbf{r})\right) = \int f\left[\rho(\mathbf{r}), \nabla\rho(\mathbf{r}), \tau(\mathbf{r})\right] \mathrm{d}\mathbf{r}. \tag{2.13}$$

The exchange part is slightly modified compared to its GGA counterpart by making the enhancement factor also dependent on the kinetic energy density:

$$E_{\mathrm{X}}^{\mathrm{MGGA}}\left(\rho(\mathbf{r}), \nabla\rho(\mathbf{r}), \tau(\mathbf{r})\right) = \int \rho(\mathbf{r})\epsilon_{\mathrm{X}}(\rho(\mathbf{r}))F(s, \tau(\mathbf{r}))\,\mathrm{d}\mathbf{r}, \tag{2.14}$$

where the functional form of the enhancement factor again depends on the specific DF. In the "made simple" (MS) scheme[21], the enhancement factor is defined as

$$F^{\mathrm{MS}}(s, \alpha) = F^{1}(s) + f(\alpha)(F^{0}(s; c) - F^{1}(s)), \tag{2.15}$$

where $F^{1}(s)$ and $F^{0}(s; c)$ are the enhancement factors for the jellium and single-orbital cases, respectively, which are only dependent on the gradient of the electron density. The interpolation function $f(\alpha)$ depends on $\tau(\mathbf{r})$ through the inhomogeneity parameter

$$\alpha = \frac{\tau(\mathbf{r}) - \tau^{\mathrm{W}}(\mathbf{r})}{\tau^{\mathrm{jellium}}(\mathbf{r})}, \tag{2.16}$$

where $\tau^{\mathrm{jellium}}$ is the kinetic energy density for the jellium, and $\tau^{\mathrm{W}}$ is the von Weizsäcker kinetic energy density for the single-orbital electron density. Crucially, with the $\alpha$ parameter a distinction can be made between a molecular orbital regime ($\alpha \approx 0$), a metalic orbital regime ($\alpha \approx 1$), and a weakly bonding regime ($\alpha \gg 1$), which allows for the design of a DF that is able to be accurate for both molecules and solids. This accurate description of the different density regimes can be achieved through switching between the $F^{0}$ and $F^{1}$ enhancement factors using a specific form for the interpolation function, e.g.[21],

$$f(\alpha) = \frac{1 - \alpha^{2}}{1 + \alpha^{3} + b\alpha^{6}}, \tag{2.17}$$

where $b$ is a constant dependent on the DF design, and, here, is taken to be equal to one. Again, the form of the enhancement factor is dependent on the design of the DF, of which the PBE-like (MS-PBEl) and RPBE-like (MS-RPBEl)

expressions are highlighted here:

$$F^1_{\mathrm{PBE}}(s) = 1 + \kappa \left(1 - \frac{1}{1 + \mu s^2/\kappa}\right), \tag{2.18}$$

$$F^1_{\mathrm{RPBE}}(s) = 1 + \kappa \left(1 - e^{-\mu s^2/\kappa}\right). \tag{2.19}$$

Note that for the MS-PBEl and MS-RPBEl DFs $\kappa = 0.804$ (i.e., the value for (R)PBE) and $\mu = 10/81$. The $\mu$ value is taken from PBEsol[22], as is appropriate for metallic electron densities[23], and not from (R)PBE. This way, in metallic bonding regimes, the MS-(R)PBEl DF performs (almost) as well as the PBEsol DF, which yields excellent results for metals. Furthermore, $F^0$ can be obtained by simply replacing $\mu s^2$ with $(\mu s^2 + c)$. Subsequently, this $c$ parameter is optimized to ensure that the DF reproduces the exact exchange energy for the free hydrogen atom, yielding an approximate correction in the molecular orbital regime for the self-interaction error (SIE) fundamental to DFT[24]. Moreover, since the correlation functional for MGGA DFs is a rather large expression, the reader is referred to, e.g., Refs. [25] (TPSS) and [26] (revTPSS, which is used in the MS DFs). Nevertheless, $E_{\mathrm{C}}^{\mathrm{MGGA}}$ is extended from $E_{\mathrm{C}}^{\mathrm{GGA}}$ in a similar way as has been done for $E_{\mathrm{X}}^{\mathrm{MGGA}}$.

### Non-local Exchange

Another potential route to improve DFs is to go from a semi-local to a non-local functional. This way, the error in the non-local classical self-interaction can be corrected for since a non-local XC energy is required to do so[27]. One way to achieve this is by replacing a part of the local DFT exchange with Hartree-Fock (HF) exact exchange, yielding a so-called hybrid DF. The most commonly used hybrid DFs (e.g., B3LYP[28] and PBE0[29]) are the global hybrid DFs, where a fixed ratio $\alpha_{\mathrm{X}}$ of HF and DFT exchange is employed, while keeping the full DFT correlation energy:

$$E_{\mathrm{XC}}^{\mathrm{Hybrid}} = \alpha_{\mathrm{X}} E_{\mathrm{X}}^{\mathrm{HF}} + (1 - \alpha_{\mathrm{X}}) E_{\mathrm{X}}^{\mathrm{DFT}} + E_{\mathrm{C}}^{\mathrm{DFT}}. \tag{2.20}$$

Note that these hybrid DFs are often used with GGA DFs, but can in principle be combined with any type of (semi-)local DF (e.g., MGGA). However, global hybrid DFs yield an incorrect description of the long-range Coulomb interaction, which can be especially catastrophic for extended systems such as metals. Therefore, screened hybrid DFs have been developed that do yield the correct asymptotic behaviour. This screening is the result of separating the Coulomb operator in a short-range (SR) and long-range (LR) part, which usually leads

to the following operator[30–32]:

$$\frac{1}{r_{12}} = \underbrace{\frac{\mathrm{erfc}(\omega r_{12})}{r_{12}}}_{\mathrm{SR}} + \underbrace{\frac{\mathrm{erf}(\omega r_{12})}{r_{12}}}_{\mathrm{LR}}, \tag{2.21}$$

where $r_{12}$ is the interelectronic distance and $\omega$ is the screening length parameter. $\omega$ can then be determined empirically by fitting databases[32, 33], optimally tuned to reproduce physical constraints for ionization potentials[34–37], or optimized to ensure the reproduction of the energy of a free hydrogen atom[38, 39]. The total XC energy can then be expressed as

$$E_{\mathrm{XC}}^{\text{Screened hybrid}} = \alpha_{\mathrm{X}} E_{\mathrm{x,HF}}^{\mathrm{SR}} + (1-\alpha_{\mathrm{X}}) E_{\mathrm{x,DFT}}^{\mathrm{SR}} + E_{\mathrm{x,DFT}}^{\mathrm{LR}} + E_{\mathrm{c,DFT}}. \tag{2.22}$$

In addition to retrieving the correct asymptotic behaviour for the Coulomb interaction, a screened hybrid DF also lowers the computational cost considerably for an extended system, making screened hybrid DFs tractable for metal systems. However, it should also be noted that while including HF exchange diminishes the SIE, at the same time it introduces a static correlation error as well, especially for multi-reference systems[40]. Post HF methods employing multiple Slater determinants might be able to diminish the static correlation error while simultaneously reducing the SIE, but are at present intractable for extended systems.

### Non-local Correlation

The correlation energy can also be treated non-locally. A very popular way to include non-local correlation effects is include dispersion corrections in a *a posteriori* scheme such as the empirical Grimme[41, 42] or Tkatchenko-Scheffler[43] dispersion corrections. The benefit of these a posteriori dispersion corrected DFT calculations is that the increase in the computational cost compared to non-corrected DFT calculations is negligible. Self-consistent non-local correlation DFs have also been developed, such as the vdW-DF family[44–46] and (r)VV10 DFs[47, 48]. Due to the integration of a non-local double integral, the vdW and VV10 type of DFs are considerably more expensive than dispersion corrected DFs, even with efforts to improve the efficiency with which the integral is integrated[49]. The VV10 type of DFs can be combined with any type of correlation DF as long as that DF does not include any long-range correlation effects, i.e., the DF is (semi-)local:

$$E_{\mathrm{XC}}^{\mathrm{VV10}} = E_{\mathrm{X}} + E_{\mathrm{C}}^{\text{(Semi-)Local}} + E_{\mathrm{C}}^{\mathrm{VV10}}. \tag{2.23}$$

In contrast, the vdW-DF DFs consist of a fully local correlation part (i.e., LDA correlation) in addition to a non-local correlation part:

$$E_{\mathrm{XC}}^{\mathrm{vdW\text{-}DF}} = E_{\mathrm{X}} + E_{\mathrm{C}}^{\mathrm{LDA}} + E_{\mathrm{C}}^{\mathrm{Non\text{-}local}}. \tag{2.24}$$

Another way to include non-local correlation is to derive a correlation DF in the same way as a hybrid exchange DF by mixing DFT correlation with non-local exact partial correlation (e.g., second-order Møller-Plesset):

$$E_{\mathrm{XC}}^{\mathrm{Double\ hybrid}} = \alpha_{\mathrm{X}} E_{\mathrm{X}}^{\mathrm{HF}} + (1-\alpha_{\mathrm{X}}) E_{\mathrm{X}}^{\mathrm{DFT}} + \alpha_{\mathrm{C}} E_{\mathrm{C}}^{\mathrm{Non\text{-}local}} (1-\alpha_{\mathrm{C}}) E_{\mathrm{C}}^{\mathrm{DFT}}, \tag{2.25}$$

which is also called a double hybrid DF[50]. A single hybrid DF where only hybrid correlation is employed, and no hybrid exchange, is also possible but uncommon. Unfortunately, exact partial correlation is even more expensive than non-local vdW DFs and, so far, has been intractable to apply to molecule-metal surface reactions. The correlation mixing ratio $\alpha_{\mathrm{C}}$ can again be optimized empirically, or from physical constraints such as the one-parameter double-hybrid approximation[51].

#### Specific Reaction Parameter Approach

Finally, a pragmatic semi-empirical approach in the construction of an XC-DF is the so-called specific reaction parameter (SRP) approach. In the original approach devised by Truhlar and coworkers, one or a few parameters of an XC-DF is fitted to a set of experimental data for a specific gas-phase reaction[52, 53]. Subsequently, this optimized XC-DF, or SRP-DF, can be tested against different experimental data sets for the same reaction. Kroes and coworkers have extended this approach to molecule-metal surface reactions[54, 55]. A weighted average of two DFs is used, of which the mixing ratio is again fitted against a single set of experimental data for a specific molecule-metal surface reaction. Likewise, this DF is subsequently tested for different experimental sets, and if successful, a single parameter SRP-DF is obtained. Interestingly, in some cases, such an SRP-DF is observed to even reproduce experiments for other chemically related systems, even though these systems have not been included in the fitting procedure[56].

### 2.1.2 Plane Wave DFT

DFT calculations require some form of basis set in order to represent the wave functions. According to Bloch's theorem[57], plane waves are a convenient

way to represent the basis set for periodic systems:

$$\psi_j(\mathbf{r}, \mathbf{k}) = N \sum_{\mathbf{G}} c_{j\mathbf{Gk}} e^{i(\mathbf{k}+\mathbf{G})\mathbf{r}}, \tag{2.26}$$

where $j$ runs over the KS orbitals, $\mathbf{k}$ is a vector in the first Brillouin zone, $\mathbf{G}$ is a reciprocal lattice vector, $c_{j\mathbf{Gk}}$ is an expansion coefficient, and $N$ is a normalization factor. An additional advantage of a plane wave basis set is the computational ease with which the forces are calculated analytically due to the Pulay forces being zero if a basis set is employed that is independent of the ionic positions[58]. In order to have a tractable finite number of plane waves, the Brillouin zone is discretized with a $k$-point grid and Eq. 2.26 is truncated with a kinetic energy cut-off for the plane waves:

$$\frac{1}{2}|\mathbf{k} + \mathbf{G}|^2 \leq E_{\text{cut}}. \tag{2.27}$$

For the accuracy of the calculations, both the $k$-point grid and $E_{\text{cut}}$ have to be checked for convergence. Furthermore, the strong oscillations of the wave functions of the core electrons close to the nuclei require a very large $E_{\text{cut}}$. Therefore, pseudopotentials are employed that replace core electrons with a smooth potential[59, 60], resulting in a reduction of $E_{\text{cut}}$. Moreover, since only valence electrons are treated explicitly, the computational cost is reduced even further.

## 2.2 Dynamics Methods

For performing (quasi-)classical trajectory ((Q)CT) calculations, forces are required to integrate Newton's equations of motion and to propagate the ions (Section 2.2.1). These forces can be obtained, e.g., directly from plane wave DFT or from a fitted PES at negligible or minimal costs, respectively (see Section 2.3).

### 2.2.1 Integration Algorithm

In this thesis, Newton's equations of motion are integrated with the leapfrog algorithm when employing ab initio molecular dynamics (AIMD) and VASP[60–64] (Chapters 6, 7, 9 and 10), the Bulirsch-Stoer algorithm[65, 66] when employing the corrugation reducing procedure (CRP)[67] and the inhouse-built program QCTraj (Chapter 5), or the velocity Verlet algorithm[68] when employing

a high-dimensional neural network potential (HDNNP)[69] and LAMMPS[70, 71] (Chapters 3, 4 and 8).

### Velocity Verlet

In the velocity Verlet algorithm[68], first the velocity $\mathbf{v}$ is advanced with half a timestep $\Delta t$:

$$\mathbf{v}(t + \Delta t/2) = \mathbf{v}(t) + \mathbf{a}(t)\Delta t/2. \tag{2.28}$$

Subsequently, the position $\mathbf{x}$ is advanced with a full time step

$$\mathbf{x}(t + \Delta t) = \mathbf{x}(t) + \mathbf{v}(t + \Delta t/2)\Delta t, \tag{2.29}$$

from which the new acceleration $\mathbf{a}(t + \Delta t)$ is computed. Finally, the velocity is advanced with another half a timestep:

$$\mathbf{v}(t + \Delta t) = \mathbf{v}(t + \Delta t/2) + \mathbf{a}(t + \Delta t)\Delta t/2. \tag{2.30}$$

### Leapfrog

The leapfrog algorithm is similar to the velocity Verlet algorithm, but the velocity and position are advanced at staggered time points, i.e., the velocity and position updates "leapfrog" each other. The advantage of the leapfrog over the velocity Verlet algorithm is that the velocity is only updated once per timestep instead of twice. However, one needs to be careful with the initial conditions (see Section 2.4) since the initial velocity is at half a time step earlier than the initial position. First, the acceleration is determined at time $t$, with which $\mathbf{v}(t - \Delta t/2)$ can be advanced a full time step:

$$\mathbf{v}(t + \Delta t/2) = \mathbf{v}(t - \Delta t/2) + \mathbf{a}(t)\Delta t. \tag{2.31}$$

Then, the position can be propagated:

$$\mathbf{x}(t + \Delta t) = \mathbf{x}(t) + \mathbf{v}(t + \Delta t/2)\Delta t. \tag{2.32}$$

### Bulirsch-Stoer

The Bulirsch-Stoer algorithm[65, 66] is more involved and is therefore only briefly discussed. Initially, a large timestep $H$ is chosen. Then, $H$ is subdivided in $n$ pieces, or smaller timesteps, after which the position at $t + H$ is determined through polynomial extrapolation towards an infinite number of timesteps within $H$, i.e., $\Delta t \to 0$ and $n \to \infty$. This subdivision is repeated with

an increasing number of timesteps using the sequence[72, 73]

$$n_j = 2, 4, 6, \ldots, 2j, \ldots, 2j_{\max}, \tag{2.33}$$

where $j$ indicates the iteration. If the estimated error associated with the extrapolation is sufficiently low, the integration is considered to be accurate and the position is updated. If the desired accuracy is not achieved within $j_{\max}$ iterations, $H$ is halved and the procedure is repeated. The advantage of the Bulirsch-Stoer integrator is that it allows for adaptive timesteps and concomitant reduction in computational time while maintaining the desired accuracy.

### 2.2.2 (Quasi-)Classical and Quantum Dynamics

Nowadays, QCT is preferred over CT for molecule-metal surface reactions since QCT generally yields results in good agreement with quantum dynamics (QD)[74–77]. The good performance of QCT is achieved by including the quantum mechanical vibrational zero-point energy (ZPE) in the initial conditions (see also Section 2.4.2), opposed to CT where ZPE is not included. Note that occasionally CT outperforms QCT, but this is caused by artificial ZPE leakage in the QCT approach[78, 79]. However, when quantum effects such as tunneling play an important role, the QCT approach often fails, especially for (light) molecules with a total kinetic energy below the barrier height. Full dimensional QD simulations would include all quantum effects, but are intractable due to the large number of degrees of freedom (DOFs) and concomitant computational cost. Therefore, surface atom motion is not included in QD and QD simulations are limited to small molecules or reduced dimensionality Hamiltonians. One way to include quantum effects in simulations with a large number of DOFs is to employ ring polymer molecular dynamics (RPMD)[75, 80, 81]. However, RPMD is computationally still demanding due to its linear scaling with the number of beads, especially at low temperatures (the number of beads required to approximate QD scales inversely with the temperature), and remains largely untested for molecule-metal surface reactions[75]. Fortunately, precomputed PESs and the generally high temperatures involved in molecule-metal surface reactions allow for tractable RPMD calculations.

## 2.3 Fitting Potential Energy Surfaces

Evaluation of the forces required for MD can be performed *ab initio* (i.e., on-the-fly) with DFT, which is commonly referred to as ab initio molecu-

lar dynamics (AIMD), density functional molecular dynamics (DFMD), or Born-Oppenheimer molecular dynamics (BOMD). The large advantages of performing AIMD are that no prior knowledge of the dynamics is required and that many degrees of freedom can be modeled explicitly, which tends to be complicated or unfeasible in procedures that fit or interpolate the PES. However, due to the associated computational costs, AIMD calculations are limited in both the system size and amount of trajectories. This is especially problematic for molecule-metal surface reactions with low reactivity (i.e., $< 1\%$) in that it limits the statistical accuracy with which these probabilities can be calculated. Therefore, many different approaches have been developed where the PES is precomputed and subsequently fitted, leading to a considerable reduction in computational cost. Two different approaches are discussed here, namely the CRP[67] and Behler-Parrinello approach to neural network potentials[69]. Both approaches are capable of fitting or interpolating a PES with chemical accuracy, i.e., with an RMSE lower than 4.2 kJ/mol.

### 2.3.1 Corrugation Reducing Procedure (CRP)

A 6D PES for a diatomic molecule interacting with a metal surface can be easily constructed with the CRP[67]. The accuracy of this method comes from a procedure that reduces the energetic corrugation of the 6D function that is interpolated. This reduction is achieved by subtracting the single atom-surface PESs (i.e., the 3D PES $V_i^{3D}$) from the molecular PES (i.e., the full 6D PES $V^{6D}$), yielding the smoother 6D interpolation function $I^{6D}$:

$$I^{6D}\left(\mathbf{R},\mathbf{q}\right) = V^{6D}\left(\mathbf{R},\mathbf{q}\right) - \sum_{i=1}^{2} V_i^{3D}\left(\mathbf{r}_i\right), \tag{2.34}$$

where $\mathbf{R}$ is the vector of the cartesian coordinates of the center of mass (i.e., $X$, $Y$ and $Z$) and $\mathbf{q}$ is the vector of the spherical internal coordinates of the molecule (i.e., $r$, $\theta$ and $\phi$) Subsequently, $I^{6D}$ can be interpolated. Similarly, the atom-surface PES can also be made smoother prior to the interpolation by subtracting a sum of potentials for each atom in the molecule interacting with the surface atoms:

$$I_{\mathrm{A}}^{3D}\left(\mathbf{R}\right) = V_{\mathrm{A}}^{3D}\left(\mathbf{R}\right) - \sum_{j=1}^{N} V^{1D}\left(R_{\mathrm{A},j}\right). \tag{2.35}$$

Here, $V^{1D}\left(R_{\mathrm{A},j}\right)$ is taken to be directly above the top site, $R_{\mathrm{A},j}$ is the distance between the surface atom $j$ and atom A, and N is the number of surface atoms

in the reference cluster. For the evaluation of the energy from the full 6D PES, the atom-surface PESs are added back to the interpolated PES:

$$V^{6D}(\mathbf{R}, \mathbf{q}) = I^{6D}(\mathbf{R}, \mathbf{q}) + \sum_{i=1}^{2} V_i^{3D}(\mathbf{r}_i). \tag{2.36}$$

Likewise, the same procedure is employed for the atom-surface interaction energy. In the construction of the DFT data set employed in the interpolation, the symmetry of both the surface and the molecule are taken into account in order to reduce the size of the data set and concomitant computational effort. Another benefit of this approach is that it is general, i.e., it can be employed for any diatomic molecule and surface. In principle the CRP can also be extended to polyatomic molecules, however, the increase in degrees of freedom would severely complicate the applied symmetry, increase the data set size, and no guarantee exists that the PES would be sufficiently smooth for the interpolation.

### 2.3.2 Behler-Parrinello Approach to High-Dimensional Neural Network Potentials (HD-NNPs)

A procedure for obtaining a fit of the potential for a high-dimensional system that is relatively cheap from a computational point of view is the HD-NNP approach proposed by Behler and Parrinello[69]. The benefit of this approach is that it is system-size independent and allows for tractable simulations while explicitly modeling surface atom motion. In the HD-NNP, the total energy is evaluated as a sum of atomic contributions that are dependent on their energetically relevant local environment, which is described by many-body atom-centered symmetry functions[82]. Considering that the used symmetry functions and fitting procedure have been described in earlier studies[69, 82–85], only a short summary is given here for the symmetry functions[82]. The local environment of an atom is defined by the following cut-off function

$$f_c(R) = \begin{cases} \frac{1}{2}\left[\cos\left(\pi \frac{R}{R_c}\right) + 1\right] & R < R_c \\ 0 & R \geq R_c, \end{cases} \tag{2.37}$$

where only atomic contributions within the cut-off radius are taken into account. This cut-off radius needs to be large enough to ensure that long-range interactions are included as well, but not too large in order to avoid interactions with periodic images. The radial symmetry functions (effectively

two-body interactions) are[69, 82]

$$G_i^2 = \sum_{j \neq i} e^{-\eta(R_{i,j}-R_s)^2} f_c(R_{i,j}), \tag{2.38}$$

where $R_{i,j}$ is the internuclear distance between atoms $i$ and $j$, and $\eta$ and $R_s$ are parameters characterizing the function form, for which $R_s = 0$ in this thesis. Furthermore, the angular symmetry functions (effectively three-body interactions) are taken as[69, 82]

$$G_i^4 = 2^{1-\zeta} \sum_{j,k \neq i} (1 + \lambda \cos\theta_{i,j,k})^{\zeta} e^{-\eta(R_{i,j}+R_{i,k}+R_{j,k})} f_c(R_{i,j}) f_c(R_{i,k}) f_c(R_{j,k}), \tag{2.39}$$

where $\theta_{i,j,k} = \frac{R_{i,j} \cdot R_{i,k}}{R_{i,j} R_{i,k}}$, and $\eta$, $\zeta$ and $\lambda$ are parameters characterizing the function form. Note that since a summation over all two- and three-body interactions inside the cut-off radius is performed, a many-body description is achieved.

## 2.4 Initial Condition Sampling

Accurate simulations of experiments require one to faithfully represent the experiment, and thus special consideration of the initial conditions in MD simulations is required. Here, the initial conditions of both the metal surface and molecular beam are discussed in order to accurately simulate reactive scattering of molecules on metal surfaces.

### 2.4.1 Metal Surface

In order to simulate the effect of surface temperature ($T_s$), a procedure can be employed as described in Refs. [55] and [86]. An independent 1D harmonic oscillator model is used to mimic the local distortion of the ideal surface and the thermal motion of the surface atoms, by assigning initial displacements and velocities to the atoms of the mobile layers. Using $K = 1/2mv^2$ and $U = 1/2kx^2$, where $K$ and $U$ are the kinetic and potential energies, respectively, the following Boltzmann distributions for the velocities and positions are obtained:

$$f(v) = \left(\frac{m}{2\pi k_B T}\right)^{\frac{1}{2}} e^{\frac{-mv^2}{2k_B T}} \tag{2.40}$$

$$f(q) = \left(\frac{m\omega^2}{2\pi k_B T}\right)^{\frac{1}{2}} e^{\frac{-m\omega^2 q^2}{2k_B T}} \tag{2.41}$$

The frequency $\omega$ is obtained by performing normal mode calculations for a single atom in an ideal metal slab, which are performed for each of the mobile layers. This yields the frequencies that are employed in the aforementioned Boltzmann distributions. Furthermore, the theoretically computed lattice constant is expanded by an experimentally obtained lattice expansion coefficient in order to account for the thermal expansion from $T_s = 0\,\mathrm{K}$ to the simulated surface temperature[87]. Several differently-initialized slabs are generated using the aforementioned procedure, which are then equilibrated for 2 ps by doing NVE (constant number of particles, volume and total energy) MD runs with an 1 fs time step and allowing the atoms in the mobile layers to move in all directions. The configurations (positions and velocities) in the last picosecond of these simulations are then used to form a pool of initial conditions. Typically, the atoms in the bottom layer(s) of the metal slab are kept fixed in their ideal positions during the calculations.

### 2.4.2 Molecular Beam

Molecular beam experiments are typically simulated by reproducing both the rovibrational state and the velocity distributions present in the experiment. The rovibrational state population $F_{\nu_i,j}$ of a molecule in the molecular beam is given by

$$F_{\nu,j}\left(T_\mathrm{n}\right) = \frac{2j+1}{Z\left(T_\mathrm{n}\right)} \exp\left(-\frac{\left(E_{\nu_i,0} - E_{0,0}\right)}{k_\mathrm{B} T_\mathrm{vib}}\right) \exp\left(-\frac{\left(E_{\nu_i,j} - E_{\nu_i,0}\right)}{k_\mathrm{B} T_\mathrm{rot}}\right), \tag{2.42}$$

where $Z\left(T_\mathrm{n}\right)$ is the partition function and $T_\mathrm{n}$, $T_\mathrm{vib}$, and $T_\mathrm{rot}$ are the nozzle, vibrational, and rotational temperatures, respectively.

Throughout this thesis, molecules are treated as either a linear rigid rotor (in this thesis HCl and $O_2$) or an oblate symmetric top rigid rotor (in this thesis $NH_3$, $CHD_3$, and, after application of an appropriate approximation, $CH_3OH$) for the sampling of the rotational state[88]. Here, the two quantum numbers $J$ and $M$ define the orientation of the angular momentum vector in a space fixed reference frame, where the $Z$ axis (i.e., the vector normal to the surface plane) is fixed in space. $J$ corresponds to the total rotational angular momentum $\mathbf{L}$ and $M$ to its projection on the $Z$ axis:

$$|\mathbf{L}| = \hbar\sqrt{J\left(J+1\right)}, \tag{2.43}$$

$$\mathbf{L}_Z = \hbar M. \tag{2.44}$$

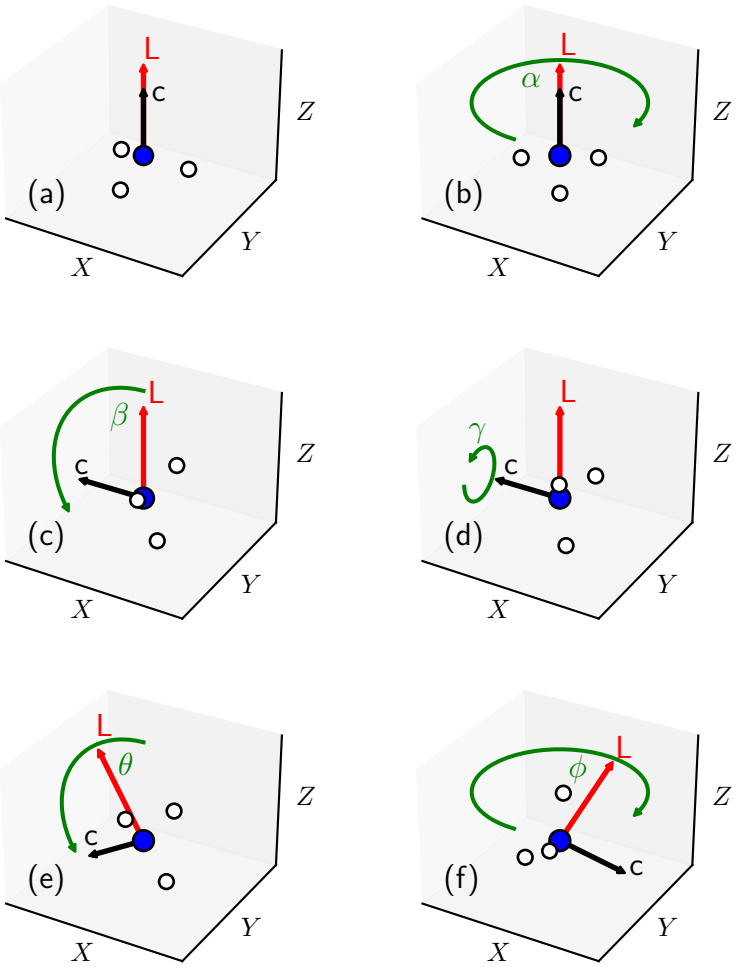


FIGURE 2.1: (a) The initial orientation of an oblate symmetric top molecule (black arrow), here an ammonia molecule, and its angular momentum vector (red arrow) are fixed with respect to the space fixed reference frame ($XYZ$). (b-f) Same as panel a, but indicating the rotations (green arrows) of the molecular orientation and the angular momentum vectors required according to the quantum numbers $J$, $M$, and $K$. See the text for the meaning of the rotations.

Additionally, the quantum number $K$ fixes the orientation of the figure axis (here, taken to be the principle axis **C**) with respect to the angular momentum vector:

$$\mathbf{L}_{\text{figure}} = \hbar K, \tag{2.45}$$

Furthermore, $M$ and $K$ are integers in the range $[-J, +J]$. Note that $K$ is only relevant for the symmetric top rotor as the linear rotor obviously does not rotate about its intramolecular (figure) axis. The orientation of the molecule and the angular momentum vector can then be obtained as follows. First, both the figure axis **C** of the molecule and the angular momentum vector **L** are oriented parallel to the surface normal $Z$ (Figure 2.1a). Then, the figure axis is rotated by the $\alpha$, $\beta$, and $\gamma$ Euler angles using the ZYZ convention (Figures 2.1b-d, respectively). The rotations by the $\alpha$ and $\gamma$ angles are both in the interval $[0, 2\pi]$. The angle $\beta$ is computed from $J$ and $K$ as follows:

$$\cos(\beta) = \frac{K}{\sqrt{J(J+1)}}. \tag{2.46}$$

Finally, both the figure axis and the angular momentum vector are rotated by the spherical $\theta$ and $\phi$ angles (Figures 2.1e,f, respectively) about the $Z$ axis. The polar angle $\theta$ is computed from $J$ and $M$ as follows:

$$\cos(\theta) = \frac{M}{\sqrt{J(J+1)}}. \tag{2.47}$$

The azimuthal angle is in the interval $\phi \in [0, 2\pi]$ (or $\phi \in [0, 2\pi/2n]$ when taking into account the $C_{nv}$ symmetry of the molecule). If $J = 0$, one can simply obtain the molecular orientation by randomly sampling $\beta$ from a $\sin(\beta)$ distribution, and $\alpha$ and $\gamma$ from the $[0, 2\pi]$ interval, where the angular momentum is zero (i.e., $|\mathbf{L}| = 0$).

The vibrational state of a molecule is obtained by performing a microcanonical sampling for each of its vibrational modes. An 1D QCT simulation is performed along each mode, from which the initial displacement (compared to the equilibrium geometry) and concomitant velocity is selected by randomly sampling the phase of the vibration. Subsequently, the sum of displacements and velocities are added to the atomic positions and velocities, while also taking into account the orientation of the molecule given by its rotational state.

The center of mass (COM) velocity $v$ of the molecule in the molecular beam is given by the flux weighted probability distribution[89, 90]

$$f(v; T_{\text{n}})\, \mathrm{d}v = A v^3 e^{-(v-v_0)^2/\alpha^2}\, \mathrm{d}v, \tag{2.48}$$

where $A$ is a normalization constant, $v_0$ is the stream velocity, and $\alpha$ is the width of the distribution.

In order to keep DFT calculations tractable, often a smaller vacuum distance is employed than what would be considered to be converged. This is typically the case when a Van der Waals correlation DF is employed since the Van der Waals interactions cause long-range interaction between the molecule and metal surface. The interaction energy, defined as $E_{\mathrm{R}} = E_{\mathrm{b}}^{\text{small vacuum}} - E_{\mathrm{b}}^{\text{large vacuum}}$, at a large distance between the molecule and the metal surface is only dependent on the molecular coordinate $Z$, i.e., the distance between the molecule and the metal surface. To correct for the artificial increase in barrier height due to the interaction energy, this energy is added to the initial velocity ($v = \sqrt{2E/M_{\text{molecule}}}$) of the molecule, similar to what has been done and justified in previous work[55].

Finally, the molecule's center of mass is placed halfway between the two periodic slabs (i.e., the value of $Z$ is half of the vacuum distance) and samples randomly the entire unit cell in $X$ and $Y$.

## 2.5 Calculation of Observables

Here, the computation of several observables in MD simulations is discussed. First, three different possible outcomes have been defined for MD simulations, i.e., scattering, reaction and trapping. A molecule is considered to be scattered when the value of $Z$ for the center of mass is larger than half of the vacuum distance (i.e., larger than as in the initial conditions) and its momentum is pointing away from the surface. Furthermore, throughout this thesis, the molecule is considered to be reacted if one of the intramolecular bonds is either longer than 3 Å, or longer than 2 Å for 100 fs, unless noted otherwise. Finally, if none of the aforementioned results are obtained within the simulation time, the molecule is considered to be trapped.

The reaction probability $p$ is defined as $p = N_{\mathrm{r}}/N_{\mathrm{i}}$, where $N_{\mathrm{r}}$ and $N_{\mathrm{i}}$ are the amount of reacted and initial trajectories, respectively. Similarly, the sticking probability $S_0$, which includes contributions of both reacted and trapped trajectories, is defined as $S_0 = (N_{\mathrm{r}} + N_{\mathrm{t}})/N_{\mathrm{i}}$, where $N_{\mathrm{t}}$ is the amount of trapped trajectories. The standard deviation of probabilities is $\sigma = \sqrt{p(1-p)/N}$, where $N$ is the sample size. However, for probabilities that are 0 or 100% the one-sided interval $\alpha^{1/N}$ is used[91], where $\alpha$ is the confidence interval.

Vibrational ($\chi_v$) and rotational ($\chi_J$) efficacies indicate how effective it is to promote the reaction by increasing the vibrational and rotational energy compared to increasing the translational energy. This efficacy is computed as

follows:

$$\chi_\nu(J, \langle E_\mathrm{i} \rangle) = \frac{\langle E_\mathrm{i}(\nu = 0, J; S_0) \rangle - \langle E_\mathrm{i}(\nu, J; S_0) \rangle}{E_\mathrm{vib}(\nu, J) - E_\mathrm{vib}(\nu = 0, J)}, \tag{2.49}$$

$$\chi_J(\nu, \langle E_\mathrm{i} \rangle) = \frac{\langle E_\mathrm{i}(\nu, J = 0; S_0) \rangle - \langle E_\mathrm{i}(\nu, J; S_0) \rangle}{E_\mathrm{rot}(\nu, J) - E_\mathrm{rot}(\nu, J = 0)}, \tag{2.50}$$

where it is assumed that $S_0$ is a bijective or invertible function, i.e., only one value of $E_\mathrm{i}$ corresponds to a particular value of $S_0$. This will usually be true as $S_0$ tends to be a monotonically increasing function of $E_\mathrm{i}$.

The energy transfer $E_\mathrm{T}$ from the molecule to the metal surface is defined as

$$E_\mathrm{T} = (V_\mathrm{i} + K_\mathrm{i}) - (V_\mathrm{f} + K_\mathrm{f}), \tag{2.51}$$

where $V$ and $K$ are the potential electronic and kinetic energy of the molecule, respectively, at the initial (i) and final (f) time steps of the scattered trajectories. The hard sphere Baule model[92] is often used to provide a rough prediction of the energy transfer, where the mass ratio between the molecule and the surface atom plays a large role in the energy transfer. This energy transfer is described by

$$E_\mathrm{T} = \frac{4\mu \cos^2 \gamma}{(1+\mu)^2} \langle E_\mathrm{i} \rangle, \tag{2.52}$$

where $\mu = m/M$ ($m$ is the mass of the projectile and $M$ is the mass of a surface atom), $\gamma$ is the angle between the velocity vector of the molecule and the line connecting the centers of the hard spheres of the molecule and surface atom at impact, and $\langle E_\mathrm{i} \rangle$ is the average incidence energy. In general, it is observed that the lower the surface atom mass is, the higher the energy transfer is from the molecule to the surface atoms due to the masses of the molecule and the surface atom being more similar. Typically, the Baule model is actually taken as an upper limit by treating the collision as a head-on collision ($\gamma = 0$), from which one obtains the well-known Baule limit

$$E_\mathrm{T} = \frac{4\mu}{(1+\mu)^2} \langle E_\mathrm{i} \rangle. \tag{2.53}$$

However, when an empirical average for the $\gamma$ angle distribution is used, in what here is called the refined Baule model, the following equation for the average energy transfer is obtained[93]:

$$\langle E_\mathrm{T} \rangle = \frac{2.4\mu}{(1+\mu)^2} \langle E_\mathrm{i} \rangle. \tag{2.54}$$

## References


(1) Born, M.; Oppenheimer, R. Zur Quantentheorie Der Molekeln. *Ann. Phys.* **1927**, *389*, 457–484, DOI: 10.1002/andp.19273892002.

(2) Hohenberg, P.; Kohn, W. Inhomogeneous Electron Gas. *Phys. Rev.* **1964**, *136*, B864–B871, DOI: 10.1103/PhysRev.136.B864.

(3) Kohn, W.; Sham, L. J. Self-Consistent Equations Including Exchange and Correlation Effects. *Phys. Rev.* **1965**, *140*, A1133–A1138, DOI: 10.1103/PhysRev.140.A1133.

(4) Perdew, J. P.; Schmidt, K. Jacob's Ladder of Density Functional Approximations for the Exchange-Correlation Energy. *AIP Conf. Proc.* **2001**, *577*, 1–20, DOI: 10.1063/1.1390175.

(5) Dirac, P. a. M. Note on Exchange Phenomena in the Thomas Atom. *Math. Proc. Camb. Philos. Soc.* **1930**, *26*, 376–385, DOI: 10.1017/S0305004100016108.

(6) Alder, B.; Ceperly, D. Ground State of the Electron Gas by a Stochastic Method. *Phys. Rev. Lett.* **1980**, *45*, 566–569, DOI: 10.1103/PhysRevLett.45.566.

(7) Vosko, S. H.; Wilk, L.; Nusair, M. Accurate Spin-Dependent Electron Liquid Correlation Energies for Local Spin Density Calculations: A Critical Analysis. *Can. J. Phys.* **1980**, *58*, 1200–1211, DOI: 10.1139/p80-159.

(8) Perdew, J. P.; Zunger, A. Self-Interaction Correction to Density-Functional Approximations for Many-Electron Systems. *Phys. Rev. B* **1981**, *23*, 5048–5079, DOI: 10.1103/PhysRevB.23.5048.

(9) Perdew, J. P.; Wang, Y. Accurate and Simple Analytic Representation of the Electron-Gas Correlation Energy. *Phys. Rev. B* **1992**, *45*, 13244–13249, DOI: 10.1103/PhysRevB.45.13244.

(10) Chachiyo, T. Communication: Simple and Accurate Uniform Electron Gas Correlation Energy for the Full Range of Densities. *J. Chem. Phys.* **2016**, *145*, 021101, DOI: 10.1063/1.4958669.

(11) Peverati, R.; Truhlar, D. G. Exchange–Correlation Functional with Good Accuracy for Both Structural and Energetic Properties While Depending Only on the Density and Its Gradient. *J. Chem. Theory Comput.* **2012**, *8*, 2310–2319, DOI: 10.1021/ct3002656.

(12) Peverati, R.; Truhlar, D. G. Quest for a Universal Density Functional: The Accuracy of Density Functionals across a Broad Spectrum of Databases in Chemistry and Physics. *Philos. Trans. R. Soc. A* **2014**, *372*, 20120476, DOI: 10.1098/rsta.2012.0476.

(13) Perdew, J. P.; Burke, K.; Ernzerhof, M. Generalized Gradient Approximation Made Simple. *Phys. Rev. Lett.* **1996**, *77*, 3865–3868, DOI: 10.1103/PhysRevLett.77.3865.

(14) Hammer, B.; Hansen, L. B.; Nørskov, J. K. Improved Adsorption Energetics within Density-Functional Theory Using Revised Perdew-Burke-Ernzerhof Functionals. *Phys. Rev. B* **1999**, *59*, 7413–7421, DOI: 10.1103/PhysRevB.59.7413.

(15) Lieb, E. H.; Oxford, S. Improved Lower Bound on the Indirect Coulomb Energy. *Int. J. Quantum Chem.* **1981**, *19*, 427–439, DOI: 10.1002/qua.560190306.

(16) Odashima, M. M.; Capelle, K.; Trickey, S. B. Tightened Lieb-Oxford Bound for Systems of Fixed Particle Number. *J. Chem. Theory Comput.* **2009**, *5*, 798–807, DOI: 10.1021/ct8005634.

(17) Seidl, M.; Vuckovic, S.; Gori-Giorgi, P. Challenging the Lieb–Oxford Bound in a Systematic Way. *Mol. Phys.* **2016**, *114*, 1076–1085, DOI: 10.1080/00268976.2015.1136440.

(18) Perdew, J. P.; Ruzsinszky, A.; Csonka, G. I.; Vydrov, O. A.; Scuseria, G. E.; Constantin, L. A.; Zhou, X.; Burke, K. Perdew et al. Reply: *Phys. Rev. Lett.* **2008**, *101*, 239702, DOI: 10.1103/PhysRevLett.101.239702.

(19) Śmiga, S.; Constantin, L. A.; Della Sala, F.; Fabiano, E. The Role of the Reduced Laplacian Renormalization in the Kinetic Energy Functional Development. *Computation* **2019**, *7*, 65, DOI: 10.3390/computation7040065.

(20) Perdew, J. P.; Constantin, L. A. Laplacian-Level Density Functionals for the Kinetic Energy Density and Exchange-Correlation Energy. *Phys. Rev. B* **2007**, *75*, 155109, DOI: 10.1103/PhysRevB.75.155109.

(21) Sun, J.; Xiao, B.; Ruzsinszky, A. Communication: Effect of the Orbital-Overlap Dependence in the Meta Generalized Gradient Approximation. *J. Chem. Phys.* **2012**, *137*, 051101, DOI: 10.1063/1.4742312.

(22) Perdew, J. P.; Ruzsinszky, A.; Csonka, G. I.; Vydrov, O. A.; Scuseria, G. E.; Constantin, L. A.; Zhou, X.; Burke, K. Restoring the Density-Gradient Expansion for Exchange in Solids and Surfaces. *Phys. Rev. Lett.* **2008**, *100*, 136406, DOI: 10.1103/PhysRevLett.100.136406.

(23) Antoniewicz, P. R.; Kleinman, L. Kohn-Sham Exchange Potential Exact to First Order in $\rho(K \rightarrow)/\rho_0$. *Phys. Rev. B* **1985**, *31*, 6779–6781, DOI: 10.1103/PhysRevB.31.6779.

(24) Perdew, J. P.; Ruzsinszky, A.; Constantin, L. A.; Sun, J.; Csonka, G. I. Some Fundamental Issues in Ground-State Density Functional Theory: A Guide for the Perplexed. *J. Chem. Theory Comput.* **2009**, *5*, 902–908, DOI: 10.1021/ct800531s.

(25) Tao, J.; Perdew, J. P.; Staroverov, V. N.; Scuseria, G. E. Climbing the Density Functional Ladder: Nonempirical Meta–Generalized Gradient Approximation Designed for Molecules and Solids. *Phys. Rev. Lett.* **2003**, *91*, 146401, DOI: 10.1103/PhysRevLett.91.146401.

(26) Perdew, J. P.; Ruzsinszky, A.; Csonka, G. I.; Constantin, L. A.; Sun, J. Workhorse Semilocal Density Functional for Condensed Matter Physics and Quantum Chemistry. *Phys. Rev. Lett.* **2009**, *103*, 026403, DOI: 10.1103/PhysRevLett.103.026403.

(27) Perdew, J. P.; Ruzsinszky, A.; Tao, J.; Staroverov, V. N.; Scuseria, G. E.; Csonka, G. I. Prescription for the Design and Selection of Density Functional Approximations: More Constraint Satisfaction with Fewer Fits. *J. Chem. Phys.* **2005**, *123*, 062201, DOI: 10.1063/1.1904565.

(28) Stephens, P. J.; Devlin, F. J.; Chabalowski, C. F.; Frisch, M. J. Ab Initio Calculation of Vibrational Absorption and Circular Dichroism Spectra Using Density Functional Force Fields. *J. Phys. Chem.* **1994**, *98*, 11623–11627, DOI: 10.1021/j100096a001.

(29) Adamo, C.; Barone, V. Toward Reliable Density Functional Methods without Adjustable Parameters: The PBE0 Model. *J. Chem. Phys.* **1999**, *110*, 6158–6170, DOI: 10.1063/1.478522.

(30) Leininger, T.; Stoll, H.; Werner, H.-J.; Savin, A. Combining Long-Range Configuration Interaction with Short-Range Density Functionals. *Chem. Phys. Lett.* **1997**, *275*, 151–160, DOI: 10.1016/S0009-2614(97)00758-6.

(31) Iikura, H.; Tsuneda, T.; Yanai, T.; Hirao, K. A Long-Range Correction Scheme for Generalized-Gradient-Approximation Exchange Functionals. *J. Chem. Phys.* **2001**, *115*, 3540–3544, DOI: 10.1063/1.1383587.

(32) Heyd, J.; Scuseria, G. E.; Ernzerhof, M. Hybrid Functionals Based on a Screened Coulomb Potential. *J. Chem. Phys.* **2003**, *118*, 8207–8215, DOI: 10.1063/1.1564060.

(33) Krukau, A. V.; Vydrov, O. A.; Izmaylov, A. F.; Scuseria, G. E. Influence of the Exchange Screening Parameter on the Performance of Screened Hybrid Functionals. *J. Chem. Phys.* **2006**, *125*, 224106, DOI: 10.1063/1.2404663.

(34) Baer, R.; Livshits, E.; Salzner, U. Tuned Range-Separated Hybrids in Density Functional Theory. *Annu. Rev. Phys. Chem.* **2010**, *61*, 85–109, DOI: 10.1146/annurev.physchem.012809.103321.

(35) Refaely-Abramson, S.; Sharifzadeh, S.; Govind, N.; Autschbach, J.; Neaton, J. B.; Baer, R.; Kronik, L. Quasiparticle Spectra from a Nonempirical Optimally Tuned Range-Separated Hybrid Density Functional. *Phys. Rev. Lett.* **2012**, *109*, 226405, DOI: 10.1103/PhysRevLett.109.226405.

(36) Karolewski, A.; Kronik, L.; Kümmel, S. Using Optimally Tuned Range Separated Hybrid Functionals in Ground-State Calculations: Consequences and Caveats. *J. Chem. Phys.* **2013**, *138*, 204115, DOI: 10.1063/1.4807325.

(37) Tamblyn, I.; Refaely-Abramson, S.; Neaton, J. B.; Kronik, L. Simultaneous Determination of Structures, Vibrations, and Frontier Orbital Energies from a Self-Consistent Range-Separated Hybrid Functional. *J. Phys. Chem. Lett.* **2014**, *5*, 2734–2741, DOI: 10.1021/jz5010939.

(38) Brémond, É.; Pérez-Jiménez, Á. J.; Sancho-García, J. C.; Adamo, C. Range-Separated Hybrid Density Functionals Made Simple. *J. Chem. Phys.* **2019**, *150*, 201102, DOI: 10.1063/1.5097164.

(39) Brémond, É.; Pérez-Jiménez, Á. J.; Sancho-García, J. C.; Adamo, C. Range-Separated Hybrid and Double-Hybrid Density Functionals: A Quest for the Determination of the Range-Separation Parameter. *J. Chem. Phys.* **2020**, *152*, 244124, DOI: 10.1063/5.0010976.

(40) Handy, N. C.; Cohen, A. J. A Dynamical Correlation Functional. *J. Chem. Phys.* **2002**, *116*, 5411–5418, DOI: 10.1063/1.1457432.

(41) Grimme, S. Accurate description of van der Waals complexes by density functional theory including empirical corrections. *J. Comput. Chem.* **2004**, *25*, 1463–1473, DOI: 10.1002/jcc.20078.

(42) Grimme, S.; Antony, J.; Ehrlich, S.; Krieg, H. A Consistent and Accurate Ab Initio Parametrization of Density Functional Dispersion Correction (DFT-D) for the 94 Elements H-Pu. *J. Chem. Phys.* **2010**, *132*, 154104, DOI: 10.1063/1.3382344.

(43) Tkatchenko, A.; Scheffler, M. Accurate Molecular Van Der Waals Interactions from Ground-State Electron Density and Free-Atom Reference Data. *Phys. Rev. Lett.* **2009**, *102*, 073005, DOI: 10.1103/PhysRevLett.102.073005.

(44) Dion, M.; Rydberg, H.; Schröder, E.; Langreth, D. C.; Lundqvist, B. I. Van Der Waals Density Functional for General Geometries. *Phys. Rev. Lett.* **2004**, *92*, 246401, DOI: 10.1103/PhysRevLett.92.246401.

(45) Lee, K.; Murray, É. D.; Kong, L.; Lundqvist, B. I.; Langreth, D. C. Higher-Accuracy van Der Waals Density Functional. *Phys. Rev. B* **2010**, *82*, 081101(R), DOI: 10.1103/PhysRevB.82.081101.

(46) Chakraborty, D.; Berland, K.; Thonhauser, T. Next-Generation Non-Local van Der Waals Density Functional. *J. Chem. Theory Comput.* **2020**, *16*, 5893–5911, DOI: 10.1021/acs.jctc.0c00471.

(47) Vydrov, O. A.; Van Voorhis, T. Nonlocal van Der Waals Density Functional: The Simpler the Better. *J. Chem. Phys.* **2010**, *133*, 244103, DOI: 10.1063/1.3521275.

(48) Sabatini, R.; Gorni, T.; de Gironcoli, S. Nonlocal van Der Waals Density Functional Made Simple and Efficient. *Phys. Rev. B* **2013**, *87*, 041108(R), DOI: 10.1103/PhysRevB.87.041108.

(49) Román-Pérez, G.; Soler, J. M. Efficient Implementation of a van Der Waals Density Functional: Application to Double-Wall Carbon Nanotubes. *Phys. Rev. Lett.* **2009**, *103*, 096102, DOI: 10.1103/PhysRevLett.103.096102.

(50) Ernzerhof, M. Construction of the Adiabatic Connection. *Chem. Phys. Lett.* **1996**, *263*, 499–506, DOI: 10.1016/S0009-2614(96)01225-0.

(51) Toulouse, J.; Sharkas, K.; Brémond, E.; Adamo, C. Communication: Rationale for a New Class of Double-Hybrid Approximations in Density-Functional Theory. *J. Chem. Phys.* **2011**, *135*, 101102, DOI: 10.1063/1.3640019.

(52) Chakraborty, A.; Zhao, Y.; Lin, H.; Truhlar, D. G. Combined Valence Bond-Molecular Mechanics Potential-Energy Surface and Direct Dynamics Study of Rate Constants and Kinetic Isotope Effects for the H + $C_2H_6$ Reaction. *J. Chem. Phys.* **2006**, *124*, 044315, DOI: 10.1063/1.2132276.

(53) Chuang, Y.-Y.; Radhakrishnan, M. L.; Fast, P. L.; Cramer, C. J.; Truhlar, D. G. Direct Dynamics for Free Radical Kinetics in Solution: Solvent Effect on the Rate Constant for the Reaction of Methanol with Atomic Hydrogen. *J. Phys. Chem. A* **1999**, *103*, 4893–4909, DOI: 10.1021/jp990969d.

(54) Díaz, C.; Pijper, E.; Olsen, R. A.; Busnengo, H. F.; Auerbach, D. J.; Kroes, G. J. Chemically Accurate Simulation of a Prototypical Surface Reaction: $H_2$ Dissociation on Cu(111). *Science* **2009**, *326*, 832–834, DOI: 10.1126/science.1178722.

(55) Nattino, F.; Migliorini, D.; Kroes, G.-J.; Dombrowski, E.; High, E. A.; Killelea, D. R.; Utz, A. L. Chemically Accurate Simulation of a Polyatomic Molecule-Metal Surface Reaction. *J. Phys. Chem. Lett.* **2016**, *7*, 2402–2406, DOI: 10.1021/acs.jpclett.6b01022.

(56) Migliorini, D.; Chadwick, H.; Nattino, F.; Gutiérrez-González, A.; Dombrowski, E.; High, E. A.; Guo, H.; Utz, A. L.; Jackson, B.; Beck, R. D.; Kroes, G.-J. Surface Reaction Barriometry: Methane Dissociation on Flat and Stepped Transition-Metal Surfaces. *J. Phys. Chem. Lett.* **2017**, *8*, 4177–4182, DOI: 10.1021/acs.jpclett.7b01905.

(57) Bloch, F. Über die Quantenmechanik der Elektronen in Kristallgittern. *Z. Physik* **1929**, *52*, 555–600, DOI: 10.1007/BF01339455.

(58) In *Heterogeneous Materials: Nonlinear and Breakdown Properties and Atomistic Modeling*, Sahimi, M., Ed.; Interdisciplinary Applied Mathematics; Springer: New York, NY, 2003, pp 455–548, DOI: 10.1007/0-387-21704-5_10.

(59) Blöchl, P. E. Projector Augmented-Wave Method. *Phys. Rev. B* **1994**, *50*, 17953–17979, DOI: 10.1103/PhysRevB.50.17953.

(60) Kresse, G.; Joubert, D. From Ultrasoft Pseudopotentials to the Projector Augmented-Wave Method. *Phys. Rev. B* **1999**, *59*, 1758–1775, DOI: 10.1103/PhysRevB.59.1758.

(61) Kresse, G.; Hafner, J. Ab Initio Molecular-Dynamics Simulation of the Liquid-Metal–Amorphous-Semiconductor Transition in Germanium. *Phys. Rev. B* **1994**, *49*, 14251–14269, DOI: 10.1103/PhysRevB.49.14251.

(62) Kresse, G.; Hafner, J. Ab Initio Molecular Dynamics for Liquid Metals. *Phys. Rev. B* **1993**, *47*, 558–561, DOI: 10.1103/PhysRevB.47.558.

(63) Kresse, G.; Furthmüller, J. Efficient Iterative Schemes for Ab Initio Total-Energy Calculations Using a Plane-Wave Basis Set. *Phys. Rev. B* **1996**, *54*, 11169–11186, DOI: 10.1103/PhysRevB.54.11169.

(64) Kresse, G.; Furthmüller, J. Efficiency of Ab-Initio Total Energy Calculations for Metals and Semiconductors Using a Plane-Wave Basis Set. *Comput. Mater. Sci.* **1996**, *6*, 15–50, DOI: 10.1016/0927-0256(96)00008-0.

(65) Bulirsch, R.; Stoer, J. Numerical Treatment of Ordinary Differential Equations by Extrapolation Methods. *Numer. Math.* **1966**, *8*, 1–13, DOI: 10.1007/BF02165234.

(66) Stoer, J.; Bulirsch, R. In *Introduction to Numerical Analysis*, Stoer, J., Bulirsch, R., Eds.; Springer: New York, NY, 1980, pp 244–313, DOI: 10.1007/978-1-4757-5592-3_5.

(67) Busnengo, H. F.; Salin, A.; Dong, W. Representation of the 6D Potential Energy Surface for a Diatomic Molecule near a Solid Surface. *J. Chem. Phys.* **2000**, *112*, 7641–7651, DOI: 10.1063/1.481377.

(68) Verlet, L. Computer "Experiments" on Classical Fluids. I. Thermodynamical Properties of Lennard-Jones Molecules. *Phys. Rev.* **1967**, *159*, 98–103, DOI: 10.1103/PhysRev.159.98.

(69) Behler, J.; Parrinello, M. Generalized Neural-Network Representation of High-Dimensional Potential-Energy Surfaces. *Phys. Rev. Lett.* **2007**, *98*, 146401, DOI: 10.1103/PhysRevLett.98.146401.

(70) Plimpton, S. Fast Parallel Algorithms for Short-Range Molecular Dynamics. *J. Comput. Phys.* **1995**, *117*, 1–19, DOI: 10.1006/jcph.1995.1039.

(71) Singraber, A.; Behler, J.; Dellago, C. Library-Based LAMMPS Implementation of High-Dimensional Neural Network Potentials. *J. Chem. Theory Comput.* **2019**, *15*, 1827–1840, DOI: 10.1021/acs.jctc.8b00770.

(72) Deuflhard, P. Order and Stepsize Control in Extrapolation Methods. *Numer. Math.* **1983**, *41*, 399–422, DOI: 10.1007/BF01418332.

(73) Deuflhard, P. Recent Progress in Extrapolation Methods for Ordinary Differential Equations. *SIAM Rev.* **1985**, *27*, 505–535, DOI: 10.1137/1027140.

(74) Jackson, B.; Nattino, F.; Kroes, G.-J. Dissociative Chemisorption of Methane on Metal Surfaces: Tests of Dynamical Assumptions Using Quantum Models and Ab Initio Molecular Dynamics. *J. Chem. Phys.* **2014**, *141*, 054102, DOI: 10.1063/1.4891327.

(75) Liu, Q.; Zhang, L.; Li, Y.; Jiang, B. Ring Polymer Molecular Dynamics in Gas–Surface Reactions: Inclusion of Quantum Effects Made Simple. *J. Phys. Chem. Lett.* **2019**, *10*, 7475–7481, DOI: 10.1021/acs.jpclett.9b02570.

(76) Rodríguez-Fernández, A.; Bonnet, L.; Crespos, C.; Larrégaray, P.; Díez Muiño, R. When Classical Trajectories Get to Quantum Accuracy: The Scattering of $H_2$ on Pd(111). *J. Phys. Chem. Lett.* **2019**, *10*, 7629–7635, DOI: 10.1021/acs.jpclett.9b02742.

(77) Ghassemi, E. N.; Smeets, E. W. F.; Somers, M. F.; Kroes, G.-J.; Groot, I. M. N.; Juurlink, L. B. F.; Füchsel, G. Transferability of the Specific Reaction Parameter Density Functional for $H_2$ + Pt(111) to $H_2$ + Pt(211). *J. Phys. Chem. C* **2019**, *123*, 2973–2986, DOI: 10.1021/acs.jpcc.8b11018.

(78) Kroes, G.-J. Six-Dimensional Quantum Dynamics of Dissociative Chemisorption of $H_2$ on Metal Surfaces. *Prog. Surf. Sci.* **1999**, *60*, 1–85, DOI: 10.1016/S0079-6816(99)00006-4.

(79) Kroes, G.-J.; Somers, M. F. Six-Dimensional Dynamics of Dissociative Chemisorption of $H_2$ on Metal Surfaces. *J. Theor. Comput. Chem.* **2005**, *04*, 493–581, DOI: 10.1142/S0219633605001647.

(80) Craig, I. R.; Manolopoulos, D. E. Quantum Statistics and Classical Mechanics: Real Time Correlation Functions from Ring Polymer Molecular Dynamics. *J. Chem. Phys.* **2004**, *121*, 3368–3373, DOI: 10.1063/1.1777575.

(81) Habershon, S.; Manolopoulos, D. E.; Markland, T. E.; Miller, T. F. Ring-Polymer Molecular Dynamics: Quantum Effects in Chemical Dynamics from Classical Trajectories in an Extended Phase Space. *Annu. Rev. Phys. Chem.* **2013**, *64*, 387–413, DOI: 10.1146/annurev-physchem-040412-110122.

(82) Behler, J. Atom-Centered Symmetry Functions for Constructing High-Dimensional Neural Network Potentials. *J. Chem. Phys.* **2011**, *134*, 074106, DOI: 10.1063/1.3553717.

(83) Behler, J. Representing Potential Energy Surfaces by High-Dimensional Neural Network Potentials. *J. Phys.: Condens. Matter* **2014**, *26*, 183001, DOI: 10.1088/0953-8984/26/18/183001.

(84) Shakouri, K.; Behler, J.; Meyer, J.; Kroes, G.-J. Accurate Neural Network Description of Surface Phonons in Reactive Gas–Surface Dynamics: $N_2$ + Ru(0001). *J. Phys. Chem. Lett.* **2017**, *8*, 2131–2136, DOI: 10.1021/acs.jpclett.7b00784.

(85) Shakouri, K.; Behler, J.; Meyer, J.; Kroes, G.-J. Analysis of Energy Dissipation Channels in a Benchmark System of Activated Dissociation: $N_2$ on Ru(0001). *J. Phys. Chem. C* **2018**, *122*, 23470–23480, DOI: 10.1021/acs.jpcc.8b06729.

(86) Nattino, F.; Díaz, C.; Jackson, B.; Kroes, G.-J. Effect of Surface Motion on the Rotational Quadrupole Alignment Parameter of $D_2$ Reacting on Cu(111). *Phys. Rev. Lett.* **2012**, *108*, 236104, DOI: 10.1103/PhysRevLett.108.236104.

(87) Mondal, A.; Wijzenbroek, M.; Bonfanti, M.; Díaz, C.; Kroes, G.-J. Thermal Lattice Expansion Effect on Reactive Scattering of $H_2$ from Cu(111) at $T_s$ = 925 K. *J. Phys. Chem. A* **2013**, *117*, 8770–8781, DOI: 10.1021/jp4042183.

(88) Brink, D.; Satchler, G., *Angular Momentum*, 2nd ed.; Oxford University Press: 1968; 87 pp.

(89) Auerbach, D. J. In *Atomic and Molecular Beam Methods*, Scoles, G., Ed.; Oxford University Press: 1988; Vol. 1, pp 362–379.

(90) Michelsen, H. A.; Auerbach, D. J. A Critical Examination of Data on the Dissociative Adsorption and Associative Desorption of Hydrogen at Copper Surfaces. *J. Chem. Phys.* **1991**, *94*, 7502–7520, DOI: 10.1063/1.460182.

(91) Louis, T. A. Confidence Intervals for a Binomial Parameter after Observing No Successes. *Am. Stat.* **1981**, *35*, 154–154, DOI: 10.1080/00031305.1981.10479337.

(92) Baule, B. Theoretische Behandlung Der Erscheinungen in Verdünnten Gasen. *Ann. Phys.* **1914**, *349*, 145–176, DOI: 10.1002/andp.19143490908.

(93) Goodman, F. O.; Wachman, H. Y. *Formula for Thermal Accommodation Coefficient*; 66-1; Cambridge, Massachusetts: M.I.T. Fluid Dynamics Research, 1966, DOI: 10.21236/ad0631007.

# Chapter 3

# Closing the Gap Between Experiment and Theory: Reactive Scattering of HCl from Au(111

This chapter is based on Gerrits, N.; Geweke, J.; Smeets, E. W. F.; Voss, J.; Wodtke, A. M.; Kroes, G.-J. Closing the Gap Between Experiment and Theory: Reactive Scattering of HCl from Au(111). *J. Phys. Chem. C* **2020**, *124*, 15944–15960, DOI: 10.1021/acs.jpcc.0c03756

## Abstract

Accurate simulation of molecules reacting on metal surfaces, which can help in improving heterogeneous catalysts, remains out of reach for several reactions. For example, a large disagreement between theory and experiment for HCl reacting on Au(111) still remains, despite many efforts. In this chapter, the dissociative chemisorption of HCl on Au(111) is investigated with a recently developed density functional (MS-RPBEl) at the meta-generalized gradient approximation level and a high-dimensional neural network potential. Computed sticking probabilities are compared with a new experimental data set that results from a recent re-examination of the data. A considerably improved agreement between experiment and theory is obtained, although theory still overestimates experimental sticking probabilities by a factor 2 - 7 at the highest incidence energy. Computed and measured vibrational transition probabilities are also in improved agreement. Several dynamical effects such as angular steering and energy transfer from the molecule to the surface are found to play an important role.

## 3.1 Introduction

Accurate first-principles simulation of the reaction of molecules on metal surfaces is of vital importance to understanding heterogeneous catalysis. Such simulations are continuously subject to improvements. For example, the development of high-dimensional neural network potentials (HD-NNP) allows molecular dynamics (MD) calculations on sticking while fully including the movement of surface atoms with computational costs orders of magnitude lower than those of Born-Oppenheimer molecular dynamics (BOMD)[1–5]. Developments in density functional (DF) design[6–14] and wave function theory with DFT embedding[15, 16] have led to an increasing number of surface reactions being described accurately. Furthermore, including the dissipative effect of electron-hole pair (ehp) excitations has enabled several accurate simulations that hitherto were impossible[17–22]. Nevertheless, many molecule-metal surface scattering processes[23] and reactions[5, 24–27] exist for which accurate simulations remain elusive.

One molecule-metal surface reaction of particular interest is the dissociative chemisorption of HCl on Au(111). Although a large body of both theoretical and experimental work has shrunk the gap between theory and experiment[2, 27–36], quantitative agreement between the two is still out of reach. Dynamics calculations based on DFT potentials or forces have consistently overestimated experimental sticking probabilities by more than an order of magnitude[2, 27, 30, 32, 34, 36]. Throughout the years, development in theory often resulted in a lowering of the reactivity of HCl + Au(111): Going from a relatively attractive DF like PBE[37] or PW91[38] towards a repulsive DF like RPBE[39] lowers the initial sticking probability[2, 34, 36]. Including Van der Waals correlation into the DF lowers the sticking probability even further[27]. Performing the MD with quasi-classical trajectories (QCT) or quantum dynamics (QD) appears to have little effect on the sticking probability[36]. Switching from a frozen to a mobile thermal surface is observed to lower the sticking probability, albeit only marginally[2, 27, 34]. Finally, treating the ehp excitations with the local density friction approximation (LDFA)[40] likewise has a small effect on the sticking probability[2, 27, 34]. Even so, in the most recent calculations theory still overestimated the sticking probability by more than an order of magnitude[2, 27].

Not only the sticking probability is subject of debate from a theoretical point of view, the vibrationally (in)elastic scattering of HCl on Au(111) seems to be described inaccurately as well: No matter which model and method was employed, vibrational transition probabilities are systematically overestimated by theory[2, 27]. Enabling ehp excitation within the LDFA decreases transition

probabilities by only a small amount[2]. A potential problem arises from the prevalent use of QCT as the rovibrational states are not quantized during MD when employing QCT. Therefore, final rovibrational states need to be binned in order to obtain quantized rovibrational state populations. Although it is observed that Gaussian binning lowers the excitation probabilities compared to histogram binning, it remains to be seen what kind of binning method is the most appropriate one. For example, for $H_2$ + Pd(111) a single energy based Gaussian binning method, where also the diffraction quantum numbers are binned, performs comparatively well[41]. However, violation of Bohr's quantization does not present a problem as many rovibrational states are available for HCl + Au(111), and thus histogram binning should perform accurately as well[42]. An adiabatic correction was also employed for $H_2$ + Pd(111)[41, 43], but for HCl + Au(111) such a correction would not make sense since many adiabatic paths are possible[43]. Finally, for elevated surface temperatures it is necessary to take into account surface atom motion[2, 27].

The transition and sticking probabilities measured by experiment are also subject to uncertainty[27, 31, 33, 34]. An error was found in an initial report of $\nu = 0 \rightarrow \nu = 1$ inelastic scattering probabilities[44]. Revised probabilities are however now available with small uncertainty[31]. As will become clear, it is also necessary to re-investigate the experimental sticking probabilities, of which accurate measurement poses considerable challenges. For this reason, a comparison is made here with experimental results on sticking that result from a re-examination[45] of the original data[33] in the hope of more accurately characterizing the uncertainty of the measured sticking probabilities, thereby better clarifying the true magnitude of the discrepancy between experiment and theory.

As discussed above, many improvements have been made by theory and experiment for the description of the sticking and vibrational transition probabilities of HCl on Au(111). Nevertheless, the current state of affairs remains unsatisfactory. Therefore, in this chapter the focus is on improving the employed DF in the hope of thereby improving the aforementioned observables in MD simulations. Recently, a meta generalized gradient approximation (MGGA) DF has been developed, the "made simple" RPBE-like (MS-RPBEl) DF, which can describe both the molecule and the surface accurately, as well as the interaction between the two[14]. The MS-RPBEl DF yields chemically accurate (errors smaller than 1 kcal/mol or 4.2 kJ/mol) sticking probabilities for $H_2$ + Cu(111) and almost chemically accurate results for $H_2$ + Ag(111)[14]. Interestingly, for $H_2$ + Cu(111) the MS-RPBEl DF outperforms even state-of-the-art MGGA DFs like the revTPSS DF[46] by a large margin[14]. The MS-RPBEl DF is able to describe both the metallic and molecular orbital regimes by

relying on a switching function that depends on the kinetic energy density. The overall functional form is derived from the RPBE DF[39]. To limit the self-interaction error (SIE) in the molecular orbital regime, which is fundamental to DFT[47], the hydrogen atom is considered as the extreme case where any amount of electronic interaction constitutes an SIE. The analytical solution to the H charge density and SIE is used to parametrize the single-electron limit of the meta-GGA, and correctly reproducing this limit has been shown to improve surface reaction energetics also for multi-electron adsorbates[14, 48]. For the metallic density regime on the other hand, the low order gradient expansion of the exchange energy of the homogeneous electron gas is reproduced, ensuring good description of lattice constants and elastic properties. Since the MS-RPBEl DF has provided promising initial results and contains fundamental advantages that might be of importance for the reaction of HCl on Au(111), this DF will be tested on HCl + Au(111) in this chapter. Additionally, in order to be able to perform MD calculations with surface atom motion modeled explicitly an HD-NNP will be employed, allowing observables with low probability to be obtained with relatively small statistical errors.

To summarize, in this chapter the newly developed MS-RPBEl DF is tested for vibrationally inelastic scattering and sticking of HCl on Au(111). As will be shown, a considerably improved agreement between theory and experiment is obtained, although discrepancies still remain. Furthermore, several aspects of the reaction dynamics, such as the influence of surface atom motion, energy transfer, vibrational efficacies, the bobsled effect, and site specificity, are discussed as well.

## 3.2 Method

### 3.2.1 Theory

For the electronic structure (density functional theory, DFT) calculations the Vienna Ab-initio Simulation Package (VASP version 5.4.4)[49–53] is used. The "made simple" revised Perdew, Burke and Ernzerhof (MS-RPBEl) meta-GGA exchange-correlation DF is used, which has been introduced in Ref. [14]. The design of this DF is based on the MS philosophy underlying earlier DFs of this kind[54, 55]. The first Brillouin zone is sampled by a $\Gamma$-centered $8 \times 8 \times 1$ $k$-point grid and the plane wave kinetic energy cutoff is 600 eV. Moreover, the core electrons have been represented with the projector augmented wave (PAW) method[53, 56]. The surface is modeled using a 4 layer $(3 \times 3)$ supercell, where the top three layers have been relaxed in the $Z$ direction and a vacuum distance of 15 Å is used between the slabs. The bulk optimized

TABLE 3.1: Beam parameters from Ref. [29] that describe the simulated HCl velocity distributions. The stream energy $E_0$, stream velocity $v_0$, and width parameter $\alpha$ were determined through time-of-flight measurements. The nozzle temperature was assumed to be room temperature.

| $T_n$ (K) | $\langle E_i \rangle$ (kJ/mol) | $E_0$ (kJ/mol) | $v_0$ (m/s) | $\alpha$ (m/s) |
|---|---|---|---|---|
| 300 | 27 | 27 | 1210 | 52 |
| 300 | 31 | 31 | 1297 | 60 |
| 300 | 43 | 43 | 1542 | 67 |
| 300 | 50 | 51 | 1665 | 48 |
| 300 | 75 | 75 | 2031 | 114 |
| 300 | 94 | 94 | 2276 | 98 |
| 300 | 122 | 123 | 2601 | 81 |

lattice constant is 4.092 Å, which is in good agreement with the experimental value of 4.078 Å[57]. Furthermore, the outward interlayer relaxation of the top two layers is 3.0%, which is in reasonable agreement with the experimental value of 1.5%[58]. Note that the interlayer relaxation is not well converged, but this does not affect the results presented in this chapter considerably (see Section 3.A). In order to simulate a surface temperature of 170 K, the lattice constant obtained from energy minimization of bulk Au is multiplied with a thermal expansion coefficient of 1.0014, as has been done in Refs. [34] and [27]. First-order Methfessel-Paxton smearing[59] with a width parameter of 0.2 eV has been employed. The aforementioned computational setup is confirmed to yield a barrier height that is converged with respect to the input parameters to within chemical accuracy (1 kcal/mol, or 4.2 kJ/mol), as shown in Section 3.A.

The transition state (TS) is obtained with the dimer method[60–63] as implemented in the VASP Transition State Tools (VTST) package[64], and is confirmed to be a first-order saddle point. Forces along the degrees of freedom are converged to within 5 meV/Å, where only HCl is relaxed in all its six degrees of freedom and the surface atoms are kept fixed in their ideal positions.

The initial conditions of the HCl molecules are generated in the same way as in Ref. [34] (see also Section 2.4.2), which is summarized here. The center of mass (COM) velocity $v$ of HCl is given by the flux weighted probability distribution

$$f\left(v; T_n\right)\, \mathrm{d}v = A v^3 e^{-(v-v_0)^2/\alpha^2}\, \mathrm{d}v, \tag{3.1}$$

where $T_n$ is the nozzle temperature, $A$ is a normalization constant, $v_0 = \sqrt{2E_0/M_{\mathrm{HCl}}}$ is the stream velocity, and $\alpha$ is the width of the distribution. The

TABLE 3.2: Same as Table 3.1 but from Ref. [33].

| $T_n$ (K) | $\langle E_i \rangle$ (kJ/mol) | $E_0$ (kJ/mol) | $v_0$ (m/s) | $\alpha$ (m/s) |
|---|---|---|---|---|
| 296 | 91 | 90 | 2219 | 158 |
| 400 | 114 | 110 | 2456 | 245 |
| 500 | 124 | 120 | 2562 | 207 |
| 620 | 150 | 144 | 2808 | 292 |
| 740 | 174 | 167 | 3026 | 323 |
| 910 | 205 | 196 | 3278 | 364 |
| 1060 | 247 | 238 | 3616 | 371 |

rovibrational state population $F_{\nu,j}$ is given by

$$F_{\nu,j}(T_n) = \frac{2j+1}{Z(T_n)} e^{-(E_{\nu,0}-E_{0,0})/k_B T_{vib}} e^{-(E_{\nu,j}-E_{\nu,0})/k_B T_{rot}}, \tag{3.2}$$

where $Z(T_n)$ is the partition function, $T_{vib} = T_n$, and $T_{rot} = -181.1 + 0.648 T_n$[34]. All incidence conditions are normal to the surface (i.e., $v_X = v_Y = 0$). The beam parameters describing the velocity and rovibrational state distributions are obtained from Refs. [29] and [33], and are summarized in Tables 3.1 and 3.2. In general, the parameters of Tables 3.1 and 3.2 are used when investigating vibrational transition and sticking probabilities (and their related observables), respectively. When the parameters of both Tables are employed due to the need of describing a large incidence energy range, Table 3.1 is used up to 94 kJ/mol and Table 3.2 is used from 114 kJ/mol. The initial thermal distortions and velocities of the surface atoms are sampled from 50 slabs, yielding 50 000 initial surface configurations. Additional details about the surface atom motion sampling procedure can be found in Section 2.4.1.

Molecular dynamics calculations have been performed using LAMMPS[65, 66]. All trajectories are propagated up to 3 ps using a time step of 0.4 fs, or until HCl either scattered ($Z_{COM} > 7.5$ Å) or reacted ($r > 3$ Å or $r > 2$ Å for 100 fs). The time step size is deemed adequate as the energy conservation error is quite good for the vibrational ground state (1 - 2 meV) and reasonably good for the $\nu = 2$ vibrationally excited HCl (5 - 10 meV) during the trajectories. A smaller time step would decrease the energy conservation error, but it has been checked that the choice of time step size does not affect the reaction and vibrational transition probabilities. For each sticking data point 10 000 trajectories have been simulated. Where 10 000 trajectories yield too large statistical errors in the desired observables, e.g., when scattering to specific rovibrational states was investigated, 100 000 trajectories have been run.

TABLE 3.3: Parameters used to generate configurations in the DFT calculations to generate the training and testing data set for the HD-NNP.

| Surface atom motion | $Z_{\mathrm{Cl}}$ (Å) | $r$ (Å) | $N$ |
|---|---|---|---|
| No | 2.5-8.0 | 1.0-1.6 | 6000 |
| No | 1.5-2.5 | 1.0-3.2 | 2500 |
| Yes | 2.5-8.0 | 1.0-1.6 | 6000 |
| Yes | 1.5-2.5 | 1.0-3.2 | 15 000 |

The vibrational and rotational action ($x$ and $J$) of scattering trajectories are given by

$$x = \frac{1}{2\pi} \oint p_r \, \mathrm{d}r - \frac{1}{2} = \frac{1}{2\pi} \int_0^\tau p_r \dot{r} \, \mathrm{d}\tau - \frac{1}{2}, \tag{3.3}$$

$$J = -\frac{1}{2} + \sqrt{\frac{1}{4} + L_{\mathrm{f}}^2}, \tag{3.4}$$

and

$$L_{\mathrm{f}} = p_\theta^2 + \frac{p_\phi^2}{\sin^2(\theta)}, \tag{3.5}$$

where $r$ is the HCl bond length and $p_r$ its conjugate momentum, and $p_\theta$ and $p_\phi$ are the momenta conjugate to the $\theta$ and $\phi$ angles of HCl, which will be discussed later. In the vibrational action integral (Eq. 3.3) the vibrational momentum $p_r$ is evaluated over a single vibrational period $\tau$. Furthermore, the concomitant quantum number is obtained by rounding the action to the nearest integer (so-called standard or histogram binning).

Previous studies show that ehp excitation, when modeled with electronic friction at the local density friction approximation level, has only a marginal effect on the sticking and the vibrationally (in)elastic scattering of HCl on Au(111)[2, 27, 34]. Moreover, since a fairly large discrepancy persists between theory and experiment, as will be shown even with an improved setup, in this chapter the effect of ehp excitation is neglected, and instead the effect of the exchange-correlation DF is focused on.

To develop the HD-NNP, the Behler-Parrinello approach[67, 68] is used. In this approach, the total energy is constructed as a sum of atomic contributions that are dependent on their chemical local environment and are described by many-body atom-centered symmetry functions[69]. In total, 29 500 DFT calculations were performed, of which 90% were used to train and 10% to test the HD-NNP. The configurations that were used in the DFT calculations to generate the data set are summarized in Table 3.3. 8500 configurations were generated that excluded surface atom motion (i.e., for the ideal frozen

surface) and 21 000 configurations were generated including surface atom motion. Surface atom motion was included by displacing surface atoms according to a harmonic oscillator model, as described in Section 2.4.1. $Z_{Cl}$ and $r$ were sampled randomly in the ranges described in Table 3.3, and the other degrees of freedom of HCl ($X_{Cl}$, $Y_{Cl}$, $\theta$ and $\phi$) were also sampled randomly, with the only constraint that $Z_H > 0.5$ Å. Finally, it was confirmed that the occurrence of extrapolation errors due to missing structures in the data set was sufficiently low that it had a negligible effect on the sticking probability. The RMSE of the energies and forces of the training data set is 1.0 kJ/mol and 2.3 kJ/mol/Å, respectively, which is well within chemical accuracy for the energies. Additional details regarding the fitting accuracy are provided in Section 3.A. For the neural network, two hidden layers are used, each with 15 nodes. The training has been carried out using the RuNNer code[70–72]. The employed symmetry functions are described in Section 2.3.2 and the concomitant parameters have been obtained following the procedure of Ref. [73] and are provided in Section 3.B.

### 3.2.2 Experiment

This section describes the experimental work that was done on HCl + Au(111). It was not part of this thesis, but is included here to allow a better assessment of the comparison between experiment and theory. The experimental apparatus has been described in detail before[33, 44] as were the methods to determine the initial sticking probabilities[33]. Thus, after briefly recalling the most important experimental details here, further on the focus is on the changes in data *analysis*.

Pulsed molecular beams of 4% HCl seeded in $H_2$ were directed at a Au(111) single-crystal (orientation accuracy better than 0.1°, purity 99.999%, MaTecK) with a surface temperature of $T_s = 170$ K held in an ultra-high vacuum chamber with base pressure $\sim 2 \times 10^{-10}$ Torr. A wide range of translational energies, $\langle E_i \rangle = 91 - 247$ kJ/mol, was obtained by mounting a ~20 mm long SiC tube to the front of the home-built, solenoid-based valve and resistively heating it to as high as $T_n = 1140$ K. Resonance-enhanced multiphoton ionization is used to quantify the ro-vibrational population distributions which also varied with $T_n$ according to Eq. 3.2. During exposure, the $H_2$ pressure rise in the UHV chamber was recorded with a mass spectrometer (SRS RGA-200) from which the dose of HCl molecules $\phi_{HCl}$ was derived *via* the previously determined HCl/$H_2$ pressure ratio in the gas mix. After dosing, the chlorine coverage, $\Theta_{Cl}$, was derived using an Auger electron spectrometer (Physical

Electronics Φ15-255G) by measuring the ratio of the peak heights at 181 eV (Cl) and 239 eV (Au).

## 3.3 Results

### 3.3.1 Experimental Sticking Probabilities

This section describes the re-examination of the experimental data that was performed by Jan Geweke[45]. It was not part of this thesis, but is included here to allow a better assessment of the comparison between experiment and theory.

Initial sticking probabilities $S_0$ are determined from the dependency of the chlorine coverage $\Theta_{\mathrm{Cl}}$ on the applied HCl dose $\phi_{\mathrm{HCl}}$, both of which have recently been re-analyzed. In general, the incident dose is calculated as:

$$\phi_{\mathrm{HCl}} = \frac{N_{\mathrm{H_2}}}{A_{\mathrm{MB}}} \times \frac{c_{\mathrm{HCl}}}{c_{\mathrm{H_2}}} \times f_{\mathrm{e}} \times \frac{1}{N_{\mathrm{ML}}} \tag{3.6}$$

Here, $N_{\mathrm{H_2}}$ is the number of incident $H_2$ molecules, $A_{\mathrm{MB}}$ is the cross-sectional area of the incident molecular beam, $c_{\mathrm{HCl}}$ and $c_{\mathrm{H_2}}$ are the concentrations in the prepared gas mixture, and $f_{\mathrm{e}}$ is the correction factor for the hydrodynamic enrichment of the heavier HCl molecules. Due to the higher mass of HCl relative to that of $H_2$, the concentration of HCl molecules in the center of the molecular beam is up to ten times higher in the UHV chamber than in the prepared gas mixture (see the SI of Ref. [33]). Furthermore, $N_{\mathrm{ML}}$ is the areal number density of Cl atoms per monolayer (ML) on the unreconstructed Au(111) surface (assuming one ML coverage corresponds to one Cl atom per every surface top layer Au atom). Compared to a previously published analysis [33], its value was more accurately determined to be $1.39 \times 10^{15}\,\mathrm{cm^{-2}ML^{-1}}$ instead of $1 \times 10^{15}\,\mathrm{cm^{-2}ML^{-1}}$, in accordance with values reported by Kastanas and Koel [74].

The chlorine coverage resulting from a controlled HCl dose, $\Theta_{\mathrm{Cl}}$, is calculated from the atomic concentration of Cl on the surface, $C_{\mathrm{Cl}}$, relative to the saturation coverage. The latter can be obtained from the Auger peak heights $I_{\mathrm{Cl}}$ and $I_{\mathrm{Au}}$ for Cl and Au, which can be combined to obtain the peak-height ratio $P_{\mathrm{r}} = I_{\mathrm{Cl}}/I_{\mathrm{Au}}$, and the corresponding Auger sensitivities $S_{\mathrm{Au}}$ and $S_{\mathrm{Cl}}$ [33]:

$$C_{\mathrm{Cl}} = \frac{I_{\mathrm{Cl}}}{S_{\mathrm{Cl}}} \Bigg/ \left( \frac{I_{\mathrm{Cl}}}{S_{\mathrm{Cl}}} + \frac{I_{\mathrm{Au}}}{S_{\mathrm{Au}}} \right) = \frac{P_{\mathrm{r}} \times S_{\mathrm{Au}}}{P_{\mathrm{r}} \times S_{\mathrm{Au}} + S_{\mathrm{Cl}}}. \tag{3.7}$$

The chlorine coverage is then obtained from

$$\Theta_{\mathrm{Cl}} = \frac{C_{\mathrm{Cl}}}{C_{\mathrm{Cl,sat.}}}. \tag{3.8}$$

Re-evaluating the literature for the saturation value of $P_{\mathrm{r}}$ [75] and the element-specific Auger sensitivity factors [76] reveals the saturation value for the atomic concentration of Cl on Au(111) ($C_{\mathrm{Cl,sat.}}$) to be $0.13\,\mathrm{ML}^{-1}$, which is slightly lower than the one ($0.2\,\mathrm{ML}^{-1}$) used in the previous analysis [33]. As a result the new measured $S_0$ values presented here have, to a good approximation, increased by a factor $0.2/0.13 = 1.54$. For this work, the possible influence of diffusion of Cl atoms on the gold surface has also been considered. This could dilute the chlorine concentration in the center of the surface spot which was hit by the molecular beam, resulting in a radial gradient of $C_{\mathrm{Cl}}$.

Resulting coverage *vs.* dose data is shown in Figure 3.1 for two representative conditions chosen to cover high and low incidence energies. Note that Figures 3.1a and 3.1b are representative in the sense that they show the amount of scatter that may occur in the measurement of coverage vs. HCl exposure, but not in the sense that the scatter is systematically higher at higher incidence energies. To obtain initial sticking probabilities, the data are fitted with a bounded growth model according to Eq. 3.9. Assuming an asymptotic saturation coverage of $\Theta_{\mathrm{Cl}} = 1\,\mathrm{ML}$, the only fit parameter is $S_0$ which corresponds to the initial slopes of the dashed lines in Figure 3.1.

$$\Theta_{\mathrm{Cl}} = 1 - \exp(-S_0 \times \phi_{\mathrm{HCl}}) \tag{3.9}$$

Two further systematic corrections to the data upon which the derivation of $S_0$ is based are needed. First, additional calibration experiments have shown that in comparison with an ion gauge, the mass spectrometer overestimated the $H_2$ partial pressure, which is integrated to obtain $N_{H_2}$, by a factor of $f_{\mathrm{IG}} = 1.8$. That is, the dose determined with the mass spectrometer needs to be decreased by the same factor. Unfortunately, $f_{\mathrm{IG}}$ was determined with an ion gauge that itself was not calibrated against any known standard which limits the correction's accuracy[1]. Second, as reported in the SI of Ref. [33], the derived Cl-surface coverage exhibited a surface temperature dependence: for high $T_{\mathrm{s}}$ the resulting $\Theta_{\mathrm{Cl}}$ was reduced. More specifically, the coverage derived at the lowest accessible temperature, $T_{\mathrm{s}} = 80\,\mathrm{K}$, was a factor of $f_{T_{\mathrm{s}}} = 1.4$ higher than that obtained at 170 K, the temperature used for the reactive

[1]See the SRS user manual for the IGC100 ion gauge controller for an overview of ion gauge accuracy and stability, available at their website under https://www.thinksrs.com/products/igc100.html.

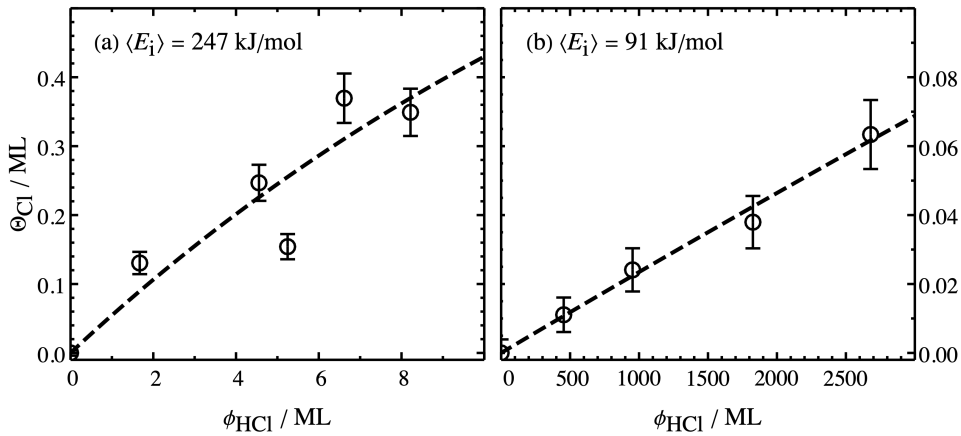


FIGURE 3.1: Representative plots of the Cl coverage $\Theta_{Cl}$ on the surface *vs.* the applied dose $\phi_{HCl}$ for $\langle E_i \rangle = 247\,kJ/mol$ (a) and $\langle E_i \rangle = 91\,kJ/mol$ (b). Open symbols denote the data calculated according to Eqs. 3.6 and 3.8, the dashed lines show fits according to Eq. 3.9.

dosing experiments. These differences are attributed to additional sticking of undissociated HCl by a physisorption interaction possible at 80 K but not at 170 K and to changes in the competitive kinetics for the associative desorption of $H_2$ and HCl with changes in surface temperature.

Despite the fact that the combined effect of these two corrections is not clear, the systematic direction of their influence on $S_0$ is; hence, lower and upper limits to the dissociative sticking probabilities can be derived. If both $f_{IG}$ and $f_{T_s}$ corrections are applied, an upper limit to the sticking probability is obtained. If both corrections are ignored, a lower limit is obtained. This is shown in Figure 3.2 for the sticking probability of HCl on Au(111) as a function of mean translational incidence energy. There, the two limits comprise all statistical and systematical uncertainties resulting from the experiments and the analysis. These also include the uncertainties from the fitting process due to the aforementioned scatter in the coverage vs. HCl exposure data.

### 3.3.2 Potential Energy Surface

In Figure 3.3 the minimum barrier geometry obtained with the MS-RPBEl DF and the spherical coordinate system used throughout this chapter are depicted: The distance between the Cl atom and the surface $Z_{Cl}$, the HCl bond length $r$, and the polar and azimuthal angles of the HCl bond $\theta$ and $\phi$ with respect to the surface normal and lateral skewed vector $u$, respectively. The HCl bond

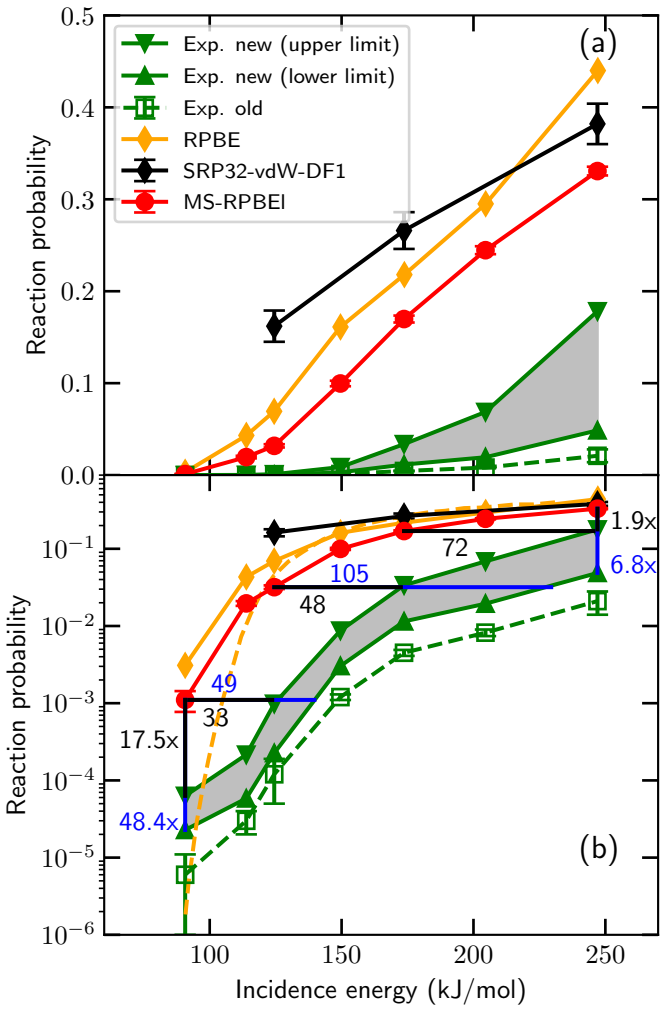


FIGURE 3.2: (a) Sticking probability of HCl on Au(111) for normal incidence and $T_s = 170$ K. The open green squares connected with a dashed line indicate the experimental results from Ref. [33] and the closed green triangles indicate the new experimental results, where the gray area indicates the area between the lower and upper limits. The theoretical results obtained with the SRP32-vdW-DF1[27], RPBE[2] and MS-RPBEl DFs are indicated by black diamonds, orange diamonds, and red circles, respectively. The error bars represent 68% confidence intervals. (b) Same as panel a, but using a logarithmic scale. The solid orange line with diamonds and the dashed orange line without diamonds indicate results for the RPBE DF employing QCT and QD, respectively. The horizontal and vertical black (blue) lines indicate the difference between the computed and measured results for the newly determined upper (lower) limit.

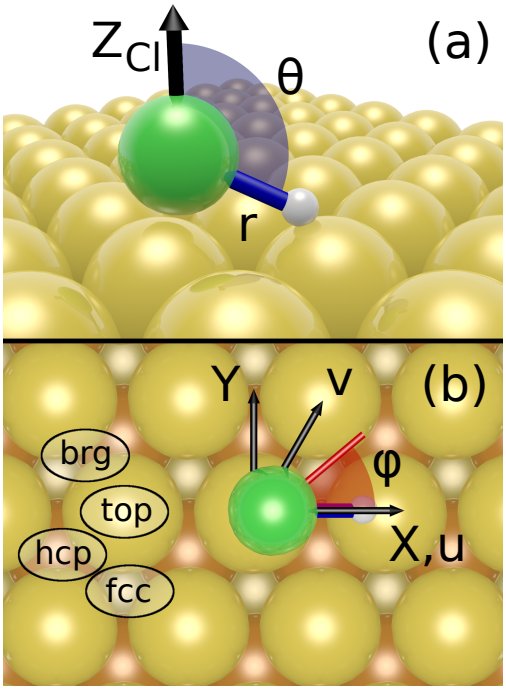


FIGURE 3.3: Minimum barrier geometry of HCl on Au(111) using the MS-RPBEl DF. The Cl atom is indicated in green, the H atom in white, and the Au atoms in gold, orange and gray (first, second and third layer, respectively). The spherical coordinate system used throughout this chapter is depicted: (a) the distance between the Cl atom and the surface $Z_{\mathrm{Cl}}$, the HCl bond length $r$, and the polar angle $\theta$ giving the vector pointing from Cl to H makes with the surface normal; (b) the lateral coordinates $X$ and $Y$, the lateral skewed coordinates $u$ and $v$, and the azimuthal angle $\phi$, which defines the projection of the Cl to H vector on the surface. The lateral coordinates may refer to Cl or the COM. Note that for $\phi$ not the value for the barrier is depicted but an arbitrary value. The top, bridge (brg), and hcp and fcc hollow sites are indicated as well.

is defined as the vector going from the Cl atom to the H atom. Furthermore, the lateral coordinates $X$ and $Y$ indicate the $XY$ plane, where $X$ and $u$ are identical. The angle between the lateral skewed coordinates $u$ and $v$ is 60°. Since the interaction between HCl and the fcc and hcp sites is similar, they are also referred to as hollow sites throughout this chapter.

The minimum barrier geometries and heights computed with DFT using the MS-RPBEl, RPBE, RPBE-vdW-DF1 and SRP32-vdW-DF1 DFs are compared in Table 3.4. All barrier geometries are similar, except for the RPBE DF for which the COM is near the top2fcc site (i.e., the site midway between the top and fcc sites) and the HCl bond points towards the fcc site. The RPBE DF yields an earlier barrier ($r = 1.95$ Å) than the other DFs ($r \approx 2.2$ Å). Furthermore, RPBE yields for HCl a gas phase equilibrium bond length of 1.27 Å, whereas the other DFs yield a equilibrium bond length of 1.28 - 1.29 Å. The COM of the other barrier geometries is near the top site and the HCl bond points towards the bridge site. Several other GGA DFs incorporating the nonlocal Van der Waals correlation DF of Dion and co-workers (vdW-DF1)[77] have been tried as well and yield similar geometries, where only the barrier height is considerably affected[27]. Furthermore, the PBE DF yields a similar barrier geometry as RPBE but again different barrier heights are obtained[27]. Interestingly, the MS-RPBEl DF yields a similar geometry as the GGA-vdW-DF1 DFs, even though it is lacking Van der Waals correlation and for this reason might be expected to yield results more similar to the (R)PBE DFs. Moreover, with the MS-RPBEl DF one of the highest barrier heights so far is obtained, where to the best of our knowledge, with the DFs tested only with RPBE a slightly higher barrier height was obtained.

The barrier geometries and heights obtained from the HD-NNP fit to the MS-RPBEl data at several high symmetry sites are provided in Table 3.5, where $X_{\mathrm{Cl}}$ and $Y_{\mathrm{Cl}}$ are fixed above the high symmetry sites. Note that the small differences between Tables 3.4 and 3.5 for the minimum barrier obtained with DFT is due to excluding or including the lattice expansion corresponding to $T_{\mathrm{s}} = 170$ K, respectively. Moreover, the minimum barrier geometries and heights obtained with the HD-NNP are in excellent agreement with DFT. The order of the barrier heights is global $<$ bridge $<$ top $<$ hollow. It is also expected that the hollow site barrier is the highest on the basis of the location of the minimum barrier, which is located near the top site and for which the Cl-H bond points towards the bridge site. Furthermore, the geometry at the hollow sites is similar to the minimum barrier geometry, where the HCl also points towards a top site (see Figure 3.3). The bridge site geometry is also similar to the minimum barrier, with the only differences being that it is an earlier barrier (i.e., a smaller $r$ value) and the HCl bond is oriented towards the

TABLE 3.4: Minimum barrier geometry and height of HCl on Au(111) obtained with DFT using different DFs for $T_s = 0\,K$. The lateral skewed coordinates $u$ and $v$ of the center of mass (COM) is given in units of the surface lattice constant L.

| Density functional | $Z_{Cl}$ (Å) | $r$ (Å) | $\theta$ (°) | $\phi$ (°) | $COM_u$ [L] | $COM_v$ [L] | $E_b$ (kJ/mol) |
|---|---|---|---|---|---|---|---|
| MS-RPBEl | 2.43 | 2.18 | 115 | 1 | 0.145 | 0.023 | 100.6 |
| RPBE[34] | 2.44 | 1.95 | 135 | 30 | 0.328 | 0.164 | 101.3 |
| RPBE-vdW-DF1[27] | 2.45 | 2.20 | 115 | 0 | 0.199 | 0.016 | 78.9 |
| SRP32-vdW-DF1[27] | 2.43 | 2.22 | 114 | 0 | 0.197 | 0.026 | 62.1 |

TABLE 3.5: Barrier geometries and heights of HCl on Au(111) on different sites obtained from the HD-NNP fit to the MS-RPBEl data for $T_s = 170\,K$ (i.e., including the lattice expansion according to the surface temperature). The minimum barrier obtained directly from DFT is included as well. The lateral skewed coordinates $u$ and $v$ of the center of mass (COM) is given in units of the surface lattice constant L.

| Site | $Z_{Cl}$ (Å) | $r$ (Å) | $\theta$ (°) | $\phi$ (°) | $COM_u$ [L] | $COM_v$ [L] | $E_b$ (kJ/mol) |
|---|---|---|---|---|---|---|---|
| Global (DFT) | 2.45 | 2.08 | 117 | 0 | 0.117 | 0.009 | 100.4 |
| Global | 2.46 | 2.08 | 117 | 0 | 0.200 | 0.005 | 99.9 |
| Bridge | 2.39 | 1.96 | 119 | 30 | 0.509 | 0.509 | 109.3 |
| Top | 2.59 | 1.89 | 135 | 2 | 0.000 | 0.012 | 115.5 |
| Fcc | 2.42 | 2.20 | 113 | 90 | 0.322 | 0.356 | 128.0 |
| Hcp | 2.42 | 2.20 | 113 | 30 | 0.678 | 0.678 | 128.3 |

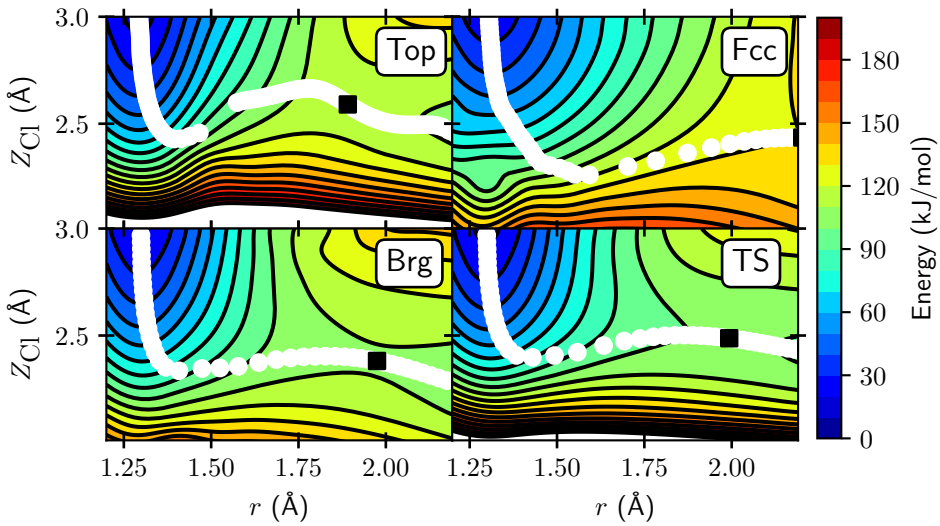


FIGURE 3.4: Elbow plots of HCl on Au(111) as a function of $Z_{Cl}$ and $r$ using the MS-RPBEl DF for the top, fcc and bridge sites, and the minimum TS. All other degrees of freedom are relaxed. Black contour lines are drawn at an interval of 10 kJ/mol between 0 and 200 kJ/mol. The white circles indicate the MEP in reduced dimensionality and the black square indicates the highest point along the MEP. Note that the break along the MEP for the top site is an artifact caused by the procedure employed to obtain the MEP (see Figure 3.D.1).

hcp site. Finally, the top site geometry is different in location, and length ($r$) and polar orientation ($\theta$) of the HCl bond compared to the minimum barrier, while the only similarity between the two being the azimuthal orientation ($\phi$).

Elbow plots corresponding to the aforementioned site specific and global minimum barrier geometries are shown in Figure 3.4. The procedure for obtaining the minimum energy path (MEP) is described in Section 3.D (see also Figure 3.D.1). In general, the barrier is late and high. Furthermore, most of the barriers seem to exhibit reasonable dynamical accessibility as the MEP typically does not make a sharp turn. However, the top site clearly is an exception as the MEP does not only make a sharp turn, but also goes up sharply in the $Z_{Cl}$ coordinate after the turn, leading to low dynamical accessibility of the minimum barrier at the top site. Moreover, it is quite possible that HCl would not follow the MEP's turn at the top site at all, but rather would go down further along the $Z_{Cl}$ coordinate. This would result in HCl hitting a large repulsive wall and subsequent scattering of the molecule,

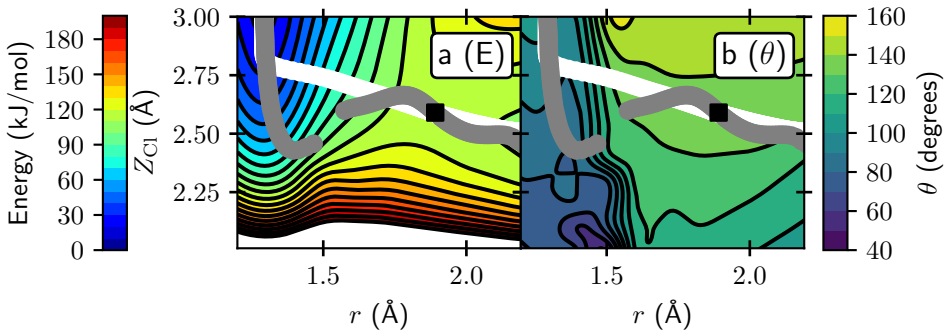


FIGURE 3.5: Elbow plots of HCl on Au(111) as a function of $Z_{Cl}$ and $r$ using the MS-RPBEl DF for the top site showing the energy (a, kJ/mol) and the $\theta$ angle (b, degrees). All degrees of freedom other than $Z_{Cl}$ and $r$ are relaxed. Black contour lines are drawn at an interval of 10 kJ/mol between 0 and 200 kJ/mol (energy) or at an interval of 10° between 40° and 160° ($\theta$). The grey circles indicate the MEP in reduced dimensionality and the black square indicates the highest point along the MEP. Note that the break along the MEP is an artifact caused by the procedure employed to obtain the MEP (see Figure 3.D.1). The white circles indicate the MEP as it is obtained conventionally using a steepest descent from the TS.

reducing the overall reactivity of the top site. In Figure 3.5 the MEP is also shown as it is obtained in a more conventional way, performing a steepest descent from the top site minimum barrier. Figure 3.5b suggests that HCl would need to undergo a considerable reorientation in the $\theta$ angle going from the gas phase to the TS, which could reduce the dynamical availability of the top site TS even further as large dynamical steering in the $\theta$ angle is required. Also, since the MEP leading to the TS (grey circles) is different from the steepest descent away from the TS (white circles), it is possible that desorption would follow a different path than dissociative chemisorption.

Electronic ($\beta$) and mechanical ($\alpha$) couplings of the minimum barrier of HCl on Au(111) computed using the MS-RPBEl DF are shown in Figure 3.6. The electronic coupling indicates the change in barrier height as a function of surface atom puckering, whereas mechanical coupling indicates the change in location, i.e., $Z_{Cl}$, as a function of surface atom puckering. The effect of puckering of the two top layer atoms nearest to the Cl and H atoms appears to be additive, i.e., the effect of the simultaneous puckering of the two multiple surface atoms nearest to Cl and H and the concomitant coupling parameters can be approximated by summing the contributions due to the puckering of the individual surface atoms. Furthermore, the surface atom near the H atom

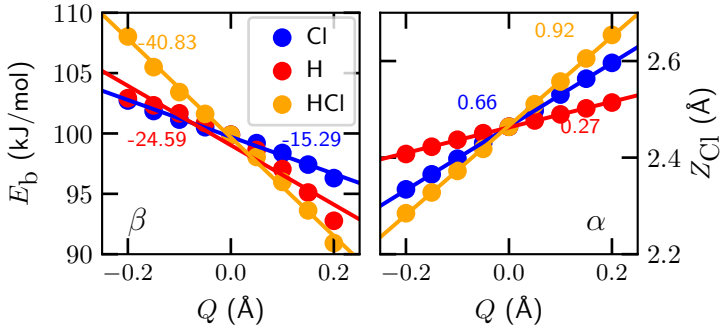


FIGURE 3.6: Electronic ($\beta$) and mechanical ($\alpha$) coupling at the minimum barrier of HCl on Au(111) using the MS-RPBEl DF. Variation of the barrier height $E_b$, and the distance of Cl to the surface $Z_{Cl}$, with the coordinate associated with the (simultaneous) motion(s) of the top layer surface atom(s) ($Q$) nearest to Cl, H, or both is indicated by the blue, red and orange circles, respectively. A positive value of Q indicates one atom or both atoms puckering out of the surface. The lines are linear regression fits to the data. The numbers in the plot indicate the electronic ($\beta$, kJ/mol/Å) and mechanical ($\alpha$) coupling parameters, which are obtained from the slope of the linear regression fits.

has a larger effect on the electronic coupling than the surface atom near the Cl atom, and vice versa for the mechanical coupling. The electronic coupling of HCl with the surface atom nearest to H is weaker by a factor 4.6 than that found in $CH_4$ + Ni(111) (112 kJ/mol/Å), while the mechanical coupling of HCl with the surface atom nearest to Cl is of similar magnitude as that in $CH_4$ + Ni(111)[78].

### 3.3.3 Sticking Probabilities Computed by Theory

In Figure 3.2a the sticking probabilities computed for normal incidence and $T_s = 170$ K with the MS-RPBEl DF are compared to both the old and new experimental sticking probabilities and are found to be in improved agreement. Nevertheless, a large discrepancy still remains, where the overestimation is a factor 2 to 7 at the highest incidence energy (see Figure 3.2b). Sticking probabilities previously obtained with the SRP32-vdW-DF1 and RPBE DFs are included as well, and these are higher than those obtained with the MS-RPBEl DF. The QCT and QD results sticking probabilities obtained with the RPBE DF in Ref. [2] are compared in Figure 3.2b. For incidence energies well above the minimum barrier height the QCT and QD results are in good

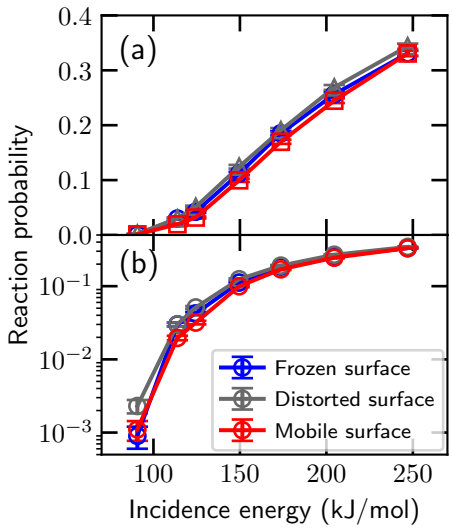


FIGURE 3.7: (a) Sticking probability of HCl on Au(111) using the MS-RPBEl DF for normal incidence and $T_s = 170\,K$. Results employing a frozen, thermally distorted, and mobile surface are indicated by the blue, gray, and red symbols, respectively. The error bars represent 68% confidence intervals. (b) Same as panel a, but using a logarithmic scale.

agreement, whereas for energies near and below the minimum barrier QD yields a considerably lower sticking probability than QCT, which is likely to be caused by ZPE leakage in the QCT. Moreover, for the experimental sticking probability only reacted, and not trapped, molecules were taken into account. In the calculations presented in this chapter, trapping hardly occurs and has a negligible effect on the sticking probability. Thus, sticking and reaction probabilities (i.e., the probabilities of dissociative chemisorption) can be considered to be the same.

The effect of surface atom motion on the sticking probability is investigated in Figure 3.7. In the frozen ideal surface model, both the energy transfer from the molecule to the surface phonons and the thermal variation in barrier heights (due to puckering of surface atoms[79]) are excluded. The difference between the frozen and the mobile surface results is minimal, the sticking probability of the frozen surface being at most one percentage point (0.01) higher than that of the mobile surface. As previously seen for $CHD_3$ + Cu(111)[3], the effects of energy transfer and variation in barrier heights on the sticking probability are opposite and can (partially) cancel each other. This can be seen by also comparing with results obtained using a thermally distorted surface, which model takes into account the thermal variation in barrier heights, i.e., electronic and mechanical coupling, in an approximate way. The thermally distorted surface yields sticking probabilities that are at most two percentage points higher than those obtained with the mobile surface. Thus, it can be con-

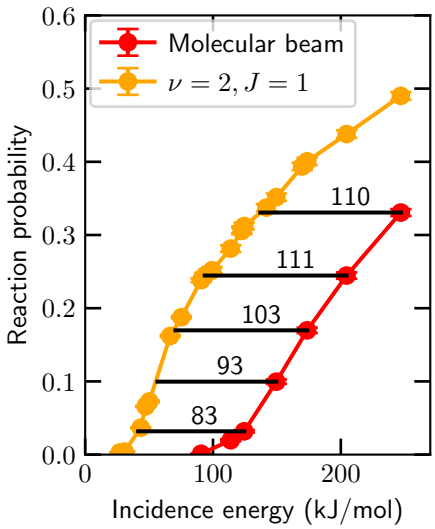


FIGURE 3.8: Sticking probability of HCl on Au(111) computed with the MS-RPBEl DF. Results for a molecular beam with the initial rovibrational population according to the nozzle temperature (see Table 3.2) are indicated by the red circles, and the $\nu = 2, j = 1$ initial state selected results are indicated by the orange circles. Distances between the two curves along the energy axis are indicated by the horizon black lines and numbers (kJ/mol). The error bars represent 68% confidence intervals.

cluded that in the present calculation not only the total effect of surface atom motion on the sticking is small, but also its important individual components (energy transfer, and thermal barrier height and location variation), as these components taken by themselves all have a small effect on the sticking probability. It is suspected that the effect of surface atom motion on the sticking of HCl on Au(111) is small because the electronic couplings between HCl and the surface atoms are small, i.e., they are smaller than for, e.g., $CH_4$ + Ni(111) by a factor 4.6[78] (see Section 3.3.2). Also note that the electronic coupling has a larger effect on sticking than mechanical coupling[78] and that the surface temperature is rather low (170 K).

The sticking probability of vibrationally excited ($\nu = 2, j = 1$) HCl is shown in Figure 3.8. The effect of vibrationally pre-exciting molecules on a reaction is typically described with the so-called vibrational efficacy $\eta(S_0)$, which is the shift in translational energy for a particular sticking probability $S_0$ divided by the increase in vibrational energy relative to the vibrational ground state. For $S_0 = 0.03$ the vibrational efficacy is 1.2 and for $S_0 = 0.33$ it is 1.6, i.e., vibrational energy is more efficient at promoting reaction than translational energy for both values of $S_0$. This may be expected from the barrier geometry previously discussed in Section 3.3.2 when one invokes the Polanyi rules[80] and assumes additionally that the molecule may slide off the MEP (i.e., the bobsled effect), especially for $\nu = 0$[3, 81–84]. According to Polanyi, if the barrier is late (as is the case for HCl + Au(111)), vibrational energy may be

more efficient in promoting reaction than translational energy. A similarly high value for the vibrational efficacy was previously found for $\nu_1 = 2$ $CHD_3$ + Cu(111)[3] (see also Chapter 8).

### 3.3.4 Dynamics During the Reaction Obtained with Theory

#### Vibrational Excitation

The transition probabilities for vibrationally inelastic scattering ($T_{\nu=1,j=1\rightarrow\nu=2}$ and $T_{\nu=0,j=0\rightarrow\nu=1}$) are shown in Figures 3.9a and b, respectively. In order to directly compare the computed results with the experimental results, the vibrational transition probabilities are defined as[31]

$$T_{\nu=i\rightarrow\nu=i+1} = \frac{N_{\nu=i+1}}{N_{\nu=i} + N_{\nu=i+1}}, \tag{3.10}$$

where $N_\nu$ is the number of molecules scattered to the $\nu$ vibrational state. Here a few observations regarding the theoretical results are discussed.

First, the agreement between experiment and theory is improved with the MS-RPBEl DF compared with the SRP32-vdW-DF1 and RPBE DFs. Second, both modeling the effect of ehp excitation and using Gaussian binning instead of histogram binning would lower the computed transition probabilities[2]. Unfortunately, it remains unclear whether ehp excitations play a major role for HCl + Au(111); to determine this, calculations modeling ehp excitation using orbital dependent friction (ODF)[22, 85–88] are needed as calculations with the LDFA predict only a small effect[2, 27, 34]. Several binning procedures exist, and the binning procedure selected can influence the results[41]. It remains unclear what method would be best suitable, but this is not the focus of the present work. Third, the surface temperature employed in the DF MD simulations using the SRP32-vdW-DF1 DF is considerably higher ($T_s = 575$ K) than used in this chapter ($T_s = 170$ K), but for this temperature range experimental results suggest that the effect of $T_s$ on the transition probability should be small[28, 31], i.e., transition probabilities increase only marginally with the surface temperature. Finally, though a difference between theory and experiment remains for absolute transition probabilities, the enhancement of the $\nu = 1, j = 1 \rightarrow \nu = 2$ channel relative to the $\nu = 0, j = 0 \rightarrow \nu = 1$ channel is approximately of the same order of magnitude.

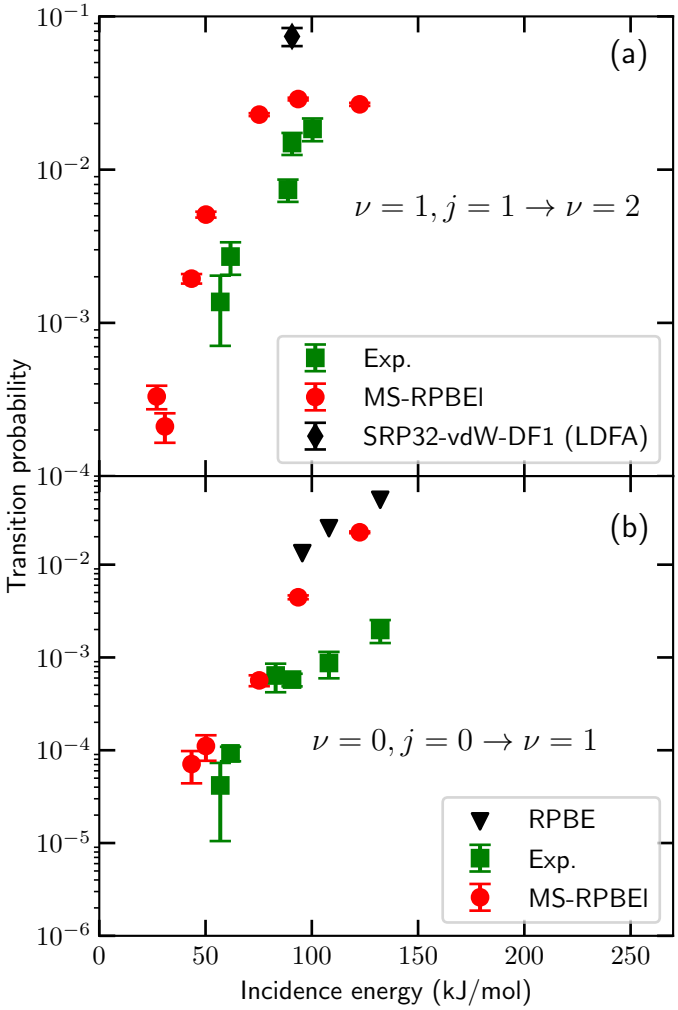


FIGURE 3.9: Vibrational transition probability computed with the MS-RPBEl DF (red circles) for $\nu = 1, j = 1 \rightarrow \nu = 2$ (a) and $\nu = 0, j = 0 \rightarrow \nu = 1$ (b) at $T_s = 170\,\mathrm{K}$ for normal incidence. Experimental results[31] and their error bars were taken for the lowest $T_s$ for which they are available; below this value of $T_s$ the experimental transition probabilities were essentially independent of $T_s$. The experimental results are indicated by the green squares. Computed results using the SRP32-vdW-DF1 DF from Ref. [27] (black diamonds) and the RPBE DF from Ref. [2] (black triangles) are included as well. Note that the results obtained with the SRP32-vdW-DF1 DF employed the LDFA and assumed $T_s = 575\,\mathrm{K}$. The results using the RPBE DF employed a mono-energetic beam and assumed $T_s = 323\,\mathrm{K}$.

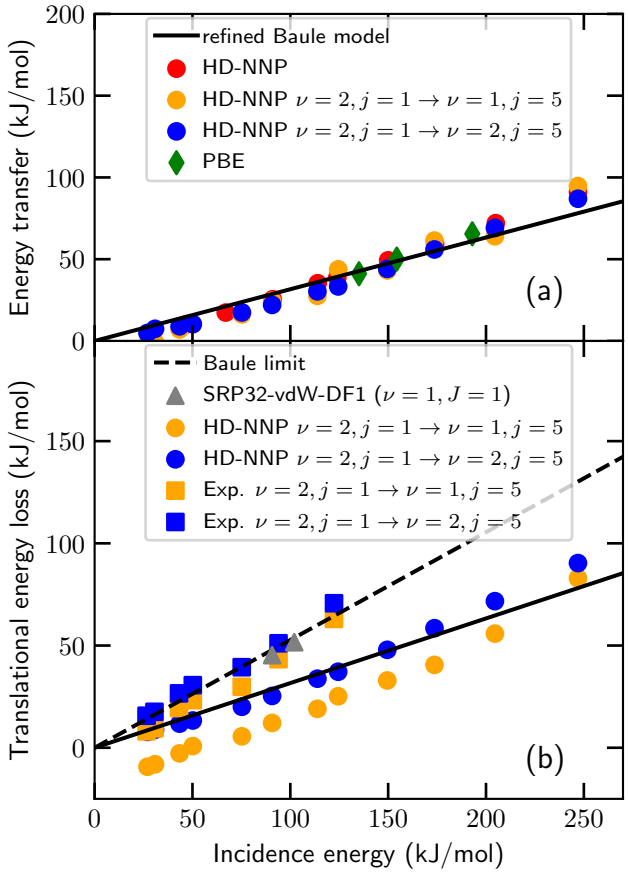


FIGURE 3.10: (a) Computated energy transfer to the surface phonons in scattering of HCl from Au(111) as a function of the incidence energy for $T_s = 170\,K$. The initial rovibrational state distribution is either sampled according to the nozzle temperature (red and green) or HCl is in the $\nu = 2$ and $j = 1$ state (orange and blue). Orange and blue indicate results for inelastic ($\nu = 2 \rightarrow \nu = 1$) and elastic ($\nu = 2 \rightarrow \nu = 2$) scattering, respectively. The circles and diamonds indicate results obtained with the MS-RPBEl and PBE[34] DFs, respectively. The PBE results are obtained for $T_s = 298\,K$ (b) Difference of the initial and final translational energy in scattering of HCl from Au(111). Experiment[29] and theory are indicated by squares and circles, respectively. Results for $\nu = 1, J = 1$ pre-excited HCl with the SRP32-vdW-DF1 DF[27] are indicated by grey triangles. The refined Baule model average (Baule limit) is indicated by the solid (dashed) black line. The experimental results are for $T_s = 300\,K$, and the SRP32-vdW-DF1 results are obtained with BOMD with the LDFA calculations modeling energy transfer to the phonons as well as ehp excitations in scattering of ($\nu = 1, J = 1$) HCl for $T_s = 900\,K$.

### Energy Transfer

The computed energy transfer from scattered HCl to the surface phonons of Au(111) is shown in Figure 3.10a. Results obtained by Füchsel et al. employing the PBE DF[34] are in good agreement with the results obtained with the MS-RPBEl DF. Note that the PBE results were obtained for $T_s = 298\,\mathrm{K}$, which is slightly higher than the surface temperature used with the MS-RPBEl DF ($T_s = 170\,\mathrm{K}$), but also that calculations suggest that this has only a minor effect on the energy transfer[34, 35]. Furthermore, simulations employing the RPBE DF resulted in about 10 - 15 % lower energy transfer than simulations using the PBE DF[34]. Interestingly, the energy transfer predicted with the SRP32-vdW-DF1 DF for $T_s = 900\,\mathrm{K}$[27] is about 80% higher than with the MS-RPBEl DF for $T_s = 170\,\mathrm{K}$. Including ehp excitation hardly has any effect on the energy transfer, at least not at the LDFA level[2, 34]. This suggests that Van der Waals correlation increases energy transfer from the molecule to the surface phonons considerably. At present it is unknown what the underlying reason is. A possibility would be that the molecule is accelerated by the physisorption well (which effect is missing with the MS-RPBEl and (R)PBE DFs), and would thus hit the surface with a higher velocity and transfer more energy.

The energy transfer obtained from the MS-RPBEl simulations compares well with the Baule average obtained with the refined Baule model[89, 90] (see also Section 2.5), which is defined as

$$\langle E_T \rangle = \frac{2.4\mu}{(1+\mu)^2} \langle E_i \rangle \,, \tag{3.11}$$

where $\mu = m/M$ ($m$ is the mass of the projectile and $M$ is the mass of a surface atom) and $\langle E_i \rangle$ is the average incidence energy. Good agreement between the refined Baule model and computed energy transfer has also been observed for several other systems such as $CHD_3$ and methanol scattering from Cu(111), Pd(111) and Pt(111)[90–92] (see Chapters 7, 9 and 10). Füchsel et al. reported that the Baule model severely overestimated the energy transfer for HCl scattering from Au(111)[34] while employing GGA DFs without Van der Waals correlation. However, the comparison was made with the more approximate Baule limit, where every collision is treated as a head-on collision, which could overestimate the energy transfer as this is a rather severe approximation. As has been shown in Figure 3.10a the PBE results obtained in Ref. [34] are instead in good agreement with the refined Baule model average, which is lower than the Baule limit. However, the energy transfer predicted with the SRP32-vdW-DF1 DF compares well with that obtained in the Baule limit.

A comparison between theory (with the MS-RPBEl DF) and experiment[29]

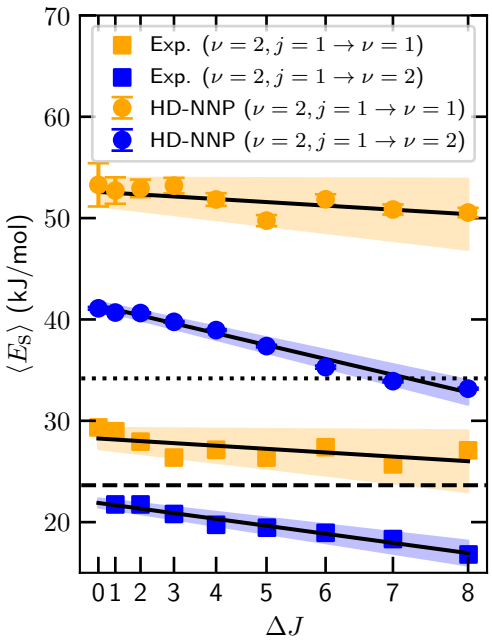


FIGURE 3.11: Average translational energy of HCl scattered from Au(111) as a function of change in rotational state for $\langle E_i \rangle = 50\,\text{kJ/mol}$. The initial rovibrational state is $\nu = 2$ and $j = 1$ and the final vibrational state is $\nu = 1$ or $\nu = 2$ (orange and blue, respectively). Experimental ($T_s = 300\,\text{K}$)[29] and theoretical ($T_s = 170\,\text{K}$) results are indicated by squares and circles, respectively. The solid black lines are linear regression lines fitted to the results and the blue and orange shaded areas are the $2\sigma$ (95%) confidence intervals of those fits. The dotted (dashed) black line is the refined Baule model average (Baule limit). The error bars represent 68% confidence intervals.

is made in Figure 3.10b for the change in translational energy (i.e., the loss of translational energy). Note that the energy transfer in Figure 3.10a is different to the translational energy loss in Figure 3.10b, which also arises from energy transfer involving molecular rotation and vibration, and not the energy transfer to the phonons only. A qualitative agreement is obtained for the translational energy loss, but not a quantitative one. As expected vibrational de-excitation is accompanied by a smaller loss in translational energy than vibrationally elastic scattering as some of the vibrational energy lost will be transferred to translation (V-T, Figure 3.10b). In contrast, for vibrational de-excitation a similar energy transfer from the molecule to the surface is observed as for vibrationally elastic scattering, i.e., the vibrational energy lost is apparently not transferred to the phonons (V-P, Figure 3.10a). Interestingly, the experimental results suggest that the Baule limit, and not the Baule average, is an accurate prediction for the energy transfer, if one compares the elastic scattering results to the Baule limit (i.e., no vibrational energy transfer and little effect from rotational energy transfer). Since the SRP32-vdW-DF1 BOMD with the LDFA results also compare well to the Baule limit, Van der Waals correlation and modeling energy transfer to ehps might both be necessary to accurately model energy transfer between HCl and Au(111).

The average translational energy of vibrationally (in)elastically scattered HCl from Au(111) is shown in Figure 3.11 as a function of the final rotational quantum number. Again, only a qualitative agreement is obtained between experiment and theory in the sense that the trends are recovered that vibrationally de-excited HCl retains more translational energy and that the final translational energy of vibrationally de-excited HCl shows a weaker dependence on its final rotational state. It is likely that the aforementioned lack of Van der Waals correlation in this work causes at least part of the quantitative difference between experiment and theory. The decrease in translational energy with increasing rotational quantum number is due to translational energy being transferred to rotational energy. After making comparisons to the Baule model, coupling of the projectile's translation to the ehps of the solid was previously suggested[29]. This is the first time a high quality first principles adiabatic theory has been compared to these experiments. The fact that the differences between the translational energy of vibrationally elastically and vibrationally inelastically scattered HCl as computed with electronically adiabatic calculations are larger than the measured differences confirms the suggestion of Ref. [29] that part of the vibrational energy is lost to electron-hole pair excitation.

The effect of the impact site on the energy transfer is visualized in Figure 3.12. Two observations stand out: More energy is transferred to the surface atoms in collisions with the hollow and bridge sites, and, when considering only collisions with the area assigned to the top site, more energy is transferred in (head-on) collisions with the actual top site than in collisions that have a larger impact parameter with respect to the top site. The latter observation is in agreement with the Baule model, but the former observation is not. It is possible that while the energy transfer near a hollow or bridge site with a single surface atom is comparable to that of the top site (i.e., is in agreement with the Baule model), the molecule interacts with multiple surface atoms in a single collision and therefore the total energy transfer is larger near the hollow and bridge sites than near the top site. These multiple molecule-surface interactions cannot be evaluated within a single collision in the Baule model, as one might do by artificially increasing the surface atom mass in equation 3.11 since this would actually lower the energy transfer. Thus, it is concluded here that the Baule model is too simplistic for a good qualitative description of the energy transfer. Also, a model where the energy transfer is modeled within a simplistic single oscillator model such as the generalized Langevin oscillator (GLO) model[93] would probably also incorrectly describe the energy transfer of HCl to Au(111) since such a model would also rely on energy transfer to a single surface oscillator at a given specific time, and not to more than

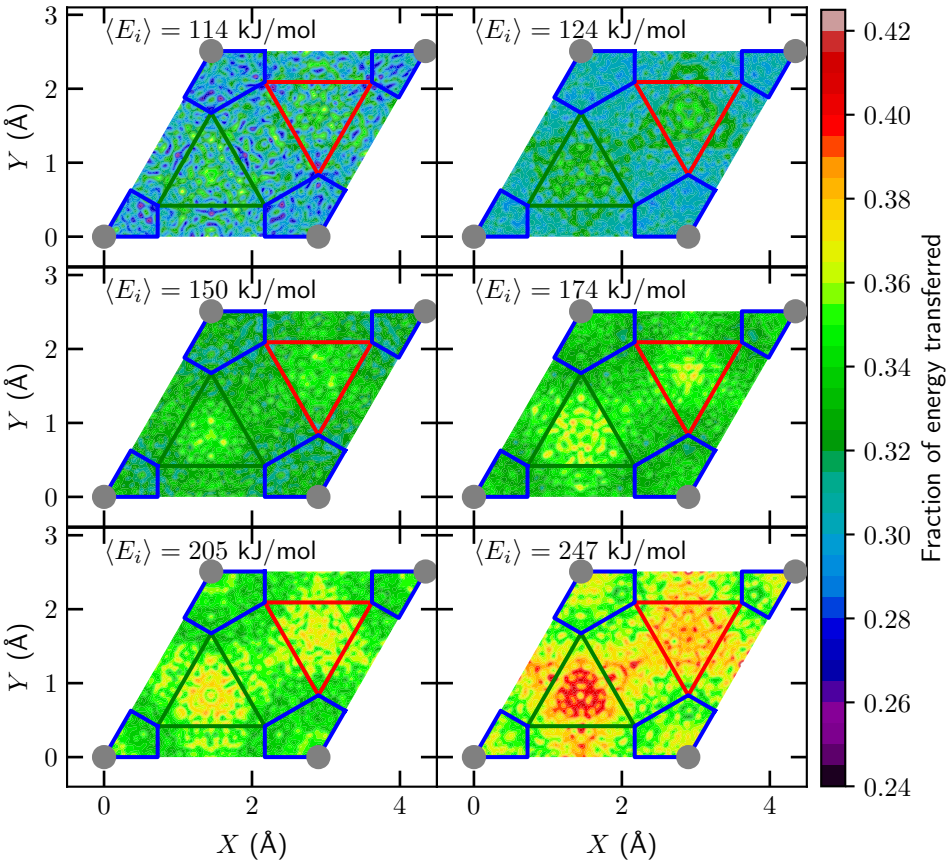


FIGURE 3.12: Fraction of the translational energy of scattered HCl transferred to the surface phonons of Au(111) as a function of the initial impact site ($t = 0$) on the surface unit cell and incidence energy. The areas enclosed by the blue, green, and red lines are the areas closest to the top, fcc, and hcp sites, while the rest is closest to the bridge site.

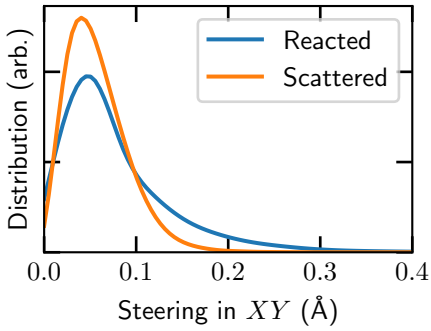


FIGURE 3.13: Steering of HCl in the $XY$ plane when reacting on or scattering from Au(111) (blue and orange line, respectively). For scattering HCl the steering is defined as the distance between the location of the COM in the $XY$ plane at the first classical turning point in the $Z$ direction and its location at $t = 0$. For reacting HCl the locations in the $XY$ plane are taken at the moment of reaction ($r = r^{\ddagger}$) and at $t = 0$.

one surface atom simultaneously. Furthermore, in the introduction of the modified GLO model it was suggested that its accuracy can be improved by including not only the $Z$ location in the coupling potential, but also the $X$ and $Y$ coordinates[94]. However, for HCl + Au(111) the mechanical and electronic coupling is not only dependent on the position of the COM (i.e., $X$, $Y$ and $Z$) but also on the molecule's orientation (i.e., $\theta$ and $\phi$). Therefore, it is likely that an accurate description of HCl + Au(111) using the MGLO model would require a coupling potential depending on all HCl's six degrees of freedom.

### Site Specific Reaction

The dynamical steering of reacting and scattering HCl on Au(111) (i.e., change in the projection of the COM of HCl on the surface during trajectories) in the $XY$ direction is shown in Figure 3.13. For reacting HCl, the distance is shown between the initial $XY$ position and the $XY$ position at the moment of reaction ($r = r^{\ddagger}$) of the COM of HCl. For scattering HCl, instead of the $XY$ position at the moment of reaction ($r = r^{\ddagger}$), the $XY$ position is taken at the first classical turning point in the $Z$ direction. For reacting HCl slightly more steering is observed than for scattering HCl, but in any case for both processes the amount of steering is fairly small. Therefore, a sudden impact model[95] regarding the $X$ and $Y$ positions should be sufficient for modeling the reaction. This was also observed by Liu et al.[30], who showed that a model in which 4D sticking results are averaged over several fixed locations of $X$ and $Y$, i.e., the COM of the molecule cannot move in the $X$ and $Y$ directions, can accurately reproduce 6D sticking probabilities, as long as enough sites are included.

The importance of the impact site for the sticking can also be seen in Figure 3.14, where the sticking probability is shown as a function of impact site. At

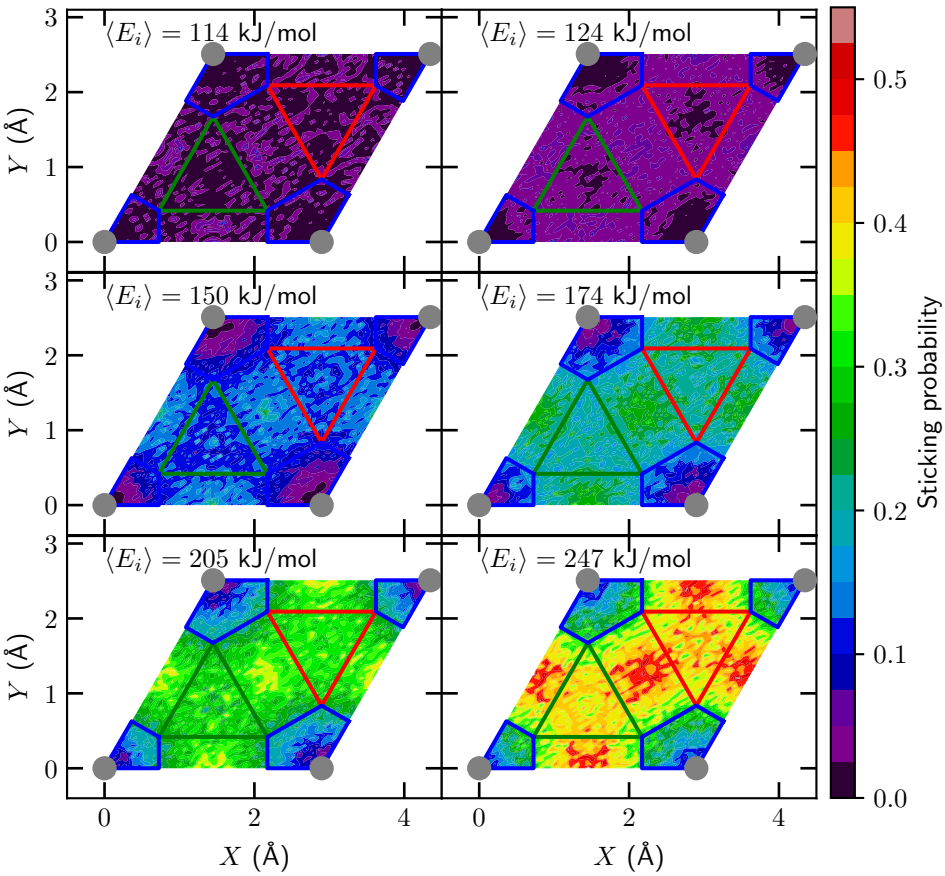


FIGURE 3.14: Sticking probability of HCl on Au(111) as a function of the initial impact site ($t = 0$) of the COM on the surface unit cell and incidence energy. The areas enclosed by the blue, green, and red lines are the areas closest to the top, fcc, and hcp sites, while the rest is closest to the bridge site.

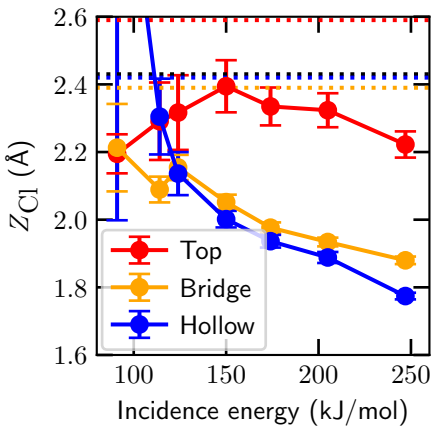


FIGURE 3.15: Distance between Cl and the surface ($Z_{Cl}$) for HCl reacting on Au(111) near the top, bridge and hollow sites (red, orange, and blue, respectively) at the moment of reaction ($r = r^{\ddagger}$, see Table 3.5) using the MS-RPBEl DF. The sites are determined as the nearest high symmetry site for a reacted trajectory at $t = 0$. The dashed lines indicate the values associated with the minimum barriers at these sites, while the global TS is indicated by the black line.

low incidence energy reaction occurs mostly near the bridge site, followed by the hollow and top site. At high incidence energy the hollow site becomes relatively more reactive and reaction occurs almost equally near the bridge and hollow sites, while the top site is still considerably less reactive. Interestingly, from the barrier heights in Table 3.5 it is expected that the hollow site should be the least reactive site, while the top site should be considerably more reactive. Additionally, a site with a barrier that is earlier (i.e., has a lower $r$ value, like the top site) is often more reactive. These results suggest that these particular static aspects of the PES (i.e., the height of the barrier and the corresponding H-Cl distance) do not play a very large role, as the hollow site is clearly more reactive than the top site.

Since the impact sites considered in Figure 3.14 differ in the shape of the MEP (see Figure 3.4), one might expect that the bobsled effect plays a role. In the bobsled effect, the molecule slides off the MEP up the repulsive wall, if the MEP has a too sharp turn compared to the translational energy of the molecule, so that the molecule encounters a higher barrier than the minimum barrier[81, 82]. Although Figure 3.15 strongly suggests that the bobsled effect does play a role overall (as the molecules appear to react much closer to the surface than suggested by the location of the minimum barrier), if anything the observations suggest that the negative impact on the reactivity should be largest in collisions with the bridge and hollow sites. Thus, the bobsled effect cannot explain the variation of reactivity with impact site.

It is known that a molecule might not be able to react over the minimum barrier if it is dynamically inaccessible, e.g., as observed for the dissociation of HOD on Ni(111)[96]. In Section 3.3.2 (see also Figures 3.4 and 3.5) it is

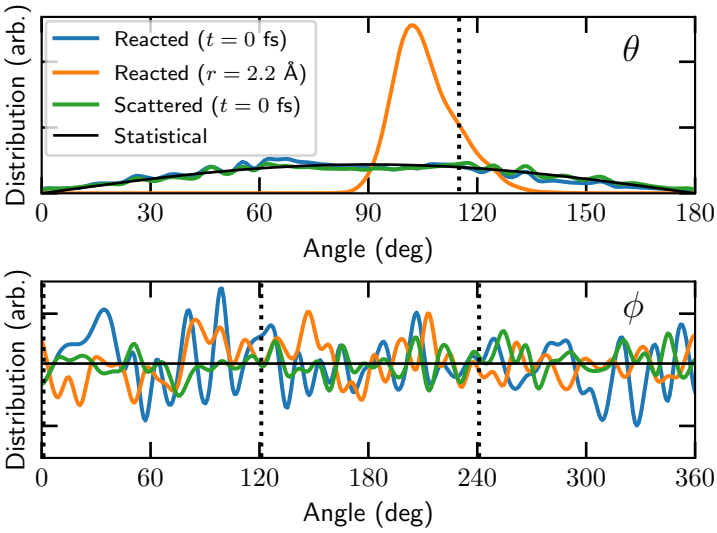


FIGURE 3.16: Distribution of $\theta$ and $\phi$ angles for HCl on Au(111). The distributions at the initial time step ($t = 0$) for reacted and scattered HCl are indicated in blue and green, respectively, whereas the distribution for reacted HCl at the moment of reaction ($r = 2.2$ Å) is indicated in orange. The statistical distribution is indicated by the solid black line and the values from the global TS are indicated by the dotted black line.

hypothesized that the top site barrier might be dynamically less accessible due to the shape of the MEP. Furthermore, it is possible that due to the different site specific dependence of the potential on $\theta$ and $\phi$ (the polar and azimuthal angles, respectively), the site specific reactivity might be affected differently depending on the anisotropy in the $\theta$ and $\phi$ angles (see Figure 3.D.2). These observations are also supported by the site specific reaction probabilities obtained by Liu et al. employing the PW91 DF and QD[30]: Top site reaction favors a cartwheel orientation (steering in $\theta$), bridge site reaction favors a helicopter orientation (steering in $\phi$), and hollow site reaction shows no clear preference. A large amount of steering in the $\theta$ angle is suggested by the results of Figure 3.16, where the orientation distributions of scattering and reacting HCl are shown. Moreover, the initial angular distributions are statistical. Thus, here it is concluded that the observed site specific reactivity is probably due to the dynamical accessibility of the barriers. Furthermore, if the initial angular distribution that leads to reaction is statistical and concomitant steering would appear to occur, typically a rotationally adiabatic approximation should be adequate[95]. However, as will be shown in Chapter 4, the low reactivity at the top site is due to the dependence of the optimum $\theta$ value on the reaction coordinate and a rotationally adiabatic approximation is not expected to work well.

Figure 3.17 again shows the site specificity of the reaction. The upper panel shows clearly that more molecules react at the bridge site than expected on the basis of the area associated with this site (see Figure 3.14 for how the surface unit cell is partitioned), while fewer molecules react at the top site than expected on this basis. The lower panel shows that overall most molecules react at the bridge site, followed by the hollow and top sites. It is also observed that if a frozen surface is employed instead of a mobile surface, i.e., if energy transfer and the thermal variation of barrier heights are not taken into account, only the bridge site becomes more reactive.

Additionally, for $\nu = 2$ vibrationally excited HCl a statistical site specific reactivity is obtained for $S_0 > 0.2$ (see Figure 3.18). In contrast, for $S_0 < 0.2$ the site specific reactivity is non-statistical, but it does not follow the trend of the barrier heights in Table 3.5 either, nor is the state specificity similar to that found under molecular beam conditions. Rather, the order of the sites in terms of reactivity is now top $>$ bridge $>$ hollow. This observation implies that adding vibrational energy increases the dynamical accessibility of specific barriers, especially that of the top site.

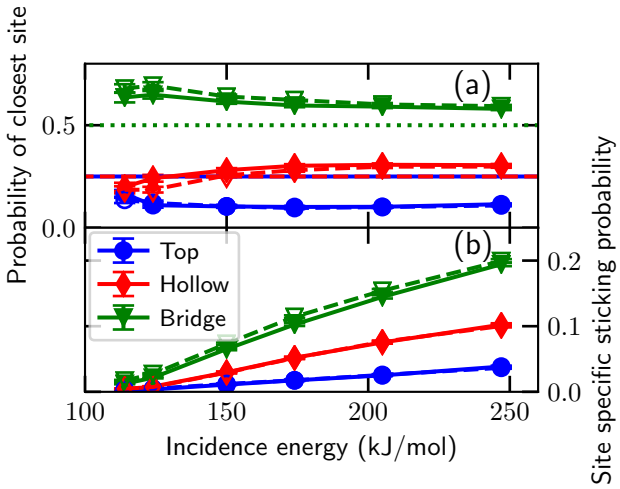


FIGURE 3.17: (a) Fractions of the closest high symmetry sites encountered by HCl, i.e., the top, hollow, and bridge (blue, red, and green, respectively) sites, as a function of the incidence energy at the time of dissociation, that is, when $r = r^{\ddagger}$. The dashed and dotted lines indicate the statistical average for the high symmetry sites. The open and solid symbols indicate the use of a frozen and mobile surface, respectively. (b) Sticking probability of HCl on the high symmetry sites as a function of the incidence energy. Note that the site specific sticking probabilities add up to the total sticking probability. The error bars represent 68% confidence intervals.

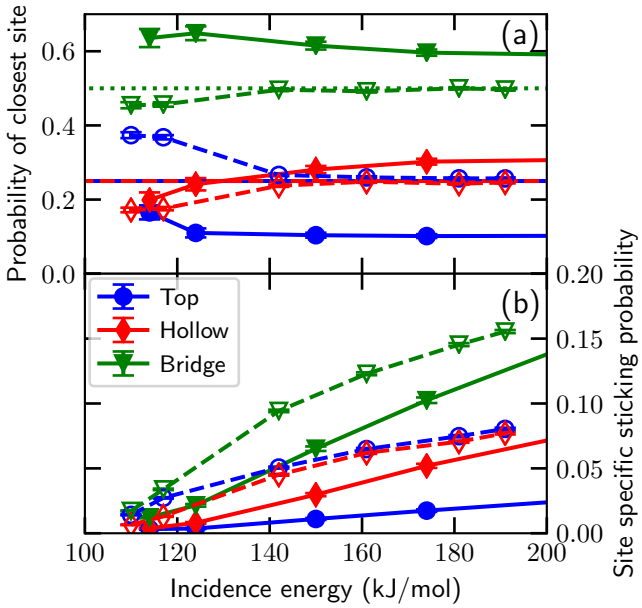


FIGURE 3.18: (a) Fractions of the closest high symmetry sites encountered by HCl, i.e., the top, hollow, and bridge (blue, red, and green, respectively) sites, as a function of the incidence energy at the time of dissociation, i.e., when $r = r^{\ddagger}$. The dashed and dotted lines indicate the statistical average for the high symmetry sites. The open and solid symbols indicate the use of a rovibrational population of only $\nu = 2, J = 1$ and according to a Boltzmann distribution, respectively. The $\nu = 2, J = 1$ state selected HCl results are shifted by 66 kJ/mol (i.e., the energy difference between $\nu = 0, J = 0$ and $\nu = 2, J = 1$) in order to compare to the results where the vibrational population of HCl is sampled with a Boltzmann distribution according to the nozzle temperature. (b) Same as a but for the sticking probability of HCl on the high symmetry sites as a function of the incidence energy. Note that the site specific sticking probabilities add up to the total sticking probability. The error bars represent 68% confidence intervals.

## 3.4 Additional Discussion

A considerable disagreement between theory and experiment remains, even though the difference between the two is diminishing. Here a few remaining issues are discussed that could potentially explain the difference between theory and experiment for sticking and vibrationally inelastic scattering.

First, experience suggests that including ehp excitations with the LDFA will not yield a substantially improved description of the sticking probability. Description of ehp excitation with a higher level of theory such as independent electron surface hopping[97, 98] or ODF[22, 85–88] might improve the results: ODF has been observed to alter the dynamics[87], e.g., modeling ehp excitation with ODF had a larger effect on the sticking probability than modeling ehp excitation at the LDFA level of theory for $N_2$ + Ru(0001)[22]. Indeed, there is some evidence now that the translational motion of the HCl molecule may be able to excite ehps of Au. This could reduce the reactivity since translational energy is necessary to surmount the barrier.

Second, experimentally not an ideal (111) surface is employed, but a reconstructed herringbone patterned surface. Such a surface reconstruction is well known to occur for gold, and might alter the reactivity of the surface[99]. Unfortunately, the surface unit cell associated with such a reconstruction is quite large, making tractable MD simulations difficult. An embedded atom model might make such MD simulations tractable[100], but this might lead to loss of accuracy of the molecule-metal surface interaction.

Furthermore, the presence or absence of a physisorption well can influence the dynamics[101] and therefore the reactivity as well, even when the barrier height is similar (e.g., $CHD_3$ + Pt(111) using the PBE and SRP32-vdW-DF1 DFs[102]). Therefore, it is possible that adding Van der Waals correlation to the MS-RPBEl DF might lower the sticking probability even further. Also, it is likely that the discrepancy between the measured and computed energy transfer will be diminished by using Van der Waals correlation (see Section 3.3.4). Moreover, the use of the non-local vdW-DF2 correlation[103] instead of the vdW-DF1 correlation typically increases the barrier height[8, 104], and might therefore improve the description of HCl + Au(111) compared to that previously obtained with vdW-DF1[27].

Fourth, and probably most importantly, Füchsel et al. have shown that a considerable amount of charge transfer occurs when HCl is near the surface with the use of the (R)PBE DFs[34]. Since GGA DFs suffer from delocalization errors (due to the SIE, see Chapter 5 and the references therein), the barrier height might be artificially lowered when employing DFs that suffer from SIEs. For example, compared to standard GGA DFs, the embedded correlation

wave function method and (range-separated) hybrid DFs yield considerably better sticking probabilities and/or barriers for $O_2$ + Al(111)[7, 15, 16, 24, 105, 106], a system known for a large charge transfer (see also Chapter 5). In this framework it is highly significant that the DF used here to describe the interaction between HCl and Au(111), which was explicitly designed to correct for the SIE at the meta-GGA level of theory, yields significantly improved results for this system compared to results obtained earlier using GGA exchange DFs. Future work involving advanced methods that would remedy the SIE at a higher level of theory could perhaps further increase the barrier height of HCl dissociating on Au(111) and lead to further improved computed sticking probabilities.

As has been briefly mentioned in Section 3.3.4, the binning method can influence the rovibrational state populations obtained. Thus, a combined QCT and QD study that would investigate the binning method is necessary. It should also be noted that a change in sticking probability due to the use of a different binning method, as has recently been observed by Rodríguez et al.[41] for $H_2$ + Pd(111), is not expected here. For $H_2$ + Pd(111) only the vibrational ground state and a few rotational states are available, and analyzing the QCT sticking probabilities in a quantum spirit is necessary. In contrast, for HCl + Au(111) many rovibrational states are available, justifying the use of quasi-classical theory with histogram binning in the analysis of the QCT calculations[42]. Moreover, QD and BOMD calculations performed with the RPBE DF lead to similar sticking probabilities[36].

Turning to scattering, the (in)elastic scattering experiments were performed only for a final scattering angle of 15°[31], whereas in the simulations presented in this chapter all scattering angles are taken into account. However, the experimental results are corrected in such a way that they should yield the average over the entire angular distribution, where this correction is valid when no significant difference in angular distribution between different rotational states exists[31]. Also, the experimental incidence angle is between 0° and 5°, while the simulations are performed for normal incidence, i.e., the incidence angle is 0°. However, results by Füchsel et al.[34] suggest that this has only a minor effect on the energy transfer of HCl scattering from Au(111). In this work, for the vibrational transition probabilities a larger effect of the scattering angle is observed (see Figure 3.C.1): The vibrational transition probabilities ($T_{v=1,j=1\rightarrow v=2}$) are increased by a factor 1.2 for low incidence energy and up to a factor 2.3 for high incidence energy, resulting in a larger discrepancy between experiment and theory. Qualitatively similar results are expected when employing other DFs and thus it is expected that the MS-RPBEl DF would also yield the best agreement between experiment and theory for

the excitation probabilities if the theoretical results for the other DFs would also be obtained for a restricted range of scattering angles, as done here.

Finally, as has been shown in this chapter, a large uncertainty regarding the experimental sticking probabilities remains. Future experiments reducing the uncertainty would help with testing theory, but first theory should be brought into better agreement with experiment. Furthermore, molecular beam studies where HCl is state-selectively prepared with laser excitation could serve as an improved benchmark for theory. Not only might such studies provide potentially more accurate sticking probabilities since they might be easier to measure, but also vibrational efficacies could be compared. Such experiments are in an early preparation stage.

## 3.5 Conclusions

In this chapter the dissociative chemisorption of HCl on Au(111) is re-investigated with molecular dynamics and a high-dimensional neural network potential and previous experiments are re-examined to better characterize their error margins. By employing a recently developed MGGA DF (MS-RPBEl) and comparing with re-analyzed experimental data, the agreement between computed and measured sticking probabilities is improved considerably. The computed minimum barrier height is high (100.6 kJ/mol) and the barrier geometry is late (i.e., the HCl bond is extended from 1.28 Å in the gas phase to 2.18 Å at the TS), which results in a decrease of the sticking probability relative to dynamics calculations based on the other DFs tested so far. Furthermore, surface atom motion is found to be of minor influence on the sticking probability. Moreover, computed and measured vibrational transition probabilities are also in improved agreement, although the employed binning method warrants additional research. Dynamical effects play an important role in the overall reactivity, leading to a dependence of the reactivity on impact sites that cannot be explained on the basis of site-specific barrier heights and locations. A qualitative, but not quantitative agreement between experiment and theory is obtained for the energy transfer of the HCl molecule to the surface. Finally, a number of possibilities are discussed that might account for the remaining discrepancies between experiment and theory.

# Appendix

## 3.A Convergence

Convergence of the minimum barrier height of HCl on Au(111) employing the MS-RPBEl DF is shown in Figure 3.A.1 and Table 3.A.1. Furthermore, the absolute error distribution for the training and testing data set of the HD-NNP compared to DFT calculations is shown in Figure 3.A.2. For the test set, the HD-NNP predicts energies for 85% of all structures that agree with the raw DFT data within 1 kJ/mol, for 97% of all structures within 2.5 kJ/mol, and for 98.4% of all structures within chemical accuracy (4.2 kJ/mol). Finally, the energy along the global MEP in Figure 3.4 as obtained with the HD-NNP is compared to the raw DFT data in Figure 3.A.3, where it is shown that the HD-NNP reproduces the raw DFT data within chemical accuracy. Since both the RMSE and Figure 3.A.2 indicate an excellent fit quality, similar behavior is expected for the site-specific MEPs.

The interlayer relaxation in this chapter is performed for a slab with a $1 \times 1$ surface unit cell employing an $8 \times 8 \times 1$ $k$-point grid, which yields an outward interlayer relaxation of the top two layers of 3.0% for a 4 layer slab. However, calculations employing a $24 \times 24 \times 1$ or $32 \times 32 \times 1$ $k$-point grid yield an outward interlayer relaxation of 0.5% and 0.7%, respectively. DFT calculations employing the computational setup used throughout this chapter, but with converged interlayer distances obtained with a $24 \times 24 \times 1$ $k$-point grid, suggest that both the minimum barrier and geometry are not affected significantly. For example, the barrier height is only increased by 0.2 kJ/mol. Additionally, the surface is equilibrated prior to the generation of the snapshots employed in the initial conditions (see Section 2.4.1), hence the MD results should be unaffected as well. Since experimentally a herringbone patterned surface instead of an ideal (111) surface is employed, it is possible that employing unconverged interlayer spacings might not matter for the comparison between experiment and theory. Moreover, computationally it would be untractable to redo all the calculations that have been performed for the PES. Therefore, unconverged interlayer spacings are employed throughout this chapter, but it is also noted that this should not affect results considerably.

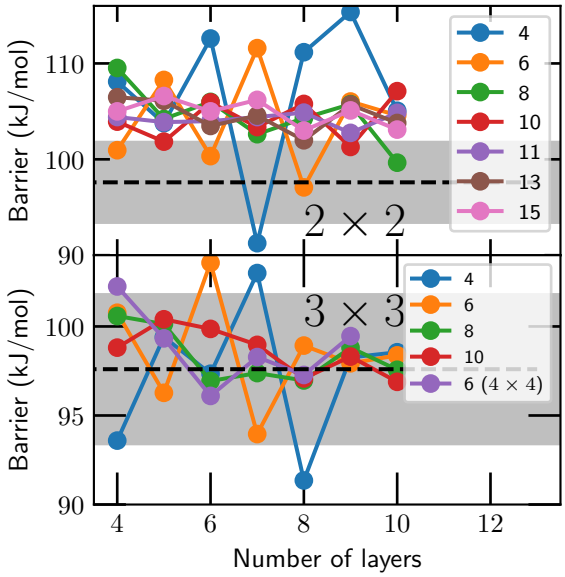


FIGURE 3.A.1: Convergence of the minimum barrier height (kJ/mol) of HCl on Au(111) as a function of the amount of layers and $k$-points using the MS-RPBEl DF. The upper panel and lower panel used a $2 \times 2$ and $3 \times 3$ supercell, respectively. The second panel also includes the convergence for a $4 \times 4$ supercell using a $6 \times 6 \times 1$ $k$-point grid. The dashed lines indicate the converged barrier height. The calculations of the PES were done with a $3 \times 3$ surface unit cell, 4 layers, and an $8 \times 8 \times 1$ $k$-point grid. The amount of $k$-points is indicated in the legend.

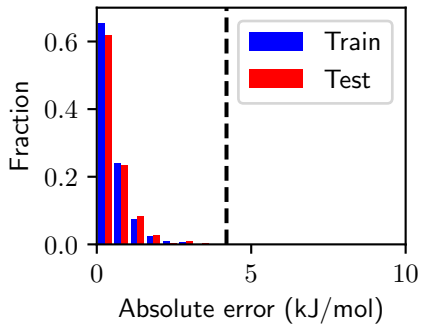


FIGURE 3.A.2: Distribution of absolute total energy errors (kJ/mol) of the HD-NNP compared to the DFT total energy. Blue indicates the training set, whereas red indicates the test set. The dashed line indicates chemical accuracy, i.e., 4.2 kJ/mol.

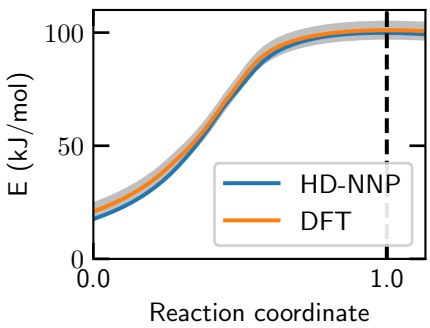


FIGURE 3.A.3: Energy along the reaction coordinate of the minimum barrier's MEP (as defined in Figure 3.4) obtained from the HD-NNP and raw DFT data. The reaction coordinate value of zero is taken to be HCl with $Z_{Cl} = 3$ Å, and the value of one is the TS. The grey area indicates chemical accuracy (i.e., 4.2 kJ/mol) and the dashed black line indicates the TS.

TABLE 3.A.1: Same as Figure 3.A.1. The results obtained with the employed computational set up in the DFT calculations for the training data set is in bold and the most converged result (i.e., obtained with the largest setup) is in italic.

| Layers | $k$-points | $E_b, 2 \times 2$ | $E_b, 3 \times 3$ |
|---|---|---|---|
| 4 | $4 \times 4 \times 1$ | 108.1 | 93.6 |
| 4 | $6 \times 6 \times 1$ | 101.0 | 100.8 |
| 4 | $8 \times 8 \times 1$ | 109.5 | **100.6** |
| 4 | $10 \times 10 \times 1$ | 103.9 | 98.8 |
| 4 | $11 \times 11 \times 1$ | 104.4 | |
| 4 | $13 \times 13 \times 1$ | 106.5 | |
| 4 | $15 \times 15 \times 1$ | 105.0 | |
| 5 | $4 \times 4 \times 1$ | 103.8 | 99.4 |
| 5 | $6 \times 6 \times 1$ | 108.3 | 96.3 |
| 5 | $8 \times 8 \times 1$ | 104.2 | 100.1 |
| 5 | $10 \times 10 \times 1$ | 101.8 | 100.4 |
| 5 | $11 \times 11 \times 1$ | 103.9 | |
| 5 | $13 \times 13 \times 1$ | 106.1 | |
| 5 | $15 \times 15 \times 1$ | 106.6 | |
| 6 | $4 \times 4 \times 1$ | 112.6 | 97.3 |
| 6 | $6 \times 6 \times 1$ | 100.3 | 103.6 |
| 6 | $8 \times 8 \times 1$ | 106.0 | 96.9 |
| 6 | $10 \times 10 \times 1$ | 105.9 | 99.9 |
| 6 | $11 \times 11 \times 1$ | 104.0 | |
| 6 | $13 \times 13 \times 1$ | 103.5 | |
| 6 | $15 \times 15 \times 1$ | 105.0 | |
| 7 | $4 \times 4 \times 1$ | 91.3 | 103.0 |
| 7 | $6 \times 6 \times 1$ | 111.6 | 94.0 |
| 7 | $8 \times 8 \times 1$ | 102.6 | 97.4 |
| 7 | $10 \times 10 \times 1$ | 103.4 | 99.0 |
| 7 | $11 \times 11 \times 1$ | 104.4 | |
| 7 | $13 \times 13 \times 1$ | 104.6 | |
| 7 | $15 \times 15 \times 1$ | 106.2 | |
| 8 | $4 \times 4 \times 1$ | 111.2 | 91.4 |
| 8 | $6 \times 6 \times 1$ | 97.1 | 98.9 |
| 8 | $8 \times 8 \times 1$ | 104.3 | 97.0 |
| 8 | $10 \times 10 \times 1$ | 105.8 | 97.1 |
| 8 | $11 \times 11 \times 1$ | 104.9 | |
| 8 | $13 \times 13 \times 1$ | 102.0 | |
| 8 | $15 \times 15 \times 1$ | 103.0 | |
| 9 | $4 \times 4 \times 1$ | 115.4 | 98.3 |
| 9 | $6 \times 6 \times 1$ | 106.0 | 97.9 |
| 9 | $8 \times 8 \times 1$ | 105.7 | 98.8 |
| 9 | $10 \times 10 \times 1$ | 101.3 | 98.3 |
| 9 | $11 \times 11 \times 1$ | 102.8 | |
| 9 | $13 \times 13 \times 1$ | 105.7 | |
| 9 | $15 \times 15 \times 1$ | 105.1 | |
| 10 | $4 \times 4 \times 1$ | 105.1 | 98.5 |
| 10 | $6 \times 6 \times 1$ | 104.6 | 98.4 |
| 10 | $8 \times 8 \times 1$ | 99.6 | 97.6 |
| 10 | $10 \times 10 \times 1$ | 107.1 | *96.9* |
| 10 | $11 \times 11 \times 1$ | 104.9 | |
| 10 | $13 \times 13 \times 1$ | 103.8 | |
| 10 | $15 \times 15 \times 1$ | 103.1 | |

TABLE 3.B.1: Parameters used for the radial symmetry functions describing the interaction of a reference atom (Ref.) with its neighbouring atoms (Neighb.) within the cut-off radius.

| Ref. | Neighb. | $\eta$ | Ref. | Neighb. | $\eta$ | Ref. | Neighb. | $\eta$ |
|---|---|---|---|---|---|---|---|---|
| Au | Cl | 0.00453515 | H | Cl | 0.00453515 | Cl | H | 0.00453515 |
| Au | Cl | 0.00598145 | H | Cl | 0.00598145 | Cl | H | 0.00598145 |
| Au | Cl | 0.00824846 | H | Cl | 0.00824846 | Cl | H | 0.00824846 |
| Au | Cl | 0.01209877 | H | Cl | 0.01209877 | Cl | H | 0.01209877 |
| Au | Cl | 0.01944059 | H | Cl | 0.01944059 | Cl | H | 0.01944059 |
| Au | Cl | 0.0362426 | H | Cl | 0.0362426 | Cl | H | 0.0362426 |
| Au | Cl | 0.08999082 | H | Cl | 0.08999082 | Cl | H | 0.08999082 |
| Au | Cl | 0.5 | H | Cl | 0.5 | Cl | H | 0.5 |
| Au | H | 0.00453515 | H | Au | 0.00453515 | Cl | Au | 0.00453515 |
| Au | H | 0.00598145 | H | Au | 0.00598145 | Cl | Au | 0.00598145 |
| Au | H | 0.00824846 | H | Au | 0.00824846 | Cl | Au | 0.00824846 |
| Au | H | 0.01209877 | H | Au | 0.01209877 | Cl | Au | 0.01209877 |
| Au | H | 0.01944059 | H | Au | 0.01944059 | Cl | Au | 0.01944059 |
| Au | H | 0.0362426 | H | Au | 0.0362426 | Cl | Au | 0.0362426 |
| Au | H | 0.08999082 | H | Au | 0.08999082 | Cl | Au | 0.08999082 |
| Au | H | 0.5 | H | Au | 0.5 | Cl | Au | 0.5 |
| Au | Au | 0.00453515 | | | | | | |
| Au | Au | 0.00593499 | | | | | | |
| Au | Au | 0.00809917 | | | | | | |
| Au | Au | 0.01170534 | | | | | | |
| Au | Au | 0.01838994 | | | | | | |
| Au | Au | 0.03299386 | | | | | | |
| Au | Au | 0.07561728 | | | | | | |
| Au | Au | 0.32 | | | | | | |

## 3.B Symmetry Functions

The parameters used in the HD-NNP for the radial and angular symmetry functions are given in Tables 3.B.1 and 3.B.2, which have been generated following the procedure of Ref. [73], and the cut-off radius $R_c = 11\,a_0$.

## 3.C Vibrational Excitation Probabilities

The scattering angle dependence of the vibrational excitation probabilities of HCl is shown in Figure 3.C.1. The vibrational transition probabilities ($T_{\nu=1,j=1\rightarrow\nu=2}$) are increased by a factor 1.6 for low incidence energy up to a factor 2.7 for high incidence energy, when only a range of scattering angles is considered relative to all scattering angles. The increase in transition probabilities also results in a larger discrepancy between experiment and theory.

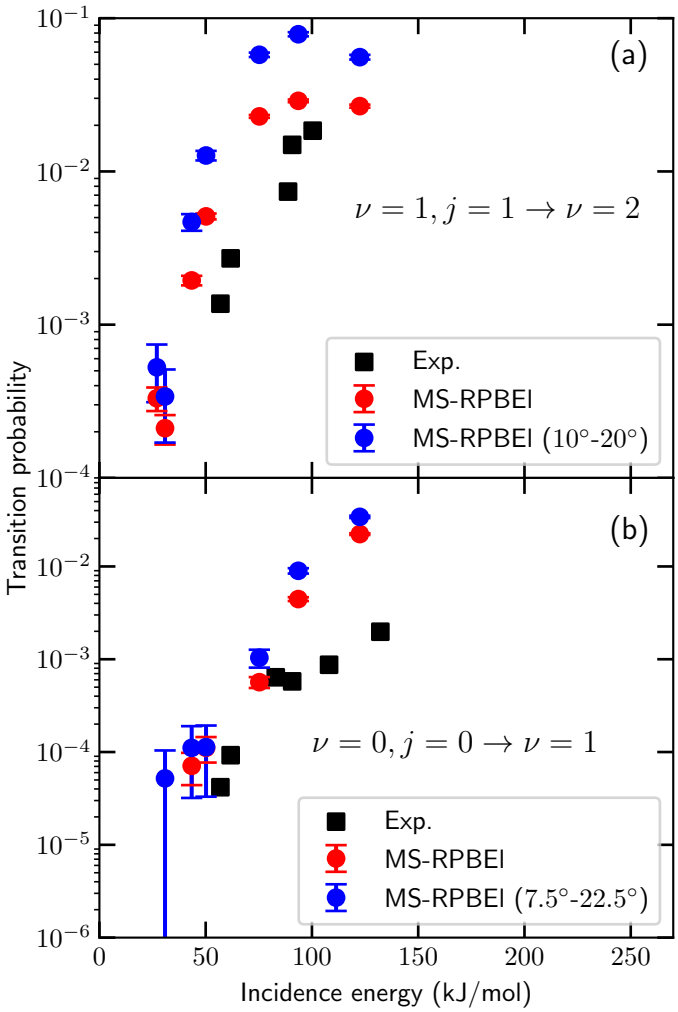


FIGURE 3.C.1: Vibrational excitation probability of HCl scattered from Au(111) ($T_s$ = 170 K) using the MS-RPBEl DF for $\nu = 1, j = 1 \rightarrow \nu = 2$ (a) and $\nu = 0, j = 0 \rightarrow \nu = 1$ (b). Experimental results from Ref. [31] are indicated by the black squares. Computed results with the MS-RPBEl DF including all scattering angles or only angles in the range of 10° to 20° (a) or 7.5° to 22.5° (b) are indicated by the red and blue circles, respectively.

TABLE 3.B.2: Parameters used for the angular symmetry functions describing the interaction of a reference atom with its neighbouring atoms within the cut-off radius.

| $\eta$ | $\lambda$ | $\zeta$ |
|---|---|---|
| 0.00453514739 | 1 | 1 |
| 0.00929752066 | 1 | 1 |
| 0.02880000000 | 1 | 1 |
| 0.00453514739 | 1 | 4 |
| 0.00929752066 | 1 | 4 |
| 0.02880000000 | 1 | 4 |
| 0.00453514739 | -1 | 1 |
| 0.00929752066 | -1 | 1 |
| 0.02880000000 | -1 | 1 |
| 0.00453514739 | -1 | 4 |
| 0.00929752066 | -1 | 4 |
| 0.02880000000 | -1 | 4 |

However, as discussed in Section 3.4, the experimental correction for the determination of the excitation probability in only a specific range of scattering angles is likely to be accurate, and therefore including all scattering angles in the theoretical analysis should be adequate.

The beam parameters of Ref. [31] have not been published previously, and are included in Table 3.C.1 for future reference, but note that these parameters have not been employed in this chapter. The velocity distributions of Ref. [31] are somewhat broader than the ones simulated in this chapter. Nevertheless, as can be seen from Figure 3.C.2, the transition probability does not depend considerably on the width of the velocity distribution.

## 3.D Elbow Plots of the Potential Energy Surface

Figure 3.D.1 shows an elbow plot of the PES incorporating the minimum TS, which is also shown in Figure 3.4. The white dashed lines are drawn from the top right corner, where the lowest energy along these lines (i.e., the white circles) yields the MEP in the main procedure used in this chapter to compute an MEP.

The barrier height as a function of $\theta$ and $\phi$ (the polar and azimuthal angles, respectively) for the high symmetry sites and the minimum barrier impact site is shown in Figure 3.D.2. Depending on the site, the PES around the site-specific minimum TS is narrow in the $\theta$ coordinate (top site), the $\phi$ coordinate

TABLE 3.C.1: Beam parameters from Ref. [31] that describe the experimental HCl velocity distributions in the experiments on vibrationally inelastic scattering. The stream energy $E_0$, stream velocity $v_0$, and width parameter $\alpha$ are determined through time-of-flight measurements. Note that only in the case of the $\nu = 1 \rightarrow 2$ excitation experiments (Figure 3.9a) all of these incident conditions were employed, whereas in the $\nu = 0 \rightarrow 1$ experiments (Figure 3.9b) only $\langle E_\mathrm{i} \rangle = 62\,\mathrm{kJ/mol}$ and $\langle E_\mathrm{i} \rangle = 91\,\mathrm{kJ/mol}$ were employed. The remaining experimental data points in Figure 3.9b were taken from Ref. [28], where only the mean incidence energy was provided.

| $\langle E_\mathrm{i} \rangle$ (kJ/mol) | $E_0$ (kJ/mol) | $v_0$ (m/s) | $\alpha$ (m/s) |
|---|---|---|---|
| 57 | 57 | 1765 | 101 |
| 62 | 61 | 1831 | 95 |
| 89 | 87 | 2190 | 150 |
| 91 | 90 | 2226 | 110 |
| 100 | 100 | 2343 | 136 |

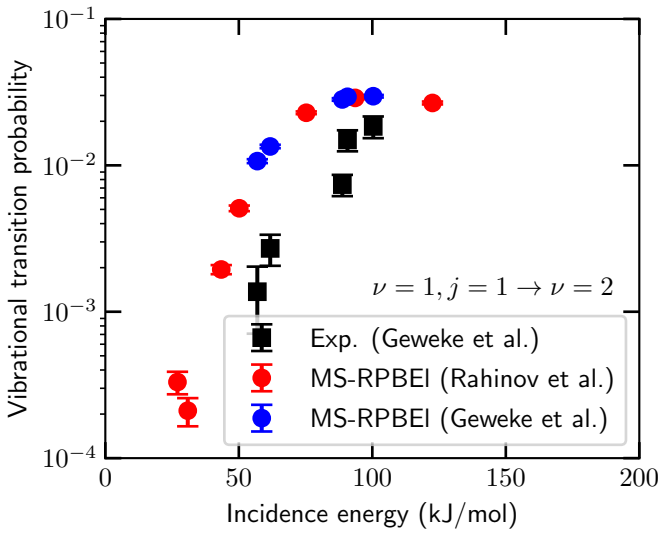


FIGURE 3.C.2: Vibrational excitation probability of HCl scattered from Au(111) ($T_\mathrm{s} = 170\,\mathrm{K}$) using the MS-RPBEl DF for $\nu = 1, j = 1 \rightarrow \nu = 2$. Experimental results from Ref. [31] are indicated by the black squares. Computed results with the MS-RPBEl DF employing beam parameters from Refs. [29] (which are employed in Figure 3.9) and [31] are indicated by the red and blue circles, respectively.

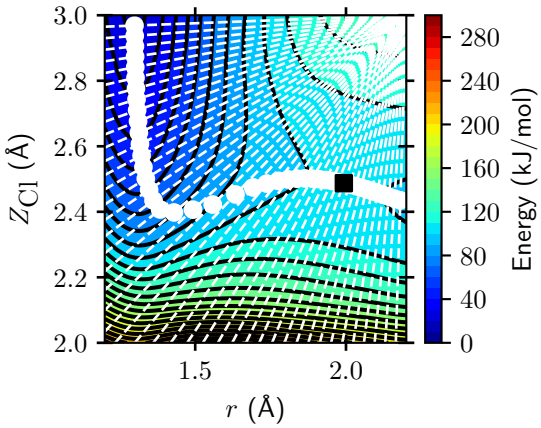


FIGURE 3.D.1: Elbow plot of HCl on Au(111) as a function of $Z_{Cl}$ and $r$ using the MS-RPBEl DF for the minimum TS. All other degrees of freedom are relaxed. Black contour lines are drawn at an interval of 10 kJ/mol between 0 and 200 kJ/mol. The white circles indicate the MEP in reduced dimensionality and the black square indicates the highest point along the MEP. The white dashed lines indicate the lines from which the MEP is determined.

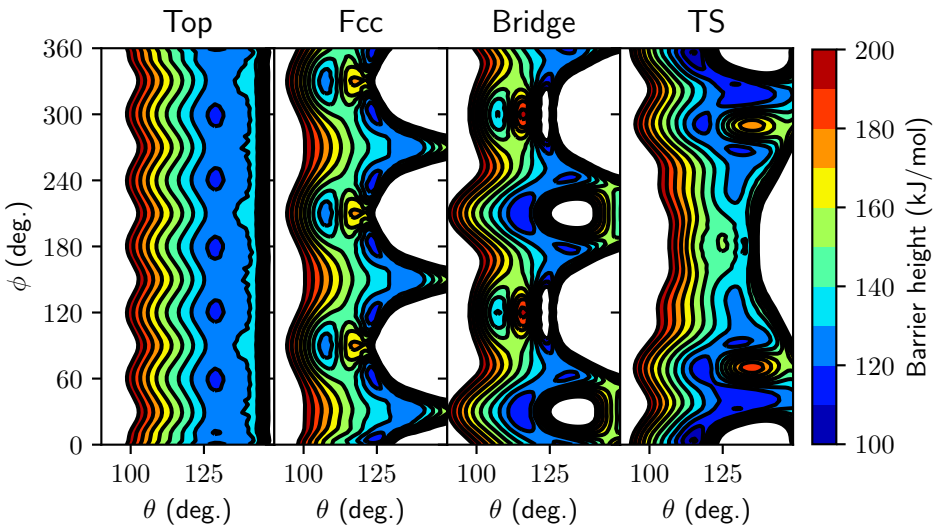


FIGURE 3.D.2: Barrier height of HCl on Au(111) as a function of the $\theta$ and $\phi$ angles for the top, fcc and bridge sites, and the minimum TS. The black contour lines are drawn at a interval of 10 kJ/mol from 100 to 200 kJ/mol.

(bridge site and global minimum TS), or neither (fcc site). Especially for the global minimum TS it seems that the orientation in the $XY$ plane (i.e., the $\phi$ coordinate) is extremely important. Hence, the overall reactivity near the top site is mainly limited by the azimuthal orientation of HCl.

## References


(1) Shakouri, K.; Behler, J.; Meyer, J.; Kroes, G.-J. Accurate Neural Network Description of Surface Phonons in Reactive Gas–Surface Dynamics: $N_2$ + Ru(0001). *J. Phys. Chem. Lett.* **2017**, *8*, 2131–2136, DOI: 10.1021/acs.jpclett.7b00784.

(2) Liu, Q.; Zhou, X.; Zhou, L.; Zhang, Y.; Luo, X.; Guo, H.; Jiang, B. Constructing High-Dimensional Neural Network Potential Energy Surfaces for Gas–Surface Scattering and Reactions. *J. Phys. Chem. C* **2018**, *122*, 1761–1769, DOI: 10.1021/acs.jpcc.7b12064.

(3) Gerrits, N.; Shakouri, K.; Behler, J.; Kroes, G.-J. Accurate Probabilities for Highly Activated Reaction of Polyatomic Molecules on Surfaces Using a High-Dimensional Neural Network Potential: $CHD_3$ + Cu(111). *J. Phys. Chem. Lett.* **2019**, *10*, 1763–1768, DOI: 10.1021/acs.jpclett.9b00560.

(4) Zhang, Y.; Zhou, X.; Jiang, B. Bridging the Gap between Direct Dynamics and Globally Accurate Reactive Potential Energy Surfaces Using Neural Networks. *J. Phys. Chem. Lett.* **2019**, *10*, 1185–1191, DOI: 10.1021/acs.jpclett.9b00085.

(5) Yin, R.; Zhang, Y.; Jiang, B. Strong Vibrational Relaxation of NO Scattered from Au(111): Importance of the Adiabatic Potential Energy Surface. *J. Phys. Chem. Lett.* **2019**, *10*, 5969–5974, DOI: 10.1021/acs.jpclett.9b01806.

(6) Díaz, C.; Pijper, E.; Olsen, R. A.; Busnengo, H. F.; Auerbach, D. J.; Kroes, G. J. Chemically Accurate Simulation of a Prototypical Surface Reaction: $H_2$ Dissociation on Cu(111). *Science* **2009**, *326*, 832–834, DOI: 10.1126/science.1178722.

(7) Liu, H.-R.; Xiang, H.; Gong, X. G. First Principles Study of Adsorption of $O_2$ on Al Surface with Hybrid Functionals. *J. Chem. Phys.* **2011**, *135*, 214702, DOI: 10.1063/1.3665032.

(8) Wijzenbroek, M.; Kroes, G. J. The Effect of the Exchange-Correlation Functional on $H_2$ Dissociation on Ru(0001). *J. Chem. Phys.* **2014**, *140*, 084702, DOI: 10.1063/1.4865946.

(9) Nattino, F.; Migliorini, D.; Kroes, G.-J.; Dombrowski, E.; High, E. A.; Killelea, D. R.; Utz, A. L. Chemically Accurate Simulation of a Polyatomic Molecule-Metal Surface Reaction. *J. Phys. Chem. Lett.* **2016**, *7*, 2402–2406, DOI: 10.1021/acs.jpclett.6b01022.

(10) Migliorini, D.; Chadwick, H.; Nattino, F.; Gutiérrez-González, A.; Dombrowski, E.; High, E. A.; Guo, H.; Utz, A. L.; Jackson, B.; Beck, R. D.; Kroes, G.-J. Surface Reaction Barriometry: Methane Dissociation on Flat and Stepped Transition-Metal Surfaces. *J. Phys. Chem. Lett.* **2017**, *8*, 4177–4182, DOI: 10.1021/acs.jpclett.7b01905.

(11) Zhou, X.; Jiang, B.; Guo, H. Dissociative Chemisorption of Methane on Stepped Ir(332) Surface: Density Functional Theory and Ab Initio Molecular Dynamics Studies. *J. Phys. Chem. C* **2019**, *123*, 20893–20902, DOI: 10.1021/acs.jpcc.9b04651.

(12) Ghassemi, E. N.; Smeets, E. W. F.; Somers, M. F.; Kroes, G.-J.; Groot, I. M. N.; Juurlink, L. B. F.; Füchsel, G. Transferability of the Specific Reaction Parameter Density Functional for $H_2$ + Pt(111) to $H_2$ + Pt(211). *J. Phys. Chem. C* **2019**, *123*, 2973–2986, DOI: 10.1021/acs.jpcc.8b11018.

(13) Lončarić, I.; Alducin, M.; Juaristi, J. I.; Novko, D. CO Stretch Vibration Lives Long on Au(111). *J. Phys. Chem. Lett.* **2019**, *10*, 1043–1047, DOI: 10.1021/acs.jpclett.9b00069.

(14) Smeets, E. W.; Voss, J.; Kroes, G.-J. Specific Reaction Parameter Density Functional Based on the Meta-Generalized Gradient Approximation: Application to $H_2$ + Cu(111) and $H_2$ + Ag(111). *J. Phys. Chem. A* **2019**, *123*, 5395–5406, DOI: 10.1021/acs.jpca.9b02914.

(15) Libisch, F.; Huang, C.; Liao, P.; Pavone, M.; Carter, E. A. Origin of the Energy Barrier to Chemical Reactions of $O_2$ on Al(111): Evidence for Charge Transfer, Not Spin Selection. *Phys. Rev. Lett.* **2012**, *109*, 198303, DOI: 10.1103/PhysRevLett.109.198303.

(16) Yin, R.; Zhang, Y.; Libisch, F.; Carter, E. A.; Guo, H.; Jiang, B. Dissociative Chemisorption of $O_2$ on Al(111): Dynamics on a Correlated Wave-Function-Based Potential Energy Surface. *J. Phys. Chem. Lett.* **2018**, *9*, 3271–3277, DOI: 10.1021/acs.jpclett.8b01470.

(17) Blanco-Rey, M.; Juaristi, J. I.; Díez Muiño, R.; Busnengo, H. F.; Kroes, G. J.; Alducin, M. Electronic Friction Dominates Hydrogen Hot-Atom Relaxation on Pd(100). *Phys. Rev. Lett.* **2014**, *112*, 103203, DOI: 10.1103/PhysRevLett.112.103203.

(18) Janke, S. M.; Auerbach, D. J.; Wodtke, A. M.; Kandratsenka, A. An Accurate Full-Dimensional Potential Energy Surface for H–Au(111): Importance of Nonadiabatic Electronic Excitation in Energy Transfer and Adsorption. *J. Chem. Phys.* **2015**, *143*, 124708, DOI: 10.1063/1.4931669.

(19) Rittmeyer, S. P.; Meyer, J.; Juaristi, J. I.; Reuter, K. Electronic Friction-Based Vibrational Lifetimes of Molecular Adsorbates: Beyond the Independent-Atom Approximation. *Phys. Rev. Lett.* **2015**, *115*, 046102, DOI: 10.1103/PhysRevLett.115.046102.

(20) Bünermann, O.; Jiang, H.; Dorenkamp, Y.; Kandratsenka, A.; Janke, S.; Auerbach, D. J.; Wodtke, A. M. Electron-Hole Pair Excitation Determines the Mechanism of Hydrogen Atom Adsorption. *Science* **2015**, *350*, 1346–1349, DOI: 10.1126/science.aad4972.

(21) Kandratsenka, A.; Jiang, H.; Dorenkamp, Y.; Janke, S. M.; Kammler, M.; Wodtke, A. M.; Bünermann, O. Unified Description of H-Atom–Induced Chemicurrents and Inelastic Scattering. *PNAS* **2018**, *115*, 680–684, DOI: 10.1073/pnas.1710587115.

(22) Spiering, P.; Shakouri, K.; Behler, J.; Kroes, G.-J.; Meyer, J. Orbital-Dependent Electronic Friction Significantly Affects the Description of Reactive Scattering of $N_2$ from Ru(0001). *J. Phys. Chem. Lett.* **2019**, *10*, 2957–2962, DOI: 10.1021/acs.jpclett.9b00523.

(23) Zhou, X.; Kolb, B.; Luo, X.; Guo, H.; Jiang, B. Ab Initio Molecular Dynamics Study of Dissociative Chemisorption and Scattering of $CO_2$ on Ni(100): Reactivity, Energy Transfer, Steering Dynamics, and Lattice Effects. *J. Phys. Chem. C* **2017**, *121*, 5594–5602, DOI: 10.1021/acs.jpcc.6b12686.

(24) Sun, S.; Xu, P.; Ren, Y.; Tan, X.; Li, G. First-Principles Study of Dissociation Processes of $O_2$ Molecular on the Al (111) Surface. *Curr. Appl. Phys.* **2018**, *18*, 1528–1533, DOI: 10.1016/j.cap.2018.09.010.

(25) Gerrits, N.; Kroes, G.-J. Curious Mechanism of the Dissociative Chemisorption of Ammonia on Ru(0001). *J. Phys. Chem. C* **2019**, *123*, 28291–28300, DOI: 10.1021/acs.jpcc.9b09121.

(26) Chadwick, H.; Gutiérrez-González, A.; Beck, R. D.; Kroes, G.-J. $CHD_3$ Dissociation on the Kinked Pt(210) Surface: A Comparison of Experiment and Theory. *J. Phys. Chem. C* **2019**, *123*, 14530–14539, DOI: 10.1021/acs.jpcc.9b03051.

(27) Füchsel, G.; Zhou, X.; Jiang, B.; Juaristi, J. I.; Alducin, M.; Guo, H.; Kroes, G.-J. Reactive and Nonreactive Scattering of HCl from Au(111): An Ab Initio Molecular Dynamics Study. *J. Phys. Chem. C* **2019**, *123*, 2287–2299, DOI: 10.1021/acs.jpcc.8b10686.

(28) Ran, Q.; Matsiev, D.; Auerbach, D. J.; Wodtke, A. M. Observation of a Change of Vibrational Excitation Mechanism with Surface Temperature: HCl Collisions with Au(111). *Phys. Rev. Lett.* **2007**, *98*, 237601, DOI: 10.1103/PhysRevLett.98.237601.

(29) Rahinov, I.; Cooper, R.; Yuan, C.; Yang, X.; Auerbach, D. J.; Wodtke, A. M. Efficient Vibrational and Translational Excitations of a Solid Metal Surface: State-to-State Time-of-Flight Measurements of HCl($v$=2,J=1) Scattering from Au(111). *J. Chem. Phys.* **2008**, *129*, 214708, DOI: 10.1063/1.3028542.

(30) Liu, T.; Fu, B.; Zhang, D. H. Six-Dimensional Quantum Dynamics Study for the Dissociative Adsorption of HCl on Au(111) Surface. *J. Chem. Phys.* **2013**, *139*, 184705, DOI: 10.1063/1.4829508.

(31) Geweke, J.; Shirhatti, P. R.; Rahinov, I.; Bartels, C.; Wodtke, A. M. Vibrational Energy Transfer near a Dissociative Adsorption Transition State: State-to-State Study of HCl Collisions at Au(111). *J. Chem. Phys.* **2016**, *145*, 054709, DOI: 10.1063/1.4959968.

(32) Kolb, B.; Guo, H. Communication: Energy Transfer and Reaction Dynamics for DCl Scattering on Au(111): An Ab Initio Molecular Dynamics Study. *J. Chem. Phys.* **2016**, *145*, 011102, DOI: 10.1063/1.4956453.

(33) Shirhatti, P. R.; Geweke, J.; Steinsiek, C.; Bartels, C.; Rahinov, I.; Auerbach, D. J.; Wodtke, A. M. Activated Dissociation of HCl on Au(111). *J. Phys. Chem. Lett.* **2016**, *7*, 1346–1350, DOI: 10.1021/acs.jpclett.6b00289.

(34) Füchsel, G.; del Cueto, M.; Díaz, C.; Kroes, G.-J. Enigmatic HCl + Au(111) Reaction: A Puzzle for Theory and Experiment. *J. Phys. Chem. C* **2016**, *120*, 25760–25779, DOI: 10.1021/acs.jpcc.6b07453.

(35) Kolb, B.; Luo, X.; Zhou, X.; Jiang, B.; Guo, H. High-Dimensional Atomistic Neural Network Potentials for Molecule–Surface Interactions: HCl Scattering from Au(111). *J. Phys. Chem. Lett.* **2017**, *8*, 666–672, DOI: 10.1021/acs.jpclett.6b02994.

(36) Liu, T.; Fu, B.; Zhang, D. H. HCl Dissociating on a Rigid Au(111) Surface: A Six-Dimensional Quantum Mechanical Study on a New Potential Energy Surface Based on the RPBE Functional. *J. Chem. Phys.* **2017**, *146*, 164706, DOI: 10.1063/1.4982051.

(37) Perdew, J. P.; Burke, K.; Ernzerhof, M. Generalized Gradient Approximation Made Simple. *Phys. Rev. Lett.* **1996**, *77*, 3865–3868, DOI: 10.1103/PhysRevLett.77.3865.

(38) Perdew, J. P.; Chevary, J. A.; Vosko, S. H.; Jackson, K. A.; Pederson, M. R.; Singh, D. J.; Fiolhais, C. Atoms, Molecules, Solids, and Surfaces: Applications of the Generalized Gradient Approximation for Exchange and Correlation. *Phys. Rev. B* **1992**, *46*, 6671–6687, DOI: 10.1103/PhysRevB.46.6671.

(39) Hammer, B.; Hansen, L. B.; Nørskov, J. K. Improved Adsorption Energetics within Density-Functional Theory Using Revised Perdew-Burke-Ernzerhof Functionals. *Phys. Rev. B* **1999**, *59*, 7413–7421, DOI: 10.1103/PhysRevB.59.7413.

(40) Juaristi, J. I.; Alducin, M.; Muiño, R. D.; Busnengo, H. F.; Salin, A. Role of Electron-Hole Pair Excitations in the Dissociative Adsorption of Diatomic Molecules on Metal Surfaces. *Phys. Rev. Lett.* **2008**, *100*, 116102, DOI: 10.1103/PhysRevLett.100.116102.

(41) Rodríguez-Fernández, A.; Bonnet, L.; Crespos, C.; Larrégaray, P.; Díez Muiño, R. When Classical Trajectories Get to Quantum Accuracy: The Scattering of $H_2$ on Pd(111). *J. Phys. Chem. Lett.* **2019**, *10*, 7629–7635, DOI: 10.1021/acs.jpclett.9b02742.

(42) Bonnet, L. Classical Dynamics of Chemical Reactions in a Quantum Spirit. *Int. Rev. Phys. Chem.* **2013**, *32*, 171–228, DOI: 10.1080/0144235X.2012.752905.

(43) Crespos, C.; Decock, J.; Larrégaray, P.; Bonnet, L. Classical Molecule–Surface Scattering in a Quantum Spirit: Application to $H_2$/Pd(111) Nonactivated Sticking. *J. Phys. Chem. C* **2017**, *121*, 16854–16863, DOI: 10.1021/acs.jpcc.7b04829.

(44) Ran, Q.; Matsiev, D.; Wodtke, A. M.; Auerbach, D. J. An Advanced Molecule-Surface Scattering Instrument for Study of Vibrational Energy Transfer in Gas-Solid Collisions. *Rev. Sci. Instrum.* **2007**, *78*, 104104, DOI: 10.1063/1.2796149.

(45) Geweke, J. D. Scattering HCl Molecules from Au(111) and Ag(111) Surfaces, Lausanne: EPFL, 2019, DOI: 10.5075/epfl-thesis-9742.

(46) Perdew, J. P.; Ruzsinszky, A.; Csonka, G. I.; Constantin, L. A.; Sun, J. Workhorse Semilocal Density Functional for Condensed Matter Physics and Quantum Chemistry. *Phys. Rev. Lett.* **2009**, *103*, 026403, DOI: 10.1103/PhysRevLett.103.026403.

(47) Perdew, J. P.; Ruzsinszky, A.; Constantin, L. A.; Sun, J.; Csonka, G. I. Some Fundamental Issues in Ground-State Density Functional Theory: A Guide for the Perplexed. *J. Chem. Theory Comput.* **2009**, *5*, 902–908, DOI: 10.1021/ct800531s.

(48) Mallikarjun Sharada, S.; Karlsson, R. K. B.; Maimaiti, Y.; Voss, J.; Bligaard, T. Adsorption on Transition Metal Surfaces: Transferability and Accuracy of DFT Using the ADS41 Dataset. *Phys. Rev. B* **2019**, *100*, 035439, DOI: 10.1103/PhysRevB.100.035439.

(49) Kresse, G.; Hafner, J. Ab Initio Molecular-Dynamics Simulation of the Liquid-Metal–Amorphous-Semiconductor Transition in Germanium. *Phys. Rev. B* **1994**, *49*, 14251–14269, DOI: 10.1103/PhysRevB.49.14251.

(50) Kresse, G.; Hafner, J. Ab Initio Molecular Dynamics for Liquid Metals. *Phys. Rev. B* **1993**, *47*, 558–561, DOI: 10.1103/PhysRevB.47.558.

(51) Kresse, G.; Furthmüller, J. Efficient Iterative Schemes for Ab Initio Total-Energy Calculations Using a Plane-Wave Basis Set. *Phys. Rev. B* **1996**, *54*, 11169–11186, DOI: 10.1103/PhysRevB.54.11169.

(52) Kresse, G.; Furthmüller, J. Efficiency of Ab-Initio Total Energy Calculations for Metals and Semiconductors Using a Plane-Wave Basis Set. *Comput. Mater. Sci.* **1996**, *6*, 15–50, DOI: 10.1016/0927-0256(96)00008-0.

(53) Kresse, G.; Joubert, D. From Ultrasoft Pseudopotentials to the Projector Augmented-Wave Method. *Phys. Rev. B* **1999**, *59*, 1758–1775, DOI: 10.1103/PhysRevB.59.1758.

(54) Sun, J.; Xiao, B.; Ruzsinszky, A. Communication: Effect of the Orbital-Overlap Dependence in the Meta Generalized Gradient Approximation. *J. Chem. Phys.* **2012**, *137*, 051101, DOI: 10.1063/1.4742312.

(55) Sun, J.; Haunschild, R.; Xiao, B.; Bulik, I. W.; Scuseria, G. E.; Perdew, J. P. Semilocal and Hybrid Meta-Generalized Gradient Approximations Based on the Understanding of the Kinetic-Energy-Density Dependence. *J. Chem. Phys.* **2013**, *138*, 044113, DOI: 10.1063/1.4789414.

(56) Blöchl, P. E. Projector Augmented-Wave Method. *Phys. Rev. B* **1994**, *50*, 17953–17979, DOI: 10.1103/PhysRevB.50.17953.

(57) Maeland, A.; Flanagan, T. B. Lattice Spacings of Gold–Palladium Alloys. *Can. J. Phys.* **1964**, *42*, 2364–2366, DOI: 10.1139/p64-213.

(58) Nichols, R. J.; Nouar, T.; Lucas, C. A.; Haiss, W.; Hofer, W. A. Surface Relaxation and Surface Stress of Au(111). *Surf. Sci.* **2002**, *513*, 263–271, DOI: 10.1016/S0039-6028(02)01510-8.

(59) Methfessel, M.; Paxton, A. T. High-Precision Sampling for Brillouin-Zone Integration in Metals. *Phys. Rev. B* **1989**, *40*, 3616–3621, DOI: 10.1103/PhysRevB.40.3616.

(60) Henkelman, G.; Jónsson, H. A Dimer Method for Finding Saddle Points on High Dimensional Potential Surfaces Using Only First Derivatives. *J. Chem. Phys.* **1999**, *111*, 7010–7022, DOI: 10.1063/1.480097.

(61) Heyden, A.; Bell, A. T.; Keil, F. J. Efficient Methods for Finding Transition States in Chemical Reactions: Comparison of Improved Dimer Method and Partitioned Rational Function Optimization Method. *J. Chem. Phys.* **2005**, *123*, 224101, DOI: 10.1063/1.2104507.

(62) Kästner, J.; Sherwood, P. Superlinearly Converging Dimer Method for Transition State Search. *J. Chem. Phys.* **2008**, *128*, 014106, DOI: 10.1063/1.2815812.

(63) Xiao, P.; Sheppard, D.; Rogal, J.; Henkelman, G. Solid-State Dimer Method for Calculating Solid-Solid Phase Transitions. *J. Chem. Phys.* **2014**, *140*, 174104, DOI: 10.1063/1.4873437.

(64) Transition State Tools Package for VASP https://theory.cm.utexas.edu/vtsttools/index.html (accessed 02/08/2021).

(65) Plimpton, S. Fast Parallel Algorithms for Short-Range Molecular Dynamics. *J. Comput. Phys.* **1995**, *117*, 1–19, DOI: 10.1006/jcph.1995.1039.

(66) Singraber, A.; Behler, J.; Dellago, C. Library-Based LAMMPS Implementation of High-Dimensional Neural Network Potentials. *J. Chem. Theory Comput.* **2019**, *15*, 1827–1840, DOI: 10.1021/acs.jctc.8b00770.

(67) Behler, J.; Parrinello, M. Generalized Neural-Network Representation of High-Dimensional Potential-Energy Surfaces. *Phys. Rev. Lett.* **2007**, *98*, 146401, DOI: 10.1103/PhysRevLett.98.146401.

(68) Behler, J. Representing Potential Energy Surfaces by High-Dimensional Neural Network Potentials. *J. Phys.: Condens. Matter* **2014**, *26*, 183001, DOI: 10.1088/0953-8984/26/18/183001.

(69) Behler, J. Atom-Centered Symmetry Functions for Constructing High-Dimensional Neural Network Potentials. *J. Chem. Phys.* **2011**, *134*, 074106, DOI: 10.1063/1.3553717.

(70) Behler, J. Constructing High-Dimensional Neural Network Potentials: A Tutorial Review. *Int. J. Quantum Chem.* **2015**, *115*, 1032–1050, DOI: 10.1002/qua.24890.

(71) Behler, J. First Principles Neural Network Potentials for Reactive Simulations of Large Molecular and Condensed Systems. *Angew. Chem. Int. Ed.* **2017**, *56*, 12828–12840, DOI: 10.1002/anie.201703114.

(72) Behler, J. RuNNer - A Neural Network Code for High-Dimensional Neural Network Potential-Energy Surfaces; Universität Göttingen http://www.uni-goettingen.de/de/560580.html (accessed 02/14/2019).

(73) Gastegger, M.; Schwiedrzik, L.; Bittermann, M.; Berzsenyi, F.; Marquetand, P. wACSF—Weighted Atom-Centered Symmetry Functions as Descriptors in Machine Learning Potentials. *J. Chem. Phys.* **2018**, *148*, 241709, DOI: 10.1063/1.5019667.

(74) Kastanas, G. N.; Koel, B. E. Interaction of $Cl_2$ with the Au(111) Surface in the Temperature Range of 120 to 1000 K. *Appl. Surf. Sci.* **1993**, *64*, 235–249, DOI: 10.1016/0169-4332(93)90030-F.

(75) Spencer, N. D.; Lambert, R. M. Chlorine Chemisorption and Surface Chloride Formation on Au(111). *Surf. Sci.* **1981**, *107*, 237–248, DOI: 10.1016/0039-6028(81)90623-3.

(76) Davis, L. E.; MacDonald, N. C.; Palmberg, P. W.; Riach, G. E.; Weber, R. E., *Handbook of Auger Electron Spectroscopy: A Reference Book of Standard Data for Identification and Interpretation of Auger Electron Spectroscopy Data*, 2nd edition; Physical Electronics Industries: Eden Prairie, Minn., 1976.

(77) Dion, M.; Rydberg, H.; Schröder, E.; Langreth, D. C.; Lundqvist, B. I. Van Der Waals Density Functional for General Geometries. *Phys. Rev. Lett.* **2004**, *92*, 246401, DOI: 10.1103/PhysRevLett.92.246401.

(78) Jackson, B.; Nave, S. The Dissociative Chemisorption of Methane on Ni(111): The Effects of Molecular Vibration and Lattice Motion. *J. Chem. Phys.* **2013**, *138*, 174705, DOI: 10.1063/1.4802008.

(79) Guo, H.; Farjamnia, A.; Jackson, B. Effects of Lattice Motion on Dissociative Chemisorption: Toward a Rigorous Comparison of Theory with Molecular Beam Experiments. *J. Phys. Chem. Lett.* **2016**, *7*, 4576–4584, DOI: 10.1021/acs.jpclett.6b01948.

(80) Polanyi, J. C. Concepts in Reaction Dynamics. *Acc. Chem. Res.* **1972**, *5*, 161–168, DOI: 10.1021/ar50053a001.

(81) Marcus, R. A. On the Analytical Mechanics of Chemical Reactions. Quantum Mechanics of Linear Collisions. *J. Chem. Phys.* **1966**, *45*, 4493–4499, DOI: 10.1063/1.1727528.

(82) McCullough, E. A.; Wyatt, R. E. Quantum Dynamics of the Collinear (H, $H_2$) Reaction. *J. Chem. Phys.* **1969**, *51*, 1253–1254, DOI: 10.1063/1.1672133.

(83) Smith, R. R.; Killelea, D. R.; DelSesto, D. F.; Utz, A. L. Preference for Vibrational over Translational Energy in a Gas-Surface Reaction. *Science* **2004**, *304*, 992–995, DOI: 10.1126/science.1096309.

(84) Díaz, C.; Olsen, R. A. A Note on the Vibrational Efficacy in Molecule-Surface Reactions. *J. Chem. Phys.* **2009**, *130*, 094706, DOI: 10.1063/1.3080613.

(85) Head-Gordon, M.; Tully, J. C. Molecular Dynamics with Electronic Frictions. *J. Chem. Phys.* **1995**, *103*, 10137–10145, DOI: 10.1063/1.469915.

(86) Askerka, M.; Maurer, R. J.; Batista, V. S.; Tully, J. C. Role of Tensorial Electronic Friction in Energy Transfer at Metal Surfaces. *Phys. Rev. Lett.* **2016**, *116*, 217601, DOI: 10.1103/PhysRevLett.116.217601.

(87) Maurer, R. J.; Jiang, B.; Guo, H.; Tully, J. C. Mode Specific Electronic Friction in Dissociative Chemisorption on Metal Surfaces: $H_2$ on Ag(111). *Phys. Rev. Lett.* **2017**, *118*, 256001, DOI: 10.1103/PhysRevLett.118.256001.

(88) Spiering, P.; Meyer, J. Testing Electronic Friction Models: Vibrational De-Excitation in Scattering of $H_2$ and $D_2$ from Cu(111). *J. Phys. Chem. Lett.* **2018**, *9*, 1803–1808, DOI: 10.1021/acs.jpclett.7b03182.

(89) Goodman, F. O.; Wachman, H. Y. *Formula for Thermal Accommodation Coefficient*; 66-1; Cambridge, Massachusetts: M.I.T. Fluid Dynamics Research, 1966, DOI: 10.21236/ad0631007.

(90) Gerrits, N.; Chadwick, H.; Kroes, G.-J. Dynamical Study of the Dissociative Chemisorption of $CHD_3$ on Pd(111). *J. Phys. Chem. C* **2019**, *123*, 24013–24023, DOI: 10.1021/acs.jpcc.9b05757.

(91) Gerrits, N.; Migliorini, D.; Kroes, G.-J. Dissociation of $CHD_3$ on Cu(111), Cu(211), and Single Atom Alloys of Cu(111). *J. Chem. Phys.* **2018**, *149*, 224701, DOI: 10.1063/1.5053990.

(92) Gerrits, N.; Kroes, G.-J. An AIMD Study of Dissociative Chemisorption of Methanol on Cu(111) with Implications for Formaldehyde Formation. *J. Chem. Phys.* **2019**, *150*, 024706, DOI: 10.1063/1.5070129.

(93) Tully, J. C. Theories of the Dynamics of Inelastic and Reactive Processes at Surfaces. *Annu. Rev. Phys. Chem.* **1980**, *31*, 319–343, DOI: 10.1146/annurev.pc.31.100180.001535.

(94) Zhou, X.; Jiang, B. A Modified Generalized Langevin Oscillator Model for Activated Gas-Surface Reactions. *J. Chem. Phys.* **2019**, *150*, 024704, DOI: 10.1063/1.5078541.

(95) Jackson, B.; Nattino, F.; Kroes, G.-J. Dissociative Chemisorption of Methane on Metal Surfaces: Tests of Dynamical Assumptions Using Quantum Models and Ab Initio Molecular Dynamics. *J. Chem. Phys.* **2014**, *141*, 054102, DOI: 10.1063/1.4891327.

(96) Migliorini, D.; Nattino, F.; Tiwari, A. K.; Kroes, G.-J. HOD on Ni(111): Ab Initio Molecular Dynamics Prediction of Molecular Beam Experiments. *J. Chem. Phys.* **2018**, *149*, 244706, DOI: 10.1063/1.5059357.

(97) Shenvi, N.; Roy, S.; Tully, J. C. Nonadiabatic Dynamics at Metal Surfaces: Independent-Electron Surface Hopping. *J. Chem. Phys.* **2009**, *130*, 174107, DOI: 10.1063/1.3125436.

(98) Cooper, R.; Bartels, C.; Kandratsenka, A.; Rahinov, I.; Shenvi, N.; Golibrzuch, K.; Li, Z.; Auerbach, D. J.; Tully, J. C.; Wodtke, A. M. Multiquantum Vibrational Excitation of NO Scattered from Au(111): Quantitative Comparison of Benchmark Data to Ab Initio Theories of Nonadiabatic Molecule–Surface Interactions. *Angew. Chem. Int. Ed.* **2012**, *51*, 4954–4958, DOI: 10.1002/anie.201201168.

(99) Hanke, F.; Björk, J. Structure and Local Reactivity of the Au(111) Surface Reconstruction. *Phys. Rev. B* **2013**, *87*, 235422, DOI: 10.1103/PhysRevB.87.235422.

(100) Zhang, Y.; Hu, C.; Jiang, B. Embedded Atom Neural Network Potentials: Efficient and Accurate Machine Learning with a Physically Inspired Representation. *J. Phys. Chem. Lett.* **2019**, *10*, 4962–4967, DOI: 10.1021/acs.jpclett.9b02037.

(101) Kumar, S.; Jiang, H.; Schwarzer, M.; Kandratsenka, A.; Schwarzer, D.; Wodtke, A. M. Vibrational Relaxation Lifetime of a Physisorbed Molecule at a Metal Surface. *Phys. Rev. Lett.* **2019**, *123*, 156101, DOI: 10.1103/PhysRevLett.123.156101.

(102) Chadwick, H.; Migliorini, D.; Kroes, G. J. $CHD_3$ Dissociation on Pt(111): A Comparison of the Reaction Dynamics Based on the PBE Functional and on a Specific Reaction Parameter Functional. *J. Chem. Phys.* **2018**, *149*, 044701, DOI: 10.1063/1.5039458.

(103) Lee, K.; Murray, É. D.; Kong, L.; Lundqvist, B. I.; Langreth, D. C. Higher-Accuracy van Der Waals Density Functional. *Phys. Rev. B* **2010**, *82*, 081101(R), DOI: 10.1103/PhysRevB.82.081101.

(104) Migliorini, D.; Nattino, F.; Kroes, G.-J. Application of van Der Waals Functionals to the Calculation of Dissociative Adsorption of $N_2$ on W(110) for Static and Dynamic Systems. *J. Chem. Phys.* **2016**, *144*, 084702, DOI: 10.1063/1.4942198.

(105) Behler, J.; Delley, B.; Lorenz, S.; Reuter, K.; Scheffler, M. Dissociation of $O_2$ at Al(111): The Role of Spin Selection Rules. *Phys. Rev. Lett.* **2005**, *94*, 036104, DOI: 10.1103/PhysRevLett.94.036104.

(106) Livshits, E.; Baer, R.; Kosloff, R. Deleterious Effects of Long-Range Self-Repulsion on the Density Functional Description of $O_2$ Sticking on Aluminum. *J. Phys. Chem. A* **2009**, *113*, 7521–7527, DOI: 10.1021/jp900892r.

# Chapter 4

# Large Effect of Rotational Pre-excitation of HCl on its Reaction on Au(111): A Rotational Phase Lock-in Effect

This chapter is based on Gerrits, N.; Geweke, J.; Auerbach, D. J.; Beck, R. D.; Kroes, G.-J. Highly Efficient Activation of HCl Dissociation on Au(111) via Rotational Preexcitation. *J. Phys. Chem. Lett.* **2021**, *12*, 7252–7260, DOI: 10.1021/acs.jpclett.1c02093

## Abstract

Dissociative chemisorption of molecules on metal surfaces, which is relevant to heterogeneous catalysis, can be subject to important non-statistical effects. Cases have been recorded in which adding energy to the molecule's vibration promotes reaction more effectively than increasing the collision energy, but similar results have not yet been presented for rotational pre-excitation. In this chapter, it is shown that adding energy to the rotation of HCl can promote its dissociation on Au(111) 20 times more effectively than increasing its translational energy. Our prediction can be tested by experiments within the present state-of-the-art. In the underlying mechanism the molecule needs to rotate initially in the polar angle $\theta$ of its orientation relative to the surface so that it can pass through a critical region of the reaction path in a region in front of the barrier, where this path shows a strong and non-monotonic dependence on $\theta$.

## 4.1 Introduction

Fundamental understanding of molecule-metal surface reaction (MMSR) mechanisms is vital for heterogeneous catalysis as MMSRs play an important role in many industrial processes[1–5]. The efficiency or the rate of an industrial heterogeneously catalyzed process, which consists of a sequence of elementary surface reactions, is often controlled[6] by the transition state (TS) of a dissociative chemisorption reaction on a metal surface[6–8], as is the case in ammonia production[2] and steam reforming[3]. However, not only statistical effects, which can be associated with the TS, but also dynamical effects on the dissociation reaction can play an important role in an MMSR[9–28].

An important example of dynamical effects on dissociative chemisorption reactions is mode-specifity. For instance, many[29–31], although not all dissociative chemisorption reactions[32], display sticking probabilities that depend only on the fraction of the molecule's translational energy that is normal to the surface (normal energy scaling, NES). Putting additional vibrational energy in an incident molecule usually increases its reaction probability, with an efficacy that differs from that achieved by enhancing its incident translational energy by the same amount[9–14, 17, 18, 33–35]. For some systems, increasing the vibrational energy is even more effective at increasing the reaction probability than increasing the translational energy, in which case we say that the vibrational efficacy exceeds one[10, 17, 21, 22, 25, 34, 35] (see also Chapters 3 and 8 to 10). In contrast, increasing the rotational energy of a molecule incident on a metal surface is usually not very effective at increasing the reaction probability, and to the best of our knowledge the rotational efficacy has always been found to be lower than one: adding rotational energy is less effective at promoting reaction than adding the same amount of translational energy. For example, in the benchmark MMSR of $H_2$ + Cu(111) rotational energy only has a small influence on the dissociation probability[30, 31, 36, 37] (the rotational efficacy is 0.3 - 0.5[30, 31]), and a similar effect has been observed for $H_2$ on other metal surfaces[38–42]. In the mechanism found to be operative for $H_2$ reacting on coinage metal surfaces, rotational energy is converted to energy in motion along the reaction path because the rotational constant of the molecule decreases as its bond length extends upon approaching the late barrier[30, 31]. Adding rotational energy has an even smaller effect on the sticking of methane on Ni(111)[43]. Moreover, rotational effects are not expected to be easily visible in molecular beam experiments on sticking of small molecules not containing hydrogen atoms: these molecules tend to have small rotational constants, so that rotational cooling should be very efficient in such molecular beams[44–47].

The dissociative chemisorption of HCl on Au(111) has been called an enigmatic reaction[48] for several reasons. For example, the first measured sticking probabilities[49] were found to exceed previously predicted values[50] by about two orders of magnitude, and the analysis of the experiments suggested a very high vibrational efficacy. Subsequent dynamics calculations managed to reduce the discrepancies between computed and measured $S_0$ values, but the computed $S_0$ still exceeded the measured values by one order of magnitude[48, 51, 52]. Only recently considerably better agreement between theory and experiment was achieved for sticking at normal incidence[25] (see Chapter 3). The improved agreement resulted from the theory using a better density functional (the MS-RPBEl meta-GGA functional[53]), and a reanalysis of the experiments concerning, for instance, the relationship between the sticking probability and the Auger signals used to establish the coverage of Au by Cl[25]. As a result, the discrepancy between the computed and measured sticking probabilities at normal incidence was reduced to a factor ranging from 2 to 7, depending on the incidence energy. Also, the trends observed experimentally in the energy transfer[54] and (in)elastic scattering probabilities[55] were reproduced qualitatively, suggesting that the new PES should be adequate for describing the reaction mechanism of HCl + Au(111). However, sticking at off-normal incidence and the unusually large vibrational efficacy implicit in a former analysis of the experiments[49] were not yet addressed in Chapter 3.

In this chapter, we consider the sticking of HCl on Au(111) at off-normal incidence, paying special attention to the effects of the rotational temperature of the incident molecular beam and its average incidence energy parallel to the surface. For this, the previous experiments on sticking at off-normal incidence were re-analyzed in the same way as done before for normal incidence[25]. Also, the same improved potential energy surface was used as in the previous successful study on scattering at normal incidence[25] in Chapter 3. For technical details of this chapter, the reader is referred to Chapter 3. The theory based on the meta-GGA functional yields an even better description of sticking at off-normal incidence than obtained for normal incidence[25] in Chapter 3. Surprisingly, the calculations show very high rotational efficacies for reaction, i.e., values exceeding a factor 10. This high rotational efficacy is caused by a strong and non-monotonic dependence of the reaction path on the polar angle $\theta$ of the orientation of HCl relative to the Au(111) surface in a region of this path that just precedes the barrier. To traverse this region, the molecule needs to rotate initially, and it needs to arrive at this region with the right rotational phase.

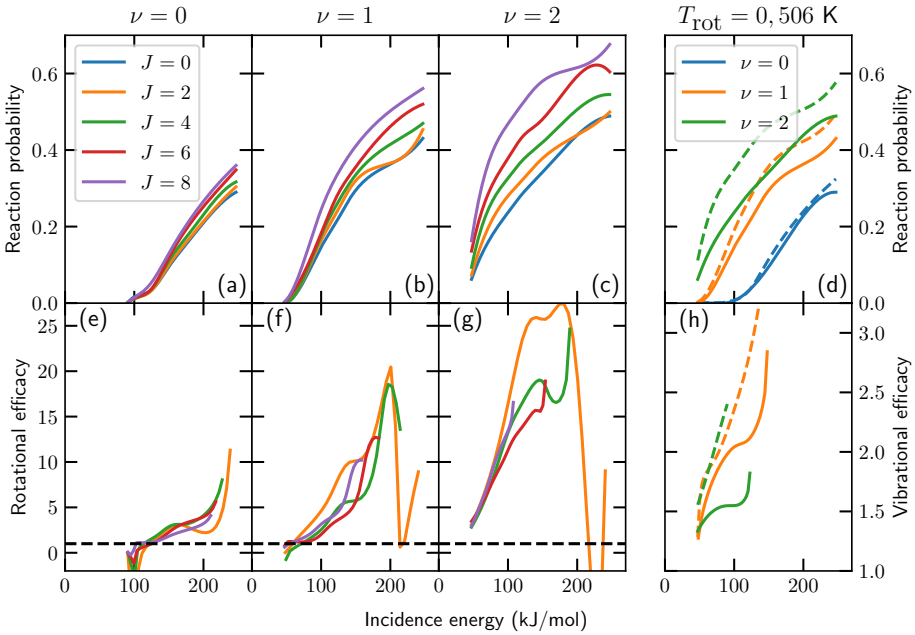


FIGURE 4.1: (a-c) Reaction probability for normally incident HCl on Au(111) and (e-g) the corresponding rotational efficacy. Results for $\nu = 0$ are shown in panels a and d, for $\nu = 1$ in panels b and e, and for $\nu = 2$ in panels c and f. The rotational efficacy is computed relative to $J = 0$ with the same vibrational state. The dashed line indicates a rotational efficacy of unity. (d) Reaction probability and (h) concomitant vibrational efficacy. The vibrational efficacy is computed relative to $\nu = 0$ with the same rotational state distribution. The solid (dashed) lines indicate results for $T_{\rm rot} = 0\,\mathrm{K}$ ($T_{\rm rot} = 506\,\mathrm{K}$).

## 4.2 Results

### 4.2.1 Rotational and Vibrational Efficacies

For now, we consider normally incident HCl only, dropping the incidence angle from our notation and writing the initial state selected reaction probability simply as $R_{\nu,J}(E_{\rm i})$, where $\nu$ is the initial vibrational and $J$ the rotational quantum number (see also Section 4.C). Figures 4.1a-c show a large dependence of $R_{\nu,J}(E_{\rm i})$ on $J$ for $\nu = 0, 1$, and especially 2. We may define the rotational efficacy, which measures how effective adding rotational energy is at promoting the reaction (i.e., at achieving an initial state-selected reaction probability

TABLE 4.1: Rotational ($\chi_J$) and vibrational ($\chi_\nu$) efficacies of HCl on Au(111) as a function of the reaction probability (Eq. 4.1).

| $R$ \ $\nu$ | $\chi_{J=2}$ | | | $\chi_{J=4}$ | | | $\chi_{J=6}$ | | | $\chi_{J=8}$ | | | $\chi_\nu(J=0)$ | | $\chi_\nu(T_{\rm rot}=506\,{\rm K})$ | |
|---|---|---|---|---|---|---|---|---|---|---|---|---|---|---|---|---|
| | 0 | 1 | 2 | 0 | 1 | 2 | 0 | 1 | 2 | 0 | 1 | 2 | $0\to1$ | $0\to2$ | $0\to1$ | $0\to2$ |
| 0.05 | 0.5 | 2.0 | - | 1.0 | 0.8 | - | 0.6 | 1.2 | - | 1.1 | 1.2 | - | 1.7 | - | 1.8 | - |
| 0.10 | 2.2 | 3.8 | 5.3 | 2.2 | 1.8 | 3.1 | 1.4 | 1.2 | - | 1.2 | 1.6 | - | 1.9 | 1.4 | 2.0 | - |
| 0.15 | 3.1 | 6.5 | 10.9 | 3.1 | 3.1 | 6.0 | 2.6 | 1.6 | 4.0 | 1.9 | 2.2 | - | 2.0 | 1.5 | 2.2 | 1.7 |
| 0.20 | 2.3 | 9.8 | 18.7 | 3.4 | 5.0 | 9.9 | 3.4 | 2.8 | 6.0 | 2.4 | 3.1 | 4.1 | 2.1 | 1.5 | 2.4 | 1.9 |
| 0.25 | 2.9 | 10.4 | 25.3 | 4.7 | 5.7 | 13.9 | 4.0 | 3.7 | 8.4 | 3.0 | 3.8 | 5.9 | 2.2 | 1.6 | 2.7 | 2.1 |
| 0.30 | - | 14.6 | 25.7 | - | 6.6 | 16.6 | - | 4.6 | 10.8 | - | 4.5 | 7.9 | - | | 3.1 | 2.3 |
| 0.35 | - | 19.1 | 27.5 | - | 12.3 | 18.8 | - | 7.7 | 13.0 | - | 6.8 | 10.1 | - | | - | |
| 0.40 | - | 3.9 | 20.2 | - | 18.3 | 17.7 | - | 12.5 | 14.6 | - | 9.9 | 11.9 | - | | - | |

equal to $R$), relative to increasing $E_{\rm i}$ and for HCl in the state $\nu$, as follows:

$$\chi_J(R;\nu) = \frac{E_{\rm i}(\nu, J=0; R) - E_{\rm i}(\nu, J; R)}{E_{\rm rot}(\nu, J) - E_{\rm rot}(\nu, J=0)}. \tag{4.1}$$

Here, $E_{\rm i}(\nu, J; R)$ is the incidence energy at which $R_{\nu,J}(E_{\rm i}) = R$. Table 4.1 shows that rotational efficacies defined in this way may be large, e.g., for $J = 6$ it takes on the values of 4.0 for $\nu = 0$ and $R = 0.25$, of 12.5 for $\nu = 1$ and $R = 0.40$, and of 14.6 for $\nu = 2$ and $R = 0.40$. In writing and applying Eq. 4.1 we have tentatively assumed that $R_{\nu,J}(E_{\rm i})$ is a bijective or invertible function, i.e., only one value of $E_{\rm i}$ corresponds to a particular value of $R_{\nu,J}$. This will usually be true as $R_{\nu,J}(E_{\rm i})$ tends to be a monotonically increasing function of $E_{\rm i}$. We may then also define a function $E_{\rm i}^{\nu,J}(R)$, which is equal to the incidence energy $E_{\rm i}$ at which $R_{\nu,J}(E_{\rm i}) = R$. This allows us to define a rotational efficacy that depends on incidence energy for the molecule in the state $\nu$ as follows:

$$\chi_J(E_{\rm i};\nu) = \frac{E_{\rm i}(\nu, J=0; R) - E_{\rm i}(\nu, J; R)}{E_{\rm rot}(\nu, J) - E_{\rm rot}(\nu, J=0)}. \tag{4.2}$$

In Eq. 4.2, the argument $E_{\rm i}$ is the incidence energy for which a reaction probability $R$ is obtained for the higher rotational state. The rotational efficacy defined in this way is plotted in Figures 4.1e-g. The plots show that the rotational efficacy strongly depends on the value of $E_{\rm i}$ at which it is evaluated for the higher rotational state, and it also strongly depends on the value of $\nu$. For example, for $J = 6$ the rotational efficacy takes on values of up to 4 for $\nu = 0$, up to 12 for $\nu = 1$, and up to 20 for $\nu = 2$.

Figure 4.1d also shows a large dependence of $R_{\nu,J}(E_{\rm i})$ on $\nu$ for $J = 0$. To determine the effectiveness of vibrational pre-excitation for promoting

reaction, the vibrational efficacies $\chi_\nu(R;J)$ and $\chi_\nu(E_\mathrm{i};J)$ may be defined in a way that is entirely analogous to Eqs. 4.1 and 4.2, respectively. As can be seen from Table 4.1, $\chi_\nu(R;J)$ can also take on large values (for $J=0$, these values are up to 2.2 for $\nu=1$, and up to 1.6 for $\nu=2$), which are considerably larger than one. However, they are much smaller than the values achieved for $\chi_J(R;\nu)$ (e.g., up to 14.6 for $\nu=2, J=6$). This suggests that rotational pre-excitation of the molecules present in a molecular beam may have a greater effect on the sticking probability $S_0(E_\mathrm{i}, T_\mathrm{N}, \Theta_\mathrm{i})$ measured in a molecular beam experiment than vibrational pre-excitation. We will come back to this different efficacy later. A similar picture emerges from the plots of $\chi_\nu(E_\mathrm{i};J)$, which takes on values of up to 2.8 for $\nu=1$ and up to 1.8 for $\nu=2$, respectively (Figure 4.1h).

Vibrational efficacies may also be evaluated for a thermal rotational distribution instead of for $J=0$ only. In Figure 4.1h, we show $\chi_\nu(E_\mathrm{i};T_\mathrm{rot}=506\,\mathrm{K})$ for the highest rotational temperature achieved in the recent molecular beam experiments on HCl + Au(111), i.e., $T_\mathrm{rot}=506\,\mathrm{K}$. Here, we see a synergistic effect, i.e., the effects of increased vibrational and rotational pre-excitation are mutually reinforcing, which, to the best of our knowledge, has not been observed before (see also Section 4.F).

In the literature, values of vibrational efficacies have often been based on fits of $R_{\nu,J}(E_\mathrm{i})$ where the fit function is taken as an S-shaped function of $E_\mathrm{i}$, e.g., as a function containing an error function or tanh function of $E_\mathrm{i}$[30, 31, 56–58]. If these functions are taken to be of the same shape (i.e., if they have the same "width" and "saturation value"), the efficacies $\chi_\nu(R;J)$ and $\chi_\nu(E_\mathrm{i};J)$ become independent of $R$ and of $E_\mathrm{i}$, respectively, and the vibrational efficacy may be evaluated simply as

$$\chi_\nu(J) = \frac{E_0(\nu=0,J) - E_0(\nu,J)}{E_\mathrm{vib}(\nu,J) - E_\mathrm{vib}(\nu=0,J)}, \tag{4.3}$$

where $E_0(\nu,J)$ is simply defined as the incidence energy at which $R_{\nu,J}(E_\mathrm{i})$ becomes equal to half its maximum value (i.e., its "saturation value"), as achieved at high $E_\mathrm{i}$. One could attempt to extract the vibrational efficacy with the aid of Eq. 4.3 in a procedure where experiments are performed for normal incidence, varying the nozzle temperature to increase the (normal) incidence energy and the vibrational state populations, and for off-normal incidence at a high nozzle temperature, varying the normal incidence energy by varying the incidence angle while keeping the vibrational state populations constant. Such a procedure was recently used to extract $E_0(\nu)$ parameters for $\nu=0$ and 1 for HCl + Au(111), assuming rotational effects to be negligible and assuming

TABLE 4.2: Sticking probabilities for off-normally incident HCl on Au(111) shown in Figure 4.2 for laser-off and laser-on conditions.

| $E_n$ (kJ/mol) | $S_0^{\text{laser-off}}$ | $S_{0,\nu=1,J=2}^{\text{laser-on}}$ | $S_{0,\nu=1,J=8}^{\text{laser-on}}$ | $S_{0,\nu=2,J=2}^{\text{laser-on}}$ | $S_{0,\nu=2,J=8}^{\text{laser-on}}$ |
|---|---|---|---|---|---|
| 47 | $0.000 \pm 0.000$ | $0.000 \pm 0.000$ | $0.000 \pm 0.000$ | $0.006 \pm 0.000$ | $0.008 \pm 0.000$ |
| 67 | $0.001 \pm 0.000$ | $0.004 \pm 0.001$ | $0.004 \pm 0.000$ | $0.015 \pm 0.001$ | $0.015 \pm 0.001$ |
| 99 | $0.010 \pm 0.001$ | $0.022 \pm 0.001$ | $0.021 \pm 0.001$ | $0.030 \pm 0.001$ | $0.029 \pm 0.001$ |
| 123 | $0.044 \pm 0.002$ | $0.061 \pm 0.002$ | $0.060 \pm 0.002$ | $0.068 \pm 0.002$ | $0.067 \pm 0.002$ |
| 142 | $0.088 \pm 0.003$ | $0.109 \pm 0.003$ | $0.106 \pm 0.003$ | $0.113 \pm 0.003$ | $0.111 \pm 0.003$ |
| 170 | $0.169 \pm 0.004$ | $0.193 \pm 0.004$ | $0.191 \pm 0.004$ | $0.197 \pm 0.004$ | $0.196 \pm 0.004$ |
| 247 | $0.331 \pm 0.005$ | $0.353 \pm 0.005$ | $0.351 \pm 0.005$ | $0.356 \pm 0.005$ | $0.355 \pm 0.005$ |

TABLE 4.3: State-specific reaction probabilities for off-normally incident HCl on Au(111) used to compute the laser-off and laser-on sticking probabilities shown in Figure 4.2.

| $E_n$ (kJ/mol) | $R_{\nu=0,J=3}$ | $R_{\nu=0,J=7}$ | $R_{\nu=1,J=2}$ | $R_{\nu=1,J=8}$ | $R_{\nu=2,J=2}$ | $R_{\nu=2,J=8}$ |
|---|---|---|---|---|---|---|
| 47 | $0.000 \pm 0.000$ | $0.000 \pm 0.000$ | $0.001 \pm 0.000$ | $0.005 \pm 0.001$ | $0.073 \pm 0.003$ | $0.163 \pm 0.004$ |
| 67 | $0.000 \pm 0.000$ | $0.000 \pm 0.000$ | $0.033 \pm 0.002$ | $0.071 \pm 0.003$ | $0.183 \pm 0.004$ | $0.327 \pm 0.005$ |
| 99 | $0.006 \pm 0.001$ | $0.008 \pm 0.001$ | $0.161 \pm 0.004$ | $0.243 \pm 0.004$ | $0.279 \pm 0.005$ | $0.466 \pm 0.005$ |
| 123 | $0.032 \pm 0.002$ | $0.043 \pm 0.002$ | $0.236 \pm 0.004$ | $0.342 \pm 0.005$ | $0.332 \pm 0.005$ | $0.531 \pm 0.005$ |
| 142 | $0.079 \pm 0.003$ | $0.095 \pm 0.003$ | $0.291 \pm 0.005$ | $0.393 \pm 0.005$ | $0.369 \pm 0.005$ | $0.561 \pm 0.005$ |
| 170 | $0.158 \pm 0.004$ | $0.176 \pm 0.004$ | $0.350 \pm 0.005$ | $0.460 \pm 0.005$ | $0.407 \pm 0.005$ | $0.604 \pm 0.005$ |
| 247 | $0.304 \pm 0.005$ | $0.354 \pm 0.005$ | $0.453 \pm 0.005$ | $0.561 \pm 0.005$ | $0.499 \pm 0.005$ | $0.676 \pm 0.005$ |

$S_0$ to depend only on normal incidence energy[49]. Applying this procedure blindly using Eq. 4.3 would yield a vibrational efficacy of 6.4 (see Section 4.B and Table 4.B.1), which is considerably higher than the computed efficacy ($\chi_{\nu=1} = 1.8 - 3.1$). We attribute this discrepancy not only to the neglect of rotational effects in the aforementioned procedure to obtain the vibrational efficacy, but also to the procedure used to obtain the effective barrier heights (see Section 4.B).

Our prediction of a high rotational efficacy will of course be most useful if it can be confirmed with experiments within the present state-of-the-art. In Figure 4.2 and Tables 4.2 and 4.3, we show that it is possible to do. To enable excitation to high $J$, the experiments suggested (see also Section 4.C) would employ a high $T_N$ and off-normal incidence to vary the normal incidence energy, as done before in the off-normal incidence experiments on HCl + Au(111)[49]. Furthermore, the experiments we suggest would pre-excite HCl to the $J = 2$ and $J = 8$ states in $\nu = 1$ or $\nu = 2$, and would therefore be able to verify that the reaction of $J = 8$ HCl is far more efficient than that of $J = 2$ HCl. Specifically, such an experiment would pre-excite HCl to a specific rovibrational state (here, from $\nu = 0$ and $J = 3$ to $\nu = 1$ or 2 and $J = 2$; or from

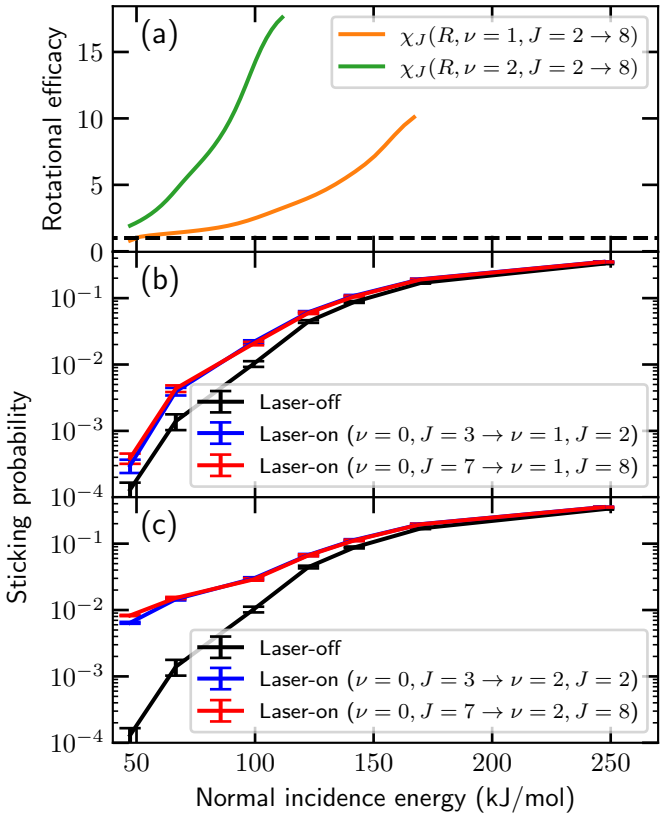


FIGURE 4.2: (a) Predicted rotational efficacy of off-normally incident HCl on Au(111) as a function of normal incidence energy. The $J = 2 \to 8$ rotational efficacy is determined for $\nu = 1$ (orange) and $\nu = 2$ (green). The dashed line indicates a rotational efficacy of unity. (b) Sticking probability of off-normally incident HCl on Au(111) as a function of normal incidence energy. The black lines indicate "laser-off" results for $T_{\text{vib}} = 1060\,\text{K}$ and $T_{\text{rot}} = 506\,\text{K}$. "Laser-on" results, where part of the molecules in the $\nu = 0, J = 3$ ($\nu = 0, J = 7$) state are excited to the $\nu = 1, J = 2$ ($\nu = 1, J = 8$) state, are indicated by the blue (red) lines. The error bars represent 68% confidence intervals. (c) Same as panel b, except that the laser-on results are for the $\nu = 2, J = 2$ and $\nu = 2, J = 8$ excited states.

$\nu = 0$ and $J = 7$ to $\nu = 1, 2$ and $J = 8$) with a laser. Then, from the "laser-off" and "laser-on" results, a state-specific sticking probability can be obtained (for the procedure see Section 4.C). Note that we have also accounted for the excitation efficiency in such an experiment. For incidence energies below the barrier height (i.e., 100 kJ/mol), the differences between the laser-off and laser-on results are likely to be measurable, especially for $\nu = 2$ (Figure 4.2c). For incidence energies above the barrier height, the differences between the laser-on and laser-off results are small and likely difficult to measure. Fortunately, since it is probable that the employed DF underestimates the barrier height compared to experiment (with an estimated 30 - 50 kJ/mol)[25], a considerably larger range of incidence energies where the state-specific sticking probability is measurable should be available for such an experiment than predicted here.

### 4.2.2 Reaction Mechanism

We now turn to the cause of the high rotational efficacy. Our explanation is based on the following remarkable observations. First of all, results for $\nu = 0$ and $\nu = 2$ at $E_i = 247$ kJ/mol show that $S_{\nu,J}(\theta)$ is non-zero for all initial values of the polar orientation angle of HCl for all $J$-values except for $J = 0$ (Figures 4.3a and 4.E.3). This already suggests a partial explanation for the high rotational efficacy: Reaction of molecules with high $J$ is comparatively efficient, because reaction of $J = 0$ HCl is notoriously inefficient. Similarly, vibrational efficacies $> 1$ are only observed if the reaction of a molecule in $\nu = 0$ is remarkably inefficient, as found in cases where the reaction of molecules in the vibrational ground state is hampered by the bobsled effect[10, 22] (see also Chapters 8 and 9).

Another intriguing observation is that $S_{\nu,J=6}(\theta)$ is larger for $\theta < 90°$ than for $\theta > 90°$ (Figures 4.3a and 4.E.3), even though the barrier for reaction is at $\theta \geq 113°$ for reaction at the top, bridge, fcc, and hcp sites, and at the global TS geometry (which occurs close to, but not at the top site, see Chapter 3)[25]. Note that $\theta = 0°$ corresponds to the H atom pointing away from the surface, and $\theta = 180°$ to the H atom pointing to the surface. Furthermore, independent of the vibrational state, whether or not molecules with $J = 6$ stick not only depends on the initial value of $\theta$, but also on its conjugate momentum, i.e., the sense of rotation (see Figures 4.3b and 4.E.4-4.E.6). This is even more obvious for the $J = 2$ states of $\nu = 0, 1$, and 2 (see Figures 4.E.4 to 4.E.6). These observations suggest that reaction is promoted if the molecule is initially rotating and if it approaches the barrier with an appropriate rotational phase. Inspection of how $\theta$ varies with the MEP for the TS and the high symmetry top, bridge, and fcc sites (Figure 4.3c) suggests an explanation. On the way

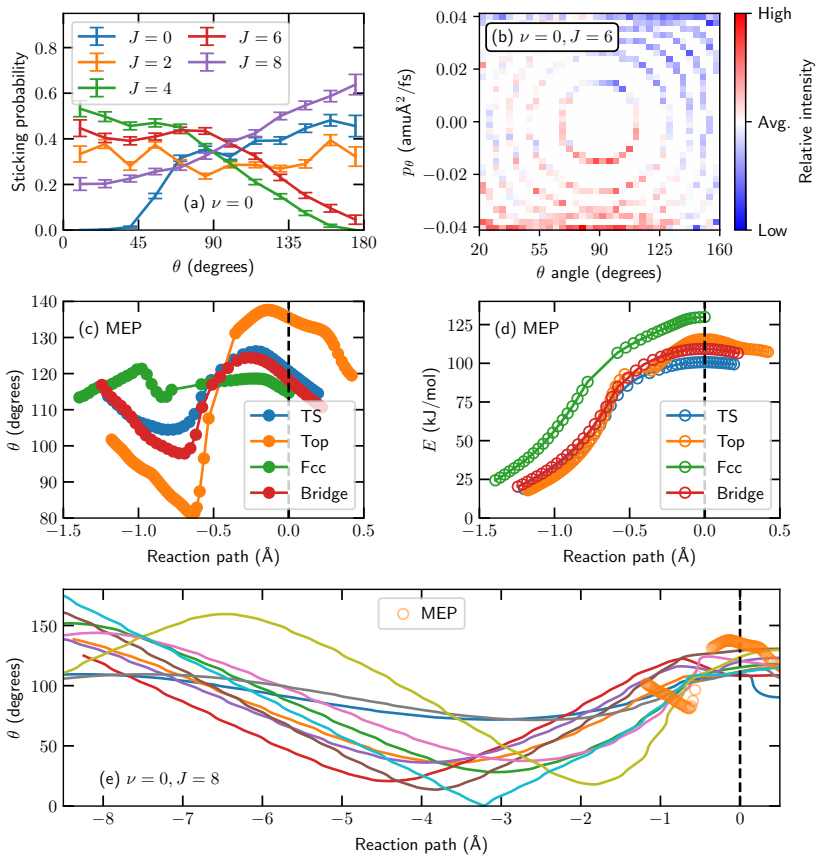


FIGURE 4.3: (a) Sticking probability as a function of the initial $\theta$ angle of HCl on Au(111) for $\langle E_i \rangle = 247$ kJ/mol. Results for several rotational states within $\nu = 0$ are shown, which are indicated in the figure. The error bars represent 68% confidence intervals. (b) Distribution of the initial $\theta$ angle and its conjugate momentum of reacting HCl on Au(111) for $\nu = 0$ and $J = 6$. The colors indicate the intensity of reactive combinations of $\theta$ and $p_\theta$ relative to the statistical distribution in the simulated molecular beam; i.e., blue indicates that the combination is less reactive compared to its statistical occurrence whereas red indicates a relatively higher reactivity. The data have been normalized along the $\theta$ angle to remove the $\sin\theta$ distribution in the initial statistical distribution, i.e., with the renormalization performed all initial $\theta$ angles have equal probability. (c) Polar angle $\theta$ of HCl on Au(111) along the MEP of the global TS (blue), and the top (orange), fcc (green), and bridge (red) sites. The black dashed line indicates the TS, i.e., the value of the reaction path is zero. (d) Same as panel c, but showing the potential energy instead of $\theta$. (e) $\theta$ angle along the reaction path for a few representative trajectories reacting at the top site for $\nu = 0$ and $J = 8$. The $\theta$ angle along the MEP for the top site is indicated by the orange red circles. The black dashed line indicates the location of the reaction barrier, where $r = r^\ddagger = 1.89$ Å[25].

to the barrier, $\theta$ depends on the reaction coordinate in a clear non-monotonic manner, especially for the top, TS, and bridge MEPs. The optimal $\theta$ value first decreases with the reaction coordinate, then it sharply increases, after which it decreases again, before the molecule reaches the minimum barrier geometry (Figure 4.3c). For the initially non-rotating molecules, "steering" (i.e., the effect that the molecule is steered to the most favorable orientation for reaction by the forces acting on it[59]) cannot take place under these conditions, because the molecule will "overshoot" its most favorable orientation once the most favorable value of $\theta$ starts changing in the opposite direction, due to the angular momentum the molecule has acquired. Hence, steering, which can be especially effective for an initially non-rotating molecule[59], will be counterproductive, and on a relative basis molecules with $J = 0$ will be non-reactive. Rather the opposite is observed: the faster the molecule is rotating initially, the higher the probability is that the molecule arrives at the barrier with an appropriate rotational phase (i.e., orientation and angular momentum) to react (see Figures 4.3e and 4.E.7). In chapter 3, it has been found[25] that the top site is relatively unreactive, whereas the hollow site is relatively reactive, even though the barrier heights would suggest the opposite (Figure 4.3d). The strong non-monotonic dependence of the most favorable value of $\theta$ on the reaction coordinate is observed to a lesser extent at the fcc site than at the other sites (Figure 4.3c), suggesting that the behaviour of the $\theta$ angle along the MEP plays an important role in the dynamical accessibility of the TS, hence also the observed site-specific reactivity in Chapter 3 (i.e., bridge $\geq$ hollow $>$ top).

Our admittedly tentative explanation of the non-monotonic dependence of the value of $\theta$ on the reaction path observed for most impact sites is as follows. We suspect that the initial bonding of the dissociating molecule to the surface goes via the more electronegative Cl atom; its increasingly attractive interaction with the surface and the purely repulsive interaction of the H atom with the surface could explain why $\theta$ decreases initially with the reaction path coordinate in Figure 4.3c for all sites but the fcc site. For long enough distance between the H and Cl atoms, the H atom will also start bonding with the surface, which can explain the increase in the $\theta$ value of the reaction path starting at the value of roughly $-0.6$ Å of the reaction path coordinate in Figure 4.3c.

### 4.2.3 Sticking Probabilities

We now come back to the possibility that rotational excitation may have a larger effect on $S_0$ than vibrational excitation. Figures 4.4a,b show the experimental and theoretical sticking probabilities of normally (red diamonds) and

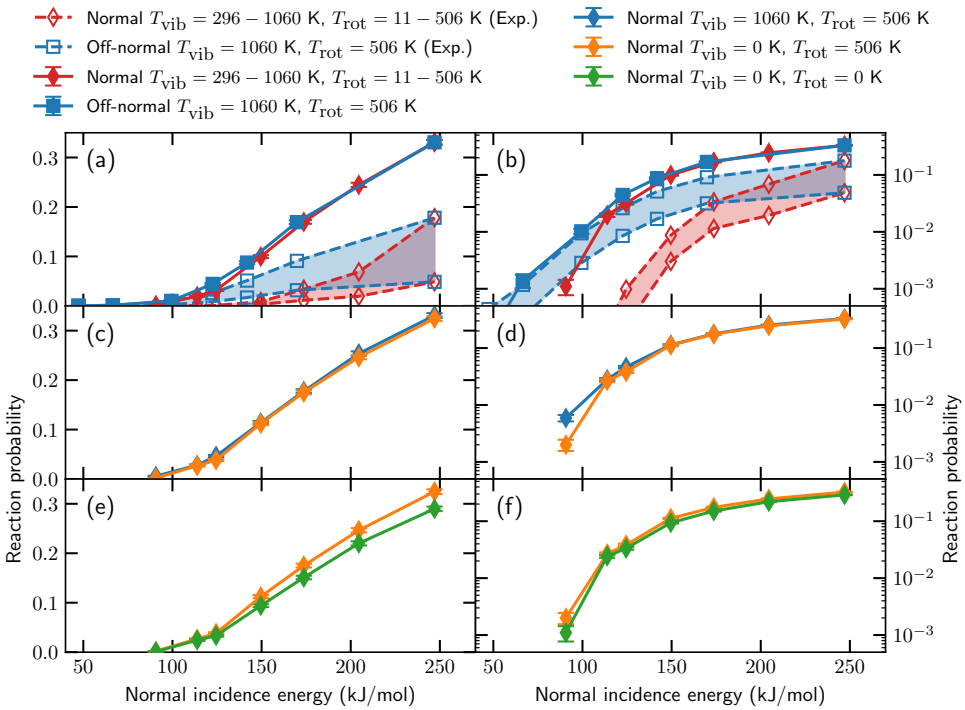


FIGURE 4.4: Sticking probability of HCl on Au(111) as a function of normal incidence energy for various conditions ((off-)normal indicidence, and vibrational and rotational temperatures). The open symbols and dashed lines indicate experimental results, where the shaded area indicates their uncertainty. The solid symbols and lines indicate computed results. The diamonds (squares) are for (off-)normal incidence, where the color indicates the rotational and vibrational temperatures (see legend). The error bars represent 68% confidence intervals. Panels b, d, and f are identical to panels a, c, and e, respectively, except that a logarithmic scale is used instead. For further explanation see the text.

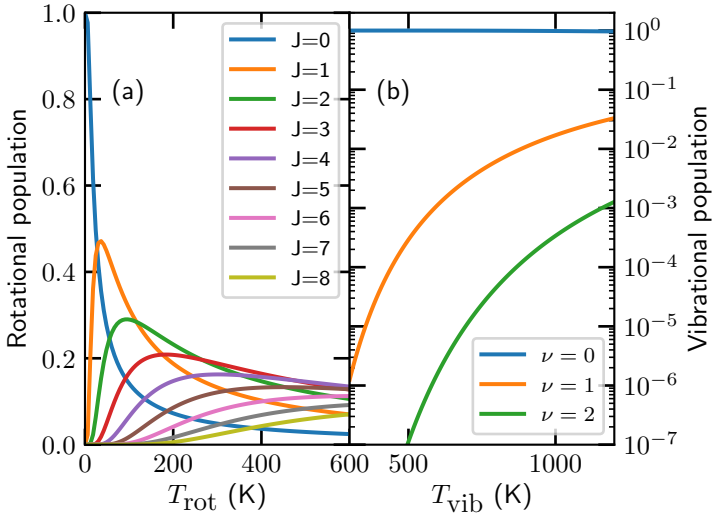


FIGURE 4.5: Rotational (a) and vibrational (b) state populations of HCl according to a Boltzmann distribution as a function of temperature. The rovibrational energies are obtained from the PES.

off-normally (blue squares) incident HCl. Interestingly, it seems that the agreement between theory (solid lines and filled symbols) and experiment (dashed lines and open symbols) is better for off-normally than normally incident HCl. The difference in the sticking probability between the two experimental data sets has previously been explained from the difference in vibrational temperature[49]. Whether this analysis is correct may be gleaned from Figures 4.4c,d, which compares results of calculations for normal incidence and one and the same rotational temperature, but different vibrational temperatures, i.e., $T_{\mathrm{vib}} = 0\,\mathrm{K}$ (orange diamonds) and $T_{\mathrm{vib}} = 1060\,\mathrm{K}$ (blue diamonds). No difference between the computed reaction probabilities is visible using a linear scale (panel c), while a difference is only visible with the use of a logarithmic scale (panel d) if the incidence energy is lower than the minimum barrier in the PES, i.e., 100 kJ/mol. The reason is that, even though the vibrational efficacy for sticking ($\chi_{\nu=1} = 2 - 3$) is high for the energies shown, only two percent of the molecules is vibrationally pre-excited (to $\nu = 1$) at $T_{\mathrm{vib}} = 1060\,\mathrm{K}$ (see Figure 4.5), which is the highest vibrational temperature used in the experiments. Thus, the difference between the normal and off-normal incidence data sets cannot be attributed to the difference in vibrational temperature only.

It has been suggested that the translational energy parallel to the metal

surface might increase the sticking probability as well[60], i.e., the assumption of NES might break down. However, here we do not observe an influence of motion parallel to the surface on the sticking probability (see also Figures 4.D.1g,h). Furthermore, Figures 4.4e,f compare sticking of normally incident HCl with the rotational state distribution either being completely in $J = 0$ (green) or according to a Boltzmann distribution at the maximum rotational temperature achieved in the experiments (orange). Here, we see that also the rotational temperature influences the sticking probability. From Figure 4.4 we conclude that the difference between the sticking probabilities measured for normal and off-normal incidence (presented in Ref. [49], Chapter 3, and the present chapter) are for a large part due to rotational effects. These rotational effects (see also Figure 4.D.1 and Section 4.D) prevent the direct determination of vibrational effects from the experiments discussed, as the vibrational effects are much weaker than the rotational effects over most of the incidence energy range probed.

## 4.3 Conclusion

In this chapter, a large effect of rotational excitation is found for the dissociative chemisorption of HCl on Au(111). This rotational effect is the cause for a considerable difference in the sticking probability between two experimental data sets, which was previously attributed to vibrational excitation instead. The predicted rotational efficacy can be as large as 20; i.e., rotational energy is much more efficient at promoting the reaction than translational energy. To the best of our knowledge a rotational efficacy this large, or even larger than one, has not been observed so far. Furthermore, pre-exciting both rotation and vibration has a mutually reinforcing effect: The rotational efficacy is increased considerably (from a factor of about 4 to a factor 20). Moreover, the high rotational efficacy is not due to a steering effect, but a lock-in effect where only specific initial rotational phases (i.e., combinations of the polar angle $\theta$ and its conjugate momentum) are reactive, which is caused by a non-monotonic dependence of the reaction path on the polar angle $\theta$ in the region just in front of the minimum barrier. As a result, the reaction of HCl in the rotational ground state on Au(111) is inefficient, in contrast to that of rotationally pre-excited HCl.

# Appendix

## 4.A Definition of the Sticking Probability

Here, we define the sticking probability as

$$S_0(\langle E_\mathrm{i}(v_0,\alpha)\rangle, T_\mathrm{N}, \Theta_\mathrm{i}) = S_0(\langle E_\mathrm{i}\rangle, T_\mathrm{N}, \Theta_\mathrm{i}) = S_0(E_\mathrm{i}, T_\mathrm{N}, \Theta_\mathrm{i}), \tag{4.4}$$

where $T_\mathrm{N}$ is the nozzle temperature and $\Theta_\mathrm{i}$ the incidence angle. We usually drop the dependence of the average incidence energy $\langle E_\mathrm{i}(v_0,\alpha)\rangle$ on the molecular beam parameters defining the velocity distribution (i.e., the stream velocity $v_0$ and velocity width $\alpha$) and write it simply like $\langle E_\mathrm{i}\rangle$. In writing the sticking probability like $S_0(E_\mathrm{i}, T_\mathrm{N}, \Theta_\mathrm{i})$ we tacitly assume that the reader knows that $E_\mathrm{i}$ is in fact equal to $\langle E_\mathrm{i}\rangle$. If we consider normal incidence ($\Theta_\mathrm{i} = 0$), we may also drop the incidence angle from the expression and write the sticking probability like $S_0(E_\mathrm{n}, T_\mathrm{N}) = S_0(E_\mathrm{i}, T_\mathrm{N})$, where $E_\mathrm{n}$ is the normal incidence energy and in writing this equation we have again tacitly assumed that in fact it is the average normal incidence energy, i.e., $E_\mathrm{n} = \langle E_\mathrm{n}\rangle$. Here,

$$E_\mathrm{n} = \cos^2(\Theta_\mathrm{i})E_\mathrm{i}. \tag{4.5}$$

If normal energy scaling (NES) holds, we then may simply substitute $S_0(E_\mathrm{n}, T_\mathrm{N})$ for $S_0(E_\mathrm{i}, T_\mathrm{N}, \Theta_\mathrm{i})$.

We also define the initial-state selected reaction probability $R_{\nu,J}(E_\mathrm{i}, \Theta_\mathrm{i})$, where $\nu$ and $J$ are the initial vibrational and rotational quantum numbers, respectively. Of course, if we decide to only consider normal incidence, we may also write this as $R_{\nu,J}(E_\mathrm{n})$ or as $R_{\nu,J}(E_\mathrm{i})$, as long as we remember that we are considering normal incidence. And, if we assume NES, we may substitute $R_{\nu,J}(E_\mathrm{n})$ for $R_{\nu,J}(E_\mathrm{i}, \Theta_\mathrm{i})$. Which assumption is made (normal incidence only, or NES holds) has to be clearly stated and we make a decision on this when we present this in this chapter. Here, the symbol $R$ is used instead of $S_0(E_\mathrm{i}, T_\mathrm{N}, \Theta_\mathrm{i})$ to clearly distinguish between an initial-state selected reaction probability that can usually not be directly measured in a molecular beam experiment and the sticking probability, which can be directly measured, but represents an

average over the distribution of incidence energies and of the rovibrational states of the molecules in the incident beam.

## 4.B Determination of Effective Barrier Heights and Concomitant Vibrational Efficacy

An effective barrier height indicates the incidence energy at which $S_0 = 1/2 S_0^{\max}$, and is typically a parameter in error function fits to experimental sticking probabilities[31, 49, 61]. Previously, the following vibrational state specific S-shaped sticking curves were employed for HCl + Au(111)[49]:

$$S_0^{\nu=i}(E) = \frac{A_i}{2}\left[1 + \mathrm{erf}\left(\frac{E - E_{0,i}}{W_i}\right)\right], \tag{4.6}$$

where $A_i$ is the saturation value (i.e., $S_0^{\max}$), $E_{0,i}$ is the effective barrier height, $W_i$ is a broadening parameter, and $i$ indicates the vibrational state. Furthermore, it is assumed that only $\nu = 0$ and $\nu = 1$ HCl are present in the molecular beam. The constraints employed in the original fitting procedure[49] are $A_0 = A_1 = 1$ and $W_0 = W_1$, whereas for the newly determined lower and upper limits (see Ref. [25]) the constraint of $W_0 = W_1$ is lifted. The parameters of the fitted curves are provided in Table 4.B.1. However, in this approach the role of rotational excitation is assumed to be negligible, which we have shown to be incorrect. For example, neglecting rotational excitation in making the fit, even if the sticking probability of vibrationally excited HCl is unity ($S_0^{\nu=1}(E_\mathrm{i}) = 1$), the difference between the measured normal and off-normal incidence sticking probabilities is larger than the maximum contribution of the vibrationally excited molecules in the beam (i.e., 0.02, which would be the population of $\nu = 1$ HCl at $T_\mathrm{N} = 1060\,\mathrm{K}$, see Figures 4.4a,b and 4.5b). Moreover, the agreement between the fitted curves and the experimental data is poor (see Figure 4.B.1). Additionally, $E_0$ parameters determined for energies larger than the employed normal incidence energy (i.e., $E_0 \geq 299\,\mathrm{kJ/mol}$ (Table 4.B.1), whereas $E_\mathrm{n} \leq 247\,\mathrm{kJ/mol}$ (Tables 4.D.1 and 4.D.2)) may be expected to be inaccurate.

Rotational and vibrational efficacies are often obtained from the aforementioned effective barrier heights as follows (see also Eq. 4.3 and the discussion thereof)[30, 31]:

$$\chi_J(\nu) = \frac{E_0(\nu, J=0) - E_0(\nu, J)}{E_\mathrm{rot}(\nu, J) - E_\mathrm{rot}(\nu, J=0)}, \tag{4.7}$$

TABLE 4.B.1: Parameters for the S-shaped curves shown in Figure 4.B.1 fitted to the original[49] and newly determined experimental sticking probabilities for $\nu = 0$ and 1 HCl. $E_{0,\nu}$ and $W_\nu$ are in kJ/mol, whereas $A_\nu$ is unitless.

| Results | $E_{0,0}$ | $W_0$ | $A_0$ | $E_{0,1}$ | $W_1$ | $A_1$ |
|---|---|---|---|---|---|---|
| Old | 385.9 | 48.2 | 1.0 | 164.0 | 48.2 | 1.0 |
| New (lower limit) | 395.6 | 106.1 | 1.0 | 115.8 | 9.6 | 1.0 |
| New (upper limit) | 299.1 | 77.2 | 1.0 | 96.5 | 19.3 | 1.0 |

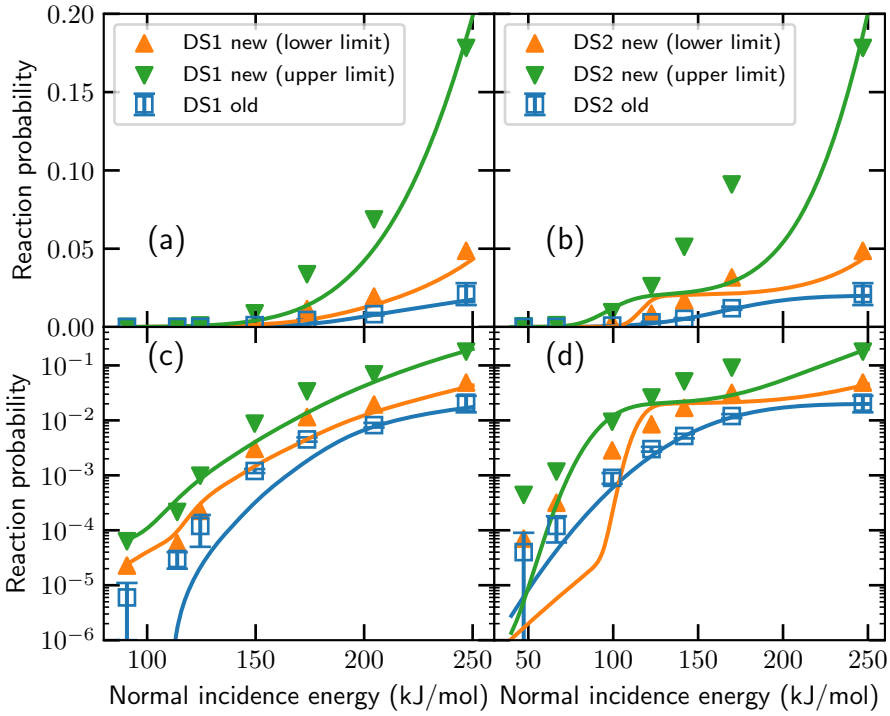


FIGURE 4.B.1: Experimental sticking probabilities of HCl on Au(111) for normally (DS1; a,c) and off-normally (DS2; b,d) incident HCl, where DS1 and DS2 refer to the employed beam parameters (see text). The blue diamonds indicate the original experimental results[49], whereas the orange upwards facing (green downwards facing) triangles indicate the newly determined lower (upper) limit (see Chapter 3). The solid lines are the error function fits to the data discussed in Section 4.B. Panels c and d are identical to panels a and b, respectively, except that a logarithmic scale is used instead.

$$\chi_\nu(J) = \frac{E_0(\nu = 0, J) - E_0(\nu, J)}{E_{\text{vib}}(\nu, J) - E_{\text{vib}}(\nu = 0, J)}. \tag{4.8}$$

The vibrational efficacies are 6.4, 8.1 and 5.9 for the original, and newly determined lower and upper limit $E_0$ parameters, respectively. This is clearly much too large when compared to our calculations (see Table 4.1). At the same time, this approach does not take into account the $R$ dependence of the efficacy, which we also consider to be a too severe approximation since efficacies can vary wildly with $R$ (see Figure 4.1 and Table 4.1). In conclusion, an analysis of the experimental results based on the assumption of a rotational efficacy of 0, and in terms of vibrational effects only, is too simple and will lead to overestimated vibrational efficacies.

## 4.C Experimental State-Specific Sticking Probabilities

For the predicted laser-on sticking probabilities shown in Figure 4.4, several experimental limitations are taken into account. First, in the molecular beam two HCl isotopes, i.e., $^{35}$HCl and $^{37}$HCl, would usually be present, of which only one can be excited due to the mass mismatch between the two isotopes and concomitant frequency shift. As such, in the simulated laser-on results only $3/4^{\text{th}}$ of the molecules (the fraction of $^{35}$HCl in an HCl gas) in the targeted rovibrational state can be excited.

An excitation efficiency of close to 100%, which can be achieved for some molecules by rapid adiabatic passage (RAP)[14, 62–65], cannot be achieved with RAP for HCl. The reason is that the narrow frequency bandwidth of the laser that would be required for RAP would make it impossible to transfer all of the population in the ($\nu = 0, J$) to the upper ($\nu = 1$ or 2, $J'$) state: The energy ranges spanned between the fine structure states associated with the nuclear spin of Cl and $J$ in both the upper and lower levels exceed the required laser band width by too much to achieve a laser excitation efficiency greater than 50%[66–68]. Thus, only $3/4 \times 1/2 = 3/8^{\text{th}}$ of the molecules initially in a specific ($\nu, J$) state can be excited. Furthermore, the selection rules for the R branch ($\nu = 0, J$ to $\nu' = 1$ or 2, $J' = J + 1$) and P branch ($\nu = 0, J$ to $\nu' = 1$ or 2, $J' = J - 1$) excitations are taken into account.

Experiments using laser excitation would measure both a "laser-off" and a "laser-on" sticking probability, where the latter can be written as

$$S_0^{\text{laser-on}}(E_\text{i}) = S_0^{\text{laser-off}}(E_\text{i}) + f_{\text{exc}} \left( S_0^{v',J'}(E_\text{i}) - S_0^{v,J=J'\pm1}(E_\text{i}) \right) \tag{4.9}$$

if excitation takes place from the $(\nu, J)$ to the $(\nu', J')$ state, and if the fraction of HCl molecules transferred between these states, $f_{\text{exc}}$, is given by

$$f_{\text{exc}} = f_{\text{sat}} f_\nu(T_{\text{vib}}) f_J(T_{\text{rot}}). \tag{4.10}$$

Here, $f_{\text{sat}}$ is equal to 3/8, as already established above. The product $f_\nu(T_{\text{vib}}) \times f_J(T_{\text{rot}})$ yields a Boltzmann-like population of the $(\nu, J)$ state excited from in the molecular beam, where we take into account that the rotational and vibrational temperatures of the molecules in the beam may differ, assume that these can be related to the nozzle temperature in some way (see Tables 4.D.1 and 4.D.2 for their values), and have made the approximation that the rotational constants of the molecule are independent of the vibrational state. Obviously, the initial-state selected reaction probability $S_0^{v',J'}(E_{\text{i}})$ that we are after can be calculated from Eqs. 4.9 and 4.10 using the equation also used when extracting these probabilities from experiments, i.e.,

$$S_0^{\nu',J'}(E_{\text{i}}) = \frac{S_0^{\text{laser-on}}(E_{\text{i}}) - S_0^{\text{laser-off}}(E_{\text{i}})}{f_{\text{exc}}} + S_0^{\nu=0,J=J'\pm1}(E_{\text{i}}). \tag{4.11}$$

As can be seen from Eq. 4.11, it will be possible to extract accurate values of $S_0^{v',J'}(E_{\text{i}})$ from experiments if the difference between the laser-on and laser-off sticking probabilities is sufficiently large (as addressed by Figures 4.2b,c) in comparison to the error bars with which these quantities are measured (this is not addressed in Figure 4.2), and if $S_0^{v,J=J'\pm1}(E_{\text{i}})$ is either known in advance, or can be assumed to be zero or approximately equal to the laser-off sticking probability. Of course, in calculations we do not have this difficulty and in the simulation of the experiment we can simply use a calculated value for $S_0^{v,J=J'\pm1}(E_{\text{i}})$. Another way to obtain $S_0^{\nu=0,J=J'\pm1}$ is to employ the ratio of $S_0^{\nu=0,J=J'\pm1}/S_0^{\text{laser-off}}$ from simulations[17], although this might require a PES that is in better quantitative agreement with the experimental sticking probabilities than employed in this chapter. Here, however, the problem is solved by simply using the calculated $S_0^{\text{laser-off}}$, $S_0^{\nu=0,J=J'\pm1}$ and $S_0^{v',J'}(E_{\text{i}})$ to predict $S_0^{\text{laser-on}}(E_{\text{i}})$.

## 4.D The Two Experimental Data Sets and the Origin of Their Differences

Specifically, the main differences between the experiments yielding the DS1 and the DS2 datasets are as follows[49]. The DS1 experiments were per-

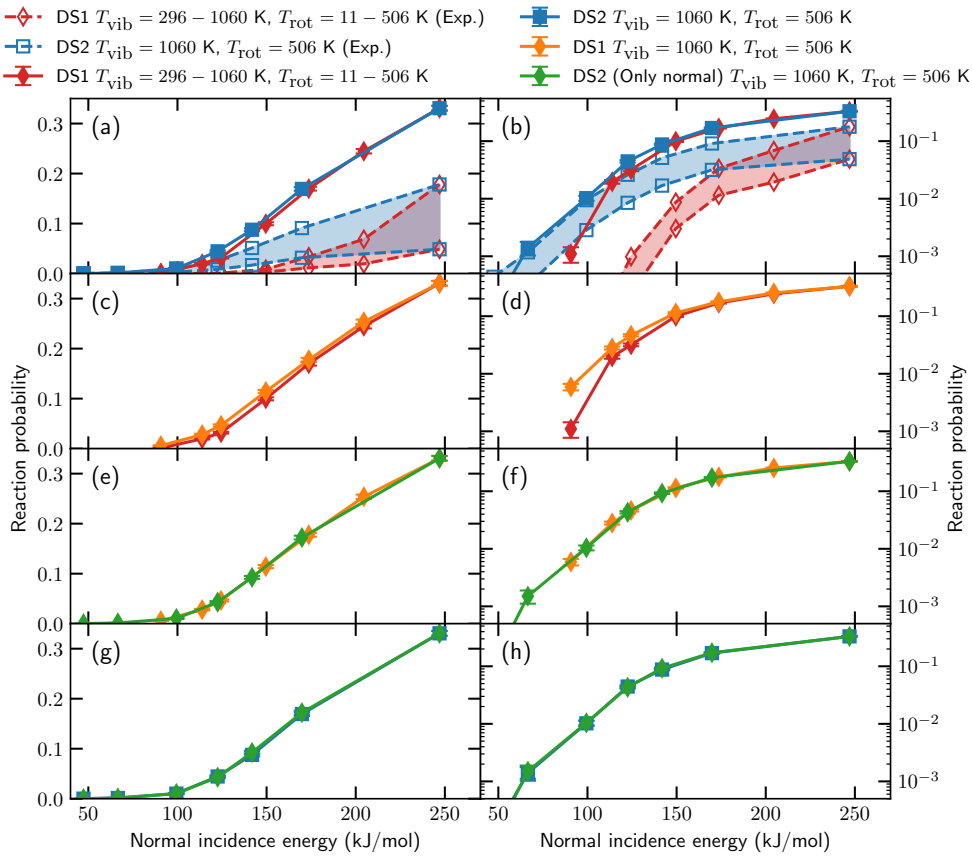


FIGURE 4.D.1: Sticking probability of HCl on Au(111) as a function of normal incidence energy for various conditions ((off-)normal indicidence, and vibrational and rotational temperatures). The open symbols and dashed lines indicate experimental results, where the shaded area indicates their uncertainty. The solid symbols and lines indicate computed results. The diamonds (squares) are for (off-)normal incidence, where the color indicates the rotational and vibrational temperatures (see legend). DS1 and DS2 refer to the employed beam parameters (see text in Section 4.D). The error bars represent 68% confidence intervals. Panels b, d, f and h are identical to panels a, c, e, and g, respectively, except that a logarithmic scale is used instead. For further details see Section 4.D.

formed for normal incidence, and the (normal) incidence energy was varied by changing the nozzle temperature, so that the normal incidence energy on the one hand and the vibrational and rotational temperatures on the other hand were not varied independently in these experiments. In contrast, the DS2 experiments were performed while keeping the nozzle temperature (and therefore $T_{\mathrm{vib}}$ and $T_{\mathrm{rot}}$) constant, while varying the normal incidence energy by varying the incidence angle and the seeding gas mixture. Therefore, in these experiments the normal incidence energy could be varied independently from the rovibrational state populations; however, in the DS2 case there is parallel translational energy present, and this varies with the normal incidence angle. As can be seen from Figures 4.D.1a,b, for similar normal incidence energy the computed DS2 sticking probabilities are higher than the computed DS1 sticking probabilities. The same is true for the measured values as first published[49], but also for the upper and lower bounds to these probabilities obtained by reanalyzing the data (Figures 4.D.1a,b)[25, 69].

With the "experimental knobs" that can be turned to change conditions between the two experiments yielding sticking probabilities as functions of normal incidence energy, one cannot vary all quantities determining these sticking probabilities independently, as discussed above. Of course in theory, one can, as discussed already to some extent in the discussion of Figure 4.4. Here, we enter into additional details. In the first step going from the DS1 to the DS2 conditions, i.e., in turning the first "computational knob" to stay with our previous analogy, we keep all conditions in the DS1 experiment the same, except that we now adopt the same $T_{\mathrm{vib}}$ and $T_{\mathrm{rot}}$ temperature as used in all the DS2 experiments. We keep the beam parameters describing the velocity distributions in the DS1 experiments the same, and perform the simulations for normal incidence. Figures 4.D.1c,d then show the effect of changing to DS2 conditions for $T_{\mathrm{vib}}$ and $T_{\mathrm{rot}}$ while keeping all other conditions the same as in the DS1 experiments. Here, we see that the sticking probability increases with the rovibrational temperature. As discussed in Section 4.2.3, this increase is mostly caused by the increase in rotational temperature, and not by the increase in vibrational temperature (see also Figures 4.4c,d,g,h). Only for incidence energies below the barrier height does the vibrational temperature have a considerable effect on the sticking probability (Figure 4.4d).

The second step is to additionally employ the beam parameters describing the velocity distributions of DS2 (green) instead of DS1 (orange, see Figures 4.D.1e,f), but without including the effect of changing the incidence angle (i.e., the translational energy parallel to the surface remains zero). No considerable changes are observed and therefore we conclude that the change in stream velocity and width when going from DS1 to DS2 does not influence the sticking

TABLE 4.D.1: Beam parameters from Ref. [49] that describe the simulated HCl velocity distributions of data set 1 (DS1). The stream energy $E_0$, stream velocity $v_0$, and velocity width parameter $\alpha$ have been determined through time-of-flight measurements. The incidence angle is normal to the surface.

| $T_{\mathrm{N,vib}}$ (K) | $T_{\mathrm{rot}}$ (K) | $\langle E_{\mathrm{i}} \rangle$ (kJ/mol) | $E_0$ (kJ/mol) | $v_0$ (m/s) | $\alpha$ (m/s) |
|---|---|---|---|---|---|
| 296 | 11 | 91 | 90 | 2219 | 158 |
| 400 | 78 | 114 | 110 | 2456 | 245 |
| 500 | 143 | 124 | 120 | 2562 | 207 |
| 620 | 221 | 150 | 144 | 2808 | 292 |
| 740 | 298 | 174 | 167 | 3026 | 323 |
| 910 | 409 | 205 | 196 | 3278 | 364 |
| 1060 | 506 | 247 | 238 | 3616 | 371 |

TABLE 4.D.2: Beam parameters from Ref. [49] that describe the simulated HCl velocity distributions of data set 2 (DS2). The stream energy $E_0$, stream velocity $v_0$, and velocity width parameter $\alpha$ have been determined through time-of-flight measurements. The nozzle temperature is 1060 K, yielding $T_{\mathrm{vib}} = 1060$ K and $T_{\mathrm{rot}} = 506$ K.

| $\langle E_{\mathrm{i}} \rangle$ (kJ/mol) | $\langle E_{\perp} \rangle$ (kJ/mol) | $\langle E_{\parallel} \rangle$ (kJ/mol) | $\Theta_{\mathrm{i}}$ (°) | $E_0$ (kJ/mol) | $v_0$ (m/s) | $\alpha$ (m/s) |
|---|---|---|---|---|---|---|
| 114 | 47 | 67 | 50 | 114 | 2500 | 273 |
| 114 | 67 | 47 | 40 | 114 | 2500 | 273 |
| 241 | 99 | 142 | 50 | 234 | 3586 | 321 |
| 236 | 123 | 114 | 44 | 230 | 3549 | 322 |
| 241 | 142 | 99 | 40 | 234 | 3586 | 321 |
| 236 | 170 | 67 | 32 | 230 | 3549 | 322 |
| 247 | 247 | 0 | 0 | 238 | 3616 | 371 |

probability considerably.

The final step is to also include the translational energy parallel to the surface (Figures 4.D.1g,h), which is present due to an off-normal incidence angle, thus completely employing the DS2 conditions (blue). Similar to the beam parameters, including parallel translational energy does not influence the sticking probability considerably.

In summary, the difference between the DS1 and DS2 sticking probabilities is caused mainly by the rotational temperature, whereas the vibrational temperature only has an effect for incidence energies below the barrier height, and the stream velocity and width, and motion parallel to the surface have no visible effect on the sticking probability.

## 4.E The Mechanism Underlying the High Rotational Efficacy

The distributions of the $\theta$ angle of reacting HCl are shown for several HCl bond lengths and rovibrational states in Figure 4.E.1. Similarly, Figure 4.E.2 shows the distribution of the $\theta$ angle along the reaction coordinate. The reaction coordinate $S$ is defined here through the change in $Z_{\mathrm{HCl}}$ and $r_{\mathrm{HCl}}$ along the MEP or during a trajectory:

$$S = \Delta Z_{\mathrm{HCl}} + \Delta r_{\mathrm{HCl}}, \tag{4.12}$$

where at the TS $S = 0$. Although generally the reaction coordinate is taken to be mass weighted, here, the masses are neglected due to the small dependence of the reaction coordinate on $r$. Additionally, movement of the center of mass in the $XY$ plane is neglected, since little movement in the $XY$ plane is observed in normally incident HCl MD simulations (see Chapter 3). In general, the initial $\theta$ distributions are broad and become more narrow when the bond is extended, eventually moving the distributions close to the minimum TS value ($\theta = 117°$) (Figures 4.E.1 and 4.E.2). At lower $r$ values, increasing the rotational energy ($J = 2 \rightarrow 8$) increases the width of the $\theta$ distribution, making low initial $\theta$ values more reactive (Figure 4.E.1a). Similarly, increasing the vibrational energy ($\nu = 0 \rightarrow 2$) increases the width of the initial $\theta$ distribution as well (Figure 4.E.1b). This effect is also observed in Figure 4.E.3, where $S_0$ is shown as a function of $\theta$. Furthermore, when the vibrational energy is increased, the focusing of the distribution towards the TS value occurs at a larger $r$ value (compare Figures 4.E.1e,f and Figures 4.E.1g,h).

Figures 4.E.4, 4.E.5 and 4.E.6 show the relative reactivity of combinations of the initial values of $\theta$ and its conjugate momentum compared to its statistical distribution in the simulated molecular beams. Interestingly, the reactivity depends on the combination of the orientation and angular momentum (i.e., the rotational phase), and is also rotational state specific. Furthermore, the results suggest that since the higher $J$ states allow for more different orientations and angular momenta, the molecule is perhaps more easily focused towards a reactive pathway if it is in a high $J$ state.

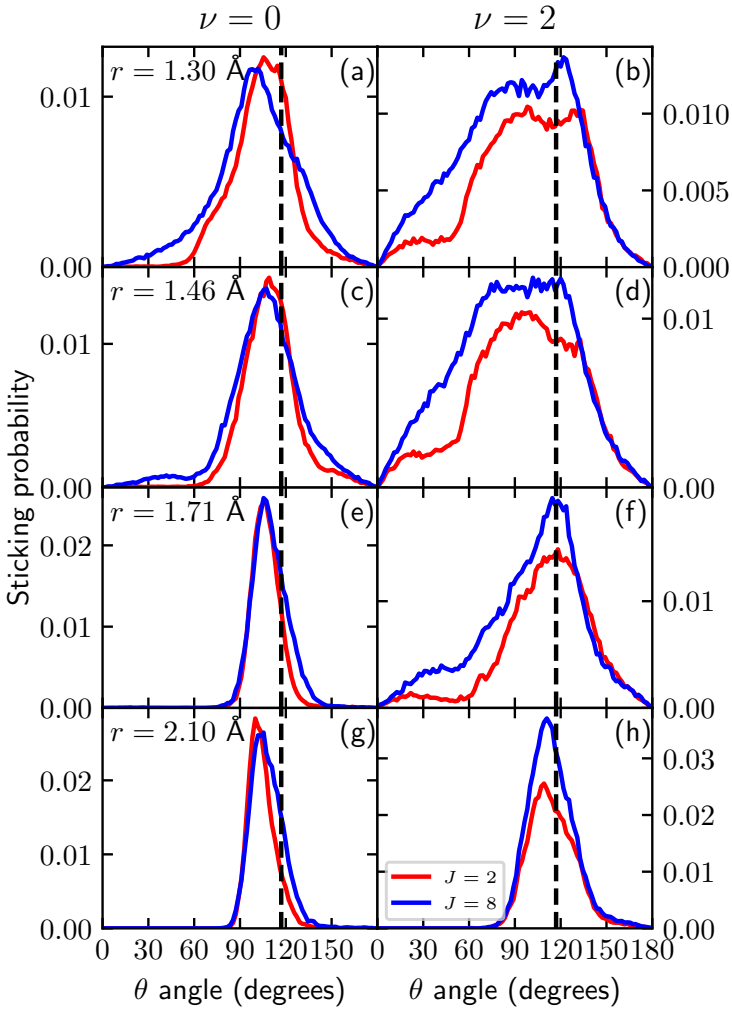


FIGURE 4.E.1: Distribution of the $\theta$ angle of reacting HCl on Au(111) for several bond lengths. Red and blue indicate $J = 2$ and 8, respectively. The left panels are for $\nu = 0$ and the right panels are for $\nu = 2$. The average normal indicidence energy is 247 kJ/mol. For the analysis of the trajectories only $Z_{Cl} < 2.5$ Å is considered. The black dashed line indicates the minimum TS value.

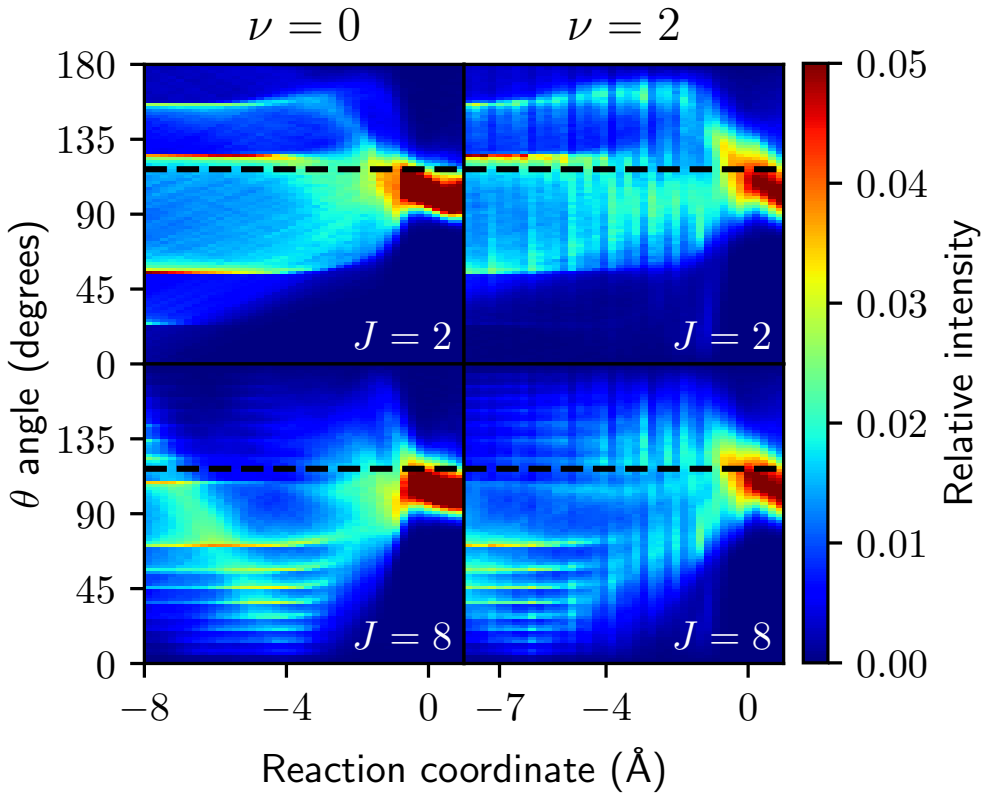


FIGURE 4.E.2: Distribution of the $\theta$ angle of reacting HCl on Au(111) along the reaction path. The average normal indicidence energy is 247 kJ/mol, $\nu = 0$ or 2 (left and right panels, respectively), and $J = 2$ or 8 (top and bottom panels, respectively). The black dashed line indicates the minimum TS value.

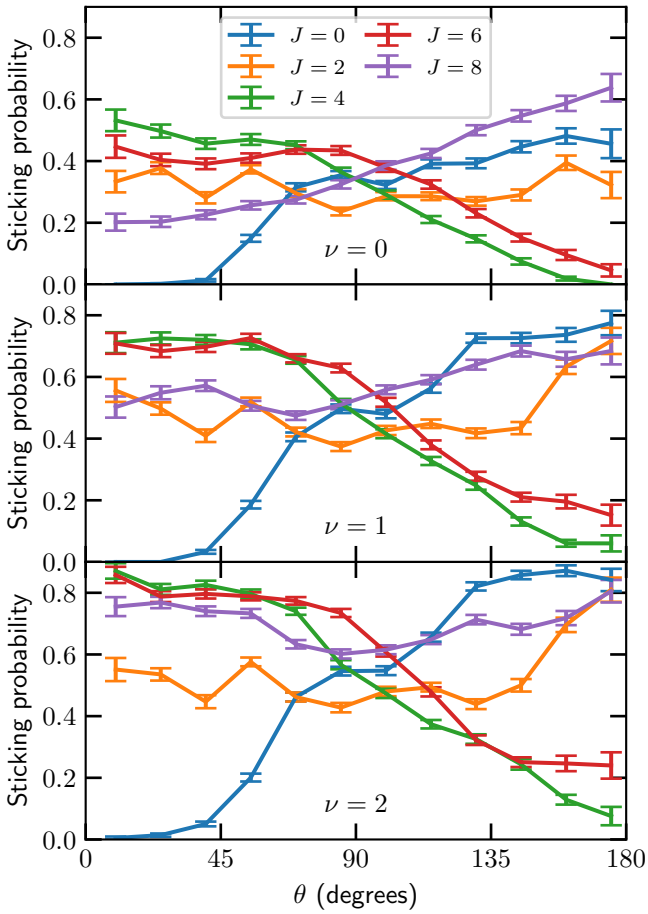


FIGURE 4.E.3: Sticking probability as a function of the initial $\theta$ angle of HCl on Au(111) for $\langle E_i \rangle = 247\,\mathrm{kJ/mol}$. Results for several rovibrational states are shown, as indicated in the legend of the upper panel. The error bars represent 68% confidence intervals.

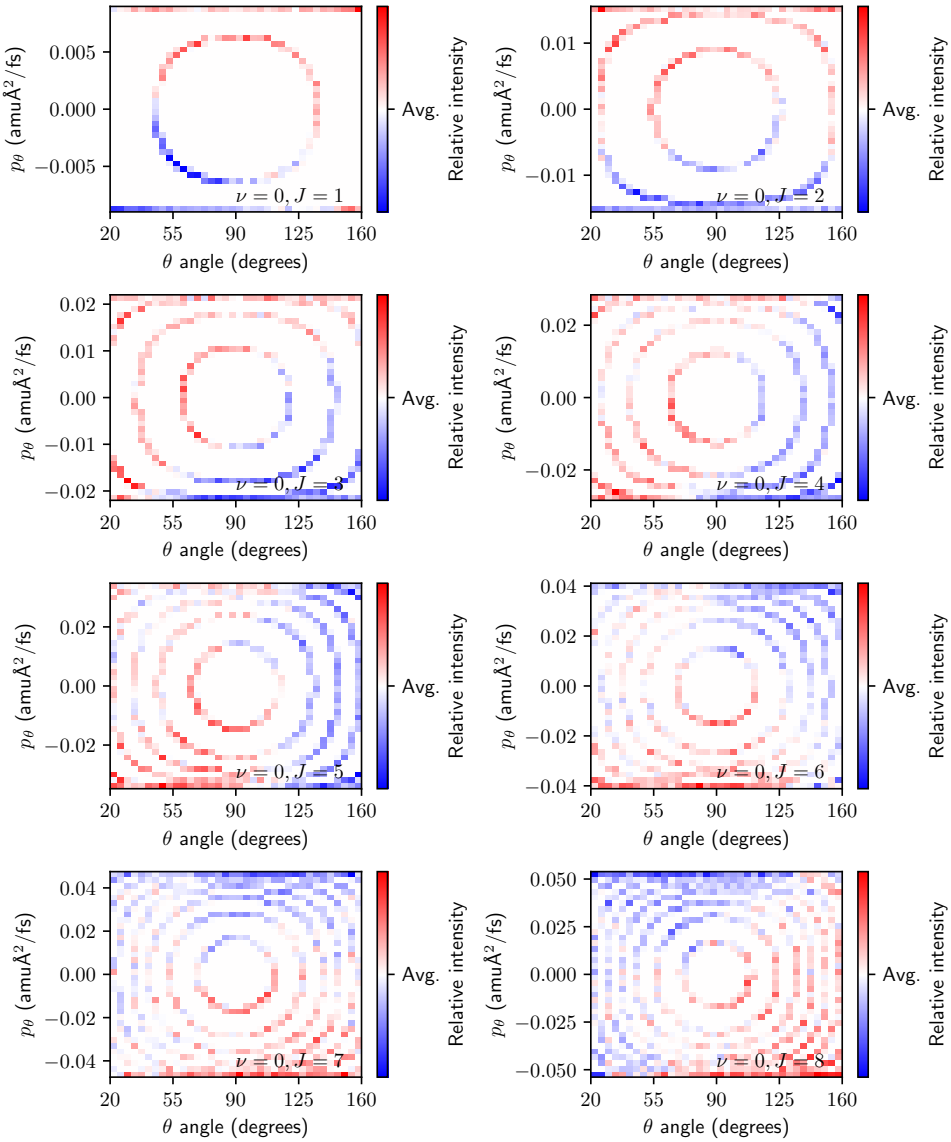


FIGURE 4.E.4: Distribution of the initial $\theta$ angle and its conjugate momentum of reacting HCl on Au(111) for $\nu = 0$ and $J = 1 - 8$. The colors indicate the intensity of reactive combinations of $\theta$ and $p_\theta$ relative to the statistical distribution in the simulated molecular beam; i.e., blue indicates that the combination is less reactive compared to its statistical occurrence whereas red indicates a relatively higher reactivity. The data have been normalized along the $\theta$ angle to remove the $\sin\theta$ distribution in the initial statistical distribution, i.e., with the renormalization performed all initial $\theta$ angles have equal probability.

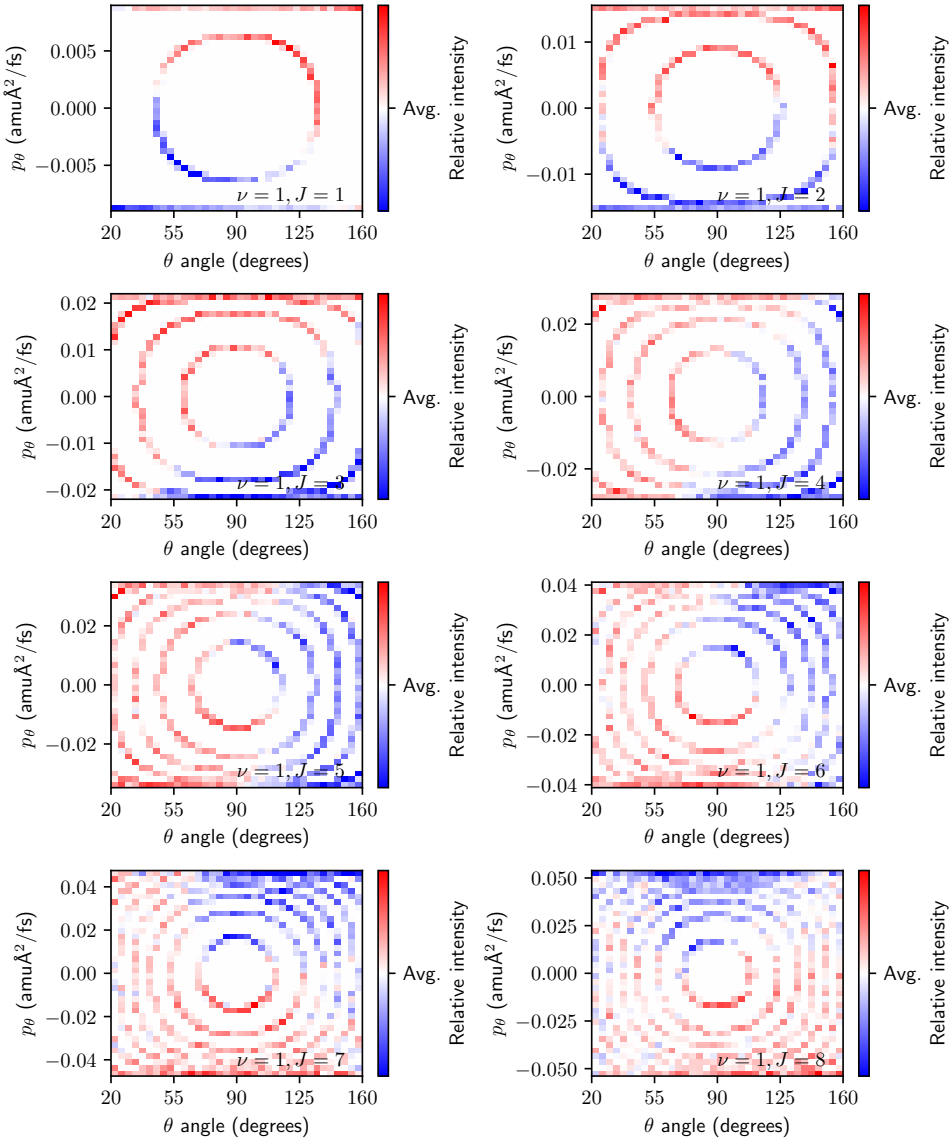


FIGURE 4.E.5: Same as Figure 4.E.4 but for $\nu = 1$.

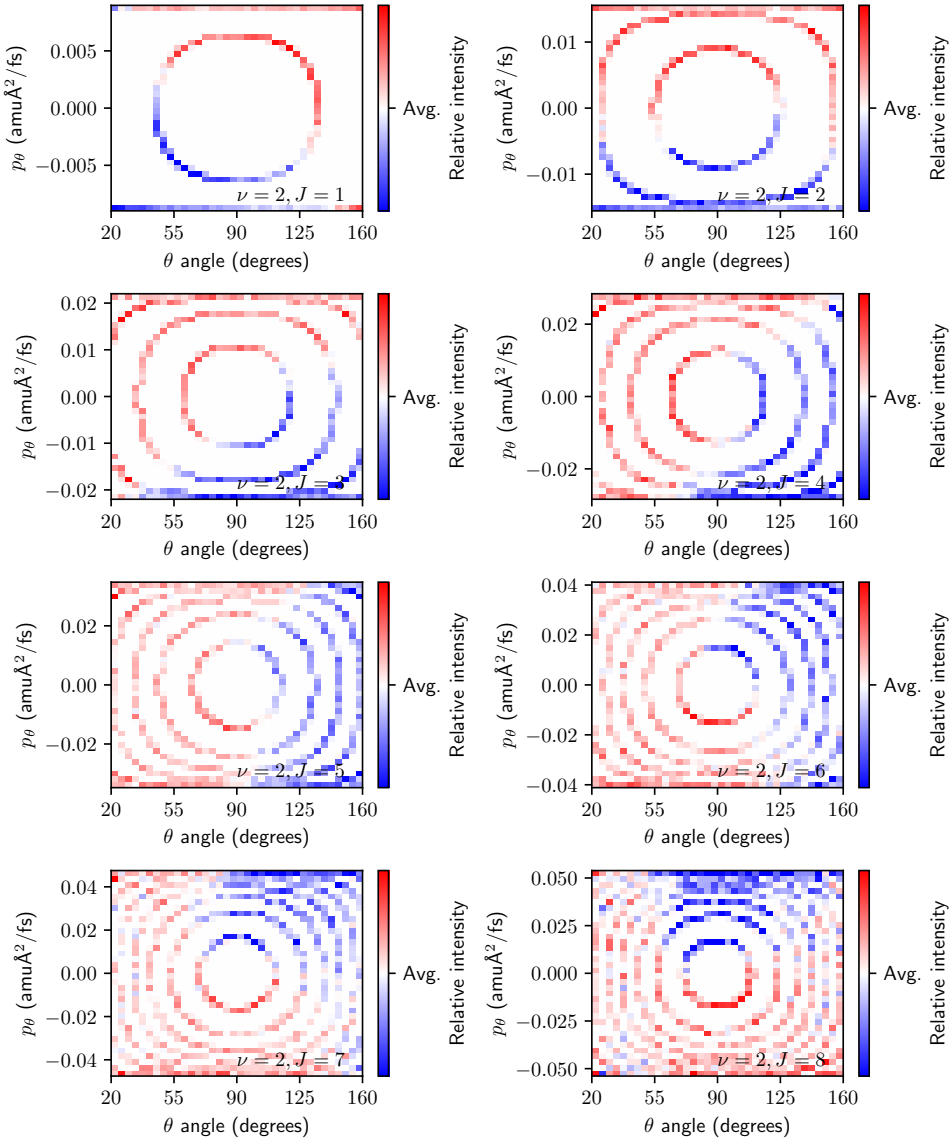


FIGURE 4.E.6: Same as Figure 4.E.4 but for $\nu = 2$.

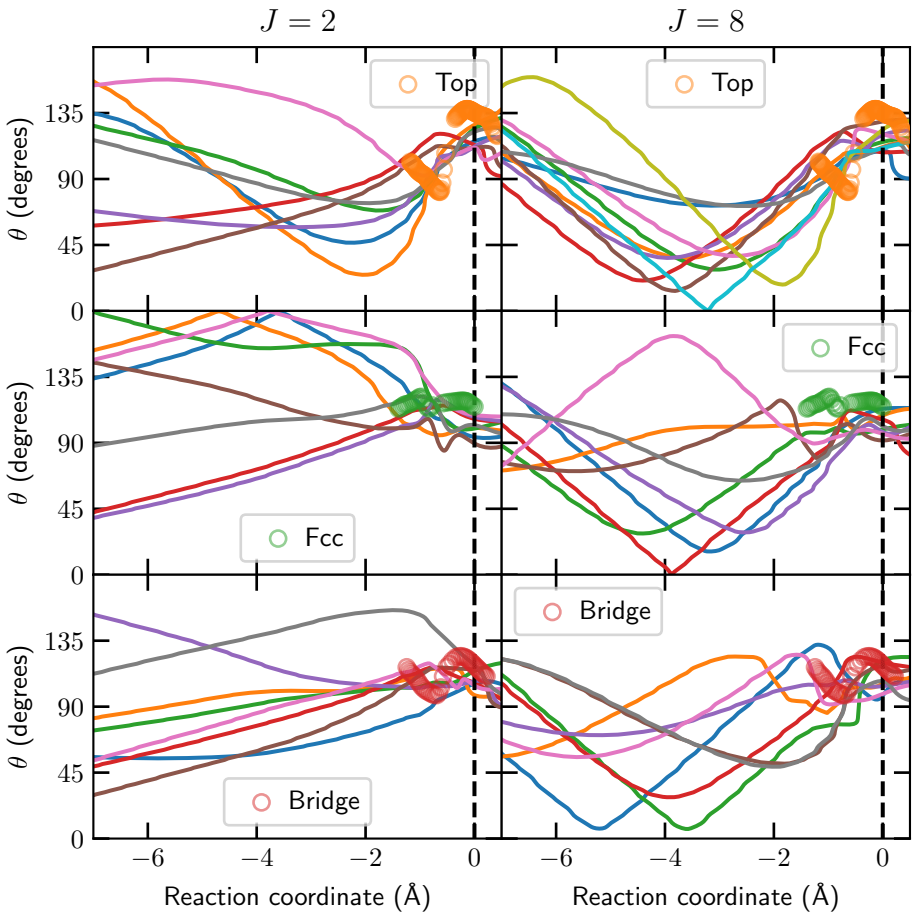


FIGURE 4.E.7: $\theta$ angle along the reaction path for a few representative trajectories reacting at the top, fcc, and bridge sites for $v = 0$ and $J = 2$ (left panels) or 8 (right panels). The $\theta$ angle along the MEP for the top, fcc, and bridge sites is indicated by the orange, green, and red circles, respectively. The dashed line indicates the location of the reaction barrier, i.e., $r = r^{\ddagger}$.

## 4.F Synergistic Effect of Rotational and Vibrational Pre-excitation

Rotational and vibrational pre-excitation of HCl has a synergistic effect on $S_0$, which we will discuss now. The initial distribution of the $\theta$ angle is broad for all rovibrational states considered, whereas at the moment of reaction (i.e., $r = r^{\ddagger} = 2.18$ Å) the distribution is more narrow and nearer the TS value (see Figures 4.E.1 and 4.E.2). Both rotational and vibrational pre-excitation cause a broader initial $\theta$ distribution to be reactive (Figures 4.E.1a,b). Furthermore, rotational reorientation is required due to large changes in the optimum value along the MEP and due to a narrow bottleneck in $\theta$ leading up to the dissociation (see Section 4.2.2). On the other hand, vibrational excitation causes the bottleneck to occur later along the reaction path, while the rotational reorientation occurs in a shorter timeframe (see especially Figure 4.E.1). It is possible that this shortening of the reorientation timeframe causes rotational excitation to have an even larger effect on $S_0$. In any case, we see that pre-exciting rotation and vibration simultaneously has a mutually reinforcing effect on the sticking probability.

## References


(1) Sorgenti, H. A.; Sachsel, G. F. Nitric Acid Manufacture—Theory and Practice. *Ind. Eng. Chem.* **1960**, *52*, 101–104, DOI: 10.1021/ie50602a019.

(2) Ertl, G. Primary Steps in Catalytic Synthesis of Ammonia. *J. Vac. Sci. Technol. A* **1983**, *1*, 1247–1253, DOI: 10.1116/1.572299.

(3) Rostrup-Nielsen, J. R.; Sehested, J.; Nørskov, J. K. In *Advances in Catalysis*; Academic Press: 2002; Vol. 47, pp 65–139, DOI: 10.1016/S0360-0564(02)47006-X.

(4) Sá, S.; Silva, H.; Brandão, L.; Sousa, J. M.; Mendes, A. Catalysts for Methanol Steam Reforming—A Review. *Appl. Catal. B* **2010**, *99*, 43–57, DOI: 10.1016/j.apcatb.2010.06.015.

(5) Fisch, A. G. In *Kirk-Othmer Encyclopedia of Chemical Technology*; John Wiley & Sons: 2019, pp 1–22, DOI: 10.1002/0471238961.2609050703050303.a01.pub2.

(6) Wolcott, C. A.; Medford, A. J.; Studt, F.; Campbell, C. T. Degree of Rate Control Approach to Computational Catalyst Screening. *J. Catal.* **2015**, *330*, 197–207, DOI: 10.1016/j.jcat.2015.07.015.

(7) Ertl, G. Elementary Steps in Heterogeneous Catalysis. *Angew. Chem. Int. Ed.* **1990**, *29*, 1219–1227, DOI: 10.1002/anie.199012191.

(8) Sabbe, M. K.; Reyniers, M.-F.; Reuter, K. First-Principles Kinetic Modeling in Heterogeneous Catalysis: An Industrial Perspective on Best-Practice, Gaps and Needs. *Catal. Sci. Technol.* **2012**, *2*, 2010–2024, DOI: 10.1039/C2CY20261A.

(9) Juurlink, L. B. F.; McCabe, P. R.; Smith, R. R.; DiCologero, C. L.; Utz, A. L. Eigenstate-Resolved Studies of Gas-Surface Reactivity: $CH_4$ $\nu_3$ Dissociation on Ni(100). *Phys. Rev. Lett.* **1999**, *83*, 868–871, DOI: 10.1103/PhysRevLett.83.868.

(10) Smith, R. R.; Killelea, D. R.; DelSesto, D. F.; Utz, A. L. Preference for Vibrational over Translational Energy in a Gas-Surface Reaction. *Science* **2004**, *304*, 992–995, DOI: 10.1126/science.1096309.

(11) Killelea, D. R.; Campbell, V. L.; Shuman, N. S.; Utz, A. L. Bond-Selective Control of a Heterogeneously Catalyzed Reaction. *Science* **2008**, *319*, 790–793, DOI: 10.1126/science.1152819.

(12) Juurlink, L. B. F.; Killelea, D. R.; Utz, A. L. State-Resolved Probes of Methane Dissociation Dynamics. *Prog. Surf. Sci.* **2009**, *84*, 69–134, DOI: 10.1016/j.progsurf.2009.01.001.

(13) Shen, X. J.; Lozano, A.; Dong, W.; Busnengo, H. F.; Yan, X. H. Towards Bond Selective Chemistry from First Principles: Methane on Metal Surfaces. *Phys. Rev. Lett.* **2014**, *112*, 046101, DOI: 10.1103/PhysRevLett.112.046101.

(14) Hundt, P. M.; Ueta, H.; van Reijzen, M. E.; Jiang, B.; Guo, H.; Beck, R. D. Bond-Selective and Mode-Specific Dissociation of $CH_3D$ and $CH_2D_2$ on Pt(111). *J. Phys. Chem. A* **2015**, *119*, 12442–12448, DOI: 10.1021/acs.jpca.5b07949.

(15) Jiang, B.; Guo, H. Dynamics of Water Dissociative Chemisorption on Ni(111): Effects of Impact Sites and Incident Angles. *Phys. Rev. Lett.* **2015**, *114*, 166101, DOI: 10.1103/PhysRevLett.114.166101.

(16) Zhang, Z.; Liu, T.; Fu, B.; Yang, X.; Zhang, D. H. First-Principles Quantum Dynamical Theory for the Dissociative Chemisorption of $H_2O$ on Rigid Cu(111). *Nat. Commun.* **2016**, *7*, 11953, DOI: 10.1038/ncomms11953.

(17) Nattino, F.; Migliorini, D.; Kroes, G.-J.; Dombrowski, E.; High, E. A.; Killelea, D. R.; Utz, A. L. Chemically Accurate Simulation of a Polyatomic Molecule-Metal Surface Reaction. *J. Phys. Chem. Lett.* **2016**, *7*, 2402–2406, DOI: 10.1021/acs.jpclett.6b01022.

(18) Migliorini, D.; Chadwick, H.; Nattino, F.; Gutiérrez-González, A.; Dombrowski, E.; High, E. A.; Guo, H.; Utz, A. L.; Jackson, B.; Beck, R. D.; Kroes, G.-J. Surface Reaction Barriometry: Methane Dissociation on Flat and Stepped Transition-Metal Surfaces. *J. Phys. Chem. Lett.* **2017**, *8*, 4177–4182, DOI: 10.1021/acs.jpclett.7b01905.

(19) Gerrits, N.; Migliorini, D.; Kroes, G.-J. Dissociation of $CHD_3$ on Cu(111), Cu(211), and Single Atom Alloys of Cu(111). *J. Chem. Phys.* **2018**, *149*, 224701, DOI: 10.1063/1.5053990.

(20) Chadwick, H.; Migliorini, D.; Kroes, G. J. $CHD_3$ Dissociation on Pt(111): A Comparison of the Reaction Dynamics Based on the PBE Functional and on a Specific Reaction Parameter Functional. *J. Chem. Phys.* **2018**, *149*, 044701, DOI: 10.1063/1.5039458.

(21) Gerrits, N.; Kroes, G.-J. An AIMD Study of Dissociative Chemisorption of Methanol on Cu(111) with Implications for Formaldehyde Formation. *J. Chem. Phys.* **2019**, *150*, 024706, DOI: 10.1063/1.5070129.

(22) Gerrits, N.; Shakouri, K.; Behler, J.; Kroes, G.-J. Accurate Probabilities for Highly Activated Reaction of Polyatomic Molecules on Surfaces Using a High-Dimensional Neural Network Potential: $CHD_3$ + Cu(111). *J. Phys. Chem. Lett.* **2019**, *10*, 1763–1768, DOI: 10.1021/acs.jpclett.9b00560.

(23) Gerrits, N.; Chadwick, H.; Kroes, G.-J. Dynamical Study of the Dissociative Chemisorption of $CHD_3$ on Pd(111). *J. Phys. Chem. C* **2019**, *123*, 24013–24023, DOI: 10.1021/acs.jpcc.9b05757.

(24) Gerrits, N.; Kroes, G.-J. Curious Mechanism of the Dissociative Chemisorption of Ammonia on Ru(0001). *J. Phys. Chem. C* **2019**, *123*, 28291–28300, DOI: 10.1021/acs.jpcc.9b09121.

(25) Gerrits, N.; Geweke, J.; Smeets, E. W. F.; Voss, J.; Wodtke, A. M.; Kroes, G.-J. Closing the Gap Between Experiment and Theory: Reactive Scattering of HCl from Au(111). *J. Phys. Chem. C* **2020**, *124*, 15944–15960, DOI: 10.1021/acs.jpcc.0c03756.

(26) Moiraghi, R.; Lozano, A.; Peterson, E.; Utz, A.; Dong, W.; Busnengo, H. F. Nonthermalized Precursor-Mediated Dissociative Chemisorption at High Catalysis Temperatures. *J. Phys. Chem. Lett.* **2020**, *11*, 2211–2218, DOI: 10.1021/acs.jpclett.0c00260.

(27) Jackson, B. Direct and Trapping-Mediated Pathways to Dissociative Chemisorption: $CH_4$ Dissociation on Ir(111) with Step Defects. *J. Chem. Phys.* **2020**, *153*, 034704, DOI: 10.1063/5.0012252.

(28) Zeng, X.; Qiu, Z.; Li, P.; Li, Z.; Yang, J. Steric Hindrance Effect in High-Temperature Reactions. *CCS Chem.* **2020**, *2*, 460–467, DOI: 10.31635/ccschem.020.202000155.

(29) Rettner, C. T.; DeLouise, L. A.; Auerbach, D. J. Effect of Incidence Kinetic Energy and Surface Coverage on the Dissociative Chemisorption of Oxygen on W(110). *J. Chem. Phys.* **1986**, *85*, 1131–1149, DOI: 10.1063/1.451310.

(30) Michelsen, H. A.; Rettner, C. T.; Auerbach, D. J.; Zare, R. N. Effect of Rotation on the Translational and Vibrational Energy Dependence of the Dissociative Adsorption of $D_2$ on Cu(111). *J. Chem. Phys.* **1993**, *98*, 8294–8307, DOI: 10.1063/1.464535.

(31) Rettner, C. T.; Michelsen, H. A.; Auerbach, D. J. Quantum-state-specific Dynamics of the Dissociative Adsorption and Associative Desorption of $H_2$ at a Cu(111) Surface. *J. Chem. Phys.* **1995**, *102*, 4625–4641, DOI: 10.1063/1.469511.

(32) Luntz, A. C.; Brown, J. K.; Williams, M. D. Molecular Beam Studies of $H_2$ and $D_2$ Dissociative Chemisorption on Pt(111). *J. Chem. Phys.* **1990**, *93*, 5240–5246, DOI: 10.1063/1.459669.

(33) Chadwick, H.; Guo, H.; Gutiérrez-González, A.; Menzel, J. P.; Jackson, B.; Beck, R. D. Methane Dissociation on the Steps and Terraces of Pt(211) Resolved by Quantum State and Impact Site. *J. Chem. Phys.* **2018**, *148*, 014701, DOI: 10.1063/1.5008567.

(34) Migliorini, D.; Nattino, F.; Tiwari, A. K.; Kroes, G.-J. HOD on Ni(111): Ab Initio Molecular Dynamics Prediction of Molecular Beam Experiments. *J. Chem. Phys.* **2018**, *149*, 244706, DOI: 10.1063/1.5059357.

(35) Chen, J.; Zhou, X.; Zhang, Y.; Jiang, B. Vibrational Control of Selective Bond Cleavage in Dissociative Chemisorption of Methanol on Cu(111). *Nat. Commun.* **2018**, *9*, 4039, DOI: 10.1038/s41467-018-06478-6.

(36) Díaz, C.; Olsen, R. A.; Auerbach, D. J.; Kroes, G. J. Six-Dimensional Dynamics Study of Reactive and Non Reactive Scattering of $H_2$ from Cu(111) Using a Chemically Accurate Potential Energy Surface. *Phys. Chem. Chem. Phys.* **2010**, *12*, 6499–6519, DOI: 10.1039/C001956A.

(37) Donald, S. B.; Harrison, I. Rice–Ramsperger–Kassel–Marcus Simulation of Hydrogen Dissociation on Cu(111): Addressing Dynamical Biases, Surface Temperature, and Tunneling. *J. Phys. Chem. C* **2014**, *118*, 320–337, DOI: 10.1021/jp408714s.

(38) Xiao, Y.; Dong, W.; Busnengo, H. F. Reactive Force Fields for Surface Chemical Reactions: A Case Study with Hydrogen Dissociation on Pd Surfaces. *J. Chem. Phys.* **2010**, *132*, 014704, DOI: 10.1063/1.3265854.

(39) Chen, J.-C.; Ramos, M.; Arasa, C.; Juanes-Marcos, J. C.; Somers, M. F.; Martínez, A. E.; Díaz, C.; Olsen, R. A.; Kroes, G.-J. Dynamics of $H_2$ Dissociation on the 1/2 ML c(2x2)-Ti/Al(100) Surface. *Phys. Chem. Chem. Phys.* **2012**, *14*, 3234–3247, DOI: 10.1039/C2CP23693A.

(40) Wijzenbroek, M.; Helstone, D.; Meyer, J.; Kroes, G.-J. Dynamics of $H_2$ Dissociation on the Close-Packed (111) Surface of the Noblest Metal: $H_2$ + Au(111). *J. Chem. Phys.* **2016**, *145*, 144701, DOI: 10.1063/1.4964486.

(41) Shuai, Q.; Kaufmann, S.; Auerbach, D. J.; Schwarzer, D.; Wodtke, A. M. Evidence for Electron–Hole Pair Excitation in the Associative Desorption of $H_2$ and $D_2$ from Au(111). *J. Phys. Chem. Lett.* **2017**, *8*, 1657–1663, DOI: 10.1021/acs.jpclett.7b00265.

(42) Kaufmann, S.; Shuai, Q.; Auerbach, D. J.; Schwarzer, D.; Wodtke, A. M. Associative Desorption of Hydrogen Isotopologues from Copper Surfaces: Characterization of Two Reaction Mechanisms. *J. Chem. Phys.* **2018**, *148*, 194703, DOI: 10.1063/1.5025666.

(43) Juurlink, L. B.; Smith, R. R.; Utz, A. L. The Role of Rotational Excitation in the Activated Dissociative Chemisorption of Vibrationally Excited Methane on Ni(100). *Faraday Discuss.* **2000**, *117*, 147–160, DOI: 10.1039/B003708G.

(44) Friedrich, B.; Pullman, D. P.; Herschbach, D. R. Alignment and Orientation of Rotationally Cool Molecules. *J. Phys. Chem.* **1991**, *95*, 8118–8129, DOI: 10.1021/j100174a021.

(45) Aquilanti, V.; Ascenzi, D.; Cappelletti, D.; Pirani, F. Velocity Dependence of Collisional Alignment of Oxygen Molecules in Gaseous Expansions. *Nature* **1994**, *371*, 399–402, DOI: 10.1038/371399a0.

(46) Aquilanti, V.; Ascenzi, D.; Cappelletti, D.; Pirani, F. Rotational Alignment in Supersonic Seeded Beams of Molecular Oxygen. *J. Phys. Chem.* **1995**, *99*, 13620–13626, DOI: 10.1021/j100037a008.

(47) Lenzer, T.; Bürsing, R.; Dittmer, A.; Panja, S. S.; Wild, D. A.; Oum, K. Rotational and Vibrational Cooling in Pulsed High-Pressure Molecular Beam Expansions from 3 Bar into the Supercritical Regime. *J. Phys. Chem. A* **2010**, *114*, 6377–6383, DOI: 10.1021/jp9092207.

(48) Füchsel, G.; del Cueto, M.; Díaz, C.; Kroes, G.-J. Enigmatic HCl + Au(111) Reaction: A Puzzle for Theory and Experiment. *J. Phys. Chem. C* **2016**, *120*, 25760–25779, DOI: 10.1021/acs.jpcc.6b07453.

(49) Shirhatti, P. R.; Geweke, J.; Steinsiek, C.; Bartels, C.; Rahinov, I.; Auerbach, D. J.; Wodtke, A. M. Activated Dissociation of HCl on Au(111). *J. Phys. Chem. Lett.* **2016**, *7*, 1346–1350, DOI: 10.1021/acs.jpclett.6b00289.

(50) Liu, T.; Fu, B.; Zhang, D. H. Six-Dimensional Quantum Dynamics Study for the Dissociative Adsorption of HCl on Au(111) Surface. *J. Chem. Phys.* **2013**, *139*, 184705, DOI: 10.1063/1.4829508.

(51) Liu, Q.; Zhou, X.; Zhou, L.; Zhang, Y.; Luo, X.; Guo, H.; Jiang, B. Constructing High-Dimensional Neural Network Potential Energy Surfaces for Gas–Surface Scattering and Reactions. *J. Phys. Chem. C* **2018**, *122*, 1761–1769, DOI: 10.1021/acs.jpcc.7b12064.

(52) Füchsel, G.; Zhou, X.; Jiang, B.; Juaristi, J. I.; Alducin, M.; Guo, H.; Kroes, G.-J. Reactive and Nonreactive Scattering of HCl from Au(111): An Ab Initio Molecular Dynamics Study. *J. Phys. Chem. C* **2019**, *123*, 2287–2299, DOI: 10.1021/acs.jpcc.8b10686.

(53) Smeets, E. W.; Voss, J.; Kroes, G.-J. Specific Reaction Parameter Density Functional Based on the Meta-Generalized Gradient Approximation: Application to $H_2$ + Cu(111) and $H_2$ + Ag(111). *J. Phys. Chem. A* **2019**, *123*, 5395–5406, DOI: 10.1021/acs.jpca.9b02914.

(54) Rahinov, I.; Cooper, R.; Yuan, C.; Yang, X.; Auerbach, D. J.; Wodtke, A. M. Efficient Vibrational and Translational Excitations of a Solid Metal Surface: State-to-State Time-of-Flight Measurements of HCl($v$=2,J=1) Scattering from Au(111). *J. Chem. Phys.* **2008**, *129*, 214708, DOI: 10.1063/1.3028542.

(55) Geweke, J.; Shirhatti, P. R.; Rahinov, I.; Bartels, C.; Wodtke, A. M. Vibrational Energy Transfer near a Dissociative Adsorption Transition State: State-to-State Study of HCl Collisions at Au(111). *J. Chem. Phys.* **2016**, *145*, 054709, DOI: 10.1063/1.4959968.

(56) Díaz, C.; Olsen, R. A. A Note on the Vibrational Efficacy in Molecule-Surface Reactions. *J. Chem. Phys.* **2009**, *130*, 094706, DOI: 10.1063/1.3080613.

(57) Wijzenbroek, M.; Klein, D. M.; Smits, B.; Somers, M. F.; Kroes, G.-J. Performance of a Non-Local van Der Waals Density Functional on the Dissociation of $H_2$ on Metal Surfaces. *J. Phys. Chem. A* **2015**, *119*, 12146–12158, DOI: 10.1021/acs.jpca.5b06008.

(58) Smeets, E. W. F.; Kroes, G.-J. Designing New SRP Density Functionals Including Non-Local vdW-DF2 Correlation for $H_2$ + Cu(111) and Their Transferability to $H_2$ + Ag(111), Au(111) and Pt(111). *Phys. Chem. Chem. Phys.* **2021**, *23*, 7875–7901, DOI: 10.1039/D0CP05173J.

(59) Gross, A.; Wilke, S.; Scheffler, M. Six-Dimensional Quantum Dynamics of Adsorption and Desorption of $H_2$ at Pd(100): Steering and Steric Effects. *Phys. Rev. Lett.* **1995**, *75*, 2718–2721, DOI: 10.1103/PhysRevLett.75.2718.

(60) Roscioli, J. R.; Bell, D. J.; Nelson, D. J.; Nesbitt, D. J. State-Resolved Velocity Map Imaging of Surface-Scattered Molecular Flux. *Phys. Chem. Chem. Phys.* **2012**, *14*, 4070–4080, DOI: 10.1039/C1CP22938A.

(61) Luntz, A. C. A Simple Model for Associative Desorption and Dissociative Chemisorption. *J. Chem. Phys.* **2000**, *113*, 6901–6905, DOI: 10.1063/1.1311280.

(62) Yoder, B. L.; Bisson, R.; Beck, R. D. Steric Effects in the Chemisorption of Vibrationally Excited Methane on Ni(100). *Science* **2010**, *329*, 553–556, DOI: 10.1126/science.1191751.

(63) Yoder, B. L.; Bisson, R.; Morten Hundt, P.; Beck, R. D. Alignment Dependent Chemisorption of Vibrationally Excited $CH_4(\nu_3)$ on Ni(100), Ni(110), and Ni(111). *J. Chem. Phys.* **2011**, *135*, 224703, DOI: 10.1063/1.3665136.

(64) Morten Hundt, P.; Bisson, R.; Beck, R. D. The Sticking Probability of $D_2O$-Water on Ice: Isotope Effects and the Influence of Vibrational Excitation. *J. Chem. Phys.* **2012**, *137*, 074701, DOI: 10.1063/1.4742914.

(65) Pan, H.; Mondal, S.; Yang, C.-H.; Liu, K. Imaging Characterization of the Rapid Adiabatic Passage in a Source-Rotatable, Crossed-Beam Scattering Experiment. *J. Chem. Phys.* **2017**, *147*, 013928, DOI: 10.1063/1.4982615.

(66) Klaus, T.; Belov, S. P.; Winnewisser, G. Precise Measurement of the Pure Rotational Submillimeter-Wave Spectrum of HCl and DCl in Their $\nu = 0, 1$ States. *J. Mol. Spectrosc.* **1998**, *187*, 109–117, DOI: 10.1006/jmsp.1997.7465.

(67) Cazzoli, G.; Puzzarini, C. Hyperfine Structure of the J=1←0 Transition of $H^{35}Cl$ and $H^{37}Cl$: Improved Ground State Parameters. *J. Mol. Spectrosc.* **2004**, *226*, 161–168, DOI: 10.1016/j.jms.2004.03.020.

(68) Iwakuni, K.; Sera, H.; Abe, M.; Sasada, H. Hyperfine-Resolved Transition Frequency List of Fundamental Vibration Bands of $H^{35}Cl$ and $H^{37}Cl$. *J. Mol. Spectrosc.* **2014**, *306*, 19–25, DOI: 10.1016/j.jms.2014.09.013.

(69) Geweke, J. D. Scattering HCl Molecules from Au(111) and Ag(111) Surfaces, Lausanne: EPFL, 2019, DOI: 10.5075/epfl-thesis-9742.

# Chapter 5

# When Does GGA-DFT Get Molecule-Metal Surface Reaction Barriers Right, and What to Do if it Doesn't

This chapter is based on Gerrits, N.; Smeets, E. W. F.; Vuckovic, S.; Powell, A. D.; Doblhoff-Dier, K.; Kroes, G.-J. Density Functional Theory for Molecule–Metal Surface Reactions: When Does the Generalized Gradient Approximation Get It Right, and What to Do If It Does Not. *J. Phys. Chem. Lett.* **2020**, *11*, 10552–10560, DOI: 10.1021/acs.jpclett.0c02452

## Abstract

While density functional theory (DFT) is perhaps the most used electronic structure theory in chemistry, many of its practical aspects remain poorly understood. For instance, DFT at the generalized gradient approximation (GGA) level tends to fail miserably at describing gas phase reaction barriers, while it performs surprisingly well for many molecule-metal surface reactions. GGA-DFT also fails for many systems in the latter category, and up to now it has not been clear when one may expect it to work. This chapter shows that GGA-DFT tends to work if the difference between the work function of the metal and the molecule's electron affinity is greater than ≈7 eV, and to fail if this difference is smaller, with sticking of $O_2$ on Al(111) being a spectacular example. Using dynamics calculations it is shown that, for this system, the DFT problem may be solved as done for gas phase reactions, i.e., by resorting to hybrid functionals, but using screening at long range to obtain a correct description of the metal. The results suggest the GGA error in the $O_2$ + Al(111) barrier height to be functional driven. The results also suggest the possibility to compute potential energy surfaces for the difficult-to-treat systems with

computationally cheap non-self-consistent calculations in which a hybrid functional is applied to a GGA density.

## 5.1 Introduction

Kohn-Sham DFT has become very popular and is now being used in more than 30 000 papers per year[1]. Nevertheless, much of the theory remains not yet well understood, even concerning much of its practical aspects. One surprising practical aspect is that density functionals (DFs) at the generalized gradient approximation (GGA) level are quite accurate for barriers for dissociative chemisorption (DC) reactions on metal surfaces. In contrast, semi-local functionals tend to systematically underestimate reaction barrier heights of gas phase reactions[2, 3], and it has been assumed that this overestimation should carry over to surface reactions in general[4]. Nonetheless, a semi-empirical version of DFT, the specific reaction parameter (SRP) approach to DFT, has achieved chemically accurate descriptions of sticking in many molecule-metal surface systems by using functionals in which the exchange part is a weighted average of GGA exchange functionals[5–13]. Here, often (the exchange part of) the PBE[14] (or PW91[15]) and the RPBE[16] DFs are used, with PBE and PW91 often yielding too low, and RPBE often too high barriers[5, 7]. Dynamics studies using non-empirical GGA DFs have semi-quantitatively described many experiments on DC on metals[17–21]. Perhaps even more surprisingly a recent comparison of DFT results for a database of molecule-metal surface reactions based on experiments and SRP-DFT (SBH10) suggested a better performance for a GGA-exchange based DF (i.e., BEEF-vdW[22]) than for the meta-GGA and screened hybrid representative examples that were tested[23].

In spite of the above, also many molecule-metal surface systems exist for which SRP-DFs based on GGA exchange DFs do not work. By this we mean that even the most repulsive GGA exchange DFs still obeying the uniform electron gas limit (such as RPBE, a non-empirical functional which describes adsorption on metals with quite high accuracy, but already performs rather poorly at describing solid state properties[22, 24]) are too reactive compared to experiment, even when simulating the effect of energy dissipation to electron-hole pairs and surface phonons[25–30]. As a result, the barrier height cannot be "tweaked" to a good value by mixing exchange DFs yielding too high barriers (such as RPBE) and too low barriers (as often the case with PBE or PW91). That is a pity, as a DC transition state (TS) on a metal surface is often the rate-controlling state in industrially important heterogeneously catalyzed processes[31–33] like ammonia production[34] and steam reforming[35]. A

further problem is that it is not clear which property of the system determines whether GGA-DFT may yield a reliable barrier height. Reasons to explain the GGA-DFT failure for individual systems have, however, been cited, with an often cited reason being that electron transfer occurs from the metal surface to the molecule[36, 37].

In this connection often reference is made to the following explanation for why GGA-DFT fails at describing gas phase reactions: the GGA's tendency to underestimate gas phase barrier heights is caused by the electrons delocalizing over additional atoms at the TS, artificially lowering the GGA energy of the TS relative to that of the reactants[3, 38, 39]. The delocalization error finds its origin in what has been called "the lack of derivative discontinuities of semi-local functionals" or alternatively the violation of the Perdew-Parr-Levy-Balduz condition[40] by these functionals. According to Yang and co-workers[41] the delocalization error is similar, but not equal to the self-interaction error (SIE)[42], which is also often invoked to explain the underestimation of gas phase reaction barrier heights. However, the above does not yet explain why GGA-DFT *does* work for many molecule-metal surface reactions. Also, a property of the system on the basis of which one could straightforwardly predict whether GGA-DFT should, at least in principle, work is still missing. Fortunately, the "charge transfer" explanation does suggest such a criterion, as will be shown here.

This chapter shows that a single, albeit composite, property of molecule-metal surface systems exists on the basis of which one can decide whether it should be possible to find a GGA functional with which one can describe the barrier to dissociative chemisorption with chemical accuracy. This allows one to define a single corresponding criterion stating whether GGA functionals should be able to deliver chemical accuracy for the corresponding "easy-to-handle" reactions. Also, the solution applicable to the problem that gas phase reaction barriers are not well-described with GGA functionals (i.e., resorting to hybrid functionals) also works for a prominent example of "difficult" surface reactions, i.e., that of $O_2$ + Al(111). These findings suggest the possibility of extending SRP-DFT to the full range of dissociative chemisorption reactions on metals. Such an extension should enable the development of databases for such reactions[43] without bias to specific rungs of functionals, similar to databases that already exist for gas phase reactions[2, 3].

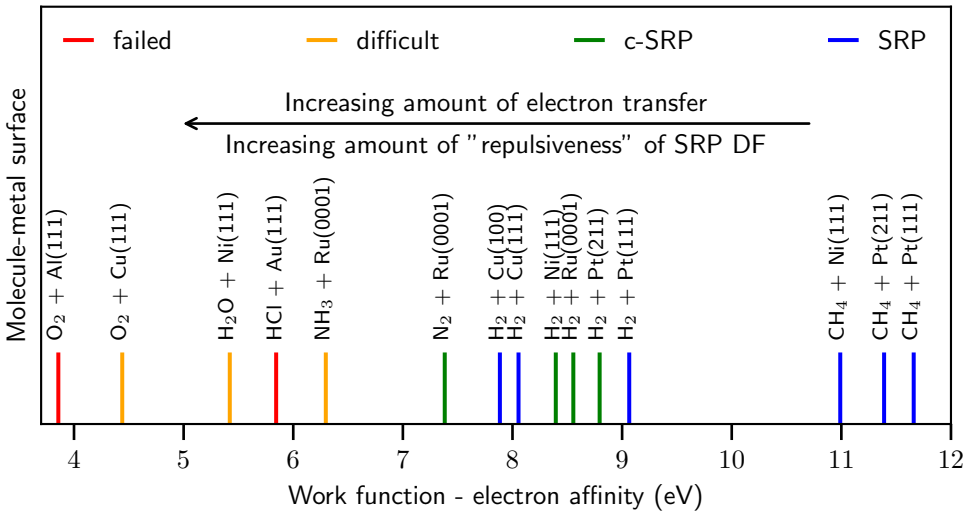


FIGURE 5.1: Correlation between the difference of the work function of the metal surface and the electron affinity of the molecule (eV) with the ability of GGA exchange-based DFs to accurately describe barrier heights to DC in the systems described. Red, orange, green and blue indicate whether efforts to develop an SRP DF based on GGA exchange for a molecule-metal surface reaction have failed, proven difficult, yielded a candidate SRP (c-SRP) DF, or yielded an SRP DF, respectively. The values of the work functions (Table 5.A.1) and electron affinities (Table 5.A.2) are obtained as described in Section 5.A.2.

## 5.2 Analysis of Previous Results

Obviously, one would expect the tendency of a system to display charge transfer to correlate with the difference $(W - E_{ea})$ between the work function $W$ of the metal and the electron affinity $E_{ea}$ of the molecule. Systematic evidence is collected in Figure 5.1, where it is shown how the ability to accurately describe the measured reactivity of molecule-metal surface systems with DFs containing GGA exchange correlates with $(W - E_{ea})$. Figure 5.1 shows that it has been possible to achieve chemical accuracy in descriptions of sticking experiments with GGA-exchange based SRP-DFs[5, 6, 8–10] (in blue) and candidate SRP-DFs[7, 11–13] (in green) if $(W - E_{ea})$ exceeds 7 eV. (Candidate SRP-DFs usually describe a sticking experiment on a specific system with chemical accuracy, but their validity has not (yet) been confirmed through comparison with another experiment on the same system[7, 12, 13].) However, for systems with $(W - E_{ea}) < 7$ eV DFs with repulsive RPBE exchange either overestimate sticking notoriously [25, 26, 29, 44–46] (red), or they show a suspect performance[27, 28, 30, 47] (orange). In Figure 5.1 a trend is also observed that when the difference between $W$ and $E_{ea}$ decreases, so that one might also expect the amount of electron transfer to increase, the SRP or GGA DF needs to be made increasingly repulsive to describe the system's reactivity with chemical accuracy. For example, $CH_4$ + Ni(111)[48] and Pt(111)[49] are quite well-described with the attractive PBE functional[14], and this is also true for $H_2$ + Pt(111)[50] (here the PW91[15] functional was used, which may be considered the predecessor to PBE, which was designed to replace it[14]) and Ru(0001)[7]. On the other hand, the SRP DF for $H_2$ + Cu(111)[5] and Cu(100)[6] needs to contain about 50% RPBE exchange, and a good description of $N_2$ + Ru(0001) was recently obtained with the RPBE DF[11].

A caveat with the above comparison between dynamics based on DFT and experiment is that the difference $(W - E_{ea})$ has also been correlated with the extent to which (reactive) scattering in a system may be affected by energy dissipation through electron-hole pair excitation[51]. Here, the reasoning used could be that (electronically adiabatic) dynamics simulations using repulsive RPBE exchange might overestimate the DC probability because the dissipation of the molecule's incident kinetic energy to electron-hole pairs is not modeled. However, in this type of analysis evidence for strongly nonadiabatic molecule-metal surface scattering comes mostly from experiments on vibrationally inelastic scattering[52, 53] and scattering of H-atoms from metal surfaces[54], whereas dynamics calculations only suggested small effects of electron-hole pair excitation in some of the hard-to-model systems in Figure 5.1, i.e., $D_2O$ + Ni(111)[55] and HCl + Au(111)[29]. More definite evidence

TABLE 5.1: Barrier heights (in kJ/mol) computed with DMC are compared with values calculated with the RPBE and PBE (or PW91‡) DFs of DFT for three different $H_2$ + metal surface systems. Also shown are the differences ($W - E_{ea}$, in eV) between the work function of the metal, and the electron affinity of $H_2$ as computed at the semi-empirical composite G4 level of theory[60]. The values for Mg(0001) are calculated with PBE-DFT[a][61] or measured for a thin layer of Mg[b][62].

| Molecule-metal surface | $E_b^{DMC}$ | $E_b^{RPBE}$ | $E_b^{PBE}$ | $W - E_{ea}$ |
|---|---|---|---|---|
| $H_2$ + Cu(111) | $54.4 \pm 4.2$[57] | 79.1[5] | 46.9‡[5] | 8.06 |
| $H_2$ + Al(110) | $105.0 \pm 0.8$[58] | 100.4[58] | 79.9[58] | 7.39 |
| $H_2$ + Mg(0001) | $113.8 \pm 2.9$[59] | 103.3[59] | 84.9[59] | 6.92[a], 6.82[b] |

that electronically nonadiabatic effects are most likely not the explanation for the trend observed in Figure 5.1 comes from a direct comparison between barrier heights obtained with first-principles and RPBE calculations. Barrier heights obtained with diffusion Monte Carlo (DMC)[56] and DFT using the RPBE and PBE DFs are compared for three $H_2$ + metal surface systems in Table 5.1. For $H_2$ + Cu(111)[57] and Al(110)[58] GGA DFT is able to reproduce the DMC barrier height, and $(W - E_{ea}) > 7\,\text{eV}$. In contrast, the RPBE DF underestimates the DMC barrier height for $H_2$ + Mg(0001)[59] ($W - E_{ea} < 7\,\text{eV}$). Note that for $H_2$ + Cu(111) DMC was shown[57] to be able to reproduce the best estimate of the barrier height to within $(6.7 \pm 4.2)\,\text{kJ/mol}$. Below an explanation is attempted of the success of exchange-correlation functionals containing semi-local exchange at describing reaction barrier heights for molecule-metal surface systems with $(W - E_{ea}) > 7\,\text{eV}$ and of their failure for systems with $(W - E_{ea}) < 7\,\text{eV}$. However, first we investigate whether and how the problem can be fixed for one of the "difficult" systems decribed above.

The standard way of dealing with errors in barriers for gas phase reactions is to ascend the DFT ladder to higher level functionals, i.e., to use meta-GGA or hybrid DFs[2, 3]. As will be shown now, this route can also be successful when dealing with molecule-metal surface reactions. One clear example where DFT tends to overestimate the reactivity is for useful benchmark systems[43] of activated dissociation of $O_2$ on metal surfaces[25, 27] (see also the SI), with $O_2$ + Al(111) being an infamous example[25]. Molecular dynamics (MD) simulations employing GGA DFs predict a non-activated reaction[25, 44], whereas experiments show that the reaction is activated[63, 65] (see Figure 5.2a). So far, of the MD simulations that use a GGA DF (or a semi-empirical potential energy surface (PES) based on a GGA DF)[25, 44, 66] only calculations that

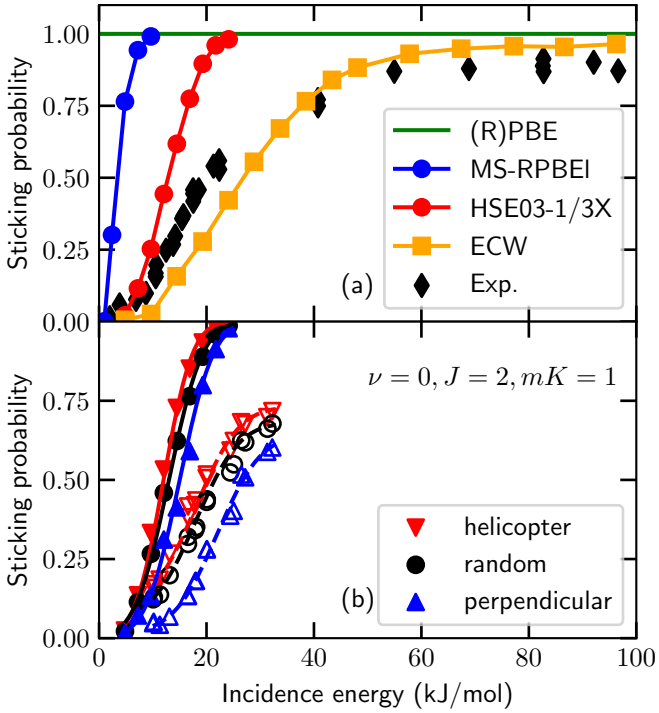


FIGURE 5.2: (a) Sticking probability of $O_2$ on Al(111) as a function of translational energy for normal incidence. The green line indicates results obtained with the (R)PBE DF[25, 44], whereas the blue and red circles indicate QCT results obtained here with the MS-RPBEl and HSE03-1/3X DFs, respectively. The black diamonds and orange squares indicate experimental results[63] and QCT results obtained with an ECW PES[64], respectively. (b) Sticking probability of $O_2$ ($\nu = 0, J = 2, K = 1$) on Al(111) for the helicopter (red downward pointing triangle), random (black circle), and perpendicular (blue upward pointing triangle) alignments of the molecule relative to the surface. The solid and open symbols indicate the computed (HSE03-1/3X) and the experimental[65] results, respectively. The lines merely guide the eye.

treat the $O_2$-metal system nonadiabatically have been shown to yield sticking probabilities in semi-quantitative agreement with experiment. On the other hand, electronically adiabatic simulations that use embedded correlated wave function (ECW) theory for the PES have also yielded quite good agreement with experiment[64] (see Figure 5.2a). The latter results led Carter and co-workers to suggest that modeling electronically nonadiabatic effects should not be necessary for $O_2$ + Al(111)[37]. Specifically, electronic structure calculations based not only on ECW theory but also on hybrid DFT yield adiabatic barriers[37, 67–72], suggesting that an electronically adiabatic approach could well be valid, but that the way the electronic structure is treated is crucial. However, drawbacks of the ECW method are that it is expensive to use and that it is hard to converge the molecule-surface interaction energy with respect to the size of the embedded cluster[37]. Consequently, Yin et al.[64] had to base their PES on a limited amount of points, which forced them to adopt a fitting method that is of only medium accuracy (i.e., a flexible periodic London-Eyring-Polanyi-Sato (FPLEPS) function[73]) to represent their ECW data. Additionally, it is not so clear how the ECW method could be used in an SRP approach, whereas this is rather obvious for DFT.

## 5.3 Method

Here, the dissociative chemisorption of $O_2$ is investigated on a static Al(111) surface with the quasi-classical trajectory (QCT)[74] method using PESs based on DFs that go beyond the standard GGA. Like Carter and co-workers, the static surface approximation and the Born-Oppenheimer approximation is made, thereby neglecting non-adiabatic effects related to the spin- and charge-states of $O_2$ and to electron-hole pair excitation. For the calculations, 6D PESs have been developed with the meta-GGA MS-RPBEl DF[75] and the screened hybrid HSE03-1/3X DF[76, 77]. The MS-RPBEl DF[75] is able to describe both covalent and metallic interactions accurately by relying on a switching function dependent on the kinetic energy density[78]. In principle, with this DF the SIE is reduced by ensuring that the exact energy of the free hydrogen atom is reproduced. For the metallic density regime the low-order gradient expansion of the exchange energy of the homogeneous electron gas is reproduced, which ensures a good description of the metal. The HSE03-1/3X DF is based on the HSE03 DF[76, 77], with the only difference being the maximum fraction of exact exchange $\alpha_X$, which may be viewed as a semi-empirical parameter. Specifically, $\alpha_X = 1/3$ is used instead of $\alpha_X = 1/4$, since Cortona and coworkers[79, 80] have shown that increasing $\alpha_X$ to 1/3 is also

valid according to the standard DFT adiabatic connection[79], and that the increase from 1/4 as in PBE0 to 1/3 improves the description of gas phase reaction barriers[80]. More generally, it is known that hybrid functionals with high fractions of exact exchange tend to perform better at describing reaction barrier heights[3, 81–83]. Importantly, the HSE03 DF uses screened exact exchange so that a correct description of the long-range Coulomb interaction is recovered for the metal, and screened hybrid DFT is an order of magnitude cheaper than global hybrid DFT for metals[84–89].

For the MS-RPBEl (HSE03-1/3X) DF a $2 \times 2$ Al supercell with 4 layers and 15 (10) Å vacuum distance is used. Furthermore, a plane wave kinetic energy cutoff of 600 (400) eV and an $8 \times 8 \times 1$ $\Gamma$-centered $k$-point grid are used. All DFT calculations are performed with the Vienna Ab-initio Simulation Package (VASP version 5.4.4)[90–94], with a user modification to allow the use of the MS-RPBEl DF, using spin polarization when necessary. The core electrons have been represented with the projector augmented wave (PAW) method[94, 95]. In order to speed up convergence, first-order Methfessel-Paxton smearing[96] with a width parameter of 0.2 eV has been employed. Additional information is provided in the appendix to this chapter.

The slabs are constructed with the ideal DFT lattice constants obtained for the tested functionals (4.045 and 4.022 Å for the MS-RPBEl and HSE03-1/3X DFs, respectively), which have been obtained from bulk calculations. The computed bulk lattice constants are in good agreement with the experimental value of 4.032 Å[97]. Furthermore, all interlayer distances have been optimized, yielding an outer layer expansion of 1.4% for the HSE03-1/3X DF and 1.1% for the MS-RPBEl DF, which is in reasonable agreement with the experimental value of 2.2%[98]. Calculations employing the HSE03-1/3X DF are started from converged spin polarized calculations employing the RPBE DF and then iterated until convergence. Using 2 octa-core Intel E5-2630v3 cpus (i.e., a total of 16 cores), single-point calculations for the $O_2$ + Al(111) PES take 2 - 6 hours or 1.5 - 5 days for the MS-RPBEl and HSE03-1/3X DFs, respectively. Non-self-consistent single-point calculations employing the HSE03-1/3X DF on the self-consistent electron density yielded by RPBE take 1 - 2 hours.

The PESs are constructed with the CRP[99] (see Section 2.3.1) with the same set-up of geometries sampled as in Ref. [7], except that the $r_{O_2}$ and $Z_{O_2}$ grids are non-equidistant in order to increase the accuracy near the barrier. For the MS-RPBEl DF $r_{O_2}$ =[0.9, 1.0, 1.1, 1.15, 1.2, 1.225, 1.25, 1.275, 1.3, 1.35, 1.4, 1.5, 1.6, 1.7, 1.8] Å and $Z_{O_2}$ =[0.25, 0.75, 1.00, 1.25, 1.50, 1.75, 2.0, 2.25, 2.50, 2.75, 3.00, 3.25, 3.50, 4.00, 4.50] Å are employed. Likewise, for the HSE03-1/3X DF $r_{O_2}$ =[1.0, 1.1, 1.15, 1.175, 1.2, 1.225, 1.25, 1.3, 1.4, 1.5, 1.6] Å and $Z_{O_2}$ =[1.00, 1.50, 2.00, 2.25, 2.50, 2.75, 3.00, 3.25, 3.50] Å are employed. It is checked that

the maximum value of $r_{O_2}$ used is large enough for an accurate evaluation of the sticking probability ($S_0$, see also below). Furthermore, the atomic 3D PES for the HSE03-1/3X DF is taken from the MS-RPBEl DF, i.e., it is computed with the MS-RPBEl DF instead of the HSE03-1/3X DF. This does not affect the accuracy of the interpolation as the 3D potential is merely to ensure an accurate fit of the PES (i.e., to ensure that the corrugation of the resulting 6D interpolation function is low), and therefore results should not be affected by the choice of the 3D potential as long as it is physically reasonable.

For the MD, the QCT method[74, 100] is employed (see Section 2.2). The sticking probabilities are computed as described in the SI of Ref [64]. A sufficient number of trajectories (at least 1500 ) are run in order to obtain standard error bars that are smaller than 0.01 (one percentage point). The oxygen molecule is initially placed halfway between the two periodic images of the slab, with the azimuthal and polar angles sampled according to the rotational state[101] (see Section 2.4.2). Trajectories are considered to be reacted when the $O_2$ bond is extended beyond 1.59 Å for the HSE03-1/3X DF or 1.79 Å for the MS-RPBEl DF. Lowering the dissociation criterium for the MS-RPBEl DF from 1.79 Å to 1.59 Å does not affect $S_0$. When the distance between the molecule and the surface is larger than the initial value (7.5 Å for MS-RPBEl and 5 Å for HSE03-1/3X) and the velocity vector is pointing away from the surface, the trajectory is considered to be scattered. With the employed propagation time of 10 ps each trajectory ends with one of these two outcomes (i.e., trapping at the surface does not lead to ambiguous outcomes). Furthermore, the equations of motion are integrated with the Stoer and Bulirsch method, using a variable time step[102, 103] (see Section 2.2.1). In using the QCT method[74], the usual assumption is made that the dynamics calculations are not affected by problems related to zero-point energy conversion or the neglect of other quantum effects like tunneling. These assumptions have also been made in previous dynamics studies of the $O_2$ + Al(111) reaction[44, 64]. Quantum and quasi-classical studies of the $CH_4$ + Pt(111) system[104] suggest that these conditions should be met in QCT calculations of sticking probabilities exceeding 0.01, where sticking usually proceeds in a classical, over the barrier fashion.

## 5.4 Results

### 5.4.1 Potential Energy Surface

Table 5.2 compares several barrier heights and locations (i.e., the distance to the surface $Z_{O_2}$) obtained with ECW theory[64], the MS-RPBEl DF, and the HSE03-1/3X DF. Some of the trends in how the barrier height varies with the

TABLE 5.2: Barrier location ($Z_{O_2}$, Å) and height ($E_b$, kJ/mol) of $O_2$ on Al(111) obtained from raw ECW data[64], and the MS-RPBEl and HSE03-1/3X CRP PESs generated in this work. The nomenclature of the different orientations is taken from Ref. [64]. The zero-point energy corrected barriers are provided in the brackets.

| | | $Z_{O_2}$ (Angstrom) | | | $E_b$ (kJ/mol) | | |
|---|---|---|---|---|---|---|---|
| site | orientation | ECW | MS-RPBEl | HSE03-1/3X | ECW | MS-RPBEl | HSE03-1/3X |
| fcc | //1 | 1.9 | 3.0 | 2.6 | 60 | 3.7 (3.7) | 12.3 (12.9) |
| | //2 | 2.2 | 3.0 | 2.7 | 43 | 3.4 (2.0) | 11.4 (10.7) |
| | //3 | 2.4 | 3.0 | 2.6 | 18 | 3.7 (1.0) | 12.3 (10.0) |
| | ⊥ | 1.9 | 3.0 | 2.8 | 41 | 8.8 (7.4) | 26.9 (26.7) |
| top | // | 2.6 | 2.8 | 2.6 | 64 | 9.3 (7.8) | 22.2 (21.3) |
| | ⊥ | 2.8 | 3.1 | 2.8 | 64 | 12.0 (10.6) | 26.8 (26.8) |
| bridge | // | 2.4 | 2.7 | 2.5 | 54 | 14.3 (12.9) | 29.4 (28.8) |
| | ⊥ | 2.7 | 3.2 | 2.9 | 43 | 7.3 (5.9) | 19.4 (15.7) |

impact site and orientation are rather different for ECW theory than for MS-RPBEl and HSE03-1/3X. Generally, both the barrier heights and the anisotropy are lower with the DFs than with ECW theory, and the discrepancies between MS-RPBEl and ECW theory are larger than between HSE03-1/3X and ECW theory. More specifically, among the barrier heights listed the minimum barriers are 3.4, 11.4, and 18 kJ/mol for the meta-GGA DF, the hybrid GGA DF, and ECW theory, respectively. Furthermore, the difference between the smallest and largest barrier heights listed, which measures how the barrier height varies with impact site (energetic corrugation) and molecular orientation (anisotropy) increases in the same order as 10.9, 17.1, and 46 kJ/mol, respectively. Qualitative predictions regarding the dependence of the sticking (or dissociative chemisorption) probability ($S_0$) on the incidence energy ($E_\mathrm{i}$) can then be made with the hole model[105]. This model holds that $S_0(E_\mathrm{i})$ is proportional to the fraction of impact sites and orientations for which $E_\mathrm{i}$ exceeds the barrier height. The hole model then predicts that the meta-GGA DF yields the lowest energy threshold in the $S_0$ curve, while the highest threshold should be found for the ECW results, with the HSE03-1/3X threshold being intermediate. Additionally, based on the barrier height variation the model predicts the steepest $S_0$ curve for the meta-GGA DF and the slowest rising curve for the ECW method. Two-dimensional cuts through the computed PESs are shown for the minimum barrier geometry (i.e., the second parallel orientation at the fcc site) in Figures 5.3a (MS-RPBEl) and 5.3b (HSE03-1/3X).

### 5.4.2 Sticking Probability

The computed $S_0(E_\mathrm{i})$ curves shown in Figure 5.2a display the behavior predicted by the hole model on the basis of the barrier heights shown in Table 5.2. Here, the focus is on the overall sticking of $O_2$ on Al(111) even though this includes contributions from both dissociative chemisorption and abstraction[106]. The MS-RPBEl DF yields a qualitative improvement over the (R)PBE GGA DF by describing the reaction as activated, but with its low energy threshold and steep rise with $E_\mathrm{i}$ it still overestimates the reactivity considerably. The HSE03-1/3X DF yields considerably better agreement with experiment. The comparison suggests that the minimum barrier height is well-described with the HSE03-1/3X DF, although the slope of the sticking curve is still too steep. In line with the above the latter observation suggests that the anisotropy of the barrier height in $\theta$ and $\phi$ is underestimated and that the energetic corrugation of the barrier height may be too low. The too low anisotropy of the HSE03-1/3X PES also explains why the rotational alignment dependence of the sticking probability is underestimated, even though the calculations

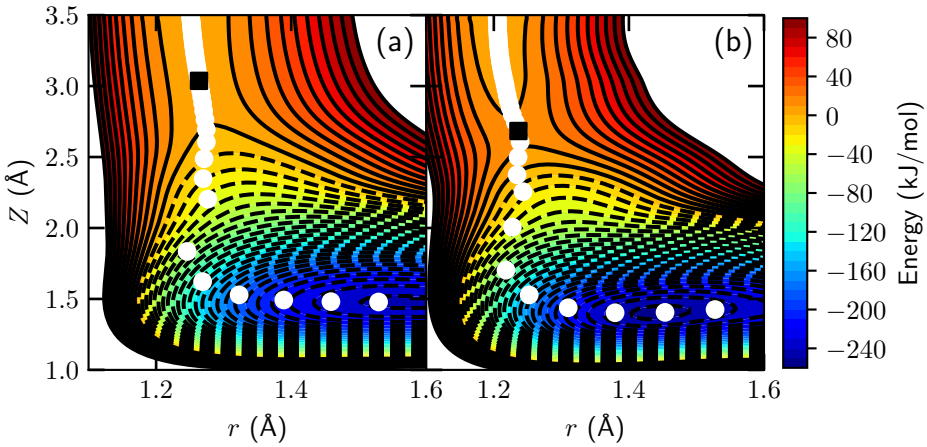


FIGURE 5.3: Elbow plot of the molecule-surface interaction energy of $O_2$ on Al(111) as a function of $Z_{O_2}$ and $r$ computed with the MS-RPBEl (a) and HSE03-1/3X (b) DFs for the second parallel configuration at the fcc site (see Ref. [64]). Black contour lines are drawn at an interval of 10 kJ/mol between -260 and 100 kJ/mol. The white circles indicate the MEP in reduced dimensionality and the black square indicates the highest point along the MEP. The zero of the energy corresponds to the gas phase equilibrium geometry of $O_2$.

qualitatively reproduce the dependence found experimentally (see Figure 5.2b, and Section 5.B.5 for further discussion). ECW theory yields the best overall agreement with experiment, especially regarding the slope. However, the reaction threshold appears to be better described with the tested hybrid functional, suggesting that the HSE03-1/3X minimum barrier height is more accurate than the ECW value. It is also noted that the ECW results are based on an approximately fitted FPLEPS PES whereas the dynamics results in this chapter are based on PESs accurately interpolating the DFT data with the CRP. Furthermore, the agreement of the ECW results with experiment at low incidence energies may have been improved artificially by simulating the reaction of non-rotating $O_2$ instead of using the appropriate rotational distribution[64] (see Figure 5.B.2 and Section 5.B.4).

The above conclusions are valid provided that the sticking is not much affected by electron-hole pair (ehp) excitation and surface atom motion, the effects of which could lower the energy threshold and the steepness of $S_0(E_\mathrm{i})$. These possible effects are believed to be unimportant for the following reasons. First, experimental results indicate that the surface temperature does not influence $S_0$[63]. Second, according to the local density friction approximation, the probability to excite ehps will only be high if the dynamics sample high electron densities. However, for $O_2$ + Al(111), the barrier is early (far away from the surface), so that the electron density sampled by $O_2$ before it encounters a barrier is low. Third, the location of the barrier far away from the surface also suggests small electronic and mechanical couplings[107, 108] with surface atom motion, i.e., the barrier height and location should not vary much with the motion of the nearest surface atom. According to the lattice relaxation sudden model[107, 108], surface atom motion should then not much affect $S_0$.

The reasonably good description of the minimum barrier obtained with the HSE03-1/3X DF is possibly due to the reduction of the delocalization error (or the SIE) as a fraction of exact exchange energy is included[39, 109–112]. Furthermore, the HSE03-1/3X DF also qualitatively reproduces experimental alignment and incidence angle dependent sticking probabilities (see Sections 5.B.5 and 5.B.6, respectively). It is concluded that the HSE03-1/3X DF already gives a reasonable description of the reaction of $O_2$ on Al(111), suggesting that an accurate SRP-DF for this system can be developed on the basis of screened hybrid DFs. As further discussed in Section 5.C.2, it is expected that a functional better describing the sticking in $O_2$ + Al(111) would contain a correlation function approximately describing the Van der Waals dispersion interaction[113–115], while $\alpha_\mathrm{X}$ should then probably be increased in the hybrid functional.

### 5.4.3 Functional-Driven Error

We now come to a tentative explanation of why semi-local DFT may be quite accurate for barriers to dissociative chemisorption on metals if $(W - E_{\mathrm{ea}}) > 7\,\mathrm{eV}$. Some have recently suggested[8] a possible reason for this success in terms of the delocalization error of Yang and co-workers[38, 39, 41]. The explanation is necessarily of a hand waving nature, as delocalization errors, like self-interaction errors[111, 116], are usually hard to quantify for most systems of practical interest. The explanation takes its cue from the explanation of the GGA's tendency to underestimate gas phase barrier heights given in the introductory paragraphs of our letter. The explanation of the GGA's success in describing molecule-metal surface reactions that may be applied if $(W - E_{\mathrm{ea}}) > 7\,\mathrm{eV}$ runs as follows: The electrons coming from the molecule to form new bonds are too delocalized at the TS, and this leads to a delocalization error[41], but the electrons coming from the metal were already quite delocalized in the metal, and they become more localized at the TS, leading to a localization error. If electron transfer does not occur too easily (i.e., $(W - E_{\mathrm{ea}}) > 7\,\mathrm{eV}$), then apparently a cancellation of errors occurs, allowing one to tweak the barrier by mixing GGA-exchange-based DFs. Presumably, the cancellation effect disappears once $(W - E_{\mathrm{ea}}) < 7\,\mathrm{eV}$ and the electrons coming from the metal start to spill over to the molecule due to charge transfer. The diffuse charge distribution on the negatively charged molecule upsets the balance leading to too much electron delocalization and therefore an underestimation of the TS energy. The explanation finds quantitative support in the high Bader charges found on the molecules in the TSs of the difficult systems (see Table 5.B.6 and Section 5.B.3).

A remaining question concerns the origin of the delocalization error that plagues the accuracy of GGA barrier heights for systems with $(W - E_{\mathrm{ea}}) < 7\,\mathrm{eV}$, which is addressed here for $O_2$ + Al(111). There are two possibilities. First, it is possible that the change from reactants to the TS (at which the true electron density will usually be more delocalized) by itself drives the underestimation of the barrier height, i.e., that the error in the barrier height is functional driven[117, 118]. Second, the error may also come about, or be further increased, because semi-local functionals yield self-consistent electron densities at the TS that differ from the true densities to the extent that density driven errors, which may result from over-delocalization, result[117, 118]. The question is relevant: even for stretched $H_2{}^+$, which is a prototypical case for delocalization error[39], the error of GGAs is still predominantly functional-driven[119]. In other words, the self-consistent results are not much improved when GGAs are evaluated on the exact density of stretched $H_2{}^+$[119].

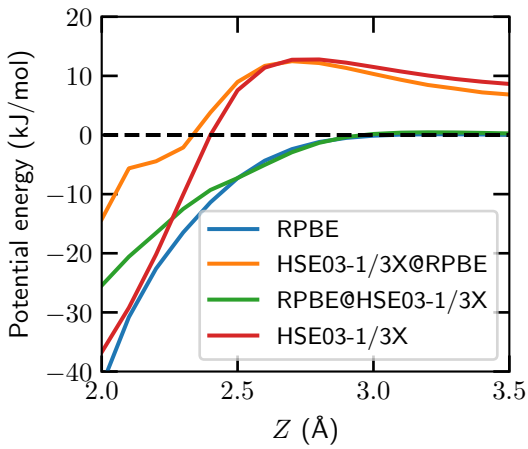


FIGURE 5.4: Potential energy of $O_2$ + Al(111) as a function of $Z_{O_2}$ for $r = 1.25$ Å and the fcc //3 configuration computed self-consistently and non-self-consistently with the RPBE and HSE03-1/3X functionals applied to self-consistent RPBE and HSE03-1/3X electron densities.

To estimate the RPBE's density-driven error (DDE) for the barrier height of $O_2$ + Al(111), RPBE is evaluated on the presumably more accurate HSE03-1/3X DF electron density, i.e., RPBE@HSE03-1/3X. Interestingly, this yields almost the same barrier height as the self-consistent RPBE (see Figure 5.4). This shows, at least for the early barrier system investigated here, that the error of RPBE is functional-driven and not density-driven. At the same time, to a good approximation, the HSE03-1/3X@RPBE energy equals the HSE03-1/3X energy in the entrance and barrier region of the $O_2$ + Al(111) PES (see Figure 5.4 and Table 5.B.4). The results therefore show that the RPBE error in the barrier height is not due to "spuriously easy charge transfer" as suggested in Ref. [37] since this should be reflected in the RPBE density to which the HSE03-1/3X is applied in HSE03-1/3X@RPBE. The result that HSE03-1/3X@RPBE yields similar energies as HSE03-1/3X in the entrance and barrier regions of the $O_2$ + Al(111) PES suggests that the HSE03-1/3X@RPBE approach might accurately describe the sticking probability for this and other DC on metal systems. This is a potentially useful finding because, as discussed in Section 5.3, using the HSE03-1/3X@RPBE approach to compute energies is roughly an order of magnitude less expensive than using the HSE03-1/3X DF[120], with obvious implications for dynamics studies based on hybrid density functionals. While the DDE has a small contribution to the total RPBE error around the TS, its DDE becomes large when the molecule gets closer to the surface (see Figure 5.4 and Section 5.B.2). This finding is consistent with the results of Perdew and co-workers for molecular adsorption of CO on Pt(111), who also find that the DDE of semi-local DFT is large when the molecule is close to the surface[121].

## 5.5 Conclusion

In conclusion, comparison of experiment and DFT-based theory, and of DMC and RPBE DFT calculations for sticking of molecules on metal surfaces suggests that GGA-DFT starts to fail for molecule-metal surface reaction barriers when $(W - E_{\mathrm{ea}}) < 7\,\mathrm{eV}$. The results obtained for $O_2$ + Al(111) with the MS-RPBEl DF suggest that meta-GGA DFs of the "made simple (MS)" kind can slightly remedy the SIE problem, but not sufficiently for this system. Screened hybrid DFs like HSE03-1/3X, and its much cheaper HSE03-1/3X@RPBE alternative, offer a considerably improved description of $O_2$ + Al(111) in that they yield sticking probabilities in semi-quantitative agreement with experiment, thus offering more promise, as also implied by single point calculations performed at reaction barrier geometries of two other difficult systems (see Table 5.B.5 and Section 5.B.2). The HSE03-1/3X DF gives a good description of the reaction threshold but still overestimates the slope of the sticking probability curve for $O_2$ + Al(111). The results suggest that SRP-DFs can be built on the basis of screened hybrid exchange DFs for DC systems in which $(W - E_{\mathrm{ea}}) < 7\,\mathrm{eV}$, i.e., when electron transfer is facile. Such calculations have the potential to widen the scope of existing databases (now only SBH10[23]) of barriers for molecule-metal-surface systems. Indeed, it is likely that the choice of systems in this database (SBH10 contains only $H_2$-metal, $CH_4$-metal, and $N_2$-metal systems that are all in the green-blue part of the spectrum made up by Figure 5.1) has led to systematic bias: The inadvertent choice of systems for which GGA-based exchange works well may actually be responsible for the outcome[23] that the GGA-exchange-based DF performed better than the also tested meta-GGA and hybrid functionals. Even more importantly, the calculations referred to might also increase the range of heterogeneously catalyzed processes that may be simulated reliably based on accurate DFT calculations on the constituent elementary molecule-metal surface reactions.

# Appendix

## 5.A Method

### 5.A.1 Density Functionals Used in This Chapter

The three DFs selected in this chapter are the RPBE DF (in the sense that its results serve as a yardstick to measure other results against), and the MS-RPBEl[75] and HSE03-1/3X[76, 77, 122] DFs used in the study of the dissociative chemisorption of $O_2$ on Al(111). Here, the choice of these functionals is briefly discussed.

The RPBE DF[16] may be viewed as a non-empirical GGA functional just like the PBE DF[14], as Hammer et al. made sure that the constraints imposed on the PBE DF are also imposed on the RPBE-DF[8, 14]. This includes the recovery of the uniform electron gas (UEG) limit, which ensures the functional's applicability to metals[123]. The RPBE DF, which was originally designed to improve the chemisorption energies of atoms and molecules on metals, which are severely overestimated with PBE, yields higher barriers for gas phase reaction barriers than PBE, thereby improving on their description (e.g., the mean unsigned error for the barrier heights in the HTBH38/08 and NHTBH38/08 databases is reduced from 8.9 to 6.6 kcal/mol going from PBE to RPBE[2]). The RPBE DF also yields consistently higher barriers for dissociative chemisorption reactions on metals[5, 7] than the PBE DF and, in fact, than any non-empirical GGA DF obeying the UEG limit that we know of. Hence, RPBE[16] (or RPBE-vdW-DF1[16, 124]) results are used as yardstick to measure other results for dissociative chemisorption systems against: if the RPBE (RPBE-vdW-DF1) DF yields a barrier that is too low, perhaps a meta-GGA but probably a hybrid DF will have to be used to obtain a higher barrier.

Some important advantages of the MS-RPBEl meta-GGA DF tested on $O_2$ + Al(111) have already been mentioned above. They include an approximate correction for one electron-self interaction, which is ensured by demanding that the functional reproduces the exact energy of the H-atom and the atomic/-molecular orbital limit. Based on this approximate correction one might expect

the functional to perform well on reaction barrier heights, the description of which may suffer from self-interaction errors[38, 39, 109]. The MS-RPBEl DF gives a chemically accurate description of the dissociative chemisorption of $H_2$ on Cu(111), and also a quite accurate description of that of $H_2$ on Ag(111)[75], which are additional reasons for including it here. The performance of this MS functional is in contrast to that of the meta-GGA MS2 DF[78], which, although based on similar design principles, with a mean signed error of −7.8 kcal/mol showed a rather poor performance on the dissociative chemisorption barriers in the SBH10 database[23].

The hybrid DF HSE03-1/3X that is applied to $O_2$ + Al(111) may be viewed as a re-parameterized version of HSE06[122]. HSE06 is a screened hybrid DF with an exact exchange ratio $\alpha_X$ equal to 0.25 as in the PBE0 DF[125, 126]; at very short range it equals PBE0 and at long range the PBE DF is obtained. As originally intended[76], the HSE03 DF (which at the start suffered from an implementation error[77]) is the HSE06 DF with a slightly different range parameter (0.15 $\text{bohr}^{-1}$)[76] than used in HSE06 (0.11 $\text{bohr}^{-1}$)[122]. However, the most important change made going from HSE06 to HSE03-1/3X is that a higher exact exchange ratio ($\alpha_X = 1/3$) is used than the value implemented originally in HSE06 and PBE0 (($\alpha_X = 1/4$)). Increasing the ratio of exact exchange in a hybrid DF is a longstanding[81–83] and accepted[3, 127] practice for improving its performance on gas phase reaction barrier heights. For example, the M08-SO and MO8-HX DFs[83] have $\alpha_X = 0.57$ and 0.52, respectively, and are among the best three performing functionals for the BH206 database[3]. An example that is pertinent to using HSE03-1/3X instead of HSE03, as done here, showed that changing $\alpha_X$ from 1/4 to 1/3 in PBE0 reduces the mean absolute error in the reaction barrier heights of the DBH24/08 database from 4.0 to 2.9 kcal/mol[80]. A more minor change made here to HSE06 mentioned already above is that a somewhat larger value is used for the screening parameter, i.e., the one corresponding to HSE03. Note that with the recommended VASP settings (screening parameters of 0.2 $\text{Å}^{-1}$ ($\approx$ 0.106 $\text{bohr}^{-1}$) and 0.3 $\text{Å}^{-1}$ ($\approx$ 0.159 $\text{bohr}^{-1}$)) the settings used for HSE03 and HSE06 are actually a bit different than the ones in the original papers (0.11 and 0.15 $\text{bohr}^{-1}$ for HSE06 and HSE03, respectively), but this slight difference should not affect the results much.

### 5.A.2 Work Function and Electron Affinity Values

The choice of how to compute the difference of the work function and the electron affinity ($W - E_{\text{ea}}$) has been a pragmatic one. The $W$-values in this chapter have been mostly taken from Ref. [128], which gives recommended

values for a number of metal surfaces based on an evaluation of experimental results, so here empirical values are used (see Table 5.A.1). The electron affinities have been mostly taken from a NIST database (Ref. [60]) using semi-empirical composite theory with the G4 basis set (see also Table 5.A.2). Note that the electron affinity of $CH_4$ is obtained by taking the difference between the exciplex state (−40.240 409 Hartree (−1094.9978 eV), see Table S3 of Ref. [129]) and the ground state (−40.451 691 Hartree (−1100.7471 eV), see Table S2 of Ref. [129]) energies obtained with CCSD(T)/aug-cc-pVQZ.

Of course, one might also want to use an all-DFT approach. Results of Perdew and co-workers[121] suggest that metal surface work functions can be computed with a mean absolute error of 0.16, 0.21, 0.11, 0.11, and 0.08 eV using the LDA[130, 131], PBE[14], PBEsol[132], SCAN[133], and SCAN+rVV10[134] DFs, respectively. Furthermore $W$-values computed for a large range of metal surfaces with DFT have been tabulated for the LDA, the PBE, and the RPBE[16] DFs in the supporting information of Ref. [135].

The calculation of electron affinities of small molecules is not so straightforward[129, 136, 137], and this is also true for DFT[137, 138]. This is especially true if the electron affinity is negative, which means that the anion is unstable with respect to the dissociation into the neutral molecule and a free electron, as the calculation of a metastable state state is then required (see, e.g., the calculation of the electron affinity of $CH_4$[129]). As can be seen from Table 5.A.2, this is true for all but one ($O_2$) of the molecules in the molecule-surface systems considered here. Studies that perform benchmarks on the thermochemistry of large numbers of DFs[2, 3] typically employ databases containing back corrected experimental electron affinities (G21EA)[137] or electron affinities computed with a high-level ab initio electronic structure method (EA13/03)[2], which exclusively or predominantly contain positive electron affinities of atoms and small molecules only. Given how complicated it is to compute negative electron affinities, it is recommended to simply use the results from Ref. [60] as obtained using semi-empirical composite theory with the G4 basis set (see Table 5.A.2), for reasons discussed in Ref. [129].

## 5.B Results

### 5.B.1 Self-Consistent DFT Results for $O_2$ + Al(111)

An one-dimensional cut through the HSE03-1/3X PES along the molecule-surface distance is shown in Figure 5.4 for the fcc //3 configuration and $r = 1.25$ Å, for which the barrier height is 12.3 kJ/mol (see Table 5.2). The barrier is found at $Z = 2.6$ Å. For this configuration and $r$-value, the total

TABLE 5.A.1: Work function values of several metal surfaces, which are taken from Ref. [128], except for the value for Pt(211), which is taken as the aforementioned value for Pt(111) plus the difference of calculated LDA values for Pt(211) and Pt(111) from Ref. [139].

| Surface | Work function (eV) |
|---|---|
| Al(111) | 4.32 |
| Ni(111) | 5.24 |
| Au(111) | 5.33 |
| Ru(0001) | 5.4 |
| Cu(100) | 4.73 |
| Cu(111) | 4.9 |
| Pt(111) | 5.91 |
| Pt(211) | 5.64 |

TABLE 5.A.2: Electron affinity values of several molecules, which are taken from Ref. [60] using semi-empirical composite theory with the G4 basis set, except for $H_2O$ (CCSD(T) with a daug-cc-pVTZ basis set) and HCl (B97D3 DF with an aug-cc-pVTZ basis set), and except for $CH_4$, which is taken from Ref. [129].

| Surface | Electron affinity (eV) |
|---|---|
| $CH_4$ | -5.75 |
| $H_2$ | -3.155 |
| $O_2$ | 0.463 |
| HCl | -0.514 |
| $N_2$ | -1.982 |
| $NH_3$ | -0.897 |
| $H_2O$ | -0.181 |

TABLE 5.B.1: Minimum barrier heights and bulk lattice constants computed with different variations of the screened hybrid PBE DF, i.e., different exact exchange ratios and screening length parameters are employed. The barrier is taken to be at $Z = 2.8$ Å, $r = 1.25$ Å, and in the fcc //3 configuration. The row shown in bold face lists the functional used in the dynamics calculations, and presents the results obtained with it. The experimental value of the lattice constant is 4.032 Å[97].

| DF | Exact exchange ratio | Screening length parameter (Å$^{-1}$) | Bulk lattice constant (Å) | $E_b$ (kJ/mol) |
|---|---|---|---|---|
| HSE06[122] | 1/4 | 0.2 | 4.023 | 7.9 |
| HSE06-1/3X | 1/3 | 0.2 | 4.018 | 13.2 |
| HSE06-1/2X | 1/2 | 0.2 | 4.009 | 25.0 |
| **HSE03-1/3X** | **1/3** | **0.3** | **4.022** | **12.8** |
| RSX-PBE0[140] | 1/4 | 0.39 | 4.029 | 3.6 |
| RSX-PBE0-1/3[140] | 1/3 | 0.37 | 4.025 | 11.4 |

magnetic moment (i.e., the number of unpaired electrons) of the $O_2$ + Al(111) system as a function of $Z$ for $r = 1.25$ Å and the fcc //3 orientation is shown in Figure 5.B.1. The magnetic moment is an indicator of charge transfer in the sense that a spin-flip and concomitant change in magnetic moment can only take place after charge transfer from the surface to the molecule has occurred[37]. Here, it can be seen that when a DF is employed that (roughly) corrects for the SIE (i.e., HSE03-1/3X), the magnetic moment drops more gradually when approaching the surface than with the standard RPBE DF. Previously, this effect has also been shown for the charge of $O_2$ approaching an $Al_5$ cluster using (screened) hybrid DFs[68]. Furthermore, from visual inspection it is observed that the charge density is more localized on the $O_2$ molecule when employing SIE-correcting DFs than when using the RPBE DF (results not shown here).

How the barrier height for $O_2$ + Al(111) depends on the parameters of the HSE functional used here is investigated as well. As Table 5.B.1 shows, the barrier height is rather insensitive to changing the screening parameter (i.e., using HSE03-1/3X rather than HSE06-1/3X changes the barrier height by just 0.4 kJ/mol), while increasing $\alpha_X$ from 1/4 to 1/3 to 1/2 leads to clear increases in the barrier height, as one would expect from the discussion in Section 5.A.1. Increasing the exact exchange ratio also decreases the lattice constant of Al somewhat, while the lattice constant is not much affected by changing the screening length parameter (Table 5.B.1).

TABLE 5.B.2: Vibrational frequencies of the molecule at the reaction barrier geometries (see Table 5.2). Total zero point vibrational energies (ZPE) are also listed. Results are obtained from the HSE03-1/3X PES. The nomenclature of the different configurations is taken from Ref. [64].

| site | orientation | Vibrational mode (meV) 1 | 2 | 3 | 4 | 5 | 6 | ZPE (meV) |
|---|---|---|---|---|---|---|---|---|
| fcc | //1 | 138.4 | 18.5 | 8.2 | 5.9i | 17.4i | 87.2i | 82.6 |
| | //2 | 121.0 | 12.8 | 8.8 | 4.4i | 15.7i | 121.0i | 71.3 |
| | //3 | 89.5 | 14.9 | 4.1i | 14.1i | 18.8i | 138.4i | 52.2 |
| | ⊥ | 106.5 | 20.7 | 1.0 | 2.9i | 20.6i | 106.4i | 64.1 |
| top | // | 115.6 | 14.9 | 5.9 | 5.9i | 14.7i | 115.6i | 68.2 |
| | ⊥ | 131.2 | 21.8 | 1.1 | 0.9i | 21.8i | 131.2i | 77.1 |
| bridge | // | 107.6 | 17.1 | 7.0 | 7.9i | 15.6i | 107.6i | 65.9 |
| | ⊥ | 113.8 | 15.3 | 2.6 | 1.6i | 15.9i | 113.7i | 65.9 |
| gas phase | | 153.0 | - | - | - | - | - | 76.5 |

TABLE 5.B.3: Same as Table 5.B.2 but results are obtained from the MS-RPBEl PES.

| site | orientation | Vibrational mode (meV) 1 | 2 | 3 | 4 | 5 | 6 | ZPE (meV) |
|---|---|---|---|---|---|---|---|---|
| fcc | //1 | 142.2 | 4.7 | 3.3 | 3.8i | 5.8i | 89.6i | 75.1 |
| | //2 | 118.9 | 3.9 | 2.6 | 3.9i | 4.6i | 118.9i | 62.7 |
| | //3 | 89.4 | 6.5 | 5.9 | 3.6i | 5.6i | 142.5i | 50.9 |
| | ⊥ | 111.4 | 9.3 | 2.8 | 5.5i | 9.1i | 111.7i | 61.8 |
| top | // | 113.3 | 8.3 | 0.9 | 4.3i | 7.0i | 113.3i | 61.3 |
| | ⊥ | 115.9 | 8.1 | 0.1 | 2.0i | 7.9i | 115.9i | 62.1 |
| bridge | // | 102.7 | 9.6 | 5.5 | 6.0i | 8.6i | 102.7i | 58.9 |
| | ⊥ | 115.6 | 6.4 | 0.6 | 1.4i | 6.9i | 115.5i | 61.3 |
| gas phase | | 146.6 | - | - | - | - | - | 73.3 |

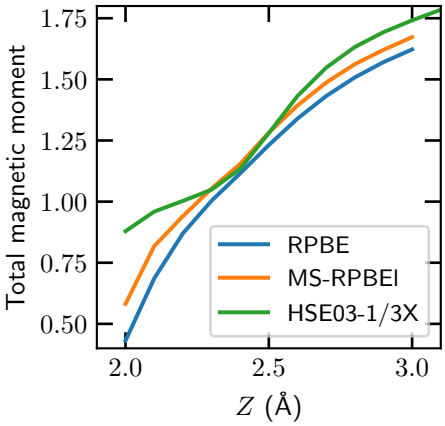


FIGURE 5.B.1: Total magnetic moment of the $O_2$ + Al(111) system as a function of $Z_{O_2}$ for $r = 1.25$ Å and the fcc //3 configuration using several DFs.

### 5.B.2 Non-Self-Consistent DFT Results for $O_2$ + Al(111), HCl + Au(111), and $NH_3$ + Ru(0001)

The barrier heights resulting from non-self-consistent calculations employing a self-consistent density from a different DF, as described in Ref. [117, 118], are shown in Table 5.B.4 for $O_2$ + Al(111). Interestingly, the non-self-consistent calculations yield similar barrier energies as the self-consistent calculations (see also Figure 5.4). As discussed above, this implies that even when a different electron density is employed, the relative energy does not change considerably; i.e., the failure of RPBE in yielding an accurate adiabatic barrier for $O_2$ + Al(111) is not caused by a density-driven error but by a functional-driven error. Only when the molecule is closer to the surface (i.e., the value of $Z$ is lower) does the density driven error play a considerable role. Interestingly, the appearance of the density driven error (see Figure 5.4) coincides with an increasing difference of the magnetic moment between HSE03-1/3X and RPBE (see Figure 5.B.1).

Non-self-consistent calculations of the same kind have also been performed for HCl + Au(111) and $NH_3$ + Ru(0001) (see Table 5.B.5). In general, increasing the fraction of exact exchange, and therefore diminishing the amount of semi-local PBE exchange, leads to barrier heights higher than those found with PBE. These results suggest that employing screened hybrid DFs to systems where $(W - E_{ea}) < 7$ eV may improve the comparison between theory and experiment compared to that obtained with GGA DFs. The barrier for $NH_3$ + Ru(0001) obtained with non-self-consistent HSE calculations is not yet higher than the previous RPBE-vdW-DF1 result (Table 5.B.5), but this will

TABLE 5.B.4: Barrier height (in kJ/mol) of $O_2$ on Al(111) obtained from the HSE03-1/3X CRP PES and HSE03-1/3X@RPBE calculations. The nomenclature of the different configurations is taken from Ref. [64].

| site | orientation | $E_{b,\text{HSE03-1/3X}}$ | $E_{b,\text{HSE03-1/3X@RPBE}}$ |
|---|---|---|---|
| fcc | //1 | 12.3 | 11.5 |
| | //2 | 11.4 | 10.3 |
| | //3 | 12.3 | 11.4 |
| | ⊥ | 26.9 | 30.1 |
| top | // | 22.2 | 21.5 |
| | ⊥ | 26.8 | 29.0 |
| bridge | // | 29.4 | 31.1 |
| | ⊥ | 19.4 | 22.7 |

probably change if a screened hybrid function is used that employs semi-local RPBE exchange instead of PBE exchange. The barrier obtained with the HSE03@RPBE-vdW-DF1 approach for HCl + Au(111) is higher than those obtained with any semi-local exchange functional tested thus far (see Table 3.4, the highest barrier (101.3 kJ/mol) thus far was obtained with RPBE), which should help to get better agreement between theory and experiment for this system.

### 5.B.3 Correlation Between $(W - E_{\mathbf{ea}})$ and Charge Transfer at the TS

The excess charge at the molecule for the TS of several molecule-metal surface systems (i.e., the charge transferred from the metal surface to the molecule) is shown in Table 5.B.6. The results show a clear correlation between the amount of charge transferred to the molecule and the difference between the work function and the electron affinity; i.e., when $(W - E_{\text{ea}})$ decreases, the amount of excess negative charge on the molecule increases. One might then also argue that the barriers of the difficult systems should be too low because the difficult systems are affected by charge transfer at the barrier, as semi-local functionals may severely overestimate the interaction of charge transfer complexes[38].

### 5.B.4 Dynamics: Dependence of $S_0$ on Molecular Beam Conditions

The sticking probability in Figure 5.1 is obtained for a simulated mono-energetic molecular beam. Simulation of only a single energy instead of a velocity distribution does not affect results considerably for weakly activated

TABLE 5.B.5: Barrier heights (in kJ/mol) obtained self-consistently and non-self-consistently for three of the five difficult systems discussed in this chapter (see Figure 5.1). All calculations are performed for a $2 \times 2$ supercell, $8 \times 8 \times 1$ $k$-point grid and a kinetic energy cut-off of 400 eV.

| System | DF | $E_{b,DF}$ | $E_{b,HSE03\text{-}1/3X@DF}$ | $E_{b,HSE03\text{-}1/2X@DF}$ | $E_{b,PBE}$ | $W - E_{ea}$ (eV) | Excess charge ($e^-$) |
|---|---|---|---|---|---|---|---|
| Al(111) + $O_2$ | RPBE | 0.1 | 12.5 | 29.9 | - | 3.857 | 0.332 |
| Au(111) + HCl[29] | RPBE-vdW-DF1 | 85.1 | 106.2 | 122.9 | 72.9 | 5.844 | 0.318 |
| Ru(0001) + $NH_3$[30] | RPBE-vdW-DF1 | 68.6 | 53.8 | 60.6 | 38.7 | 6.297 | 0.348 |

TABLE 5.B.6: Excess charge at the molecule for the TS compared to a neutral molecule for several systems obtained with the Bader charge decomposition scheme.

| System | DF | $W - E_{ea}$ (eV) | Excess charge ($e^-$) |
|---|---|---|---|
| Al(111) + $O_2$ | HSE03-1/3X | 3.857 | 0.332 |
| Ni(111) + $H_2O$[141] | SRP32-vdW-DF1 | 5.421 | 0.472 |
| Au(111) + HCl[26] | RPBE | 5.844 | 0.348 |
| Ru(0001) + $NH_3$[30] | SRP32-vdW-DF1 | 6.297 | 0.348 |
| Cu(111) + $H_2$[142] | SRP48 | 8.055 | 0.229 |
| Pt(111) + $H_2$[10] | PBEa57-vdW-DF2 | 9.065 | -0.047 |
| Ni(111) + $CH_4$[8] | SRP32-vdW-DF1 | 10.99 | 0.241 |

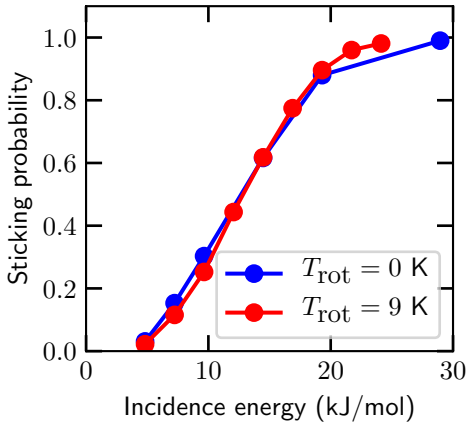


FIGURE 5.B.2: Sticking probability of $O_2$ on Al(111) as a function of translational energy for normal incidence. The blue circles indicate results for $O_2$ in the rovibrational ground state, whereas the red circles indicate results for a rovibrational state population according to $T_{vib} = 300$ K and $T_{rot} = 9$ K.

systems[143]. The rovibrational state population is sampled according to a Boltzmann-like distribution (see for example Ref. [144]), where it is assumed that the vibrational temperature $(T_{\mathrm{vib}}) = 300\,\mathrm{K}$ and the rotational temperature $(T_{\mathrm{rot}}) = 9\,\mathrm{K}$, as should be appropriate[145] for supersonic molecular beams containing $O_2$ and using a room temperature nozzle[63]. Simulating only the rotational ground state of $O_2$ instead of the distribution according to $T_{\mathrm{rot}}$ should lead to a too high sticking probability at low incidence energies (this is true even for a rotationally cold beam, see Figure 5.B.2), as is also confirmed by experiment[106]. Moreover, even though $T_{\mathrm{vib}} = 300\,\mathrm{K}$ is simulated, the population of the vibrational excited states is negligible (0.1%), and therefore the results for the simulated molecular beam can be considered to be for $O_2$ in the vibrational ground state. Since the previous results obtained with the FPLEPS PES based on ECW data are for $O_2$ in the rotational ground state[64], the agreement between the reactivity obtained with the ECW method and the experiments may well have been artificially improved somewhat for low $E_{\mathrm{i}}$ in this way (see Figure 5.B.2).

### 5.B.5 Dynamics: Dependence of $S_0$ on the Alignment of $O_2$

Figure 5.2b shows the sticking probabilities of $O_2$ in the helicopter, random, and perpendicular orientations relative to the surface (see Ref. [64] for explanations of the orientation distributions), as obtained experimentally and with the HSE03-1/3X DF. Note that different incident energy distributions (and, indeed, incidence energies) have been simulated than employed in the experiment as Kurahashi et al. did not publish experimentally determined beam parameters[65], and that the HSE03-1/3X DF yields a sticking probability of unity for $E_{\mathrm{i}} > 25\,\mathrm{kJ/mol}$. Qualitatively, the simulations reproduce the experimental alignment trends[65]: The helicopter orientation is the most reactive one, whereas the perpendicular orientation is least reactive. Quantitatively, the differences between the sticking probabilities obtained for different alignments appear smaller in the theory than in the experiment. This observation gives support to the argument that the slope of the sticking probability curve computed with the HSE03-1/3X DF may be too high because the computed anisotropy of the barrier height at the minimum barrier impact site and at other impact sites is too low.

### 5.B.6 Dynamics: Dependence of $S_0$ on Incidence Angle

Figure 5.B.3 shows the sticking probability of off-normal incident $O_2$ on Al(111), where the normal incidence energy is computed as

$$E_{\text{normal}} = \cos^2(\theta) E_{\text{i}}. \tag{5.1}$$

Experimental trends in the sticking probability as a function of incidence angle of $O_2$ in its helicopter and cartwheel orientations are reproduced (see Figure 5.B.3a). Furthermore, normal energy scaling (NES)[146] is observed both experimentally and in this work (Figure 5.B.3a), while ECW theory slightly deviates from NES (Figure 5.B.3b).

## 5.C Discussion

### 5.C.1 $O_2$ + Metal Systems That Are Useful Benchmark Systems for Dissociative Chemisorption

Systems that are useful as benchmarks for dissociative chemisorption exhibit activated dissociation, so that sticking probabilities measured in molecular beam experiments increase with incidence energy[43]. Ideally, the dissociation is not affected by precursor dynamics, and the dissociative chemisorption probability rises to several tens of percent. Unfortunately, there are few $O_2$-metal systems exhibiting this simple behavior that we know of. As discussed in a recent review paper[147], many $O_2$-metal surface systems exhibit precursor dynamics, where $O_2$ first adsorbs molecularly as a superoxo- and/or peroxo-state, and only then dissociates. This complicates the analysis of the dissociation of $O_2$ on all group 10 metals (Ni, Pd, and Pt)[147]. While it has been known for some time that DFT with GGA functionals can be used to compute properties of these precursor states in reasonable agreement with experiments and that barriers to dissociation can be computed[148, 149], comparison of the latter to experimental values is very difficult, and it is hard to establish the reliability of experimental values of barrier heights, which may differ depending on the technique used and the analysis of the experiments[147]. Studies of the $O_2$ + Pt(111) system[150, 151] show how difficult it is to extract information on the dissociative chemisorption in this system, which is activated through thermal fluctuations at low surface temperature[151]."

Extracting accurate information on dissociative chemisorption of $O_2$ on the group 11 metals Ag and Au likewise is extremely difficult. Au surfaces show very high barriers to $O_2$ dissociation[147]. As discussed by Juaristi and co-workers, the major disagreement now seen in dynamics calculations on the

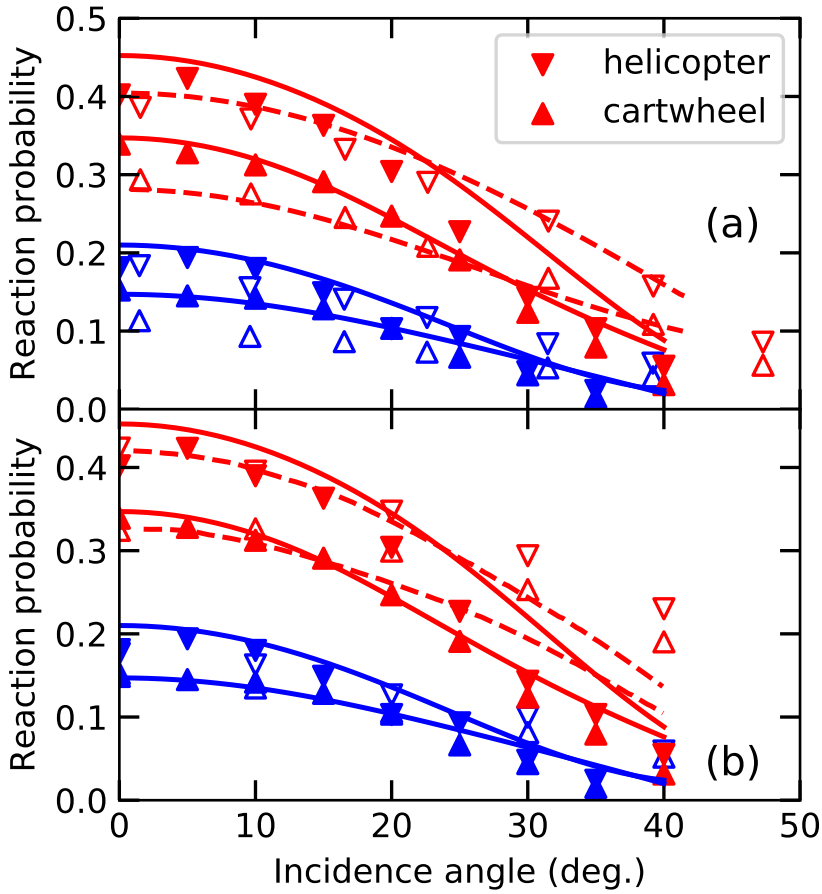


FIGURE 5.B.3: Sticking probability of $O_2$ ($v = 0, J = 2, K = 1$) on Al(111) as a function of incidence angle (degrees). (a) The solid symbols and lines indicate results obtained with the HSE03-1/3X DF for $E_i = 8.2\,\mathrm{kJ/mol}$ (blue) and $E_i = 11.1\,\mathrm{kJ/mol}$ (red). The open symbols and dashed lines indicate results from experiment[65] for $E_i = 9.6\,\mathrm{kJ/mol}$ (blue) and $E_i = 17.4\,\mathrm{kJ/mol}$ (red). The downward and upward pointing triangles correspond to the helicopter and cartwheel orientations, respectively. The lines correspond to results obtained with the assumption of normal energy scaling. (b) Same as panel a, but instead of experimental results, the results from a FPLEPS PES based on ECW data[64] for $E_i = 14.5\,\mathrm{kJ/mol}$ (blue) and $E_i = 22.2\,\mathrm{kJ/mol}$ (red) are shown. In both cases, the incidence energies in the calculations have been chosen such that similar reaction probabilities are obtained in the calculations as in the experiments.

dissociative chemisorption of $O_2$ on Ag(110), Ag(100), and Ag(111) is due to the difficulty on unraveling the contributions of molecular and dissociative chemisorption to sticking (see Figure 11 of their work)[152].

The only $O_2$-metal systems we are aware of that obey the following two conditions that (i) the sticking is activated, not precursor-mediated in a major way, and results in dissociative chemisorption with sticking probabilities equal to a few tens of percent, and that (ii) dynamics calculations using the RPBE density functional have been performed are the $O_2$ + Al(111)[44] example discussed extensively in this chapter, $O_2$ + Cu(111)[27], and $O_2$ + CuML/Ru(0001)[27]. In all cases, the dynamics calculations using a RPBE PES substantially overestimated the sticking probability. In the calculations on Cu and Cu/Ru surfaces, the effect of surface atom motion and surface temperature was modeled in an approximate manner, using the GLO model[27].

### 5.C.2 Towards an SRP Density Functional for $O_2$ + Al(111)

The HSE03-1/3X DF clearly is not yet an SRP DF for $O_2$ + Al(111). The suggestions below are based on how a SRP-DF may be developed in view of the following observations: (i) Compared to the ECW barrier geometries, the HSE03-1/3X geometries are too early, i.e., the barriers occur too far from the surface, and (ii) the too steep slope in the $S_0(E_i)$ curves obtained with standard GGA exchange-correlation DFs for $H_2$ + Ru(0001), which is also an early barrier system, could be remedied[7] by using correlation functionals approximately describing the attractive van der Waals dispersion interaction[124, 153].

We therefore suggest to proceed with the development of an SRP DF for $O_2$ + Al(111) as follows. First, the correlation DF in HSE03 (or alternatively HSE06), i.e., the PBE correlation DF, can be replaced with a Van der Waals correlation functional, obvious candidates being the vdW DFs developed for hybrids by Hyldgaard and co-workers[113, 114]. Alternatively, one could add the TS-vdW correction as used by Tkatchenko and co-workers to the HSE03 functional[115]. This would probably move the barrier geometries closer to the surface when compared to the HSE03-1/3X geometries. In turn, this would also increase the energetic corrugation and the anisotropy of the barrier heights, and lower the barrier heights. While the former change would probably result in better agreement with experiment for the steepness and the alignment dependence of $S_0(E_i)$ (Figures 5.2a and 5.2b, respectively), the energetic threshold of $S_0(E_i)$ would probably also be decreased, possibly resulting in worse agreement with experiment. However, this can probably be offset by increasing the fraction of exact exchange in HSE03 (see Section

5.B.1). Alternatively, one might think of replacing (a fraction of) the local PBE exchange[14] in HSE03 with RPBE exchange[16]. Finally, a screened meta-GGA hybrid DF might perform better[154] than a screened GGA hybrid DF. Especially a meta-GGA DF of the MS kind could perform well, as the MS-RPBEl DF already has shown to improve results for $O_2$ + Al(111) compared to the RPBE DF. Furthermore, using screened hybrid DFs where the range-separation parameter is either optimally pre-tuned (or self-consistently during calculations) or constrained to reproduce the energy of a free hydrogen atom could also improve results[85, 140, 155–158]. It is expected that the approaches sketched can go a long way towards improving the results for $O_2$ + Al(111), and developing an SRP DF for this system.

## References


(1) Pribram-Jones, A.; Gross, D. A.; Burke, K. DFT: A Theory Full of Holes? *Annu. Rev. Phys. Chem.* **2015**, *66*, 283–304, DOI: 10.1146/annurev-physchem-040214-121420.

(2) Peverati, R.; Truhlar, D. G. Quest for a Universal Density Functional: The Accuracy of Density Functionals across a Broad Spectrum of Databases in Chemistry and Physics. *Philos. Trans. R. Soc. A* **2014**, *372*, 20120476, DOI: 10.1098/rsta.2012.0476.

(3) Mardirossian, N.; Head-Gordon, M. Thirty Years of Density Functional Theory in Computational Chemistry: An Overview and Extensive Assessment of 200 Density Functionals. *Mol. Phys.* **2017**, *115*, 2315–2372, DOI: 10.1080/00268976.2017.1333644.

(4) Janesko, B. G. In *Density Functionals: Thermochemistry*, Johnson, E. R., Ed.; Topics in Current Chemistry, Vol. 365; Springer International Publishing: Cham, 2015, pp 25–51, DOI: 10.1007/128_2014_555.

(5) Díaz, C.; Pijper, E.; Olsen, R. A.; Busnengo, H. F.; Auerbach, D. J.; Kroes, G. J. Chemically Accurate Simulation of a Prototypical Surface Reaction: $H_2$ Dissociation on Cu(111). *Science* **2009**, *326*, 832–834, DOI: 10.1126/science.1178722.

(6) Sementa, L.; Wijzenbroek, M.; van Kolck, B. J.; Somers, M. F.; Al-Halabi, A.; Busnengo, H. F.; Olsen, R. A.; Kroes, G. J.; Rutkowski, M.; Thewes, C.; Kleimeier, N. F.; Zacharias, H. Reactive Scattering of $H_2$ from Cu(100): Comparison of Dynamics Calculations Based on the Specific Reaction Parameter Approach to Density Functional Theory with Experiment. *J. Chem. Phys.* **2013**, *138*, 044708, DOI: 10.1063/1.4776224.

(7) Wijzenbroek, M.; Kroes, G. J. The Effect of the Exchange-Correlation Functional on $H_2$ Dissociation on Ru(0001). *J. Chem. Phys.* **2014**, *140*, 084702, DOI: 10.1063/1.4865946.

(8) Nattino, F.; Migliorini, D.; Kroes, G.-J.; Dombrowski, E.; High, E. A.; Killelea, D. R.; Utz, A. L. Chemically Accurate Simulation of a Polyatomic Molecule-Metal Surface Reaction. *J. Phys. Chem. Lett.* **2016**, *7*, 2402–2406, DOI: 10.1021/acs.jpclett.6b01022.

(9) Migliorini, D.; Chadwick, H.; Nattino, F.; Gutiérrez-González, A.; Dombrowski, E.; High, E. A.; Guo, H.; Utz, A. L.; Jackson, B.; Beck, R. D.; Kroes, G.-J. Surface Reaction Barriometry: Methane Dissociation on Flat and Stepped Transition-Metal Surfaces. *J. Phys. Chem. Lett.* **2017**, *8*, 4177–4182, DOI: 10.1021/acs.jpclett.7b01905.

(10) Ghassemi, E. N.; Wijzenbroek, M.; Somers, M. F.; Kroes, G.-J. Chemically Accurate Simulation of Dissociative Chemisorption of $D_2$ on Pt(111). *Chem. Phys. Lett.* **2017**, *683*, 329–335, DOI: 10.1016/j.cplett.2016.12.059.

(11) Spiering, P.; Shakouri, K.; Behler, J.; Kroes, G.-J.; Meyer, J. Orbital-Dependent Electronic Friction Significantly Affects the Description of Reactive Scattering of $N_2$ from Ru(0001). *J. Phys. Chem. Lett.* **2019**, *10*, 2957–2962, DOI: 10.1021/acs.jpclett.9b00523.

(12) Ghassemi, E. N.; Smeets, E. W. F.; Somers, M. F.; Kroes, G.-J.; Groot, I. M. N.; Juurlink, L. B. F.; Füchsel, G. Transferability of the Specific Reaction Parameter Density Functional for $H_2$ + Pt(111) to $H_2$ + Pt(211). *J. Phys. Chem. C* **2019**, *123*, 2973–2986, DOI: 10.1021/acs.jpcc.8b11018.

(13) Tchakoua, T.; Smeets, E. W. F.; Somers, M.; Kroes, G.-J. Toward a Specific Reaction Parameter Density Functional for $H_2$ + Ni(111): Comparison of Theory with Molecular Beam Sticking Experiments. *J. Phys. Chem. C* **2019**, *123*, 20420–20433, DOI: 10.1021/acs.jpcc.9b05928.

(14) Perdew, J. P.; Burke, K.; Ernzerhof, M. Generalized Gradient Approximation Made Simple. *Phys. Rev. Lett.* **1996**, *77*, 3865–3868, DOI: 10.1103/PhysRevLett.77.3865.

(15) Perdew, J. P.; Chevary, J. A.; Vosko, S. H.; Jackson, K. A.; Pederson, M. R.; Singh, D. J.; Fiolhais, C. Atoms, Molecules, Solids, and Surfaces: Applications of the Generalized Gradient Approximation for Exchange and Correlation. *Phys. Rev. B* **1992**, *46*, 6671–6687, DOI: 10.1103/PhysRevB.46.6671.

(16) Hammer, B.; Hansen, L. B.; Nørskov, J. K. Improved Adsorption Energetics within Density-Functional Theory Using Revised Perdew-Burke-Ernzerhof Functionals. *Phys. Rev. B* **1999**, *59*, 7413–7421, DOI: 10.1103/PhysRevB.59.7413.

(17) Jackson, B.; Nave, S. The Dissociative Chemisorption of Methane on Ni(100): Reaction Path Description of Mode-Selective Chemistry. *J. Chem. Phys.* **2011**, *135*, 114701, DOI: 10.1063/1.3634073.

(18) Jiang, B.; Liu, R.; Li, J.; Xie, D.; Yang, M.; Guo, H. Mode Selectivity in Methane Dissociative Chemisorption on Ni(111). *Chem. Sci.* **2013**, *4*, 3249–3254, DOI: 10.1039/C3SC51040A.

(19) Shen, X.; Zhang, Z.; Zhang, D. H. Communication: Methane Dissociation on Ni(111) Surface: Importance of Azimuth and Surface Impact Site. *J. Chem. Phys.* **2016**, *144*, 101101, DOI: 10.1063/1.4943128.

(20) Guo, H.; Jackson, B. Mode-Selective Chemistry on Metal Surfaces: The Dissociative Chemisorption of $CH_4$ on Pt(111). *J. Chem. Phys.* **2016**, *144*, 184709, DOI: 10.1063/1.4948941.

(21) Moiraghi, R.; Lozano, A.; Peterson, E.; Utz, A.; Dong, W.; Busnengo, H. F. Nonthermalized Precursor-Mediated Dissociative Chemisorption at High Catalysis Temperatures. *J. Phys. Chem. Lett.* **2020**, *11*, 2211–2218, DOI: 10.1021/acs.jpclett.0c00260.

(22) Wellendorff, J.; Lundgaard, K. T.; Møgelhøj, A.; Petzold, V.; Landis, D. D.; Nørskov, J. K.; Bligaard, T.; Jacobsen, K. W. Density Functionals for Surface Science: Exchange-Correlation Model Development with Bayesian Error Estimation. *Phys. Rev. B* **2012**, *85*, 235149, DOI: 10.1103/PhysRevB.85.235149.

(23) Mallikarjun Sharada, S.; Bligaard, T.; Luntz, A. C.; Kroes, G.-J.; Nørskov, J. K. SBH10: A Benchmark Database of Barrier Heights on Transition Metal Surfaces. *J. Phys. Chem. C* **2017**, *121*, 19807–19815, DOI: 10.1021/acs.jpcc.7b05677.

(24) Schimka, L.; Harl, J.; Stroppa, A.; Grüneis, A.; Marsman, M.; Mittendorfer, F.; Kresse, G. Accurate Surface and Adsorption Energies from Many-Body Perturbation Theory. *Nat. Mater.* **2010**, *9*, 741–744, DOI: 10.1038/nmat2806.

(25) Behler, J.; Delley, B.; Lorenz, S.; Reuter, K.; Scheffler, M. Dissociation of $O_2$ at Al(111): The Role of Spin Selection Rules. *Phys. Rev. Lett.* **2005**, *94*, 036104, DOI: 10.1103/PhysRevLett.94.036104.

(26) Füchsel, G.; del Cueto, M.; Díaz, C.; Kroes, G.-J. Enigmatic HCl + Au(111) Reaction: A Puzzle for Theory and Experiment. *J. Phys. Chem. C* **2016**, *120*, 25760–25779, DOI: 10.1021/acs.jpcc.6b07453.

(27) Ramos, M.; Díaz, C.; Martínez, A. E.; Busnengo, H. F.; Martín, F. Dissociative and Non-Dissociative Adsorption of $O_2$ on Cu(111) and $Cu_{ML}$/Ru(0001) Surfaces: Adiabaticity Takes Over. *Phys. Chem. Chem. Phys.* **2017**, *19*, 10217–10221, DOI: 10.1039/C7CP00753A.

(28) Hu, X.; Yang, M.; Xie, D.; Guo, H. Vibrational Enhancement in the Dynamics of Ammonia Dissociative Chemisorption on Ru(0001). *J. Chem. Phys.* **2018**, *149*, 044703, DOI: 10.1063/1.5043517.

(29) Füchsel, G.; Zhou, X.; Jiang, B.; Juaristi, J. I.; Alducin, M.; Guo, H.; Kroes, G.-J. Reactive and Nonreactive Scattering of HCl from Au(111): An Ab Initio Molecular Dynamics Study. *J. Phys. Chem. C* **2019**, *123*, 2287–2299, DOI: 10.1021/acs.jpcc.8b10686.

(30) Gerrits, N.; Kroes, G.-J. Curious Mechanism of the Dissociative Chemisorption of Ammonia on Ru(0001). *J. Phys. Chem. C* **2019**, *123*, 28291–28300, DOI: 10.1021/acs.jpcc.9b09121.

(31) Ertl, G. Elementary Steps in Heterogeneous Catalysis. *Angew. Chem. Int. Ed.* **1990**, *29*, 1219–1227, DOI: 10.1002/anie.199012191.

(32) Sabbe, M. K.; Reyniers, M.-F.; Reuter, K. First-Principles Kinetic Modeling in Heterogeneous Catalysis: An Industrial Perspective on Best-Practice, Gaps and Needs. *Catal. Sci. Technol.* **2012**, *2*, 2010–2024, DOI: 10.1039/C2CY20261A.

(33) Wolcott, C. A.; Medford, A. J.; Studt, F.; Campbell, C. T. Degree of Rate Control Approach to Computational Catalyst Screening. *J. Catal.* **2015**, *330*, 197–207, DOI: 10.1016/j.jcat.2015.07.015.

(34) Ertl, G. Primary Steps in Catalytic Synthesis of Ammonia. *J. Vac. Sci. Technol. A* **1983**, *1*, 1247–1253, DOI: 10.1116/1.572299.

(35) Rostrup-Nielsen, J. R.; Sehested, J.; Nørskov, J. K. In *Advances in Catalysis*; Academic Press: 2002; Vol. 47, pp 65–139, DOI: 10.1016/S0360-0564(02)47006-X.

(36) Perdew, J. P.; Ruzsinszky, A.; Constantin, L. A.; Sun, J.; Csonka, G. I. Some Fundamental Issues in Ground-State Density Functional Theory: A Guide for the Perplexed. *J. Chem. Theory Comput.* **2009**, *5*, 902–908, DOI: 10.1021/ct800531s.

(37) Libisch, F.; Huang, C.; Liao, P.; Pavone, M.; Carter, E. A. Origin of the Energy Barrier to Chemical Reactions of $O_2$ on Al(111): Evidence for Charge Transfer, Not Spin Selection. *Phys. Rev. Lett.* **2012**, *109*, 198303, DOI: 10.1103/PhysRevLett.109.198303.

(38) Zhang, Y.; Yang, W. A Challenge for Density Functionals: Self-Interaction Error Increases for Systems with a Noninteger Number of Electrons. *J. Chem. Phys.* **1998**, *109*, 2604–2608, DOI: 10.1063/1.476859.

(39) Cohen, A. J.; Mori-Sánchez, P.; Yang, W. Insights into Current Limitations of Density Functional Theory. *Science* **2008**, *321*, 792–794, DOI: 10.1126/science.1158722.

(40) Perdew, J. P.; Parr, R. G.; Levy, M.; Balduz, J. L. Density-Functional Theory for Fractional Particle Number: Derivative Discontinuities of the Energy. *Phys. Rev. Lett.* **1982**, *49*, 1691–1694, DOI: 10.1103/PhysRevLett.49.1691.

(41) Li, C.; Zheng, X.; Su, N. Q.; Yang, W. Localized Orbital Scaling Correction for Systematic Elimination of Delocalization Error in Density Functional Approximations. *Natl. Sci. Rev.* **2018**, *5*, 203–215, DOI: 10.1093/nsr/nwx111.

(42) Perdew, J. P.; Zunger, A. Self-Interaction Correction to Density-Functional Approximations for Many-Electron Systems. *Phys. Rev. B* **1981**, *23*, 5048–5079, DOI: 10.1103/PhysRevB.23.5048.

(43) Kroes, G.-J. Toward a Database of Chemically Accurate Barrier Heights for Reactions of Molecules with Metal Surfaces. *J. Phys. Chem. Lett.* **2015**, *6*, 4106–4114, DOI: 10.1021/acs.jpclett.5b01344.

(44) Behler, J.; Reuter, K.; Scheffler, M. Nonadiabatic Effects in the Dissociation of Oxygen Molecules at the Al(111) Surface. *Phys. Rev. B* **2008**, *77*, 115421, DOI: 10.1103/PhysRevB.77.115421.

(45) Liu, T.; Fu, B.; Zhang, D. H. HCl Dissociating on a Rigid Au(111) Surface: A Six-Dimensional Quantum Mechanical Study on a New Potential Energy Surface Based on the RPBE Functional. *J. Chem. Phys.* **2017**, *146*, 164706, DOI: 10.1063/1.4982051.

(46) Liu, Q.; Zhou, X.; Zhou, L.; Zhang, Y.; Luo, X.; Guo, H.; Jiang, B. Constructing High-Dimensional Neural Network Potential Energy Surfaces for Gas–Surface Scattering and Reactions. *J. Phys. Chem. C* **2018**, *122*, 1761–1769, DOI: 10.1021/acs.jpcc.7b12064.

(47) Jiang, B.; Guo, H. Towards an Accurate Specific Reaction Parameter Density Functional for Water Dissociation on Ni(111): RPBE versus PW91. *Phys. Chem. Chem. Phys.* **2016**, *18*, 21817–21824, DOI: 10.1039/C6CP03707K.

(48) Campbell, V. L.; Chen, N.; Guo, H.; Jackson, B.; Utz, A. L. Substrate Vibrations as Promoters of Chemical Reactivity on Metal Surfaces. *J. Phys. Chem. A* **2015**, *119*, 12434–12441, DOI: 10.1021/acs.jpca.5b07873.

(49) Chadwick, H.; Migliorini, D.; Kroes, G. J. $CHD_3$ Dissociation on Pt(111): A Comparison of the Reaction Dynamics Based on the PBE Functional and on a Specific Reaction Parameter Functional. *J. Chem. Phys.* **2018**, *149*, 044701, DOI: 10.1063/1.5039458.

(50) Ludwig, J.; Vlachos, D. G. Ab Initio Molecular Dynamics of Hydrogen Dissociation on Metal Surfaces Using Neural Networks and Novelty Sampling. *J. Chem. Phys.* **2007**, *127*, 154716, DOI: 10.1063/1.2794338.

(51) Golibrzuch, K.; Bartels, N.; Auerbach, D. J.; Wodtke, A. M. The Dynamics of Molecular Interactions and Chemical Reactions at Metal Surfaces: Testing the Foundations of Theory. *Annu. Rev. Phys. Chem.* **2015**, *66*, 399–425, DOI: 10.1146/annurev-physchem-040214-121958.

(52) White, J. D.; Chen, J.; Matsiev, D.; Auerbach, D. J.; Wodtke, A. M. Conversion of Large-Amplitude Vibration to Electron Excitation at a Metal Surface. *Nature* **2005**, *433*, 503–505, DOI: 10.1038/nature03213.

(53) Nahler, N. H.; White, J. D.; LaRue, J.; Auerbach, D. J.; Wodtke, A. M. Inverse Velocity Dependence of Vibrationally Promoted Electron Emission from a Metal Surface. *Science* **2008**, *321*, 1191–1194, DOI: 10.1126/science.1160040.

(54) Bünermann, O.; Jiang, H.; Dorenkamp, Y.; Kandratsenka, A.; Janke, S.; Auerbach, D. J.; Wodtke, A. M. Electron-Hole Pair Excitation Determines the Mechanism of Hydrogen Atom Adsorption. *Science* **2015**, *350*, 1346–1349, DOI: 10.1126/science.aad4972.

(55) Jiang, B.; Alducin, M.; Guo, H. Electron–Hole Pair Effects in Polyatomic Dissociative Chemisorption: Water on Ni(111). *J. Phys. Chem. Lett.* **2016**, *7*, 327–331, DOI: 10.1021/acs.jpclett.5b02737.

(56) Foulkes, W. M. C.; Mitas, L.; Needs, R. J.; Rajagopal, G. Quantum Monte Carlo Simulations of Solids. *Rev. Mod. Phys.* **2001**, *73*, 33–83, DOI: 10.1103/RevModPhys.73.33.

(57) Doblhoff-Dier, K.; Meyer, J.; Hoggan, P. E.; Kroes, G.-J. Quantum Monte Carlo Calculations on a Benchmark Molecule–Metal Surface Reaction: $H_2$ + Cu(111). *J. Chem. Theory Comput.* **2017**, *13*, 3208–3219, DOI: 10.1021/acs.jctc.7b00344.

(58) Powell, A. D.; Kroes, G.-J.; Doblhoff-Dier, K. Quantum Monte Carlo Calculations on Dissociative Chemisorption of $H_2$ + Al(110): Minimum Barrier Heights and Their Comparison to DFT Values. *J. Chem. Phys.* **2020**, *153*, 224701, DOI: 10.1063/5.0022919.

(59) Pozzo, M.; Alfè, D. Hydrogen Dissociation on Mg(0001) Studied via Quantum Monte Carlo Calculations. *Phys. Rev. B* **2008**, *78*, 245313, DOI: 10.1103/PhysRevB.78.245313.

(60) Johnson III, R. D. Computational Chemistry Comparison and Benchmark Database, NIST Standard Reference Database 101, National Institute of Standards and Technology: 2020, DOI: 10.18434/T47C7Z.

(61) Ji, D.-P.; Zhu, Q.; Wang, S.-Q. Detailed First-Principles Studies on Surface Energy and Work Function of Hexagonal Metals. *Surf. Sci.* **2016**, *651*, 137–146, DOI: 10.1016/j.susc.2016.04.007.

(62) Garron, R. Photoelectricité - Rendement Photoelectriques Des Couches Minces de Magnesium. *C.R. Hebd. Seances Acad. Sci.* **1964**, *258*, 1458.

(63) Österlund, L.; Zorić, I.; Kasemo, B. Dissociative Sticking of $O_2$ on Al(111). *Phys. Rev. B* **1997**, *55*, 15452–15455, DOI: 10.1103/PhysRevB.55.15452.

(64) Yin, R.; Zhang, Y.; Libisch, F.; Carter, E. A.; Guo, H.; Jiang, B. Dissociative Chemisorption of $O_2$ on Al(111): Dynamics on a Correlated Wave-Function-Based Potential Energy Surface. *J. Phys. Chem. Lett.* **2018**, *9*, 3271–3277, DOI: 10.1021/acs.jpclett.8b01470.

(65) Kurahashi, M.; Yamauchi, Y. Steric Effect in $O_2$ Sticking on Al(111): Preference for Parallel Geometry. *Phys. Rev. Lett.* **2013**, *110*, 246102, DOI: 10.1103/PhysRevLett.110.246102.

(66) Katz, G.; Kosloff, R.; Zeiri, Y. Abstractive Dissociation of Oxygen over Al(111): A Nonadiabatic Quantum Model. *J. Chem. Phys.* **2004**, *120*, 3931–3948, DOI: 10.1063/1.1635360.

(67) Mosch, C.; Koukounas, C.; Bacalis, N.; Metropoulos, A.; Gross, A.; Mavridis, A. Interaction of Dioxygen with Al Clusters and Al(111): A Comparative Theoretical Study. *J. Phys. Chem. C* **2008**, *112*, 6924–6932, DOI: 10.1021/jp711991b.

(68) Livshits, E.; Baer, R.; Kosloff, R. Deleterious Effects of Long-Range Self-Repulsion on the Density Functional Description of $O_2$ Sticking on Aluminum. *J. Phys. Chem. A* **2009**, *113*, 7521–7527, DOI: 10.1021/jp900892r.

(69) Bacalis, N. C.; Metropoulos, A.; Gross, A. Theoretical Study of the $O_2$ Interaction with a Tetrahedral $Al_4$ Cluster. *J. Phys. Chem. A* **2010**, *114*, 11746–11750, DOI: 10.1021/jp1052198.

(70) Liu, H.-R.; Xiang, H.; Gong, X. G. First Principles Study of Adsorption of $O_2$ on Al Surface with Hybrid Functionals. *J. Chem. Phys.* **2011**, *135*, 214702, DOI: 10.1063/1.3665032.

(71) Cheng, J.; Libisch, F.; Carter, E. A. Dissociative Adsorption of $O_2$ on Al(111): The Role of Orientational Degrees of Freedom. *J. Phys. Chem. Lett.* **2015**, *6*, 1661–1665, DOI: 10.1021/acs.jpclett.5b00597.

(72) Paranthaman, S.; Moon, J.; Hong, K.; Kim, J.; Kim, D. E.; Kim, J.; Kim, T. K. Reactivity of Molecular Oxygen with Aluminum Clusters: Density Functional and Ab Initio Molecular Dynamics Simulation Study. *Int. J. Quantum Chem.* **2016**, *116*, 547–554, DOI: 10.1002/qua.25080.

(73) Martin-Gondre, L.; Crespos, C.; Larrégaray, P.; Rayez, J. C.; Conte, D.; van Ootegem, B. Detailed Description of the Flexible Periodic London–Eyring–Polanyi–Sato Potential Energy Function. *Chem. Phys.* **2010**, *367*, 136–147, DOI: 10.1016/j.chemphys.2009.11.012.

(74) Karplus, M.; Porter, R. N.; Sharma, R. D. Exchange Reactions with Activation Energy. I. Simple Barrier Potential for (H, $H_2$). *J. Chem. Phys.* **1965**, *43*, 3259–3287, DOI: 10.1063/1.1697301.

(75) Smeets, E. W.; Voss, J.; Kroes, G.-J. Specific Reaction Parameter Density Functional Based on the Meta-Generalized Gradient Approximation: Application to $H_2$ + Cu(111) and $H_2$ + Ag(111). *J. Phys. Chem. A* **2019**, *123*, 5395–5406, DOI: 10.1021/acs.jpca.9b02914.

(76) Heyd, J.; Scuseria, G. E.; Ernzerhof, M. Hybrid Functionals Based on a Screened Coulomb Potential. *J. Chem. Phys.* **2003**, *118*, 8207–8215, DOI: 10.1063/1.1564060.

(77) Heyd, J.; Scuseria, G. E.; Ernzerhof, M. Erratum: "Hybrid Functionals Based on a Screened Coulomb Potential" [J. Chem. Phys. 118, 8207 (2003)]. *J. Chem. Phys.* **2006**, *124*, 219906, DOI: 10.1063/1.2204597.

(78) Sun, J.; Xiao, B.; Fang, Y.; Haunschild, R.; Hao, P.; Ruzsinszky, A.; Csonka, G. I.; Scuseria, G. E.; Perdew, J. P. Density Functionals That Recognize Covalent, Metallic, and Weak Bonds. *Phys. Rev. Lett.* **2013**, *111*, 106401, DOI: 10.1103/PhysRevLett.111.106401.

(79) Cortona, P. Note: Theoretical Mixing Coefficients for Hybrid Functionals. *J. Chem. Phys.* **2012**, *136*, 086101, DOI: 10.1063/1.3690462.

(80) Guido, C. A.; Brémond, E.; Adamo, C.; Cortona, P. Communication: One Third: A New Recipe for the PBE0 Paradigm. *J. Chem. Phys.* **2013**, *138*, 021104, DOI: 10.1063/1.4775591.

(81) Truong, T. N.; Duncan, W. A New Direct Ab Initio Dynamics Method for Calculating Thermal Rate Constants from Density Functional Theory. *J. Chem. Phys.* **1994**, *101*, 7408–7414, DOI: 10.1063/1.468299.

(82) Lynch, B. J.; Fast, P. L.; Harris, M.; Truhlar, D. G. Adiabatic Connection for Kinetics. *J. Phys. Chem. A* **2000**, *104*, 4811–4815, DOI: 10.1021/jp000497z.

(83) Zhao, Y.; Truhlar, D. G. Exploring the Limit of Accuracy of the Global Hybrid Meta Density Functional for Main-Group Thermochemistry, Kinetics, and Noncovalent Interactions. *J. Chem. Theory Comput.* **2008**, *4*, 1849–1868, DOI: 10.1021/ct800246v.

(84) Zhao, Y.; Truhlar, D. G. Density Functional Theory for Reaction Energies: Test of Meta and Hybrid Meta Functionals, Range-Separated Functionals, and Other High-Performance Functionals. *J. Chem. Theory Comput.* **2011**, *7*, 669–676, DOI: 10.1021/ct1006604.

(85) Brémond, É.; Pérez-Jiménez, Á. J.; Sancho-García, J. C.; Adamo, C. Range-Separated Hybrid Density Functionals Made Simple. *J. Chem. Phys.* **2019**, *150*, 201102, DOI: 10.1063/1.5097164.

(86) Moltved, K. A.; Kepp, K. P. The Metal Hydride Problem of Computational Chemistry: Origins and Consequences. *J. Phys. Chem. A* **2019**, *123*, 2888–2900, DOI: 10.1021/acs.jpca.9b02367.

(87) Zhao, Q.; Kulik, H. J. Stable Surfaces That Bind Too Tightly: Can Range-Separated Hybrids or DFT+U Improve Paradoxical Descriptions of Surface Chemistry? *J. Phys. Chem. Lett.* **2019**, *10*, 5090–5098, DOI: 10.1021/acs.jpclett.9b01650.

(88) Laikov, D. N. Simple Exchange Hole Models for Long-Range-Corrected Density Functionals. *J. Chem. Phys.* **2019**, *151*, 094106, DOI: 10.1063/1.5110633.

(89) Jana, S.; Patra, A.; Constantin, L. A.; Samal, P. Screened Range-Separated Hybrid by Balancing the Compact and Slowly Varying Density Regimes: Satisfaction of Local Density Linear Response. *J. Chem. Phys.* **2020**, *152*, 044111, DOI: 10.1063/1.5131530.

(90) Kresse, G.; Hafner, J. Ab Initio Molecular-Dynamics Simulation of the Liquid-Metal–Amorphous-Semiconductor Transition in Germanium. *Phys. Rev. B* **1994**, *49*, 14251–14269, DOI: 10.1103/PhysRevB.49.14251.

(91) Kresse, G.; Hafner, J. Ab Initio Molecular Dynamics for Liquid Metals. *Phys. Rev. B* **1993**, *47*, 558–561, DOI: 10.1103/PhysRevB.47.558.

(92) Kresse, G.; Furthmüller, J. Efficient Iterative Schemes for Ab Initio Total-Energy Calculations Using a Plane-Wave Basis Set. *Phys. Rev. B* **1996**, *54*, 11169–11186, DOI: 10.1103/PhysRevB.54.11169.

(93) Kresse, G.; Furthmüller, J. Efficiency of Ab-Initio Total Energy Calculations for Metals and Semiconductors Using a Plane-Wave Basis Set. *Comput. Mater. Sci.* **1996**, *6*, 15–50, DOI: 10.1016/0927-0256(96)00008-0.

(94) Kresse, G.; Joubert, D. From Ultrasoft Pseudopotentials to the Projector Augmented-Wave Method. *Phys. Rev. B* **1999**, *59*, 1758–1775, DOI: 10.1103/PhysRevB.59.1758.

(95) Blöchl, P. E. Projector Augmented-Wave Method. *Phys. Rev. B* **1994**, *50*, 17953–17979, DOI: 10.1103/PhysRevB.50.17953.

(96) Methfessel, M.; Paxton, A. T. High-Precision Sampling for Brillouin-Zone Integration in Metals. *Phys. Rev. B* **1989**, *40*, 3616–3621, DOI: 10.1103/PhysRevB.40.3616.

(97) Haas, P.; Tran, F.; Blaha, P. Calculation of the Lattice Constant of Solids with Semilocal Functionals. *Phys. Rev. B* **2009**, *79*, 085104, DOI: 10.1103/PhysRevB.79.085104.

(98) Jona, F.; Sondericker, D.; Marcus, P. M. Al(111) Revisited. *J. Phys. C: Solid State Phys.* **1980**, *13*, L155–L158, DOI: 10.1088/0022-3719/13/8/004.

(99) Busnengo, H. F.; Salin, A.; Dong, W. Representation of the 6D Potential Energy Surface for a Diatomic Molecule near a Solid Surface. *J. Chem. Phys.* **2000**, *112*, 7641–7651, DOI: 10.1063/1.481377.

(100) Porter, R. N.; Raff, L. M. In *Dynamics of Molecular Collisions: Part B*, Miller, W. H., Ed.; Modern Theoretical Chemistry; Springer US: Boston, MA, 1976, pp 1–52, DOI: 10.1007/978-1-4757-0644-4_1.

(101) Brink, D.; Satchler, G., *Angular Momentum*, 2nd ed.; Oxford University Press: 1968; 87 pp.

(102) Bulirsch, R.; Stoer, J. Numerical Treatment of Ordinary Differential Equations by Extrapolation Methods. *Numer. Math.* **1966**, *8*, 1–13, DOI: 10.1007/BF02165234.

(103) Stoer, J.; Bulirsch, R. In *Introduction to Numerical Analysis*, Stoer, J., Bulirsch, R., Eds.; Springer: New York, NY, 1980, pp 244–313, DOI: 10.1007/978-1-4757-5592-3_5.

(104) Nattino, F.; Ueta, H.; Chadwick, H.; van Reijzen, M. E.; Beck, R. D.; Jackson, B.; van Hemert, M. C.; Kroes, G.-J. Ab Initio Molecular Dynamics Calculations versus Quantum-State-Resolved Experiments on $CHD_3$ + Pt(111): New Insights into a Prototypical Gas–Surface Reaction. *J. Phys. Chem. Lett.* **2014**, *5*, 1294–1299, DOI: 10.1021/jz500233n.

(105) Karikorpi, M.; Holloway, S.; Henriksen, N.; Nørskov, J. K. Dynamics of Molecule-Surface Interactions. *Surf. Sci.* **1987**, *179*, L41–L48, DOI: 10.1016/0039-6028(87)90111-7.

(106) Binetti, M.; Weiße, O.; Hasselbrink, E.; Katz, G.; Kosloff, R.; Zeiri, Y. The Role of Nonadiabatic Pathways and Molecular Rotations in the Oxygen Abstraction Reaction on the Al(111) Surface. *Chem. Phys. Lett.* **2003**, *373*, 366–371, DOI: 10.1016/S0009-2614(03)00586-4.

(107) Tiwari, A. K.; Nave, S.; Jackson, B. The Temperature Dependence of Methane Dissociation on Ni(111) and Pt(111): Mixed Quantum-Classical Studies of the Lattice Response. *J. Chem. Phys.* **2010**, *132*, 134702, DOI: 10.1063/1.3357415.

(108) Tiwari, A. K.; Nave, S.; Jackson, B. Methane Dissociation on Ni(111): A New Understanding of the Lattice Effect. *Phys. Rev. Lett.* **2009**, *103*, 253201, DOI: 10.1103/PhysRevLett.103.253201.

(109) Mori-Sánchez, P.; Cohen, A. J.; Yang, W. Many-Electron Self-Interaction Error in Approximate Density Functionals. *J. Chem. Phys.* **2006**, *125*, 201102, DOI: 10.1063/1.2403848.

(110) Mori-Sánchez, P.; Cohen, A. J.; Yang, W. Localization and Delocalization Errors in Density Functional Theory and Implications for Band-Gap Prediction. *Phys. Rev. Lett.* **2008**, *100*, 146401, DOI: 10.1103/PhysRevLett.100.146401.

(111) Bao, J. L.; Gagliardi, L.; Truhlar, D. G. Self-Interaction Error in Density Functional Theory: An Appraisal. *J. Phys. Chem. Lett.* **2018**, *9*, 2353–2358, DOI: 10.1021/acs.jpclett.8b00242.

(112) Bartlett, R. J. Adventures in DFT by a Wavefunction Theorist. *J. Chem. Phys.* **2019**, *151*, 160901, DOI: 10.1063/1.5116338.

(113) Berland, K.; Jiao, Y.; Lee, J.-H.; Rangel, T.; Neaton, J. B.; Hyldgaard, P. Assessment of Two Hybrid van Der Waals Density Functionals for Covalent and Non-Covalent Binding of Molecules. *J. Chem. Phys.* **2017**, *146*, 234106, DOI: 10.1063/1.4986522.

(114) Jiao, Y.; Schröder, E.; Hyldgaard, P. Extent of Fock-Exchange Mixing for a Hybrid van Der Waals Density Functional? *J. Chem. Phys.* **2018**, *148*, 194115, DOI: 10.1063/1.5012870.

(115) Marom, N.; Tkatchenko, A.; Rossi, M.; Gobre, V. V.; Hod, O.; Scheffler, M.; Kronik, L. Dispersion Interactions with Density-Functional Theory: Benchmarking Semiempirical and Interatomic Pairwise Corrected Density Functionals. *J. Chem. Theory Comput.* **2011**, *7*, 3944–3951, DOI: 10.1021/ct2005616.

(116) Lonsdale, D. R.; Goerigk, L. The One-Electron Self-Interaction Error in 74 Density Functional Approximations: A Case Study on Hydrogenic Mono- and Dinuclear Systems. *Phys. Chem. Chem. Phys.* **2020**, *22*, 15805–15830, DOI: 10.1039/D0CP01275K.

(117) Kim, M.-C.; Sim, E.; Burke, K. Understanding and Reducing Errors in Density Functional Calculations. *Phys. Rev. Lett.* **2013**, *111*, 073003, DOI: 10.1103/PhysRevLett.111.073003.

(118) Vuckovic, S.; Song, S.; Kozlowski, J.; Sim, E.; Burke, K. Density Functional Analysis: The Theory of Density-Corrected DFT. *J. Chem. Theory Comput.* **2019**, *15*, 6636–6646, DOI: 10.1021/acs.jctc.9b00826.

(119) Song, S.; Sim, E.; Vuckovic, S.; Burke, K. How Errors in Densities Contaminate Empirical Density Functionals http://arxiv.org/abs/2008.01261 (accessed 10/28/2020).

(120) Skelton, J. M.; Gunn, D. S. D.; Metz, S.; Parker, S. C. Accuracy of Hybrid Functionals with Non-Self-Consistent Kohn–Sham Orbitals for Predicting the Properties of Semiconductors. *J. Chem. Theory Comput.* **2020**, *16*, 3543–3557, DOI: 10.1021/acs.jctc.9b01218.

(121) Patra, A.; Peng, H.; Sun, J.; Perdew, J. P. Rethinking CO Adsorption on Transition-Metal Surfaces: Effect of Density-Driven Self-Interaction Errors. *Phys. Rev. B* **2019**, *100*, 035442, DOI: 10.1103/PhysRevB.100.035442.

(122) Krukau, A. V.; Vydrov, O. A.; Izmaylov, A. F.; Scuseria, G. E. Influence of the Exchange Screening Parameter on the Performance of Screened Hybrid Functionals. *J. Chem. Phys.* **2006**, *125*, 224106, DOI: 10.1063/1.2404663.

(123) Perdew, J. P.; Ruzsinszky, A.; Tao, J.; Staroverov, V. N.; Scuseria, G. E.; Csonka, G. I. Prescription for the Design and Selection of Density Functional Approximations: More Constraint Satisfaction with Fewer Fits. *J. Chem. Phys.* **2005**, *123*, 062201, DOI: 10.1063/1.1904565.

(124) Dion, M.; Rydberg, H.; Schröder, E.; Langreth, D. C.; Lundqvist, B. I. Van Der Waals Density Functional for General Geometries. *Phys. Rev. Lett.* **2004**, *92*, 246401, DOI: 10.1103/PhysRevLett.92.246401.

(125) Perdew, J. P.; Ernzerhof, M.; Burke, K. Rationale for Mixing Exact Exchange with Density Functional Approximations. *J. Chem. Phys.* **1996**, *105*, 9982–9985, DOI: 10.1063/1.472933.

(126) Adamo, C.; Barone, V. Toward Reliable Density Functional Methods without Adjustable Parameters: The PBE0 Model. *J. Chem. Phys.* **1999**, *110*, 6158–6170, DOI: 10.1063/1.478522.

(127) Cohen, A. J.; Mori-Sánchez, P.; Yang, W. Challenges for Density Functional Theory. *Chem. Rev.* **2012**, *112*, 289–320, DOI: 10.1021/cr200107z.

(128) Derry, G. N.; Kern, M. E.; Worth, E. H. Recommended Values of Clean Metal Surface Work Functions. *J. Vac. Sci. Technol. A* **2015**, *33*, 060801, DOI: 10.1116/1.4934685.

(129) Ramírez-Solís, A.; Vigué, J.; Hinojosa, G.; Saint-Martin, H. Solving the $CH_4^-$ Riddle: The Fundamental Role of Spin to Explain Metastable Anionic Methane. *Phys. Rev. Lett.* **2020**, *124*, 056001, DOI: 10.1103/PhysRevLett.124.056001.

(130) Kohn, W.; Sham, L. J. Self-Consistent Equations Including Exchange and Correlation Effects. *Phys. Rev.* **1965**, *140*, A1133–A1138, DOI: 10.1103/PhysRev.140.A1133.

(131) Perdew, J. P.; Wang, Y. Accurate and Simple Analytic Representation of the Electron-Gas Correlation Energy. *Phys. Rev. B* **1992**, *45*, 13244–13249, DOI: 10.1103/PhysRevB.45.13244.

(132) Perdew, J. P.; Ruzsinszky, A.; Csonka, G. I.; Vydrov, O. A.; Scuseria, G. E.; Constantin, L. A.; Zhou, X.; Burke, K. Restoring the Density-Gradient Expansion for Exchange in Solids and Surfaces. *Phys. Rev. Lett.* **2008**, *100*, 136406, DOI: 10.1103/PhysRevLett.100.136406.

(133) Sun, J.; Ruzsinszky, A.; Perdew, J. P. Strongly Constrained and Appropriately Normed Semilocal Density Functional. *Phys. Rev. Lett.* **2015**, *115*, 036402, DOI: 10.1103/PhysRevLett.115.036402.

(134) Peng, H.; Yang, Z.-H.; Perdew, J. P.; Sun, J. Versatile van Der Waals Density Functional Based on a Meta-Generalized Gradient Approximation. *Phys. Rev. X* **2016**, *6*, 041005, DOI: 10.1103/PhysRevX.6.041005.

(135) Tran, R.; Li, X.-G.; Montoya, J. H.; Winston, D.; Persson, K. A.; Ong, S. P. Anisotropic Work Function of Elemental Crystals. *Surf. Sci.* **2019**, *687*, 48–55, DOI: 10.1016/j.susc.2019.05.002.

(136) Richard, R. M.; Marshall, M. S.; Dolgounitcheva, O.; Ortiz, J. V.; Brédas, J.-L.; Marom, N.; Sherrill, C. D. Accurate Ionization Potentials and Electron Affinities of Acceptor Molecules I. Reference Data at the CCSD(T) Complete Basis Set Limit. *J. Chem. Theory Comput.* **2016**, *12*, 595–604, DOI: 10.1021/acs.jctc.5b00875.

(137) Goerigk, L.; Grimme, S. A General Database for Main Group Thermochemistry, Kinetics, and Noncovalent Interactions - Assessment of Common and Reparameterized (Meta-)GGA Density Functionals. *J. Chem. Theory Comput.* **2010**, *6*, 107–126, DOI: 10.1021/ct900489g.

(138) Su, N. Q.; Xu, X. Insights into Direct Methods for Predictions of Ionization Potential and Electron Affinity in Density Functional Theory. *J. Phys. Chem. Lett.* **2019**, *10*, 2692–2699, DOI: 10.1021/acs.jpclett.9b01052.

(139) Feibelman, P. J. Energetics of Steps on Pt(111). *Phys. Rev. B* **1995**, *52*, 16845–16854, DOI: 10.1103/PhysRevB.52.16845.

(140) Brémond, É.; Pérez-Jiménez, Á. J.; Sancho-García, J. C.; Adamo, C. Range-Separated Hybrid and Double-Hybrid Density Functionals: A Quest for the Determination of the Range-Separation Parameter. *J. Chem. Phys.* **2020**, *152*, 244124, DOI: 10.1063/5.0010976.

(141) Migliorini, D.; Nattino, F.; Tiwari, A. K.; Kroes, G.-J. HOD on Ni(111): Ab Initio Molecular Dynamics Prediction of Molecular Beam Experiments. *J. Chem. Phys.* **2018**, *149*, 244706, DOI: 10.1063/1.5059357.

(142) Nattino, F.; Díaz, C.; Jackson, B.; Kroes, G.-J. Effect of Surface Motion on the Rotational Quadrupole Alignment Parameter of $D_2$ Reacting on Cu(111). *Phys. Rev. Lett.* **2012**, *108*, 236104, DOI: 10.1103/PhysRevLett.108.236104.

(143) Ghassemi, E. N.; Somers, M. F.; Kroes, G.-J. Assessment of Two Problems of Specific Reaction Parameter Density Functional Theory: Sticking and Diffraction of $H_2$ on Pt(111). *J. Phys. Chem. C* **2019**, *123*, 10406–10418, DOI: 10.1021/acs.jpcc.9b00981.

(144) Gerrits, N.; Geweke, J.; Smeets, E. W. F.; Voss, J.; Wodtke, A. M.; Kroes, G.-J. Closing the Gap Between Experiment and Theory: Reactive Scattering of HCl from Au(111). *J. Phys. Chem. C* **2020**, *124*, 15944–15960, DOI: 10.1021/acs.jpcc.0c03756.

(145) Kuebler, N. A.; Robin, M. B.; Yang, J. J.; Gedanken, A.; Herrick, D. R. Fully Resolved Zeeman Pattern in the Stern-Gerlach Deflection Spectrum of $O_2$ $(^3\Sigma_g^-, K = 1)$. *Phys. Rev. A* **1988**, *38*, 737–749, DOI: 10.1103/PhysRevA.38.737.

(146) Rettner, C. T.; DeLouise, L. A.; Auerbach, D. J. Effect of Incidence Kinetic Energy and Surface Coverage on the Dissociative Chemisorption of Oxygen on W(110). *J. Chem. Phys.* **1986**, *85*, 1131–1149, DOI: 10.1063/1.451310.

(147) Montemore, M. M.; van Spronsen, M. A.; Madix, R. J.; Friend, C. M. $O_2$ Activation by Metal Surfaces: Implications for Bonding and Reactivity on Heterogeneous Catalysts. *Chem. Rev.* **2018**, *118*, 2816–2862, DOI: 10.1021/acs.chemrev.7b00217.

(148) Eichler, A.; Hafner, J. Molecular Precursors in the Dissociative Adsorption of $O_2$ on Pt(111). *Phys. Rev. Lett.* **1997**, *79*, 4481–4484, DOI: 10.1103/PhysRevLett.79.4481.

(149) Eichler, A.; Mittendorfer, F.; Hafner, J. Precursor-Mediated Adsorption of Oxygen on the (111) Surfaces of Platinum-Group Metals. *Phys. Rev. B* **2000**, *62*, 4744–4755, DOI: 10.1103/PhysRevB.62.4744.

(150) Sendner, C.; Groß, A. Kinetic Monte Carlo Simulations of the Interaction of Oxygen with Pt(111). *J. Chem. Phys.* **2007**, *127*, 014704, DOI: 10.1063/1.2748379.

(151) Zhou, Y.; Zhou, L.; Hu, X.; Xie, D. Dynamics Studies of $O_2$ Collision on Pt(111) Using a Global Potential Energy Surface. *J. Phys. Chem. C* **2020**, *124*, 10573–10583, DOI: 10.1021/acs.jpcc.0c01247.

(152) Lončarić, I.; Alducin, M.; Juaristi, J. I.; Novko, D. CO Stretch Vibration Lives Long on Au(111). *J. Phys. Chem. Lett.* **2019**, *10*, 1043–1047, DOI: 10.1021/acs.jpclett.9b00069.

(153) Lee, K.; Murray, É. D.; Kong, L.; Lundqvist, B. I.; Langreth, D. C. Higher-Accuracy van Der Waals Density Functional. *Phys. Rev. B* **2010**, *82*, 081101(R), DOI: 10.1103/PhysRevB.82.081101.

(154) Sun, J.; Haunschild, R.; Xiao, B.; Bulik, I. W.; Scuseria, G. E.; Perdew, J. P. Semilocal and Hybrid Meta-Generalized Gradient Approximations Based on the Understanding of the Kinetic-Energy-Density Dependence. *J. Chem. Phys.* **2013**, *138*, 044113, DOI: 10.1063/1.4789414.

(155) Baer, R.; Livshits, E.; Salzner, U. Tuned Range-Separated Hybrids in Density Functional Theory. *Annu. Rev. Phys. Chem.* **2010**, *61*, 85–109, DOI: 10.1146/annurev.physchem.012809.103321.

(156) Refaely-Abramson, S.; Sharifzadeh, S.; Govind, N.; Autschbach, J.; Neaton, J. B.; Baer, R.; Kronik, L. Quasiparticle Spectra from a Nonempirical Optimally Tuned Range-Separated Hybrid Density Functional. *Phys. Rev. Lett.* **2012**, *109*, 226405, DOI: 10.1103/PhysRevLett.109.226405.

(157) Karolewski, A.; Kronik, L.; Kümmel, S. Using Optimally Tuned Range Separated Hybrid Functionals in Ground-State Calculations: Consequences and Caveats. *J. Chem. Phys.* **2013**, *138*, 204115, DOI: 10.1063/1.4807325.

(158) Tamblyn, I.; Refaely-Abramson, S.; Neaton, J. B.; Kronik, L. Simultaneous Determination of Structures, Vibrations, and Frontier Orbital Energies from a Self-Consistent Range-Separated Hybrid Functional. *J. Phys. Chem. Lett.* **2014**, *5*, 2734–2741, DOI: 10.1021/jz5010939.

# Chapter 6

# The Curious Reaction Mechanism of Ammonia on Ru(0001)

This chapter is based on Gerrits, N.; Kroes, G.-J. Curious Mechanism of the Dissociative Chemisorption of Ammonia on Ru(0001). *J. Phys. Chem. C* **2019**, *123*, 28291–28300, DOI: 10.1021/acs.jpcc.9b09121

## Abstract

Dissociative chemisorption of polyatomic molecules on metals, which is relevant to heterogeneous catalysis, usually proceeds through a rotationally adiabatic or rotational sudden mechanism. The reaction is usually either direct, or proceeds through a trapped molecular physisorped state. Here, ab initio molecular dynamics is used to model the dissociative chemisorption of ammonia on Ru(0001). The reaction mechanism is neither rotationally adiabatic nor rotational sudden, with clearly distinct and non-statistical initial and time-of-reaction orientation distributions. Reasonably good agreement is obtained between computed and previously measured sticking probabilities. Under the conditions investigated the reaction of $NH_3$ goes through a molecular chemisorption-like state, but the reaction is direct.

## 6.1 Introduction

Recent ab initio molecular dynamics (AIMD)[1–7] and quasi-classical trajectory (QCT)[8, 9] calculations on high-dimensional potential energy surfaces (PESs) are providing a wealth of information on the dynamics of polyatomic molecules reacting on metal surfaces. Of these, direct reactions on metal surfaces are typically either rotationally adiabatic[10] (e.g., water + Ni(111)[4, 11]) or in a sudden regime[12, 13] (e.g., $CHD_3$ + Pt(111)[5] and methanol + Cu(111)[7] (see also Chapter 10)). In the former case, the initial orientation distribution of the reacting molecules is statistical (i.e., it resembles a $\sin(\theta)$ distribution of the $\theta_d$ angle shown in Figure 6.1a) and is steered towards transition state (TS) values[4]. In the latter case, the initial orientation distribution is already close to the orientation at the barrier geometry[5, 7, 14, 15]. Approximate methods such as the Reaction Path Hamiltonian (RPH) approach[16] often use either a rotationally adiabatic or a sudden approximation[13, 14]. Furthermore, if a reaction proceeds through a molecular chemisorption-like state, it is usually trapping mediated[3]. However, as will be shown here, ammonia reacts on Ru(0001) through a very different mechanism, in which both the incident orientation distribution and the distribution at the TS are non-statistical, but clearly distinct. Furthermore, the reaction is observed to be direct, even though the molecule proceeds through a molecular chemisorption-like geometry as observed in trapping-mediated reaction.

Due to the high pressures and temperatures involved in the Haber-Bosch process[18], whereby $N_2$ is converted to $NH_3$, ammonia is not only a product in this process, but also a reactant, and Ru is a good catalyst for ammonia production[19]. Therefore, predicting and understanding the reaction of ammonia on Ru(0001) is not only of interest for fundamental reasons, it is also of practical importance, as $NH_3$ is a raw material for the production of synthetic fertilizer that helps feed a substantial part of the world's population[20]. Additionally, Ru is the best single metal catalyst for ammonia decomposition[21–23], which is relevant to the production of $CO_x$-free $H_2$ for hydrogen fuel cell applications[22]. In the kinetics of ammonia decomposition, the breaking of the first NH-bond is an important step[22–24].

Molecular beam sticking experiments on dissociative chemisorption of ammonia on Ru(0001) have been performed by Mortensen et al.[25] at surface temperatures ($T_s$) of 475 and 1100 K. They found the dissociation to be activated and independent of $T_s$ at incidence energies larger than 85 kJ/mol. Consequently, they proposed a direct reaction mechanism for these conditions. For the lower $E_i$ their detailed experiments allowed them to propose a mechanism involving a molecularly chemisorbed state reacting at defect sites. In the

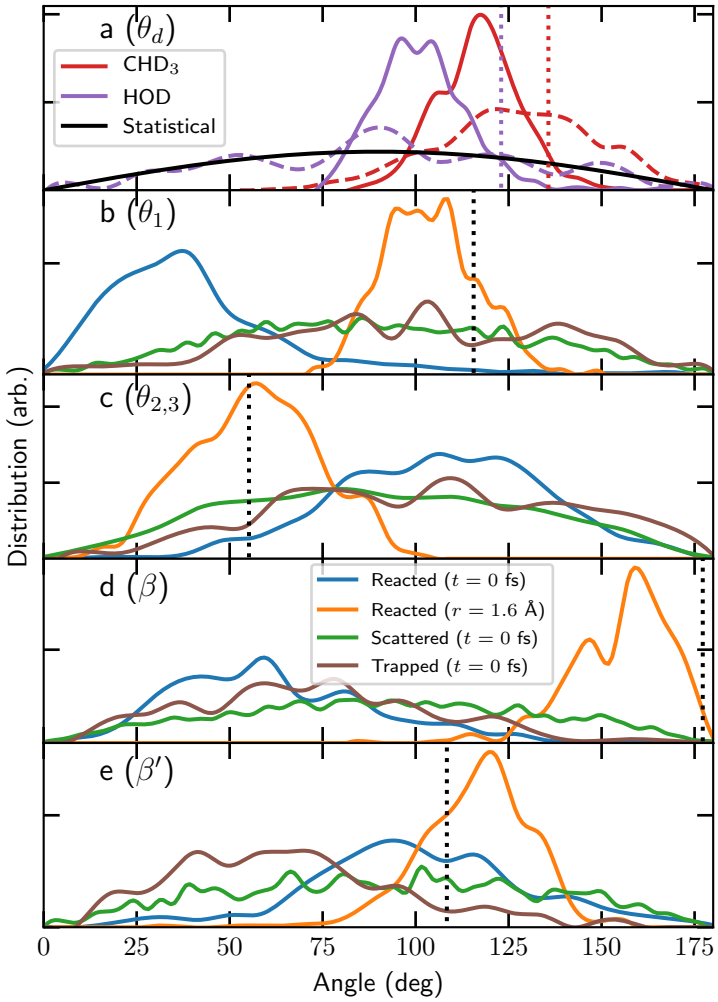


FIGURE 6.1: (a) $\theta_d$ angle (i.e., the dissociating bond) of $CHD_3$[17] (red) and HOD[4] (purple) for all reacted trajectories at the initial time step (dashed lines) and when a dissociating bond reaches the TS value (solid lines). The solid black line indicates a statistical $\sin(\theta)$ distribution. The dotted lines indicate the TS values. (b, c, d, e) $\theta_1$, $\theta_{2,3}$, $\beta$, and $\beta'$ angles of ammonia for all scattered (green), trapped (brown), and reacted trajectories, where the results for the reacted trajectories are shown at the initial time step (blue) and when the dissociating bond reaches the TS value (orange). The angles of the non-dissociating hydrogen atoms with respect to the surface normal are indicated by $\theta_{2,3}$. $\beta'$ indicates the angle between the surface normal and the umbrella axis, which is defined as the vector going from the geometric center of the three hydrogen atoms to the nitrogen atom. The dotted lines indicate the TS values belonging to the top2fcc barrier geometry.

latter mechanism, diffusion of reactants to and products away from the defects limits the sticking at very low $T_s$, and desorption of $NH_3$ prior to reaching the defects limits trapping-mediated reaction at high $T_s$.

So far, only Hu et al.[26] used dynamics calculations to model the experimentally measured sticking probabilities on $NH_3$ + Ru(0001), performing QCT calculations on a twelve-dimensional (12D) PES fitted with a neural network approach[27]. Their work focused on vibrational enhancement of the reaction, and they found vibrational efficacies near unity for each of the four vibrational modes of $NH_3$. Although the dynamical behaviour of the ammonia molecule was included, the metal surface atoms were kept frozen. They did not model energy transfer to the surface atoms, even though this can play a major role in the computed reactivity for molecule-metal surface reactions[8, 12, 13]. The Perdew, Burke and Ernzerhof (PBE) exchange-correlation (xc) density functional (DF)[28] was used. For high incidence energies the computed sticking probabilities for $NH_3$ in its initial vibrational ground state were considerably higher (by a factor 2 - 2.5) than the experimental sticking probabilities, which the authors attributed to the use of the PBE DF. Indeed, this DF, like its very similar[28] predecessor PW91[29], often overestimates the reactivity of molecules on metal surfaces[5, 30–33] (see also Chapter 5 where the ease of charge transfer between the molecule and metal surface is related to the ability of a DF to accurately describe a molecule-metal surface barrier height).

Here, the reaction is studied at the higher incidence energy conditions for which the experimentalists did not yet characterize the reaction mechanism in detail, and for which AIMD calculations can be used: For high incidence energies the system can be kept small as defects do not play an important role, and propagation times can be kept short. In the AIMD calculations, the motions of $NH_3$ as well as that of the surface atoms of Ru(0001) are modelled explicitly. Different aspects are adressed of the reaction mechanism, i.e., the orientation distribution of the reacting molecules, and the role of the molecular chemisorption state in the reaction at high incidence energies. A DF is used containing revised PBE (RPBE)[34] exchange (more repulsive than PBE exchange) and the Van der Waals correlation DF of Dion et al. (vdW-DF1)[35], and is therefore called the RPBE-vdW-DF1 DF. In this chapter, it is shown that the reaction proceeds through an unusual mechanism, in which the initial orientation distribution of the reacting molecules is non-statistical, but is clearly distinct from the non-statistical distribution at the time of reaction, which resembles the orientation at the TS. Additionally, although the reaction is direct, the reacting molecules go through a geometry that is similar to the geometry that would be taken on by the molecular

precursor state dominating the reaction mechanism at low $E_i$. Compared to the earlier dynamics calculations[26] the agreement with the experimental sticking probabilities is improved.

## 6.2 Method

For the AIMD and electronic structure (Density Functional Theory, DFT) calculations the Vienna Ab-initio Simulation Package (VASP version 5.3.5)[36–40] is used. The first Brillouin zone is sampled by a Γ-centered $4 \times 4 \times 1$ $k$-point grid and the plane wave basis set kinetic energy cutoff is 400 eV. Moreover, the core electrons have been represented with the projector augmented wave (PAW) method[40, 41]. The surface is modeled using a 4 layer ($3 \times 3$) supercell, where the top three layers have been relaxed in the $Z$ direction and a vacuum distance of 15 Å is used between the slabs. Due to the use of the vdW-DF1 correlation DF the employed vacuum distance causes a small interaction energy between the surface and the molecule in the gas phase, which effectively raises the barrier height by 3.0 kJ/mol. However, due to the computational cost a larger vacuum distance is untractable in the AIMD. Therefore, 3.0 kJ/mol is added to the translational energy to counteract this shift (see Section 2.4.2). In order to speed up convergence, first-order Methfessel-Paxton smearing[42] with a width parameter of 0.2 eV has been applied. The employed computational setup is confirmed to be converged within chemical accuracy (1 kcal/mol, or 4.2 kJ/mol), as shown in Section 6.A.

Transition states are obtained with the dimer method[43–46] as implemented in the VASP Transition State Tools package (VTST)[47], and are confirmed to be first-order saddle points. Forces on the degrees of freedom are converged within 5 meV/Å, where only the ammonia is relaxed in all its degrees of freedom, i.e., when computing TSs the surface is kept fixed in its relaxed surface-vacuum geometry.

The RPBE-vdW-DF1 DF is used, which is defined as

$$E_{xc} = E_x^{\text{RPBE}} + E_c^{\text{vdW-DF1}}, \tag{6.1}$$

where $E_x^{\text{RPBE}}$ is the exchange part of the revised Perdew, Burke and Ernzerhof (RPBE)[34] exchange-correlation DF and $E_c^{\text{vdW-DF1}}$ is the non-local Van der Waals correlation DF of Dion et al. (vdW-DF1)[35].

A surface temperature of 475 K and 1100 K is simulated in the AIMD calculations, where the atoms in the top three layers are allowed to move. The

TABLE 6.1: Thermal expansion coefficients for the $a$ and $c$ lattice vectors, which are taken from Ref. [48].

| Temperature (K) | $\alpha_a(\mathrm{K}^{-1})$ | $\alpha_c(\mathrm{K}^{-1}))$ |
|---|---|---|
| 475 | 1.00110 | 1.00168 |
| 1100 | 1.00684 | 1.01045 |

TABLE 6.2: Experimental beam parameters that describe the simulated $NH_3$ velocity distributions. $\nu_0$ and $\alpha$ are based on time-of-flight measurements on $CHD_3/H_2$ beams (see the text)[17, 50].

| $T_n$ (K) | $\langle E_i \rangle$ (kJ/mol) | $\nu_0$ (m/s) | $\alpha$ (m/s) |
|---|---|---|---|
| 400[50] | 74.0 | 2899 | 290 |
| 500[50] | 89.2 | 3157 | 316 |
| 600[17] | 102.9 | 3418 | 342 |
| 700[17] | 119.5 | 3683 | 368 |

expansion of the bulk due to the surface temperature is simulated by multiplying[49] the computed ideal lattice constants ($a = 2.7524$ Å, $c = 4.3334$ Å) with the thermal expansion coefficients[48] that are provided in Table 6.1.

Since ammonia has a similar mass as methane, the parameters used to simulate the molecular beam bundles (the stream velocity and width parameters, see Table 6.2) are taken from Refs. [17] and [50], which reported experiments performed for $CHD_3$ + Pt(111) and Ni(111). The width parameter $\alpha$ is taken as 10% of the stream velocity $\nu_0$, which is somewhat larger than was obtained for $CHD_3$[17, 50]. Note that this procedure was not employed in Ref. [26], where ammonia was in its vibrational ground state and the velocity distribution was not taken into account. For every AIMD data point at a surface temperature of 475 K and 1100 K, 1000 and 500 trajectories were run, respectively, using a time step of 0.4 fs. Other technical details of the AIMD calculations and the sampling of the initial conditions can be found in recent work[17, 32, 50] and in Chapter 2. Note that since $NH_3$ is an oblate symmetric top rotor, the rotational states have been described in the same manner as for $CHD_3$[17, 50] (see Section 2.4.2), which is also a symmetric top rotor.

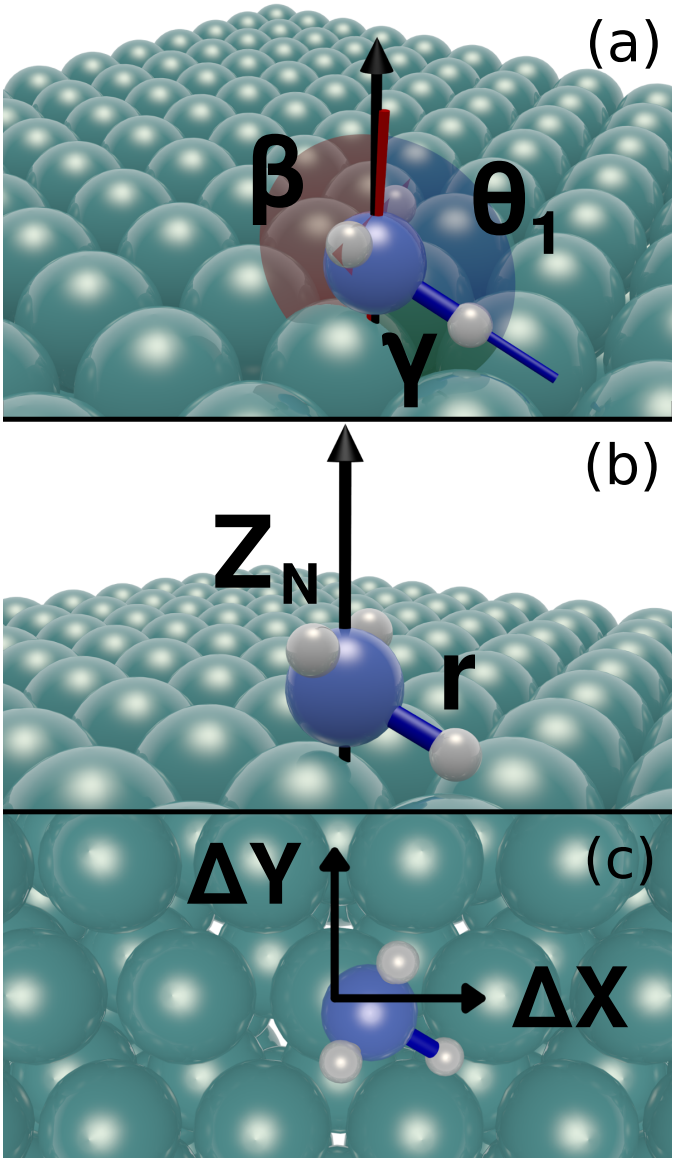


FIGURE 6.2: (a) Top2fcc TS of ammonia on Ru(0001), indicating the orientation angles as used in Table 6.3. $\theta_1$ is the angle between the dissociating NH bond and the surface normal, $\beta$ is the angle between the principal axis of $NH_2$ (i.e., the vector going from the geometric center of the two non-dissociating hydrogen atoms to the nitrogen atom) and the surface normal, and $\gamma$ is the angle between $\theta_1$ and this principal axis. (b) Same as panel a but here the length of the dissociating NH bond ($r$) and distance of the nitrogen atom to the surface ($Z_N$) are illustrated. (c) Top view of the top2fcc TS geometry.

TABLE 6.3: Minimum barrier geometries and barrier heights of ammonia on Ru(0001) using different XC-DFs. The zero-point energy corrected barriers are given in the brackets. Barriers corrected for the usage of a too small vacuum distance are indicated by $E_b^c$.

| Barrier | $Z_N$(Å) | $r$(Å) | $\theta_1$ (°) | $\beta$ (°) | $\gamma$ (°) | $E_b$ (kJ/mol) | $E_b^c$ (kJ/mol) |
|---|---|---|---|---|---|---|---|
| top2fcc (RPBE-vdW) | 2.04 | 1.62 | 115.6 | 177.2 | 61.6 | 65.9 (50.0) | 62.9 (47.0) |
| top2hcp (RPBE-vdW) | 2.03 | 1.60 | 116.1 | 176.5 | 60.3 | 63.2 (47.4) | 60.2 (44.4) |
| top2fcc (SRP32-vdW) | 2.01 | 1.62 | 113.8 | 177.6 | 63.9 | 41.4 (26.1) | 38.4 (23.1) |
| top2hcp (SRP32-vdW) | 2.01 | 1.59 | 114.8 | 175.0 | 60.2 | 42.0 (26.9) | 39.0 (23.9) |
| top2fcc (PBE) | 1.99 | 1.63 | 115.1 | 176.9 | 61.8 | 43.3 (29.6) | - |
| top2fcc (PBE)[26] | 2.06 | 1.64 | - | - | - | 45.6 (31.8) | - |
| top2hcp (PBE) | 1.99 | 1.61 | 115.6 | 176.2 | 60.6 | 40.2 (26.7) | - |

TABLE 6.4: Top2fcc and top2hcp barrier geometries of ammonia on Ru(0001) using different XC-DFs. The relative cartesian coordinates of the nitrogen atom to the closest top atom are given by $\Delta X_N$ and $\Delta Y_N$ and the distance between the nitrogen atom and the surface is given by $Z_N$. The positions of the hydrogen atoms relative to the nitrogen atom are given in spherical coordinates. The zero-point energy corrected barriers are given in the brackets and in kJ/mol. Barriers corrected for the usage of a too small vacuum distance are indicated by $E_b^c$.

| | top2fcc (RPBE-vdW) | top2hcp (RPBE-vdW) | top2fcc (SRP32-vdW) | top2hcp (SRP32-vdW) | top2fcc (PBE) | top2hcp (PBE) |
|---|---|---|---|---|---|---|
| $\Delta X_N$ (Å) | 0.47 | 0.00 | 0.51 | 0.00 | 0.45 | 0.00 |
| $\Delta Y_N$ (Å) | -0.28 | -0.56 | -0.29 | -0.60 | -0.25 | -0.53 |
| $Z_N$ (Å) | 2.04 | 2.03 | 2.01 | 2.01 | 1.99 | 1.99 |
| $r_{NH_1}$ (Å) | 1.62 | 1.60 | 1.59 | 1.62 | 1.63 | 1.61 |
| $r_{NH_2}$ (Å) | 1.02 | 1.02 | 1.02 | 1.02 | 1.02 | 1.02 |
| $r_{NH_3}$ (Å) | 1.02 | 1.02 | 1.02 | 1.03 | 1.02 | 1.02 |
| $\theta_{NH_1}$ (°) | 115.6 | 116.1 | 114.8 | 113.8 | 115.1 | 115.6 |
| $\theta_{NH_2}$ (°) | 55.2 | 55.2 | 55.2 | 54.6 | 55.8 | 55.6 |
| $\theta_{NH_3}$ (°) | 55.3 | 55.2 | 55.4 | 55.9 | 55.5 | 55.7 |
| $\phi_{NH_1}$ (°) | -30.0 | -89.9 | -29.7 | -88.0 | -30.1 | -90.1 |
| $\phi_{NH_2}$ (°) | 61.9 | 2.5 | 63.3 | 0.7 | 62.2 | 2.6 |
| $\phi_{NH_3}$ (°) | -122.0 | 177.6 | -123.6 | 177.6 | -122.0 | 177.4 |
| $E_b$ (kJ/mol) | 65.9 (50.0) | 63.2 (47.4) | 41.4 (26.1) | 42.0 (26.9) | 43.3 (29.6) | 40.2 (26.7) |
| $E_b^c$ (kJ/mol) | 62.9 (47.0) | 60.2 (44.4) | 38.4 (23.1) | 39.0 (23.9) | - | - |

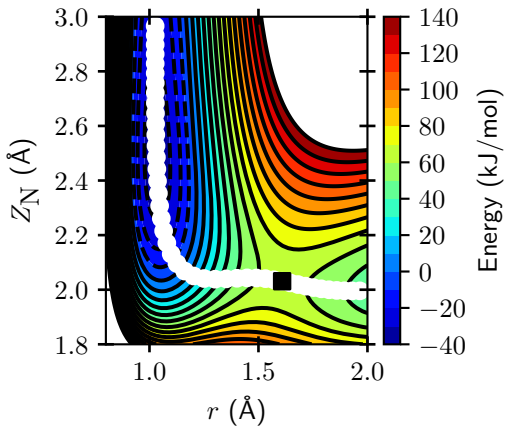


FIGURE 6.3: Elbow plot of ammonia on Ru(0001) as a function of $Z_N$ and $r$ (distance between the nitrogen atom and the surface, and the length of the dissociating NH bond, respectively), where other degrees of freedom are fixed according to the top2fcc TS geometry. Contour lines are drawn at intervals of 10 kJ/mol between -40 and 200 kJ/mol. The white circles indicate the MEP and the black square indicates the highest point along the MEP.

## 6.3 Results

### 6.3.1 Activation Barriers and Adsorption Energies

Figures 6.2a-c show the top2fcc barrier geometry obtained with the RPBE-vdW-DF1 DF and depicts the angles that are used in the description of the barrier heights and geometries obtained with the RPBE-vdW-DF1, SRP32-vdW[17] and PBE[28] DFs shown in Tables 6.3 and 6.3. The $\theta_1$ angle is the angle between the dissociating bond and the surface normal. The $\beta$ angle is the angle between the surface normal and the principal axis of the $NH_2$ fragment, which is defined as the vector going from the geometric center of the two non-dissociating hydrogen atoms to the nitrogen atom. The $\gamma$ angle indicates the angle between the axis defined and the dissociating bond (see Figure 6.2a). $Z_N$ indicates the distance of the nitrogen atom to the surface and the length of the dissociating NH bond is indicated by $r$ (see Figure 6.2b).

Two barriers have been obtained, the top2fcc and top2hcp barriers, of which the top2hcp barrier height (63.2 kJ/mol) is 2.7 kJ/mol lower than the top2fcc barrier height (65.9 kJ/mol). Moreover, in terms of the five coordinates shown in Figures 6.2a and 6.2b the two barrier geometries are very similar, with an important difference being the location of the dissociating hydrogen atom, i.e., towards the fcc and hcp hollow sites. Additionally, Figure 6.3 shows the elbow plot of ammonia on Ru(0001), where $Z_N$ and $r$ are allowed to vary but the remaining $NH_3$ coordinates are fixed to the top2fcc TS values. For this geometry, an adsorption well of about 36 kJ/mol is found before the MEP makes a turn. The top2fcc barrier geometry obtained by Hu et al.[26] using the PBE DF is similar to the one obtained with the RPBE-vdW-DF1

DF but their top2fcc barrier height is 20.3 kJ/mol lower. Moreover, with the computational setup described in Section 6.2, but with the PBE DF, a similar top2fcc barrier height and geometry is obtained as Hu et al.[26], where the difference in barrier heights is only 2.3 kJ/mol. Interestingly, for PBE the top2hcp barrier height obtained in this chapter is also lower than the top2fcc barrier height (by 3.1 kJ/mol), but the top2hcp barrier was not mentioned previously by Hu et al[26]. Nevertheless, the top2hcp barrier is confirmed to be present and to yield the lowest barrier height in the work of Hu et al. as well (private communication). It should also be noted that the converged surface lattice constant for PBE in this work is slightly smaller ($a = 2.7148$ Å) than the one obtained by Hu et al.[26] ($a = 2.7251$ Å) due to Hu et al. employing tetrahedron smearing with Blöchl corrections[51] for the bulk optimization instead of Fermi-Dirac smearing[52], which is employed throughout the rest of their DFT calculations.

With the SRP32-vdW DF previously developed for $CHD_3$ + Ni(111)[17] barrier heights for $NH_3$ + Ru(0001) are obtained that are similar to the PBE barrier heights, although now the top2fcc barrier height is 0.6 kJ/mol lower than the top2hcp barrier height (Tables 6.3 and 6.3). Again, the geometries are similar to the geometries obtained with the RPBE-vdW-DF1 DF. This was also observed for the barriers of $CHD_3$ on Pt(111) obtained with the PBE and SRP32-vdW DFs[5]. In general, it seems that the vdW interactions mostly lower the barrier height, and do not affect the barrier geometry much: Mixing in repulsive RPBE exchange (by going from PBE to SRP32 or RPBE exchange) while retaining PBE correlation would raise the barrier, but replacing PBE by vdW correlation fully (in case of SRP32 exchange) or partly (for RPBE exchange) compensates for this. However, the inclusion of vdW interactions may affect other areas of the PES in different ways, and therefore the dynamics may change as well, as has been shown for $CHD_3$ + Pt(111)[5].

The adsorption well of ammonia on Ru(0001) is shown in Figure 6.4, which is obtained by fixing the ammonia in the gas phase geometry. It is observed that the adsorption well is considerably deeper when the nitrogen atom points downwards (74.5 kJ/mol) than when the hydrogen atoms point downwards (18.5 kJ/mol), which corresponds to a chemisorbed and physisorbed state, respectively. When the ammonia molecule is fully relaxed at the surface an adsorption energy of 75.7 kJ/mol is obtained (see Table 6.5), which is in reasonable agreement with experiment (88.7 kJ/mol)[53]. Moreover, allowing the surface atoms to relax in response to the molecule as well yields an adsorption energy of 81.4 kJ/mol (Table 6.5), which is in even better agreement with experiment. When also the interaction energy of 3.0 kJ/mol is taken into account due to the employed vacuum distance (see Section 6.2), an adsorption

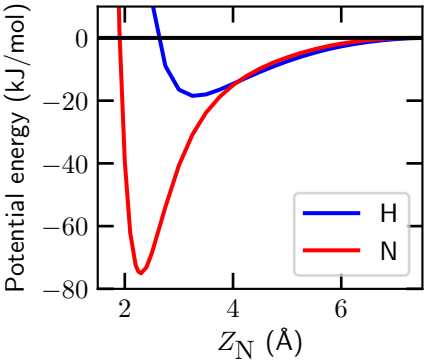


FIGURE 6.4: Physorption and chemisorption well of ammonia on Ru(0001). The blue and red lines indicate whether the hydrogen atoms (physisorption) or nitrogen atom (chemisorption) are closest to the surface, respectively. The asymptotic gas phase energy is taken as zero.

TABLE 6.5: Adsorption energies ($E_{ads}$) of $NH_3$ on Ru(0001) computed with the RPBE-vdW-DF1 DF, where the metal surface is kept fixed and relaxed. Ammonia is always relaxed. The corrected adsorption energies due to the interaction energy caused by the smaller vacuum distance are provided in the brackets.

| | Surface relaxed w.r.t. vacuum | | Surface relaxed w.r.t. $NH_3$ | |
|---|---|---|---|---|
| Site | $Z_N$ (Å) | $E_{ads}$ (kJ/mol) | $Z_N$ (Å) | $E_{ads}$ (kJ/mol) |
| Bridge | 2.61 | -29.8 (-32.8) | 2.55 | -32.4 (-35.4) |
| Fcc | 2.75 | -26.2 (-29.2) | 2.70 | -28.1 (-31.1) |
| Hcp | 2.78 | -25.6 (-28.6) | 2.78 | -26.3 (-29.3) |
| Top | 2.30 | -75.7 (-78.7) | 2.36 | -81.4 (-84.4) |
| T2f | 2.34 | -50.7 (-53.7) | 2.36 | -62.1 (-65.1) |
| T2b | 2.32 | -56.2 (-59.2) | 2.36 | -66.6 (-69.6) |
| Top (PBE)[26] | 2.23 | -83.7 | - | - |
| Top (Exp.)[53] | - | - | - | -88.7 |

energy of 84.4 kJ/mol is obtained (Table 6.5), which reproduces the experiment with almost chemical accuracy. With the PBE DF a similar adsorption energy (83.5 kJ/mol)[26] is obtained. This similarity in adsorption energy is attributed to the PBE exchange typically binding more than the RPBE exchange, combined with the vdW correlation compensating for this effect. Furthermore, the preferred adsorption site is the top site, which is in agreement with theory and experiments by Maier et al.[54] and Hu et al.[26], who both used the PBE DF without long-range correlation effects.

The barrier heights computed with the RPBE-vdW-DF1 DF can also be corrected for the unconverged value of the vacuum distance, obtaining $E_b^c$. Values of $E_b^c$ and the associated zero-point energy corrected values are listed in Tables 6.3 and 6.4.

### 6.3.2 Sticking Probability

The computed sticking probability of ammonia on Ru(0001) is shown in Figure 6.5a. The sticking probabilities computed by Hu et al. for vibrationally ground state $NH_3$[26] and the sticking probabilities measured by Mortensen et al.[25] are also shown. The sticking probability obtained with the RPBE-vdW-DF1 DF for a mobile surface is in better agreement with experiment than the sticking probabilities computed using the PBE DF within the static surface approximation[26]. The computed RPBE-vdW-DF1 sticking probabilities are smaller than the PBE sticking probabilities even though in the calculation of the latter the contribution from excited vibrational states to the sticking was omitted, and no averaging over the velocity distribution in the molecular beam was performed. Performing both averaging procedures would have led to even higher PBE sticking probabilities (see Figure 6.6 for sticking probabilities for vibrationally ground state $NH_3$). Furthermore, when the experimental results are multiplied with a factor 1.5 (Figure 6.5b), excellent agreement between the computed RPBE-vdW-DF1 and the measured sticking probabilities is obtained. This multiplication improves the mean absolute deviation (the mean of the distances between the theoretical and experimental sticking probability curves along the energy axis) from 23.1 kJ/mol to 4.5 kJ/mol, which is almost within chemical accuracy. Moreover, in agreement with experiment, no difference in reactivity is obtained using a surface temperature of 475 K or 1100 K at high incidence energy, i.e., the sticking probability has no surface temperature dependence. Trapping is also observed (see Figure 6.B.1), but the trapped molecules will most likely desorb when the corresponding trajectories are propagated longer for the incidence energies considered, where the measured sticking is independent of surface temperature.

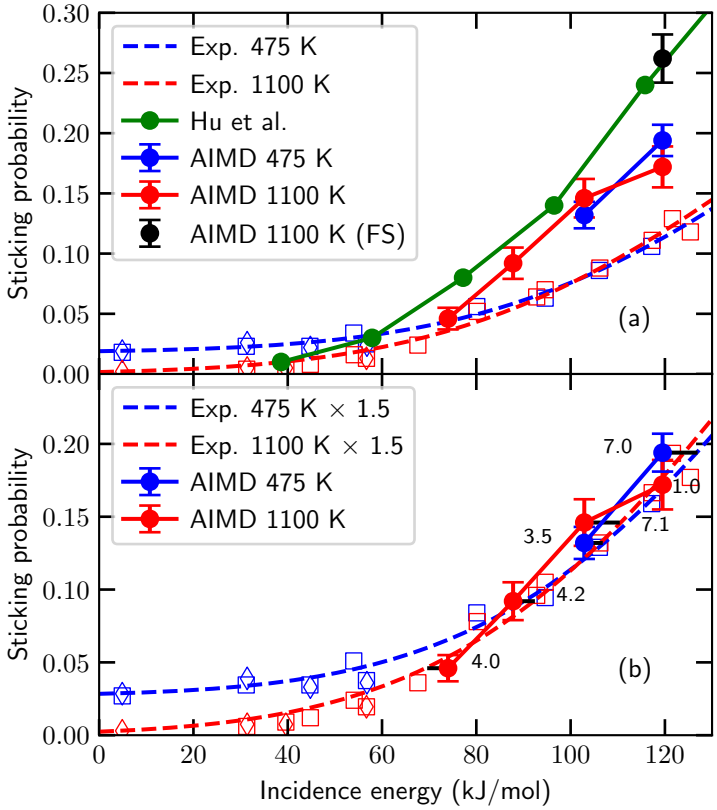


FIGURE 6.5: (a) Sticking probability of ammonia on Ru(0001). All theoretical results are indicated by closed circles and the experimental results are indicated by open diamonds and squares, of which the diamonds and squares are measurements using hydrogen or nitrogen desorption, respectively. Experimental results are taken from Ref. [25], and previous theoretical results without surface motion (closed green circles) are from Ref. [26]. The AIMD results are the closed blue ($T_s = 475\,K$) and red ($T_s = 1100\,K$) circles. The error bars represent 68% confidence intervals. (b) Same as panel a, but with the experimental results multiplied with a factor 1.5. The horizontal offsets between the computed and fitted experimental sticking probabilities are indicated by the numbers (in kJ/mol).

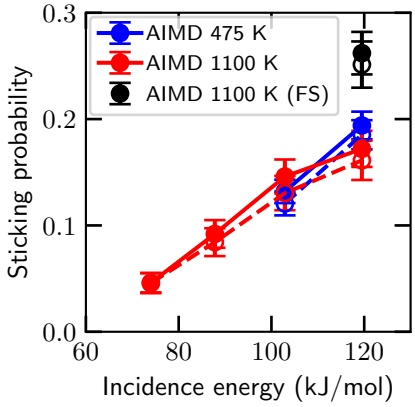


FIGURE 6.6: Sticking probability of $NH_3$ on Ru(0001). Theoretical results including vibrational states sampled with a Boltzmann distribution according to $T_n$ or only the ground state are indicated by closed and open circles, respectively. $T_s = 475\,K$ and 1100 K with(out) surface motion are represented by the blue and red (black) symbols, respectively. The error bars represent 68% confidence intervals.

The effect of surface motion is investigated as well by fixing the surface atoms in their ideal positions, commonly referred to as a frozen surface or Born-Oppenheimer static surface model, but using a lattice expansion coefficient corresponding to $T_s = 1100\,K$. This excludes any energy transfer from ammonia to the surface atoms, and corrugation in barrier heights and positions due to the movement of the surface atoms. In Figure 6.5a the sticking probability on the frozen surface is considerably higher than on the mobile surface. The thermal modulation of barrier heights and positions typically has a negligible effect on the sticking probability when the incidence energy is near or above the barrier height, as has been shown previously for methane reacting on several surfaces[8, 55, 56]. Furthermore, since both in this work and the experiments performed by Mortensen et al.[25] no surface temperature dependence is found for the incidence energies addressed, it is expected that this holds true for $NH_3$ + Ru(0001) as well. Therefore, it is likely that the increase in sticking is mainly caused by the lack of energy transfer from the molecule to the surface atoms, and thus including surface motion into the modeling of $NH_3$ + Ru(0001) is necessary.

The difference between the computed sticking probabilities in this chapter and those by Hu et al.[26] for vibrationally ground state ammonia is somewhat smaller than might have been expected from the difference between the $E_b$ value of PBE (45.6 kJ/mol)[26] and RPBE-vdW-DF1 (62.9 kJ/mol). However, note that the sticking probability of Hu et al. should be underestimated as also the contribution of vibrationally excited $NH_3$ should be taken into account (see Figure 6.6). Furthermore, as will be shown in the next section, the dynamics plays an important role in the dissociation of ammonia, especially the reorientation of ammonia. Therefore, the minimum barrier height might play a

TABLE 6.6: Average value of the $\theta_1$, $\beta$ and $\gamma$ angles with the standard error ($\sigma_m$) and standard deviation ($\sigma$) for all reacted and scattered trajectories. The top2fcc and top2hcp TS values are included as well.

| | $\theta_1(^\circ) \pm \sigma_m(\sigma)$ | $\beta(^\circ) \pm \sigma_m(\sigma)$ | $\gamma(^\circ) \pm \sigma_m(\sigma)$ |
|---|---|---|---|
| Reacted ($t = 0$) | $41.0 \pm 1.1$ (25.5) | $62.2 \pm 1.1$ (26.6) | $62.3 \pm 0.4$ (9.8) |
| Reacted ($r = r^\ddagger$) | $103.6 \pm 0.5$ (12.5) | $155.2 \pm 0.6$ (13.4) | $74.6 \pm 0.8$ (19.1) |
| Scattered ($t = 0$) | $89.7 \pm 0.7$ (38.4) | $90.6 \pm 0.7$ (40.1) | $62.2 \pm 0.2$ (9.8) |
| top2fcc | 115.6 | 177.2 | 61.6 |
| top2hcp | 116.1 | 176.5 | 60.3 |

smaller role than expected.

The sticking probabilities measured on Ru(0001) were not absolute sticking probabilities, but relative sticking probabilities measured by a combination of three different methods using partial pressures and temperature programmed desorption (TPD) of $H_2$ and $N_2$. The relative sensitivities of these three methods were calibrated to one another for overlapping regimes of surface temperatures where the methods were applicable. Absolute sticking probabilities were then obtained by also performing a King and Wells experiment[57] on a surface with an artificially high defect concentration created by sputtering, against which the other methods for measuring sticking of $NH_3$ on defect free Ru(0001) were then calibrated[25]. This procedure was needed due to the tendency of $NH_3$ to stick to the walls of the chamber. However, the uncertainty of the absolute sticking probabilities obtained in this manner was not stated. Since the shape of the sticking probability curve is predicted correctly if the experimental data is multiplied with a factor 1.5 (see Figure 6.5b), and the experimental error margin is unknown, it is possible that the disagreement between experiment and theory in this chapter is at least in part caused by an error in the calibration of the sticking probabilities. On the other hand, the results of Chapter 5 suggest that a GGA DF will always underestimate the barrier height of $NH_3$ + Ru(0001) since the difference between the molecule's electron affinity and the metal surface's work function is smaller than 7 eV, thus likely requiring a DF that reduces the self-interaction error (e.g., a screened hybrid DF). Nevertheless, additional experiments are required in order to validate both theory and experiment. For further discussion of the agreement between theory and experiment, see Section 6.4.

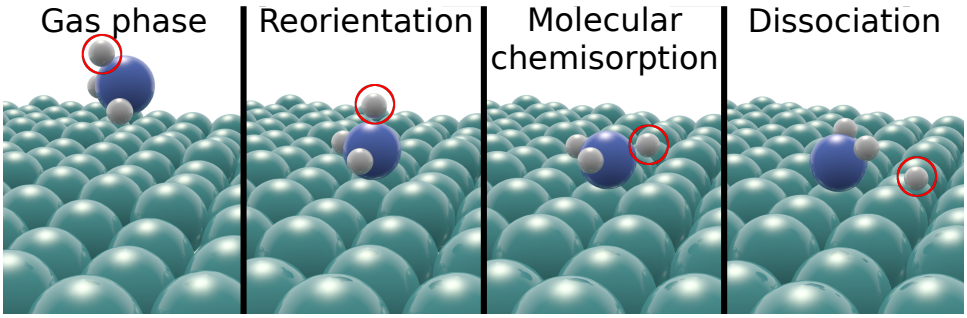


FIGURE 6.7: Snapshots from a typical trajectory of reacting ammonia on Ru(0001). The gas phase (a), first moment of reorientation (b), molecular chemisorbed state (c), and moment of reaction (d) are depicted. The dissociating hydrogen atom is indicated by the red circles. The simulation time portrayed in these panels is about 50 fs.

### 6.3.3 Dynamics During the Reaction

In order to elucidate the reaction mechanism of ammonia on Ru(0001), the dynamics of the reaction is now investigated. First, all reacted trajectories, except for one, occurred without bouncing, so the reaction proceeds directly, without the system going through a long-lived molecular precursor state. However, looking at the angles of ammonia during a reaction (see Figure 6.1, Table 6.6, and Figures 6.7a-d, which present snapshots from a representative example of the reactive trajectories) paints a different picture. The initial distribution of $\theta_1$ is centered on values smaller than 90° (Figure 6.1b), so typically the leaving H atom initially points away from the surface (Figure 6.7a). The dissociating hydrogen atom is only reoriented towards the surface (as in the TS, see Figure 6.2a) near the moment of the reaction (i.e., when $r = r^{\ddagger}$), see Figures 6.1b and 6.7d. Moreover, the non-dissociating hydrogen atoms are initially oriented towards the surface ($\theta_{2,3} > 90°$ and $\beta < 90°$, Figures 6.1c,d and 6.7a), while at the time of reaction they point upwards ($\theta_{2,3} < 90°$ and $\beta > 90°$, Figures 6.1c,d and 6.7d). Closer inspection of the reacted trajectories suggests that the nitrogen atom first binds to the surface (Figures 6.7b and 6.7c), while the two non-dissociating hydrogen atoms are oriented along (Figure 6.7b) and then away from (Figure 6.7c) the surface. After this, a rapid reorientation of all hydrogen atoms occurs and subsequently a hydrogen atom dissociates (Figure 6.7d), which is the hydrogen atom that was originally oriented away from the surface (Figure 6.7a). It is possible that by first binding the nitrogen atom to the surface, and thus forming a chemisorbed molecule, the NH bond is destabilized so that it can dissociate more easily after reorientation. Furthermore, this reaction occurs rapidly and without

bounces on the surface, where typically the time between ammonia impacting on the surface and dissociation of an NH bond is about 50 to 150 fs. Several movies of dissociation events are provided in the supporting information of Ref. [58] to illustrate the mechanism. Since the dissociative chemisorption of ammonia on Ru(0001) occurs initially through molecular chemisorption and only subsequently an NH bond dissociates, this is arguably not a simple direct reaction mechanism as reported before[25, 26], but rather a molecular chemisorption mediated direct reaction mechanism.

Importantly, at the initial time step the orientation distribution of the reacting molecule is non-statistical, i.e., it does not resemble a $\sin(\theta)$ distribution as shown in Figure 6.1a. A non-statistical initial distribution has also been observed for other polyatomic molecules reacting on metal surfaces (Figure 6.1a) (e.g., $CHD_3$[15, 17, 50] and methanol[7], see Chapters 7, 9 and 10) for which cases the reaction mechanism can be described reasonably well as a rotational sudden mechanism. Interestingly, unlike for the aforementioned cases, the initial orientation distribution of $NH_3$ does not resemble the barrier geometry or the orientation distribution at the time of reaction. Only at the moment of dissociation, i.e., when $r = r^{\ddagger}$ for the dissociating bond, does the time-evolved orientation distribution of ammonia resemble the barrier geometry, which to the best of our knowledge has not been observed before. This has consequences for the approximations that can be made in modeling the reaction. For example, the HOD + Ni(111) reaction can be treated as rotationally adiabatic[4, 59], while the reaction of $CHD_3$ + Ni(111) can be treated reasonably well with a rotational sudden approximation[14] (see also Figure 6.1a). However, the unique behaviour of ammonia, where rotationally non-adiabatic dynamics is coupled with a non-statistical distribution of the orientation of the reacting molecule at $t = 0$, prevents the usage of such approximations and only models where the full dynamics is included, such as AIMD, can describe $NH_3$ + Ru(0001) correctly. It should be noted that although HCl + Au(111) appears to exhibit a statistical initial distribution and a time-evolved distribution of the orientation of HCl resembling the barrier geometry (i.e., a rotational adiabatic mechanism, see Chapter 3), a careful analysis of the reaction mechanism suggests that the reaction is, in fact, rotationally non-adiabatic, similar to $NH_3$ + Ru(0001) (see Chapter 4. Furthermore, quantum dynamics might be necessary to describe the reaction of $NH_3$ on Ru(0001)[26] at low $E_i$, but performing quantum dynamics (QD) calculations using the full 12D hamiltonian is probably computationally prohibitive. So far QD employing a hamiltonian including all degrees of freedom of the molecule has been performed up to 9D, e.g., on $H_2O$ + Cu(111)[60]. For molecule-surface systems with more than nine molecular degrees of freedom reduced dimensionality

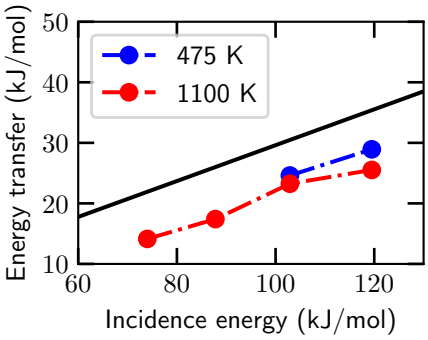


FIGURE 6.8: Average energy transfer from scattered ammonia to Ru(0001) compared to the refined Baule model. The black line is the energy transfer predicted by the refined Baule model, whereas the blue and red circles indicate the energy transfer predicted by AIMD at $T_s = 475\,K$ and $1100\,K$, respectively.

hamiltonians have been employed, e.g., with nine degrees of freedom for $CH_4$ + Ni(111)[61], and the use of the rotationally adiabatic or rotational sudden approximation might therefore be desirable. However, as has been noted here, these approximations are not valid for the reaction of $NH_3$ on Ru(0001), and therefore employing a reduced dimensionality hamiltonian may not be straightforward.

Figure 6.8 shows the predicted energy transfer of the scattered trajectories obtained with AIMD and by the refined Baule model[62, 63] (see also Section 2.5), which is defined as

$$\langle E_T \rangle = \frac{2.4\mu}{(1+\mu)^2} \langle E_i \rangle \,, \tag{6.2}$$

where $\mu = m/M$ (m is the mass of ammonia and M is the mass of a ruthenium atom) and $\langle E_i \rangle$ is the average incidence energy. Here it is seen that the energy transfer computed with AIMD is about 20%, whereas the refined Baule model predicts an energy transfer of about 30%. This disagreement is larger than has generally been observed for $CHD_3$[63] (Chapter 9) and methanol[7] (Chapter 10). It is possible that trajectories that transfer less energy from ammonia to the metal surface are also less likely to trap, and therefore that the average energy transfer is lower than one would expect from the comparatively simple refined Baule model.

Molecules are most likely to trap when the lone pair on the nitrogen atom is pointing away from the surface ($\beta' < 90°$, see Figure 6.1e). When the lone pair is oriented more towards the surface, it is considerably more likely to react, probably due to the possibility of forming the chemisorption-like state required for the reaction. An obvious reason for trapping would be the translational energy transfer from the ammonia to the metal surface.

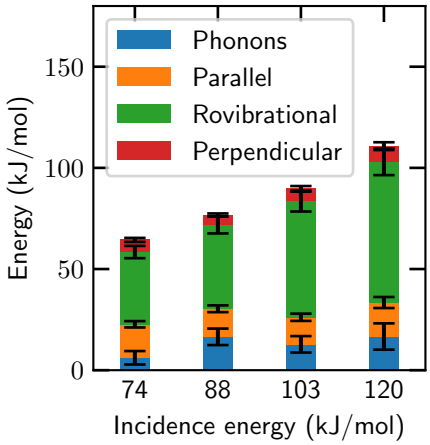


FIGURE 6.9: Kinetic energy of trapped ammonia parallel ($XY$ direction, orange) and perpendicular ($Z$ direction, red) to the surface, the energy transfered from $NH_3$ to the surface phonons (compared to $t = 0$, blue), and increase in the rovibrational energy of $NH_3$ (compared to $t = 0$, green) at the final time step, i.e., when $t = 1.0$ ps, as a function of incidence energy. The error bars represent 68% confidence intervals.

However, even when energy transfer from the molecule to the surface is not allowed by employing a frozen surface, trapping is still observed (about 2% at $\langle E_i \rangle = 119$ kJ/mol, versus 5% if surface motion is included, see Figure 6.B.1). This suggests that energy transfer to other motions, i.e., motions of $NH_3$, may also cause ammonia to be trapped. For instance, it is possible to excite the vibrational bending mode of ammonia when the umbrella is pointing towards the surface, thereby converting translational energy into vibrational energy. Also, a large fraction of the translational energy of trapped molecules is oriented parallel to the surface instead of perpendicular to the surface after the initial collision. These energy transfer effects are quantified in Figure 6.9. The largest energy transfer is observed to vibrations and rotations, and this represents about 60% of the energy transfered. The energy transfer from motion normal to the surface to motion parallel to the surface and to the phonons and rovibrational motion make it less likely to scatter. It is expected that these trapped trajectories are likely to scatter back into the gas phase at longer simulation times, as they might be able at some point to escape both the chemisorption and physisorption wells. This has also been observed for some of the scattered trajectories, which scattered after one or two bounces on the surface. The observation of trajectories that scattered after one or two bounces, and the observation that only one of the reacted trajectories was indirect (occurred with bouncing) is in accordance with the original proposal by the experimentalists[25] of a direct mechanism for the high $E_i$ addressed here, and the surface temperature independence of reaction they observed.

Figure 6.10 shows that the reaction occurs relatively more near (i.e., more than expected on the basis of relative surface areas) the bridge site than near

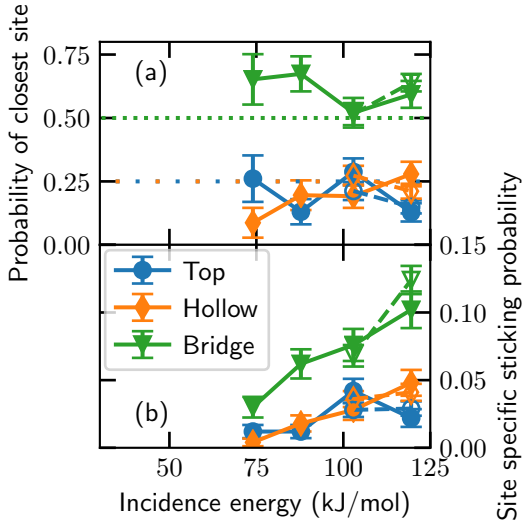


FIGURE 6.10: (a) Fraction of closest high symmetry site, i.e., the top, hollow and bridge (blue, orange and green, respectively) sites, to the impact site of reacting ammonia as a function of the incidence energy when a bond dissociates, i.e., when $r = r^{\ddagger}$. The open and closed symbols indicate a surface temperature of 475 K and 1100 K, respectively. The dotted lines indicate the statistical average for the high symmetry sites. (b) The sticking probability of $NH_3$ on the high symmetry sites as a function of the incidence energy. The error bars represent 68% confidence intervals.

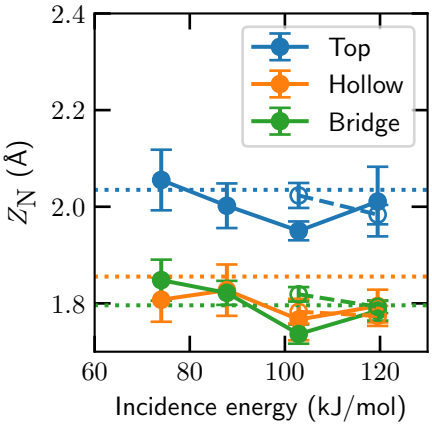


FIGURE 6.11: Distance of the nitrogen atom to the surface when a bond dissociates, i.e., when $r = r^{\ddagger}$, as a function of incidence energy. The open and closed circles indicate a surface temperature of 475 K and 1100 K, respectively. The blue, orange, and green lines indicate the top, hollow, and bridge sites. The horizontal dotted lines indicate the TS values of $Z_N$, where the values belonging to the hollow and bridge sites are taken from Ref. [26]. The error bars represent 68% confidence intervals.

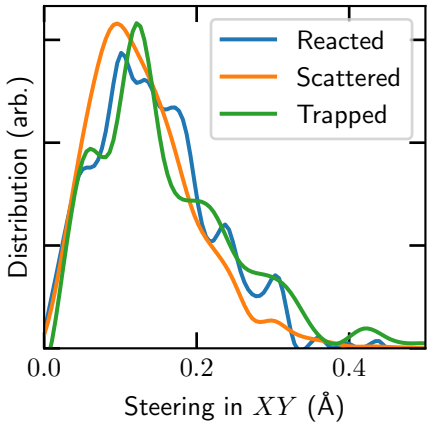


FIGURE 6.12: Distribution of steering of ammonia in the $XY$ direction for all reacted (blue), scattered (orange) and trapped (green) trajectories. Steering is here defined as the distance travelled by $NH_3$ in the $XY$ plane between the initial time step and first classical turning point for the scattered and trapped trajectories, and between the initial time step and when a bond dissociates, i.e., when $r = r^{\ddagger}$, for reacted trajectories.

the top and hollow sites. However, from the minimum barrier location (near the top site, see Section 6.3.1) one would expect that the top site should be relatively more reactive than the other sites. The barrier height on the bridge site was predicted by Hu et al. to be 11 kJ/mol higher than the minimum barrier height[26]. Furthermore, the reactivity of the top and hollow sites is similar, even though compared to the minimum barrier the barriers on the hcp and fcc sites were predicted to be higher by 49 and 38 kJ/mol, respectively[26]. The possibility is considered here that the relatively low reactivity near the top site is caused by the bobsled effect[64, 65], which can reduce the reactivity as it causes the molecule to slide off the MEP and react over a higher barrier than the lowest barrier[8, 63]. However, Figure 6.11 shows that the average distance of the nitrogen atom to the surface is close to the TS value for all three sites. Therefore, it seems unlikely that the bobsled effect plays a large role. At present, it remains unclear why the bridge site is more reactive than the top and hollow sites. It can be speculated that the use of vdW-DF1 correlation leads to the barriers being relatively lower (i.e., compared to PBE) above the bridge and hollow sites, where the barriers are closer to the surface.

Interestingly, a considerable amount of steering in the $XY$ plane is observed (see Figure 6.12). The steering also seems to be independent of incidence energy and whether the trajectory will go on to react, scatter or trap. Moreover, looking at Figure 6.13, the dynamical steering in the $XY$ direction mostly steers the ammonia away from the hollow sites towards the bridge sites. At high incidence energy steering from the bridge site towards the top site occurs as well.

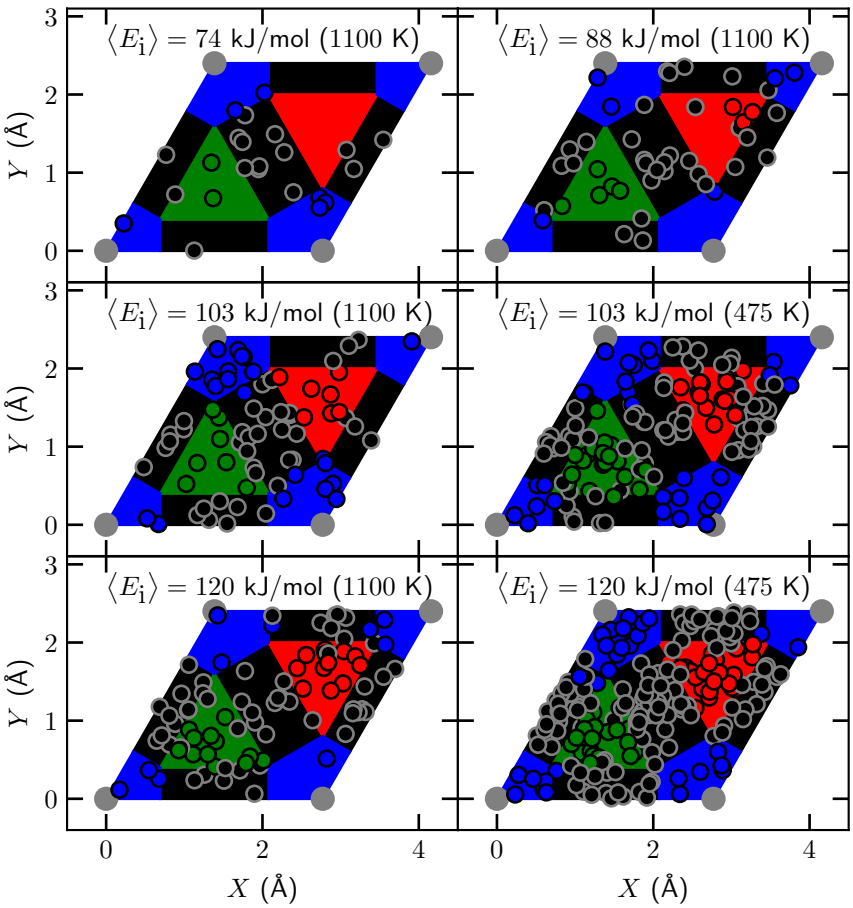


FIGURE 6.13: Impact site of reacting ammonia on Ru(0001) indicated with circles at the initial time step, i.e., $t = 0$ fs and $Z_{\mathrm{COM}} = 7.5$ Å, whereas the color of the circle indicates the closest high symmetry site when a bond dissociates, i.e., when $r = r^{\ddagger}$. The top, fcc, hcp and bridge sites are indicated in blue, green, red and black, respectively, and the top layer atoms are indicate by the gray circles.

## 6.4 Discussion of the Comparison of Experiment and Theory

Here, potential issues are discussed with both theory and experiment that could further affect the comparison between the measured and computed reaction probabilities. First, the inversion of the umbrella of the ammonia molecule during the dynamics might be treated incorrectly with the QCT approach in the AIMD[66, 67]. Especially when higher nozzle temperatures are employed, the probability of having vibrationally excited bending modes is considerable. However, in the AIMD the inversion of the umbrella does not occur before reaching the surface, and the inversion of ammonia occurs on a timescale (once per 21 ps[68]) that is considerably longer than the time it takes to reach the surface in the AIMD (100 fs). Therefore, it is concluded that the QCT approach should be valid at high incidence energies where reaction occurs in a "classical over the barrier fashion", and thus tunneling should not play a significant role. Another issue is that the experimental beam parameters[25] are not exactly known, making a direct quantitative comparison difficult as beam parameters can have a large effect on the reaction probability of molecules reacting on metal surfaces[30, 69, 70]. This effect can also be seen in Figure 6.6 where results are compared for ammonia in the vibrational ground state with ammonia vibrationally excited according to a Boltzmann distribution. At the higher incidence energies and concomitant higher nozzle temperatures, the sticking probability of vibrational ground state ammonia is somewhat lower than when the vibrational excitations in the molecular beam are taken into account.

## 6.5 Conclusions

In this chapter the dissociative chemisorption of ammonia on Ru(0001) is investigated with AIMD. Not only is surface motion included for this reaction for the first time, a DF incorporating attractive Van der Waals correlation (RPBE-vdW-DF1) is employed as well. With respect to earlier work employing the PBE DF and modeling the Ru(0001) surface as static the computed sticking probability is found to be in improved agreement with experiment. This improvement is attributed to both modeling the Ru(0001) as a mobile surface, and using the RPBE-vdW-DF1 DF. Also, the lack of surface temperature dependence at high incidence energy observed by experiment is confirmed with AIMD. It is found that the modeling of surface motion is required to accurately describe the sticking probability. The reaction mechanism is neither

rotationally adiabatic nor rotational sudden, with initial and intermediate (i.e., at time of reaction) orientation distributions that are both non-statistical, but do not resemble one another, which to the best of our knowledge has not been observed before. Furthermore, it is observed that under the conditions investigated the dissociation of ammonia on Ru(0001) is not described by a simple direct, or by an indirect trapping-mediated reaction mechanism, but rather by a direct reaction mechanism in which $NH_3$ goes through a very short-lived molecularly chemisorbed state. Direct dissociative chemisorption of a polyatomic molecule where the molecular chemisorption of a molecule is immediately followed by dissociation has also not been observed before.

# Appendix

## 6.A Convergence

Figure 6.A.1 and Table 6.A.1 illustrate the convergence of the minimum barrier height for ammonia dissociation on Ru(0001) ($E_b$) as a function of number of layers for different numbers of $k$-points using a kinetic energy cut-off of 400 eV, yielding a converged barrier height of 44.8 kJ/mol. The SRP32-vdW DF that was originally developed for $CHD_3$ + Ni(111)[17] is used here instead of the RPBE-vdW-DF1 DF used throughout the rest of this chapter. Moreover, a vacuum distance of 13 Å is used, instead of 15 Å used in the rest of this chapter. However, similar convergence behaviour is expected. The computational set up employed for the AIMD calculations (4 layers, $3 \times 3$ surface unit cell, $4 \times 4 \times 1$ $k$-points, kinetic energy cut-off of 400 eV), with the exception noted for the vacuum distance, gave a barrier height of 44.0 kJ/mol. It is confirmed that the computational set up is also converged with respect to the kinetic energy cut-off. Furthermore, Table 6.A.2 shows the top2hcp barrier heights obtained with the SRP32-vdW DF as a function of the vacuum distance. Here it can be seen that 30 Å yields converged barrier heights. Note that in Table 6.A.2 for only a vacuum distance of 13 and 30 Å a dimer calculation is performed, whereas for the other values of the vacuum distance the barrier geometry yielded by 13 Å is employed, i.e., a so-called single point calculation is performed. For a vacuum distance of 30 Å it is confirmed that a single point calculation reproduces the result of the dimer calculation. However, for 15 Å a small difference of 1.4 kJ/mol is obtained between the single point and dimer calculations (see Table 6.3, where $E_b = 42.0$ kJ/mol instead of 40.6 kJ/mol). Hence, a translational energy shift of 4.4 kJ/mol instead of 3.0 kJ/mol would have been more appropriate due to the interaction energy (see Section 6.2), but we consider this difference to be small enough to not affect the results presented in this chapter considerably. It is also confirmed that employing the RPBE-vdW-DF1 DF yields the same difference in barrier heights between 15 Å and 30 Å as the SRP32-vdW DF.

TABLE 6.A.1: Convergence of the minimum barrier height (kJ/mol) on Ru(0001) (top2hcp geometry) is shown as a function of the amount of layers, *k*-points, and the size of the surface unit cell ($3 \times 3$ and $4 \times 4$) for a plane wave energy cutoff of 400 eV using the SRP32-vdW DF. A vacuum distance of 13 Å instead of 15 Å (used throughout the rest of this chapter) is employed. The results obtained with the employed computational set up in the AIMD (except the vacuum distance) is in bold and the most converged result (i.e., obtained with the largest setup) is in italic.

| Layers | *k*-points | $E_b, 3 \times 3$ | $E_b, 4 \times 4$ |
|---|---|---|---|
| 4 | $3 \times 3 \times 1$ | | 44.0 |
| 4 | $4 \times 4 \times 1$ | **44.0** | 42.2 |
| 4 | $6 \times 6 \times 1$ | 43.5 | 42.8 |
| 4 | $8 \times 8 \times 1$ | 42.9 | 42.8 |
| 4 | $10 \times 10 \times 1$ | 42.9 | |
| 5 | $3 \times 3 \times 1$ | | 46.0 |
| 5 | $4 \times 4 \times 1$ | 46.6 | 45.8 |
| 5 | $6 \times 6 \times 1$ | 45.7 | 45.7 |
| 5 | $8 \times 8 \times 1$ | 46.3 | 45.3 |
| 5 | $10 \times 10 \times 1$ | 46.2 | |
| 6 | $3 \times 3 \times 1$ | | 48.2 |
| 6 | $4 \times 4 \times 1$ | 47.9 | 46.8 |
| 6 | $6 \times 6 \times 1$ | 47.5 | 47.5 |
| 6 | $8 \times 8 \times 1$ | 47.4 | 47.4 |
| 6 | $10 \times 10 \times 1$ | 47.3 | |
| 7 | $3 \times 3 \times 1$ | | 46.1 |
| 7 | $4 \times 4 \times 1$ | 45.8 | 45.9 |
| 7 | $6 \times 6 \times 1$ | 45.3 | 45.5 |
| 7 | $8 \times 8 \times 1$ | 45.3 | 45.6 |
| 7 | $10 \times 10 \times 1$ | 45.6 | |
| 8 | $3 \times 3 \times 1$ | | 44.7 |
| 8 | $4 \times 4 \times 1$ | 45.1 | 45.1 |
| 8 | $6 \times 6 \times 1$ | 45.3 | 44.8 |
| 8 | $8 \times 8 \times 1$ | 45.2 | 44.5 |
| 8 | $10 \times 10 \times 1$ | 44.9 | |
| 9 | $3 \times 3 \times 1$ | | 43.9 |
| 9 | $4 \times 4 \times 1$ | 44.0 | 44.3 |
| 9 | $6 \times 6 \times 1$ | 44.1 | 43.8 |
| 9 | $8 \times 8 \times 1$ | 43.9 | 43.6 |
| 9 | $10 \times 10 \times 1$ | 43.7 | |
| 10 | $3 \times 3 \times 1$ | | 44.8 |
| 10 | $4 \times 4 \times 1$ | 44.6 | 44.9 |
| 10 | $6 \times 6 \times 1$ | 44.9 | 45.0 |
| 10 | $8 \times 8 \times 1$ | 44.6 | *44.8* |
| 10 | $10 \times 10 \times 1$ | 44.6 | |

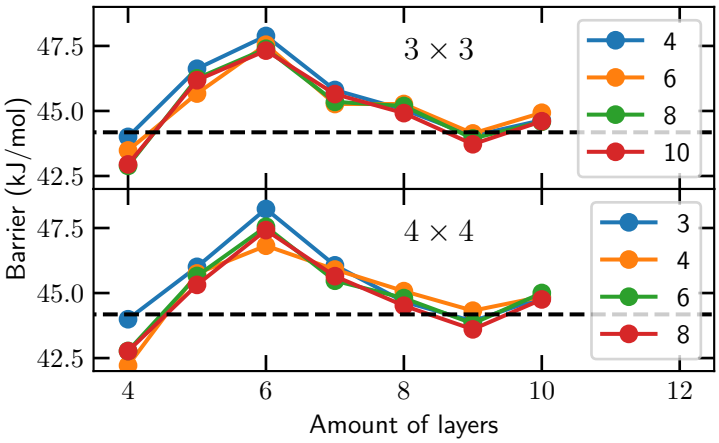


FIGURE 6.A.1: Convergence of the minimum barrier height on Ru(0001) (top2hcp geometry) as a function of the amount of layers for the number of $k$-points equal to $(n \times n \times 1)$, where $n$ is indicated in the legend. The SRP32-vdW DF is used. The upper panel and lower panel used a $3 \times 3$ and $4 \times 4$ supercell, respectively. The dashed lines indicate the converged barrier height.

TABLE 6.A.2: Minimum barrier height (kJ/mol) on Ru(0001) (top2hcp geometry) is shown as a function of the vacuum distance with the computational set up used in the AIMD employing the SRP32-vdW DF.

| Vacuum distance | $E_b$ (kJ/mol) |
|---|---|
| 13 | 44.0 |
| 15 | 40.6 |
| 17 | 39.0 |
| 20 | 38.2 |
| 25 | 37.7 |
| 30 | 37.5 |

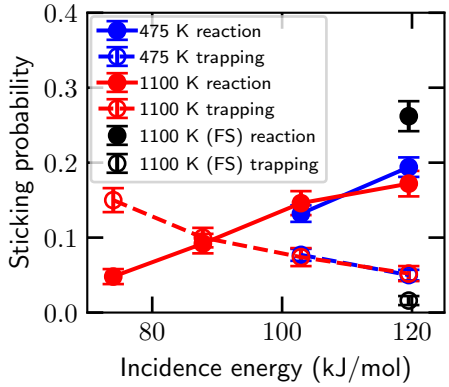


FIGURE 6.B.1: Sticking probability of ammonia on Ru(0001) obtained with AIMD. $T_s = 475\,K$ and $1100\,K$ are represented by the blue and red symbols, respectively. The closed and open symbols indicate reaction probabilities and trapping probabilities, respectively. The error bars represent 68% confidence intervals.

## 6.B Trapping

Figure 6.B.1 shows the reaction probabilities of $NH_3$ on Ru(0001) obtained with AIMD, where the trapping probabilities are shown as well. At the lowest incidence energy about three times as much trapping occurs as reaction, whereas at the highest incidence energy the trapping probability is about a factor 4 smaller than the reaction probability. Under the conditions shown in Figure 6.B.1, trapping is not expected to contribute to reaction[25]. If trapping were to affect the reaction probability, it is expected the measured sticking probability to depend on $T_s$, while it does not.

# References


(1) Lin, X.; Yoon, Y.; Petrik, N. G.; Li, Z.; Wang, Z.-T.; Glezakou, V.-A.; Kay, B. D.; Lyubinetsky, I.; Kimmel, G. A.; Rousseau, R.; Dohnálek, Z. Structure and Dynamics of $CO_2$ on Rutile $TiO_2$(110)-1x1. *J. Phys. Chem. C* **2012**, *116*, 26322–26334, DOI: 10.1021/jp308061j.

(2) Naderian, M.; Groß, A. From Single Molecules to Water Networks: Dynamics of Water Adsorption on Pt(111). *J. Chem. Phys.* **2016**, *145*, 094703, DOI: 10.1063/1.4961870.

(3) Zhou, X.; Kolb, B.; Luo, X.; Guo, H.; Jiang, B. Ab Initio Molecular Dynamics Study of Dissociative Chemisorption and Scattering of $CO_2$ on Ni(100): Reactivity, Energy Transfer, Steering Dynamics, and Lattice Effects. *J. Phys. Chem. C* **2017**, *121*, 5594–5602, DOI: 10.1021/acs.jpcc.6b12686.

(4) Migliorini, D.; Nattino, F.; Tiwari, A. K.; Kroes, G.-J. HOD on Ni(111): Ab Initio Molecular Dynamics Prediction of Molecular Beam Experiments. *J. Chem. Phys.* **2018**, *149*, 244706, DOI: 10.1063/1.5059357.

(5) Chadwick, H.; Migliorini, D.; Kroes, G. J. $CHD_3$ Dissociation on Pt(111): A Comparison of the Reaction Dynamics Based on the PBE Functional and on a Specific Reaction Parameter Functional. *J. Chem. Phys.* **2018**, *149*, 044701, DOI: 10.1063/1.5039458.

(6) Migliorini, D.; Chadwick, H.; Kroes, G.-J. Methane on a Stepped Surface: Dynamical Insights on the Dissociation of $CHD_3$ on Pt(111) and Pt(211). *J. Chem. Phys.* **2018**, *149*, 094701, DOI: 10.1063/1.5046065.

(7) Gerrits, N.; Kroes, G.-J. An AIMD Study of Dissociative Chemisorption of Methanol on Cu(111) with Implications for Formaldehyde Formation. *J. Chem. Phys.* **2019**, *150*, 024706, DOI: 10.1063/1.5070129.

(8) Gerrits, N.; Shakouri, K.; Behler, J.; Kroes, G.-J. Accurate Probabilities for Highly Activated Reaction of Polyatomic Molecules on Surfaces Using a High-Dimensional Neural Network Potential: $CHD_3$ + Cu(111). *J. Phys. Chem. Lett.* **2019**, *10*, 1763–1768, DOI: 10.1021/acs.jpclett.9b00560.

(9) Zhang, Y.; Zhou, X.; Jiang, B. Bridging the Gap between Direct Dynamics and Globally Accurate Reactive Potential Energy Surfaces Using Neural Networks. *J. Phys. Chem. Lett.* **2019**, *10*, 1185–1191, DOI: 10.1021/acs.jpclett.9b00085.

(10) Farjamnia, A.; Jackson, B. The Dissociative Chemisorption of Water on Ni(111): Mode- and Bond-Selective Chemistry on Metal Surfaces. *J. Chem. Phys.* **2015**, *142*, 234705, DOI: 10.1063/1.4922625.

(11) Jiang, B. Rotational and Steric Effects in Water Dissociative Chemisorption on Ni(111). *Chem. Sci.* **2017**, *8*, 6662–6669, DOI: 10.1039/C7SC02659E.

(12) Campbell, V. L.; Chen, N.; Guo, H.; Jackson, B.; Utz, A. L. Substrate Vibrations as Promoters of Chemical Reactivity on Metal Surfaces. *J. Phys. Chem. A* **2015**, *119*, 12434–12441, DOI: 10.1021/acs.jpca.5b07873.

(13) Guo, H.; Farjamnia, A.; Jackson, B. Effects of Lattice Motion on Dissociative Chemisorption: Toward a Rigorous Comparison of Theory with Molecular Beam Experiments. *J. Phys. Chem. Lett.* **2016**, *7*, 4576–4584, DOI: 10.1021/acs.jpclett.6b01948.

(14) Jackson, B.; Nattino, F.; Kroes, G.-J. Dissociative Chemisorption of Methane on Metal Surfaces: Tests of Dynamical Assumptions Using Quantum Models and Ab Initio Molecular Dynamics. *J. Chem. Phys.* **2014**, *141*, 054102, DOI: 10.1063/1.4891327.

(15) Gerrits, N.; Migliorini, D.; Kroes, G.-J. Dissociation of $CHD_3$ on Cu(111), Cu(211), and Single Atom Alloys of Cu(111). *J. Chem. Phys.* **2018**, *149*, 224701, DOI: 10.1063/1.5053990.

(16) Jackson, B.; Nave, S. The Dissociative Chemisorption of Methane on Ni(100): Reaction Path Description of Mode-Selective Chemistry. *J. Chem. Phys.* **2011**, *135*, 114701, DOI: 10.1063/1.3634073.

(17) Nattino, F.; Migliorini, D.; Kroes, G.-J.; Dombrowski, E.; High, E. A.; Killelea, D. R.; Utz, A. L. Chemically Accurate Simulation of a Polyatomic Molecule-Metal Surface Reaction. *J. Phys. Chem. Lett.* **2016**, *7*, 2402–2406, DOI: 10.1021/acs.jpclett.6b01022.

(18) Ertl, G. Primary Steps in Catalytic Synthesis of Ammonia. *J. Vac. Sci. Technol. A* **1983**, *1*, 1247–1253, DOI: 10.1116/1.572299.

(19) Nielsen, A., *Ammonia: Catalysis and Manufacture*; Springer Science & Business Media: 2012; 352 pp.

(20) Erisman, J. W.; Sutton, M. A.; Galloway, J.; Klimont, Z.; Winiwarter, W. How a Century of Ammonia Synthesis Changed the World. *Nat. Geosci.* **2008**, *1*, 636–639, DOI: 10.1038/ngeo325.

(21) Choudhary, T.; Sivadinarayana, C.; Goodman, D. Catalytic Ammonia Decomposition: $CO_x$-Free Hydrogen Production for Fuel Cell Applications. *Catal. Lett.* **2001**, *72*, 197–201, DOI: 10.1023/A:1009023825549.

(22) Schüth, F.; Palkovits, R.; Schlögl, R.; Su, D. S. Ammonia as a Possible Element in an Energy Infrastructure: Catalysts for Ammonia Decomposition. *Energy Environ. Sci.* **2012**, *5*, 6278–6289, DOI: 10.1039/C2EE02865D.

(23) Mukherjee, S.; Devaguptapu, S. V.; Sviripa, A.; Lund, C. R. F.; Wu, G. Low-Temperature Ammonia Decomposition Catalysts for Hydrogen Generation. *Appl. Catal. B* **2018**, *226*, 162–181, DOI: 10.1016/j.apcatb.2017.12.039.

(24) Bradford, M. C. J.; Fanning, P. E.; Vannice, M. A. Kinetics of $NH_3$ Decomposition over Well Dispersed Ru. *J. Catal.* **1997**, *172*, 479–484, DOI: 10.1006/jcat.1997.1877.

(25) Mortensen, H.; Diekhöner, L.; Baurichter, A.; Jensen, E.; Luntz, A. C. Dynamics of Ammonia Decomposition on Ru(0001). *J. Chem. Phys.* **2000**, *113*, 6882–6887, DOI: 10.1063/1.1310662.

(26) Hu, X.; Yang, M.; Xie, D.; Guo, H. Vibrational Enhancement in the Dynamics of Ammonia Dissociative Chemisorption on Ru(0001). *J. Chem. Phys.* **2018**, *149*, 044703, DOI: 10.1063/1.5043517.

(27) Jiang, B.; Guo, H. Permutation Invariant Polynomial Neural Network Approach to Fitting Potential Energy Surfaces. III. Molecule-Surface Interactions. *J. Chem. Phys.* **2014**, *141*, 034109, DOI: 10.1063/1.4887363.

(28) Perdew, J. P.; Burke, K.; Ernzerhof, M. Generalized Gradient Approximation Made Simple. *Phys. Rev. Lett.* **1996**, *77*, 3865–3868, DOI: 10.1103/PhysRevLett.77.3865.

(29) Perdew, J. P.; Wang, Y. Accurate and Simple Analytic Representation of the Electron-Gas Correlation Energy. *Phys. Rev. B* **1992**, *45*, 13244–13249, DOI: 10.1103/PhysRevB.45.13244.

(30) Díaz, C.; Pijper, E.; Olsen, R. A.; Busnengo, H. F.; Auerbach, D. J.; Kroes, G. J. Chemically Accurate Simulation of a Prototypical Surface Reaction: $H_2$ Dissociation on Cu(111). *Science* **2009**, *326*, 832–834, DOI: 10.1126/science.1178722.

(31) Wijzenbroek, M.; Kroes, G. J. The Effect of the Exchange-Correlation Functional on $H_2$ Dissociation on Ru(0001). *J. Chem. Phys.* **2014**, *140*, 084702, DOI: 10.1063/1.4865946.

(32) Nattino, F.; Ueta, H.; Chadwick, H.; van Reijzen, M. E.; Beck, R. D.; Jackson, B.; van Hemert, M. C.; Kroes, G.-J. Ab Initio Molecular Dynamics Calculations versus Quantum-State-Resolved Experiments on $CHD_3$ + Pt(111): New Insights into a Prototypical Gas–Surface Reaction. *J. Phys. Chem. Lett.* **2014**, *5*, 1294–1299, DOI: 10.1021/jz500233n.

(33) Nattino, F.; Migliorini, D.; Bonfanti, M.; Kroes, G.-J. Methane Dissociation on Pt(111): Searching for a Specific Reaction Parameter Density Functional. *J. Chem. Phys.* **2016**, *144*, 044702, DOI: 10.1063/1.4939520.

(34) Hammer, B.; Hansen, L. B.; Nørskov, J. K. Improved Adsorption Energetics within Density-Functional Theory Using Revised Perdew-Burke-Ernzerhof Functionals. *Phys. Rev. B* **1999**, *59*, 7413–7421, DOI: 10.1103/PhysRevB.59.7413.

(35) Dion, M.; Rydberg, H.; Schröder, E.; Langreth, D. C.; Lundqvist, B. I. Van Der Waals Density Functional for General Geometries. *Phys. Rev. Lett.* **2004**, *92*, 246401, DOI: 10.1103/PhysRevLett.92.246401.

(36) Kresse, G.; Hafner, J. Ab Initio Molecular-Dynamics Simulation of the Liquid-Metal–Amorphous-Semiconductor Transition in Germanium. *Phys. Rev. B* **1994**, *49*, 14251–14269, DOI: 10.1103/PhysRevB.49.14251.

(37) Kresse, G.; Hafner, J. Ab Initio Molecular Dynamics for Liquid Metals. *Phys. Rev. B* **1993**, *47*, 558–561, DOI: 10.1103/PhysRevB.47.558.

(38) Kresse, G.; Furthmüller, J. Efficient Iterative Schemes for Ab Initio Total-Energy Calculations Using a Plane-Wave Basis Set. *Phys. Rev. B* **1996**, *54*, 11169–11186, DOI: 10.1103/PhysRevB.54.11169.

(39) Kresse, G.; Furthmüller, J. Efficiency of Ab-Initio Total Energy Calculations for Metals and Semiconductors Using a Plane-Wave Basis Set. *Comput. Mater. Sci.* **1996**, *6*, 15–50, DOI: 10.1016/0927-0256(96)00008-0.

(40) Kresse, G.; Joubert, D. From Ultrasoft Pseudopotentials to the Projector Augmented-Wave Method. *Phys. Rev. B* **1999**, *59*, 1758–1775, DOI: 10.1103/PhysRevB.59.1758.

(41) Blöchl, P. E. Projector Augmented-Wave Method. *Phys. Rev. B* **1994**, *50*, 17953–17979, DOI: 10.1103/PhysRevB.50.17953.

(42) Methfessel, M.; Paxton, A. T. High-Precision Sampling for Brillouin-Zone Integration in Metals. *Phys. Rev. B* **1989**, *40*, 3616–3621, DOI: 10.1103/PhysRevB.40.3616.

(43) Henkelman, G.; Jónsson, H. A Dimer Method for Finding Saddle Points on High Dimensional Potential Surfaces Using Only First Derivatives. *J. Chem. Phys.* **1999**, *111*, 7010–7022, DOI: 10.1063/1.480097.

(44) Heyden, A.; Bell, A. T.; Keil, F. J. Efficient Methods for Finding Transition States in Chemical Reactions: Comparison of Improved Dimer Method and Partitioned Rational Function Optimization Method. *J. Chem. Phys.* **2005**, *123*, 224101, DOI: 10.1063/1.2104507.

(45) Kästner, J.; Sherwood, P. Superlinearly Converging Dimer Method for Transition State Search. *J. Chem. Phys.* **2008**, *128*, 014106, DOI: 10.1063/1.2815812.

(46) Xiao, P.; Sheppard, D.; Rogal, J.; Henkelman, G. Solid-State Dimer Method for Calculating Solid-Solid Phase Transitions. *J. Chem. Phys.* **2014**, *140*, 174104, DOI: 10.1063/1.4873437.

(47) Transition State Tools Package for VASP https://theory.cm.utexas.edu/vtsttools/index.html (accessed 02/08/2021).

(48) Arblaster, J. W. Crystallographic Properties of Ruthenium. *Platin. Met. Rev.* **2013**, *57*, 127–136, DOI: 10.1595/147106713X665030.

(49) Mondal, A.; Wijzenbroek, M.; Bonfanti, M.; Díaz, C.; Kroes, G.-J. Thermal Lattice Expansion Effect on Reactive Scattering of $H_2$ from Cu(111) at $T_s$ = 925 K. *J. Phys. Chem. A* **2013**, *117*, 8770–8781, DOI: 10.1021/jp4042183.

(50) Migliorini, D.; Chadwick, H.; Nattino, F.; Gutiérrez-González, A.; Dombrowski, E.; High, E. A.; Guo, H.; Utz, A. L.; Jackson, B.; Beck, R. D.; Kroes, G.-J. Surface Reaction Barriometry: Methane Dissociation on Flat and Stepped Transition-Metal Surfaces. *J. Phys. Chem. Lett.* **2017**, *8*, 4177–4182, DOI: 10.1021/acs.jpclett.7b01905.

(51) Blöchl, P. E.; Jepsen, O.; Andersen, O. K. Improved Tetrahedron Method for Brillouin-Zone Integrations. *Phys. Rev. B* **1994**, *49*, 16223–16233, DOI: 10.1103/PhysRevB.49.16223.

(52) Mermin, N. D. Thermal Properties of the Inhomogeneous Electron Gas. *Phys. Rev.* **1965**, *137*, A1441–A1443, DOI: 10.1103/PhysRev.137.A1441.

(53) Benndorf, C.; Madey, T. E. Adsorption and Orientation of $NH_3$ on Ru(001). *Surf. Sci.* **1983**, *135*, 164–183, DOI: 10.1016/0039-6028(83)90217-0.

(54) Maier, S.; Stass, I.; Cerda, J. I.; Salmeron, M. Bonding of Ammonia and Its Dehydrogenated Fragments on Ru(0001). *J. Phys. Chem. C* **2012**, *116*, 25395–25400, DOI: 10.1021/jp308835x.

(55) Luntz, A. C.; Bethune, D. S. Activation of Methane Dissociation on a Pt(111) Surface. *J. Chem. Phys.* **1989**, *90*, 1274–1280, DOI: 10.1063/1.456132.

(56) Tiwari, A. K.; Nave, S.; Jackson, B. The Temperature Dependence of Methane Dissociation on Ni(111) and Pt(111): Mixed Quantum-Classical Studies of the Lattice Response. *J. Chem. Phys.* **2010**, *132*, 134702, DOI: 10.1063/1.3357415.

(57) King, D. A.; Wells, M. G. Reaction Mechanism in Chemisorption Kinetics: Nitrogen on the {100} Plane of Tungsten. *Proc. R. Soc. Lond. A* **1974**, *339*, 245–269, DOI: 10.1098/rspa.1974.0120.

(58) Gerrits, N.; Kroes, G.-J. Curious Mechanism of the Dissociative Chemisorption of Ammonia on Ru(0001). *J. Phys. Chem. C* **2019**, *123*, 28291–28300, DOI: 10.1021/acs.jpcc.9b09121.

(59) Jiang, B.; Guo, H. Dynamics of Water Dissociative Chemisorption on Ni(111): Effects of Impact Sites and Incident Angles. *Phys. Rev. Lett.* **2015**, *114*, 166101, DOI: 10.1103/PhysRevLett.114.166101.

(60) Zhang, Z.; Liu, T.; Fu, B.; Yang, X.; Zhang, D. H. First-Principles Quantum Dynamical Theory for the Dissociative Chemisorption of $H_2O$ on Rigid Cu(111). *Nat. Commun.* **2016**, *7*, 11953, DOI: 10.1038/ncomms11953.

(61) Shen, X.; Zhang, Z.; Zhang, D. H. Communication: Methane Dissociation on Ni(111) Surface: Importance of Azimuth and Surface Impact Site. *J. Chem. Phys.* **2016**, *144*, 101101, DOI: 10.1063/1.4943128.

(62) Goodman, F. O.; Wachman, H. Y. *Formula for Thermal Accommodation Coefficient*; 66-1; Cambridge, Massachusetts: M.I.T. Fluid Dynamics Research, 1966, DOI: 10.21236/ad0631007.

(63) Gerrits, N.; Chadwick, H.; Kroes, G.-J. Dynamical Study of the Dissociative Chemisorption of $CHD_3$ on Pd(111). *J. Phys. Chem. C* **2019**, *123*, 24013–24023, DOI: 10.1021/acs.jpcc.9b05757.

(64) Marcus, R. A. On the Analytical Mechanics of Chemical Reactions. Quantum Mechanics of Linear Collisions. *J. Chem. Phys.* **1966**, *45*, 4493–4499, DOI: 10.1063/1.1727528.

(65) McCullough, E. A.; Wyatt, R. E. Quantum Dynamics of the Collinear (H, $H_2$) Reaction. *J. Chem. Phys.* **1969**, *51*, 1253–1254, DOI: 10.1063/1.1672133.

(66) David, C. W. IR Vibration-Rotation Spectra of the Ammonia Molecule. *J. Chem. Educ.* **1996**, *73*, 46, DOI: 10.1021/ed073p46.

(67) Marquardt, R.; Sagui, K.; Zheng, J.; Thiel, W.; Luckhaus, D.; Yurchenko, S.; Mariotti, F.; Quack, M. Global Analytical Potential Energy Surface for the Electronic Ground State of $NH_3$ from High Level Ab Initio Calculations. *J. Phys. Chem. A* **2013**, *117*, 7502–7522, DOI: 10.1021/jp4016728.

(68) Halpern, A. M.; Ramachandran, B. R.; Glendening, E. D. The Inversion Potential of Ammonia: An Intrinsic Reaction Coordinate Calculation for Student Investigation. *J. Chem. Educ.* **2007**, *84*, 1067, DOI: 10.1021/ed084p1067.

(69) Bisson, R.; Sacchi, M.; Dang, T. T.; Yoder, B.; Maroni, P.; Beck, R. D. State-Resolved Reactivity of $CH_4(2\nu_3)$ on Pt(111) and Ni(111): Effects of Barrier Height and Transition State Location. *J. Phys. Chem. A* **2007**, *111*, 12679–12683, DOI: 10.1021/jp076082w.

(70) Ghassemi, E. N.; Somers, M. F.; Kroes, G.-J. Assessment of Two Problems of Specific Reaction Parameter Density Functional Theory: Sticking and Diffraction of $H_2$ on Pt(111). *J. Phys. Chem. C* **2019**, *123*, 10406–10418, DOI: 10.1021/acs.jpcc.9b00981.

# Chapter 7

# $CHD_3$ + Cu(111), Cu(211), and Single-Atom Cu(111) Alloys

This chapter is based on Gerrits, N.; Migliorini, D.; Kroes, G.-J. Dissociation of $CHD_3$ on Cu(111), Cu(211), and Single Atom Alloys of Cu(111). *J. Chem. Phys.* **2018**, *149*, 224701, DOI: 10.1063/1.5053990

## Abstract

In order to model accurately reactions of polyatomic molecules with metal surfaces important for heterogeneous catalysis in industry, the Specific Reaction Parameter (SRP) approach to density functional theory has been developed. This approach has been shown to describe the dissociation of $CHD_3$ on Ni(111), Pt(111), and Pt(211) with chemical accuracy. In this work, predictions have been made for the reaction of $CHD_3$ on Cu(111) and Cu(211) using barriers, elbow plots, and Born-Oppenheimer molecular dynamics. Hopefully, future experiments can prove the transferability of the SRP density functional to systems in which methane reacts with flat and stepped surfaces of adjacent groups of the periodic table, by comparison with the present predictions. Moreover, the effect of a so-called single atom alloy on the reactivity of methane is investigated by making predictions for $CHD_3$ on Pt–Cu(111) and Pd–Cu(111). It is found that the reactivity is only increased for Pt–Cu(111) near the alloyed atom, which is not only caused by the lowering of the barrier height but also by changes in the dynamical pathway and reduction of energy transfer from methane to the surface.

## 7.1 Introduction

For heterogeneous catalysis, one of the most important processes is steam reforming, where methane and steam react over a metal catalyst and form molecular CO and hydrogen. At high temperatures, the dissociation of methane is a rate controlling step on a wide variety of metals[1, 2], and thus warrants detailed study of the breaking of the CH bond on metal surfaces. Moreover, methane dissociation on copper is a much investigated method for creating high quality graphene[3–9]. However, due to the complexity of the interaction between metals and molecules and of describing both metals and molecules accurately, this reaction remains difficult for theoretical studies[10–14]. Recently, it has been shown that chemically accurate results can be obtained for molecule-metal surface reactions by using a so-called Specific Reaction Parameter (SRP) approach[15–17]. Furthermore, the recently developed SRP32-vdW density functional (DF) not only gives chemically accurate results for the reaction for which it is developed ($CHD_3$ + Ni(111)[16]), but it is also transferable to systems in which methane interacts with metals from the same group ($CHD_3$ + Pt(111)[17]) and with stepped surfaces of the same metal ($CHD_3$ + Pt(211)[17]). In this chapter predictive calculations are performed for the reaction of methane on surfaces of a metal belonging to a neighbouring group of the periodic table, in the hope that these predictive calculations will be followed by experiments that can test the transferability of the SRP32-vdW DF to methane interacting with a flat and stepped Cu surface, i.e., Cu(111) and Cu(211).

Moreover, a way to improve catalysts is to introduce alloys[18], which can be used to both increase reactivity and selectivity[19]. For example, methane dissociation is so highly activated on Pt and Ni that the methane will completely dehydrogenate and thus poison the catalyst[20–22]. However, by combining Pt or Ni with a less reactive metal like Cu, a highly active catalyst that does not poison itself can be produced[22]. In order to be able to clearly identify the effect of the different metals, so-called Single Atom Alloys (SAA) are investigated in this chapter, where a small portion (5%) of the top surface atoms is replaced with a different metal. These alloyed metal atoms do not cluster and thus can be viewed as single isolated atoms[23–25]. So far only a limited amount of information is available for the reaction of methane on alloys[22, 26–30]. As such, the SRP32-vdW DF will not only be used to make a prediction for Cu(111) and Cu(211), but it will also be applied to SAAs of Cu(111) that incorporate metals for which the DF either gives chemically accurate results (Pt), or is expected to do so (Pd).

In short, in this chapter a prediction is made for the reactivity of $CHD_3$

on Cu(111), Cu(211), Pd-Cu(111) and Pt-Cu(111). Furthermore, a detailed analysis of the dynamical behaviour is provided. This chapter is structured as follows: a short summary of the technical details is given in Section 7.2. The barriers are discussed in Section 7.3.1 followed by the minimum energy path in Section 7.3.2. In Section 7.3.3 the sticking probabilities are presented, while Section 7.3.4 concerns the impact site associated with reactive collisions. Finally, a short summary is given in Section 7.4.

## 7.2 Method

All the Born-Oppenheimer molecular dynamics (BOMD) and electronic structure (Density Functional Theory, DFT) calculations have been performed with the Vienna Ab-initio Simulation Package (VASP version 5.3.5)[31–35]. A kinetic energy cutoff of 350 eV and a Γ-centered $6 \times 6 \times 1$ $k$-point grid are used. Furthermore, core electrons have been represented with the projector augmented wave (PAW) method[35, 36], using an Ar core PAW pseudo-potential for Cu. The (111) surfaces are modeled using a 5 layer $(3 \times 3)$ supercell, while the (211) surface is modeled using a 4 layer $(1 \times 3)$ supercell. Furthermore, the vacuum distance between the slabs is 13 Å. In order to speed up convergence, first-order Methfessel-Paxton smearing[37] with a width parameter of 0.2 eV has been applied. Calculations have been performed without spin polarization, which is not required for a diamagnetic material as Cu. This computational setup is confirmed to yield results that are converged to within chemical accuracy (1 kcal/mol, or 4.2 kJ/mol), and results with respect to this convergence are given in Section 7.A.

For the alloys, a single surface layer atom in the supercell is replaced with a Pt or Pd atom, which is similar to what is observed in experiment[22, 24], and results in a coverage of $1/9^{\text{th}}$ of a monolayer. The alloyed atom is confirmed to remain at its position, i.e., it does not travel over the surface.

Transition states (TSs) are obtained with the dimer method[38–41] as implemented in the VASP Transition State Tools package (VTST)[42], with the forces on the molecule's atoms converged within 5 meV/Å. The TSs are confirmed to be first-order saddle points by doing a frequency analysis, i.e., by checking if only one imaginary frequency was found. An ideal slab is used, where the top three layers have been relaxed in the $Z$ direction.

For the BOMD simulations a surface temperature of 550 K is used, where the atoms in the top three layers are allowed to move in all three directions and the ideal lattice constant is expanded by a factor of 1.0078 in order to reflect the expansion of the bulk due to the surface temperature[43]. The

TABLE 7.1: Experimental beam parameters that describe the simulated $CHD_3$ velocity distributions. The stream velocity ($v_0$) and the width parameter ($\alpha$) are determined through time-of-flight measurements for the nozzle temperatures ($T_n$) of 750 and 900 K[16]. The parameters for $\langle E_i \rangle = 181.3$ kJ/mol are not from experiment, but theoretical estimates obtained by extrapolation.

| $T_n$ (K) | $\langle E_i \rangle$ (kJ/mol) | $v_0$ (m/s) | $\alpha$ (m/s) |
|---|---|---|---|
| 750 | 136.4 | 3760.72 | 216.91 |
| 900 | 160.4 | 4070.12 | 274.51 |
| 1050* | 181.3 | 4320.12 | 324.01 |

frequency $\omega$ employed in the 1D harmonic oscillator model for the simulation of surface atom motion (see Section 2.4.1 for this procedure) is in the range of $1.4 < \omega < 1.8$ kJ/mol. Ten differently-initialized slabs are generated using the aforementioned procedure, resulting in a pool of 10 000 snapshots. The average temperature of the pool of snapshots is $(541 \pm 60)$ K. For every BOMD data point, 1000 trajectories were run, unless noted otherwise, with a time step of 0.4 fs. The rest of the technical details for the BOMD calculations can be found in recent work[16, 17, 44] and in Chapter 2.

The initial translational energy of the molecules has been sampled from the experimental molecular beam parameters (stream velocity and width parameter), which are provided in Table 7.1. Experiments for $\langle E_i \rangle = 181.3$ kJ/mol were not readily available, so parameters were estimated. Moreover, the nozzle temperature is merely an estimate of what is needed to obtain a beam with the required translational energy distribution, but for the state population this is not an issue since at this energy BOMD was only done for $CHD_3$ in the single rovibrational state it would be excited to in a laser-on experiment. The residual energy $E_R$ (1.9 kJ/mol) is added to the kinetic energy in order to correct for the interaction with the periodic image and reduced plane wave cutoff energy, as is described in Sections 2.4.2 and 7.A. The laser-off beams are simulated by sampling the initial vibrational states of the molecule from a Boltzman distribution at $T_n$, while its initial angular momentum has been set to zero and the molecule's orientation is randomly sampled. The $\nu_1 = 1$ and $\nu_1 = 2$ beams are simulated by initializing all molecules with one or two quanta in the CH stretch mode, respectively. Moreover, the experimental R(1) transition to the rotational state $J = 2$ and $K = 0$ is simulated in the BOMD trajectories (see Section 2.4.2 for the simulation of the rotational states). The alignment in $M$ should be erased by hyperfine coupling due to the long pathway of the excited molecules in the experiments[12]. Therefore, $M$ has

been statistically sampled, i.e., $M = -2, -1, 0, 1, 2$ with equal probability.

The SRP32-vdW DF is employed, which was previously used for $CHD_3$ + Ni(111), Pt(111) and Pt(211)[16, 17], of which the exchange part is defined as

$$E_x = x \cdot E_x^{RPBE} + (1 - x) \cdot E_x^{PBE}, \tag{7.1}$$

where $E_x^{RPBE}$ and $E_x^{PBE}$ are the exchange parts of the RPBE and PBE[45, 46] exchange-correlation DFs, respectively, and $x = 0.32$. Moreover, the vdW correlation DF of Dion and coworkers (vdW-DF1)[47] is used. Earlier work has shown that using a Van der Waals correlation DF may be important to a correct description of the energy dependence of the reaction probability[48], signifying that the variation of the barrier height with molecular orientation and impact site is correctly described[48], and that this is also true for methane interacting with metals[16, 17, 49]. With the use of an appropriate correlation DF and an appropriate weighted average of exchange DFs, SRP-DFT has been shown capable of accurately describing the minimum barrier height, the anisotropy and corrugation of the barrier height, and the position of the barrier, which determines how efficiently pre-exciting stretch vibrations may enhance the reactivity (see Ref. [15] and the supporting information of Refs. [16] and [50]). Finally, $CHD_3$ is used instead of $CH_4$ in order to avoid artificial intramolecular vibrational energy redistribution (IVR) in the dynamics when the CH stretch mode is vibrationally excited[44, 51]. For arguments regarding the reliability of the quasi-classical trajectory (QCT) approach implicit in the BOMD, the reader is referred to the supporting information of Refs. [16] and [44]. There, the authors were able to argue that the QCT approach should not suffer much from problems like zero-point energy violation, and be accurate already for reaction of molecules in their ground vibrational state just above the reaction threshold, with reaction probabilities of the order of a percent. This was established on the basis of the quality of the comparison of QCT calculations with quantum dynamics calculations for $D_2$ + Cu(111)[52], as $D_2$ has a similar vibrational frequency and reduced mass as the CH stretch vibration in $CHD_3$, and of actual BOMD calculations for $CHD_3$ + Pt(111) which showed that the reaction near the threshold only involved zero-point energy violation in only 1 out of 144 reactive trajectories[44].

TABLE 7.2: Barrier geometries for $CHD_3$ + Cu(100), Cu(111), Cu(211), Pt-Cu(111), Pd-Cu(111), Pd(111), Ni(111) and Pt(111). The naming convention from Ref. [53] is used for the (100) and (111) surfaces. Geometry names for Cu(211) indicate first the location of the methane and then the direction of the dissociating H atom. The height of the C atom on Cu(211) is taken with respect to the top step edge (EtoE and E/BtoB geometries) or to the middle of the (111) terrace (TtoB geometry). For $\theta$, $\beta$ and $\gamma$ on Cu(211), the surface normal is taken as the macroscopic surface normal. The zero-point energy corrected barriers are given in the brackets. The calculations are performed with the SRP-vdW-DF1 DF, unless indicated otherwise.

| Surface | Site | $Z_C$ (Å) | $r$ (Å) | $\theta$ (°) | $\beta$ (°) | $\gamma$ (°) | $E_b$ (kJ/mol) |
|---|---|---|---|---|---|---|---|
| Cu(100) | G2 geometry | 2.19 | 1.84 | 129.4 | 165.3 | 35.9 | 166.1 (152.1) |
| Cu(111) | C2 geometry | 2.25 | 1.79 | 136.4 | 169.4 | 33.0 | 166.6 (151.8) |
| Cu(111) | C2 geometry (550 K) | 2.25 | 1.80 | 136.6 | 168.4 | 31.9 | 167.9 (153.4) |
| Cu(111) | C2 geometry (PBE-vdW) | 2.24 | 1.77 | 136.3 | 168.3 | 32.0 | 157.2 (143.1) |
| Cu(111) | C2 geometry (optB86b-vdW) | 2.19 | 1.74 | 134.1 | 167.5 | 33.4 | 136.2 (122.4) |
| Cu(111) | C2 geometry (optB86b-vdW)[22] | - | - | - | - | - | 129.3 |
| Cu(111) | C2 geometry (SRP32-DF2) | 2.28 | 1.79 | 137.1 | 168.8 | 31.7 | 182.3 (167.8) |
| Cu(111) | Fcc | 2.25 | 1.80 | 133.4 | 162.5 | 29.2 | 187.4 (171.7) |
| Cu(111) | Bridge | 2.26 | 1.84 | 129.8 | 160.8 | 31.0 | 193.9 (178.2) |
| Cu(211) | EtoE geometry | 2.08 | 1.86 | 125.1 | 157.4 | 34.4 | 137.8 (128.4) |
| Cu(211) | E/BtoB geometry | 1.90 | 1.81 | 158.3 | 168.3 | 33.4 | 152.9 (138.8) |
| Cu(211) | TtoB geometry | 1.39 | 1.81 | 143.1 | 163.2 | 33.3 | 174.3 (159.8) |
| Pt-Cu(111) | Atop Pt | 2.36 | 1.66 | 133.2 | 165.3 | 32.1 | 134.1 (121.8) |
| Pt-Cu(111) | Atop Pt (PBE-vdW) | 2.35 | 1.65 | 132.7 | 164.9 | 32.2 | 124.8 (112.6) |
| Pt-Cu(111) | Atop Pt (optB86b-vdW) | 2.32 | 1.62 | 131.4 | 164.2 | 32.9 | 100.3 (88.1) |
| Pt-Cu(111) | Atop Pt (optB86b-vdW)[22] | - | - | - | - | - | 84.9 |
| Pt-Cu(111) | Nearest neighbour | 2.26 | 1.83 | 137.5 | 170.3 | 32.8 | 173.4 (159.2) |
| Pt-Cu(111) | Next nearest neighbour | 2.26 | 1.80 | 136.3 | 168.7 | 32.5 | 165.7 (151.8) |
| Pt-Cu(111) | Next nearest neighbour (PBE-vdW) | 2.21 | 1.79 | 135.7 | 168.2 | 32.5 | 156.4 (143.3) |
| Pt-Cu(111) | Next nearest neighbour (optB86b-vdW) | 2.16 | 1.76 | 133.4 | 167.4 | 34.0 | 135.6 (122.4) |
| Pd-Cu(111) | Atop Pd | 2.32 | 1.76 | 136.9 | 167.9 | 32.0 | 142.5 (129.2) |
| Pd-Cu(111) | Nearest neighbour | 2.26 | 1.81 | 136.7 | 169.0 | 32.4 | 172.3 (158.0) |
| Pd-Cu(111) | Next nearest neighbour | 2.25 | 1.80 | 136.2 | 168.7 | 32.5 | 167.6 (153.5) |
| Ni(111) | C2 geometry[16] | 2.18 | 1.61 | 135.7 | 164.7 | 29.1 | 97.9 (85.3) |
| Pd(111) | A2 geometry | 2.23 | 1.61 | 135.9 | 165.0 | 29.1 | 84.6 (70.7) |
| Pt(111) | D1 geometry[17] | 2.28 | 1.56 | 133 | 168 | 35 | 78.7 (66.5) |
| Pt(111) | D1 geometry (PBE-vdW)[49] | 2.29 | 1.54 | 133.9 | 168.4 | - | 73.9 (61.7) |

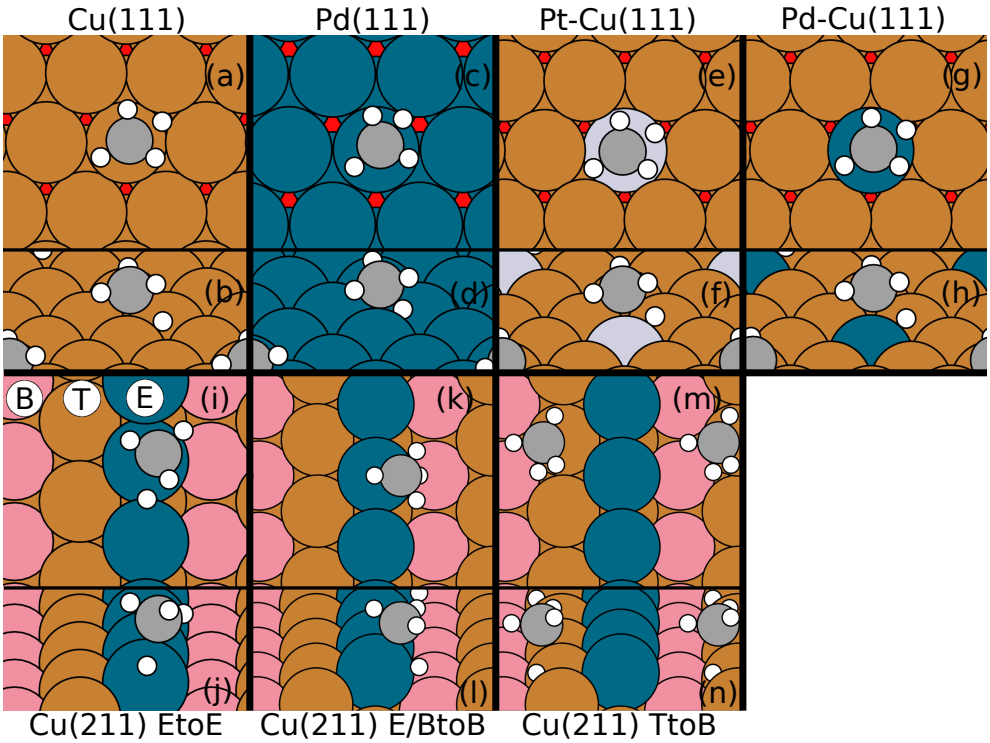


FIGURE 7.1: Top and side view of the TS of methane on Cu(111) with the C2 geometry (a,b); Pd(111) with the A2 geometry (c,d); on Pt-Cu(111) (e,f) and Pd-Cu(111) (g,h) with the C2 geometry; and on Cu(211) with the EtoE (i,j), E/BtoT (k,l), and TtoT (m,n) geometries. For the (111) surfaces, red indicates the fcc sites. For Cu(211), pink indicates the bottom step edge atoms (B), orange the terrace atoms (T), and blue the top step edge atoms (E).

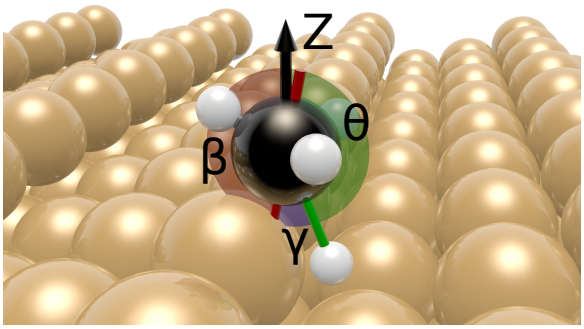


FIGURE 7.2: Methane on Cu(211) with the E/BtoB geometry, indicating the geometry angles as used in Table 7.2. $\theta$ is the angle between the dissociating CH-bond and the surface normal, $\beta$ is the angle between the umbrella axis and the surface normal, and $\gamma$ is the angle between $\theta$ and $\beta$.

## 7.3 Results

### 7.3.1 Activation Barriers and Adsorption Energies

The TS geometries for the dissociation of methane on several surfaces are summarized in Table 7.2 and in Figure 7.1, where the naming convention from Ref. [53] is used for the TSs on the (100) and (111) surfaces. Figure 7.2 depicts the angles that are used to characterize the TSs. $\theta$ is the angle between the surface normal and the dissociating CH bond and $\beta$ is the angle between the surface normal and the umbrella axis, which is defined as the vector going from the geometric center of the three H-atoms to the carbon atom. Finally, $\gamma$ is the angle between the dissociating CH bond and the umbrella axis.

The TS geometry on Cu(111) is similar to Ni(111) and Pt(111), except the CH-bond and umbrella axis of the methane have a slightly smaller tilt with respect to the surface normal (i.e., $\theta$ and $\beta$ are larger) and the bond distance ($r^{\ddagger}$) of the dissociating hydrogen is much larger; i.e., the location of the barrier is later compared to Ni(111) and Pt(111). Moreover, the barrier height is 166.6 kJ/mol, which is 68.7 kJ/mol higher than for Ni(111). Since the barrier on Cu(111) is later and higher than on Ni(111) and Pt(111), less reactivity is expected. The barrier geometry does not change considerably when PBE-vdW is used instead of SRP32-vdW, but the barrier height is 9.4 kJ/mol lower. This is to be expected since PBE is less repulsive than a mixture of PBE and RPBE[15]. Likewise, the barrier height increases only with 1.3 kJ/mol when the expanded lattice constant for 550 K is used, and the barrier geometry does not change considerably. Again, using vdW-DF2[54] instead of vdW-DF1 has little effect on the geometry, although it does increase the barrier height by 15.7 kJ/mol. However, using optB86b-vdW[55] does not only lower the barrier by 30.2 kJ/mol, it also makes the methane tilt more with respect to the surface and shortens the length of the dissociating bond, making the barrier slightly earlier. The barrier height with optB86b-vdW is in good agreement with previous work[22], being 6 kJ/mol higher when the barrier is adjusted for an adsorption well of 13 kJ/mol (the barriers in previous work were reported with respect to the physisorbed state).

The barriers on the fcc and bridge sites are found by fixing the $X$ and $Y$ coordinates of the carbon atom at these sites. While these barriers are second order saddle points, they do provide additional insight on the reactivity across the surface. The CH-bond length is longer and the methane is tilted more compared to the top site, and the barrier height is 20.8 and 27.3 kJ/mol higher for the fcc and bridge site, respectively. The barrier height on Cu(100) is similar to the barrier height on Cu(111), which has been observed previously[5].

TABLE 7.3: Adsorption energy of $CH_3$ on Cu(111). The naming convention for the geometries is from Ref. [53].

| Site | $Z_C$ (Å) | Adsorption energy (kJ/mol) |
|---|---|---|
| Bridge2 | 0.48 | -154.8 |
| Bridge3 | 0.48 | -154.1 |
| Fcc1 | 0.48 | -154.1 |
| Fcc2 | 0.48 | -140.6 |
| Hcp1 | 0.48 | -154.8 |
| Hcp2 | 0.48 | -141.6 |
| Top1 | 0.49 | -150.3 |
| Top2 | 0.49 | -150.4 |
| Top3 | 0.49 | -150.5 |

TABLE 7.4: Adsorption energy of H on Cu(111).

| Site | $Z_H$ (Å) | Adsorption energy (kJ/mol) |
|---|---|---|
| Bridge | 0.44 | -234.5 |
| Fcc | 0.44 | -245.3 |
| Hcp | 0.44 | -244.9 |
| Top | 0.47 | -196.4 |

Furthermore, the methane molecule has a larger tilt and is closer to the Cu(100) surface, while the barrier is slightly later. These differences between the (100) and (111) surfaces are observed for Ni as well[56], except that the barrier height is 15 kJ/mol lower on Ni(100) than on Ni(111).

Tables 7.3 and 7.4 show the adsorption energies for $CH_3$ and H on Cu(111), with the naming convention for the adsorption geometries from Ref. [53]. For the adsorption energies, calculations were done with spin polarization. Methyl adsorbs stronger on the hollow and bridge sites than on the top site. Moreover, the adsorption is stronger when the hydrogen atoms are oriented towards the top sites, than towards the hollow sites. Finally, the hollow sites are the most favorable adsorption site for hydrogen, followed by the bridge and top sites. These results are in agreement with earlier theoretical results[5].

For Cu(211), three distinctly different barriers are found: above the top step edge atom, between the top and bottom step edge, and on the terrace, which are referred to as the EtoE, E/BtoB and TtoB geometries, respectively. In

general, the length of the dissociating CH bond is larger than on Cu(111), i.e., the barriers for Cu(211) are even later than for Cu(111). Furthermore, the barrier on the terrace (TtoB geometry) is 7.7 kJ/mol higher than on Cu(111), while the barriers at the step (EtoE and E/BtoB geometries) are 28.8 and 13.7 kJ/mol lower, respectively. Finally, for the EtoE geometry the hydrogen dissociates towards the bridge site, which is at odds with the other TS geometries obtained on Cu(211) for which the hydrogen atom moves towards a hollow site.

For alloys, above the next nearest neighbour Cu atom, almost no changes are observed compared to Cu(111). The nearest neighbour Cu atom shows an almost identical barrier geometry, but above these Cu atoms the barrier heights for Pt-Cu(111) and Pd-Cu(111) are 7 and 6 kJ/mol higher than on Cu(111), respectively. However, above the alloyed top atoms the barrier changes considerably. The barrier above Pt is further away from the surface and the dissociating CH bond distance is smaller than for Cu(111), although the barrier is later than on Pt(111). Moreover, the barrier height is reduced with 32.7 kJ/mol relative to Cu(111), although the barrier is much higher than on Pt(111). When using another DF like PBE-vdW, these changes to the barrier are very similar, suggesting that mixing PBE with RPBE only affects the minimum barrier height and not other physics like the energetic corrugation of the barrier height. This finding is in agreement with a similar finding in quantum Monte Carlo and DFT calculations on $H_2$ + Al(110)[57]. Previous work[22] using the optB86b-vdW DF reported a much larger reduction of 44 kJ/mol relative to Cu(111), whereas here a reduction of 35.7 kJ/mol is found when using the optB86b-vdW DF. However, the barrier heights previously reported[22] were incorrect and the corrected results are available in Ref. [58]. The geometry found previously[22] is slightly different, but can only explain a small part of the difference (about 2 kJ/mol) between previous results and results in this work. Most of the difference is caused by the relaxation of the surface atoms during the dimer calculation in Ref. [22] due to the considerable resulting protrusion of the Pt atom. Furthermore, using a different XC-DF (optB86b-vdW[55]) results in smaller lattice constants for solids[59]. This could mean that due to different lattice constants caused by the different DFs, a different strain in the lattice of a SAA is observed, resulting in a different barrier height for the alloy.

Marcinkowski et al.[22] introduced the parameter

$$\alpha = \frac{E_b^{\text{Cu(111)}} - E_b^{\text{Pt-Cu(111) (atop Pt)}}}{E_b^{\text{Cu(111)}} - E_b^{\text{Pt(111)}}}, \tag{7.2}$$

where $\alpha = 0$ and $\alpha = 1$ indicate a barrier height equal to Cu(111) and Pt(111),

respectively. The lower barrier found previously[22] gives $\alpha_{\text{optB86b-vdW}} = 0.52$, i.e., the barrier is almost halfway between a Pt(111)-like and Cu(111)-like barrier, whereas the higher barrier found in this work with the SRP32-vdW DF is closest to Cu(111), i.e., $\alpha_{\text{SRP32-vdW}} = 0.37$. Moreover, PBE-vdW also results in a more Cu(111)-like barrier with $\alpha_{\text{PBE-vdW}} = 0.39$. Although additional work is needed, it seems that by allowing the Pt atom to pucker out, the barrier becomes more Pt-like for Pt-Cu(111).

Finally, it is checked that relaxing the top layer also in the $X$ and $Y$ directions does not have a large influence on the barrier height. When the top layer is also relaxed in the $X$ and $Y$ directions before the dimer calculation (but note that the top layer is kept fixed during the TS search), above Pt the barrier height is further reduced by 3.4 kJ/mol and above the next nearest neighbour Cu the barrier height is increased by 1.2 kJ/mol. It is expected that similarly small effects will occur for the case of Pd-Cu(111).

Above the alloyed Pd top atom in Pd-Cu(111) the barrier height is reduced by 24.1 kJ/mol and the changes for the geometry relative to Cu(111) are similar as for the Pt alloy, but smaller. This is to be expected, since the barrier height on Pd(111) is also higher and later than on Pt(111). Likewise, Pd-Cu(111) has a barrier height that is even more similar to a Cu(111)-like barrier height since $\alpha = 0.29$, which is also reflected by the fact that the barrier geometry above Pd is more similar to that found on Cu(111) than what is observed above Pt.

### 7.3.2 Minimum Energy Path

Figure 7.3a shows the minimum energy path (MEP) of methane dissociating above the top site on Cu(111). Methane is fixed in its TS geometry, while varying the length of the dissociating CH bond and distance from the surface. Since methane has 15 degrees of freedom, the potential along the MEP will increasingly differ from the true MEP in which other coordinates also vary, when moving away from the TS. However, points from a nudged elastic band[60] (NEB) calculation, where all degrees of freedom are relaxed, in Figure 7.3a are in excellent agreement with the MEP, and this is assumed to be also the case for other surfaces. As already stated above, the barrier is late and high on Cu(111). Moreover, the MEP does not have a smooth curvature, but makes almost a right angle in the elbow plot. Hence, incoming molecules may not be able to follow the MEP due to the requirement of a high kinetic energy to overcome the barrier combined with the sharp turn of the MEP, and thus may have to react over much higher barriers ("*the bobsled effect*"[61, 62]). This can also be seen in Figure 7.3c, where the reacted trajectories at $\langle E_i \rangle = 181.3$ kJ/mol for $\nu_1 = 1$ are superimposed on the elbow plot. Even

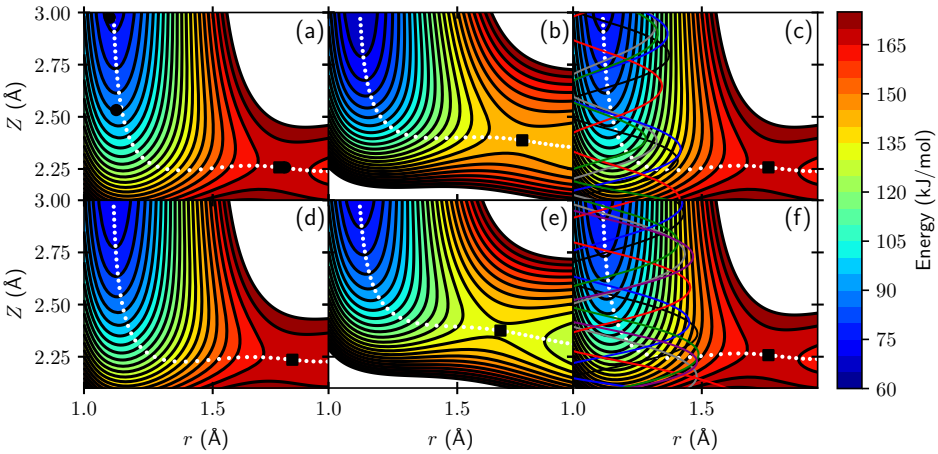


FIGURE 7.3: Elbow plot of methane on Cu(111) (a), above Pd in Pd-Cu(111) (b), above the next nearest neighbour Cu in Pt-Cu(111) (d), and above Pt in Pt-Cu(111) (e). (c) and (f) are the same as (a), but with reacted trajectories for $\langle E_i \rangle = 181.3$ kJ/mol and $\nu_1 = 1$ (c) and $\nu_1 = 2$ (f). Methane is fixed in its TS geometry above the top site, whereas Z and the distance of the dissociating CH-bond are variable. Contour lines are drawn at intervals of 5 kJ/mol between 60 and 180 kJ/mol. The colours indicate the energy (kJ/mol) with respect to methane in the gas phase. The white circles indicate the MEP. The black circles in panel (a) indicate points from a NEB calculation, while the black squares indicate the highest point along the MEP.

when the vibrational energy is increased to $\nu_1 = 2$ the trajectories are not able to follow the MEP in Figure 7.3f. Nevertheless, the trajectories do approach the minimum TS more closely when the vibrational energy is increased (see Chapter 8), but this effect is not visible in Figures 7.3c,f. Furthermore, in Figure 7.4 the top site TS geometry is taken and used to plot the PES for methane above the fcc site resulting in a similar elbow plot, although the MEP is more strongly curved. The barrier obtained from this elbow plot is 185.9 kJ/mol, which is only 1.5 kJ/mol lower than the barrier obtained using a constrained dimer search. This suggests that the barrier geometry is almost independent of the reaction site. Additionally, the change in energy when moving away from the TS at the top site is similar to the change found at the fcc site, i.e., the corrugation around the barrier geometry is again almost independent of the reaction site.

Similarly, Figure 7.3b shows the MEP of methane dissociating above the Pd atom in Pd-Cu(111). Here, the MEP is further away from the surface and through a lower barrier than for Cu(111). However, the MEP above the Pt

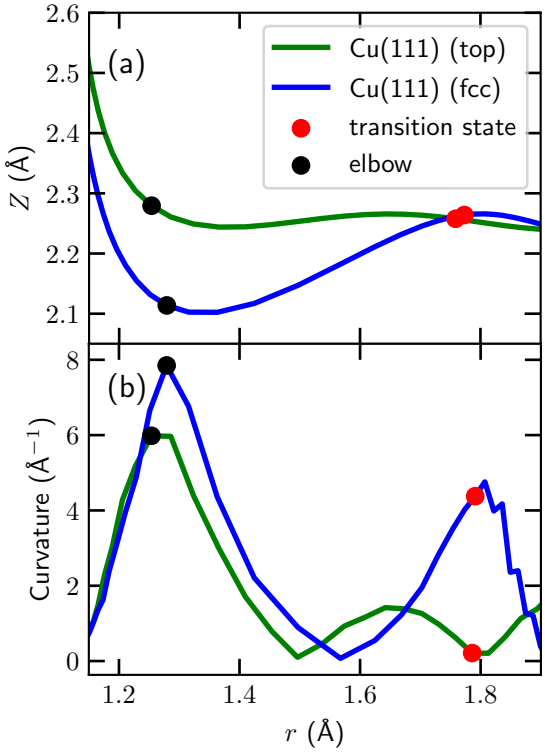


FIGURE 7.4: (a) The MEP from Figure 7.3a (green) and above the fcc site on Cu(111) (blue). The fcc PES and concomitant MEP is obtained by placing the top site TS geometry above the fcc site. (b) Curvature from the aforementioned MEPs. The red points indicate the TS, while the black squares indicate the point on the MEP with the largest curvature.

atom in Pt-Cu(111) in Figure 7.3e shows larger differences than above Pd relative to Cu(111), which could be caused by the fact that the barrier above Pd is more similar to Cu(111) than above Pt. Above Pt the barrier is lower and earlier and the MEP has a smoother curvature. Furthermore, the MEP for Pt-Cu(111) has a similar curvature, although at a higher distance to the surface, as the MEP for Pt(111) does, while the barrier is later and higher. Above the next nearest Cu atom for both alloys a similar MEP was obtained as for Cu(111), as can be seen in Figure 7.3e for Pt-Cu(111). Summarizing, the MEPs above the Pt and Pd atoms in the alloys exhibit similar, but not identical features as the MEPs for Pt(111) and Pd(111). Above the Cu atoms in the alloys the MEPs are similar to the MEP for Cu(111).

The MEP of methane above the step edge of Cu(211) in Figure 7.5a is similar to that for Cu(111) in Figure 7.3a, although closer to the surface. Moreover, the barrier is lower, but later. Figure 7.5c shows the same elbow plot, but here the $\theta$ coordinate is also optimized. The turn the MEP makes for the optimized $\theta$ is slightly smoother early on, but as soon as the bond starts extending the

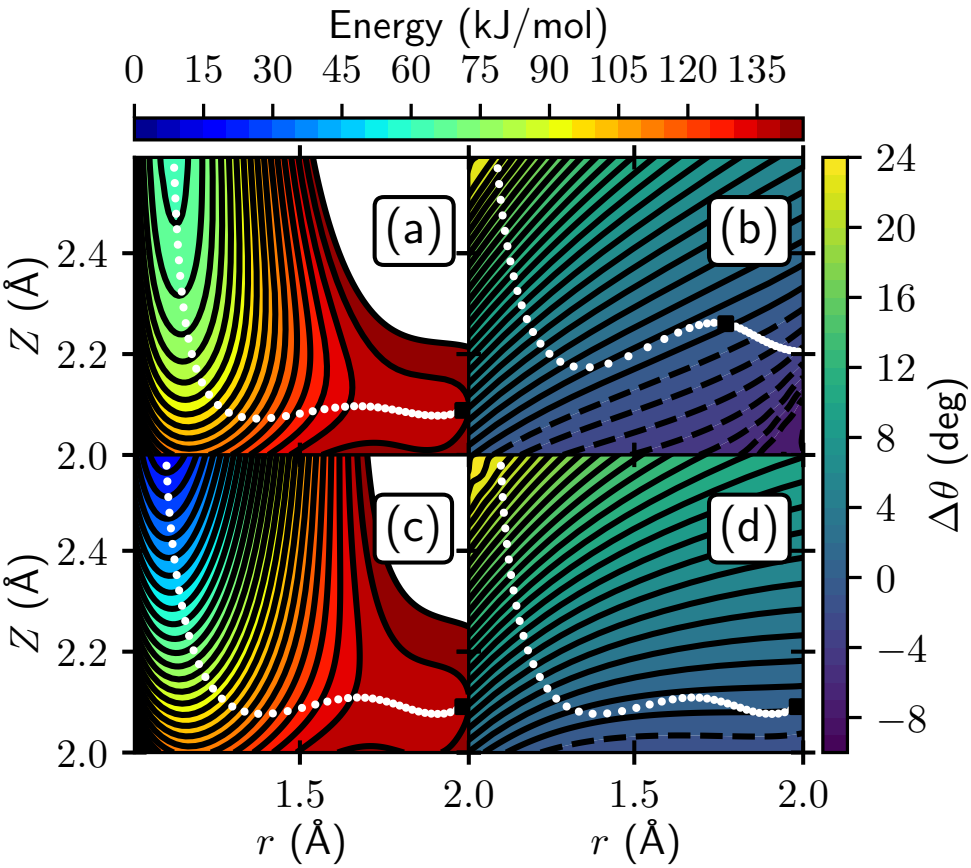


FIGURE 7.5: Same as figure 7.3, but for Cu(211) with the EtoE geometry (a) and with the $\theta$ angle optimized (c). (b) and (d) show the MEP for Cu(111) and Cu(211), where $\theta$ is optimized. The contour lines in (a) and (c) are drawn at intervals of 5 kJ/mol between 0 and 150 kJ/mol and indicate the energy (kJ/mol) with respect to methane in the gas phase. The colours in (b) and (d) indicate the difference in angle with respect to the TS, and contour lines are drawn at intervals of 0.5 degrees between -10 and 24 degrees. The black squares indicate the highest point along the MEP.

curvature actually increases compared to the case where $\theta$ is kept fixed, i.e., from the curvature point of view the MEP becomes dynamically less favorable compared to the MEP for which $\theta$ is not optimized. The difference in $\theta$ with respect to the TS for which the energy is minimized is shown in Figures 7.5b and 7.5d. If the molecule would follow the MEP, it would undergo a rapid reorientation of the CH-bond when it approaches the surface before it is able to extend the CH bond. The bending along the MEP for Cu(211) is similar as for Cu(111).

### 7.3.3 Sticking Probability

In Table 7.5 results are summarized for BOMD on several surfaces. At incidence energies close to the minimum barrier height, methane has a much lower sticking probability on Cu(111) than on Ni(111). At $\langle E_i \rangle = 160\,\mathrm{kJ/mol}$ and $\nu_1 = 1$ no reaction is observed on Cu(111), and with $\nu_1 = 2$ a reaction probability of only 2.4% is obtained. At higher incidence energy some reaction is observed, but only for vibrationally excited molecules, which also explains why only CH cleavage is observed and no CD cleavage.

Surprisingly, on Cu(211) a similar reaction probability is obtained as for Cu(111). This could imply that the lower barriers found around the step edge on Cu(211) are dynamically inaccessible. However, CD cleavage is observed, which could indicate that methane found a lower barrier to dissociate over on Cu(211) than on Cu(111) since no CD cleavage was found at Cu(111) for the same or even higher energy, although it remains unclear whether this is a statistical anomaly. It is more probable that an increase in reactivity due to the steps combined with a reduction in reactivity due to the terraces, leads to a similar reactivity for Cu(211) as Cu(111).

On Pd-Cu(111) the reaction probability is low for $\langle E_i \rangle = 160\,\mathrm{kJ/mol}$ and $\nu_1 = 1$, i.e., only $0.1\% \pm 0.1$. Apparently, the lowering of the barrier atop the Pd atom is not large enough to enable the reaction of methane for 160 kJ/mol and $\nu_1 = 1$. In contrast, on Pt-Cu(111) a higher reaction probability is observed. Interestingly, the barrier atop the Pt atom on Pt-Cu(111) is only 8 kJ/mol lower than atop Pd on Pd-Cu(111), and it is not clear whether this can fully account for the increased reaction probability at $\langle E_i \rangle = 160\,\mathrm{kJ/mol}$ and for $\nu_1 = 1$. It is possible that since the barrier on Pt is earlier and the MEP in the entrance channel is less curved than on Pd, the reaction is also dynamically more favorable on the Pt doped surface than on the Pd doped surface due to a smaller bobsled effect[61, 62]. Moreover, it was found that the energy transfer from scattered methane to the surface atoms of Pt-Cu(111) and Pd-Cu(111) surface is about 10 kJ/mol lower than to the Cu(111) surface

TABLE 7.5: Sticking probabilities obtained with BOMD for Cu(111), Cu(211), Pd-Cu(111), Pt-Cu(111) and Ni(111). For Cu(111) and Cu(211) at 160 kJ/mol and $\nu_1 =$ 1, 500 and 692 trajectories were done, respectively. The error bars represent 68% confidence intervals.

| Surface | $\langle E_i \rangle$ (kJ/mol) | Quantum states | Reaction probability (%) | Fraction CH cleavage |
|---|---|---|---|---|
| Cu(111) | 160.4 | $\nu_1 = 1$ | $0.0 \pm 0.2$ | - |
| Cu(111) | 160.4 | $\nu_1 = 2$ | $2.4 \pm 0.5$ | $1.00 \pm 0.05$ |
| Cu(111) | 181.3 | $\nu_1 = 1$ | $0.5 \pm 0.2$ | $1.00 \pm 0.20$ |
| Cu(111) | 181.3 | $\nu_1 = 2$ | $4.8 \pm 0.7$ | $1.00 \pm 0.02$ |
| Cu(211) | 160.4 | $\nu_1 = 1$ | $0.1 \pm 0.1$ | $0.00 \pm 0.32$ |
| Cu(211) | 181.3 | $\nu_1 = 1$ | $0.4 \pm 0.2$ | $0.75 \pm 0.22$ |
| Pd-Cu(111) | 160.4 | $\nu_1 = 1$ | $0.1 \pm 0.1$ | $1.00 \pm 0.32$ |
| Pt-Cu(111) | 160.4 | Laser-off | $0.6 \pm 0.2$ | $0.00 \pm 0.17$ |
| Pt-Cu(111) | 160.4 | $\nu_1 = 1$ | $1.4 \pm 0.4$ | $0.71 \pm 0.12$ |
| Ni(111)[16] | 160.4 | Laser-off | $28 \pm 2.0$ | $0.24 \pm 0.05$ |
| Ni(111)[16] | 160.4 | $\nu_1 = 1$ | $41 \pm 2.2$ | $0.53 \pm 0.03$ |

TABLE 7.6: Energy transfer (kJ/mol) of scattered methane to Cu(111), Pd-Cu(111), Pt-Cu(111) and Pt(111) at $\langle E_i \rangle = 160$ kJ/mol. The results for Pt(111) are extrapolated from earlier work[17]. The error bars represent 68% confidence intervals.

| Surface | Energy transfer | Refined Baule model |
|---|---|---|
| Cu(111) | $62 \pm 1$ | 68 |
| Pd-Cu(111) | $53 \pm 1$ | 66 |
| Pt-Cu(111) | $52 \pm 1$ | 64 |
| Pt(111)[17] | $28 \pm 1$ | 24 |

at equal incidence energy ($\langle E_i \rangle = 160$ kJ/mol) (see Table 7.6). It is possible that due to the additional lattice strain caused by the alloyed atoms, energy transfer from methane to the surface via phonon excitations is less efficient. This is also supported by the fact that the partial phonon densities of states of the Pt and nearest neighbour Cu top layer atoms in Pt-Cu(111) are found at higher energies than in Cu(111), which is shown in Section 7.C. Furthermore, it is likely that the difference in energy transfer is partially caused by the difference in mass between the Cu atoms and the alloyed atoms, as one would expect in the Baule model[63, 64] (see Section 2.5). A modified Baule model, which weights energy loss to the Pt or Pd atom in the surface layer according to its fractional coverage in the SAA, yields good agreement with the BOMD results for energy transfer to the surface atoms (Table 7.6).

In most cases, exciting the $\nu_1$ vibrational mode leads to more CH-cleavage than CD cleavage (see Table 7.5). However, it remains difficult to draw conclusions on the fraction of CH cleavage due to the limited amount of reacted trajectories. Furthermore, Figure 7.6 shows distributions of the $\theta$, $\beta$ and $\gamma$ angles of methane on Cu(111) and Pt-Cu(111) at the highest collision energies, noting that the initial conditions are similar for the two surfaces, except that methane has a higher kinetic energy and vibrational excitation on Cu(111) than on Pt-Cu(111). Here it can be seen that the angular distributions of the reacting methane are similar on both surfaces and that there is little steering in the $\theta$ and $\beta$ angles, but there is quite some steering in the bend angle $\gamma$ in order to follow the MEP. Moreover, it is to be expected on the basis of the elbow plots that the vibrational efficacy is high. Unfortunately, due to the limited amount of reactivity typically only vibrationally excited molecules react, i.e., vibrational energy promotes the reaction but it is unclear by how much, as laser-off reaction is hardly seen. Therefore, it is not possible not compute vibrational efficacies for the BOMD data computed here. Finally, no trapping is observed, which is to be expected considering the high kinetic

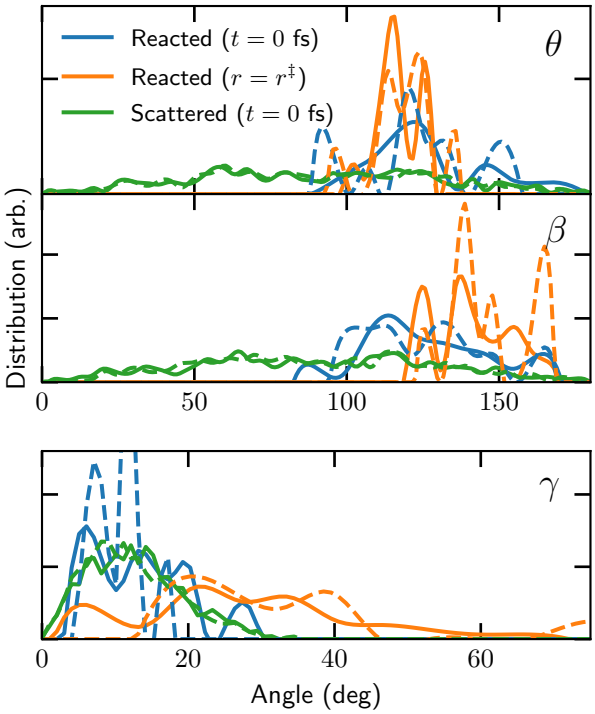


FIGURE 7.6: Distributions of the $\theta$, $\beta$ and $\gamma$ angles of methane during BOMD for scattered (green) and reacted trajectories at the initial time step (blue) and when a dissociating bond reaches the TS value (orange). Solid lines are for Cu(111) ($\langle E_i \rangle = 181$ kJ/mol and $\nu_1 = 2$) and dashed lines are for Pt-Cu(111) ($E_i = 160$ kJ/mol and $\nu_1 = 1$).

energy methane has in the performed simulations.

### 7.3.4 Reaction Site

Figures 7.7a,c show the reaction site of methane on Cu(111) for $\nu_1 = 1$ and $\nu_1 = 2$, respectively, with $\langle E_i \rangle = 181$ kJ/mol. Methane does not have a clear preference of reaction site on Cu(111), since the distribution appears to be statistical. It is likely that since the barrier above the hollow sites is only 21 kJ/mol higher than above the top site, and methane has a high energy due to both the translational and the vibrational energy, dynamically there is no preference of reaction site. Also, no significant steering in $X$ and $Y$ is observed for either scattered or reacted trajectories.

On Cu(211) methane reacts only at the step, as can be seen in Figure 7.8. Furthermore, during the dissociation the methyl moves towards the bottom step edge, while the dissociating hydrogen moves towards the terrace, with the dissociating bond located above the top step edge atom. This can also be seen from the fact that the center of mass moves from the top step edge

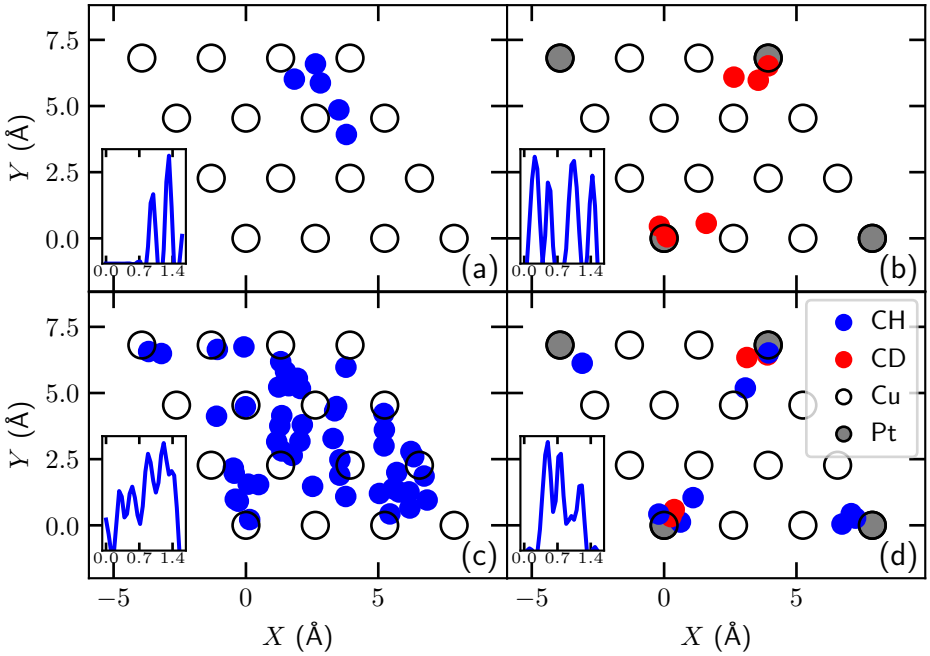


FIGURE 7.7: The impact site of reacting methane on Cu(111) for $\nu_1 = 1$ (a) and $\nu_1 = 2$ (c), with $\langle E_i \rangle = 181$ kJ/mol, and on Pt-Cu(111) for laser-off (b) and laser-on ($\nu_1 = 1$) (d), with $\langle E_i \rangle = 160$ kJ/mol. The grey circles indicate Pt atoms, while the black open circles indicate the Cu top layer surface atoms. The blue (CH cleavage) and red (CD cleavage) circles are the impact sites when dissociation takes place, i.e., when $r = r^{\ddagger}$. The distribution of distance (Å) of the reacting $CHD_3$ to the closest top site (either a Cu or Pt top layer atom) is given in the inset.

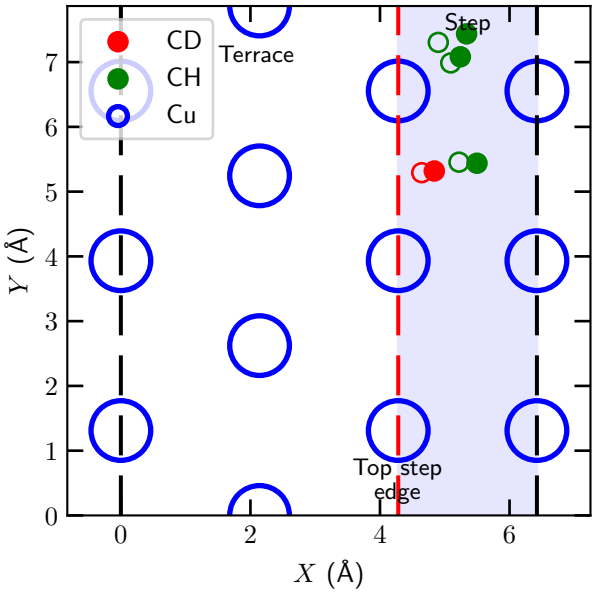


FIGURE 7.8: The impact site of reacting methane on Cu(211) for $\langle E_i \rangle = 181\,\mathrm{kJ/mol}$ and $v_1 = 1$. The blue shaded area indicates the step, while the red dashed line is the top step edge. The blue circles are the top layer surface atoms, and the green and red circles are the impact sites where dissociation of a CH (green) or CD (red) bond occurred. The empty green and red circles indicate the location of methane at $t = 0\,\mathrm{fs}$, while the solid circles are for when dissociation takes place, i.e., when $r = r^{\ddagger}$.

towards the bottom step edge, i.e., there is some steering. Interestingly, for none of the reactive events the center of mass is above the top step edge atom, which is the location of the lowest barrier, nor does the dissociation take place with the hydrogen atom moving towards the bottom step edge, in which case the dissociation would have to proceed over another barrier. Due to the limited amount of reacted trajectories it remains unclear whether this is a statistical anomaly or whether the aforementioned barriers are dynamically inaccessible, for instance due to the late barrier geometry.

On Pt-Cu(111), for both laser-off and laser-on conditions, reaction occurs near the Pt, as can be seen in Figures 7.7b and 7.7d. This means that Pt only alters the barrier locally as suggested by the elbow plots and the minimum barriers. Moreover, in contrast to Cu(111), methane reacts relatively closer to the Pt top site, with no difference being observed between CH and CD bond dissociation. Again, no significant steering in $X$ and $Y$ is observed.

## 7.4 Conclusions

In this chapter predictions have been made with BOMD on the reactivity of methane on several copper-based surfaces using the SRP32-vdW DF, combined with barriers and elbow plots in order to rationalize the results. The results

predict a much lower reactivity for Cu(111) than for Ni(111) and Pt(111) due to the high and late barrier found on Cu(111), requiring high translational and vibrational energies in order to observe reaction. Furthermore, methane has the same reaction probability on Cu(211) as on Cu(111), but with the reaction occurring only at the steps. This can be understood from the lower barriers at the step and higher barriers at the terrace relative to Cu(111). Moreover, making a so-called single-atom alloy from Cu(111) with Pt increases reactivity. This is partially caused by the reduction of the barrier height, together with changes in the dynamical pathway and reduction in energy transfer from the molecule to the surface. The minimum barrier is only affected locally around the alloyed atom, i.e., the Cu surface is unaffected, which is also reflected by the fact that methane only reacts near the top site of the Pt atom. Also, the choice of the exchange-correlation DF can have a large effect on the changes of the local barrier above the alloyed atom. For Pd-Cu(111), the reduction in barrier height and changes in the dynamical pathway were not sufficient to observe reactivity at the same energies as Pt-Cu(111). Finally, it is to be hoped that these predictive calculations will be followed by experiments in order to prove the transferability of the SRP32-vdW DF among systems in which methane interacts with flat and stepped surfaces of metals belonging to adjacent groups of the periodic table, and among systems in which the interaction is with SAAs of these metals.

In this chapter, the predictions of the reactivity of methane on copper surfaces are for a limited range of incidence energies, which additionally are at the high end of what can be achieved with molecular beams using seeding with $H_2$. In chapter 8 a larger range of incidence energies is investigated with a neural network approach, where a potential energy surface is fitted for methane interacting with a mobile copper surface.

# Appendix

## 7.A Electronic Structure Calculations

Convergence tests have been performed to ensure that the aforementioned setup produces accurate results for the interaction of methane with Cu(111). As a convergence test, calculation of the minimum reaction barrier height of $CHD_3$ on Cu(111) has been done. However, the same convergence behavior is expected for other TS geometries, metal surfaces, and exchange-correlation DFs. The barrier height is defined as $E_b = \epsilon_b - \epsilon_{asym}$, where $\epsilon_b$ and $\epsilon_{asym}$ are the absolute energies from the DFT calculations for the barrier geometry and the asymptotic configuration, respectively. The asymptotic configuration is considered to be the gas phase configuration and is obtained by putting the molecule halfway between two periodic slabs, i.e., the distance between the carbon of the methane and the surface is 6.5 Å. The results are presented in Figure 7.A.1. Converged setups yield a barrier height of 168 kJ/mol, which the employed computational setup can reproduce within chemical accuracy (i.e., 4.2 kJ/mol).

The effect of the vacuum distance has also been investigated. When a vacuum distance of 30 Å is employed, while keeping $Z = 6.5$ Å, the residual energy is about 2.5 kJ/mol, where the residual energy is defined as $E_R = E_b^{13\,\text{Å}} - E_{b,Z=6.5\,\text{Å}}^{30\,\text{Å}}$. Furthermore, the barrier height is reduced by 0.6 kJ/mol when using a cutoff energy of 350 eV compared to higher cutoff energies, which is independent of other parameters such as the amount of $k$-points and layers. In order to keep the calculations tractable, a vacuum distance of 13 Å is kept and a cutoff energy of 350 eV is used, but 1.9 kJ/mol is added to the initial kinetic energy during the BOMD (see Section 2.4.2). This is motivated by the fact that the interaction energy at this distance is only dependent on the molecular coordinate $Z$, which is shown in figure 7.A.2. Here methane is kept fixed in its gas phase equilibrium geometry, while varying $Z$ above the top site for a vacuum distance of 13 and 30 Å, where $Z$ is defined as the distance between the surface and the center of mass of methane. The Van der Waals well depth depends on the orientation of the hydrogen atoms, i.e., if more hydrogen atoms point towards the surface, the Van der Waals well is deeper.

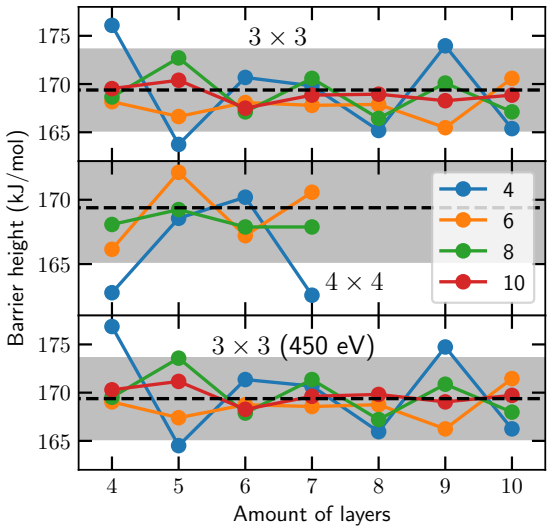


FIGURE 7.A.1: The barrier height as a function of the amount of layers for varying amount of $k$-points ($n \times n \times 1, n = 4, 6, 8, 10$). The first panel is with an energy cutoff of 350 eV and a $3 \times 3$ supercell, second panel is with an energy cutoff of 350 eV and a $4 \times 4$ supercell, and the last panel is with an energy cutoff of 450 eV and a $3 \times 3$ supercell. The dashed lines indicate the converged barrier height and the gray area indicates chemical accuracy (4.2 kJ/mol) with respect to the converged barrier height.

The number $n$ defines the amount of $k$-points and is indicated in the legend.

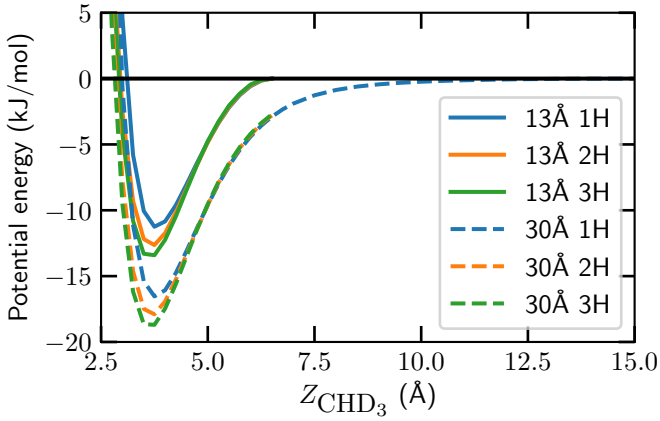


FIGURE 7.A.2: The Van der Waals interaction of methane with a Cu(111) surface as a function of the distance $Z$ between the surface and the methane, with 1 (blue), 2 (orange) or 3 (green) hydrogen atoms pointing towards the surface. The solid and dashed lines indicate results of using a vacuum distance of 13 and 30 Å, respectively. The asymptotic energy is considered to be zero.

The exact orientation and impact site of the molecule have been found not to influence the results for the Van der Waals energy significantly. For 1, 2 and 3 hydrogen atoms pointing towards the surface and a vacuum distance of 13 Å, a Van der Waals adsorption well was found of 12, 13 and 14 kJ/mol, respectively. When the vacuum distance is increased to 30 Å, the physisorption energy is 4.8 kJ/mol higher. Furthermore, the equilibrium distance to the surface is approximately 3.75 Å. These results are comparable to what Li et al. found[6], who found an adsorption energy of 15 kJ/mol and an equilibrium distance for physisorped methane of 3.532 Å.

The described computational setup is used to perform bulk calculations within the primitive unit cell for a fcc lattice, which yielded an equilibrium lattice constant $a_0 = 3.679$ Å, which is 1.8% larger than the experimental value $a_0 = 3.615$ Å[65]. The obtained lattice constant was used to model the Cu(111), Pt-Cu(111), Pd-Cu(111) and Cu(211) slabs.

## 7.B Minimum Energy Paths

Figure 7.B.1 shows the elbow plot and the MEP of methane on Cu(111) above the fcc site, using the TS geometry obtained above the top site. The MEP

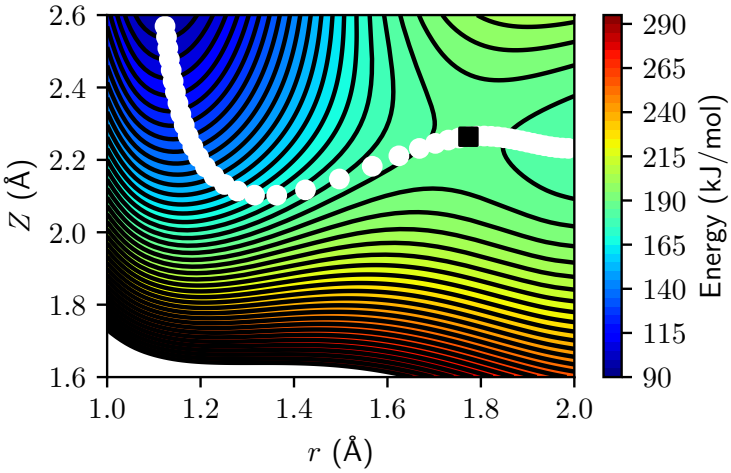


FIGURE 7.B.1: Elbow plot of methane on Cu(111) as a function of $Z$ and the distance of the dissociating CH-bond. The other coordinates of methane are kept fixed at their values at the top site C2 geometry except for the COM coordinates, which are taken such that methane is placed above the fcc site. Contour lines are drawn at intervals of 5 kJ/mol between 90 and 300 kJ/mol. The colours indicate the energy (kJ/mol) with respect to methane in the gas phase.

of methane on Cu(211) using the E/BtoB geometry is shown in Figure 7.B.2, which is similar to the MEP obtained for the EtoE geometry and on Cu(111). This can also be seen from the curvature of the MEPs on Cu(111) and Cu(211) where the $\theta$ angle was allowed to relax in Figure 7.B.3. Above the next nearest neighbour copper atom in Pt-Cu(111) the MEP is almost identical to that of Cu(111) in Figure 7.B.4. Moreover, above the Pt atom in Pt-Cu(111) the MEP is also similar to that found for Pt(111) in Figure 7.B.5, although the barrier is later than on Pt(111). Finally, the MEP on Pd(111) in Figure 7.B.6 is similar to the MEP on Pt(111).

## 7.C Energy Transfer

The energy transfer distributions from methane to the Cu(111), Pd-Cu(111), and Pt-Cu(111) surface, with $\langle E_i \rangle = 160$ kJ/mol and $\nu_1 = 1$, is shown in Figure 7.C.1. The energy transfer from methane to Pd-Cu(111) is roughly the same as to Pt-Cu(111), whereas Cu(111) yields the largest energy transfer. Figure 7.C.2 shows the total phonon density of states (DOS) for Cu(111) and Pt-Cu(111),

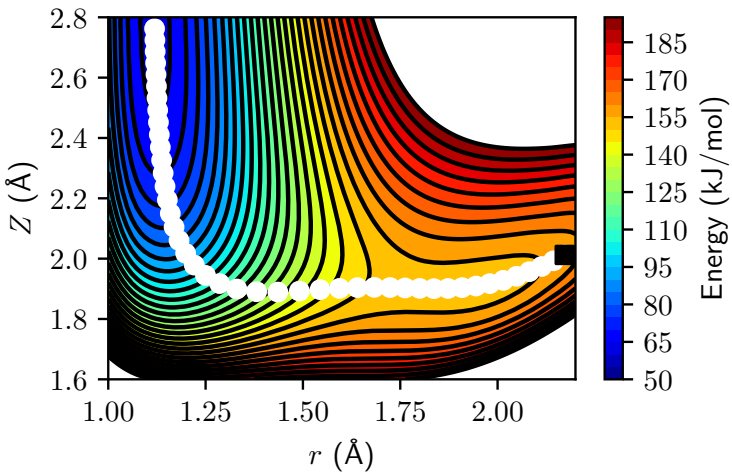


FIGURE 7.B.2: Elbow plot of methane on Cu(211) as a function of $Z$ and the distance of the dissociating CH-bond. The other coordinates of methane are kept fixed at their values at the E/BtoB geometry. Contour lines are drawn at intervals of 5 kJ/mol between 50 and 200 kJ/mol. The colours indicate the energy (kJ/mol) with respect to methane in the gas phase.

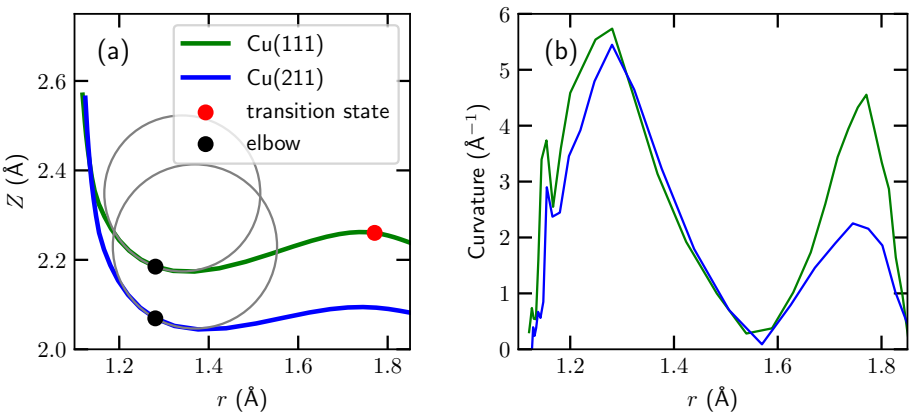


FIGURE 7.B.3: The MEP of methane on Cu(111) (green) and Cu(211) (blue) as a function of $Z$ and the distance of the dissociating CH-bond $r$ (a), and its curvature (b). The other coordinates of methane are kept fixed, except the $\theta$ angle which is relaxed, at their values at the top site C2 geometry (Cu(111)) or at the step edge EtoE geometry (Cu(211)).

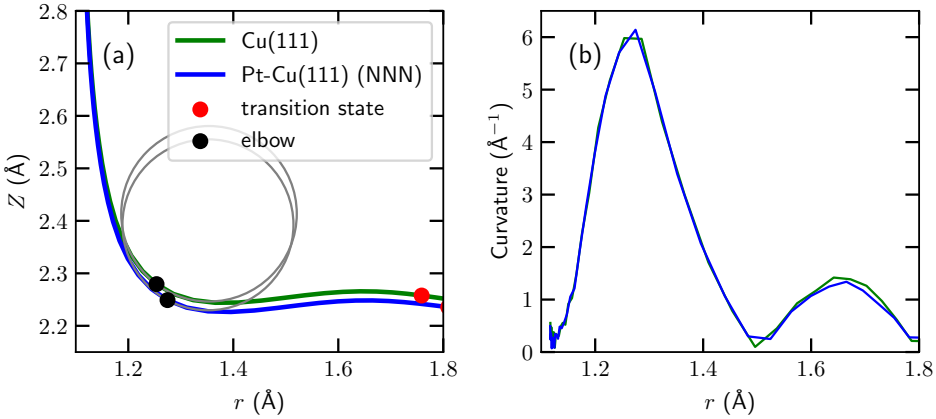


FIGURE 7.B.4: The MEP of methane on Cu(111) (green) and Pt-Cu(111) (blue, next nearest neighbour) as a function of $Z$ and the distance of the dissociating CH-bond $r$ (a), and its curvature (b). The other coordinates of methane are kept fixed at their values at the TS geometry.

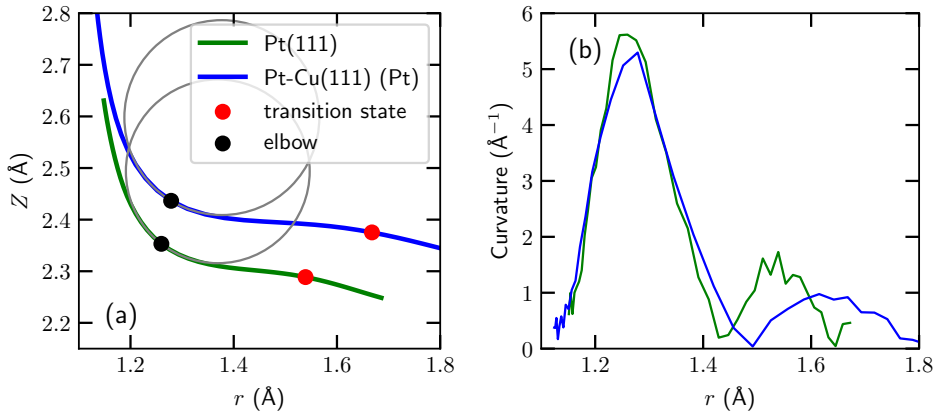


FIGURE 7.B.5: The MEP of methane on Pt(111) (green) and Pt-Cu(111) (blue, Pt) as a function of $Z$ and the distance of the dissociating CH-bond $r$ (a), and its curvature (b).The other coordinates of methane are kept fixed at their values at the TS geometry.

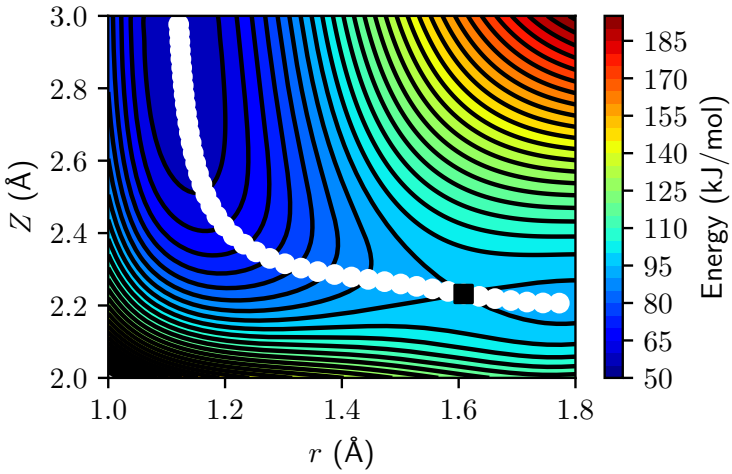


FIGURE 7.B.6: Elbow plot of methane on Pd(111) as a function of $Z$ and the distance of the dissociating CH-bond. The other coordinates of methane are kept fixed at their values at the TS geometry. Contour lines are drawn at intervals of 5 kJ/mol between 50 and 200 kJ/mol. The colours indicate the energy (kJ/mol) with respect to methane in the gas phase.

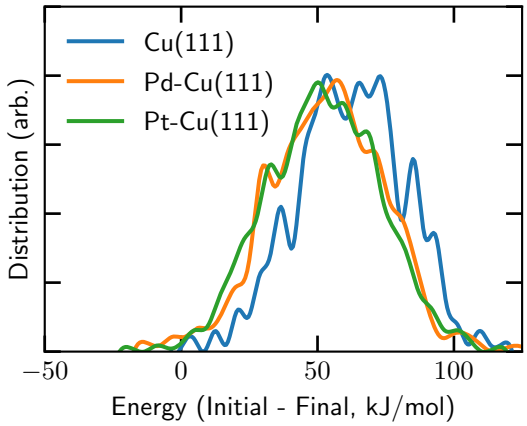


FIGURE 7.C.1: Energy transfer from methane to the Cu(111), Pd-Cu(111), and Pt-Cu(111) surface, with $\langle E_i \rangle = 160$ kJ/mol and $\nu_1 = 1$.

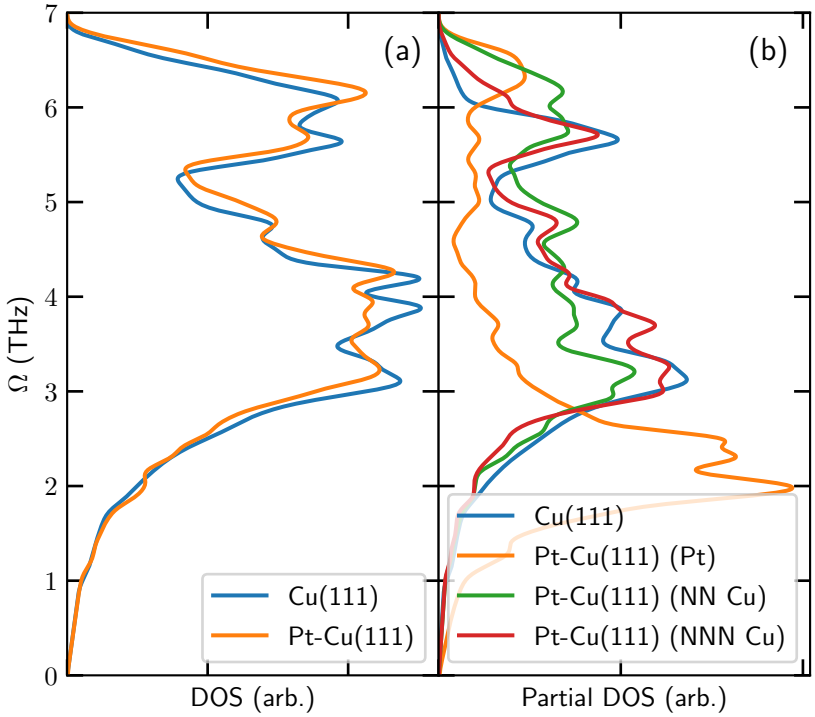


FIGURE 7.C.2: (a) Total phonon density of states (DOS) for Cu(111) (blue) and Pt-Cu(111) (orange). (b) Partial phonon DOS of the top layer Pt atom (orange), the nearest neighbour (green) and next nearest neighbour (red) Cu atoms in Pt-Cu(111), and a top layer atom in Cu(111) (blue).

which are similar. However, the partial DOS shows that the Cu top layer atoms have a similar DOS, save for the nearest neighbour Cu atom in Pt-Cu(111), whereas the partial DOS for Pt is at a lower energy.

## 7.D Surface Atom Displacement

The distributions of the displacement in the $Z$ direction of surface top layer atoms in Cu(111), Pt(111) and Pt-Cu(111) are shown in Figure 7.D.1. The atoms in the alloy are on average 0.05 Å lower than in pure Cu(111) and Pt(111). This corresponds well with an effectively 1.9 kJ/mol higher barrier above the Cu atoms in the alloy than on Cu(111) (see Figure 7.D.2).

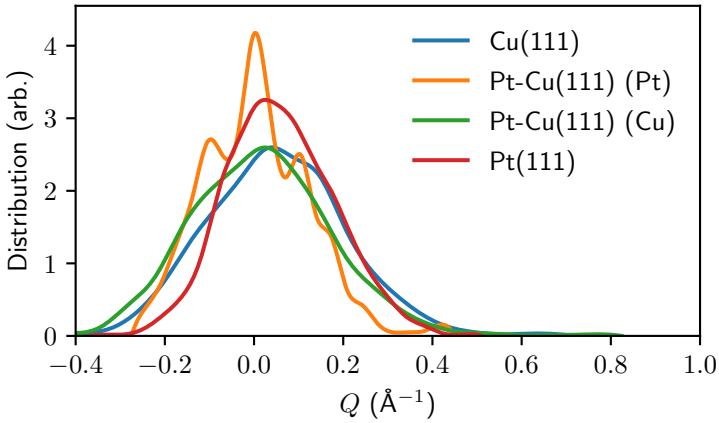


FIGURE 7.D.1: Distributions of the displacements of top layer surface atoms in the $Z$ direction for Cu(111), Pt(111) and Pt-Cu(111) during the surface equilibration at 550 K. For Pt-Cu(111) a distinction is made between Pt and Cu.

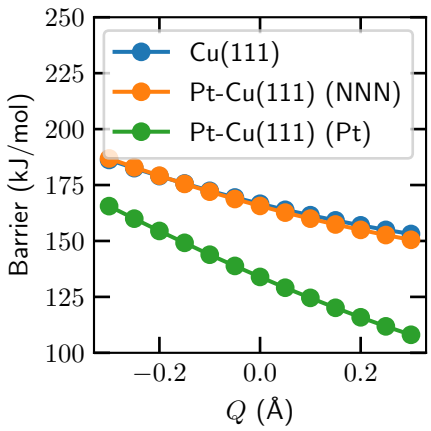


FIGURE 7.D.2: The barrier for methane dissociation on Cu(111) and Pt-Cu(111) as a function of the displacement $Q$ of the surface atom, above which methane dissociates.

## References


(1) Wei, J.; Iglesia, E. Mechanism and Site Requirements for Activation and Chemical Conversion of Methane on Supported Pt Clusters and Turnover Rate Comparisons among Noble Metals. *J. Phys. Chem. B* **2004**, *108*, 4094–4103, DOI: 10.1021/jp036985z.

(2) Jones, G.; Jakobsen, J. G.; Shim, S. S.; Kleis, J.; Andersson, M. P.; Rossmeisl, J.; Abild-Pedersen, F.; Bligaard, T.; Helveg, S.; Hinnemann, B.; Rostrup-Nielsen, J. R.; Chorkendorff, I.; Sehested, J.; Nørskov, J. K. First Principles Calculations and Experimental Insight into Methane Steam Reforming over Transition Metal Catalysts. *J. Catal.* **2008**, *259*, 147–160, DOI: 10.1016/j.jcat.2008.08.003.

(3) Li, X.; Cai, W.; An, J.; Kim, S.; Nah, J.; Yang, D.; Piner, R.; Velamakanni, A.; Jung, I.; Tutuc, E.; Banerjee, S. K.; Colombo, L.; Ruoff, R. S. Large-Area Synthesis of High-Quality and Uniform Graphene Films on Copper Foils. *Science* **2009**, *324*, 1312–1314, DOI: 10.1126/science.1171245.

(4) Losurdo, M.; Giangregorio, M. M.; Capezzuto, P.; Bruno, G. Graphene CVD Growth on Copper and Nickel: Role of Hydrogen in Kinetics and Structure. *Phys. Chem. Chem. Phys.* **2011**, *13*, 20836–20843, DOI: 10.1039/C1CP22347J.

(5) Zhang, W.; Wu, P.; Li, Z.; Yang, J. First-Principles Thermodynamics of Graphene Growth on Cu Surfaces. *J. Phys. Chem. C* **2011**, *115*, 17782–17787, DOI: 10.1021/jp2006827.

(6) Li, K.; He, C.; Jiao, M.; Wang, Y.; Wu, Z. A First-Principles Study on the Role of Hydrogen in Early Stage of Graphene Growth during the $CH_4$ Dissociation on Cu(111) and Ni(111) Surfaces. *Carbon* **2014**, *74*, 255–265, DOI: 10.1016/j.carbon.2014.03.030.

(7) Wang, X.; Yuan, Q.; Li, J.; Ding, F. The Transition Metal Surface Dependent Methane Decomposition in Graphene Chemical Vapor Deposition Growth. *Nanoscale* **2017**, *9*, 11584–11589, DOI: 10.1039/C7NR02743E.

(8) Kraus, J.; Böbel, L.; Zwaschka, G.; Günther, S. Understanding the Reaction Kinetics to Optimize Graphene Growth on Cu by Chemical Vapor Deposition. *Ann. Phys.* **2017**, *529*, 1700029, DOI: 10.1002/andp.201700029.

(9) Tian, B.; Liu, T.; Yang, Y.; Li, K.; Wu, Z.; Wang, Y. $CH_4$ Dissociation in the Early Stage of Graphene Growth on Fe–Cu(100) Surface: Theoretical Insights. *Appl. Surf. Sci.* **2018**, *427*, 953–960, DOI: 10.1016/j.apsusc.2017.09.088.

(10) Kroes, G.-J. Towards Chemically Accurate Simulation of Molecule–Surface Reactions. *Phys. Chem. Chem. Phys.* **2012**, *14*, 14966–14981, DOI: 10.1039/C2CP42471A.

(11) Jackson, B.; Nattino, F.; Kroes, G.-J. Dissociative Chemisorption of Methane on Metal Surfaces: Tests of Dynamical Assumptions Using Quantum Models and Ab Initio Molecular Dynamics. *J. Chem. Phys.* **2014**, *141*, 054102, DOI: 10.1063/1.4891327.

(12) Wellendorff, J.; Silbaugh, T. L.; Garcia-Pintos, D.; Nørskov, J. K.; Bligaard, T.; Studt, F.; Campbell, C. T. A Benchmark Database for Adsorption Bond Energies to Transition Metal Surfaces and Comparison to Selected DFT Functionals. *Surf. Sci.* **2015**, *640*, 36–44, DOI: 10.1016/j.susc.2015.03.023.

(13) Gautier, S.; Steinmann, S. N.; Michel, C.; Fleurat-Lessard, P.; Sautet, P. Molecular Adsorption at Pt(111). How Accurate Are DFT Functionals? *Phys. Chem. Chem. Phys.* **2015**, *17*, 28921–28930, DOI: 10.1039/C5CP04534G.

(14) Kroes, G.-J. Toward a Database of Chemically Accurate Barrier Heights for Reactions of Molecules with Metal Surfaces. *J. Phys. Chem. Lett.* **2015**, *6*, 4106–4114, DOI: 10.1021/acs.jpclett.5b01344.

(15) Díaz, C.; Pijper, E.; Olsen, R. A.; Busnengo, H. F.; Auerbach, D. J.; Kroes, G. J. Chemically Accurate Simulation of a Prototypical Surface Reaction: $H_2$ Dissociation on Cu(111). *Science* **2009**, *326*, 832–834, DOI: 10.1126/science.1178722.

(16) Nattino, F.; Migliorini, D.; Kroes, G.-J.; Dombrowski, E.; High, E. A.; Killelea, D. R.; Utz, A. L. Chemically Accurate Simulation of a Polyatomic Molecule-Metal Surface Reaction. *J. Phys. Chem. Lett.* **2016**, *7*, 2402–2406, DOI: 10.1021/acs.jpclett.6b01022.

(17) Migliorini, D.; Chadwick, H.; Nattino, F.; Gutiérrez-González, A.; Dombrowski, E.; High, E. A.; Guo, H.; Utz, A. L.; Jackson, B.; Beck, R. D.; Kroes, G.-J. Surface Reaction Barriometry: Methane Dissociation on Flat and Stepped Transition-Metal Surfaces. *J. Phys. Chem. Lett.* **2017**, *8*, 4177–4182, DOI: 10.1021/acs.jpclett.7b01905.

(18) Groß, A. Reactivity of Bimetallic Systems Studied from First Principles. *Top. Catal.* **2006**, *37*, 29–39, DOI: 10.1007/s11244-006-0005-x.

(19) Ramos, M.; Martínez, A. E.; Busnengo, H. F. $H_2$ Dissociation on Individual Pd Atoms Deposited on Cu(111). *Phys. Chem. Chem. Phys.* **2012**, *14*, 303–310, DOI: 10.1039/C1CP22163A.

(20) Swaan, H. M.; Kroll, V. C. H.; Martin, G. A.; Mirodatos, C. Deactivation of Supported Nickel Catalysts during the Reforming of Methane by Carbon Dioxide. *Catal. Today* **1994**, *21*, 571–578, DOI: 10.1016/0920-5861(94)80181-9.

(21) Iglesias-Juez, A.; Beale, A. M.; Maaijen, K.; Weng, T. C.; Glatzel, P.; Weckhuysen, B. M. A Combined in Situ Time-Resolved UV–Vis, Raman and High-Energy Resolution X-Ray Absorption Spectroscopy Study on the Deactivation Behavior of Pt and PtSn Propane Dehydrogenation Catalysts under Industrial Reaction Conditions. *J. Catal.* **2010**, *276*, 268–279, DOI: 10.1016/j.jcat.2010.09.018.

(22) Marcinkowski, M. D.; Darby, M. T.; Liu, J.; Wimble, J. M.; Lucci, F. R.; Lee, S.; Michaelides, A.; Flytzani-Stephanopoulos, M.; Stamatakis, M.; Sykes, E. C. H. Pt/Cu Single-Atom Alloys as Coke-Resistant Catalysts for Efficient C–H Activation. *Nat. Chem.* **2018**, *10*, 325–332, DOI: 10.1038/nchem.2915.

(23) Tierney, H. L.; Baber, A. E.; Sykes, E. C. H. Atomic-Scale Imaging and Electronic Structure Determination of Catalytic Sites on Pd/Cu Near Surface Alloys. *J. Phys. Chem. C* **2009**, *113*, 7246–7250, DOI: 10.1021/jp809766d.

(24) Lucci, F. R.; Lawton, T. J.; Pronschinske, A.; Sykes, E. C. H. Atomic Scale Surface Structure of Pt/Cu(111) Surface Alloys. *J. Phys. Chem. C* **2014**, *118*, 3015–3022, DOI: 10.1021/jp405254z.

(25) Simonovis, J. P.; Hunt, A.; Palomino, R. M.; Senanayake, S. D.; Waluyo, I. Enhanced Stability of Pt-Cu Single-Atom Alloy Catalysts: In Situ Characterization of the Pt/Cu(111) Surface in an Ambient Pressure of CO. *J. Phys. Chem. C* **2018**, *122*, 4488–4495, DOI: 10.1021/acs.jpcc.8b00078.

(26) Reyes, P.; Figueroa, A.; Pecchi, G.; Fierro, J. L. G. Catalytic Combustion of Methane on Pd–Cu/$SiO_2$ Catalysts. *Catal. Today* **2000**, *62*, 209–217.

(27) Persson, K.; Ersson, A.; Jansson, K.; Iverlund, N.; Järås, S. Influence of Co-Metals on Bimetallic Palladium Catalysts for Methane Combustion. *J. Catal.* **2005**, *231*, 139–150, DOI: 10.1016/j.jcat.2005.01.001.

(28) Kokalj, A.; Bonini, N.; de Gironcoli, S.; Sbraccia, C.; Fratesi, G.; Baroni, S. Methane Dehydrogenation on Rh@Cu(111): A First-Principles Study of a Model Catalyst. *Journal of the American Chemical Society* **2006**, *128*, 12448–12454, DOI: 10.1021/ja060114w.

(29) An, W.; Zeng, X. C.; Turner, C. H. First-Principles Study of Methane Dehydrogenation on a Bimetallic Cu/Ni(111) Surface. *J. Chem. Phys.* **2009**, *131*, 174702, DOI: 10.1063/1.3254383.

(30) Yuan, S.; Meng, L.; Wang, J. Greatly Improved Methane Dehydrogenation via Ni Adsorbed Cu(100) Surface. *J. Phys. Chem. C* **2013**, *117*, 14796–14803, DOI: 10.1021/jp400944c.

(31) Kresse, G.; Hafner, J. Ab Initio Molecular-Dynamics Simulation of the Liquid-Metal–Amorphous-Semiconductor Transition in Germanium. *Phys. Rev. B* **1994**, *49*, 14251–14269, DOI: 10.1103/PhysRevB.49.14251.

(32) Kresse, G.; Hafner, J. Ab Initio Molecular Dynamics for Liquid Metals. *Phys. Rev. B* **1993**, *47*, 558–561, DOI: 10.1103/PhysRevB.47.558.

(33) Kresse, G.; Furthmüller, J. Efficient Iterative Schemes for Ab Initio Total-Energy Calculations Using a Plane-Wave Basis Set. *Phys. Rev. B* **1996**, *54*, 11169–11186, DOI: 10.1103/PhysRevB.54.11169.

(34) Kresse, G.; Furthmüller, J. Efficiency of Ab-Initio Total Energy Calculations for Metals and Semiconductors Using a Plane-Wave Basis Set. *Comput. Mater. Sci.* **1996**, *6*, 15–50, DOI: 10.1016/0927-0256(96)00008-0.

(35) Kresse, G.; Joubert, D. From Ultrasoft Pseudopotentials to the Projector Augmented-Wave Method. *Phys. Rev. B* **1999**, *59*, 1758–1775, DOI: 10.1103/PhysRevB.59.1758.

(36) Blöchl, P. E. Projector Augmented-Wave Method. *Phys. Rev. B* **1994**, *50*, 17953–17979, DOI: 10.1103/PhysRevB.50.17953.

(37) Methfessel, M.; Paxton, A. T. High-Precision Sampling for Brillouin-Zone Integration in Metals. *Phys. Rev. B* **1989**, *40*, 3616–3621, DOI: 10.1103/PhysRevB.40.3616.

(38) Henkelman, G.; Jónsson, H. A Dimer Method for Finding Saddle Points on High Dimensional Potential Surfaces Using Only First Derivatives. *J. Chem. Phys.* **1999**, *111*, 7010–7022, DOI: 10.1063/1.480097.

(39) Heyden, A.; Bell, A. T.; Keil, F. J. Efficient Methods for Finding Transition States in Chemical Reactions: Comparison of Improved Dimer Method and Partitioned Rational Function Optimization Method. *J. Chem. Phys.* **2005**, *123*, 224101, DOI: 10.1063/1.2104507.

(40) Kästner, J.; Sherwood, P. Superlinearly Converging Dimer Method for Transition State Search. *J. Chem. Phys.* **2008**, *128*, 014106, DOI: 10.1063/1.2815812.

(41) Xiao, P.; Sheppard, D.; Rogal, J.; Henkelman, G. Solid-State Dimer Method for Calculating Solid-Solid Phase Transitions. *J. Chem. Phys.* **2014**, *140*, 174104, DOI: 10.1063/1.4873437.

(42) Transition State Tools Package for VASP https://theory.cm.utexas.edu/vtsttools/index.html (accessed 02/08/2021).

(43) Mondal, A.; Wijzenbroek, M.; Bonfanti, M.; Díaz, C.; Kroes, G.-J. Thermal Lattice Expansion Effect on Reactive Scattering of $H_2$ from Cu(111) at $T_s$ = 925 K. *J. Phys. Chem. A* **2013**, *117*, 8770–8781, DOI: 10.1021/jp4042183.

(44) Nattino, F.; Ueta, H.; Chadwick, H.; van Reijzen, M. E.; Beck, R. D.; Jackson, B.; van Hemert, M. C.; Kroes, G.-J. Ab Initio Molecular Dynamics Calculations versus Quantum-State-Resolved Experiments on $CHD_3$ + Pt(111): New Insights into a Prototypical Gas–Surface Reaction. *J. Phys. Chem. Lett.* **2014**, *5*, 1294–1299, DOI: 10.1021/jz500233n.

(45) Hammer, B.; Hansen, L. B.; Nørskov, J. K. Improved Adsorption Energetics within Density-Functional Theory Using Revised Perdew-Burke-Ernzerhof Functionals. *Phys. Rev. B* **1999**, *59*, 7413–7421, DOI: 10.1103/PhysRevB.59.7413.

(46) Perdew, J. P.; Burke, K.; Ernzerhof, M. Generalized Gradient Approximation Made Simple. *Phys. Rev. Lett.* **1996**, *77*, 3865–3868, DOI: 10.1103/PhysRevLett.77.3865.

(47) Dion, M.; Rydberg, H.; Schröder, E.; Langreth, D. C.; Lundqvist, B. I. Van Der Waals Density Functional for General Geometries. *Phys. Rev. Lett.* **2004**, *92*, 246401, DOI: 10.1103/PhysRevLett.92.246401.

(48) Wijzenbroek, M.; Kroes, G. J. The Effect of the Exchange-Correlation Functional on $H_2$ Dissociation on Ru(0001). *J. Chem. Phys.* **2014**, *140*, 084702, DOI: 10.1063/1.4865946.

(49) Nattino, F.; Migliorini, D.; Bonfanti, M.; Kroes, G.-J. Methane Dissociation on Pt(111): Searching for a Specific Reaction Parameter Density Functional. *J. Chem. Phys.* **2016**, *144*, 044702, DOI: 10.1063/1.4939520.

(50) Kroes, G.-J.; Díaz, C.; Pijper, E.; Olsen, R. A.; Auerbach, D. J. Apparent Failure of the Born–Oppenheimer Static Surface Model for Vibrational Excitation of Molecular Hydrogen on Copper. *PNAS* **2010**, *107*, 20881–20886, DOI: 10.1073/pnas.1001098107.

(51) Xie, Z.; Bowman, J. M.; Zhang, X. Quasiclassical Trajectory Study of the Reaction H+$CH_4$($\nu_3$=0,1)→$CH_3$+$H_2$ Using a New Ab Initio Potential Energy Surface. *J. Chem. Phys.* **2006**, *125*, 133120, DOI: 10.1063/1.2238871.

(52) Díaz, C.; Olsen, R. A.; Auerbach, D. J.; Kroes, G. J. Six-Dimensional Dynamics Study of Reactive and Non Reactive Scattering of $H_2$ from Cu(111) Using a Chemically Accurate Potential Energy Surface. *Phys. Chem. Chem. Phys.* **2010**, *12*, 6499–6519, DOI: 10.1039/C001956A.

(53) Nave, S.; Jackson, B. Methane Dissociation on Ni(111) and Pt(111): Energetic and Dynamical Studies. *J. Chem. Phys.* **2009**, *130*, 054701, DOI: 10.1063/1.3065800.

(54) Lee, K.; Murray, É. D.; Kong, L.; Lundqvist, B. I.; Langreth, D. C. Higher-Accuracy van Der Waals Density Functional. *Phys. Rev. B* **2010**, *82*, 081101(R), DOI: 10.1103/PhysRevB.82.081101.

(55) Klimeš, J.; Bowler, D. R.; Michaelides, A. Van Der Waals Density Functionals Applied to Solids. *Phys. Rev. B* **2011**, *83*, 195131, DOI: 10.1103/PhysRevB.83.195131.

(56) Nave, S.; Tiwari, A. K.; Jackson, B. Methane Dissociation and Adsorption on Ni(111), Pt(111), Ni(100), Pt(100), and Pt(110)-(1x2): Energetic Study. *J. Chem. Phys.* **2010**, *132*, 054705, DOI: 10.1063/1.3297885.

(57) Powell, A. D.; Kroes, G.-J.; Doblhoff-Dier, K. Quantum Monte Carlo Calculations on Dissociative Chemisorption of $H_2$ + Al(110): Minimum Barrier Heights and Their Comparison to DFT Values. *J. Chem. Phys.* **2020**, *153*, 224701, DOI: 10.1063/5.0022919.

(58) Darby, M. T.; Stamatakis, M.; Michaelides, A.; Sykes, E. C. H. Lonely Atoms with Special Gifts: Breaking Linear Scaling Relationships in Heterogeneous Catalysis with Single-Atom Alloys. *J. Phys. Chem. Lett.* **2018**, *9*, 5636–5646, DOI: 10.1021/acs.jpclett.8b01888.

(59) Park, J.; Yu, B. D.; Hong, S. Van Der Waals Density Functional Theory Study for Bulk Solids with BCC, FCC, and Diamond Structures. *Current Applied Physics* **2015**, *15*, 885–891, DOI: 10.1016/j.cap.2015.03.028.

(60) Jónsson, H.; Mills, G.; Jacobsen, K. W. In *Classical and Quantum Dynamics in Condensed Phase Simulations*; World Scientific: 1998, pp 385–404, DOI: 10.1142/9789812839664_0016.

(61) Marcus, R. A. On the Analytical Mechanics of Chemical Reactions. Quantum Mechanics of Linear Collisions. *J. Chem. Phys.* **1966**, *45*, 4493–4499, DOI: 10.1063/1.1727528.

(62) McCullough, E. A.; Wyatt, R. E. Quantum Dynamics of the Collinear (H, $H_2$) Reaction. *J. Chem. Phys.* **1969**, *51*, 1253–1254, DOI: 10.1063/1.1672133.

(63) Baule, B. Theoretische Behandlung Der Erscheinungen in Verdünnten Gasen. *Ann. Phys.* **1914**, *349*, 145–176, DOI: 10.1002/andp.19143490908.

(64) Kennard, E., *Kinetic Theory of Gases: With an Introduction to Statistical Mechanics*; McGraw-Hill Book Company, Inc.: London, 1938.

(65) Mishin, Y.; Mehl, M. J.; Papaconstantopoulos, D. A.; Voter, A. F.; Kress, J. D. Structural Stability and Lattice Defects in Copper: Ab Initio, Tight-Binding, and Embedded-Atom Calculations. *Phys. Rev. B* **2001**, *63*, 224106, DOI: 10.1103/PhysRevB.63.224106.

# Chapter 8

# A High-Dimensional Neural Network Potential for the dissociative chemisorption of $CHD_3$ + Cu(111)

This chapter is based on Gerrits, N.; Shakouri, K.; Behler, J.; Kroes, G.-J. Accurate Probabilities for Highly Activated Reaction of Polyatomic Molecules on Surfaces Using a High-Dimensional Neural Network Potential: $CHD_3$ + Cu(111). *J. Phys. Chem. Lett.* **2019**, *10*, 1763–1768, DOI: 10.1021/acs.jpclett.9b00560

## Abstract

An accurate description of reactive scattering of molecules on metal surfaces often requires the modeling of energy transfer between the molecule and the surface phonons. Although Born-Oppenheimer molecular dynamics (BOMD) can describe this energy transfer, BOMD is at present untractable for reactions with reaction probabilities smaller than 1%. Here, it is shown that it is possible to use a neural network potential to describe a polyatomic molecule reacting on a mobile metal surface, with considerably reduced computational effort compared to BOMD. The highly activated reaction of $CHD_3$ on Cu(111) is used as a test case for this method. It is observed that the reaction probability is influenced considerably by dynamical effects such as the bobsled effect and surface recoil. A special dynamical effect for $CHD_3$ + Cu(111) is that a higher vibrational efficacy is obtained for two quanta in the CH stretch mode than for a single quantum.

## 8.1 Introduction

Accurately describing molecule-metal surface reactions is of vital importance for the understanding of heterogeneously catalyzed processes such as the Haber-Bosch[1] and steam reforming processes[2]. Unfortunately, the complexity of the interaction between molecules and metals limits the accuracy of theoretical studies on these kinds of processes[3–8]. Often, chemically accurate results are obtainable at high computational cost with Born-Oppenheimer molecular dynamics (BOMD) combined with the so-called Specific Reaction Parameter (SRP) approach[9–11]. However, the investigation of reactions with low reactivity ($< 1\%$) remains challenging due to the need for a large number of trajectories in combination with a large computational cost[12]. Therefore, neural network approaches have recently been employed in order to obtain results with the accuracy of BOMD using density functional theory (DFT), but with a considerably smaller computational cost[13–16]. So far these studies involved either diatomic molecules[13–16], or they neglected the movement of surface atoms[17–21]. Very recently, a high-dimensional neural network potential (HD-NNP) has been developed for a system in which a linear triatomic molecule interacts with a metal surface, i.e., $CO_2$ + Ni(100)[22], while also including surface atom motion. The neglect of surface motion can limit the accuracy of these studies due to the neglect of energy exchange between the molecule and the surface atoms[4, 12, 15, 16, 23–28]. This lack of energy exchange represents a severe approximation for the dynamics of polyatomic molecules reacting on metal surfaces due to their high mass[29, 30]. A modified Shepard interpolation method[31] has also been used to describe the potential of a polyatomic molecule reacting on a metal surface, but again with the neglect of surface motion. Reactive force field fits have been made that do include surface motion[32–35]. Although Busnengo and coworkers have shown that these fits can be in good agreement with DFT[35], it remains unclear whether these fits are also chemically accurate, i.e., whether the root-mean-square error (RMSE) is lower than 4.2 kJ/mol for the dynamically relevant part of the potential energy surface (PES). However, at the time this work was performed, no neural network potential had been employed for non-linear polyatomic molecules interacting with metal surfaces that explicitly includes the effect of surface motion as well.

In this chapter, the focus is on the dissociative chemisorption of $CHD_3$ on Cu(111) since this system exhibits a low reactivity[12], making reactive BOMD studies untractable for most incidence energies achievable in molecular beams. Moreover, high-quality graphene can be synthesized using methane dissociation on copper[36–42], and this warrants additional study of the rate-

controlling state, namely the breaking of the first CH bond. The Eley-Rideal reaction of D with $CD_3$ preadsorbed on Cu(111) has also been studied[43]. The methane + Cu(111) system shows interesting dynamics in that the low reactivity of methane on Cu(111) is not only caused by a high barrier (167 kJ/mol), but also by specific features of the PES such as the curvature of the minimum energy path (MEP)[12] (see Chapter 7). For all of these reasons, the neural network Behler-Parrinello approach[44, 45] has been applied for the first time to a non-linear polyatomic molecule reacting on a metal surface, which makes accurate simulations feasible while including surface motion, using $CHD_3$ + Cu(111) as an example.

## 8.2 Method

### 8.2.1 Neural Network

In the HD-NNP, the total energy is evaluated as a sum of atomic contributions that are dependent on their energetically relevant local environment, which is described by many-body atom-centered symmetry functions[46] (see Section 2.3.2), of which the parameters are given in Section 8.A. In total, 38 000 DFT data points were used to train the HD-NNP, of which 14 000 points were taken from the BOMD study of Chapter 7. Points from the BOMD data set were selected with the following procedure. All reacted and 50 scattered trajectories were used from the BOMD study in Chapter 7, of which only 10% of the steps in the trajectories have initially been selected. From those selected steps, it is made sure that the methane geometry in a selected step is not too similar to other previously selected steps. The acceptance criterium for this selection is $\epsilon_{\text{min}} = 0.2$ Å, where

$$\epsilon_j > \epsilon_{\text{min}} \quad \text{for } j = 1, \ldots, N \tag{8.1}$$

$$\epsilon_j = \sqrt{\sum_i r_{i,j}^2}. \tag{8.2}$$

The atoms of the methane molecule are indicated by $i$, all previous geometries are indicated by $j$, and $r_{i,j}$ is the distance between atom $i$ of the newly selected geometry and atom $j$ of a previous methane geometry $j$. This procedure resulted in about 14 000 points in the training data set. Missing structures in the training data set (about 21 500 ) were found by running MD on the incomplete HD-NNP using the following procedure[45]. About 5000 trajectories were calculated at $\langle E_{\text{i}} \rangle = 160$ and 181 kJ/mol for laser-off conditions and $\nu_1 = 2$. The neural network implementation would then identify extrapolation errors during the MD, indicating structures that are missing in the training set. These

missing structures were then added to the training set and this procedure was repeated until the amount of extrapolation errors was considered small enough ($< 0.5\%$) and no longer affected the computed reaction probability. During the process of identifying missing structures, about 20 points in the Van der Waals well region were included as well. Also, 500 points from the elbow plot showing the minimum barrier (see Chapter 7), and where all degrees of freedom other than the molecule-surface distance $Z$ and the length of the dissociating CH-bond $r$ are relaxed, were included (see Figure 8.3c). Finally, vibrational modes were sampled in a random fashion according to a nozzle temperature of 1200 K, on both an ideal and thermally distorted surface (but note that the ideal surface still includes a lattice expansion corresponding to the simulated surface temperature of 550 K) at random locations with respect to the surface, resulting in 2000 points. Using the aforementioned procedures a total number of 38 000 of points were obtained that formed the training and testing data set. The total energy for all structures in the training and testing data set obtained with both DFT and the HD-NNP are compared in Figure 8.1, showing excellent agreement between the HD-NNP and direct DFT calculations. The employed computational setup for the DFT calculations is described in Section 7.2. Furthermore, for the neural network, two hidden layers are used, each with 15 nodes. Finally, the training has been carried out using the RuNNer code[47–49] and the MD has been performed with LAMMPS[50, 51].

### 8.2.2 Molecular Initial Conditions

The initial translational energy distribution of the molecules has been simulated according to experimental molecular beam parameters (stream velocities and width parameters)[9], which are provided in Table 8.1. Experimental beam parameters are available for nozzle temperatures lower than 900 K[9, 10], but here the choice was made to take the width parameter simply as $\alpha = 0.05\nu_0$, which is in reasonable agreement with experiment as can be seen in Figure 8.2a. The width parameters for $T_\mathrm{n} = 950$ and 1000 K were obtained by extrapolating the experimental width parameters obtained by Utz and co-workers[9]. Although $\alpha = 0.055\nu_0$ would have been a better approximation for $\nu_0 < 4000$ m/s, this does not have a large effect on the results presented in this work. The stream velocities are obtained by fitting the experimental data using a linear fit (see Figure 8.2b). The exception is the stream velocities for $T_\mathrm{n} = 900$ and 1000 K, for which the stream velocities previously used in the BOMD study in Chapter 7 are taken.

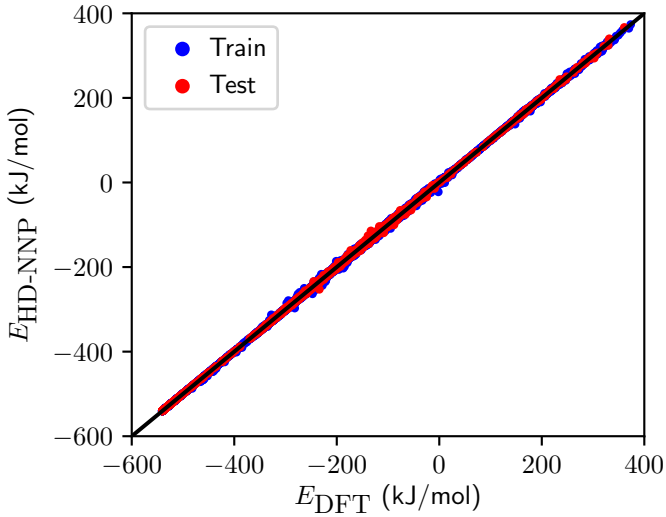


FIGURE 8.1: Total energy for all structures in the training (blue) and testing (red) data set obtained with the HD-NNP and DFT. The total energy of the methane in the gas phase with an ideal surface is taken as zero. The black line indicates $x = y$.

TABLE 8.1: Beam parameters that describe the simulated $CHD_3$ velocity distributions. $\nu_0$ and $\alpha$ are determined through time-of-flight measurements for 900 K[9]. All other parameters than $\langle E_i \rangle = 160.4$ kJ/mol are not from experiment, but theoretical estimates obtained by interpolation and extrapolation.

| $T_n$ (K) | $\langle E_i \rangle$ kJ/mol | $\nu_0$ (m/s) | $\alpha$ (m/s) |
|---|---|---|---|
| 400 | 83.4 | 2946.95 | 147.35 |
| 500 | 97.0 | 3177.70 | 158.89 |
| 600 | 111.6 | 3408.45 | 170.42 |
| 700 | 127.3 | 3639.20 | 181.96 |
| 800 | 143.9 | 3869.95 | 193.50 |
| 900* | 160.4 | 4070.12 | 274.51 |
| 950 | 172.3 | 4216.08 | 300.00 |
| 1000 | 181.3 | 4320.12 | 324.01 |

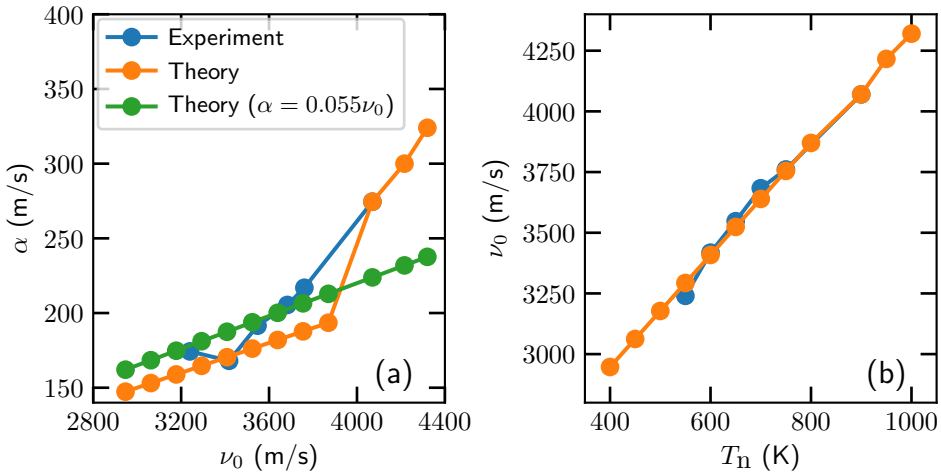


FIGURE 8.2: Width parameter $\alpha$ as a function of the stream velocity $\nu_0$ (a) and the stream velocity $\nu_0$ as a function of the nozzle temperature $T_n$ (b). Experimental parameters[9] and parameters used in this work are indicated in blue and orange, respectively. Theoretical parameters where $\alpha = 0.055\nu_0$ are indicated in green.

## 8.3 Results

First, the accuracy of the HD-NNP is tested by comparing the 2D elbow plot of methane on Cu(111) in which methane is fixed in all molecular coordinates according to its TS geometry, as depicted in Figure 8.3a, except for $Z_C$ and $r$ (the distance between the carbon atom and surface, and the length of the dissociating CH bond). The HD-NNP is compared directly with DFT calculations in Figure 8.3b. Here, it can be seen that the HD-NNP reproduces the DFT data remarkably well, even though points from the 2D cut are not included in the data set. When the methane is relaxed in all degrees of freedom other than $r$ and $Z$ (Figure 8.3c), the MEP lies slightly closer to the surface than to the MEP of the constrained methane. Again, the HD-NNP reproduces the direct DFT calculations quite well. Moreover, both the electronic and mechanical coupling[30] are in good agreement with DFT (see Figure 8.3d,e), which means that changes in the barrier height and geometry with respect to the motion of the surface atom below the dissociating molecule are described correctly. Furthermore, using 90% of the DFT data set as the training set and 10% as the test set, the RMSE is 1.7 kJ/mol for the test set, which is well within chemical accuracy (4.2 kJ/mol). (Note that all errors reported in this chapter are with respect to the full system, i.e., the total energy.) The high fitting accuracy is

also observed in Figure 8.4, where the distributions of the absolute error for the training and test set are shown and the vast majority of the errors falls within chemical accuracy. The total energy for all of the structures in the training and test set obtained with the HD-NNP and direct DFT calculations is also shown in Figure 8.1. Moreover, the RMSE for the forces in the test set is 2.3 kJ/mol/Å. The RMSE of 1.7 kJ/mol is obtained here on the basis of 38 000 DFT points for $CHD_3$ + Cu(111), where the surface atoms are allowed to move. This RMSE value compares well with the RMSE of 1.5 kJ/mol obtained for a recent 15D NN static surface PES for $CHD_3$ + Ni(111), on the basis of 200 000 DFT points[19, 28]. It should also be noted that the approximate modified generalized Langevin oscillator method used in Ref. [28] to effectively add surface atom motion to the MD may run into problems if the molecule-metal surface interaction depends on more than just one surface atom coordinate, as for instance is the case for $H_2O$ + Ni(111)[52], and may be the case for methane interacting with stepped metal surfaces[28].

The goal is to make a HD-NNP with which it is possible to accurately evaluate the energy and forces on the fly during MD simulations. Therefore, not only incidence energies with low reaction probabilities ($< 1\%$) are investigated, but also regimes with higher reaction probabilities that are obtainable with BOMD in order to test the validity of the results obtained with the HD-NNP. Figure 8.5 shows the results obtained for the dissociative chemisorption of $CHD_3$ on Cu(111) with MD using the HD-NNP and with BOMD[12] (see also Chapter 7 and Table 7.5), by simulating a molecular beam for the rovibrational ground state and under laser-off and laser-on conditions. Under laser-off conditions the molecular beam's vibrational state population is sampled according to the nozzle temperature. We also present results for the case that under laser-on conditions the CH stretch mode $\nu_1$ is excited with one or two quanta. In order to describe the reaction probability with good statistics, 10 000 - 110 000 quasiclassical trajectories were computed per incidence condition. Here, it can be seen that at high incidence energy and for vibrationally excited methane, for four sets of initial conditions resulting in reaction probabilities obtained with BOMD, good agreement exists between BOMD and MD performed with the HD-NNP (see also Table 8.2 and the statistical analysis in Section 8.C). Moreover, reaction probabilities as low as $5 \times 10^{-5}$ have been computed with the HD-NNP (Figure 8.5), which was previously not possible using accurate methods. It is observed that at the highest incidence energy (181 kJ/mol) the laser-off simulation yields a similar reaction probability as the $\nu_1 = 1$ simulation, which is caused by the high amount of vibrational excitation in the laser-off beam due to the high simulated nozzle temperature ($T_n = 1000$ K). However, it should be noted that sticking probabilities computed for laser-off

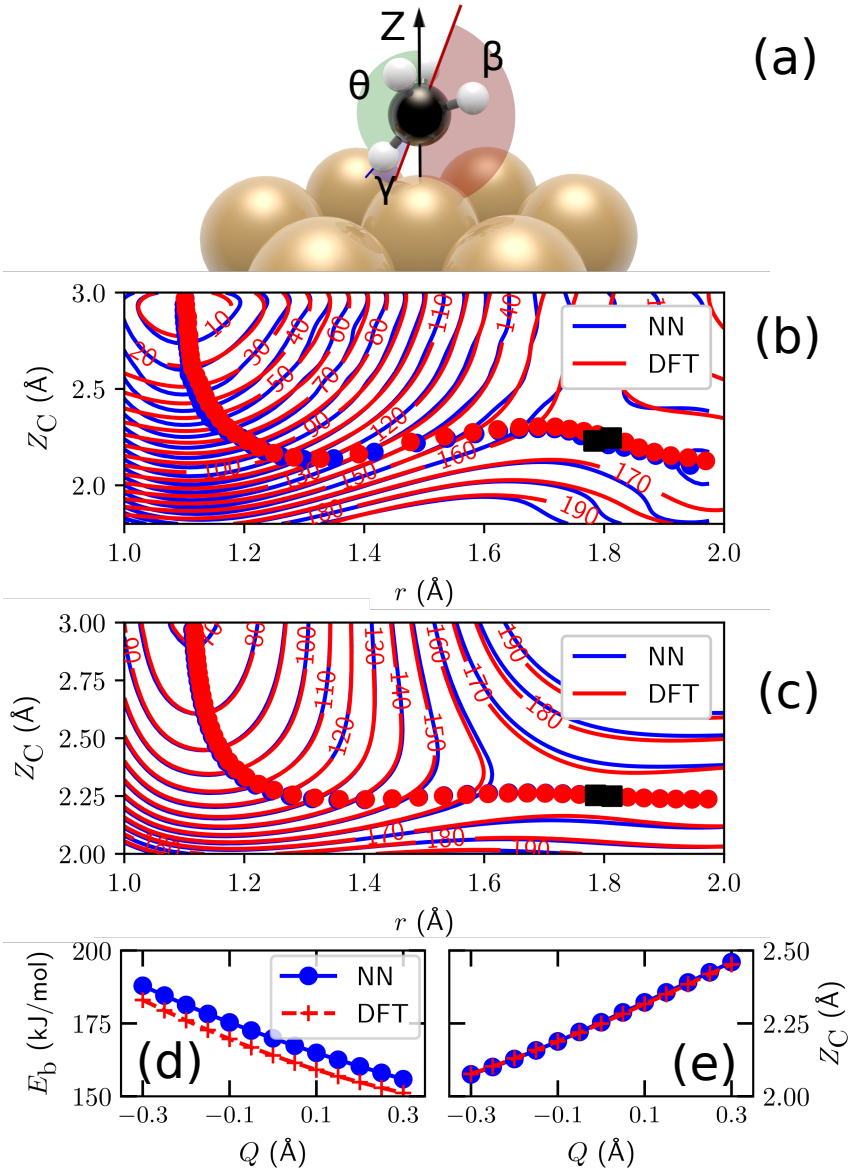


FIGURE 8.3: (a) TS geometry of methane on Cu(111), indicating the $\theta$, $\beta$ and $\gamma$ angles (see Section 7.3.1 for further explanation). (b) Elbow plot of methane on Cu(111) as a function of $Z_C$ and $r$ (distance between the carbon atom and surface, and the length of the dissociating CH-bond, respectively), where other degrees of freedom are fixed according to the TS. Contour lines are drawn at intervals of 10 kJ/mol between 0 and 200 kJ/mol. The blue and red lines are NN and DFT results, respectively. The circles indicate the MEP. (c) Same as (b), but with all degrees of freedom of the methane relaxed, except $Z_C$ and $r$. (d,e) Variation of the height (d) and location (e) of the barrier as a function of the vertical displacement $Q$ of the nearest top layer Cu atom.

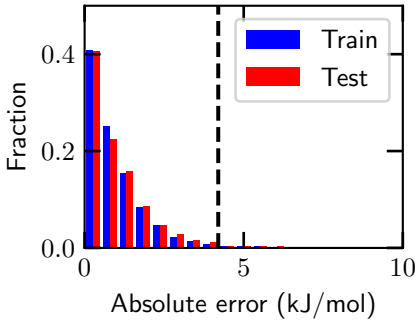


FIGURE 8.4: Distribution of absolute total energy errors (kJ/mol) of the HD-NNP compared to the DFT total energy. Blue indicates the training set, whereas red indicates the test set. The dashed line indicates chemical accuracy, i.e., 4.2 kJ/mol.

TABLE 8.2: Reaction probabilities ($P_R$) obtained with the HD-NNP and BOMD. The error bars represent 68% confidence intervals.

| $\langle E_i \rangle$ (kJ/mol) | Quantum state | $P_R$ (HD-NNP) | $P_R$ (BOMD) |
|---|---|---|---|
| 160.4 | $\nu_1 = 1$ | $0.0007 \pm 0.0002$ | $0.000 \pm 0.001$ |
| 160.4 | $\nu_1 = 2$ | $0.0246 \pm 0.0016$ | $0.024 \pm 0.005$ |
| 181.3 | $\nu_1 = 1$ | $0.0025 \pm 0.0005$ | $0.005 \pm 0.002$ |
| 181.3 | $\nu_1 = 2$ | $0.0486 \pm 0.0022$ | $0.048 \pm 0.007$ |

conditions and nozzle temperatures higher than 650 K may be unreliable due to intramolecular vibrational-energy redistribution among vibrational states in which CD bends and stretches are excited[9].

The dynamical simulations in this chapter show that the reaction of methane is promoted both by translational and vibrational energy. Plotting the reaction probability as a function of the total energy (vibrational + translational energy) shows that putting vibrational energy into the reaction is almost equally or more efficient than increasing the translational energy, depending on the amount of quanta in the $\nu_1$ CH stretch mode (see Figure 8.5b). The vibrational efficacy is equal to or larger than 0.8, which can be expected for such a late barrier system[53] combined with an MEP of the shape shown in Figure 8.3b,c, causing incoming molecules having to react over considerably higher barriers because they run off the MEP ("the bobsled effect"[54, 55]). This could play a large role at catalytic conditions, where graphene is produced from methane using very high temperatures ($> 1200$ K)[36, 41] and thus vibrational excitation is prevalent. Interestingly, the vibrational efficacy[56, 57] for the excitation from the $\nu_1 = 1$ to $\nu_1 = 2$ overtone ($\eta_{\nu_1=2,1} = 1.7$) is considerably higher than that for the excitation from the ground state to $\nu_1 = 1$ ($\eta_{\nu_1=1,0} = 0.8$). To

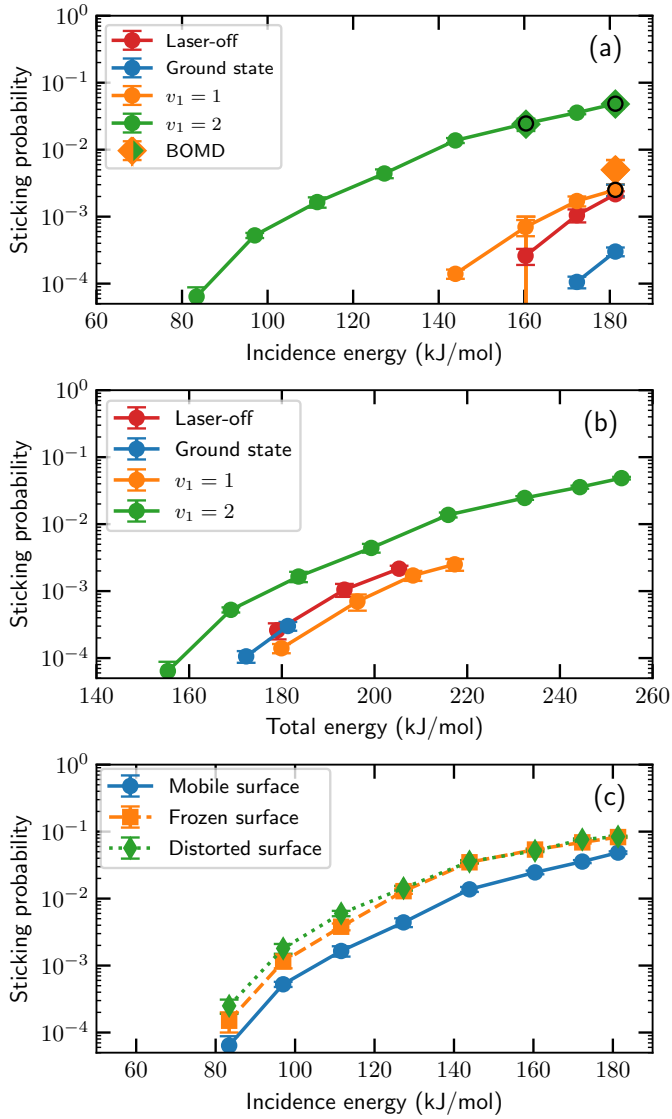


FIGURE 8.5: (a) Initial state-selected and molecular beam sticking probabilities of $CHD_3$ on Cu(111) as a function of the translational energy for a surface temperature of 550 K. Simulations for laser-off (red), rovibrational ground state (blue), $\nu_1 = 1$ (orange) and $\nu_1 = 2$ (green), where the circles and diamonds are HD-NNP and BOMD results, respectively. (b) Same as panel a, but here the reaction probability is shown as a function of the total energy (vibrational + translational energy). (c) Simulations for $\nu_1 = 2$ with (blue solid line with circles) and without surface motion, where the orange squares with a dashed line indicate an ideal surface and the green diamonds with a dotted line indicate a thermally distorted surface. The error bars represent 68% confidence intervals.

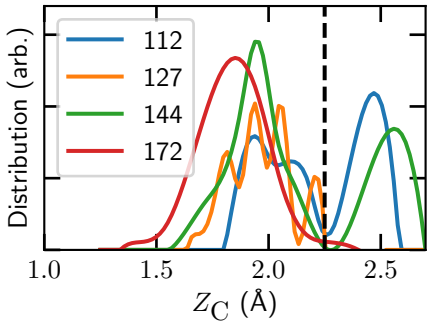


FIGURE 8.6: Distributions of the height of the carbon atom when a CH-bond dissociates (i.e., $r = r^{\ddagger}$) for $\nu_1 = 2$ at various incidence energies (numbers are in kJ/mol). The TS geometry value for $Z_C$ is indicated by the dashed line.

the best of our knowledge, a higher vibrational efficacy for an overtone has not been observed before[56–60]. In Figure 8.6, it is observed that when the incidence energy decreases, for $\nu_1 = 2$, reacted trajectories follow the MEP more closely. Furthermore, an increase of vibrational energy causes reacting trajectories to follow the MEP more closely as well (see Figure 8.7a). The dynamical effect (see Figure 8.7b) is that, because a higher incidence energy is needed to overcome the barrier for a low $\nu_1$, for low $\nu_1$ the carbon atom smashes into the repulsive wall. The hydrogen atom moves out while the carbon atom is still close to the surface, and therefore a higher barrier needs to be overcome (see Figure 8.7). Hence, a higher vibrational efficacy is observed for $\nu_1 = 2$ since the bobsled effect will be less prominent and thus lower barriers need to be overcome.

It has been already noted that the reaction probabilities at high incidence energy obtained with the HD-NNP are in good agreement with BOMD. However, the validity of the quasi-classical approximation for the low reaction probabilities needs to be tested by comparison to experiment due to the possibility of quantum effects, and potential problems with zero-point energy violation, even though it has been shown that at elevated surface temperature the reaction of methane happens in a "classical over the barrier fashion" with assistance of surface atom motion and without the need for tunneling[4, 61].

The main goal of applying the Behler-Parrinello method to polyatomic molecules is to be able to include explicitly surface motion. Therefore, to evaluate the effect of surface motion, reaction probabilities for $\nu_1 = 2$ have also been computed using a static surface model, where the surface was kept in its ideal relaxed static configuration (note that the lattice expansion corresponding to a surface temperature of 550 K was kept). This effectively removes energy transfer between the molecule and the surface and the corrugation in barrier heights and positions related to surface motion. Reaction probabilities for this

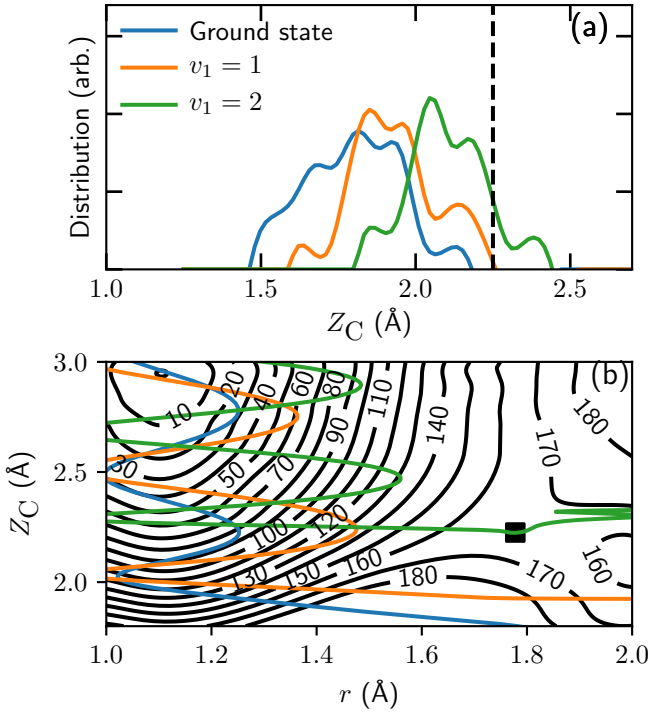


FIGURE 8.7: (a) Distributions of the height of the carbon ($Z_C$) when a CH bond dissociates, i.e., $r = r^{\ddagger}$, for the rovibrational ground state, $v_1 = 1$, and $v_1 = 2$ at incidence energies with comparable reaction probabilities (about 0.03%). The TS geometry value for $Z_C$ is indicated by the dashed line. (b) Elbow plot of methane on Cu(111) obtained with the HD-NNP, where $Z_C$ and $r$ (distance between the carbon atom and surface, and the length of the dissociating CH-bond, respectively) are variable and all other degrees of freedom are relaxed. Contour lines are drawn at intervals of 10 kJ/mol between 0 and 180 kJ/mol. Typical trajectories that go on to react for $P = 0.03\%$ are indicated by the blue (ground state), orange ($v_1 = 1$) and green ($v_1 = 2$) lines. The black square indicates the highest point along the MEP.

frozen surface are a factor 2 higher than those when surface motion is allowed (see Figure 8.5c). Furthermore, when the distortions of a hot surface are included while still excluding surface motion, i.e., modeling a static thermally disordered surface (similar to the so-called static corrugation model[62]), reaction probabilities are increased by 50% compared to the frozen ideal surface at low incidence energies. At high incidence energies, no difference is observed between the results for the static ideal and the distorted surface, with the latter including the effect of the electronic coupling (or the so-called $\beta$-coupling)[30]. The observation that explicitly including surface motion at these high incidence energies lowers the reaction probabilities suggests that the reaction probabilities are decreased due to energy transfer to the surface atoms as the molecule first impacts on the surface (Figure 8.7b) and possibly also due to surface recoil (mechanical coupling)[4, 30]. Because the surface recoil effect (which is due to surface atom vibrational averaging) tends to be small[30], it is suspected that the energy transfer is most important. This effect can only be addressed with explicit modeling of the surface motion and not by the sudden and energy averaging methods typically used with quantum dynamics simulations[30].

## 8.4 Conclusions

In this chapter the Behler-Parrinello approach is used to develop an HD-NNP that describes a polyatomic molecule reacting on a mobile metal surface, i.e., $CHD_3$ + Cu(111). The HD-NNP is found to be in good agreement with DFT, which means that MD can be performed with the accuracy of BOMD but with a considerably lower computational effort. Using this HD-NNP, reaction probabilities as low as $5 \times 10^{-5}$ have been obtained, which are untractable with previous accurate methods such as BOMD, while including surface motion. It is found that vibrational excitation plays a major role in the reactivity, where the overtone has a higher vibrational efficacy than the fundamental vibrational excitation. Moreover, allowing energy transfer from the molecule to the surface atoms considerably reduces the overall reactivity. Hence, surface motion needs to be included explicitly in simulations in order to obtain quantitative results for molecular beam simulations of methane reacting on copper. More work is still required to investigate the effect of surface temperature on the reaction of $CHD_3$ on Cu(111), since only one surface temperature (550 K) is addressed. Finally, the quasi-classical approximation needs to be tested for low reaction probabilities by comparison to experiments due to the possibility of quantum effects and zero-point energy violation. However, this would not

be an intrinsic problem of the HD-NNP as good agreement with DFT has been shown.

# Appendix

## 8.A Symmetry Functions

The parameters used for the radial and angular symmetry functions are given in Tables 8.A.1 and 8.A.2, and the cut-off radius $R_c = 13\,a_0$. Note that $\eta = 0$ for all angular symmetry functions.

## 8.B Elbow Plots

Due to the difficulty of relaxing the methane geometry in 13 degrees of freedom, a smoothing function was used for the elbow plot in Figure 8.3c and 8.7b. Figure 8.B.1 shows the elbow plot obtained with the HD-NNP in Figure 8.3c without smoothing, where the HD-NNP and direct DFT calculations are still in good agreement.

Furthermore, Figure 8.B.2 shows the elbow plots for methane on Cu(111) and Ni(111)[9]. The obtained MEPs seem very similar, where the main difference is that on Ni(111) the barrier is earlier and the barrier height is lower than on Cu(111). However, when the energy along the MEP is taken into account as well (see Figure 8.B.3), it is observed that the MEP of Cu(111) is much more repulsive. Therefore, methane needs a considerably higher energy in order to overcome the barrier, causing trajectories in general to experience the bobsled effect.

## 8.C Statistical Analysis

A statistical analysis is performed in order to see whether the HD-NNP and BOMD reaction probabilities are in agreement. Fischer's exact test[63] is used to evaluate a null hypothesis, which is defined here as $P_{\text{HD-NNP}} = P_{\text{BOMD}}$. The results obtained both with the HD-NNP and BOMD using a significance level of $\alpha = 0.05$ are in agreement, hence, the conclusion is that the reaction probabilities obtained with the HD-NNP and BOMD are in agreement.

TABLE 8.A.1: Parameters used for the radial symmetry functions (see Eq. 2.38) describing the interaction of the reference atom (Ref.) with its neighbouring atoms (Neighb.) within the cut-off radius.

| Ref. | Neighb. | $\eta$ | Ref. | Neighb. | $\eta$ | Ref. | Neighb. | $\eta$ |
|---|---|---|---|---|---|---|---|---|
| H | C | 0 | Cu | C | 0 | C | H | 0 |
| H | C | 0.007 | Cu | C | 0.007 | C | H | 0.007 |
| H | C | 0.018 | Cu | C | 0.018 | C | H | 0.018 |
| H | C | 0.036 | Cu | C | 0.035 | C | H | 0.036 |
| H | C | 0.068 | Cu | C | 0.065 | C | H | 0.068 |
| H | C | 0.13 | Cu | C | 0.12 | C | H | 0.13 |
| H | C | 0.27 | Cu | C | 0.24 | C | H | 0.27 |
| H | C | 0.7 | Cu | C | 0.55 | C | H | 0.7 |
| H | H | 0 | Cu | H | 0 | C | Cu | 0 |
| H | H | 0.007 | Cu | H | 0.007 | C | Cu | 0.007 |
| H | H | 0.018 | Cu | H | 0.018 | C | Cu | 0.018 |
| H | H | 0.035 | Cu | H | 0.035 | C | Cu | 0.035 |
| H | H | 0.065 | Cu | H | 0.068 | C | Cu | 0.065 |
| H | H | 0.12 | Cu | H | 0.13 | C | Cu | 0.12 |
| H | H | 0.24 | Cu | H | 0.27 | C | Cu | 0.24 |
| H | H | 0.55 | Cu | H | 0.7 | C | Cu | 0.55 |
| H | Cu | 0 | Cu | Cu | 0 | | | |
| H | Cu | 0.007 | Cu | Cu | 0.007 | | | |
| H | Cu | 0.018 | Cu | Cu | 0.018 | | | |
| H | Cu | 0.035 | Cu | Cu | 0.035 | | | |
| H | Cu | 0.068 | Cu | Cu | 0.065 | | | |
| H | Cu | 0.13 | Cu | Cu | 0.12 | | | |
| H | Cu | 0.27 | Cu | Cu | 0.24 | | | |
| H | Cu | 0.7 | Cu | Cu | 0.55 | | | |

TABLE 8.A.2: Parameters used for the angular symmetry functions (see Eq. 2.39) describing the interaction of the reference atom (Ref.) with its neighbouring atoms (Neighb. 1 and 2) within the cut-off radius.

| Ref. | Neighb. 1 | Neighb. 2 | $\lambda$ | $\zeta$ | Ref. | Neighb. 1 | Neighb. 2 | $\lambda$ | $\zeta$ | Ref. | Neighb. 1 | Neighb. 2 | $\lambda$ | $\zeta$ |
|---|---|---|---|---|---|---|---|---|---|---|---|---|---|---|
| H | H | H | 1 | 5 | Cu | Cu | Cu | 1 | 1 | | | | | |
| H | H | H | 1 | 7.5 | Cu | Cu | Cu | 1 | 1.7 | | | | | |
| H | H | H | 1 | 12 | Cu | Cu | Cu | 1 | 3 | | | | | |
| H | H | H | 1 | 20 | Cu | Cu | Cu | 1 | 6 | | | | | |
| H | H | H | 1 | 40 | Cu | Cu | Cu | 1 | 15 | | | | | |
| | | | | | Cu | Cu | Cu | 1 | 68 | | | | | |
| H | H | H | -1 | 1.3 | Cu | Cu | Cu | -1 | 1 | | | | | |
| H | H | H | -1 | 1.9 | Cu | Cu | Cu | -1 | 1.7 | | | | | |
| H | H | H | -1 | 2.8 | Cu | Cu | Cu | -1 | 3 | | | | | |
| H | H | H | -1 | 4.3 | Cu | Cu | Cu | -1 | 6 | | | | | |
| H | H | H | -1 | 7 | Cu | Cu | Cu | -1 | 15 | | | | | |
| H | H | C | 1 | 9 | Cu | Cu | C | 1 | 1 | | | | | |
| H | H | C | 1 | 13 | Cu | Cu | C | 1 | 1.7 | | | | | |
| H | H | C | 1 | 21 | Cu | Cu | C | 1 | 3 | | | | | |
| H | H | C | 1 | 38 | Cu | Cu | C | 1 | 6 | | | | | |
| H | H | C | 1 | 80 | Cu | Cu | C | 1 | 15 | | | | | |
| | | | | | Cu | Cu | C | 1 | 68 | | | | | |
| H | H | C | -1 | 1 | Cu | Cu | C | -1 | 1 | | | | | |
| H | H | C | -1 | 1.3 | Cu | Cu | C | -1 | 1.7 | | | | | |
| H | H | C | -1 | 1.8 | Cu | Cu | C | -1 | 3 | | | | | |
| H | H | C | -1 | 2.5 | Cu | Cu | C | -1 | 6 | | | | | |
| H | H | C | -1 | 3.5 | Cu | Cu | C | -1 | 15 | | | | | |
| H | Cu | H | 1 | 1 | Cu | H | H | 1 | 1 | C | H | H | 1 | 1.2 |
| H | Cu | H | 1 | 1.7 | Cu | H | H | 1 | 1.7 | C | H | H | 1 | 1.8 |
| H | Cu | H | 1 | 3 | Cu | H | H | 1 | 3 | C | H | H | 1 | 3 |
| H | Cu | H | 1 | 6 | Cu | H | H | 1 | 6 | C | H | H | 1 | 5.3 |
| H | Cu | H | 1 | 15 | Cu | H | H | 1 | 15 | C | H | H | 1 | 10 |
| H | Cu | H | 1 | 68 | Cu | H | H | 1 | 68 | | | | | |
| H | Cu | H | -1 | 1 | Cu | H | H | -1 | 1 | C | H | H | -1 | 5 |
| H | Cu | H | -1 | 1.7 | Cu | H | H | -1 | 1.27 | C | H | H | -1 | 8 |
| H | Cu | H | -1 | 3 | Cu | H | H | -1 | 1.65 | C | H | H | -1 | 13 |
| H | Cu | H | -1 | 6 | Cu | H | H | -1 | 2.15 | C | H | H | -1 | 23 |
| H | Cu | H | -1 | 15 | Cu | H | H | -1 | 2.9 | C | H | H | -1 | 50 |
| H | Cu | H | -1 | 68 | Cu | H | H | -1 | 4 | | | | | |
| H | Cu | C | 1 | 1 | Cu | H | C | 1 | 1 | C | H | Cu | 1 | 1 |
| H | Cu | C | 1 | 1.7 | Cu | H | C | 1 | 1.7 | C | H | Cu | 1 | 1.7 |
| H | Cu | C | 1 | 3 | Cu | H | C | 1 | 3 | C | H | Cu | 1 | 3 |
| H | Cu | C | 1 | 6 | Cu | H | C | 1 | 6 | C | H | Cu | 1 | 6 |
| H | Cu | C | 1 | 15 | Cu | H | C | 1 | 15 | C | H | Cu | 1 | 15 |
| H | Cu | C | 1 | 68 | Cu | H | C | 1 | 68 | C | H | Cu | 1 | 68 |
| H | Cu | C | -1 | 1 | Cu | H | C | -1 | 1 | C | H | Cu | -1 | 1 |
| H | Cu | C | -1 | 1.27 | Cu | H | C | -1 | 1.27 | C | H | Cu | -1 | 1.27 |
| H | Cu | C | -1 | 1.65 | Cu | H | C | -1 | 1.65 | C | H | Cu | -1 | 1.65 |
| H | Cu | C | -1 | 2.15 | Cu | H | C | -1 | 2.15 | C | H | Cu | -1 | 2.15 |
| H | Cu | C | -1 | 2.9 | Cu | H | C | -1 | 2.9 | C | H | Cu | -1 | 2.9 |
| H | Cu | C | -1 | 4 | Cu | H | C | -1 | 4 | C | H | Cu | -1 | 4 |
| H | Cu | Cu | 1 | 1 | Cu | Cu | H | 1 | 1 | C | Cu | Cu | 1 | 1 |
| H | Cu | Cu | 1 | 1.7 | Cu | Cu | H | 1 | 1.7 | C | Cu | Cu | 1 | 1.7 |
| H | Cu | Cu | 1 | 3 | Cu | Cu | H | 1 | 3 | C | Cu | Cu | 1 | 3 |
| H | Cu | Cu | 1 | 6 | Cu | Cu | H | 1 | 6 | C | Cu | Cu | 1 | 6 |
| H | Cu | Cu | 1 | 15 | Cu | Cu | H | 1 | 15 | C | Cu | Cu | 1 | 15 |
| H | Cu | Cu | 1 | 68 | Cu | Cu | H | 1 | 68 | C | Cu | Cu | 1 | 68 |
| H | Cu | Cu | -1 | 1 | Cu | Cu | H | -1 | 1 | C | Cu | Cu | -1 | 1 |
| H | Cu | Cu | -1 | 1.27 | Cu | Cu | H | -1 | 1.7 | C | Cu | Cu | -1 | 1.27 |
| H | Cu | Cu | -1 | 1.65 | Cu | Cu | H | -1 | 3 | C | Cu | Cu | -1 | 1.65 |
| H | Cu | Cu | -1 | 2.15 | Cu | Cu | H | -1 | 6 | C | Cu | Cu | -1 | 2.15 |
| H | Cu | Cu | -1 | 2.9 | Cu | Cu | H | -1 | 15 | C | Cu | Cu | -1 | 2.9 |
| H | Cu | Cu | -1 | 4 | Cu | Cu | H | -1 | 68 | C | Cu | Cu | -1 | 4 |

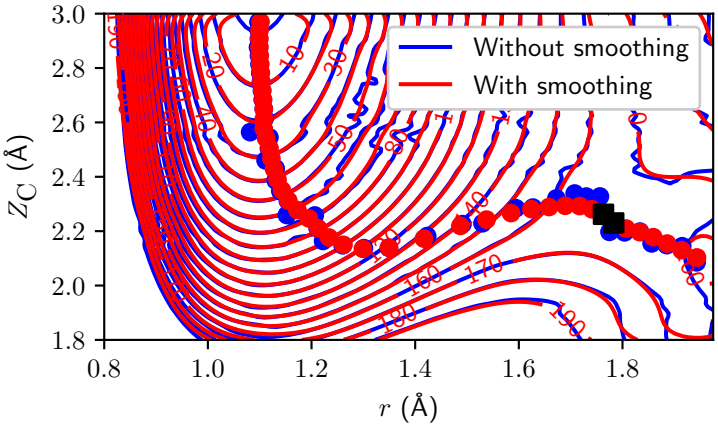


FIGURE 8.B.1: Elbow plot of methane on Cu(111) obtained with the HD-NNP with (red) and without (blue) smoothing, where $Z_C$ and $r$ (distance between the carbon atom and surface, and the length of the dissociating CH bond, respectively) are variable. Contour lines are drawn at intervals of 10 kJ/mol between 0 and 200 kJ/mol. The circles indicate the MEP and the black squares indicate the highest point along the MEPs.

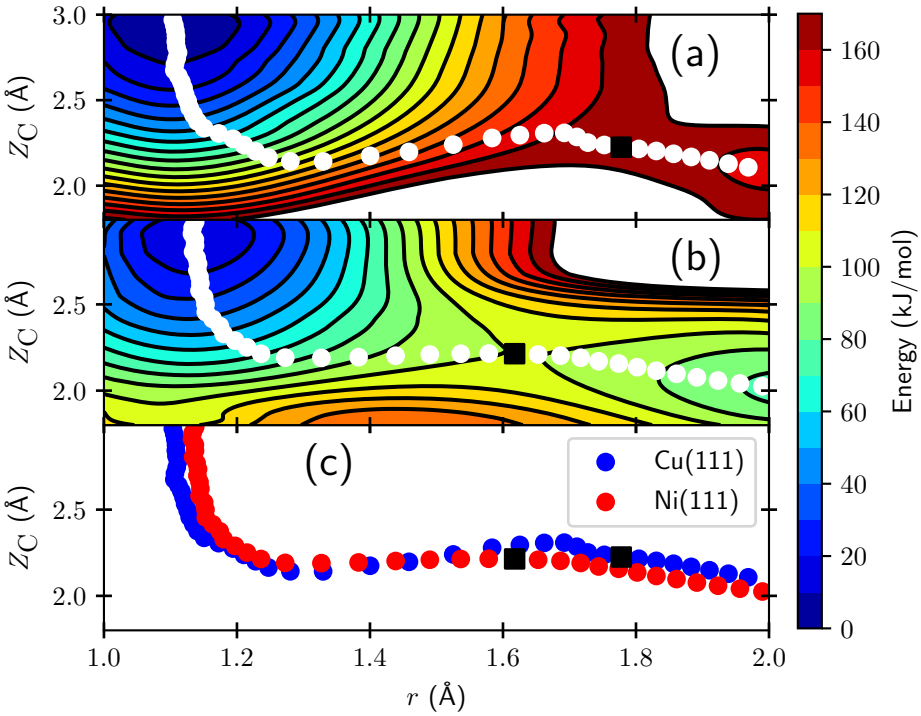


FIGURE 8.B.2: (a) Elbow plot of methane on Cu(111) obtained with the HD-NNP, where $Z$ and $r$ (distance between the carbon atom and surface, and the length of the dissociating CH bond, respectively) are variable and all other degrees of freedom are relaxed. Contour lines are drawn at intervals of 10 kJ/mol between 0 and 180 kJ/mol. The white circles indicate the MEP and the black square indicates the highest point along the MEP. (b) Same as (a) but for methane on Ni(111)[9]. (c) The MEPs for (a) (blue) and (b) (red).

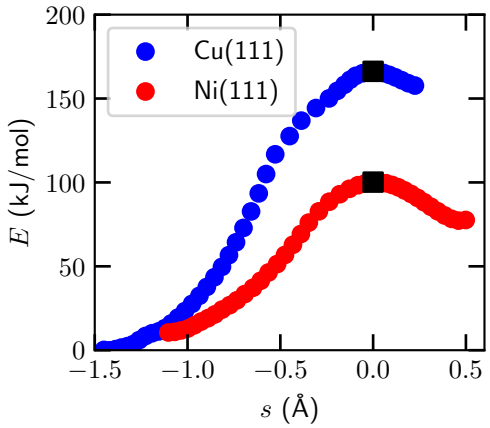


FIGURE 8.B.3: Minimum energy path of methane on Cu(111) (blue) and Ni(111) (red) as a function of the reaction coordinate $s$. The black squares indicate indicate the highest points along the MEPs.

# References


(1) Ertl, G. Primary Steps in Catalytic Synthesis of Ammonia. *J. Vac. Sci. Technol. A* **1983**, *1*, 1247–1253, DOI: 10.1116/1.572299.

(2) Wei, J.; Iglesia, E. Mechanism and Site Requirements for Activation and Chemical Conversion of Methane on Supported Pt Clusters and Turnover Rate Comparisons among Noble Metals. *J. Phys. Chem. B* **2004**, *108*, 4094–4103, DOI: 10.1021/jp036985z.

(3) Kroes, G.-J. Towards Chemically Accurate Simulation of Molecule–Surface Reactions. *Phys. Chem. Chem. Phys.* **2012**, *14*, 14966–14981, DOI: 10.1039/C2CP42471A.

(4) Jackson, B.; Nattino, F.; Kroes, G.-J. Dissociative Chemisorption of Methane on Metal Surfaces: Tests of Dynamical Assumptions Using Quantum Models and Ab Initio Molecular Dynamics. *J. Chem. Phys.* **2014**, *141*, 054102, DOI: 10.1063/1.4891327.

(5) Wellendorff, J.; Silbaugh, T. L.; Garcia-Pintos, D.; Nørskov, J. K.; Bligaard, T.; Studt, F.; Campbell, C. T. A Benchmark Database for Adsorption Bond Energies to Transition Metal Surfaces and Comparison to Selected DFT Functionals. *Surf. Sci.* **2015**, *640*, 36–44, DOI: 10.1016/j.susc.2015.03.023.

(6) Gautier, S.; Steinmann, S. N.; Michel, C.; Fleurat-Lessard, P.; Sautet, P. Molecular Adsorption at Pt(111). How Accurate Are DFT Functionals? *Phys. Chem. Chem. Phys.* **2015**, *17*, 28921–28930, DOI: 10.1039/C5CP04534G.

(7) Kroes, G.-J. Toward a Database of Chemically Accurate Barrier Heights for Reactions of Molecules with Metal Surfaces. *J. Phys. Chem. Lett.* **2015**, *6*, 4106–4114, DOI: 10.1021/acs.jpclett.5b01344.

(8) Füchsel, G.; Zhou, X.; Jiang, B.; Juaristi, J. I.; Alducin, M.; Guo, H.; Kroes, G.-J. Reactive and Nonreactive Scattering of HCl from Au(111): An Ab Initio Molecular Dynamics Study. *J. Phys. Chem. C* **2019**, *123*, 2287–2299, DOI: 10.1021/acs.jpcc.8b10686.

(9) Nattino, F.; Migliorini, D.; Kroes, G.-J.; Dombrowski, E.; High, E. A.; Killelea, D. R.; Utz, A. L. Chemically Accurate Simulation of a Polyatomic Molecule-Metal Surface Reaction. *J. Phys. Chem. Lett.* **2016**, *7*, 2402–2406, DOI: 10.1021/acs.jpclett.6b01022.

(10) Migliorini, D.; Chadwick, H.; Nattino, F.; Gutiérrez-González, A.; Dombrowski, E.; High, E. A.; Guo, H.; Utz, A. L.; Jackson, B.; Beck, R. D.; Kroes, G.-J. Surface Reaction Barriometry: Methane Dissociation on Flat and Stepped Transition-Metal Surfaces. *J. Phys. Chem. Lett.* **2017**, *8*, 4177–4182, DOI: 10.1021/acs.jpclett.7b01905.

(11) Chadwick, H.; Gutiérrez-González, A.; Migliorini, D.; Beck, R. D.; Kroes, G.-J. Incident Angle Dependence of $CHD_3$ Dissociation on the Stepped Pt(211) Surface. *J. Phys. Chem. C* **2018**, *122*, 19652–19660, DOI: 10.1021/acs.jpcc.8b05887.

(12) Gerrits, N.; Migliorini, D.; Kroes, G.-J. Dissociation of $CHD_3$ on Cu(111), Cu(211), and Single Atom Alloys of Cu(111). *J. Chem. Phys.* **2018**, *149*, 224701, DOI: 10.1063/1.5053990.

(13) Shakouri, K.; Behler, J.; Meyer, J.; Kroes, G.-J. Accurate Neural Network Description of Surface Phonons in Reactive Gas–Surface Dynamics: $N_2$ + Ru(0001). *J. Phys. Chem. Lett.* **2017**, *8*, 2131–2136, DOI: 10.1021/acs.jpclett.7b00784.

(14) Kolb, B.; Luo, X.; Zhou, X.; Jiang, B.; Guo, H. High-Dimensional Atomistic Neural Network Potentials for Molecule–Surface Interactions: HCl Scattering from Au(111). *J. Phys. Chem. Lett.* **2017**, *8*, 666–672, DOI: 10.1021/acs.jpclett.6b02994.

(15) Shakouri, K.; Behler, J.; Meyer, J.; Kroes, G.-J. Analysis of Energy Dissipation Channels in a Benchmark System of Activated Dissociation: $N_2$ on Ru(0001). *J. Phys. Chem. C* **2018**, *122*, 23470–23480, DOI: 10.1021/acs.jpcc.8b06729.

(16) Liu, Q.; Zhou, X.; Zhou, L.; Zhang, Y.; Luo, X.; Guo, H.; Jiang, B. Constructing High-Dimensional Neural Network Potential Energy Surfaces for Gas–Surface Scattering and Reactions. *J. Phys. Chem. C* **2018**, *122*, 1761–1769, DOI: 10.1021/acs.jpcc.7b12064.

(17) Jiang, B.; Guo, H. Dynamics of Water Dissociative Chemisorption on Ni(111): Effects of Impact Sites and Incident Angles. *Phys. Rev. Lett.* **2015**, *114*, 166101, DOI: 10.1103/PhysRevLett.114.166101.

(18) Shen, X.; Chen, J.; Zhang, Z.; Shao, K.; Zhang, D. H. Methane Dissociation on Ni(111): A Fifteen-Dimensional Potential Energy Surface Using Neural Network Method. *J. Chem. Phys.* **2015**, *143*, 144701, DOI: 10.1063/1.4932226.

(19) Zhou, X.; Nattino, F.; Zhang, Y.; Chen, J.; Kroes, G.-J.; Guo, H.; Jiang, B. Dissociative Chemisorption of Methane on Ni(111) Using a Chemically Accurate Fifteen Dimensional Potential Energy Surface. *Phys. Chem. Chem. Phys.* **2017**, *19*, 30540–30550, DOI: 10.1039/C7CP05993K.

(20) Hu, X.; Yang, M.; Xie, D.; Guo, H. Vibrational Enhancement in the Dynamics of Ammonia Dissociative Chemisorption on Ru(0001). *J. Chem. Phys.* **2018**, *149*, 044703, DOI: 10.1063/1.5043517.

(21) Chen, J.; Zhou, X.; Zhang, Y.; Jiang, B. Vibrational Control of Selective Bond Cleavage in Dissociative Chemisorption of Methanol on Cu(111). *Nat. Commun.* **2018**, *9*, 4039, DOI: 10.1038/s41467-018-06478-6.

(22) Zhang, Y.; Zhou, X.; Jiang, B. Bridging the Gap between Direct Dynamics and Globally Accurate Reactive Potential Energy Surfaces Using Neural Networks. *J. Phys. Chem. Lett.* **2019**, *10*, 1185–1191, DOI: 10.1021/acs.jpclett.9b00085.

(23) Tiwari, A. K.; Nave, S.; Jackson, B. The Temperature Dependence of Methane Dissociation on Ni(111) and Pt(111): Mixed Quantum-Classical Studies of the Lattice Response. *J. Chem. Phys.* **2010**, *132*, 134702, DOI: 10.1063/1.3357415.

(24) Nattino, F.; Díaz, C.; Jackson, B.; Kroes, G.-J. Effect of Surface Motion on the Rotational Quadrupole Alignment Parameter of $D_2$ Reacting on Cu(111). *Phys. Rev. Lett.* **2012**, *108*, 236104, DOI: 10.1103/PhysRevLett.108.236104.

(25) Mondal, A.; Wijzenbroek, M.; Bonfanti, M.; Díaz, C.; Kroes, G.-J. Thermal Lattice Expansion Effect on Reactive Scattering of $H_2$ from Cu(111) at $T_s$ = 925 K. *J. Phys. Chem. A* **2013**, *117*, 8770–8781, DOI: 10.1021/jp4042183.

(26) Füchsel, G.; del Cueto, M.; Díaz, C.; Kroes, G.-J. Enigmatic HCl + Au(111) Reaction: A Puzzle for Theory and Experiment. *J. Phys. Chem. C* **2016**, *120*, 25760–25779, DOI: 10.1021/acs.jpcc.6b07453.

(27) Gerrits, N.; Kroes, G.-J. An AIMD Study of Dissociative Chemisorption of Methanol on Cu(111) with Implications for Formaldehyde Formation. *J. Chem. Phys.* **2019**, *150*, 024706, DOI: 10.1063/1.5070129.

(28) Zhou, X.; Jiang, B. A Modified Generalized Langevin Oscillator Model for Activated Gas-Surface Reactions. *J. Chem. Phys.* **2019**, *150*, 024704, DOI: 10.1063/1.5078541.

(29) Baule, B. Theoretische Behandlung Der Erscheinungen in Verdünnten Gasen. *Ann. Phys.* **1914**, *349*, 145–176, DOI: 10.1002/andp.19143490908.

(30) Guo, H.; Farjamnia, A.; Jackson, B. Effects of Lattice Motion on Dissociative Chemisorption: Toward a Rigorous Comparison of Theory with Molecular Beam Experiments. *J. Phys. Chem. Lett.* **2016**, *7*, 4576–4584, DOI: 10.1021/acs.jpclett.6b01948.

(31) Frankcombe, T. J. Interpolating DFT Data for 15D Modeling of Methane Dissociation on an Fcc Metal. *Int. J. Chem. Kinet.* **2018**, *50*, 285–293, DOI: 10.1002/kin.21157.

(32) Shen, X. J.; Lozano, A.; Dong, W.; Busnengo, H. F.; Yan, X. H. Towards Bond Selective Chemistry from First Principles: Methane on Metal Surfaces. *Phys. Rev. Lett.* **2014**, *112*, 046101, DOI: 10.1103/PhysRevLett.112.046101.

(33) Lozano, A.; Shen, X. J.; Moiraghi, R.; Dong, W.; Busnengo, H. F. Cutting a Chemical Bond with Demon's Scissors: Mode- and Bond-Selective Reactivity of Methane on Metal Surfaces. *Surf. Sci.* **2015**, *640*, 25–35, DOI: 10.1016/j.susc.2015.04.002.

(34) Seminara, G. N.; Peludhero, I. F.; Dong, W.; Martínez, A. E.; Busnengo, H. F. Molecular Dynamics Study of Molecular and Dissociative Adsorption Using System-Specific Force Fields Based on Ab Initio Calculations: CO/Cu(110) and $$\text {CH_4/\text {Pt(110)$$CH4/Pt(110). *Top. Catal.* **2019**, *62*, 1044–1052, DOI: 10.1007/s11244-019-01196-9.

(35) Moiraghi, R.; Lozano, A.; Peterson, E.; Utz, A.; Dong, W.; Busnengo, H. F. Nonthermalized Precursor-Mediated Dissociative Chemisorption at High Catalysis Temperatures. *J. Phys. Chem. Lett.* **2020**, *11*, 2211–2218, DOI: 10.1021/acs.jpclett.0c00260.

(36) Li, X.; Cai, W.; An, J.; Kim, S.; Nah, J.; Yang, D.; Piner, R.; Velamakanni, A.; Jung, I.; Tutuc, E.; Banerjee, S. K.; Colombo, L.; Ruoff, R. S. Large-Area Synthesis of High-Quality and Uniform Graphene Films on Copper Foils. *Science* **2009**, *324*, 1312–1314, DOI: 10.1126/science.1171245.

(37) Losurdo, M.; Giangregorio, M. M.; Capezzuto, P.; Bruno, G. Graphene CVD Growth on Copper and Nickel: Role of Hydrogen in Kinetics and Structure. *Phys. Chem. Chem. Phys.* **2011**, *13*, 20836–20843, DOI: 10.1039/C1CP22347J.

(38) Zhang, W.; Wu, P.; Li, Z.; Yang, J. First-Principles Thermodynamics of Graphene Growth on Cu Surfaces. *J. Phys. Chem. C* **2011**, *115*, 17782–17787, DOI: 10.1021/jp2006827.

(39) Li, K.; He, C.; Jiao, M.; Wang, Y.; Wu, Z. A First-Principles Study on the Role of Hydrogen in Early Stage of Graphene Growth during the $CH_4$ Dissociation on Cu(111) and Ni(111) Surfaces. *Carbon* **2014**, *74*, 255–265, DOI: 10.1016/j.carbon.2014.03.030.

(40) Wang, X.; Yuan, Q.; Li, J.; Ding, F. The Transition Metal Surface Dependent Methane Decomposition in Graphene Chemical Vapor Deposition Growth. *Nanoscale* **2017**, *9*, 11584–11589, DOI: 10.1039/C7NR02743E.

(41) Kraus, J.; Böbel, L.; Zwaschka, G.; Günther, S. Understanding the Reaction Kinetics to Optimize Graphene Growth on Cu by Chemical Vapor Deposition. *Ann. Phys.* **2017**, *529*, 1700029, DOI: 10.1002/andp.201700029.

(42) Tian, B.; Liu, T.; Yang, Y.; Li, K.; Wu, Z.; Wang, Y. $CH_4$ Dissociation in the Early Stage of Graphene Growth on Fe–Cu(100) Surface: Theoretical Insights. *Appl. Surf. Sci.* **2018**, *427*, 953–960, DOI: 10.1016/j.apsusc.2017.09.088.

(43) Rettner, C. T.; Auerbach, D. J.; Lee, J. Dynamics of the Formation of $CD_4$ from the Direct Reaction of Incident D Atoms with $CD_3$/Cu(111). *J. Chem. Phys.* **1996**, *105*, 10115–10122, DOI: 10.1063/1.472840.

(44) Behler, J.; Parrinello, M. Generalized Neural-Network Representation of High-Dimensional Potential-Energy Surfaces. *Phys. Rev. Lett.* **2007**, *98*, 146401, DOI: 10.1103/PhysRevLett.98.146401.

(45) Behler, J. Representing Potential Energy Surfaces by High-Dimensional Neural Network Potentials. *J. Phys.: Condens. Matter* **2014**, *26*, 183001, DOI: 10.1088/0953-8984/26/18/183001.

(46) Behler, J. Atom-Centered Symmetry Functions for Constructing High-Dimensional Neural Network Potentials. *J. Chem. Phys.* **2011**, *134*, 074106, DOI: 10.1063/1.3553717.

(47) Behler, J. Constructing High-Dimensional Neural Network Potentials: A Tutorial Review. *Int. J. Quantum Chem.* **2015**, *115*, 1032–1050, DOI: 10.1002/qua.24890.

(48) Behler, J. First Principles Neural Network Potentials for Reactive Simulations of Large Molecular and Condensed Systems. *Angew. Chem. Int. Ed.* **2017**, *56*, 12828–12840, DOI: 10.1002/anie.201703114.

(49) Behler, J. RuNNer - A Neural Network Code for High-Dimensional Neural Network Potential-Energy Surfaces; Universität Göttingen http://www.uni-goettingen.de/de/560580.html (accessed 02/14/2019).

(50) Plimpton, S. Fast Parallel Algorithms for Short-Range Molecular Dynamics. *J. Comput. Phys.* **1995**, *117*, 1–19, DOI: 10.1006/jcph.1995.1039.

(51) Singraber, A.; Behler, J.; Dellago, C. Library-Based LAMMPS Implementation of High-Dimensional Neural Network Potentials. *J. Chem. Theory Comput.* **2019**, *15*, 1827–1840, DOI: 10.1021/acs.jctc.8b00770.

(52) Hundt, P. M.; Jiang, B.; van Reijzen, M. E.; Guo, H.; Beck, R. D. Vibrationally Promoted Dissociation of Water on Ni(111). *Science* **2014**, *344*, 504–507, DOI: 10.1126/science.1251277.

(53) Polanyi, J. C. Concepts in Reaction Dynamics. *Acc. Chem. Res.* **1972**, *5*, 161–168, DOI: 10.1021/ar50053a001.

(54) Marcus, R. A. On the Analytical Mechanics of Chemical Reactions. Quantum Mechanics of Linear Collisions. *J. Chem. Phys.* **1966**, *45*, 4493–4499, DOI: 10.1063/1.1727528.

(55) McCullough, E. A.; Wyatt, R. E. Quantum Dynamics of the Collinear (H, $H_2$) Reaction. *J. Chem. Phys.* **1969**, *51*, 1253–1254, DOI: 10.1063/1.1672133.

(56) Jiang, B.; Yang, M.; Xie, D.; Guo, H. Quantum Dynamics of Polyatomic Dissociative Chemisorption on Transition Metal Surfaces: Mode Specificity and Bond Selectivity. *Chem. Soc. Rev.* **2016**, *45*, 3621–3640, DOI: 10.1039/C5CS00360A.

(57) Juurlink, L. B. F.; Killelea, D. R.; Utz, A. L. State-Resolved Probes of Methane Dissociation Dynamics. *Prog. Surf. Sci.* **2009**, *84*, 69–134, DOI: 10.1016/j.progsurf.2009.01.001.

(58) Schmid, M. P.; Maroni, P.; Beck, R. D.; Rizzo, T. R. Surface Reactivity of Highly Vibrationally Excited Molecules Prepared by Pulsed Laser Excitation: $CH_4$ ($2\nu_3$) on Ni(100). *J. Chem. Phys.* **2002**, *117*, 8603–8606, DOI: 10.1063/1.1519860.

(59) Guo, H.; Jackson, B. Mode-Selective Chemistry on Metal Surfaces: The Dissociative Chemisorption of $CH_4$ on Pt(111). *J. Chem. Phys.* **2016**, *144*, 184709, DOI: 10.1063/1.4948941.

(60) Farjamnia, A.; Jackson, B. The Dissociative Chemisorption of Water on Ni(111): Mode- and Bond-Selective Chemistry on Metal Surfaces. *J. Chem. Phys.* **2015**, *142*, 234705, DOI: 10.1063/1.4922625.

(61) Campbell, V. L.; Chen, N.; Guo, H.; Jackson, B.; Utz, A. L. Substrate Vibrations as Promoters of Chemical Reactivity on Metal Surfaces. *J. Phys. Chem. A* **2015**, *119*, 12434–12441, DOI: 10.1021/acs.jpca.5b07873.

(62) Spiering, P.; Wijzenbroek, M.; Somers, M. F. An Improved Static Corrugation Model. *J. Chem. Phys.* **2018**, *149*, 234702, DOI: 10.1063/1.5058271.

(63) Fisher, R. A. On the Interpretation of $X^2$ from Contingency Tables, and the Calculation of P. *J. R. Stat. Soc.* **1922**, *85*, 87–94, DOI: 10.2307/2340521.

# Chapter 9

# Dissociative Chemisorption of $CHD_3$ on Pd(111)

This chapter is based on Gerrits, N.; Chadwick, H.; Kroes, G.-J. Dynamical Study of the Dissociative Chemisorption of $CHD_3$ on Pd(111). *J. Phys. Chem. C* **2019**, *123*, 24013–24023, DOI: 10.1021/acs.jpcc.9b05757

## Abstract

The specific reaction parameter (SRP) approach to density functional theory has been shown to model reactions of polyatomic molecules with metal surfaces important for heterogeneous catalysis in industry with chemical accuracy. However, transferability of the SRP functional among systems in which methane interacts with group 10 metals remains unclear for methane + Pd(111). Therefore, in this chapter, predictions have been made for the reaction of $CHD_3$ on Pd(111) using Born-Oppenheimer molecular dynamics, while also performing a rough comparison with experimental data for $CH_4$ + Pd(111) obtained for lower incidence energies. Hopefully, future experiments can test the transferability of the SRP functional among group 10 metals also for Pd(111). It has been found that the reactivity of $CHD_3$ on Pd(111) is intermediate between and similar to either Pt(111) or Ni(111), depending on the incidence energy and the initial vibrational state distribution. This is surprising because the barrier height and experiments performed at lower incidence energies than investigated here suggest that the reactivity of Pd(111) should be similar to that of Pt(111) only. The relative decrease in the reactivity of Pd(111) at high incidence energies can be understood from the site specificity of the reaction and from dynamical effects such as the bobsled effect and energy transfer from methane to the surface.

## 9.1 Introduction

An important heterogeneously catalyzed industrial process is steam reforming, where methane and steam react over a metal catalyst (typically Ni[1]) and subsequently form carbon monoxide and hydrogen. At high temperature, the dissociation of methane, i.e., breaking the first CH bond, is a rate-controlling state in steam reforming on a wide variety of metals[2, 3]. Therefore, a detailed study of the CH bond breaking is warranted in order to improve catalysts. However, the reaction of molecules on metal surfaces remains difficult to simulate due to the complexity of molecule-metal surface interactions[4–8]. The so-called specific reaction parameter (SRP) approach to density functional theory (DFT), though, has been shown to provide chemically accurate results, i.e., with errors smaller than 1 kcal/mol (4.2 kJ/mol), for a number of molecule-metal surface reactions[9–14].

Within the SRP-DFT approach, two density functionals are mixed, of which one overestimates and one underestimates the reaction probability, according to an empirically determined parameter in order to create an SRP functional. Recently, an SRP functional was developed (the SRP32-vdW functional) that gave chemically accurate results not only for the molecule-metal surface reaction it was developed for ($CHD_3$ + Ni(111)[12]), but also for methane interacting with a metal from the same periodic table group ($CHD_3$ + Pt(111)[13]) and with a stepped surface of Pt ($CHD_3$ + Pt(211)[13–15]). However, it remains unclear whether this transferability is common among all group 10 metals. Therefore, in this chapter, predictive Born-Oppenheimer molecular dynamics (BOMD) calculations have been performed for $CHD_3$ + Pd(111) with the SRP32-vdW functional in the hope that future experiments will test the transferability of the SRP functional describing methane interacting with all group 10 metal surfaces. Although in previous work direct dynamics calculations with SRP functionals is usually referred to as "ab initio molecular dynamics" (AIMD) calculations, the wording of the method is changed here from AIMD to BOMD as "ab initio" can be misleading in the context of calculations based on a semi-empirical density functional.

To ensure the validity of the BOMD method, conditions are adressed for which the total energy of the molecule (translational + vibrational) exceeds the minimum zero-point energy corrected barrier height of the system addressed. This ensures that the accuracy of the quasi-classical trajectory (QCT) method used in the BOMD dynamics is not much affected by quantum effects like tunneling, and classical artifacts like zero-point energy violation[16, 17]. Second, for laser-off conditions, only conditions are adressed where at least 60% of the incident $CHD_3$ is in its initial vibrational ground state, and in predictions

for initial-state selective reaction only CH stretch excited $CHD_3$ is adressed, to avoid problems with artificial intramolecular vibrational redistribution (IVR) that might otherwise affect QCT calculations[18, 19]. Third, the surface temperature employed (here, 500 K) is well above the surface Debye temperature ((140 ± 10) K for Pd(111))[20], thereby ensuring that the energy transfer between the molecule and surface can be well described with quasi-classical dynamics[13, 21, 22].

Also, a rough comparison is performed with existing experimental data for $CH_4$ + Pd(111)[23], although a direct comparison is not possible due to the low experimental reaction probabilities making BOMD calculations untractable and the employed high nozzle temperatures for which BOMD performs badly due to IVR among excited vibrational states[12].

Alloys are of special interest for catalysts[24] as they can increase both reactivity and selectivity[25]. For example, by combining a highly active metal like Pt with a less reactive metal such as Cu, a catalyst with a high activity and selectivity can be produced, without the typical issues such as catalyst poisoning[26]. The work in Chapter 7 has predicted that the Pt-Cu(111) single-atom alloy is considerably more reactive than Pd-Cu(111), even though the barrier height difference is only 8.4 kJ/mol. It was suggested that dynamical effects such as the "bobsled effect"[27, 28] played a major role in the relatively lower reactivity of Pd-Cu(111) compared to that of Pt-Cu(111)[29]. The so-called bobsled effect causes molecules with a high incidence energy to slide off the minimum energy path (MEP) for late barrier systems as the molecule is not able to make the turn in front of the barrier on the potential energy surface (PES) and therefore needs to overcome a higher barrier than the lowest barrier available[27, 28]. Since it was shown that the barrier geometries and potential energy surfaces (PES) above the doped atoms were similar to those found for the pure (111) surfaces of the respective doped elements, these dynamical effects can also be investigated by comparing methane interacting with Pd(111) and Pt(111).

The reaction of methane on metal surfaces remains fundamentally important due to many dynamically interesting effects. For example, in partially deuterated methane, the CH bond can selectively be broken by exciting the CH stretch mode[12, 13, 30–33]. Also, the dissociative chemisorption of methane is vibrational-mode-specific[34, 35] and the mode specificity is dependent on the metal surface[35–37]. Moreover, steric effects play a significant role[38]. Finally, the reaction of methane is site specific[2, 13, 15, 39]. For all of these reasons, in this chapter a detailed analysis is presented of the results from the BOMD calculations on the dissociative chemisorption of $CHD_3$ on Pd(111), and a comparison is made to the results obtained on Pt(111) and Ni(111).

## 9.2 Method

For the BOMD and electronic structure (DFT) calculations, the Vienna Ab-initio Simulation Package (VASP version 5.3.5)[40–44] is used. The first Brillouin zone is sampled by a Γ-centered $6 \times 6 \times 1$ $k$-point grid and the plane wave basis set kinetic energy cutoff is 400 eV. Moreover, the core electrons have been represented with the projector augmented wave (PAW) method[44, 45]. The surface is modeled using a 4 layer ($3 \times 3$) supercell, where the top three layers have been relaxed in the $Z$ direction and a vacuum distance of 13 Å is used between the slabs. Due to the computational cost, a small vacuum distance (i.e., 13 Å) is required, which effectively raises the barrier height by 4.9 kJ/mol. Therefore, 4.9 kJ/mol is added to the translational energy to counteract this shift (see Section 2.4.2). To speed up convergence, first-order Methfessel-Paxton smearing[46] with a width parameter of 0.2 eV has been applied. The employed computational setup is confirmed to be converged within chemical accuracy (4.2 kJ/mol), as shown by the convergence tests provided in Section 9.A.

The transition state (TS) is obtained with the dimer method[47–50] as implemented in the VASP Transition State Tools package (VTST)[51], and is confirmed to be a first-order saddle point. Forces are converged within 5 meV/Å, where only the methane is relaxed.

The SRP32-vdW functional is employed, which has been previously used for $CHD_3$ + Ni(111), Pt(111), Pt(211), Pt(110), Pt(210), Cu(111) and Cu(211) as well[12–14, 29, 52–55]. The exchange functional is defined as

$$E_x = x \cdot E_x^{RPBE} + (1 - x) \cdot E_x^{PBE}, \tag{9.1}$$

where $E_x^{PBE}$ and $E_x^{RPBE}$ are the exchange parts of the Perdew, Burke and Ernzerhof (PBE)[56] and revised PBE (RPBE)[57] exchange-correlation functionals, respectively, and $x = 0.32$. Since it has been shown that modeling Van der Waals interactions is vital for describing the reaction of methane on a metal surface[13, 14], the vdW correlation functional of Dion and coworkers (vdW-DF1)[58] is used.

A surface temperature of 500 K is simulated in the BOMD calculations, where the atoms in the top three layers are allowed to move and the expansion of the bulk due to the surface temperature is simulated by expanding the computed ideal lattice constant[59] (3.99 Å) by a factor of 1.0049[60]. The parameters used to simulate the molecular beams are taken from Ref. [13] (see Table 9.1), which describes experiments performed for $CHD_3$ + Pt(111), except for Ni(111) at $\langle E_i \rangle = 101.1$ kJ/mol, for which the parameters are taken

TABLE 9.1: Experimental beam parameters that describe the simulated $CHD_3$ velocity distributions for Pt(111). $\nu_0$ and $\alpha$ are determined through time-of-flight measurements[13]. For $T_n = 550$ K the parameters are taken from Ref. [12] for Ni(111).

| $T_n$ (K) | $\langle E_i \rangle$ kJ/mol | $\nu_0$ (m/s) | $\alpha$ (m/s) |
|---|---|---|---|
| 350 | 71.4 | 2723 | 149 |
| 450 | 89.2 | 3026 | 246 |
| 500 | 97.4 | 3157 | 270 |
| 550 | 101.0 | 3240 | 174 |
| 550 | 102.5 | 3231 | 299 |
| 600 | 111.9 | 3369 | 333 |
| 650 | 120.0 | 3483 | 367 |

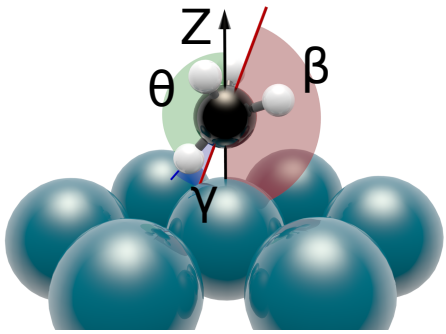


FIGURE 9.1: TS of methane on Pd(111), indicating the orientation angles as used in Table 9.2. $\theta$ is the angle between the CH-bond and the surface normal, $\beta$ is the angle between the umbrella axis and the surface normal, and $\gamma$ is the angle between $\theta$ and $\beta$ (see text for further explanation).

from Ref. [12] (experiments performed for $CHD_3$ + Ni(111)). For every BOMD data point, between 500 and 1000 trajectories were run, with a time step of 0.4 fs, for a maximum total time of 1 ps. Other technical details of the BOMD calculations and the sampling of the initial conditions can be found in recent work[12, 13, 16] and in Chapter 2.

## 9.3 Results

### 9.3.1 Activation Barriers

The barrier heights and geometries of $CHD_3$ on Pd(111) are compared to the barrier data on Ni(111) and Pt(111) in Table 9.2. $\theta$ is the angle between the

TABLE 9.2: Minimum barrier geometries and heights of methane on Ni(111)[12], Pd(111) and Pt(111)[13]. The zero-point energy corrected barrier heights are given in brackets.

| Surface | Site | $Z_C$ (Å) | $r$ (Å) | $\theta$ (°) | $\beta$ (°) | $\gamma$ (°) | $E_b$ (kJ/mol) |
|---|---|---|---|---|---|---|---|
| Ni(111) | Top[12] | 2.18 | 1.61 | 135.7 | 164.7 | 29.1 | 97.9 (85.3) |
| Ni(111) | Fcc | 2.09 | 1.63 | 128.5 | 157.3 | 30.7 | 121.1 (105.5) |
| Ni(111) | Hcp | 2.16 | 1.74 | 132.9 | 167.8 | 35.6 | 134.6 (120.7) |
| Ni(111) | Bridge | 2.06 | 1.65 | 126.3 | 154.8 | 29.5 | 135.1 (120.5) |
| Ni(111) | T2f | 2.07 | 1.90 | 126.5 | 171.1 | 45.3 | 99.1 (88.8) |
| Ni(111) | T2b | 2.12 | 1.63 | 130.4 | 160.0 | 31.0 | 113.9 (99.1) |
| Pd(111) | Top | 2.23 | 1.61 | 135.9 | 165.0 | 29.1 | 84.1 (70.1) |
| Pd(111) | Fcc | 2.14 | 1.73 | 133.0 | 160.8 | 27.8 | 132.6 (116.9) |
| Pd(111) | Hcp | 2.18 | 1.75 | 133.8 | 161.5 | 27.7 | 133.6 (118.1) |
| Pd(111) | Bridge | 2.14 | 1.76 | 130.8 | 161.9 | 31.1 | 125.6 (110.9) |
| Pd(111) | T2f | 2.17 | 1.82 | 137.5 | 178.0 | 40.6 | 108.4 (96.1) |
| Pd(111) | T2b | 2.18 | 1.76 | 132.8 | 165.8 | 33.0 | 132.5 (118.3) |
| Pt(111) | Top[13] | 2.28 | 1.56 | 133 | 168 | 35 | 78.7 (66.5) |
| Pt(111) | Fcc | 2.47 | 1.91 | 139.7 | 166.9 | 27.2 | 163.5 (145.8) |
| Pt(111) | Hcp | 2.59 | 1.90 | 122.1 | 161.2 | 39.1 | 158.0 (144.7) |
| Pt(111) | Bridge | 2.36 | 1.77 | 136.2 | 164.3 | 29.0 | 146.2 (128.1) |
| Pt(111) | T2f | 2.31 | 1.64 | 149.5 | 179.2 | 29.7 | 117.7 (101.6) |
| Pt(111) | T2b | 2.45 | 1.81 | 140.5 | 172.6 | 32.0 | 152.9 (136.5) |

dissociating bond and the surface normal, $\beta$ is the angle between the surface normal and the umbrella axis, which is defined as the vector going from the geometric center of the three non-dissociating hydrogen atoms to the carbon atom, and $\gamma$ indicates the angle between the umbrella axis and the dissociating bond (see Figure 9.1). The minimum barrier geometry on Pd(111) is similar to the minimum barrier geometry on Ni(111), with the main difference being that the barrier on Pd is at a larger distance from the surface than on Ni. However, the barrier height on Pd is much closer to that on Pt(111), being only 5.4 kJ/mol higher than on Pt(111). Based on the minimum barrier heights reported in Table 9.2, it is to be expected that the reactivity of Pd(111) is closest to that of Pt(111). Furthermore, the lowest barrier is located on the top site, which is typical for methane on a metal surface[12, 13, 29, 61].

Moreover, barriers are also obtained above the fcc, hcp, bridge, top-2-fcc (t2f), and top-2-bridge (t2b) sites, by fixing the carbon atom in the $X$ and $Y$ directions above the aforementioned sites. Here, the t2f and t2b sites are midway between the hcp and fcc, and hcp and bridge sites, respectively. For these barrier geometries, the angles are similar, but the length of the dissociating bond does increase, making the barrier even later. The distance of the carbon atom to the surface is smaller for Pd(111) and Ni(111) than at the top site, whereas in most cases it is larger for Pt(111). For Pt(111), the obtained barrier heights at the sites other than the top site are considerably higher than those of Pd(111) and Ni(111). The general trend observed here is that when going from Ni(111) to Pt(111), the difference between the barrier heights at the top site and at the other sites increases. Furthermore, among the sites other than the top sites, the lowest barrier occurs on the t2f site for all metals. For Ni(111), this barrier is almost as low as the top site so that it may play an important role in the dynamics.

Finally, the adsorption energies of $CH_3$ and H on Pd(111) are compared to those on Ni(111) and Pt(111) in Tables 9.3 and 9.4. For $CH_3$, Pd(111) is an intermediate of Ni(111) and Pt(111). The difference between the adsorption energies at the hollow and top sites is smaller for Pd(111) than for Pt(111), but for both the preferred site is the top site, as opposed to Ni(111) where the preferred sites are the hollow sites. This may also explain why the barrier for dissociation on the t2f site is so low on Ni(111). However, Pd(111) is very similar to Ni(111) concerning the adsorption of hydrogen, where the binding of hydrogen to the top site is considerably weaker than to the other sites.

TABLE 9.3: Adsorption energy of $CH_3$ on Ni(111)[62], Pd(111) and Pt(111)[62]. Note that the adsorption energies on Ni(111) and Pt(111) were calculated with the PBE functional.

| Surface | Site | $Z_C$ (Å) | Adsorption energy (kJ/mol) |
|---|---|---|---|
| Ni(111)[62] | Bridge | 1.69 | -155.2 |
| Ni(111)[62] | Fcc | 1.55 | -175.2 |
| Ni(111)[62] | Hcp | 1.56 | -172.5 |
| Ni(111)[62] | Top | 1.98 | -143.9 |
| Pd(111) | Bridge | 1.85 | -158.2 |
| Pd(111) | Fcc | 1.75 | -160.5 |
| Pd(111) | Hcp | 1.77 | -152.9 |
| Pd(111) | Top | 2.09 | -188.4 |
| Pt(111)[62] | Bridge | 1.86 | -120.2 |
| Pt(111)[62] | Fcc | 1.78 | -115.2 |
| Pt(111)[62] | Hcp | 1.82 | -105.4 |
| Pt(111)[62] | Top | 2.10 | -180.8 |

TABLE 9.4: Adsorption energy of H on Ni(111)[62], Pd(111) and Pt(111)[62]. Note that the adsorption energies on Ni(111) and Pt(111) were calculated with the PBE functional.

| Surface | Site | $Z_H$ (Å) | Adsorption energy (kJ/mol) |
|---|---|---|---|
| Ni(111)[62] | Bridge | 1.04 | -256.4 |
| Ni(111)[62] | Fcc | 0.91 | -270.2 |
| Ni(111)[62] | Hcp | 0.91 | -269.3 |
| Ni(111)[62] | Top | 1.47 | -212.8 |
| Pd(111) | Bridge | 0.98 | -255.2 |
| Pd(111) | Fcc | 0.81 | -268.0 |
| Pd(111) | Hcp | 0.81 | -262.7 |
| Pd(111) | Top | 1.56 | -223.9 |
| Pt(111)[62] | Bridge | 1.06 | -256.5 |
| Pt(111)[62] | Fcc | 0.92 | -261.3 |
| Pt(111)[62] | Hcp | 0.91 | -256.5 |
| Pt(111)[62] | Top | 1.56 | -257.2 |

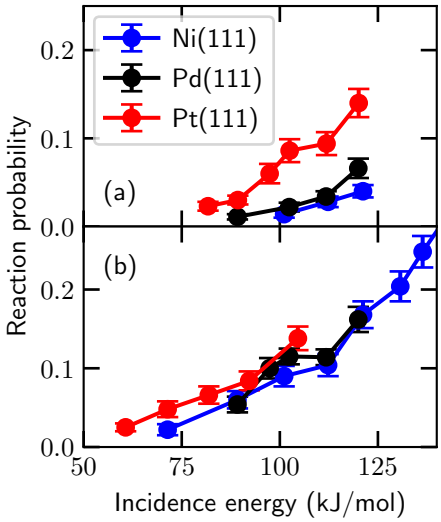


FIGURE 9.2: Reaction probability of $CHD_3$ on Ni(111) (blue), Pd(111) (black) and Pt(111) (red) for laser-off (a) and $\nu_1 = 1$ (b) using BOMD simulations. Results for Ni(111) and Pt(111) are taken from Refs. [12] and [13], respectively. The error bars represent 68% confidence intervals.

### 9.3.2 Sticking Probability

Results for the reaction of methane on Pd(111) using BOMD are compared to those on Ni(111) and Pt(111) in Figure 9.2 for laser-off conditions and $\nu_1 = 1$ (exciting the CH stretch mode with one quantum). Note that three additional points for Ni(111) have been calculated at $\langle E_i \rangle = 71.4$, 89.2, and 101.1 kJ/mol for $\nu_1 = 1$ using the same computational set up as in Ref. [12]. Additionally, results for $\langle E_i \rangle = 146.6$ kJ/mol were obtained in the original work of Ref. [12], but have not been reported before because there were no experimental data for this incidence energy. Contrary to expectations based on the minimum barrier heights only (see Table 9.2), for laser-off conditions the reaction probability on Pd(111) is similar to that on Ni(111). It should be noted that for Ni(111) a slightly higher surface temperature is used (550 K) than for Pd(111) and Pt(111) (500 K). However, this should not affect the results considerably as the surface temperature does not play a large role at high incidence energies, which will be discussed more in-depth in Section 9.3.4. For $\nu_1 = 1$ at lower incidence energy, the reaction probability is similar on all three systems investigated. Interestingly, on Pd(111) the reaction probability does not increase from 102 to 112 kJ/mol. It is possible that this is related to the site-dependence of the reaction, which will be discussed later in Section 9.3.3. The generally much lower laser-off reactivity of Pd(111) compared to that of Pt(111) at high incidence energy is also consistent with the prediction that Pt-Cu(111) is much more reactive than Pd-Cu(111) at high incidence energies[29].

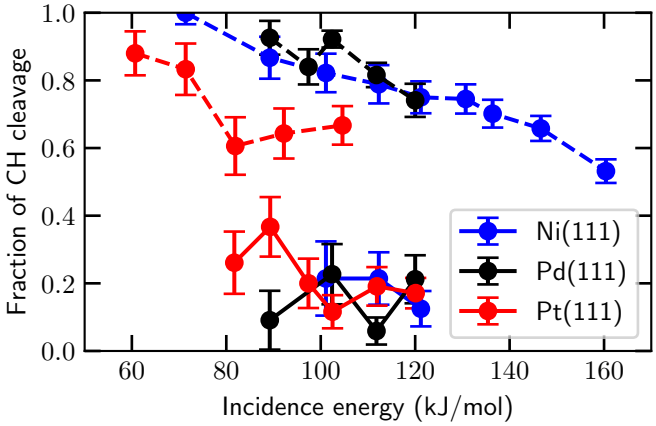


FIGURE 9.3: Fraction of reactions that occurred through CH bond cleavage for $CHD_3$ on Ni(111) (blue), Pd(111) (black), and Pt(111) (red). Laser-off and $\nu_1 = 1$ results are indicated by solid and dashed lines, respectively. The error bars represent 68% confidence intervals.

Finally, we note that the trapping probabilities are not included in the reaction probability, as they are smaller than 0.5%.

The bond selectivity is shown in Figure 9.3, where the fraction of CH bond cleavage under laser-off and state-resolved $\nu_1 = 1$ conditions are compared. When the CH stretch mode is excited the dissociation of $CHD_3$ is very selective towards CH cleavage, whereas under laser-off conditions CH cleavage is close to statistical (25%). This is similar to what has been observed for $CHD_3$ + Ni(111)[12, 30] and $CHD_3$ + Pt(111)[13]. However, it remains unclear why on Pd(111) for laser-off conditions the fraction of CH cleavage is considerably lower for 112 kJ/mol compared to the other incidence energies under laser-off conditions. This may well be a statistical anomaly since a statistical analysis using Fisher's exact test[63] cannot reject the null hypothesis that the CH dissociation probability is the same for all incidence energies. Moreover, at higher incidence energies and laser-off conditions, the CH cleavage ratio is somewhat lower than 0.25, which is attributed to the presence of CD-excited vibrational states in the beam[12] (note that there may be some artificial energy flow between these modes in classical dynamics calculations).

Finally, the obtained vibrational efficacies of $CHD_3$ on Ni(111), Pd(111) and Pt(111) are shown in Table 9.5. Generally, Ni(111) yields the highest vibrational efficacy, whereas Pt(111) yields the lowest vibrational efficacy.

TABLE 9.5: Vibrational efficacy ($\nu_1 = 1$) of $CHD_3$ on Ni(111), Pd(111) and Pt(111) as a function of the reaction probability.

| Surface | Reaction probability (%) | Vibrational efficacy |
|---|---|---|
| Ni(111) | 2.8 | 0.9 - 1.3 |
| Ni(111) | 4.0 | 0.9 - 1.3 |
| Pd(111) | 5.4 | 0.7 - 0.9 |
| Pd(111) | 6.6 | 0.7 - 0.9 |
| Pt(111) | 3.6 | 0.8 |
| Pt(111) | 4.7 | 0.6 |
| Pt(111) | 5.4 | 0.6 |
| Pt(111) | 7.1 | 0.5 |
| Pt(111) | 10.0 | 0.3 |

TABLE 9.6: Average value of the $\theta$, $\beta$ and $\gamma$ angles with the standard error ($\sigma_m$) and standard deviation ($\sigma$) for all laser-off and $\nu_1 = 1$ reacted trajectories when a dissociating bond reaches the TS value.

| Surface | $\theta(^\circ) \pm \sigma_m(\sigma)$ | $\beta(^\circ) \pm \sigma_m(\sigma)$ | $\gamma(^\circ) \pm \sigma_m(\sigma)$ |
|---|---|---|---|
| Ni(111) | $117.0 \pm 0.3$ (11.3) | $142.1 \pm 0.4$ (13.6) | $31.3 \pm 0.3$ (12.4) |
| Pd(111) | $123.5 \pm 0.5$ (11.0) | $143.9 \pm 0.6$ (14.1) | $27.9 \pm 0.5$ (11.4) |
| Pt(111) | $123.5 \pm 0.5$ (10.1) | $150.0 \pm 0.6$ (12.2) | $34.1 \pm 0.6$ (12.8) |

### 9.3.3 Dynamics of the Reaction

Distribution of the angles indicated in Figure 9.1 are shown in Figure 9.4 and average values are shown in Table 9.6 for the reacted trajectories. It is observed that both the initial $\theta$ and $\beta$ angles, i.e., the angles that describe the orientations of the dissociating bond and umbrella axis, are close to the TS geometry. Moreover, during the dynamics, a considerable amount of bending between the dissociating bond and umbrella axis ($\gamma$ angle) is observed. Finally, for all the angles considered some steering is observed, in the sense that at the time of reaction the distributions describing the reacting molecules have moved somewhat towards the TS value of the angle described. However, the reaction is not rotationally adiabatic (at the initial time step the orientation distribution of the reacting molecule is not statistical), in agreement with previous observations for Ni(111)[12] and Pt(111)[13]. This has consequences for how the rotations should be treated[5] in the reaction path Hamiltonian (RPH)

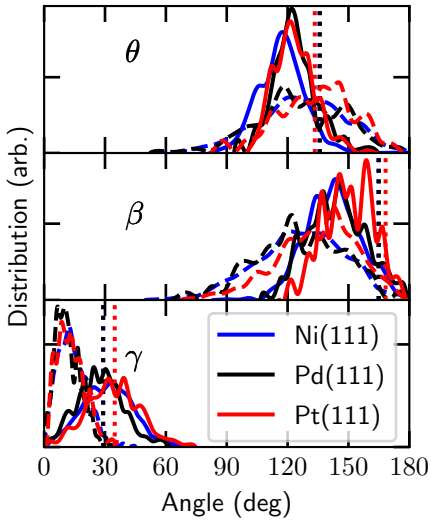


FIGURE 9.4: Distributions of the $\theta$, $\beta$ and $\gamma$ angles of methane during BOMD for all laser-off and $\nu_1 = 1$ reacted trajectories at the initial time step (dashed line) and when a dissociating bond reaches the TS value (solid line). The dotted lines indicate the TS values (note that Ni(111) and Pd(111) yield almost identical values). Blue is Ni(111)[12], black is Pd(111), and red is Pt(111)[13]

approach of Jackson and coworkers[64]. Furthermore, the aforementioned dynamical behaviour of the angles is not only typical for methane reacting on a group 10 metal surface (as can be seen in Figure 9.4), but also for methane reacting on Cu(111)[29] (see Chapter 7).

Although the barrier height on Pd(111) is considerably lower than on Ni(111), the barrier geometries are similar and thus dynamical effects such as the bobsled effect[27, 28] would be expected to play similar roles. That the bobsled effect plays a role in the reaction of $CHD_3$ on group 10 metal surfaces can be seen in Figure 9.5, where the distance of the carbon atom to the surface is shown at the time of dissociation. Both laser-off and $\nu_1 = 1$ trajectories that go on to react tend to slide off the MEP due to the bobsled effect and thus react over higher barriers. This deviation from the MEP increases with incidence energy, which is observed above all high-symmetry sites and thus is not related to the site over which the methane reacts. Furthermore, the bobsled effect is considerably smaller for Pt(111) than for Pd(111) and Ni(111), which leads to methane having to react over relatively higher barriers on Pd(111) and Ni(111) than on Pt(111) (see Figure 9.5).

For similar values of the reaction probability, the bobsled effect on the reaction dynamics of $CHD_3$ under laser-off conditions (predominantly $\nu_1 = 0$) is larger than for $\nu_1 = 1$. The reason is that a larger incidence energy is required for $\nu_1 = 0$ to react than for $\nu_1 = 1$, so that $\nu_1 = 0$ $CHD_3$ tends to slide further of the MEP than $\nu_1 = 1$ $CHD_3$. To observe this, see for

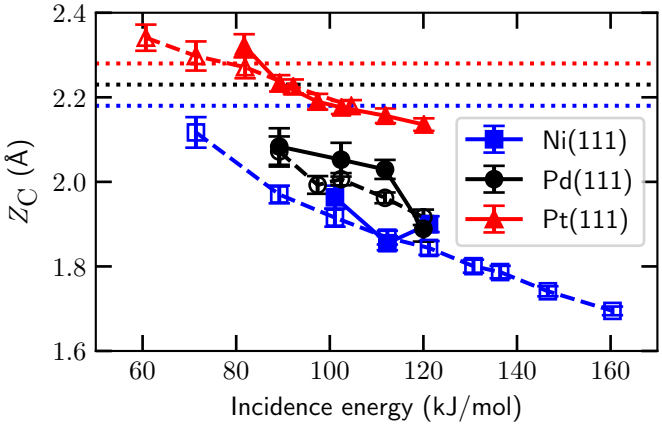


FIGURE 9.5: Distance of the carbon atom to the surface when a bond dissociates, i.e., when $r = r^{\ddagger}$, under laser-off conditions (solid lines) and for $\nu_1 = 1$ (dashed lines). The blue squares, black circles, and red triangles indicate Ni(111), Pd(111), and Pt(111), respectively. The horizontal dashed lines indicate the TS values. The error bars represent 68% confidence intervals.

example Figure 9.5 for Ni(111), observing the differences between laser-off conditions and $\nu_1 = 1$ for the lowest incidence energy for which a laser-off result is available on the one hand, and for the lowest incidence energy for which a $\nu_1 = 1$ result is available on the other hand, and Figure 9.2 to confirm that these conditions correspond to similar reaction probabilities. This has consequences for the vibrational efficacy, which is defined as the energy shift between the $\nu_1 = 1$ and $\nu_1 = 0$ (≈laser-off) reaction probability curves divided by the energy difference between $\nu_1 = 1$ and $\nu_1 = 0$, and defines how efficiently vibrational excitation promotes the reaction relative to increasing the translational energy. The larger bobsled effect on Ni(111) and Pd(111) than on Pt(111) partly explains why the vibrational efficacies for these systems (0.9 - 1.3 for Ni(111) and 0.7 - 0.9 for Pd(111)) exceed that obtained for Pt(111) (0.3 - 0.8, see Table 9.5, and also Ref. [12] for Ni(111) and Ref. [13] for Pt(111)). Furthermore, the large bobsled effect found for $CHD_3$ on Ni(111) is in line with one of the explanations Smith et al.[36] provided for the high vibrational efficacy of the asymmetric stretch mode of $CH_4$ reacting on Ni(111), i.e., that $\nu_3 = 1$ $CH_4$ reacts at the TS, while $\nu_3 = 0$ $CH_4$ slides off the MEP and has to pass over a higher barrier. Note that in the modeling of the reaction the molecule should be allowed to slide off the MEP to account for the bobsled effect on the vibrational efficacy. One reason that a too low

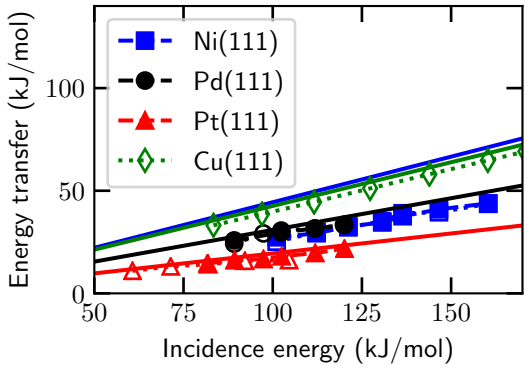


FIGURE 9.6: Energy transfer from methane to Ni(111) (blue squares), Pd(111) (black circles), Pt(111)[66] (red triangles), and Cu(111)[55] (green diamonds) compared to the refined Baule model. The solid lines without symbols indicate results predicted by the refined Baule model, whereas the dashed and dotted lines with solid and open symbols indicate laser-off and $\nu_1 = 1$ results, respectively.

vibrational efficacy was obtained for $\nu_3 = 1$ $CH_4$ on Ni(111) in Ref. [65] may have been that the RPH calculations used a harmonic approximation for motion orthogonal to the MEP and an expansion in harmonic vibrational eigenstates with up to one quantum only in all modes combined. It is possible that such a limited expansion is not capable of describing the effect that the molecule may slide off the reaction path, as perhaps indicated by the reaction probability of methane in its vibrational ground state becoming smaller for particular incidence energies if the expansion is enlarged to also contain states with up to two vibrational quanta[5].

As has also been suggested in Chapter 7, the MEP on Pd(111) is less favourable from a dynamical point of view than on Pt(111) due to the fact that the MEP makes a sharper turn on Pd(111) than on Pt(111). Therefore, it is expected that at low incidence energies and $\nu_1 = 1$ where dynamical effects such as the bobsled effect are less important, the reactivity on Pd(111) is similar to that on Pt(111), whereas at higher incidence energies and laser-off conditions dynamical effects cause the reactivity on Pd(111) to be similar to that on Ni(111) for the reaction of $CHD_3$ in its vibrational ground state (to which laser-off reaction bears a close resemblance at low nozzle temperature).

Another important dynamical aspect of the reaction of methane is the energy transfer from the molecule to the surface[55]. Figure 9.6 compares for scattered trajectories this energy transfer from $CHD_3$ to Cu(111)[55], Pt(111)[66], Ni(111)[12], and Pd(111). In general, it is observed that the lower the surface atom mass is, the higher the energy transfer is from methane to the surface atoms. This is also predicted by the hard sphere Baule model[67], where the mass ratio between the molecule and the surface atom plays a large role in the energy transfer. When the refined Baule model is employed, the following

average energy transfer (used in Figure 9.6) is obtained[68] (see Section 2.5).

$$\langle E_{\mathrm{T}} \rangle = \frac{2.4\mu}{(1+\mu)^2} \langle E_{\mathrm{i}} \rangle \,. \tag{9.2}$$

Here, $\mu = m/M$ ($m$ is the mass of the projectile and $M$ is the mass of a surface atom) and $\langle E_{\mathrm{i}} \rangle$ is the average incidence energy. Surprisingly, the relatively simple Baule model does not only qualitatively but also semi-quantitatively predict the energy transfer from methane to the metal surfaces, except to Ni(111), in contrast to what was previously predicted[66]. Considering the close to spherical shape of methane, it is probable that the hard sphere approximation made by the Baule model will typically hold. This is also suggested by Figure 9.6, which shows remarkably good agreement of the computed energy transfer with that predicted by the refined Baule model for Pt, Pd, and Cu. Additional work will be required to test the validity of the refined Baule model for other systems and investigate the considerably lower energy transfer computed to Ni(111). Since the energy transfer from methane to Pd is higher than to Pt, less energy will be available for the reaction on Pd and thus the reaction probability should be further diminished on Pd compared to that on Pt. This effect will be larger at higher incidence energies as the difference in energy transfer between Pd and Pt will increase (see Figure 9.6). Moreover, as the computed energy transfer to Pd(111) and Ni(111) is predicted to be equal, differences in reaction probabilities on Pd(111) and Ni(111) are most likely not caused by the energy transfer from methane to the metal surface.

As can be seen from Figure 9.7, at high incidence energy the distribution of sites over which $CHD_3$ reacts on Pd(111) is close to statistical for both laser-off reaction and $\nu_1 = 1$. However, at lower incidence energy it is observed that the top site is the most reactive site, followed by the bridge site. This means that at lower incidence energy mostly only the minimum barrier is accessed, since it is located at the top site as discussed in Section 9.3.1. Therefore, at lower incidence energies a large portion of the surface would be catalytically inactive. This corresponds with the lack of increase in the reactivity of $\nu_1 = 1$ on Pd(111) from 102 to 112 kJ/mol, as it is also observed that the distribution of reaction sites shifts towards the less reactive sites (i.e., the bridge and hollow sites). Moreover, the reaction of $CHD_3$ on Pt(111) shows a similar site specific behaviour as $CHD_3$ reacting on Pd(111). At lower incidence energy the reaction on Ni(111) again occurs predominantly over the top site, however, the second most reactive site is now the hollow site instead of the bridge site. In general, all the considered metal surfaces show non-statistical behaviour, where the top site is usually favored, with the main difference

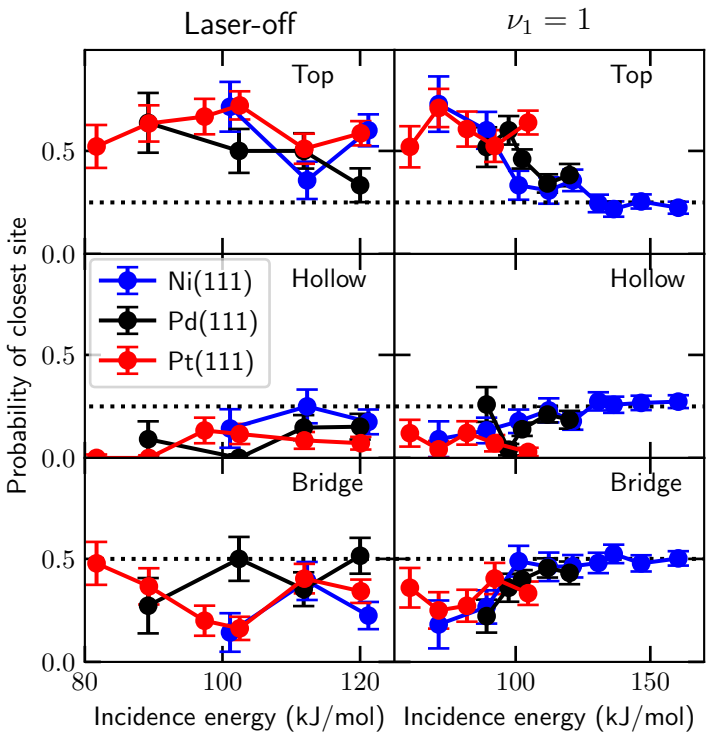


FIGURE 9.7: Fraction of closest high-symmetry site (i.e., top, hollow and bridge) to the impact site of reacting methane on Ni(111) (blue), Pd(111) (black), and Pt(111) (red) for laser-off and $\nu_1 = 1$ conditions, as a function of the incidence energy and when a bond dissociates, i.e., $r = r^{\ddagger}$. The dotted line indicates the statistical average for the high-symmetry site. The error bars represent 68% confidence intervals.

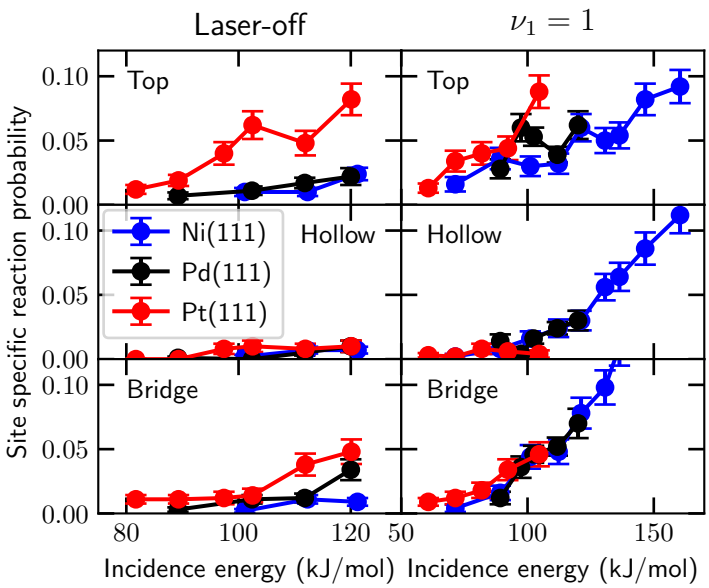


FIGURE 9.8: Reaction probability of $CHD_3$ on the high-symmetry sites (i.e., top, hollow and bridge) on Ni(111) (blue), Pd(111) (black), and Pt(111) (red) for laser-off conditions and for $\nu_1 = 1$ as a function of the incidence energy when a bond dissociates, i.e., $r = r^{\ddagger}$. The error bars represent 68% confidence intervals.

being the ordering of the sites according to their reactivity. This behaviour is also predicted by the site specific barriers discussed in Section 9.3.1.

Figure 9.8 shows site-specific reaction probabilities of $CHD_3$ which add up to total reaction probabilities. Again, Ni(111), Pd(111) and Pt(111) exhibit similar site-specific reaction probabilities. Most of the reactivity is observed above the top site, whereas the hollow and bridge sites play a considerably smaller role. Here the difference in reaction probability between Pd(111) and Pt(111) under laser-off conditions can be seen more clearly. The difference in reaction probability for the top site is large, whereas the difference for the hollow and bridge sites is generally much smaller. Therefore, the considerably lower reactivity of $CHD_3$ on Pd(111) than on Pt(111) under laser-off conditions is mostly due to the difference in the top site reactivity. However, this difference is not caused by the difference in minimum barrier heights; probably it is caused by the difference in barrier heights that can be dynamically accessed due to the bobsled effect. Furthermore, it remains unclear whether the large variation in reaction probability for Pd(111) and Ni(111) at the top site for $\nu_1 = 1$ is a statistical anomaly or a real physical feature. Also, the partial

TABLE 9.7: Dynamical features and how they qualitatively affect the reaction probability of $CHD_3$ on Ni(111), Pd(111), and Pt(111). The number of pluses and minuses indicate how much the effect increases or reduces the reaction probability, respectively, when the aforementioned surfaces are compared.

| Dynamical feature | Ni(111) | Pd(111) | Pt(111) | Largest effect on |
|---|---|---|---|---|
| Bobsled effect | $-\,-\,-$ | $-\,-\,-$ | $-$ | Laser-off |
| Energy transfer | $--$ | $--$ | $-$ | Laser-off |
| Site specificity | $-$ | $--$ | $-\,-\,-$ | Laser-off |
| Vibrational efficacy | $+\,+\,+$ | $++$ | $+$ | $\nu_1 = 1$ |
| Angular distribution | $-$ | $-$ | $-$ | Both |

contribution of each site is compared to the total reaction probability for each surface in Figure 9.B.1, which again shows the aforementioned differences in site-specific reactivity.

While the difference between the low vibrational efficacy computed for $CHD_3$ + Pt(111) on the one hand and the higher vibrational efficacies on Pd(111) and Ni(111) on the other hand could be explained on the basis of the bobsled effect (see above), the reason for the higher vibrational efficacy on Ni(111) (0.9-1.3) than on Pd(111) (0.7-0.9, see Table 9.5) could not be explained in this way. On the basis of the minimum barrier heights and geometries collected in Table 9.2, it is tempting to speculate that the t2f site could play a role in this, as it has a much lower barrier on Ni(111) than on Pd(111), and a later barrier on Ni(111) than on Pd(111). The plot of the impact sites for the reactive trajectories with $\langle E_i \rangle = 89\,\mathrm{kJ/mol}$ for $\nu_1 = 1$ on Ni(111) (Figure 9.B.2) can be construed to offer some support for this idea, as quite a few reactive impacts are seen near the corners of the triangles making up the t2f and t2h sites. However, to gather further support for this idea better statistics are needed, which can perhaps be obtained on the basis of QCT dynamics on a PES also incorporating the effect of surface atom motion, as has been done in Chapter 8 for $CHD_3$ + Cu(111).

In the reaction of $CHD_3$ on Pd(111), not much steering in the $XY$ plane is observed (on average a movement of just 0.06 Å in the $XY$ plane), as is typical for the reaction of $CHD_3$ on a metal surface[5, 12, 29, 52, 53]. As a result, it should be a good approximation to treat the reaction with a sudden approximation for motion in $X$ and $Y$, as done for instance with the RPH model of Jackson and coworkers[5], and firmly established to be valid for $CH_4$ + Ni(111)[69], and also for $H_2O$ + Ni(111)[70].

Finally, the general trends observed and how they affect the reaction probability are summarized in Table 9.7. First, the bobsled effect is considerably more important for Pd(111) and Ni(111) than for Pt(111), making Pt(111) considerably more reactive than the other surfaces, especially for laser-off conditions. Moreover, the energy transfer of methane to Pt(111) is smaller than to Pd(111) and Ni(111), again making Pt(111) relatively more reactive. However, the site-specific reactivity is increasingly more important when going from Ni(111) to Pt(111), reducing the reaction probability on Pt(111) the most. The vibrational efficacy plays an increasingly more important role when going from Pt(111) to Ni(111), increasing the reaction probability for $\nu_1 = 1$ on Ni(111) the most. Furthermore, the initial angular distribution of the molecule and concomitant steering are equally important on all surfaces considered here. These dynamical effects combined cause the reaction probability on Ni(111) and Pd(111) to be similar and on Pt(111) comparatively higher, for laser-off conditions. Additionally, they explain why the reactivity is rather similar on all of these surfaces for $\nu_1 = 1$. In this, it is suspected that the site-specificity plays the most important role in almost equalizing laser-off reaction on Pd(111) and Ni(111), while the vibrational efficacy should also be important to making the $\nu_1 = 1$ reaction probabilities almost equal on these two surfaces.

Due to the combined effects of decreased site-specificity and increased vibrational efficacy, it is conceivable that Ni(111) becomes more reactive than Pd(111), and/or Pd(111) becomes more reactive than Pt(111) towards $\nu_1 = 1$ $CHD_3$ at higher incidence energies than results are shown for in Figure 9.2b. It would be a considerable challenge to explore this experimentally, for two reasons[71, 72]: (i) At higher incidence energies, the extraction of the reactivity of $\nu_1 = 1$ $CHD_3$ requires a subtraction of an increasingly large "laser-off" signal from a "laser-on" signal that might actually decrease, because laser-excitation takes place from a rotational level that is less populated at the higher associated $T_n$, and (ii) the extraction requires the approximation that the reactivity of the vibrational ground state equals that averaged over the vibrational states populated in the beam under laser-off conditions, of which the validity decreases with incidence energy.

### 9.3.4 Discussion of Reactivity of Pd(111) vs Ni(111) and Pt(111); Comparison with Experiment

Experimentally, at low incidence energies ($< 70\,\mathrm{kJ/mol}$) (see Figure 9.9), the reactivity of Pd(111) towards $CH_4$ is similar to that of Pt(111), whereas Ni(111) is about three orders of magnitude less reactive than Pt(111)[23, 73–76]. It

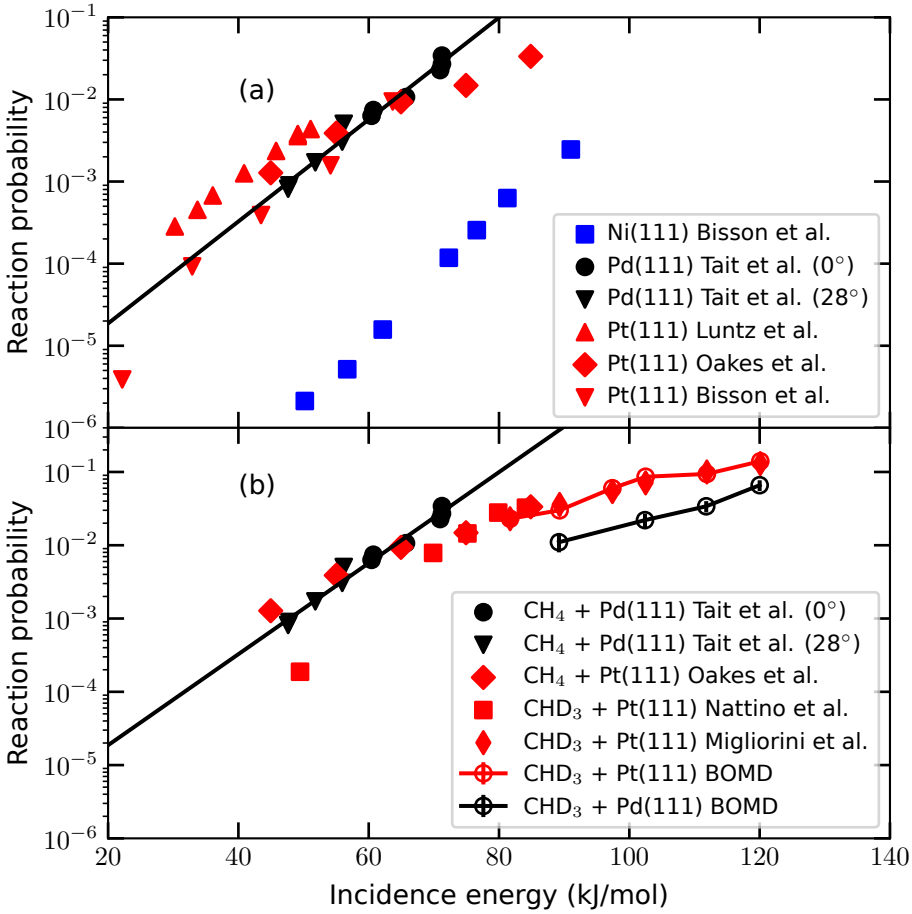


FIGURE 9.9: (a) Experimental reaction probability of $CH_4$ on Ni(111) (blue), Pd(111) (black) and Pt(111) (red) under laser-off conditions. Results for Ni(111) and Pt(111) are taken from Ref. [73] and Refs. [73–75], respectively. The Pd(111) results (black circles and triangles) are taken from Ref. [23], where the circles and triangles indicate an incidence angle of 0° and 28°, respectively, and the black line is a linear regression fit those points. (b) The reaction probability of $CH_4$ and $CHD_3$ on Pd(111) and Pt(111) obtained with experiment (closed symbols) and BOMD (open symbols) under laser-off conditions. For $CH_4$ + Pt(111) only the results from Ref. [75] are shown. The red squares and diamonds indicate results for $CHD_3$ + Pt(111) taken from Refs. [16] and [13], respectively.

TABLE 9.8: Seeding gas, surface temperature ($T_s$) and nozzle temperature ($T_n$) employed in the experiments shown Figure 9.9.

| System | Author | Seeding gas | $T_s$ (K) | $T_n$ (K) |
|---|---|---|---|---|
| $CH_4$ + Ni(111) | Bisson et al.[73] | $H_2$ | 475 | 323 - 373 |
| $CH_4$ + Pd(111) | Tait et al.[23] | He | 550 | 470 - 885 |
| $CH_4$ + Pt(111) | Luntz et al.[74] | $H_2$, He, Ar | 800 | 300 |
| $CH_4$ + Pt(111) | Oakes et al.[75] | He | 550 | 500 - 1000 |
| $CH_4$ + Pt(111) | Bisson et al.[73] | $H_2$ | 600 | 323 - 373 |
| $CHD_3$ + Pt(111) | Nattino et al.[16] | He | 120 | 500 - 850 |
| $CHD_3$ + Pt(111) | Migliorini et al.[13] | $H_2$ | 500 | 400 - 650 |

should be noted that the experiments at low incidence energies were performed with $CH_4$ using various nozzle and surface temperatures (see Table 9.8), making a direct quantitative comparison between the experiments on $CH_4$ + Pt(111) and $CH_4$ + Pd(111), and with the BOMD results for $CHD_3$ difficult. Therefore, the general trends observed for the reaction of methane on Pt(111) are discussed here and we have tried to extrapolate this to Pd(111).

In Figure 9.9b a few results concerning Pt(111) and Pd(111) are shown in order to qualitatively compare the effect of nozzle and surface temperatures, and the isotopic effect of using $CH_4$ or $CHD_3$. Nattino et al.[16] used $CHD_3$ seeded in a He beam with $T_s = 120$ K, whereas Migliorini et al.[13] used $CHD_3$ seeded in a $H_2$ beam with $T_s = 500$ K. Typically, at the high incidence energies and reaction probabilities involved here, the surface temperature does not have a large effect on the reactivity of methane[55, 74, 77]. Moreover, at high surface temperature the seeding gas influences the kinetic energy and thus also the required nozzle temperature. Therefore, the slightly higher reaction probability of Nattino et al.[16] found for $CHD_3$ + Pt(111) in the overlapping regime is caused by the higher nozzle temperature (as needed by He-seeded molecular beam studies), as a larger fraction of $CHD_3$ in the beam will be vibrationally excited.

However, the surface temperature can cause the reaction probability at lower incidence energy to vary by up to two orders of magnitude, depending on the surface temperature and incidence energy[55, 65, 74, 77, 78]. This surface temperature effect probably causes the reaction probabilities obtained by Luntz and Bethune[74] ($T_s = 800$ K) to be considerably higher than those obtained by Oakes et al.[75] ($T_s = 550$ K) and Bisson et al.[73] ($T_s = 600$ K), who all used $CH_4$. On the other hand, the higher reaction probability obtained by Oakes et al. ($T_n = 500 - 1000$ K) compared to that by Bisson et al. ($T_n =$

323 − 373 K) is probably due to the higher employed nozzle temperature used by Oakes et al.

Furthermore, the effect of partially deuterating methane can be seen by comparing the results of Nattino et al. and Oakes et al. For the incidence energy range where data are available for both sets, the difference in surface temperature (i.e., $T_s = 120$ K and $T_s = 550$ K, respectively) should only play a role for the low incidence energies. Moreover, the nozzle temperature employed by Nattino et al. is similar to that by Oakes et al., and thus should not make a large difference either. It is expected that these differences should also (partially) cancel out at high incidence energies. It has also been shown previously that using $CHD_3$ instead of $CH_4$ lowers the reaction probability[74, 79–81]. However, the reaction probabilities obtained by Nattino et al. and Oakes et al. at high incidence energy are similar, where it is expected that the reaction probabilities obtained by Oakes et al. should be slightly higher than those by Nattino et al. It remains unclear why no difference at high incidence energy is observed between the two data sets, although it is possible that the molecular beams are considerably different making direct comparison difficult.

Finally, the reaction probability of $CH_4$ on Pd(111) obtained by Tait et al.[23] is similar to that of Oakes et al. for $CH_4$ + Pt(111), except for the highest incidence energies where Pd(111) is measured to be more reactive than Pt(111) towards methane. Both used the same surface temperature and similar nozzle temperature range, but Tait et al. used relatively less seeding gas and thus a higher nozzle temperature is employed for a given incidence energy compared to Oakes et al., which perhaps explains the higher reaction probability for Pd(111) at high incidence energy. At energies that are higher than those for which $CH_4$ + Pd(111) experimental results are available, the BOMD calculations in this chapter predict a substantially lower reactivity of Pd(111) towards $CHD_3$ than that of Pt(111). While this may seem odd in light of the experimental results for $CH_4$ on Pt(111) and Pd(111), one should keep in mind that due to the simulated use of $H_2$ seeding the incidence energy is higher while the nozzle temperature is lower for the calculations on $CHD_3$ + Pd(111) and Pt(111), which leads to a larger importance of the bobsled effect and to a smaller importance of the promotion of reaction by vibrational excitation. Both effects disfavor the reaction on Pd(111). Nevertheless, experiments are clearly needed to verify the predictions for the reaction of $CHD_3$ on Pd(111). For all of these reasons it is concluded that experimentally it is expected that the reactivity of $CHD_3$ + Pd(111) should be slightly lower than that of $CHD_3$ + Pt(111) at lower incidence energies. Qualitatively, this is also what is obtained from the BOMD calculations at higher incidence energies, although there the

difference in reactivity is larger (see Figure 9.2).

## 9.4 Conclusions

In this chapter, predictive calculations using BOMD have been performed for $CHD_3$ on Pd(111) with the SRP32-vdW functional. The reactivity of Pd(111) is compared to that of Pt(111) and Ni(111), and is found to be intermediate between these systems. Although this is to be expected from the minimum barrier heights and experiments at low incidence energy, the reaction probability is also found to be dependent on dynamical effects such as the bobsled effect and energy transfer from methane to the metal surface. In general, at the lowest incidence energy and laser-off conditions when these dynamical effects are smaller, the reaction probability on Pd(111) is comparable to that on Pt(111), which is also observed by experiment. However, at higher incidence energies, these dynamical effects play a larger role and the reaction probability on Pd(111) is more comparable to that on Ni(111). Furthermore, for $\nu_1 = 1$ all three systems investigated show similar reaction probabilities. Moreover, barriers across the surface need to be considered as the reaction of methane on a group 10 metal surface is highly site specific, with the minimum barrier height and geometry varying across the surface. This variation in barrier heights across the surface also explains the similarity of the reactivity of Ni(111) and Pd(111) towards methane at high incidence energy. Interestingly, methane on Pd(111) and Ni(111) exhibits typically quite similar dynamical behaviour such as the bobsled effect, energy transfer from methane to the surface, and the site-specific reactivity, whereas the dynamical behaviour of methane on Pt(111) tends to be different from that on the aforementioned metal surfaces. This again causes reactivity of Pd(111) towards methane to shift more to that of Ni(111) than that of Pt(111). These results also suggest why Pt-Cu(111) is predicted to be much more reactive than Pd-Cu(111) at high incidence energy in Chapter 7. Hopefully, these predictions will inspire new experiments that will test the transferability of the SRP32-vdW functional to $CHD_3$ + Pd(111).

# Appendix

## 9.A Convergence

Figure 9.A.1 and Table 9.A.1 show the convergence of the minimum barrier height for methane dissociation on Pd(111) ($E_b$) as a function of the number of layers for different numbers of $k$-points using a kinetic energy cut-off of 400 eV, yielding a converged barrier height of 82.8 kJ/mol. The computational set up employed in the BOMD calculations (4 layers, $3 \times 3$ surface unit cell, $6 \times 6 \times 1$ $k$-points, kinetic energy cut-off of 400 eV, 13 Å vacuum distance) yields a barrier height of 84.1 kJ/mol. It is confirmed that the computational set up is also converged with respect to the kinetic energy cut-off.

## 9.B Site-Specific Reaction Probability

Figure 9.B.1 shows the same site-specific reaction probabilities of $CHD_3$ for each investigated surface as in Figure 9.8, but here every surface is shown separately under laser-off and $\nu_1 = 1$ conditions, showing how the site-specific reaction probabilities add up to the total reaction probability. Moreover, the impact site of the reacting methane on Ni(111), Pd(111) and Pt(111) is shown in Figure 9.B.2 for a reaction probability of about 2.5% and 5.0% under laser-off and $\nu_1 = 1$ conditions, respectively. Note that for laser-off conditions 1000 trajectories were run and for $\nu_1 = 1$ 500 trajectories were run. Here it can be seen that under laser-off conditions, most of the reaction occurs near the top site, even if the reaction occurs in the hollow or bridge region, whereas for $\nu_1 = 1$ conditions the reaction occurs across most of the surface.

TABLE 9.A.1: Convergence of the minimum barrier height (kJ/mol) on Pd(111) is shown as a function of the amount of layers, *k*-points, and the size of the surface unit cell ($3 \times 3$ and $4 \times 4$) for a plane wave energy cutoff of 400 eV. The results obtained with the employed computational set up in the BOMD is in bold and the most converged result (i.e., obtained with the largest setup) is in italic.

| Layers | *k*-points | $E_{b,3\times3}$ | $E_{b,4\times4}$ |
|---|---|---|---|
| 4 | $3 \times 3 \times 1$ | | 80.6 |
| 4 | $4 \times 4 \times 1$ | 81.1 | 86.8 |
| 4 | $6 \times 6 \times 1$ | **84.1** | 84.5 |
| 4 | $8 \times 8 \times 1$ | 85.1 | 85.6 |
| 4 | $10 \times 10 \times 1$ | 85.4 | |
| 5 | $3 \times 3 \times 1$ | | 80.2 |
| 5 | $4 \times 4 \times 1$ | 80.8 | 86.1 |
| 5 | $6 \times 6 \times 1$ | 85.3 | 85.1 |
| 5 | $8 \times 8 \times 1$ | 85.1 | 84.9 |
| 5 | $10 \times 10 \times 1$ | 85.3 | |
| 6 | $3 \times 3 \times 1$ | | 83.1 |
| 6 | $4 \times 4 \times 1$ | 82.5 | 82.6 |
| 6 | $6 \times 6 \times 1$ | 83.4 | 83.5 |
| 6 | $8 \times 8 \times 1$ | 83.6 | 83.5 |
| 6 | $10 \times 10 \times 1$ | 83.8 | |
| 7 | $3 \times 3 \times 1$ | | 79.4 |
| 7 | $4 \times 4 \times 1$ | 81.4 | 84.7 |
| 7 | $6 \times 6 \times 1$ | 83.6 | 83.4 |
| 7 | $8 \times 8 \times 1$ | 84.2 | 83.7 |
| 7 | $10 \times 10 \times 1$ | 84.7 | |
| 8 | $3 \times 3 \times 1$ | | 81.2 |
| 8 | $4 \times 4 \times 1$ | 81.7 | 84.2 |
| 8 | $6 \times 6 \times 1$ | 84.2 | 83.5 |
| 8 | $8 \times 8 \times 1$ | 83.9 | 83.4 |
| 8 | $10 \times 10 \times 1$ | 84.2 | |
| 9 | $3 \times 3 \times 1$ | | 81.1 |
| 9 | $4 \times 4 \times 1$ | 82.5 | 83.2 |
| 9 | $6 \times 6 \times 1$ | 82.9 | 82.9 |
| 9 | $8 \times 8 \times 1$ | 84.0 | 83.5 |
| 9 | $10 \times 10 \times 1$ | 84.3 | |
| 10 | $3 \times 3 \times 1$ | | 80.1 |
| 10 | $4 \times 4 \times 1$ | 81.1 | 85.1 |
| 10 | $6 \times 6 \times 1$ | 82.8 | 83.0 |
| 10 | $8 \times 8 \times 1$ | 83.7 | *82.8* |
| 10 | $10 \times 10 \times 1$ | 84.1 | |

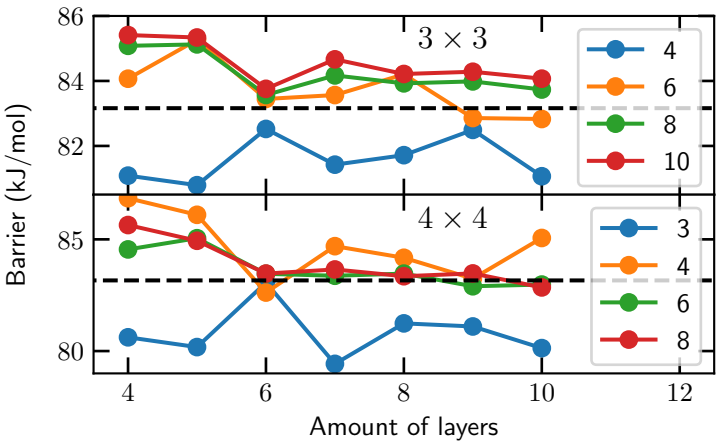


FIGURE 9.A.1: Convergence of the minimum barrier height on Pd(111) as a function of the amount of layers for the number of $k$-points equal to $(n \times n \times 1)$, where $n$ is indicated in the legend. The upper panel and lower panel used a $3 \times 3$ and $4 \times 4$ supercell, respectively. The dashed lines indicate the converged barrier height.

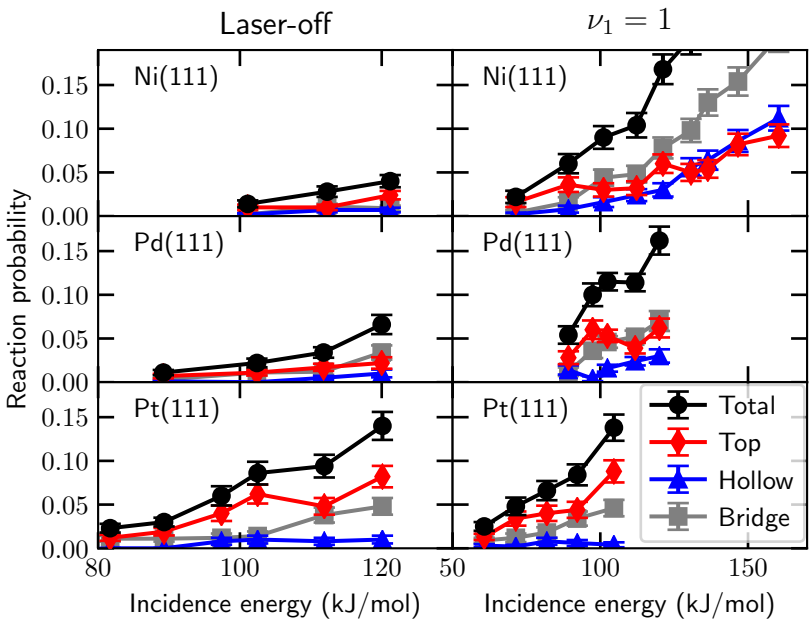


FIGURE 9.B.1: Reaction probability of $CHD_3$ on the top, hollow and bridge high-symmetry sites (red, blue and grey, respectively) and the total reaction probability (black) on Ni(111), Pd(111) and Pt(111) for laser-off conditions and for $\nu_1 = 1$, as a function of the incidence energy when a bond dissociates, i.e., $r = r^{\ddagger}$. The error bars represent 68% confidence intervals.

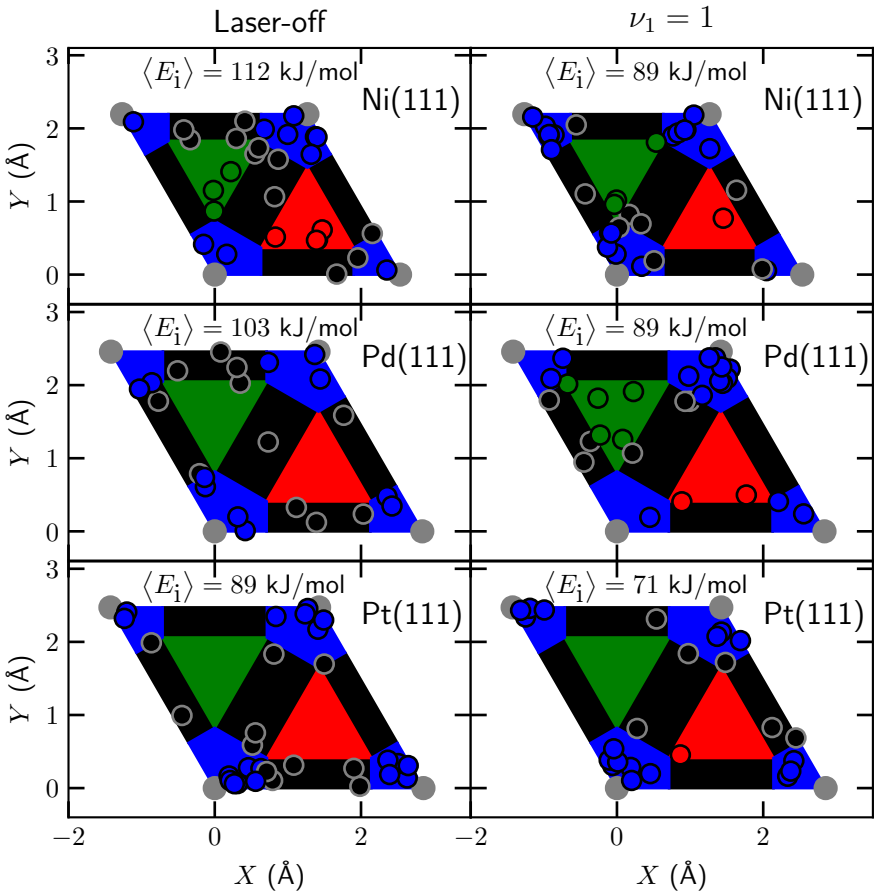


FIGURE 9.B.2: Impact site of reacting $CHD_3$ on Ni(111), Pd(111) and Pt(111) for laser-off and $\nu_1 = 1$ when a bond dissociates, i.e., $r = r^{\ddagger}$. Under laser-off conditions the reaction probability is about 2.5%, whereas for the $\nu_1 = 1$ conditions the reaction probability is about 5%. The top, fcc, hcp and bridge sites are indicated in blue, red, green and black, respectively, and the top layer atoms are indicate by the gray circles.

## References


(1) Rostrup-Nielsen, J. R.; Sehested, J.; Nørskov, J. K. In *Advances in Catalysis*; Academic Press: 2002; Vol. 47, pp 65–139, DOI: 10.1016/S0360-0564(02)47006-X.

(2) Wei, J.; Iglesia, E. Mechanism and Site Requirements for Activation and Chemical Conversion of Methane on Supported Pt Clusters and Turnover Rate Comparisons among Noble Metals. *J. Phys. Chem. B* **2004**, *108*, 4094–4103, DOI: 10.1021/jp036985z.

(3) Jones, G.; Jakobsen, J. G.; Shim, S. S.; Kleis, J.; Andersson, M. P.; Rossmeisl, J.; Abild-Pedersen, F.; Bligaard, T.; Helveg, S.; Hinnemann, B.; Rostrup-Nielsen, J. R.; Chorkendorff, I.; Sehested, J.; Nørskov, J. K. First Principles Calculations and Experimental Insight into Methane Steam Reforming over Transition Metal Catalysts. *J. Catal.* **2008**, *259*, 147–160, DOI: 10.1016/j.jcat.2008.08.003.

(4) Kroes, G.-J. Towards Chemically Accurate Simulation of Molecule–Surface Reactions. *Phys. Chem. Chem. Phys.* **2012**, *14*, 14966–14981, DOI: 10.1039/C2CP42471A.

(5) Jackson, B.; Nattino, F.; Kroes, G.-J. Dissociative Chemisorption of Methane on Metal Surfaces: Tests of Dynamical Assumptions Using Quantum Models and Ab Initio Molecular Dynamics. *J. Chem. Phys.* **2014**, *141*, 054102, DOI: 10.1063/1.4891327.

(6) Wellendorff, J.; Silbaugh, T. L.; Garcia-Pintos, D.; Nørskov, J. K.; Bligaard, T.; Studt, F.; Campbell, C. T. A Benchmark Database for Adsorption Bond Energies to Transition Metal Surfaces and Comparison to Selected DFT Functionals. *Surf. Sci.* **2015**, *640*, 36–44, DOI: 10.1016/j.susc.2015.03.023.

(7) Gautier, S.; Steinmann, S. N.; Michel, C.; Fleurat-Lessard, P.; Sautet, P. Molecular Adsorption at Pt(111). How Accurate Are DFT Functionals? *Phys. Chem. Chem. Phys.* **2015**, *17*, 28921–28930, DOI: 10.1039/C5CP04534G.

(8) Kroes, G.-J. Toward a Database of Chemically Accurate Barrier Heights for Reactions of Molecules with Metal Surfaces. *J. Phys. Chem. Lett.* **2015**, *6*, 4106–4114, DOI: 10.1021/acs.jpclett.5b01344.

(9) Díaz, C.; Pijper, E.; Olsen, R. A.; Busnengo, H. F.; Auerbach, D. J.; Kroes, G. J. Chemically Accurate Simulation of a Prototypical Surface Reaction: $H_2$ Dissociation on Cu(111). *Science* **2009**, *326*, 832–834, DOI: 10.1126/science.1178722.

(10) Sementa, L.; Wijzenbroek, M.; van Kolck, B. J.; Somers, M. F.; Al-Halabi, A.; Busnengo, H. F.; Olsen, R. A.; Kroes, G. J.; Rutkowski, M.; Thewes, C.; Kleimeier, N. F.; Zacharias, H. Reactive Scattering of $H_2$ from Cu(100): Comparison of Dynamics Calculations Based on the Specific Reaction Parameter Approach to Density Functional Theory with Experiment. *J. Chem. Phys.* **2013**, *138*, 044708, DOI: 10.1063/1.4776224.

(11) Ghassemi, E. N.; Wijzenbroek, M.; Somers, M. F.; Kroes, G.-J. Chemically Accurate Simulation of Dissociative Chemisorption of $D_2$ on Pt(111). *Chem. Phys. Lett.* **2017**, *683*, 329–335, DOI: 10.1016/j.cplett.2016.12.059.

(12) Nattino, F.; Migliorini, D.; Kroes, G.-J.; Dombrowski, E.; High, E. A.; Killelea, D. R.; Utz, A. L. Chemically Accurate Simulation of a Polyatomic Molecule-Metal Surface Reaction. *J. Phys. Chem. Lett.* **2016**, *7*, 2402–2406, DOI: 10.1021/acs.jpclett.6b01022.

(13) Migliorini, D.; Chadwick, H.; Nattino, F.; Gutiérrez-González, A.; Dombrowski, E.; High, E. A.; Guo, H.; Utz, A. L.; Jackson, B.; Beck, R. D.; Kroes, G.-J. Surface Reaction Barriometry: Methane Dissociation on Flat and Stepped Transition-Metal Surfaces. *J. Phys. Chem. Lett.* **2017**, *8*, 4177–4182, DOI: 10.1021/acs.jpclett.7b01905.

(14) Chadwick, H.; Gutiérrez-González, A.; Migliorini, D.; Beck, R. D.; Kroes, G.-J. Incident Angle Dependence of $CHD_3$ Dissociation on the Stepped Pt(211) Surface. *J. Phys. Chem. C* **2018**, *122*, 19652–19660, DOI: 10.1021/acs.jpcc.8b05887.

(15) Chadwick, H.; Guo, H.; Gutiérrez-González, A.; Menzel, J. P.; Jackson, B.; Beck, R. D. Methane Dissociation on the Steps and Terraces of Pt(211) Resolved by Quantum State and Impact Site. *J. Chem. Phys.* **2018**, *148*, 014701, DOI: 10.1063/1.5008567.

(16) Nattino, F.; Ueta, H.; Chadwick, H.; van Reijzen, M. E.; Beck, R. D.; Jackson, B.; van Hemert, M. C.; Kroes, G.-J. Ab Initio Molecular Dynamics Calculations versus Quantum-State-Resolved Experiments on $CHD_3$ + Pt(111): New Insights into a Prototypical Gas–Surface Reaction. *J. Phys. Chem. Lett.* **2014**, *5*, 1294–1299, DOI: 10.1021/jz500233n.

(17) Nave, S.; Jackson, B. Vibrational Mode-Selective Chemistry: Methane Dissociation on Ni(100). *Phys. Rev. B* **2010**, *81*, 233408, DOI: 10.1103/PhysRevB.81.233408.

(18) Nattino, F.; Migliorini, D.; Bonfanti, M.; Kroes, G.-J. Methane Dissociation on Pt(111): Searching for a Specific Reaction Parameter Density Functional. *J. Chem. Phys.* **2016**, *144*, 044702, DOI: 10.1063/1.4939520.

(19) Czakó, G.; Bowman, J. M. Dynamics of the Reaction of Methane with Chlorine Atom on an Accurate Potential Energy Surface. *Science* **2011**, *334*, 343–346, DOI: 10.1126/science.1208514.

(20) Goodman, R. M.; Farrell, H. H.; Somorjai, G. A. Mean Displacement of Surface Atoms in Palladium and Lead Single Crystals. *J. Chem. Phys.* **1968**, *48*, 1046–1051, DOI: 10.1063/1.1668759.

(21) Manson, J. R. Inelastic Scattering from Surfaces. *Phys. Rev. B* **1991**, *43*, 6924–6937, DOI: 10.1103/PhysRevB.43.6924.

(22) Manson, J. R. Multiphonon Atom-Surface Scattering. *Comput. Phys. Commun.* **1994**, *80*, 145–167, DOI: 10.1016/0010-4655(94)90101-5.

(23) Tait, S. L.; Dohnálek, Z.; Campbell, C. T.; Kay, B. D. Methane Adsorption and Dissociation and Oxygen Adsorption and Reaction with CO on Pd Nanoparticles on MgO(100) and on Pd(111). *Surf. Sci.* **2005**, *591*, 90–107, DOI: 10.1016/j.susc.2005.06.024.

(24) Groß, A. Reactivity of Bimetallic Systems Studied from First Principles. *Top. Catal.* **2006**, *37*, 29–39, DOI: 10.1007/s11244-006-0005-x.

(25) Ramos, M.; Martínez, A. E.; Busnengo, H. F. $H_2$ Dissociation on Individual Pd Atoms Deposited on Cu(111). *Phys. Chem. Chem. Phys.* **2012**, *14*, 303–310, DOI: 10.1039/C1CP22163A.

(26) Marcinkowski, M. D.; Darby, M. T.; Liu, J.; Wimble, J. M.; Lucci, F. R.; Lee, S.; Michaelides, A.; Flytzani-Stephanopoulos, M.; Stamatakis, M.; Sykes, E. C. H. Pt/Cu Single-Atom Alloys as Coke-Resistant Catalysts for Efficient C–H Activation. *Nat. Chem.* **2018**, *10*, 325–332, DOI: 10.1038/nchem.2915.

(27) Marcus, R. A. On the Analytical Mechanics of Chemical Reactions. Quantum Mechanics of Linear Collisions. *J. Chem. Phys.* **1966**, *45*, 4493–4499, DOI: 10.1063/1.1727528.

(28) McCullough, E. A.; Wyatt, R. E. Quantum Dynamics of the Collinear (H, $H_2$) Reaction. *J. Chem. Phys.* **1969**, *51*, 1253–1254, DOI: 10.1063/1.1672133.

(29) Gerrits, N.; Migliorini, D.; Kroes, G.-J. Dissociation of $CHD_3$ on Cu(111), Cu(211), and Single Atom Alloys of Cu(111). *J. Chem. Phys.* **2018**, *149*, 224701, DOI: 10.1063/1.5053990.

(30) Killelea, D. R.; Campbell, V. L.; Shuman, N. S.; Utz, A. L. Bond-Selective Control of a Heterogeneously Catalyzed Reaction. *Science* **2008**, *319*, 790–793, DOI: 10.1126/science.1152819.

(31) Shen, X. J.; Lozano, A.; Dong, W.; Busnengo, H. F.; Yan, X. H. Towards Bond Selective Chemistry from First Principles: Methane on Metal Surfaces. *Phys. Rev. Lett.* **2014**, *112*, 046101, DOI: 10.1103/PhysRevLett.112.046101.

(32) Hundt, P. M.; Ueta, H.; van Reijzen, M. E.; Jiang, B.; Guo, H.; Beck, R. D. Bond-Selective and Mode-Specific Dissociation of $CH_3D$ and $CH_2D_2$ on Pt(111). *J. Phys. Chem. A* **2015**, *119*, 12442–12448, DOI: 10.1021/acs.jpca.5b07949.

(33) Gutiérrez-González, A.; Crim, F. F.; Beck, R. D. Bond Selective Dissociation of Methane ($CH_3D$) on the Steps and Terraces of Pt(211). *J. Chem. Phys.* **2018**, *149*, 074701, DOI: 10.1063/1.5041349.

(34) Beck, R. D.; Maroni, P.; Papageorgopoulos, D. C.; Dang, T. T.; Schmid, M. P.; Rizzo, T. R. Vibrational Mode-Specific Reaction of Methane on a Nickel Surface. *Science* **2003**, *302*, 98–100, DOI: 10.1126/science.1088996.

(35) Juurlink, L. B. F.; Killelea, D. R.; Utz, A. L. State-Resolved Probes of Methane Dissociation Dynamics. *Prog. Surf. Sci.* **2009**, *84*, 69–134, DOI: 10.1016/j.progsurf.2009.01.001.

(36) Smith, R. R.; Killelea, D. R.; DelSesto, D. F.; Utz, A. L. Preference for Vibrational over Translational Energy in a Gas-Surface Reaction. *Science* **2004**, *304*, 992–995, DOI: 10.1126/science.1096309.

(37) Jiang, B.; Yang, M.; Xie, D.; Guo, H. Quantum Dynamics of Polyatomic Dissociative Chemisorption on Transition Metal Surfaces: Mode Specificity and Bond Selectivity. *Chem. Soc. Rev.* **2016**, *45*, 3621–3640, DOI: 10.1039/C5CS00360A.

(38) Yoder, B. L.; Bisson, R.; Beck, R. D. Steric Effects in the Chemisorption of Vibrationally Excited Methane on Ni(100). *Science* **2010**, *329*, 553–556, DOI: 10.1126/science.1191751.

(39) Gutiérrez-González, A.; Torio, M. E.; Busnengo, H. F.; Beck, R. D. Site Selective Detection of Methane Dissociation on Stepped Pt Surfaces. *Top. Catal.* **2019**, DOI: 10.1007/s11244-019-01170-5.

(40) Kresse, G.; Hafner, J. Ab Initio Molecular-Dynamics Simulation of the Liquid-Metal–Amorphous-Semiconductor Transition in Germanium. *Phys. Rev. B* **1994**, *49*, 14251–14269, DOI: 10.1103/PhysRevB.49.14251.

(41) Kresse, G.; Hafner, J. Ab Initio Molecular Dynamics for Liquid Metals. *Phys. Rev. B* **1993**, *47*, 558–561, DOI: 10.1103/PhysRevB.47.558.

(42) Kresse, G.; Furthmüller, J. Efficient Iterative Schemes for Ab Initio Total-Energy Calculations Using a Plane-Wave Basis Set. *Phys. Rev. B* **1996**, *54*, 11169–11186, DOI: 10.1103/PhysRevB.54.11169.

(43) Kresse, G.; Furthmüller, J. Efficiency of Ab-Initio Total Energy Calculations for Metals and Semiconductors Using a Plane-Wave Basis Set. *Comput. Mater. Sci.* **1996**, *6*, 15–50, DOI: 10.1016/0927-0256(96)00008-0.

(44) Kresse, G.; Joubert, D. From Ultrasoft Pseudopotentials to the Projector Augmented-Wave Method. *Phys. Rev. B* **1999**, *59*, 1758–1775, DOI: 10.1103/PhysRevB.59.1758.

(45) Blöchl, P. E. Projector Augmented-Wave Method. *Phys. Rev. B* **1994**, *50*, 17953–17979, DOI: 10.1103/PhysRevB.50.17953.

(46) Methfessel, M.; Paxton, A. T. High-Precision Sampling for Brillouin-Zone Integration in Metals. *Phys. Rev. B* **1989**, *40*, 3616–3621, DOI: 10.1103/PhysRevB.40.3616.

(47) Henkelman, G.; Jónsson, H. A Dimer Method for Finding Saddle Points on High Dimensional Potential Surfaces Using Only First Derivatives. *J. Chem. Phys.* **1999**, *111*, 7010–7022, DOI: 10.1063/1.480097.

(48) Heyden, A.; Bell, A. T.; Keil, F. J. Efficient Methods for Finding Transition States in Chemical Reactions: Comparison of Improved Dimer Method and Partitioned Rational Function Optimization Method. *J. Chem. Phys.* **2005**, *123*, 224101, DOI: 10.1063/1.2104507.

(49) Kästner, J.; Sherwood, P. Superlinearly Converging Dimer Method for Transition State Search. *J. Chem. Phys.* **2008**, *128*, 014106, DOI: 10.1063/1.2815812.

(50) Xiao, P.; Sheppard, D.; Rogal, J.; Henkelman, G. Solid-State Dimer Method for Calculating Solid-Solid Phase Transitions. *J. Chem. Phys.* **2014**, *140*, 174104, DOI: 10.1063/1.4873437.

(51) Transition State Tools Package for VASP https://theory.cm.utexas.edu/vtsttools/index.html (accessed 02/08/2021).

(52) Migliorini, D.; Chadwick, H.; Kroes, G.-J. Methane on a Stepped Surface: Dynamical Insights on the Dissociation of $CHD_3$ on Pt(111) and Pt(211). *J. Chem. Phys.* **2018**, *149*, 094701, DOI: 10.1063/1.5046065.

(53) Chadwick, H.; Gutiérrez-González, A.; Beck, R. D.; Kroes, G.-J. Transferability of the SRP32-vdW Specific Reaction Parameter Functional to $CHD_3$ Dissociation on Pt(110)-(2x1). *J. Chem. Phys.* **2019**, *150*, 124702, DOI: 10.1063/1.5081005.

(54) Chadwick, H.; Gutiérrez-González, A.; Beck, R. D.; Kroes, G.-J. $CHD_3$ Dissociation on the Kinked Pt(210) Surface: A Comparison of Experiment and Theory. *J. Phys. Chem. C* **2019**, *123*, 14530–14539, DOI: 10.1021/acs.jpcc.9b03051.

(55) Gerrits, N.; Shakouri, K.; Behler, J.; Kroes, G.-J. Accurate Probabilities for Highly Activated Reaction of Polyatomic Molecules on Surfaces Using a High-Dimensional Neural Network Potential: $CHD_3$ + Cu(111). *J. Phys. Chem. Lett.* **2019**, *10*, 1763–1768, DOI: 10.1021/acs.jpclett.9b00560.

(56) Perdew, J. P.; Burke, K.; Ernzerhof, M. Generalized Gradient Approximation Made Simple. *Phys. Rev. Lett.* **1996**, *77*, 3865–3868, DOI: 10.1103/PhysRevLett.77.3865.

(57) Hammer, B.; Hansen, L. B.; Nørskov, J. K. Improved Adsorption Energetics within Density-Functional Theory Using Revised Perdew-Burke-Ernzerhof Functionals. *Phys. Rev. B* **1999**, *59*, 7413–7421, DOI: 10.1103/PhysRevB.59.7413.

(58) Dion, M.; Rydberg, H.; Schröder, E.; Langreth, D. C.; Lundqvist, B. I. Van Der Waals Density Functional for General Geometries. *Phys. Rev. Lett.* **2004**, *92*, 246401, DOI: 10.1103/PhysRevLett.92.246401.

(59) Mondal, A.; Wijzenbroek, M.; Bonfanti, M.; Díaz, C.; Kroes, G.-J. Thermal Lattice Expansion Effect on Reactive Scattering of $H_2$ from Cu(111) at $T_s$ = 925 K. *J. Phys. Chem. A* **2013**, *117*, 8770–8781, DOI: 10.1021/jp4042183.

(60) Touloukian, Y.; Kirby, R.; Taylor, R.; Desai, P., Thermophysical Properties of Matter - the TPRC Data Series. Volume 12. Thermal Expansion Metallic Elements and Alloys, 14 vols.; Plenum Publishing Corporation: New York, 1975; Vol. 12; 1436 pp.

(61) Nave, S.; Tiwari, A. K.; Jackson, B. Methane Dissociation and Adsorption on Ni(111), Pt(111), Ni(100), Pt(100), and Pt(110)-(1x2): Energetic Study. *J. Chem. Phys.* **2010**, *132*, 054705, DOI: 10.1063/1.3297885.

(62) Nave, S.; Jackson, B. Methane Dissociation on Ni(111) and Pt(111): Energetic and Dynamical Studies. *J. Chem. Phys.* **2009**, *130*, 054701, DOI: 10.1063/1.3065800.

(63) Fisher, R. A. On the Interpretation of $X^2$ from Contingency Tables, and the Calculation of P. *J. R. Stat. Soc.* **1922**, *85*, 87–94, DOI: 10.2307/2340521.

(64) Jackson, B.; Nave, S. The Dissociative Chemisorption of Methane on Ni(100): Reaction Path Description of Mode-Selective Chemistry. *J. Chem. Phys.* **2011**, *135*, 114701, DOI: 10.1063/1.3634073.

(65) Guo, H.; Jackson, B. Mode-Selective Chemistry on Metal Surfaces: The Dissociative Chemisorption of $CH_4$ on Pt(111). *J. Chem. Phys.* **2016**, *144*, 184709, DOI: 10.1063/1.4948941.

(66) Chadwick, H.; Migliorini, D.; Kroes, G. J. $CHD_3$ Dissociation on Pt(111): A Comparison of the Reaction Dynamics Based on the PBE Functional and on a Specific Reaction Parameter Functional. *J. Chem. Phys.* **2018**, *149*, 044701, DOI: 10.1063/1.5039458.

(67) Baule, B. Theoretische Behandlung Der Erscheinungen in Verdünnten Gasen. *Ann. Phys.* **1914**, *349*, 145–176, DOI: 10.1002/andp.19143490908.

(68) Goodman, F. O.; Wachman, H. Y. *Formula for Thermal Accommodation Coefficient*; 66-1; Cambridge, Massachusetts: M.I.T. Fluid Dynamics Research, 1966, DOI: 10.21236/ad0631007.

(69) Shen, X.; Zhang, Z.; Zhang, D. H. Communication: Methane Dissociation on Ni(111) Surface: Importance of Azimuth and Surface Impact Site. *J. Chem. Phys.* **2016**, *144*, 101101, DOI: 10.1063/1.4943128.

(70) Jiang, B.; Guo, H. Dynamics of Water Dissociative Chemisorption on Ni(111): Effects of Impact Sites and Incident Angles. *Phys. Rev. Lett.* **2015**, *114*, 166101, DOI: 10.1103/PhysRevLett.114.166101.

(71) Juurlink, L. B. F.; McCabe, P. R.; Smith, R. R.; DiCologero, C. L.; Utz, A. L. Eigenstate-Resolved Studies of Gas-Surface Reactivity: $CH_4$ $\nu_3$ Dissociation on Ni(100). *Phys. Rev. Lett.* **1999**, *83*, 868–871, DOI: 10.1103/PhysRevLett.83.868.

(72) Schmid, M. P.; Maroni, P.; Beck, R. D.; Rizzo, T. R. Surface Reactivity of Highly Vibrationally Excited Molecules Prepared by Pulsed Laser Excitation: $CH_4$ ($2\nu_3$) on Ni(100). *J. Chem. Phys.* **2002**, *117*, 8603–8606, DOI: 10.1063/1.1519860.

(73) Bisson, R.; Sacchi, M.; Dang, T. T.; Yoder, B.; Maroni, P.; Beck, R. D. State-Resolved Reactivity of $CH_4(2\nu_3)$ on Pt(111) and Ni(111): Effects of Barrier Height and Transition State Location. *J. Phys. Chem. A* **2007**, *111*, 12679–12683, DOI: 10.1021/jp076082w.

(74) Luntz, A. C.; Bethune, D. S. Activation of Methane Dissociation on a Pt(111) Surface. *J. Chem. Phys.* **1989**, *90*, 1274–1280, DOI: 10.1063/1.456132.

(75) Oakes, D. J.; McCoustra, M. R.; Chesters, M. A. Dissociative Adsorption of Methane on Pt(111) Induced by Hyperthermal Collisions. *Faraday Discuss.* **1993**, *96*, 325–336, DOI: 10.1039/FD9939600325.

(76) Higgins, J.; Conjusteau, A.; Scoles, G.; Bernasek, S. L. State Selective Vibrational ($2\nu 3$) Activation of the Chemisorption of Methane on Pt (111). *J. Chem. Phys.* **2001**, *114*, 5277–5283, DOI: 10.1063/1.1349895.

(77) Campbell, V. L.; Chen, N.; Guo, H.; Jackson, B.; Utz, A. L. Substrate Vibrations as Promoters of Chemical Reactivity on Metal Surfaces. *J. Phys. Chem. A* **2015**, *119*, 12434–12441, DOI: 10.1021/acs.jpca.5b07873.

(78) Tiwari, A. K.; Nave, S.; Jackson, B. The Temperature Dependence of Methane Dissociation on Ni(111) and Pt(111): Mixed Quantum-Classical Studies of the Lattice Response. *J. Chem. Phys.* **2010**, *132*, 134702, DOI: 10.1063/1.3357415.

(79) Beebe, T. P.; Goodman, D. W.; Kay, B. D.; Yates, J. T. Kinetics of the Activated Dissociative Adsorption of Methane on the Low Index Planes of Nickel Single Crystal Surfaces. *J. Chem. Phys.* **1987**, *87*, 2305–2315, DOI: 10.1063/1.453162.

(80) Lee, M. B.; Yang, Q. Y.; Ceyer, S. T. Dynamics of the Activated Dissociative Chemisorption of $CH_4$ and Implication for the Pressure Gap in Catalysis: A Molecular Beam–High Resolution Electron Energy Loss Study. *J. Chem. Phys.* **1987**, *87*, 2724–2741, DOI: 10.1063/1.453060.

(81) Holmblad, P. M.; Wambach, J.; Chorkendorff, I. Molecular Beam Study of Dissociative Sticking of Methane on Ni(100). *J. Chem. Phys.* **1995**, *102*, 8255–8263, DOI: 10.1063/1.468955.

# Chapter 10

# Dissociative Chemisorption of Methanol on Cu(111) with Implications for Formaldehyde Formation

This chapter is based on Gerrits, N.; Kroes, G.-J. An AIMD Study of Dissociative Chemisorption of Methanol on Cu(111) with Implications for Formaldehyde Formation. *J. Chem. Phys.* **2019**, *150*, 024706, DOI: 10.1063/1.5070129

## Abstract

An important industrial process is methanol steam reforming, which is typically used in conjunction with copper catalysts. However, little agreement exists on the reaction mechanisms involved on a copper catalyst. Therefore, in this chapter research has been performed yielding additional insight into the reaction mechanism for dissociative chemisorption of methanol on Cu(111) using Born-Oppenheimer molecular dynamics, supported by static calculations of the molecule-metal surface interaction with density functional theory. In this chapter, it is predicted that after the initial dissociation, formaldehyde is formed through three different mechanisms. Additionally, it is observed that at high energy, CH cleavage is the dominant pathway instead of the formerly presumed OH cleavage pathway. Finally, in order to describe the interaction of methanol with the metal surface, the SRP32-vdW functional is used, which has been previously developed and tested for $CHD_3$ on Ni(111), Pt(111), and Pt(211) using the specific reaction parameter (SRP) approach. The SRP32-vdW functional is applied to methanol on Cu(111) as well, in the hope that future experiments can validate the transferability of the SRP32-vdW functional to chemically related molecule-metal surface systems.

## 10.1 Introduction

Methanol steam reforming is an important industrial process with several applications such as formaldehyde and syngas production. However, there is little agreement concerning the reaction mechanisms of methanol on metal surfaces, especially on copper-based catalysts[1]. Due to the existence of several different chemical bonds, methanol dissociation is described by a complex reaction scheme involving several products that are formed via different pathways. Furthermore, little is known about the mechanisms of the reactions that follow the breaking of the first bond in methanol. For example, experimental evidence for formaldehyde formation on copper catalysts through direct decomposition of methanol exists[2–5], although the underlying pathways remain unclear. So far, theoretical calculations have only been able to deal with this reaction scheme on a static level using transition state theory[6–12], or on a dynamical level but with a frozen surface[13]. However, these levels of theory exclude exchange of energy between the surface atoms and the molecule and transition state theory excludes any dynamical effects such as steering as well. Moreover, although the complete steam reforming reaction of methanol to $CO_2$ and hydrogen of course also involves water, water only plays a role after the initial reaction steps, i.e., after formaldehyde is formed, by hydrolyzing either a methyl formate intermediate or formaldehyde[1]. Depending on the reaction conditions, the preceding formation of formaldehyde is often the rate controlling step for methanol steam reforming[14–17], and thus an important reaction step to investigate. Therefore, in this chapter water is neglected and only the dissociative chemisorption of methanol and subsequent formation of formaldehyde on Cu(111) is investigated using Born-Oppenheimer molecular dynamics (BOMD) in order to include dynamical effects. Finally, on Pt(111) and Ru(0001) the methanol decomposition mechanism can be affected by the methanol pre-coverage, while no such dependence has been reported on Cu(111), on which methanol has a lower adsorption energy[9]. Since the simulations in this chapter are performed in the zero coverage limit, i.e., only initial sticking of methanol on a clean surface is considered, the results should therefore be relevant for catalysis at sufficiently low pressure and sufficiently high temperatures.

Moreover, to model accurately the interaction between molecules and metal surfaces remains challenging[18–22]. Therefore, the specific reaction parameter (SRP) approach has been used to develop a chemically accurate functional (SRP32-vdW) for methane on Ni(111), Pt(111) and Pt(211)[23, 24]. The SRP32-vdW functional was first developed for $CHD_3$ + Ni(111)[23]) and later shown to be transferable to methane interacting with metals within the

same periodic table group ($CHD_3$ + Pt(111)[24]) and with stepped surfaces of that group ($CHD_3$ + Pt(211)[24, 25]). In this chapter, predictive calculations have been performed on methanol, which is chemically related to methane, and on a metal surface belonging to a neighbouring group of the periodic table. Hopefully, these predictions will be followed by experiments in order to validate the transferability of the SRP32-vdW functional to methanol on a Cu(111) surface.

To summarize, this chapter makes a prediction for the reactivity of methanol on Cu(111), combined with a detailed analysis of the dynamical behaviour. Furthermore, new insights are gained for the reaction mechanisms for the formation of formaldehyde on Cu(111). The chapter is structured as follows: a short summary of the technical details is given in Section 10.2. Moreover, the barriers and elbow plots obtained with static DFT calculations are discussed in Sections 10.3.1 and 10.3.2. In Section 10.3.3 the reaction probabilities are presented, followed by the impact site associated with reactive collisions in Section 10.3.4. Furthermore, Section 10.3.5 concerns the energy transfer of methanol to the surface atoms, and Section 10.3.6 concerns the orientations methanol goes through during the reaction. Finally, formaldehyde formation is discussed in Section 10.3.7, and a short summary is given in Section 10.4.

## 10.2 Method

The Vienna Ab-initio Simulation Package (VASP version 5.3.5)[26–30] is used for the BOMD and electronic structure (Density Functional Theory, DFT) calculations. A kinetic energy cutoff of 400 eV and a Γ-centered $3 \times 3 \times 1$ $k$-point grid are used. Moreover, core electrons have been represented with the projector augmented wave (PAW) method[30, 31]. The surface is modeled using a 4 layer ($4 \times 3$) supercell, where the angle between the $u$ and $v$ vectors is 30° instead of the usual 60°, i.e., a skewed unit cell is used (see also Figure 10.B.1. Furthermore, a vacuum distance of 15 Å is used between the slabs and the top three layers have been relaxed in the $Z$ direction. In order to speed up convergence, first-order Methfessel-Paxton smearing[32] with a width parameter of 0.2 eV has been applied. Convergence of the employed computational setup is confirmed to be within chemical accuracy (1 kcal/mol, or 4.2 kJ/mol) and results connected to this convergence are given in Section 10.A.

Transition states (TSs) are obtained with the dimer method[33–36] as implemented in the VASP Transition State Tools package (VTST)[37], and are confirmed to be first-order saddle points by checking if only one imaginary

frequency is found at the TS. Forces on the degrees of freedom are converged within 5 meV/Å, where the degrees of freedom are for the motion of the methanol atoms.

In order to account for surface temperature effects, the procedure described in Section 2.4.1 is employed. For the BOMD simulations, a surface temperature of 550 K is used, where the atoms in the top three layers are allowed to move in all three directions and the ideal lattice constant is expanded by a factor of 1.0078 in order to reflect the expansion of the bulk due to the surface temperature[38]. Ten differently-initialized slabs are generated using the aforementioned procedure, resulting in a pool of 10 000 snapshots. The average temperature of the ensemble of slabs is $(537 \pm 54)$ K.

Methanol molecular beam bundles were simulated according to the parameters in Table 10.1, which were obtained for $CHD_3$ seeded in $H_2$ molecular beam bundles in Ref. [23]. It is assumed that methanol has a similar velocity slip in a molecular beam as methane; hence, beam parameters obtained for $CHD_3$ are used here for methanol. The residual energy $E_R$ (4.2 kJ/mol) is added to the kinetic energy in order to correct for the interaction with the periodic image and to take into account that the interaction of methanol with the surface has not yet decayed to zero, as is described in Sections 2.4.2 and 10.A. The laser-off beams are simulated by sampling the initial vibrational states of the molecule from a Boltzman distribution at nozzle temperature $T_n$, while the initial angular momentum of the molecules has been set to zero, and the molecules' orientations are randomly sampled. The laser-on beam ($\nu_1 = 1$) is simulated by initializing all molecules with one quantum in the OH stretch mode. Moreover, the experimental R(1) transition to the rotational state $J = 2$ and $K = 0$ is simulated in the BOMD trajectories. It is assumed that the alignment in $M$ of the molecules excited in the experiments[20] is erased by hyperfine coupling due to the long pathway to the surface. Therefore, $M$ has been statistically sampled, i.e., $M = -2, -1, 0, 1, 2$. For the rotational states, the methanol was treated like an oblate symmetric top, in an approximation in which the effect of the hydrogen in the hydroxyl is neglected, taking into account the mass mismatch between the oxygen and hydrogen atoms. The coupling between the internal rotation of the hydroxyl with respect to the methyl, i.e., the torsion vibrational mode, and the rotational states is also neglected in the generation of the initial conditions. Hence, setting up the initial rotational states is done in the same way as for $CHD_3$ in previous work[23, 24] (see also Section 2.4.2). For every BOMD data point, 500 trajectories were run for up to 1 ps, or until the trajectory was considered to be reacted or scattered, with a time step of 0.4 fs. The rest of the technical details of the BOMD calculations can be found in recent work[23, 24, 39] and in Chapter 2.

TABLE 10.1: Experimental beam parameters that describe the simulated methanol velocity distributions. $v_0$ and $\alpha$ are determined through time-of-flight measurements for 600, 750 and 900 K[23]. The parameters for $\langle E_i \rangle = 163.1$ kJ/mol are not from experiment, but theoretical estimates obtained by extrapolation. See the text for further details.

| $T_n$ (K) | $\langle E_i \rangle$ kJ/mol | $v_0$ (m/s) | $\alpha$ (m/s) |
|---|---|---|---|
| 500* | 163.1 | 3177.70 | 158.89 |
| 600 | 188.7 | 3418.09 | 168.02 |
| 750 | 229.2 | 3760.72 | 216.91 |
| 900 | 269.5 | 4070.12 | 274.51 |

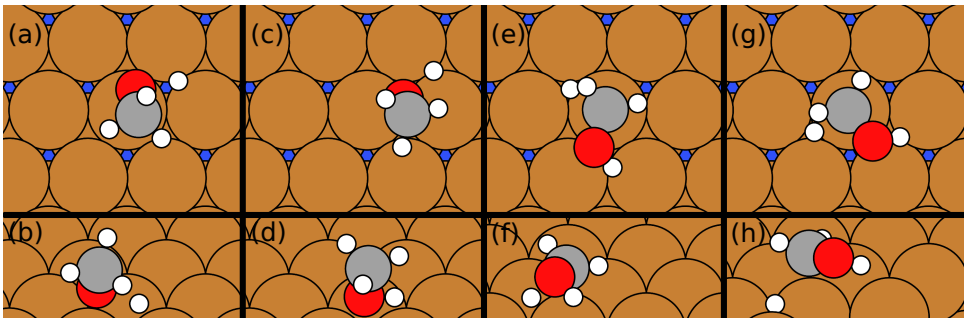


FIGURE 10.1: Top and side view of the TS of methanol on Cu(111) with the OH-fcc1 (a,b), OH-bridge1 (c,d), CH-top1 (e,f), and CH-top2 (g,h) geometries. At the surface, blue circles indicate the fcc sites.

The SRP32-vdW functional previously used for $CHD_3$ + Ni(111), Pt(111), Pt(211), Cu(111) and Cu(211)[23, 24, 40] is employed here as well, of which the exchange part is defined as

$$E_x = x \cdot E_x^{RPBE} + (1 - x) \cdot E_x^{PBE}, \tag{10.1}$$

where $E_x^{RPBE}$ and $E_x^{PBE}$ are the exchange parts of the RPBE and PBE[41, 42] exchange-correlation functionals, respectively, and $x = 0.32$. Moreover, for the correlation part, the vdW correlation functional of Dion and coworkers (vdW-DF1)[43] is used.

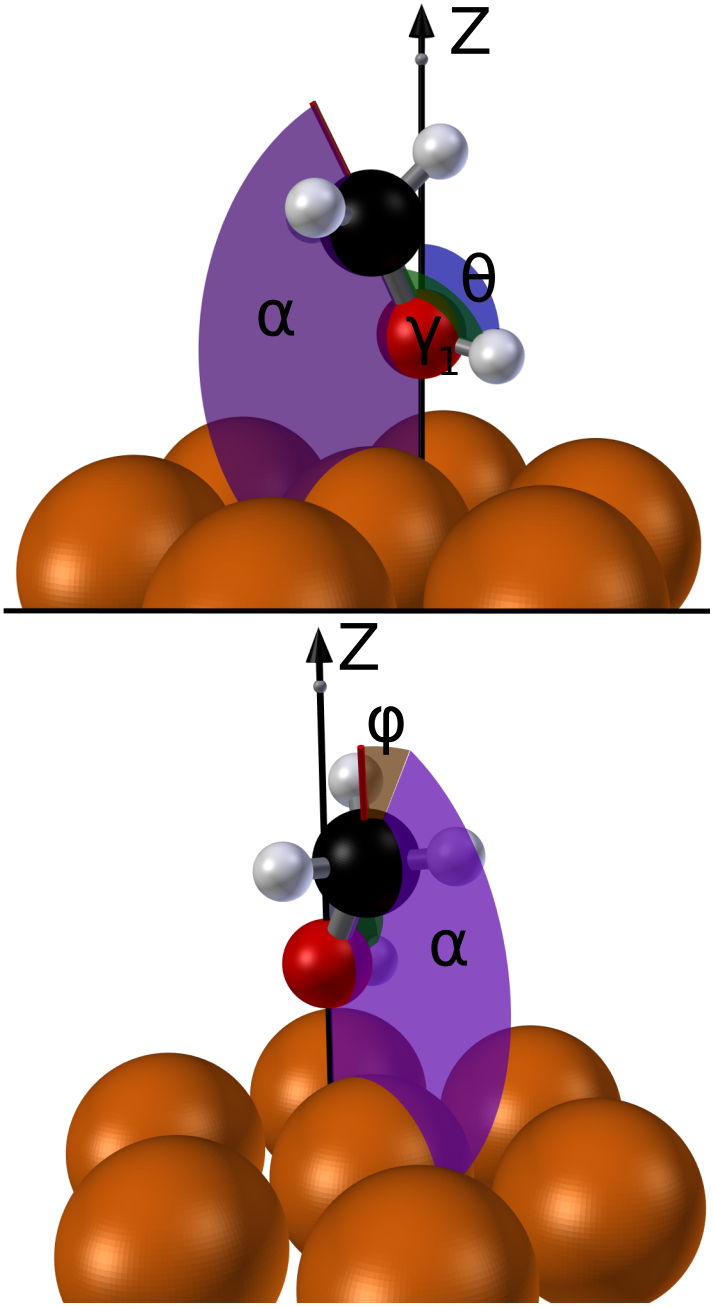


FIGURE 10.2: $\theta$, $\gamma_1$, $\alpha$ and $\phi$ angles used to describe the methanol geometry. See the text for further explanation.

TABLE 10.2: Barrier geometries for methanol on Cu(111). The labels indicate whether OH or CH cleavage occurred and the location of the broken bond. Zero-point energy corrected barriers are given in the brackets.

| Label | $Z_C$ (Å) | $Z_O$ (Å) | $r$ (Å) | $\theta$ (°) | $\beta$ (°) | $\gamma_1$ (°) | $\gamma_2$ (°) | $\alpha$ (°) | $\phi$ (°) | $E_b$ (kJ/mol) |
|---|---|---|---|---|---|---|---|---|---|---|
| OH-fcc1 | 3.06 | 1.89 | 1.62 | 117.8 | 144.4 | 64.9 | 63.9 | 144.3 | 1.0 | 92.4 (75.7) |
| OH-bridge1 | 3.11 | 1.75 | 1.49 | 112.5 | 158.9 | 59.3 | 59.6 | 159.2 | 0.4 | 95.1 (78.1) |
| CH-top1 | 2.46 | 2.85 | 2.03 | 132.5 | 110.6 | 138.0 | 24.7 | 73.5 | 130.3 | 130.4 (116.2) |
| CH-top2 | 2.46 | 2.87 | 2.02 | 134.5 | 111.8 | 135.3 | 24.4 | 72.5 | 130.0 | 130.4 (116.4) |

## 10.3 Results

### 10.3.1 Barriers

The obtained barrier geometries for methanol on Cu(111) are summarized in Figure 10.1 and Table 10.2. Additionally, the $\theta$, $\gamma_1$, $\alpha$ and $\phi$ angles used to describe the TS geometries in Table 10.2 are depicted in Figure 10.2. $\theta$ is the angle between the surface normal and the vector of the dissociating OH or CH bond pointing to the H atom. $\beta$ denotes the angle between the surface normal and the umbrella axis, which is defined as the vector from the geometric center of the three H-atoms to the carbon atom. Furthermore, $\gamma_1$ defines the angle between the vector of the CO bond pointing to the O atom and the dissociating CH or OH bond, whereas $\gamma_2$ defines the angle between the umbrella axis and the dissociating CH or OH bond. Finally, $\alpha$ describes the angle between the CO bond and surface normal and $\phi$ indicates the angle between the umbrella axis and the CO bond.

The lowest barrier height found is for the OH-fcc1 geometry, where the OH bond is broken above the fcc site. The barrier height of this geometry is 92.4 kJ/mol, which is in good agreement with earlier DFT results using the PBE DF[9]. Another barrier for OH cleavage is found above the bridge site (OH-bridge1), which is 2.6 kJ/mol higher than the OH-fcc1 barrier. Both barrier geometries are similar, except for the larger length of the dissociating bond and the larger tilt of the molecule with respect to the surface normal (i.e., $\beta$ is smaller) of the OH-fcc1 geometry compared to OH-bridge1.

Furthermore, the barrier height found for CH cleavage is considerably higher than OH cleavage (38 kJ/mol higher). The two obtained barriers for CH cleavage have identical barrier heights (130.4 kJ/mol) and similar geometries, where the major difference is the orientation of the molecule with respect to the high-symmetry sites. Moreover, the barrier for CH cleavage is considerably later than for OH cleavage, i.e., the length of the dissociating bond is much larger. From both a dynamical and energetic point of view this would mean that the minimum barrier for OH cleavage is more easily accessible than for CH cleavage. Also, in the barrier geometries for OH cleavage the CO bond is perpendicular to the surface, whereas in the geometries for CH cleavage the CO bond is parallel to the surface. Finally, no barrier is obtained for CO cleavage, but it is expected to be considerably higher than the barriers obtained in this chapter[9].

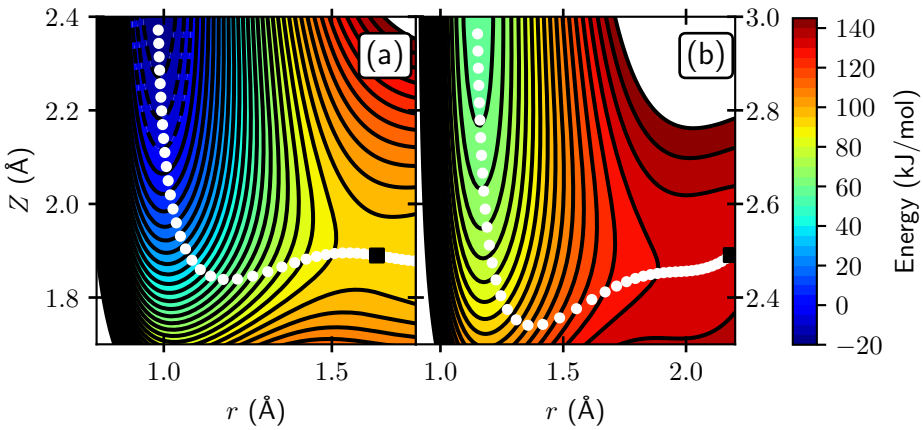


FIGURE 10.3: Elbow plot of methanol on Cu(111), where methanol is fixed in the OH-fcc1 (a) or CH-top1 (b) TS geometry, whereas $Z$ and the length $r$ of the dissociating XH bond (X is C or O) are variable. Contour lines are drawn at intervals of 5 kJ/mol between -20 and 150 kJ/mol. The colours indicate the energy (kJ/mol) with respect to methanol in the gas phase and the black squares indicate the highest point along the MEP (white circles).

### 10.3.2 Minimum Energy Path

Figure 10.3 shows the elbow plots for the OH-fcc1 and CH-top1 barriers, where methanol is kept fixed in its TS geometry while varying $Z$ and the length $r$ of the dissociating XH bond, where X is O or C. $Z$ is defined as the distance between the surface and oxygen for the OH-fcc1 barrier and between the surface and carbon for the CH-top1 barrier. The OH-fcc1 barrier is earlier (i.e., the length of the dissociating bond is smaller) and closer to the surface than the CH-top1 barrier, as also evident from the aforementioned barrier geometries in Table 10.2. Furthermore, the minimum energy path (MEP) associated with the OH-fcc1 barrier is less curved than the MEP associated with the CH-top1 barrier. This suggests that the OH-fcc1 barrier is not only more accessible than the CH-top1 barrier from a barrier height point of view, but also from a dynamical point of view in connection with the "*bobsled effect*"[44, 45]. Finally, elbow plots have not been obtained for other barrier geometries, however, similar results are expected.

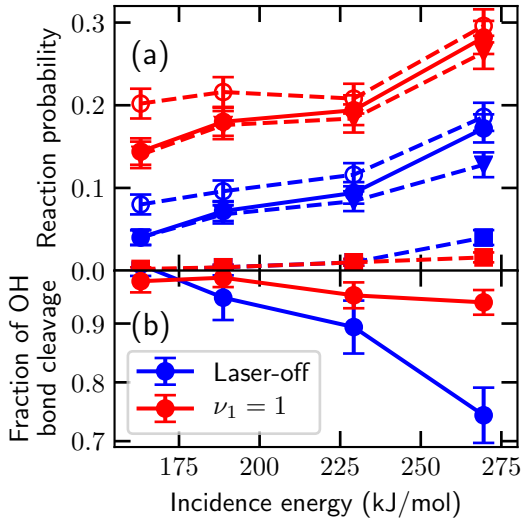


FIGURE 10.4: Reaction probability of methanol on Cu(111) for laser-off (blue) and $\nu_1 = 1$ (red) BOMD simulations (a), and the fraction of reactions that occurred through OH bond cleavage (b). In panel a, squares and triangles indicate dissociation of the CH and OH bond, while the solid circles indicate the total dissociation probability and open circles also include trapping. The error bars represent 68% confidence intervals.

### 10.3.3 Sticking Probability

A prediction for the reactivity of methanol on Cu(111) using BOMD is presented in Figure 10.4. The vibrational efficacy of exciting the OH stretch mode ($\nu_1 = 1$) is very high compared to the laser-off predictions (about 2). Furthermore, exciting the OH stretch mode suppresses CH cleavage, while for laser-off experiments a higher fraction of CH cleavage is predicted at higher incidence energies. Also, at $\langle E_i \rangle = 270\,\mathrm{kJ/mol}$ about 0.5% of the reacted trajectories were due to CO cleavage, which can be expected due to the very high translational energy of methanol, which exceeds even the high barrier for CO cleavage[9]. Finally, trapping is observed as well, however, due to the timescales involved with trapping it is not possible to obtain statistical data for a reaction probability including a trapping mechanism; i.e., only an upper bound for King and Wells experiments[46] can be given as the sum of the reaction probability and the probability that the molecule is still trapped after 1 ps.

In Figure 10.5, the reaction probabilities computed with the BOMD simulations are shown, where the ground state reaction probabilities are included as well. The ground state reaction probability is obtained from the laser-off simulations by only considering molecules initially in the vibrational ground state. However, for the purpose of obtaining good statistics in the calculation of the ground state reactivity, the torsion vibrational mode (rotation) of the hydroxyl is allowed to be excited since it is excited easily due to its compara-

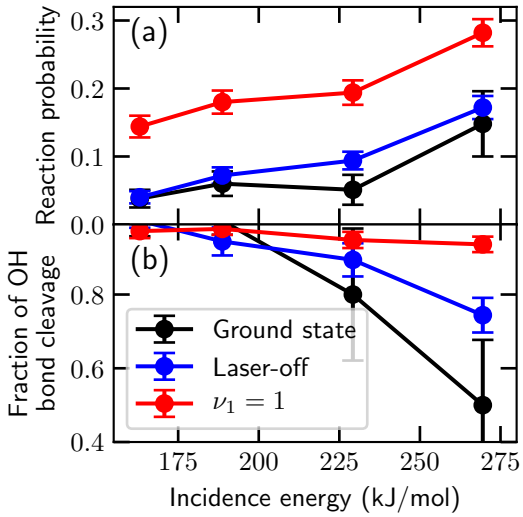


FIGURE 10.5: Reaction probability of methanol on Cu(111) for ground state (black), laser-off (blue) and $\nu_1 = 1$ (red) experimental conditions (i.e., no contribution of trapping is included), as computed with BOMD simulations (a), and the fraction of reactions that occurred through OH bond cleavage (b). The error bars represent 68% confidence intervals.

tively low energy. The ground state reaction probability curve shows similar behaviour as the laser-off curve. However, at high incidence energy, and thus high nozzle temperature, the ground state reaction probability is lower than the laser-off reaction probability due to the higher population of vibrationally excited molecules, with the excited vibrational modes being other modes than the torsion mode, in the molecular beam.

### 10.3.4 Reaction Site

The distribution of the distance of reacting methanol (only the reaction involving OH cleavage) to the high symmetry sites is given in Figure 10.6 and compared to the statistical distributions. In general, no steering is observed for the methanol in the $X$ and $Y$ directions. Furthermore, as can be seen in Figure 10.7, for the reaction of $\nu = 1$ methanol the distance to the high symmetry sites is statistical. However, at lower incidence energy and under laser-off conditions, methanol is more likely to react closer to the hollow and bridge sites than at the top site. This could mean that methanol does not react over the minimum OH cleavage barrier (OH-fcc1), for which the center of mass of methanol would be above the top site, but rather via the OH-bridge1 barrier above the hollow or bridge site. This may well be as the OH-bridge1 barrier is only 2.6 kJ/mol higher than the OH-fcc1 barrier. Furthermore, the OH-bridge1 barrier is earlier than the OH-fcc1 barrier and thus it should be dynamically more accessible. Finally, due to the small amount of trajectories leading to

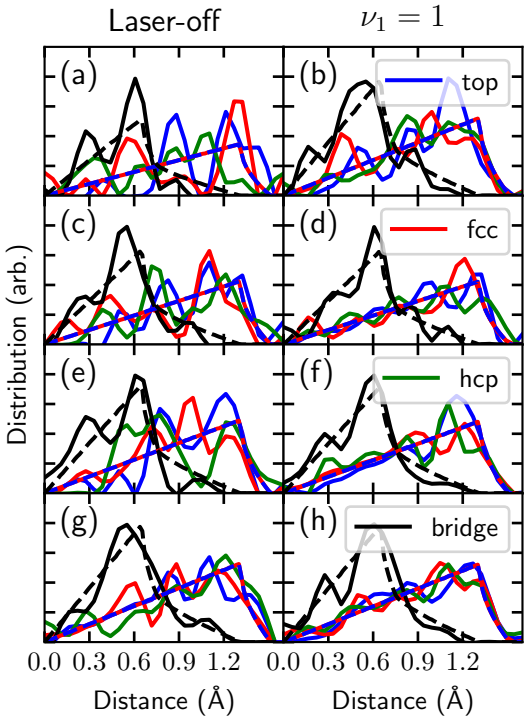


FIGURE 10.6: Distributions of the distance (Å) of the reacting methanol (through OH cleavage) to the closest top (blue), fcc (red), hcp (green) and bridge (black) sites on Cu(111) for laser-off conditions (a,c,e,g) and for $\nu_1 = 1$ (b,d,f,h), with $\langle E_i \rangle = 163$ (a,b), $\langle E_i \rangle = 189$ (c,d), $\langle E_i \rangle = 229$ (e,f) and $\langle E_i \rangle = 270$ kJ/mol (g,h). The blue and red dashed line indicates the statistical distribution for the hollow and top sites, while the black dashed line is the statistical distribution for the bridge site.

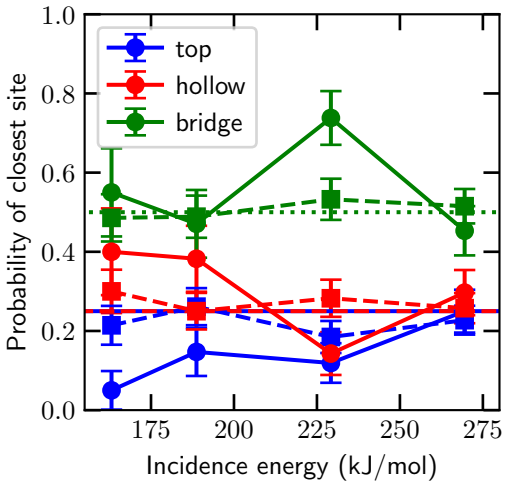


FIGURE 10.7: The probability that a reacting methanol molecule impacts closest to a high-symmetry site is shown for the top (blue), bridge (green), and hollow (red) sites for laser-off conditions (solid lines with circles) and for $\nu_1 = 1$ (dashed lines with squares), as a function of the incidence energy. The dotted green line indicates the statistical average for the bridge site, whereas the red and blue line indicates the statistical average for the hollow and top sites. The error bars represent 68% confidence intervals.

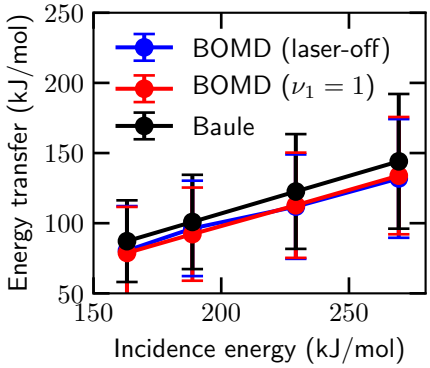


FIGURE 10.8: Energy transfer from scattered methanol to the surface atoms for laser-off conditions (blue) and for $\nu_1 = 1$ (red) as computed from BOMD simulations and the refined Baule model (black)[47, 48], as a function of incidence energy. The error bars represent 68% confidence intervals.

CH or CO cleavage, no conclusions can be drawn regarding the differences between the site specificity for CH and CO cleavage. However, it does seem that at lower energies CH cleavage happens more closely to the top site, which again can be expected from the minimum barrier.

### 10.3.5 Energy Transfer to the Surface

The average energies transferred by the scattering methanol to the surface atoms predicted by BOMD and by the refined Baule model[47, 48] are compared in Figure 10.8. The formula for the refined Baule model is $E_T = \langle E_i \rangle 2.4\mu/(1+\mu)^2$ (see Section 2.5), where $\mu = m/M$ (with $m$ being the mass of the projectile and $M$ the mass of a surface atom) and $\langle E_i \rangle$ is the average incidence energy. Here, it can be seen that the refined Baule model is in remarkably good agreement with BOMD. Half of the translational energy is transferred to the surface, which is due to the small mass difference between a Cu surface atom and the methanol molecule. Due to this large energy transfer of methanol to the surface, it is expected that surface atom motion plays a considerable role in the reactivity of methanol on Cu(111).

### 10.3.6 Angular Distributions

Angular distributions of methanol extracted from the BOMD simulations are shown in Figure 10.9. As also noted in the discussion of Figure 10.2, $\theta$ indicates the orientation of the dissociating bond, whereas $\beta$ and $\alpha$ indicate the orientation of the umbrella axis and the CO bond, respectively. Furthermore, $\phi$ concerns the angle between the CO bond and the umbrella axis, and $\gamma_1$ and $\gamma_2$ are the angles of the CO bond and umbrella axis with respect to the

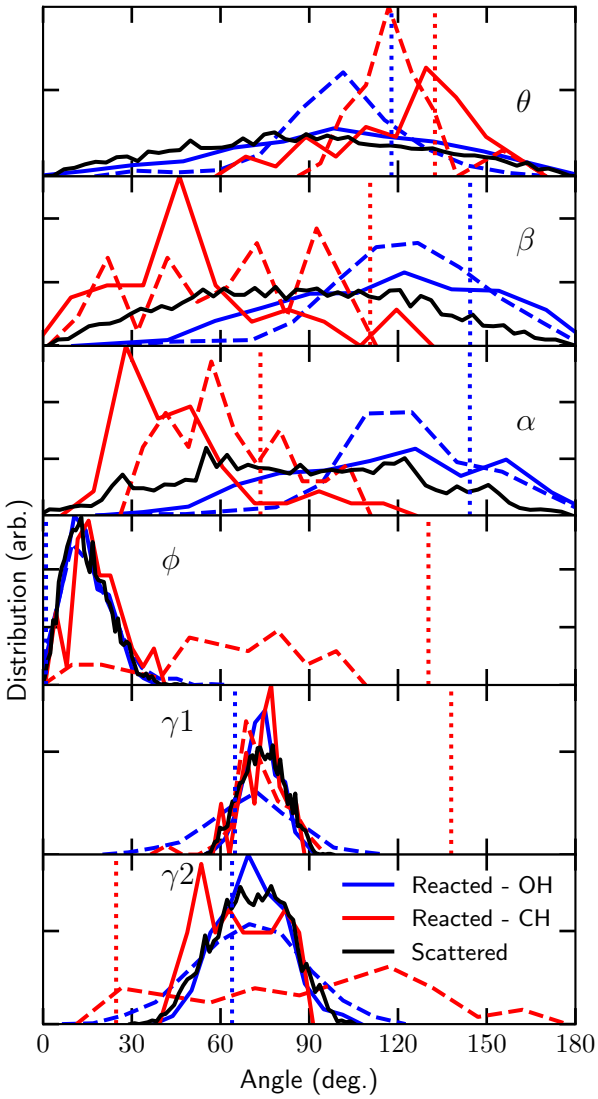


FIGURE 10.9: Angular distributions describing the orientation of methanol during BOMD for scattered (black) and reacted trajectories at the initial time step (solid lines) and when the length of the dissociating bond reaches the TS value (dashed lines). Results for all incidence energies, and simulations of laser-off conditions and for $\nu = 1$ are combined. The blue lines indicate OH cleavage, while the red lines indicate CH cleavage. The vertical dotted lines represent the TS values for the OH-fcc1 (blue) and CH-top1 (red) geometries (see Table 10.2).

dissociating bond. For the initial values, i.e., at $t = 0$ fs, no differences were found between scattered and reacted trajectories in the distributions of the $\phi$ and $\gamma$ angles. However, for the $\theta$, $\beta$ and $\alpha$ distributions differences are found not only between scattered and reacted trajectories, but also between OH and CH cleavage. These differences can be explained by the differences between the TS geometries, since the reacted trajectories tend to have orientations similar to the TS geometries. Exceptions are found for the $\beta$, $\phi$ and $\gamma$ angles for CH cleavage, where the initial angles cannot be close to the TS geometries since a rather large bend between the umbrella axis and the CO bond is required. Furthermore, for OH cleavage, steering in the $\theta$, $\beta$ and $\alpha$ angles is observed during the reaction. This means that effectively the orientation of the OH bond relative to the rest of the molecule changes, while the geometry of the rest of the molecule does not change. For CH cleavage considerably more steering is observed than for OH cleavage, with steering in all angles but $\gamma_1$ and $\gamma_2$. In general, the initial angular distributions for OH cleavage are comparable to the initial angular distributions of the scattered trajectories, whereas this is not the case for the angular distribution for CH cleavage. It seems that dynamically the barrier for OH cleavage is more accessible than the barrier for CH cleavage, which is not only caused by the barrier height and the length of the dissociating bond, but also by the large bend between the umbrella and the CO bond that is required for CH cleavage. Finally, the angle of the CO bond with respect to the surface normal is the most important angle for determining whether OH or CH cleavage will occur.

### 10.3.7 Formation of Formaldehyde

All reacted trajectories have been propagated for an additional 200 fs after a bond was broken. Some of these trajectories show formation of formaldehyde, for which the probability is provided in Figure 10.10. Formaldehyde is considered to be formed when both a CH bond and an OH bond is broken according to the definition in Section 2.5. Here we see that increasing the incidence energy leads to increased formaldehyde formation. This is probably caused by more energy remaining in the chemisorbed methanol or the hot hydrogen atom after breaking the first bond, which results in a higher chance of breaking the second bond. Furthermore, if the CH bond is broken first, more formaldehyde formation is observed than when the OH bond is broken first. Thus, the increase of CH cleavage with $\langle E_\mathrm{i} \rangle$ between 229 and 270 kJ/mol in the laser-off prediction results in a sharp increase of formaldehyde formation, while this is not observed for $\nu_1 = 1$, for which initial CH cleavage is suppressed. Interestingly, previously it was expected that the dominant pathway

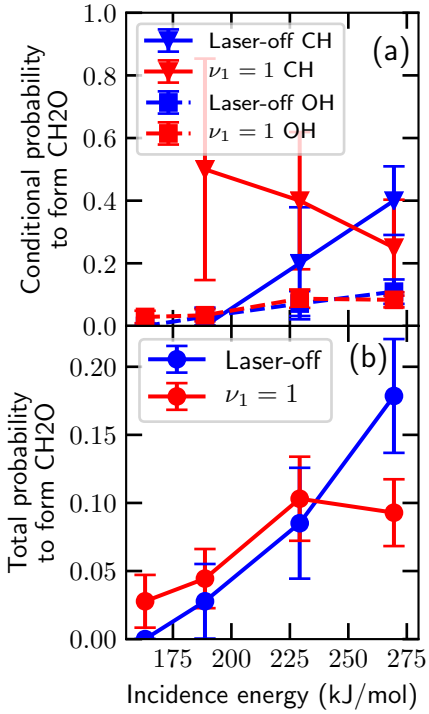


FIGURE 10.10: Probability to form formaldehyde within 200 fs after the first bond is broken for laser-off conditions (blue) and for $\nu_1 = 1$ (green) as computed with BOMD simulations, as a function of incidence energy. Panel a shows the conditional probability to form formaldehyde for when either the CH (solid lines) or the OH bond (dashed) is broken first, while panel b shows the total probability. The error bars represent 68% confidence intervals.

would be via breaking the OH bond first[9], whereas here the opposite result is obtained for high incidence energy. At low energies "OH cleavage first" is the dominant pathway, while at high energies "CH cleavage first" becomes the dominant pathway. Moreover, increasing the $\langle E_i \rangle$ from 229 to 270 kJ/mol with $\nu_1 = 1$ does not increase formaldehyde formation; instead about 1% recombinative desorption of methanol is observed at $\langle E_\mathrm{i} \rangle = 270$ kJ/mol. Also, the conditional probability for laser-off conditions at the highest incidence energy is about 10% as well, suggesting that the conditional probability limit to form formaldehyde after breaking first the OH bond is about 10%.

Three mechanisms for formaldehyde formation have been observed. The first mechanism involves a hot hydrogen atom traveling along the surface, and abstracting another hydrogen atom from the dissociated methanol resulting in formaldehyde and molecular hydrogen, after which both desorb from the surface. The second mechanism also involves a hot hydrogen atom traveling along the surface, but kinetic energy is transferred from the hot hydrogen atom to the dissociated methanol once the hydrogen atom gets close. This results then in formaldehyde and two atomic hydrogens. An accurate evaluation of

the relevance of both mechanisms is hampered by the supercell size, where effectively the hot hydrogen atom interacts with a periodic image. However, this may not be a large issue if we would consider this example to represent a methanol coverage of $1/12^{th}$ of a monolayer. The third mechanism does not suffer from this periodicity problem, since it involves two bonds to break simultaneously or subsequently, which again results in formaldehyde and atomic hydrogen. Furthermore, only two trajectories resulted in a product where two CH bonds were broken, with no clear relation to the incidence energy or vibrational excitation. Moreover, in one of the two trajectories recombination occurred to $CH_2OH$. Although these theoretical predictions are for a low methanol coverage, experimental evidence exists for formaldehyde forming from methanol at high pressure, and thus a high methanol coverage, as well[49, 50]. Finally, independent of mechanism in our BOMD calculations, formaldehyde is observed to desorb rapidly after formation due to the relatively low barrier for desorption, which is also observed experimentally[50–52].

## 10.4 Conclusions

Predictions for the reactivity of methanol on Cu(111) are made using BOMD, supported with an analysis of barriers and elbow plots. It is shown that Cu(111) is highly selective in breaking the OH bond due to the difference in barrier heights and dynamical features of the MEPs for OH and CH cleavage. Moreover, the vibrational efficacy of the OH stretch mode for dissociative chemisorption of methanol is high and vibrationally exciting this mode promotes OH cleavage but suppresses CH cleavage. Furthermore, additional insight is gained into the reaction mechanism following dissociative chemisorption of methanol by propagating reacted trajectories further. Within a short timescale (200 fs) formaldehyde formation is observed for a fraction of the dissociated methanol molecules, for which experimental evidence exists. Three different mechanisms for this formaldehyde production are identified, where two mechanisms involve a hot hydrogen atom that either abstracts another hydrogen atom forming molecular hydrogen or knocks off another hydrogen atom resulting in two hydrogen atoms (i.e., atomic hydrogen is formed) at the surface. In the third mechanism, the OH and CH bonds are broken simultaneously or subsequently without the influence of a hot hydrogen atom. In general, the probability of formaldehyde production is higher at higher incidence energy, and in this case usually a CH bond is broken first. Hopefully, these theoretical predictions will be followed by experiments in order to test

our predictions, which would also provide information on the transferability of the SRP32-vdW functional among similar systems. However, the difference between the surface's work function and molecule's electron affinity is 5.5 eV, and thus it is possible that a GGA DF is unable to correctly describe the barrier height of methanol + Cu(111) (see Chapter 5).

# Appendix

## 10.A Electronic Structure Calculations

Convergence tests have been performed to ensure that the computational setup produces accurate results for the interaction of methanol with Cu(111). To test the convergence, calculations of the minimum reaction barrier height of methanol on Cu(111), i.e., on the barrier for the OH-fcc1 geometry, have been performed. However, the same convergence behavior is expected for other TS geometries. The barrier energy is defined as $E_\mathrm{b} = \epsilon_\mathrm{b} - \epsilon_\mathrm{asym}$, where $\epsilon_\mathrm{b}$ and $\epsilon_\mathrm{asym}$ are the energies from the DFT calculations for the barrier geometry and the asymptotic configuration, respectively. The asymptotic configuration is considered to be the gas phase configuration and is obtained by putting the molecule halfway between two periodic slabs, i.e., the distance between the center of mass of methanol and the surface as well as its periodic image is 7.5 Å. The results of the convergence tests are presented in Figure 10.A.1 and Table 10.A.1. The converged setup yields a barrier height of 91.1 kJ/mol, which the employed computational setup (93.7 kJ/mol) can reproduce within chemical accuracy (4.2 kJ/mol). Note that these convergence tests have been performed with single-point calculations (i.e., no TS search was performed), with the TS geometry being obtained with a computational setup employing a $(3 \times 3)$ 5 layer supercell and a $6 \times 6 \times 1$ $k$-point grid. If a TS search is performed with the computational setup employed throughout this chapter, a barrier height of 92.4 kJ/mol is obtained, i.e., the barrier height is lowered by 1.3 kJ/mol.

The effect of the vacuum distance has also been investigated. When a vacuum distance of 30 Å is employed, while keeping $Z = 7.5$ Å, the interaction energy correction is about 4.2 kJ/mol, where the interaction energy correction is defined as $E_\mathrm{R} = E_\mathrm{b}^{15\,\text{Å}} - E_{\mathrm{b},Z=7.5\,\text{Å}}^{30\,\text{Å}}$. In order to keep the calculations tractable, a vacuum distance of 15 Å is kept, but 4.2 kJ/mol is added to the initial kinetic energy during the BOMD simulations (see Section 2.4.2). This should compensate for the interaction energy correction as at large distance to the surface the interaction energy is only dependent on molecule-surface distance $Z$, which is shown in figure 10.A.2. In this figure, methanol is kept fixed in its gas phase equilibrium geometry, while varying $Z$ above the top site for a vacuum

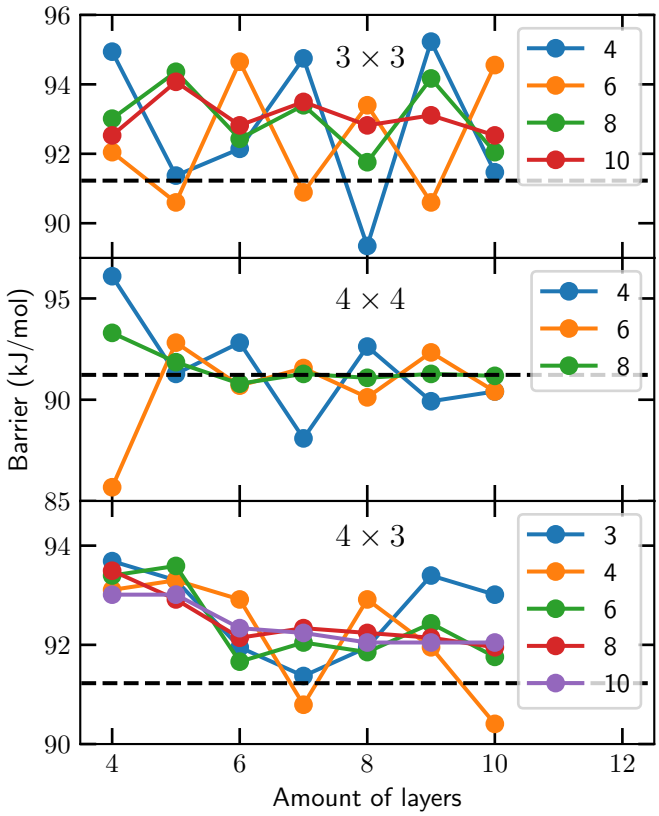


FIGURE 10.A.1: The minimum barrier height for OH cleavage (OH-fcc1 geometry) as a function of the amount of layers for the number of $k$-points equal to $(n \times n \times 1)$, where $n$ is indicated in the legend. An energy cutoff of 400 eV is used. The first panel is for a $3 \times 3$ supercell, the second panel is for a $4 \times 4$ supercell, and the last panel is for a $4 \times 3$ supercell with a skewed unit cell vector. The dashed lines indicate the converged barrier height and the gray area indicates chemical accuracy (4.2 kJ/mol) with respect to the converged barrier height.

TABLE 10.A.1: The minimum barrier height (kJ/mol) for OH cleavage (OH-fcc1 geometry, see Figures 10.1a,b and Table 10.2) as obtained with specific numbers for the amount of layers and $k$-points, with an energy cutoff of 400 eV. A $3 \times 3$, a $4 \times 4$ supercell, or a $4 \times 3$ supercell with a skewed unit cell vector is employed. The used computational setup is in bold and the most converged result (i.e., obtained with the largest setup) is in italic.

| Layers | $k$-points | $E_b, 3 \times 3$ | $E_b, 4 \times 3$ | $E_b, 4 \times 4$ |
|---|---|---|---|---|
| 4 | $3 \times 3 \times 1$ | | **93.7** | |
| 4 | $4 \times 4 \times 1$ | 94.9 | 93.1 | 96.1 |
| 4 | $6 \times 6 \times 1$ | 92.0 | 93.4 | 85.7 |
| 4 | $8 \times 8 \times 1$ | 93.0 | 93.4 | 93.3 |
| 4 | $10 \times 10 \times 1$ | 92.6 | 93.0 | |
| 5 | $3 \times 3 \times 1$ | | 93.3 | |
| 5 | $4 \times 4 \times 1$ | 91.4 | 93.3 | 91.3 |
| 5 | $6 \times 6 \times 1$ | 90.6 | 93.6 | 92.8 |
| 5 | $8 \times 8 \times 1$ | 94.4 | 92.9 | 91.9 |
| 5 | $10 \times 10 \times 1$ | 94.0 | 93.0 | |
| 6 | $3 \times 3 \times 1$ | | 91.9 | |
| 6 | $4 \times 4 \times 1$ | 92.1 | 92.9 | 92.8 |
| 6 | $6 \times 6 \times 1$ | 94.7 | 91.6 | 90.7 |
| 6 | $8 \times 8 \times 1$ | 92.5 | 92.1 | 90.8 |
| 6 | $10 \times 10 \times 1$ | 92.8 | 92.3 | |
| 7 | $3 \times 3 \times 1$ | | 91.4 | |
| 7 | $4 \times 4 \times 1$ | 94.8 | 90.8 | 88.1 |
| 7 | $6 \times 6 \times 1$ | 90.9 | 92.1 | 91.6 |
| 7 | $8 \times 8 \times 1$ | 93.4 | 92.3 | 91.3 |
| 7 | $10 \times 10 \times 1$ | 93.5 | 92.3 | |
| 8 | $3 \times 3 \times 1$ | | 91.9 | |
| 8 | $4 \times 4 \times 1$ | 89.4 | 93.0 | 92.6 |
| 8 | $6 \times 6 \times 1$ | 93.4 | 91.9 | 90.1 |
| 8 | $8 \times 8 \times 1$ | 91.7 | 92.2 | 91.1 |
| 8 | $10 \times 10 \times 1$ | 92.8 | 92.1 | |
| 9 | $3 \times 3 \times 1$ | | 93.4 | |
| 9 | $4 \times 4 \times 1$ | 95.2 | 91.9 | 90.0 |
| 9 | $6 \times 6 \times 1$ | 90.6 | 92.5 | 92.3 |
| 9 | $8 \times 8 \times 1$ | 94.1 | 92.2 | 91.2 |
| 9 | $10 \times 10 \times 1$ | 93.1 | 92.0 | |
| 10 | $3 \times 3 \times 1$ | | 93.0 | |
| 10 | $4 \times 4 \times 1$ | 91.4 | 90.4 | 90.4 |
| 10 | $6 \times 6 \times 1$ | 94.6 | 91.8 | 90.4 |
| 10 | $8 \times 8 \times 1$ | 92.1 | 92.0 | *91.1* |
| 10 | $10 \times 10 \times 1$ | 92.5 | 92.0 | |

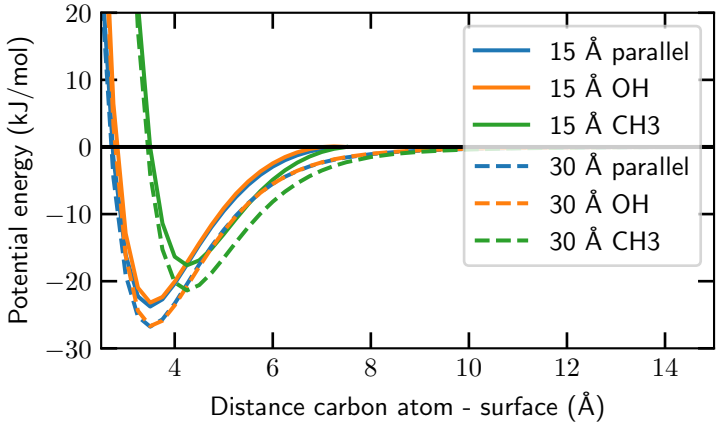


FIGURE 10.A.2: The Van der Waals interaction of methanol with a Cu(111) surface as a function of the distance $Z$ between the surface and the carbon atom, with either the hydroxyl (orange) or methyl (green) group pointing towards the surface, or with the CO bond parallel to the surface (blue). The solid and open lines indicate results obtained with a vacuum distance of 15 and 30 Å, respectively. The asymptotic energy is considered to be zero.

distance of 15 and 30 Å. The Van der Waals well depth is considerably smaller if the methyl group is pointing towards the surface (17.6 kJ/mol) than if the hydroxyl group is pointing towards the surface (23.2 kJ/mol). Moreover, if the CO bond is parallel to the surface the Van der Waals well depth is 0.7 kJ/mol larger than if the hydroxyl group points towards the surface.

Bulk calculations are performed within the primitive unit cell for a fcc lattice, yielding an equilibrium lattice constant $a_0 = 3.679$ Å, which is 1.8% larger than the experimental value $a_0 = 3.615$ Å[53]. The obtained lattice constant was used to model the Cu(111) slab.

## 10.B Impact Site

The distribution of the impact site of reacting methanol molecules on Cu(111) is provided in Figure 10.B.1 for different incidence energies and for laser-off and $\nu_1 = 1$ conditions.

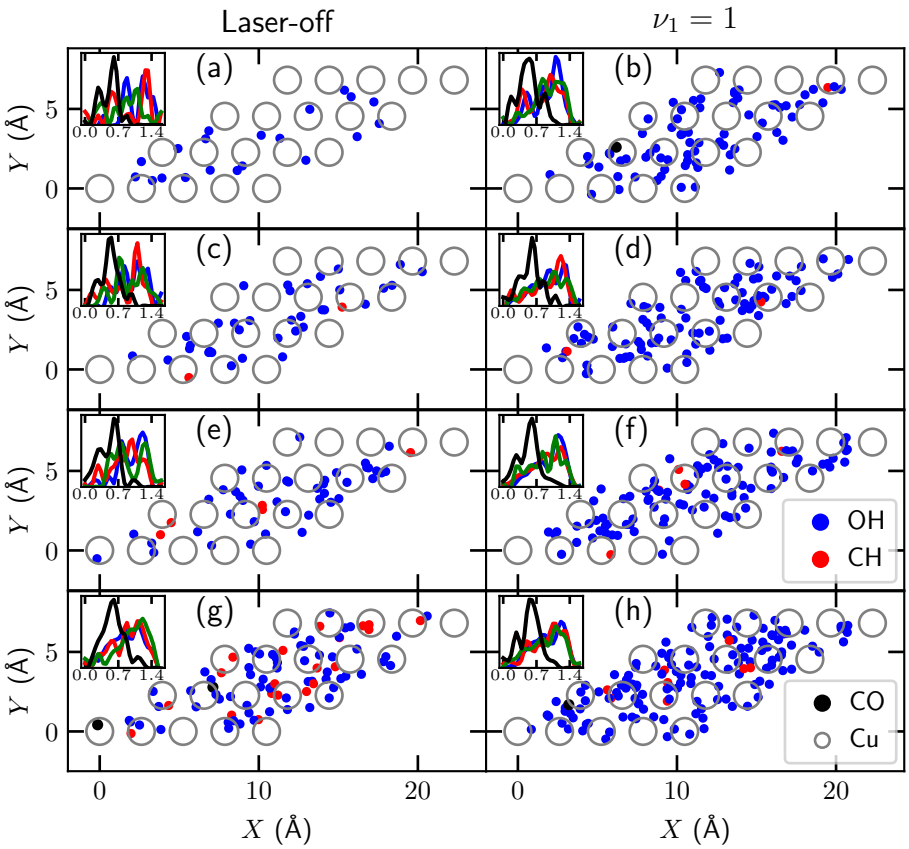


FIGURE 10.B.1: The impact site of reacting methanol on Cu(111) for laser off conditions (a,c,e,g) and for $\nu_1 = 1$ (b,d,f,h), with $\langle E_i \rangle = 163$ (a,b), $\langle E_i \rangle = 189$ (c,d), $\langle E_i \rangle = 229$ (e,f) and $\langle E_i \rangle = 270\,\mathrm{kJ/mol}$ (g,h). The grey open circles indicate the Cu top layer surface atoms, while the small solid circles indicate where dissociation of an OH (blue), CH (red) or CO (black) bond occurred, i.e., when $r = r^{\ddagger}$. The distributions of distance (Å) of the reacting methanol to the closest top (blue), fcc (red), hcp (green) and bridge (black) sites are given in the inset.

## References


(1) Sá, S.; Silva, H.; Brandão, L.; Sousa, J. M.; Mendes, A. Catalysts for Methanol Steam Reforming—A Review. *Appl. Catal. B* **2010**, *99*, 43–57, DOI: 10.1016/j.apcatb.2010.06.015.

(2) Russell, J. N.; Gates, S. M.; Yates, J. T. Reaction of Methanol with Cu(111) and Cu(111) + O(Ads). *Surf. Sci.* **1985**, *163*, 516–540, DOI: 10.1016/0039-6028(85)91077-5.

(3) Chen, A.; Masel, R. Direct Conversion of Methanol to Formaldehyde in the Absence of Oxygen on Cu(210). *Surf. Sci.* **1995**, *343*, 17–23, DOI: 10.1016/0039-6028(95)00649-4.

(4) Bowker, M. Active Sites in Methanol Oxidation on Cu(110) Determined by STM and Molecular Beam Measurements. *Top. Catal.* **1996**, *3*, 461–468, DOI: 10.1007/BF02113868.

(5) Wang, Z.-T.; Xu, Y.; El-Soda, M.; Lucci, F. R.; Madix, R. J.; Friend, C. M.; Sykes, E. C. H. Surface Structure Dependence of the Dry Dehydrogenation of Alcohols on Cu(111) and Cu(110). *J. Phys. Chem. C* **2017**, *121*, 12800–12806, DOI: 10.1021/acs.jpcc.7b02957.

(6) Mei, D.; Xu, L.; Henkelman, G. Potential Energy Surface of Methanol Decomposition on Cu(110). *J. Phys. Chem. C* **2009**, *113*, 4522–4537, DOI: 10.1021/jp808211q.

(7) Gu, X.-K.; Li, W.-X. First-Principles Study on the Origin of the Different Selectivities for Methanol Steam Reforming on Cu(111) and Pd(111). *J. Phys. Chem. C* **2010**, *114*, 21539–21547, DOI: 10.1021/jp107678d.

(8) Zuo, Z.-J.; Wang, L.; Han, P.-D.; Huang, W. Insights into the Reaction Mechanisms of Methanol Decomposition, Methanol Oxidation and Steam Reforming of Methanol on Cu(111): A Density Functional Theory Study. *Int. J. Hydrog. Energy* **2014**, *39*, 1664–1679, DOI: 10.1016/j.ijhydene.2013.11.048.

(9) García-Muelas, R.; Li, Q.; López, N. Density Functional Theory Comparison of Methanol Decomposition and Reverse Reactions on Metal Surfaces. *ACS Catal.* **2015**, *5*, 1027–1036, DOI: 10.1021/cs501698w.

(10) Jiang, Z.; Wang, B.; Fang, T. A Theoretical Study on the Complete Dehydrogenation of Methanol on Pd (100) Surface. *Appl. Surf. Sci.* **2016**, *364*, 613–619, DOI: 10.1016/j.apsusc.2015.12.204.

(11) Wang, S.-S.; Gu, X.-K.; Su, H.-Y.; Li, W.-X. First-Principles and Microkinetic Simulation Studies of the Structure Sensitivity of Cu Catalyst for Methanol Steam Reforming. *J. Phys. Chem. C* **2018**, *122*, 10811–10819, DOI: 10.1021/acs.jpcc.8b00085.

(12) Chen, W.; Cubuk, E. D.; Montemore, M. M.; Reece, C.; Madix, R. J.; Friend, C. M.; Kaxiras, E. A Comparative Ab Initio Study of Anhydrous Dehydrogenation of Linear-Chain Alcohols on Cu(110). *J. Phys. Chem. C* **2018**, *122*, 7806–7815, DOI: 10.1021/acs.jpcc.8b01698.

(13) Chen, J.; Zhou, X.; Zhang, Y.; Jiang, B. Vibrational Control of Selective Bond Cleavage in Dissociative Chemisorption of Methanol on Cu(111). *Nat. Commun.* **2018**, *9*, 4039, DOI: 10.1038/s41467-018-06478-6.

(14) Peppley, B. A.; Amphlett, J. C.; Kearns, L. M.; Mann, R. F. Methanol–Steam Reforming on $Cu/ZnO/Al_2O_3$ Catalysts. Part 2. A Comprehensive Kinetic Model. *Appl. Catal. A* **1999**, *179*, 31–49, DOI: 10.1016/S0926-860X(98)00299-3.

(15) Choi, Y.; Stenger, H. G. Fuel Cell Grade Hydrogen from Methanol on a Commercial $Cu/ZnO/Al_2O_3$ Catalyst. *Appl. Catal. B* **2002**, *38*, 259–269, DOI: 10.1016/S0926-3373(02)00054-1.

(16) Lee, J. K.; Ko, J. B.; Kim, D. H. Methanol Steam Reforming over $Cu/ZnO/Al_2O_3$ Catalyst: Kinetics and Effectiveness Factor. *Appl. Catal. A* **2004**, *278*, 25–35, DOI: 10.1016/j.apcata.2004.09.022.

(17) Patel, S.; Pant, K. K. Experimental Study and Mechanistic Kinetic Modeling for Selective Production of Hydrogen via Catalytic Steam Reforming of Methanol. *Chem. Eng. Sci.* **2007**, *62*, 5425–5435, DOI: 10.1016/j.ces.2007.01.044.

(18) Kroes, G.-J. Towards Chemically Accurate Simulation of Molecule–Surface Reactions. *Phys. Chem. Chem. Phys.* **2012**, *14*, 14966–14981, DOI: 10.1039/C2CP42471A.

(19) Jackson, B.; Nattino, F.; Kroes, G.-J. Dissociative Chemisorption of Methane on Metal Surfaces: Tests of Dynamical Assumptions Using Quantum Models and Ab Initio Molecular Dynamics. *J. Chem. Phys.* **2014**, *141*, 054102, DOI: 10.1063/1.4891327.

(20) Wellendorff, J.; Silbaugh, T. L.; Garcia-Pintos, D.; Nørskov, J. K.; Bligaard, T.; Studt, F.; Campbell, C. T. A Benchmark Database for Adsorption Bond Energies to Transition Metal Surfaces and Comparison to Selected DFT Functionals. *Surf. Sci.* **2015**, *640*, 36–44, DOI: 10.1016/j.susc.2015.03.023.

(21) Gautier, S.; Steinmann, S. N.; Michel, C.; Fleurat-Lessard, P.; Sautet, P. Molecular Adsorption at Pt(111). How Accurate Are DFT Functionals? *Phys. Chem. Chem. Phys.* **2015**, *17*, 28921–28930, DOI: 10.1039/C5CP04534G.

(22) Kroes, G.-J. Toward a Database of Chemically Accurate Barrier Heights for Reactions of Molecules with Metal Surfaces. *J. Phys. Chem. Lett.* **2015**, *6*, 4106–4114, DOI: 10.1021/acs.jpclett.5b01344.

(23) Nattino, F.; Migliorini, D.; Kroes, G.-J.; Dombrowski, E.; High, E. A.; Killelea, D. R.; Utz, A. L. Chemically Accurate Simulation of a Polyatomic Molecule-Metal Surface Reaction. *J. Phys. Chem. Lett.* **2016**, *7*, 2402–2406, DOI: 10.1021/acs.jpclett.6b01022.

(24) Migliorini, D.; Chadwick, H.; Nattino, F.; Gutiérrez-González, A.; Dombrowski, E.; High, E. A.; Guo, H.; Utz, A. L.; Jackson, B.; Beck, R. D.; Kroes, G.-J. Surface Reaction Barriometry: Methane Dissociation on Flat and Stepped Transition-Metal Surfaces. *J. Phys. Chem. Lett.* **2017**, *8*, 4177–4182, DOI: 10.1021/acs.jpclett.7b01905.

(25) Chadwick, H.; Gutiérrez-González, A.; Migliorini, D.; Beck, R. D.; Kroes, G.-J. Incident Angle Dependence of $CHD_3$ Dissociation on the Stepped Pt(211) Surface. *J. Phys. Chem. C* **2018**, *122*, 19652–19660, DOI: 10.1021/acs.jpcc.8b05887.

(26) Kresse, G.; Hafner, J. Ab Initio Molecular-Dynamics Simulation of the Liquid-Metal–Amorphous-Semiconductor Transition in Germanium. *Phys. Rev. B* **1994**, *49*, 14251–14269, DOI: 10.1103/PhysRevB.49.14251.

(27) Kresse, G.; Hafner, J. Ab Initio Molecular Dynamics for Liquid Metals. *Phys. Rev. B* **1993**, *47*, 558–561, DOI: 10.1103/PhysRevB.47.558.

(28) Kresse, G.; Furthmüller, J. Efficient Iterative Schemes for Ab Initio Total-Energy Calculations Using a Plane-Wave Basis Set. *Phys. Rev. B* **1996**, *54*, 11169–11186, DOI: 10.1103/PhysRevB.54.11169.

(29) Kresse, G.; Furthmüller, J. Efficiency of Ab-Initio Total Energy Calculations for Metals and Semiconductors Using a Plane-Wave Basis Set. *Comput. Mater. Sci.* **1996**, *6*, 15–50, DOI: 10.1016/0927-0256(96)00008-0.

(30) Kresse, G.; Joubert, D. From Ultrasoft Pseudopotentials to the Projector Augmented-Wave Method. *Phys. Rev. B* **1999**, *59*, 1758–1775, DOI: 10.1103/PhysRevB.59.1758.

(31) Blöchl, P. E. Projector Augmented-Wave Method. *Phys. Rev. B* **1994**, *50*, 17953–17979, DOI: 10.1103/PhysRevB.50.17953.

(32) Methfessel, M.; Paxton, A. T. High-Precision Sampling for Brillouin-Zone Integration in Metals. *Phys. Rev. B* **1989**, *40*, 3616–3621, DOI: 10.1103/PhysRevB.40.3616.

(33) Henkelman, G.; Jónsson, H. A Dimer Method for Finding Saddle Points on High Dimensional Potential Surfaces Using Only First Derivatives. *J. Chem. Phys.* **1999**, *111*, 7010–7022, DOI: 10.1063/1.480097.

(34) Heyden, A.; Bell, A. T.; Keil, F. J. Efficient Methods for Finding Transition States in Chemical Reactions: Comparison of Improved Dimer Method and Partitioned Rational Function Optimization Method. *J. Chem. Phys.* **2005**, *123*, 224101, DOI: 10.1063/1.2104507.

(35) Kästner, J.; Sherwood, P. Superlinearly Converging Dimer Method for Transition State Search. *J. Chem. Phys.* **2008**, *128*, 014106, DOI: 10.1063/1.2815812.

(36) Xiao, P.; Sheppard, D.; Rogal, J.; Henkelman, G. Solid-State Dimer Method for Calculating Solid-Solid Phase Transitions. *J. Chem. Phys.* **2014**, *140*, 174104, DOI: 10.1063/1.4873437.

(37) Transition State Tools Package for VASP https://theory.cm.utexas.edu/vtsttools/index.html (accessed 02/08/2021).

(38) Mondal, A.; Wijzenbroek, M.; Bonfanti, M.; Díaz, C.; Kroes, G.-J. Thermal Lattice Expansion Effect on Reactive Scattering of $H_2$ from Cu(111) at $T_s$ = 925 K. *J. Phys. Chem. A* **2013**, *117*, 8770–8781, DOI: 10.1021/jp4042183.

(39) Nattino, F.; Ueta, H.; Chadwick, H.; van Reijzen, M. E.; Beck, R. D.; Jackson, B.; van Hemert, M. C.; Kroes, G.-J. Ab Initio Molecular Dynamics Calculations versus Quantum-State-Resolved Experiments on $CHD_3$ + Pt(111): New Insights into a Prototypical Gas–Surface Reaction. *J. Phys. Chem. Lett.* **2014**, *5*, 1294–1299, DOI: 10.1021/jz500233n.

(40) Gerrits, N.; Migliorini, D.; Kroes, G.-J. Dissociation of $CHD_3$ on Cu(111), Cu(211), and Single Atom Alloys of Cu(111). *J. Chem. Phys.* **2018**, *149*, 224701, DOI: 10.1063/1.5053990.

(41) Hammer, B.; Hansen, L. B.; Nørskov, J. K. Improved Adsorption Energetics within Density-Functional Theory Using Revised Perdew-Burke-Ernzerhof Functionals. *Phys. Rev. B* **1999**, *59*, 7413–7421, DOI: 10.1103/PhysRevB.59.7413.

(42) Perdew, J. P.; Burke, K.; Ernzerhof, M. Generalized Gradient Approximation Made Simple. *Phys. Rev. Lett.* **1996**, *77*, 3865–3868, DOI: 10.1103/PhysRevLett.77.3865.

(43) Dion, M.; Rydberg, H.; Schröder, E.; Langreth, D. C.; Lundqvist, B. I. Van Der Waals Density Functional for General Geometries. *Phys. Rev. Lett.* **2004**, *92*, 246401, DOI: 10.1103/PhysRevLett.92.246401.

(44) Marcus, R. A. On the Analytical Mechanics of Chemical Reactions. Quantum Mechanics of Linear Collisions. *J. Chem. Phys.* **1966**, *45*, 4493–4499, DOI: 10.1063/1.1727528.

(45) McCullough, E. A.; Wyatt, R. E. Quantum Dynamics of the Collinear (H, $H_2$) Reaction. *J. Chem. Phys.* **1969**, *51*, 1253–1254, DOI: 10.1063/1.1672133.

(46) King, D. A.; Wells, M. G. Reaction Mechanism in Chemisorption Kinetics: Nitrogen on the {100} Plane of Tungsten. *Proc. R. Soc. Lond. A* **1974**, *339*, 245–269, DOI: 10.1098/rspa.1974.0120.

(47) Baule, B. Theoretische Behandlung Der Erscheinungen in Verdünnten Gasen. *Ann. Phys.* **1914**, *349*, 145–176, DOI: 10.1002/andp.19143490908.

(48) Goodman, F. O.; Wachman, H. Y. *Formula for Thermal Accommodation Coefficient*; 66-1; Cambridge, Massachusetts: M.I.T. Fluid Dynamics Research, 1966, DOI: 10.21236/ad0631007.

(49) Takezawa, N.; Iwasa, N. Steam Reforming and Dehydrogenation of Methanol: Difference in the Catalytic Functions of Copper and Group VIII Metals. *Catal. Today* **1997**, *36*, 45–56, DOI: 10.1016/S0920-5861(96)00195-2.

(50) Shishido, T.; Yamamoto, Y.; Morioka, H.; Takehira, K. Production of Hydrogen from Methanol over Cu/ZnO and Cu/ZnO/$Al_2O_3$ Catalysts Prepared by Homogeneous Precipitation: Steam Reforming and Oxidative Steam Reforming. *J. Mol. Catal. A: Chem.* **2007**, *268*, 185–194, DOI: 10.1016/j.molcata.2006.12.018.

(51) Barnes, C.; Pudney, P.; Guo, Q.; Bowker, M. Molecular-Beam Studies of Methanol Partial Oxidation on Cu(110). *J. Chem. Soc., Faraday Trans.* **1990**, *86*, 2693–2699, DOI: 10.1039/FT9908602693.

(52) Greeley, J.; Mavrikakis, M. Methanol Decomposition on Cu(111): A DFT Study. *J. Catal.* **2002**, *208*, 291–300, DOI: 10.1006/jcat.2002.3586.

(53) Mishin, Y.; Mehl, M. J.; Papaconstantopoulos, D. A.; Voter, A. F.; Kress, J. D. Structural Stability and Lattice Defects in Copper: Ab Initio, Tight-Binding, and Embedded-Atom Calculations. *Phys. Rev. B* **2001**, *63*, 224106, DOI: 10.1103/PhysRevB.63.224106.

# Samenvatting

Katalyse speelt een onmisbare rol in de chemie door reactieve intermediairs te stabiliseren en onderlinge verhoudingen van reactiepaden te wijzigingen. Hierdoor maakt katalyse mildere reactiecondities en selectiviteit voor gewenste producten mogelijk. Dit is van enorm belang in de context van duurzaamheid doordat er minder energie en grondstoffen nodig zijn in chemische processen. De enorme populatie op de wereld was bijvoorbeeld niet mogelijk geweest zonder het Haber-Bosch proces, wat een katalytisch proces is waarbij ammoniak wordt geproduceerd voor gebruik in onder andere kunstmest. Het is dan ook evident dat verbetering van katalyse vanuit een beter fundamenteel begrip van de werking ervan van uiterst belang is.

Een belangrijke vorm van katalyse is heterogene katalyse. Hierbij zijn de katalysator en de reactanten te onderscheiden in verschillende aggregatietoestanden. Doorgaans is de katalysator in een vaste toestand en een metaal, en zijn de reactanten moleculen in vloeibare of gas toestand. Verder omhelst een chemisch proces vrijwel altijd een divers netwerk van elementaire reacties. De kracht van heterogene katalyse is dat het invloed heeft op (relatieve) barrièrehoogtes en op diffusie van reactieve intermediairs en producten in het reactienetwerk, en dat het gemakkelijk in industriële processen toegepast kan worden. Door hierin gericht aanpassingen te doen kunnen de benodigde grondstoffen en producten in een chemisch proces beheerst worden.

Helaas zorgt het bestaan van complexe reactienetwerken in chemische processen er ook voor dat het lastig is om te begrijpen hoe katalysatoren werken. Gelukkig worden zulke reactienetwerken doorgaans gedomineerd door één of enkele toestanden, de zogenaamde snelheidsbepalende toestanden. Dat betekent dat fundamenteel onderzoek naar de werking van een katalysator zich alleen hoeft te richten op de snelheidsbepalende toestanden, wat de complexiteit van het onderzoek behoorlijk verkleint. Helaas zijn ook de industriële reactiecondities vrij complex door onder andere de gebruikte hoge temperaturen, drukken, en verscheidenheid in structuren van de katalysator. Zo bestaat het oppervlak van de katalysator uit verschillende facetten, welke weer verschillende invloeden hebben op de reactie. Deze facetten zijn snijvlakken door een metaalrooster en kunnen gekarakteriseerd worden met

behulp van de zogenaamde Miller-indices. Gelukkig bevinden snelheidsbepalende toestanden zich doorgaans op maar één of enkele facetten. Met andere woorden, hoewel een heterogeen gekatalyseerd chemisch proces zeer complex is, is het bij benadering vaak te begrijpen door alleen bepaalde elementaire reactiestappen op goed gedefinieerde oppervlakken te onderzoeken. Dit is de basis van oppervlaktechemie.

Hoewel oppervlaktechemie heterogene katalyse onderzoekt met sterk gereduceerde complexiteit, blijft het nog steeds een enorme uitdaging. Daarom wordt onderzoek aan oppervlakte chemie zowel experimenteel als theoretisch uitgevoerd, omdat geen van beide op zichzelf voldoende is. Aan dit proefschrift ligt alleen theoretisch werk ten grondslag, maar waar mogelijk wordt ander experimenteel onderzoek er bij betrokken om zo tot een beter begrip te komen.

Om de complexiteit van oppervlaktechemie nog verder terug te dringen, wordt er doorgaans gewerkt in ultrahoog vacuüm. Op deze manier wordt er bij benadering gekeken naar de reactie van één of enkele moleculen tegelijk. In een experiment wordt er vaak een moleculaire bundel geproduceerd, waarvan de snelheids- en rovibrationeletoestandsverdeling bepaald is, en gericht op een goed gedefinieerd metalen oppervlak. De eigenschappen van een moleculaire bundel kunnen gevarieerd worden met behulp van de temperatuur van het gebruikte mondstuk en het mengsel van gassen. De mondstuktemperatuur heeft invloed op de translationele, vibrationele en rotationele temperaturen. Verder heeft het mengsel van gassen met name invloed op de translationele energie, terwijl het doorgaans niet of nauwelijks invloed op de rovibrationele temperatuur. Als namelijk een zwaar molecuul gemengd wordt met een licht, vaak inert, gas, dan kunnen er fors hogere translationele energieën behaald worden voor het zware molecuul dan wanneer de mondstuktemperatuur verhoogd wordt. Uiteraard kan het omgekeerde ook bereikt worden door een molecuul met een zwaarder gas te mengen. Niet alleen de totale hoeveelheid translationele energie is van belang in de reactie van een molecuul op een metalen oppervlak, maar ook de richting geassocieerd met de translatie. Zo kan de hoek die de moleculaire bundel maakt met het oppervlak veranderd worden. Omdat voor veel reacties alleen translatie loodrecht op, en niet parallel aan, het oppervlak van belang is, is er dus een manier om effectief de translationele energie te variëren zonder de rovibrationele temperatuur te wijzigen. Daarnaast kan het gebruik van een magnetisch veld of gepolariseerd laserlicht de oriëntatie van het molecuul ten opzichte van het oppervlak beïnvloeden. Verder kan er gebruik gemaakt worden van toestandspecifieke excitatie van rovibrationele toestanden om rovibrationeletoestandspecifieke informatie te vergaren.

Tot dusver zijn alleen manieren om de moleculaire bundel te beheersen besproken, maar zoals al eerder genoemd is het facet van het metalen oppervlak ook belangrijk. Vaak wordt maar één facet tegelijk onderzocht. Verder is de temperatuur van het oppervlak van grote invloed op de desorptiesnelheid van moleculen, wat weer belangrijk is voor de bedekking van het oppervlak en de reactiekans in het geval van een indirect reactiemechanisme met gefysisorbeerde moleculen. Ook beïnvloedt de oppervlaktetemperatuur de barrièrehoogte door middel van oppervlakteatoombeweging. Kortom, in grote mate is er controle over zowel het molecuul als het metalen oppervlak in experimenten.

Door te richten met een moleculaire bundel op een metalen oppervlak kunnen vele aspecten van reactiemechanismes ontrafeld worden. De wellicht meest belangrijke grootheid is de zogenaamde plakkans, wat aangeeft hoe groot de kans is dat een molecuul aan een oppervlak blijft hangen en bij benadering vaak tevens de reactiekans is. Andere interessante grootheden zijn bijvoorbeeld de energieoverdracht van een molecuul naar de beweging van de oppervlakteatomen en de inelastischeverstrooiingswaarschijnlijkheid.

Helaas zijn vele aspecten van molecuul-metalen oppervlak reacties niet direct meetbaar. Hoewel sommige aspecten alsnog achterhaald kunnen worden door indirecte metingen, levert dit een grotere onzekerheid op en weer andere aspecten zijn simpelweg niet meetbaar. Gelukkig heeft theoretisch onderzoek andere sterktes en zwaktes dan experimenteel onderzoek waarbij bepaalde aspecten juist wel direct te bepalen zijn. Statische berekeningen kunnen het potentiële-energieoppervlak (PEO) van de interactie tussen het molecuul en het oppervlak onderzoeken. Met name overgangstoestanden (OT's) zijn interessant doordat ze vaak een goede indicator zijn van de reactiviteit. Daarentegen hebben molecuul-metalen oppervlak reacties te maken met een verzameling aan OT's, waarbij de reactie niet noodzakelijkerwijs over de laagste OT's verloopt. Verder zijn dynamische effecten vanwege het bewegen over het PEO lastig te beschrijven met statische berekeningen. Daarom worden er in dit proefschrift voornamelijk dynamische berekeningen uitgevoerd. In zo'n dynamische berekening wordt een traject van één molecuul gesimuleerd en zijn dynamische effecten een inherent onderdeel van de simulatie. Door vele van dit soort simulaties uit te voeren kunnen experimentele condities zoals hierboven besproken nagebootst worden.

Op dit moment is de grootste uitdaging van theoretisch onderzoek het vergroten van de nauwkeurigheid. Meestal wordt er gebruik gemaakt van dichtheidsfunctionaaltheorie (DFT), wat een uitwisselingcorrelatiedichtheidsfunctionaal (UC-DF) vereist. Hoewel in principe een exacte UC-DF bestaat, is deze tot op het heden niet bekend. Daarom bestaan er vele benaderende

UC-DF's en is veel onderzoek gericht op het benchmarken en verbeteren van deze UC-DF's. UC-DF's zijn min of meer te verdelen in twee groepen: (semi-)empirisch en op fysische beperkingen gebaseerd. Sommige DF's kunnen beschouwd worden als beide. Bijvoorbeeld: in de specifieke reactieparameter (SRP) aanpak worden er twee op fysische beperkingen gebaseerde DF's gemengd met één parameter die aangepast is om een experiment met chemische nauwkeurigheid te reproduceren. Van sommige SRP-DF's is aangetoond dat ze toepasbaar zijn op andere systemen dan waarvoor de aanpassing gemaakt is. In dit proefschrift wordt gebruik gemaakt van zowel SRP-DF's als op beperkingen gebaseerde DF's.

Verder heeft theoretisch onderzoek last van hoge computationele kosten. Met name de toename in het aantal expliciet behandelde vrijheidsgraden in de afgelopen jaren maakt dynamische simulaties relatief duur. Hoewel *ab initio* moleculaire dynamica (AIMD) simulaties makkelijk in gebruik zijn doordat op elke tijdstap de krachten bepaald worden door middel van berekeningen aan de electronische structuur, zijn ze om dezelfde reden duur. Gelukkig bestaan er alternatieve aanpakken die DFT data fitten of interpoleren, waardoor niet langer op elke tijdstap een berekening aan de electronische structuur gedaan hoeft te worden en wat dus behoorlijk goedkoper kan zijn dan het uitvoeren van AIMD simulaties. Weliswaar zijn deze methoden lastiger in gebruik omdat er kennis van het systeem en de bijbehorende dynamica vereist is, maar vaak wegen de significant lagere computationele kosten ten opzichte van AIMD simulaties op tegen de complexiteit van de alternatieve aanpakken. Daarom wordt in dit proefschrift naast AIMD gebruik gemaakt van vooraf bepaalde PEO's, waarbij twee alternatieve methoden zijn gebruikt om de PEO's te beschrijven: hoog-dimensionale neurale netwerk potentialen (HDNNP's) en de corrugatie reducerende procedure (CRP). HD-NNP's schalen relatief goed met het aantal vrijheidsgraden, maar werken in de praktijk grotendeels als een zwarte doos. Daarom moeten HD-NNP's rigoureus getest en verbeterd worden voordat ze gebruikt kunnen worden. De CRP is krachtig en voorspelbaar in het interpoleren van data, maar schaalt slecht met het aantal vrijheidsgraden. Dit limiteert het gebruik van de CRP voornamelijk tot (bij benadering) 6D systemen, waarbij oppervlakteatoombeweging niet expliciet behandeld wordt.

In het kort zijn er twee hoofddoelen in dit proefschrift. Ten eerste wordt er geprobeerd de nauwkeurigheid van berekeningen te vergroten door te kijken naar de rol van de UC-DF, en of er systematische verbeteringen in de UC-DF mogelijk zijn. Ten tweede worden reactiemechanismes in detail bestudeerd en opgehelderd.

In **Hoofdstuk 3** wordt de reactie van HCl op Au(111) onderzocht met

een nieuwe DF. De reden hiervoor is dat er al een lange tijd een groot verschil in resultaten tussen theorie en experiment bestaat. Voor de DF is een meta-generaliseerde gradiënt benadering (MGGB) gebruikt met behulp van het "makkelijk gemaakt" concept en een generaliseerde gradiënt benadering (GGB) expressie die lijkt op RPBE, wat de zogenaamde MS-RPBEl DF oplevert. Omdat een MGGB DF een stuk duurder is dan de doorgaans gebruikte GGB DFs, wordt er in dit hoofdstuk gebruik gemaakt van een HD-NNP. De vergelijking met opnieuw geanalyseerde experimentele resultaten laat zien dat de MS-RPBEl DF de beste overeenstemming met experiment vertoont van de tot op het heden geteste DFs, zonder dat niet-adiabatische effecten hoeven gesimuleerd te worden. Ook worden er suggesties gegeven voor toekomstige DFs die wellicht HCl + Au(111) nog beter weten te beschrijven, zoals het toevoegen van niet-lokale correlatie en gebruik van afgeschermde hybride DFs (zie ook Hoofdstuk 5). Verder worden verscheidene aspecten van het reactiemechanisme onderzocht. Opvallend daarbij is dat oppervlakteatoombeweging nauwelijks invloed heeft op de reactiekans. Daarnaast zorgen dynamische effecten ervoor dat de plaatsafhankelijke reactiekans niet te verklaren is op basis van alleen barrière hoogtes en geometriën.

**Hoofdstuk 4** bekommert zich ook om de reactie van HCl op Au(111), maar ditmaal ligt de nadruk op het effect van rotationele pre-excitatie van HCl op de reactie. Hier wordt aangetoond dat rotationele pre-excitatie van HCl een veel groter effect heeft op de reactiekans dan het verhogen van de translationele energie, zelfs nog meer dan vibrationele pre-excitatie. De vorm van het PEO is de oorzaak hiervan, omdat het minimumenergiepad (MEP) sterk varieert in wat de optimale oriëntatie van HCl is voordat het molecuul de OT voor dissociatie weet te bereiken. Hierdoor is sturing van het molecuul door de krachten die het PEO uit oefent op HCl niet alleen ineffectief, het is zelfs contraproductief, in tegenstelling tot de bekende molecuul-metalen oppervlak reactiemechanismes. Door het molecuul initieel te laten roteren weet het gemakkelijker een lage barrière te vinden dan wanneer het molecuul niet initieel roteert. Bovendien is het interessant dat vibrationele en rotationele pre-excitatie van HCl een wederzijds versterkend effect heeft op de reactiekans.

In **Hoofdstuk 5** wordt gezocht naar een criterium dat kan voorspellen wanneer DFT op het niveau van de GGB faalt in het nauwkeurig beschrijven van molecuul-metalen oppervlak reactiebarrières. Het blijkt dat het verschil tussen de uittreearbeid van het metalen oppervlak en de elektronenaffiniteit van het molecuul ($W - E_{\mathrm{ea}}$) gerelateerd is aan de bekwaamheid van GGB DF's om een molecuul-metalen oppervlak reactie nauwkeurig te beschrijven. Wanneer dit verschil kleiner is, moet een GGB DF meer "repulsief" gemaakt worden om tot een SRP-DF te komen. Bovendien, als $(W - E_{\mathrm{ea}}) < 7\,\mathrm{eV}$

dan onderschat zelfs een van meest repulsieve GGB DFs (dat wil zeggen, de RPBE DF) reactiebarrières door een toename in elektronenoverdracht van het metaal naar het molecuul in de OT, en de resulterende toename in de delokalisatiefout en zelfinteractiefout (ZIF) die fundamenteel aanwezig zijn in DFT. Gelukkig bestaan er DF's die op een of andere manier (deels) weten te corrigeren voor de ZIF. Van deze DFs is te verwachten dat ze minder vatbaar zijn voor voor de delokalisatiefout in de OT en dus mogelijk niet de barrière hoogte onderschatten wanneer $(W - E_{\mathrm{ea}})$ klein is.

Dit blijkt inderdaad het geval te zijn voor de toetssteenreactie van $O_2$ op Al(111). Alle GGB DF's, zelfs RPBE, leveren namelijk een adiabatisch barrièreloze reactie op voor dit systeem, terwijl experiment aangeeft dat er wel degelijk een barrière hoort te zijn. Vroege werken suggereerden dat de reactie wellicht nonadiabatisch is, terwijl latere werken juist suggereerden dat de reactie wel degelijk adiabatisch is maar dat DFT geen correcte barrière hoogtes kan geven voor dit systeem vanwege de delokalisatiefout. De MS-RPBEl DF, die gebruikt is voor HCl + Au(111) in Hoofdstuk 3 en 4 en op een benaderende manier corrigeert voor de ZIF, levert wel een adiabatische barrière op. Helaas is de barrière hoogte en anisotropie nog veel te laag in vergelijking met experiment. De afgeschermde hybride GGB DF HSE03-1/3X daarentegen levert wel een minimum barrière op die in overeenstemming is met experiment. Ook is de anisotropie beter beschreven dan met de MS-RPBEl DF, al is de overeenstemming met experiment maar matig. Vermoedelijk is er een afgeschermde hybride (M)GGB DF met Van der Waals-correlatie nodig om overeenstemming tussen experiment en theorie te verkrijgen. Desalniettemin lijken afgeschermde hybride DF's een uitstekende manier te zijn om molecuul-metalen oppervlak reacties te beschrijven waarvan $(W - E_{\mathrm{ea}}) < 7\,\mathrm{eV}$, wat ondersteund lijkt te worden door verkennende berekeningen aan andere systemen. Interessant is dat de fout in de beschrijving van $O_2$ + Al(111) door GGB DFs een functionaalfout is, en niet een delokalisatiefout. Verder suggereren verkennende berekeningen dat een niet-zelfconsistente aanpak, waarbij een afgeschermde hybride DF toegepast wordt op de elektronendichtheid verkregen met een GGB DF, de barrières verkregen met zelfconsistente berekeningen kan reproduceren. Dit zou onderzoek aan molecuul-metalen oppervlak reacties met afgeschermde hybride DFs fors goedkoper kunnen maken.

**Hoofdstuk 6** tracht de beschrijving van $NH_3$ + Ru(0001) te verbeteren door oppervlakteatoombeweging en Van der Waals-correlatie mee te nemen in de AIMD simulaties. De overeenstemming tussen experiment en theorie is hiermee verbeterd ten opzichte van eerder theoretisch werk. Daarnaast wordt de oppervlaktetemperatuuronafhankelijkheid van de experimentele reactiekans gereproduceerd. Doorgaans verloopt dissociatieve chemisorptie

van polyatomische moleculen via een rotationeel adiabatische of "rotationeel plotsklaps" reactiemechanisme. De reactie van $NH_3$ op Ru(0001) daarentegen verloopt via geen van beide mechanismes maar via een kortlevende moleculaire gechemisorbeerde toestand, een mechanisme dat nog niet eerder bekend was.

**Hoofdstuk 7** geeft voorspellingen met behulp van AIMD simulaties voor de reactiviteit van $CHD_3$ op het vlakke oppervlak Cu(111), het gestapte oppervlak Cu(211), en de vlakke oppervlakken bestaande uit alleenstaandeatoomlegeringen (AAL's) Pt-Cu(111) en Pd-Cu(111). De chemisch nauwkeurige SRP-DF voor $CHD_3$ + Ni(111), Pt(111), en Pt(211) wordt gebruikt in de hoop dat toekomstige experimenten kunnen testen of deze SRP-DF overdraagbaar is naar $CHD_3$ + Cu oppervlakken. De voorspellingen geven aan dat Cu(111) veel minder actief is voor de dissociatie van $CHD_3$ dan Ni(111) en Pt(111). Verder is Cu(211) verrassend genoeg even reactief als Cu(111), ondanks de lagere minimum barrière hoogte. Dit komt doordat de (100)-trede weliswaar reactiever is dan Cu(111), maar dat het (111)-terras juist minder reactief is, en dus is de totale reactiekans op Cu(111) en Cu(211) vergelijkbaar. Van de AAL's lijkt alleen Pt-Cu(111) reactiever te zijn dan Cu(111). De reactie vindt hierbij voornamelijk plaats in de buurt van het gelegeerde atoom vanwege niet alleen een verlaging in de barrièrehoogte, maar ook veranderingen in het dynamische reactiepad en vermindering in de energie-overdracht van methaan naar de oppervlakte-atomen.

In **Hoofdstuk 8** wordt gekeken of de Behler-Parrinello aanpak voor HD-NNP's werkt voor reactieve verstrooiing van polyatomige moleculen door bewegende metalen oppervlakken. Omdat de reactiekans van $CHD_3$ + Cu(111) te laag is om met AIMD simulaties statistische relevante data te vergaren voor een vergelijking met toekomstige experimenten, wordt dit systeem als toetssteen gebruikt. Hierbij wordt aangetoond dat de ontwikkelde HD-NNP nauwkeurig DFT berekeningen en reactiekansen weet te reproduceren. Daarnaast zijn er reactiekansen zo laag als $5 \times 10^{-5}$ bepaald, iets wat niet praktisch haalbaar is met AIMD simulaties. Dankzij de verbeterde statistiek met het HD-NNP ten opzichte van AIMD simulaties kunnen verschillende dynamische effecten onderzocht worden. Met name de ongebruikelijk hoge effectiviteit van vibrationele pre-excitatie op de reactiviteit van $CHD_3$ is interessant: De vibrationele CH-strek toestand aanslaan met twee quanta heeft relatief gezien een grotere werkzaamheid dan met één quantum. Wanneer de vibrationele CH-strek toestand met maar één quantum wordt aangeslagen, is translationele energie effectiever dan vibrationele energie in het verhogen van de reactiviteit, terwijl het aanslaan met twee quanta juist effectiever is dan het verhogen van de translationele energie. Dit wordt veroorzaakt door een zeer

sterk "bobslee-effect" vanwege de zeer late en hoge OT waardoor dissociatie over een relatief hogere barrière dan aanwezig in het PEO verloopt. Door het molecuul vibrationeel sterk aan te slaan kan het bobslee-effect vermeden worden en kan dissociatie makkelijker plaatsvinden.

Hoewel gedemonstreerd is dat de SRP32-vdW-DF1 DF chemisch nauwkeurig is voor $CHD_3$ + Ni(111) en Pt(111) (beide een groep-10-metaal), is de overdraagbaarheid naar Pd(111) (ook een groep-10-metaal) tot dusver niet getest. Daarom worden in **Hoofdstuk 9** voorspellingen gedaan voor de reactie van $CHD_3$ op Pd(111) met behulp van AIMD simulaties. Een ruwe vergelijking met experimentele resultaten voor $CH_4$ + Pd(111) laat zien dat de gebruikte SRP-DF mogelijk ook overdraagbaar is naar Pd(111), al zijn er nieuwe experimenten nodig om een betere vergelijking te kunnen doen. Verder wordt er gekeken naar trends in de reactiedynamica van methaan op (111)-oppervlakken bestaande uit groep-10-metalen. In het algemeen valt Pd(111) ergens tussen Pt(111) en Ni(111) qua reactiviteit, waarbij Pt en Ni het meest en minst reactief zijn, respectievelijk. De relatieve verhouding qua reactiviteit is afhankelijk van verschillende dynamische effecten zoals de plaatsafhankelijke reactiekans, bobslee-effect en energieoverdracht van het molecuul naar het metalen oppervlak. Wanneer de translationele energie laag is en de vibrationeletoestandverdeling correspondeert met een Boltzmann-verdeling, dan hebben dynamische effecten minder invloed op de reactie en is de reactiviteit van Pd(111) meer vergelijkbaar met die van Pt(111). Als de translationele energie juist hoog is en de vibrationele CH-strek toestand is aangeslagen, dan zijn dynamische effecten belangrijker en is de Pd(111) reactiviteit juist meer vergelijkbaar met die van Ni(111).

Tenslotte probeert **Hoofdstuk 10** potentiële reactiepaden op te helderen voor de dissociatie van methanol op Cu(111) en het daaropvolgende ontstaan van formaldehyde. Specifiek wordt de rol van dynamische effecten in de vertakkingsverhouding tussen de initiële dissociatie van CH en OH bekeken. Cu(111) blijkt zeer selectief te zijn in het breken van de OH binding in plaats van de CH binding, niet alleen vanwege het verschil in barrièrehoogtes maar ook kenmerken van de MEP's. Tevens wordt de opeenvolgende reactiestap, namelijk het ontstaan van formaldehyde, onderzocht. Drie verschillende mechanismes zijn gevonden voor deze reactiestap: Twee mechanismes hebben betrekking op een heet waterstofatoom dat of een ander waterstofatoom abstraheert en moleculair waterstof vormt, of een ander waterstofatoom los slaat waarbij er twee losse waterstofatomen op het oppervlak ontstaan. In het derde mechanisme worden de OH en CH bindingen (nagenoeg) tegelijk gebroken zonder dat er een heet waterstofatoom aan te pas komt. Verder is bij hogere translationele energieën juist het eerst verbreken van de CH

binding het dominante pad, en niet het eerst verbreken van de OH binding zoals doorgaans aangenomen wordt. Wederom is er gebruik gemaakt van de SRP32-vdW-DF1 DF. Hopelijk kunnen toekomstige experimenten bevestigen of deze SRP-DF niet alleen toepasbaar is op methaan en bepaalde metalen oppervlakken, maar ook chemisch verwante moleculen zoals methanol.

De resultaten van dit proefschrift leiden ook tot nieuwe vragen en mogelijke onderzoeksrichtingen. Ten eerste laten de resultaten voor HCl + Au(111) (Hoofdstuk 3 and 4), $O_2$ + Al(111) (Hoofdstuk 5), en $NH_3$ + Ru(0001) (Hoofdstuk 6) zien dat de UC-DF een grote uitdaging is voor het chemisch nauwkeurig simuleren van molecuul-metalen oppervlak reacties met DFT. In het bijzonder lijken de delokalisatiefout en de ZIF een grote rol te spelen in het falen van DFT in het kwantitatief, of zelfs kwalitatief, reproduceren van experimenten aan systemen waarbij $(W - E_{\mathrm{ea}}) < 7\,\mathrm{eV}$. Gelukkig lijken MGGB en afgeschermde hybride DF's zowel een pragmatische als fundamentele stap voorwaarts te zijn in het verkrijgen van een correcte beschrijving van zulke reacties. Toekomstig onderzoek zou zich kunnen richten op DF's die trachten de ZIF te verminderen om te proberen experimenten waar ladingoverdacht belangrijk is, zoals de eerder genoemde systemen of $O_2$ + Cu oppervlakken, (semi-)kwantitatief te reproduceren. Ook moet niet-lokale correlatie toegevoegd worden aan deze DF's omdat dit vaak een belangrijke rol speelt, terwijl dit tot op het heden nog niet gedaan is voor de behandeling van molecuul-metalen oppervlak barrières met MGGB en afschermde hybride DF's. Hoewel berekeningen met afgeschermde hybride DF's relatief gezien heel duur zijn, suggereren verkennende berekeningen in Hoofdstuk 5 dat een veel goedkopere niet-zelfconsistente aanpak ook nauwkeurige resultaten kan opleveren. Toekomstig onderzoek zou moeten uitwijzen op zo'n aanpak kan werken en hoe algemeen inzetbaar het is. Een andere potentiële onderzoeksrichting is die van het opschalen van PEO's verkregen op een bepaald niveau van theorie naar een hoger niveau door middel van HD-NNP's. Op deze manier zouden nauwkeurigere PEO's ontwikkeld kunnen worden zonder dat de computationele kosten al te erg stijgen.

Ten tweede zijn er meer, en soms betrouwbaardere, experimenten nodig. Zo is de experimentele foutmarge van HCl + Au(111) zelfs na heranalyse aanzienlijk, wat het lastiger maakt om toekomstige UC-DF's op waarde te schatten met behulp van deze toetssteen. Verder lijkt de RPBE-vdW-DF1 DF te reactief te zijn voor $NH_3$ + Ru(0001) vanwege de eerdergenoemde problemen met de ZIF. Maar er zijn ook vraagtekens bij de nauwkeurigheid van de kalibratie van het $NH_3$ + Ru(0001) experiment, en dus is er onduidelijkheid over de bijbehorende foutmarge wat het toetsen van UC-DF's voor dit systeem bemoeilijkt. Eveneens zijn er meerdere voorspellingen in dit proefschrift

gedaan welke bevestiging nodig hebben vanuit experimenten. Bijvoorbeeld voor de reactie van methanol op Cu(111), en van methaan op Pd(111) en verschillende Cu oppervlakken zijn geen directe vergelijkingen. Tevens zouden experimenten waarbij de oriëntatie van het molecuul uitgelijnd wordt verscheidene voorspellingen over reactiemechanismes kunnen toetsen. Zo wordt in dit proefschrift voorspeld dat het breken van de CH of OH binding een sterisch gehinderde reactie is. Anderzijds zou uitlijning van de oriëntatie van ammoniak en isotopologen daarvan voorspellingen omtrent het bijzondere reactiemechanisme kunnen toetsen. Ook laat Hoofdstuk 9 zien dat een systematische experimentele vergelijking van de reactie van methaan op verschillende metalen oppervlakken ontbreekt. Hoewel er ondertussen aardig wat experimenten gedaan zijn aan de dissociatieve chemisorptie van methaan op metalen oppervlakken, verschillen de experimentele condities vaak te veel om kwantitatieve vergelijkingen te maken, waarbij de condities ook nog eens niet noodzakelijkerwijs nauwgezet gedocumenteerd zijn.

# Curriculum Vitae

Nick Gerrits is geboren op 8 juli 1992 te Dordrecht. In 2010 heeft hij zijn gymnasiumdiploma *cum laude* behaald aan het Johan de Witt-gymnasium in Dordrecht. In hetzelfde jaar is hij begonnen aan de bacheloropleiding "Molecular Science and Technology" aan de Universiteit Leiden en de Technische Universiteit Delft. Na het behalen van zijn bachelordiploma in 2015 is hij begonnen aan de masteropleiding "Chemistry", tevens aan de Universiteit Leiden. Als onderdeel van deze opleiding heeft hij onderzoek gedaan onder begeleiding van dr. Jörg Meyer in de Theoretische Chemie groep in Leiden, en heeft hij een Erasmus stage gedaan bij de Centro de Física de Materiales in San Sebastian, Spanje, onder begeleiding van dr. Iñaki Juaristi. Dit onderzoek was gericht op het berekenen van elektronischefrictiecoëfficiënten met behulp van verschillende benaderingen. Tijdens zijn bachelor- en masteropleiding is hij actief geweest bij de studievereniging "Chemisch Dispuut Leiden", met als hoogtepunten het zijn van de secretaris van het bestuur en de voorzitter van de lustrumcommissie. Na het behalen van zijn masterdiploma in 2017 is hij begonnen met zijn promotieonderzoek onder begeleiding van prof. dr. Geert-Jan Kroes, wederom in de Theoretische Chemie groep in Leiden. Dit heeft geleid tot het proefschrift dat voor u ligt. Vanaf augustus 2021 zal Nick postdoctoraal onderzoek doen in Antwerpen, België, in de PLASMANT groep van prof. dr. Bogaerts, financieel gesteund door een Rubicon beurs van de Nederlandse Organisatie voor Wetenschappelijk Onderzoek. Hier zal hij fundamentele aspecten van plasmakatalyse op metalen oppervlakken onderzoeken.

Nick Gerrits is born on July 8$^{th}$ 1992 in Dordrecht. In 2010 he obtained his gymnasium diploma *cum laude* at the Johan de Witt-gymnasium in Dordrecht. In the same year he started the bachelor study "Molecular Science and Technology" at the Leiden University and the Technical University of Delft. After obtaining his bachelor's degree in 2015, he started his master study "Chemistry", also at the Leiden University. As part of this study he performed research under the supervision of Dr. Jörg Meyer in the Theoretical Chemistry group in Leiden, and he performed an Erasmus research internship

at the Centro de Física de Materiales in San Sebastian, Spain, under the supervision of Dr. Iñaki Juaristi. This research was aimed at calculating electronic friction coefficients using several approximations. During his bachelor and master studies he has been active at the study association "Chemisch Dispuut Leiden", with highlights being the secretary of board and the president of the lustrum committee. After obtaining his master's degree in 2017, he started his PhD research under supervision of Prof. Dr. Geert-Jan Kroes, again in the Theoretical Chemistry group in Leiden. This has led to the thesis in front of you. From August 2021 onward, Nick will perform postdoctoral research in Antwerp, Belgium, in the PLASMANT group of Prof. Dr. Bogaerts, financially supported by a Rubicon grant from the Dutch Research Council. Here, he will investigate fundamental aspects of plasma catalysis on metal surfaces.

# List of Publications

- Gerrits, N.; Migliorini, D.; Kroes, G.-J. Dissociation of $CHD_3$ on Cu(111), Cu(211), and Single Atom Alloys of Cu(111). *J. Chem. Phys.* **2018**, *149*, 224701, DOI: 10.1063/1.5053990
- Gerrits, N.; Shakouri, K.; Behler, J.; Kroes, G.-J. Accurate Probabilities for Highly Activated Reaction of Polyatomic Molecules on Surfaces Using a High-Dimensional Neural Network Potential: $CHD_3$ + Cu(111). *J. Phys. Chem. Lett.* **2019**, *10*, 1763–1768, DOI: 10.1021/acs.jpclett.9b00560
- Gerrits, N.; Kroes, G.-J. An AIMD Study of Dissociative Chemisorption of Methanol on Cu(111) with Implications for Formaldehyde Formation. *J. Chem. Phys.* **2019**, *150*, 024706, DOI: 10.1063/1.5070129
- Gerrits, N.; Kroes, G.-J. Curious Mechanism of the Dissociative Chemisorption of Ammonia on Ru(0001). *J. Phys. Chem. C* **2019**, *123*, 28291–28300, DOI: 10.1021/acs.jpcc.9b09121
- Gerrits, N.; Chadwick, H.; Kroes, G.-J. Dynamical Study of the Dissociative Chemisorption of $CHD_3$ on Pd(111). *J. Phys. Chem. C* **2019**, *123*, 24013–24023, DOI: 10.1021/acs.jpcc.9b05757
- Gerrits, N.; Geweke, J.; Smeets, E. W. F.; Voss, J.; Wodtke, A. M.; Kroes, G.-J. Closing the Gap Between Experiment and Theory: Reactive Scattering of HCl from Au(111). *J. Phys. Chem. C* **2020**, *124*, 15944–15960, DOI: 10.1021/acs.jpcc.0c03756
- Gerrits, N.; Juaristi, J. I.; Meyer, J. Electronic Friction Coefficients from the Atom-in-Jellium Model for $Z = 1 - 92$. *Phys. Rev. B* **2020**, *102*, 155130, DOI: 10.1103/PhysRevB.102.155130
- Gerrits, N.; Smeets, E. W. F.; Vuckovic, S.; Powell, A. D.; Doblhoff-Dier, K.; Kroes, G.-J. Density Functional Theory for Molecule–Metal Surface Reactions: When Does the Generalized Gradient Approximation Get It Right, and What to Do If It Does Not. *J. Phys. Chem. Lett.* **2020**, *11*, 10552–10560, DOI: 10.1021/acs.jpclett.0c02452

- Gerrits, N.; Geweke, J.; Auerbach, D. J.; Beck, R. D.; Kroes, G.-J. Highly Efficient Activation of HCl Dissociation on Au(111) via Rotational Pre-excitation. *J. Phys. Chem. Lett.* **2021**, *12*, 7252–7260, DOI: 10.1021/acs.jpclett.1c02093

# Afterword

Having completed my PhD thesis, I would like to thank many people that have been involved in some way or another. Since I am thankful to so many people, I am extremely sorry if I forgot to mention you. After these apocalyptic four years (e.g., Trump, Brexit, corona, Rutte's memory, and the ever increasing prices on beer), it is easy to forget.

First and foremost, I would like to thank my supervisor Geert-Jan Kroes. This thesis would not have been possible without your help and guidance. You always managed to push me to achieve more and to provide me with insights into the wonderous world of academia. Additionally, you afforded me an enormous amount of freedom in my research. Although this led to a thesis that might not resemble at all what we initially set out to do, I think we can be even happier with the end result.

I wish to thank Jörg Meyer for guiding me into the world of computational surface science during my master. You provided me with the tools to start my journey into research.

I am grateful to Mark Somers for teaching me how to approach computing and providing me with different views on university matters. While I do not share your very clear preference of La Chouffe and I think it is better in the future to avoid pitchers filled with Grimbergen Tripel, the beer-infused discussions at the Foobar were very enjoyable.

I am thankful to Thanja Lamberts for helping me to discover the next step in my career and being available for coffee or lunch during the very lonely corona office days. You always reminded me to be open minded. Also, it was funny to see such a positive person being so great at complaining about stuff.

Marc van Hemert, it was always very enjoyable to hear stories from times long past and your view on what a good scientist is supposed to be.

I thank Davide Migliorini, Helen Chadwick, and Francesco Nattino for teaching me how to do AIMD simulations on methane reactions, as this was the start of all the work forming this thesis. Without you the AIMD dance would not have existed.

I am happy that I could share some of the things I have learned during my PhD with my students Jeffrey Talboom and Sanne Starmans. I would also like

to give a honorable mention to my LO-students Felix Hall and Steven Jansen for a beautiful (meme) pie of me.

I am particularly grateful to Guido Smeets and Paul Spiering for being there during my master and PhD. You knew how to appreciate and contribute to the endless stream of jokes in the office, during breaks and, perhaps most importantly, while having drinks. With the discussions on work and matters concerning life in general combined with helping each other out with issues, I am certain our office was much better for it, despite perhaps not being the "quiet" office.

Of course, I would also like to thank the other VASPy McVASPface people, Robert van Bree and Bauke Smits. It is important to have a support group for people suffering of VASP and other related illnesses.

I am also grateful to the many other members of the Theoretical Chemistry group during my time in Leiden: Katharina Doblhoff-Dier, Süleyman Er, Celia Fonseca Guerra, Gernot Füchsel, Elham Nour Ghassemi, Michelle van der Haar, Seenivasan Hariharan, Tim Jansen, Andrew Powell, Marten Raaphorst, Soroush Rasti, Sayan Seal, Khosrow Shakouri, Fabian Sies, Derk Sjoerdsma, Hossein Tahmasbi, Theophile Tchakoua, Mark Wijzenbroek, and Peter Wright. Thank you for answering my "koffie" or "lunch" shouts, or occasionally the loud bell or megaphone for cake.

I appreciate the collaborations and discussions with Daniel Auerbach, Rainer Beck, Jörg Behler, Jan Geweke, Hannes Jónsson, Iñaki Juaristi, Ludo Juurlink, Arthur Utz, Johannes Voss, Stefan Vuckovic, and Alec Wodtke.

Although not as often as during my bachelor or master's studies, I have enjoyed many of the "extracurricular" activities with the Chemisch Dispuut Leiden and the Brouwmeesters.

I am happy to have so many friends that have supported me in some way these years. Whether we mowed the grass at a hardstyle festival, tasted (not so) excellent beer, dissected the weirdest movies, fired up the BBQ irrespective of the weather, or simply had a good time together, you helped me to stay energetic. Thanks to all of you.

Special thanks to my parents and grandparents, and Dionne's parents for their support.

Finally, I especially thank Dionne. We met when I started my PhD and you have been a constant in my life ever since.